Deep, Large Scale Surveys of Star Forming Regions throughout the Milky Way

Dissertation

zur

Erlangung des Doktorgrades (Dr. rer. nat.)

der

Mathematisch-Naturwissenschaftlichen Fakultät

der

Rheinischen Friedrich–Wilhelms–Universität Bonn

vorgelegt von

Carsten KÖNIG

aus

Düsseldorf, Deutschland

Bonn 2018

Angefertigt mit Genehmigung der Mathematisch-Naturwissenschaftlichen Fakultät der Rheinischen Friedrich–Wilhelms–Universität Bonn
Prepared with the permission from the Faculty of Mathematics and Natural Sciences of the University of Bonn

1. Gutachter / *First referee*: Prof. Dr. Karl M. Menten
2. Gutachter / *Second referee*: Prof. Dr. Pavel Kroupa

Tag der Promotion *Conferral Date*: 18.12.2018
Erscheinungsjahr *Year of Publication*: 2019

Diese Dissertation ist auf dem Hochschulschriftenserver der ULB Bonn unter http://hss.ulb.uni-bonn.de/diss_online elektronisch publiziert.
This dissertation has been published electronically at the Bonn University and State Library (ULB Bonn): http://hss.ulb.uni-bonn.de/diss_online.

Abstract

Star formation and the processes involved are not only important to the Milky Way as an astronomical object, but are also crucial to understand our own origin. For instance, only lower-mass stars like our own Sun have supposedly a long enough lifetime to allow for the development of life, whereas high-mass stars are the major source of the heavy elements beyond iron, that are needed to form life as we know it. Therefore, understanding the influence of the Galactic environment on low- to high-mass star formation is crucial to understand our own place in the Galaxy.

In order to obtain the most complete view on star formation throughout the Milky Way to date we use several different dust-continuum surveys (ATLASGAL, Hi-GAL, MSX and WISE) to obtain photometric data, and consecutively model the spectral energy distributions of the dense molecular clumps in which stars and star clusters form. From these we derive the physical properties such as dust temperatures, integrated fluxes and H_2 peak column densities. We derive distances from line-of-sight velocities obtained from CO observations for the majority of the sources, allowing us to calculate clump masses and bolometric luminosities and analyse the properties of the sources in the context of their large scale environment.

We started with a small subsample of the ATLASGAL survey, the ATLASGAL Top100, investigating the $\sim$ 100 brightest and most massive clumps in 4 distinct evolutionary stages in the inner Galaxy (König et al. 2017). The methods developed for this sample were then applied to the full ATLASGAL compact source catalogue, investigating a complete sample of $\sim$ 8000 sources located mostly in the inner part of the Milky Way (Urquhart et al. 2018). Finally, the analysis is extended to a sample of sources located in the southern outer Galaxy, unrevealing its structure and investigating star formation properties out to the edge of the Milky Way. With samples for the inner and outer Galaxy at hand, we investigate the star formation properties of the sources with respect to their evolutionary phase, their dependence on the distance to the Galactic centre and the influence of large-scale structures like the spiral arms or the second largest expanding supershell of the Galaxy.

We established an evolutionary sequence based on the dust spectral energy distributions. Using dust continuum emission we are able to assign an evolutionary phase to individual clumps, and statistically analyse the physical properties, finding the dust temperature, bolometric luminosity and luminosity-to-mass ratio to increase over time. Using this classification scheme for the ATLASGAL sample we were furthermore able to calculate statistical lifetimes, finding that the quiescent stage is indeed very short ($< 1 \times 10^4$ years) for the most massive ($>$10,000 $M_\odot$) clumps.

We find the clumps' physical properties to vary significantly with Galactocentric distance. The dust temperature increases towards the outer Galaxy, whereas the average clump masses, bolometric luminosities and peak column densities significantly drop by almost an order of magnitude within just a few kiloparsec around the solar circle. As also the gas-to-dust ratio increases and the metallicity decreases in the outer

Galaxy, we attribute the increased temperatures to a combination of less effective cooling and lower shielding against the interstellar radiation field due to the lower column densities.

In contrast, we find the star formation activity as indicated by the luminosity-to-mass ratio to stay constant on kiloparsec scales throughout the Milky Way. Furthermore, we find the clump masses to be independent of the evolutionary stage indicated by the dust temperature, showing that once a clump begins to collapse, the evolution is largely independent of its large-scale environment. This is further supported by the fact that we find no influence of the spiral arms on the physical parameters and star formation activity of the dust clumps; they only seem to be responsible for organizing the interstellar material into clumps.

List of publications related to the PhD thesis "Deep, large scale surveys of star forming regions throughout the Milky Way", Carsten König

1. **ATLASGAL-selected massive clumps in the inner Galaxy. III. Dust continuum characterization of an evolutionary sample**
   König, C.; Urquhart, J. S.; Csengeri, T.; Leurini, S.; Wyrowski, F.; Giannetti, A.; Wienen, M.; Pillai, T.; Kauffmann, J.; Menten, K. M.; Schuller, F.; 2017, A&A, 599, A139
   DOI: 10.1051/0004-6361/201526841

2. **ATLASGAL - properties of a complete sample of Galactic clumps**
   Urquhart, J. S.; König, C.; Giannetti, A.; Leurini, S.; Moore, T. J. T.; Eden, D. J.; Pillai, T.; Thompson, M. A.; Braiding, C.; Burton, M. G.; Csengeri, T.; Dempsey, J. T.; Figura, C.; Froebrich, D.; Menten, K. M.; Schuller, F.; Smith, M. D.; Wyrowski, F.; (018) MNRAS, 473, 1059
   DOI: 10.1093/mnras/stx2258

3. **A New Search for Star Forming Regions in the Outer Galaxy**
   König, C.; Urquhart, J.S.; Wyrowski, F.; Giannetti, A.; Colombo, D.; Menten, K. M.; et al., in prep.

A complete list of all publications with contributions from C. König can be found on page 249.

Acknowledgements

It was a long way, and I am grateful for everyone who accompanied me on this journey. And as this work would not have been possible without many people supporting me, I take the opportunity to thank them here.

I would like to thank Prof. Dr. Karl Menten who gave me the opportunity to write my PhD thesis at the department for millimetre and sub-millimetre astronomy at the Max Planck Institute for Radioastronomy. Without his continued trust and support, this thesis would not have been possible.

Prof. Dr. Pavel Kroupa, who kindly agreed on becoming the second referee of my thesis. Furthermore Prof. Dr. Klaus Desch and Prof. Dr. Hubert Schorle, who agreed on joining the committee.

My supervisor Dr. Friedrich Wyrowski, for his ideas, support and the freedom he gave me to explore the Galaxy. It's been a great experience!

Special thanks goes to Dr. James Urquhart, for all his advice, constructive discussions, support, hospitality and friendship. Words can't tell how grateful I am!

My family, and especially my parents. Without their love and continued support over all those years, I would never have accomplished this.

All those colleagues who were there to answer questions, discuss ideas, or so kindly invited me to collaborate. Thanks so much!

All my friends and fellow PhD students without whom the time at the Institute would not have been the same. I will always look back as you made the time most enjoyable!

Contents

Part I

Introduction & Methodology

CHAPTER 1

Introduction

1.1 Introduction

Star formation and the processes involved are not only important to the Milky Way as an astronomical object, but are also crucial to understand our own origin. For instance, only lower-mass stars like our own Sun have supposedly a long enough lifetime to allow for the development of life, whereas high-mass stars are the major source of the heavy elements like iron, that are needed to form life as we know it. Therefore, understanding the influence of the Galactic environment on low- to high-mass star formation is crucial to understand our own place in the Galaxy.

Star formation in the Milky Way is a broad field: from low-mass to high-mass stars, from small-scale to large-scale; observing single forming stars, dust clumps giving birth to clusters of new stars, giant molecular clouds being the cradle of the dust clumps, all connected by filaments of different scales; up to the largest scale structures including the spiral arms and the Milky Way as a whole. But even at these large scales the research on star formation in our Galaxy does not stop, as also the environment of the Milky-Way has an impact on Galactic star formation, as it interacts e.g. with it's satellites, the Magellanic stream or high velocity clouds moving through the halo. Furthermore, observations of nearby galaxies give us an insight into star formation on large scales, as we can observe these galaxies from the outside, without the obstruction and confusion in our own Galactic disc caused by intervening material.

Understanding star formation in the Milky Way comes with several problems. As we are located within the disk, our view is obstructed by the sheer amount of interstellar matter along any line of sight in the Galactic plane. Furthermore, as we do not have a face-on view of the disk, it is difficult to obtain a detailed view on the large scale structures due to the difficulties involved obtaining reliable distances to objects located within the disk.

A lot of progress was made overcoming the aforementioned problems after new infrared and submm observatories became available during the last two decades, and several large programs are aimed at answering the biggest questions about star formation in general and in particular on the structure and the formation of stars in our own Galaxy. Nevertheless, there are still many open questions, if not even more than before, as the better view on our own Galaxy and the much better view on nearby galaxies opened up new possibilities and details, that were inaccessible at lower resolutions, lower sensitivities or with limited sample sizes. With the availability of surveys like the APEX Telescope Large Area Survey of the Galaxy (ATLASGAL; Schuller et al. 2009) or the Herschel infrared Galactic Plane Survey (Hi-GAL; Molinari et al. 2008) providing physical parameters for tens of thousands of sources, statistical analysis of star formation in our host Galaxy is taken to the next level.

With ATLASGAL covering the whole inner Galaxy and being complete for almost all

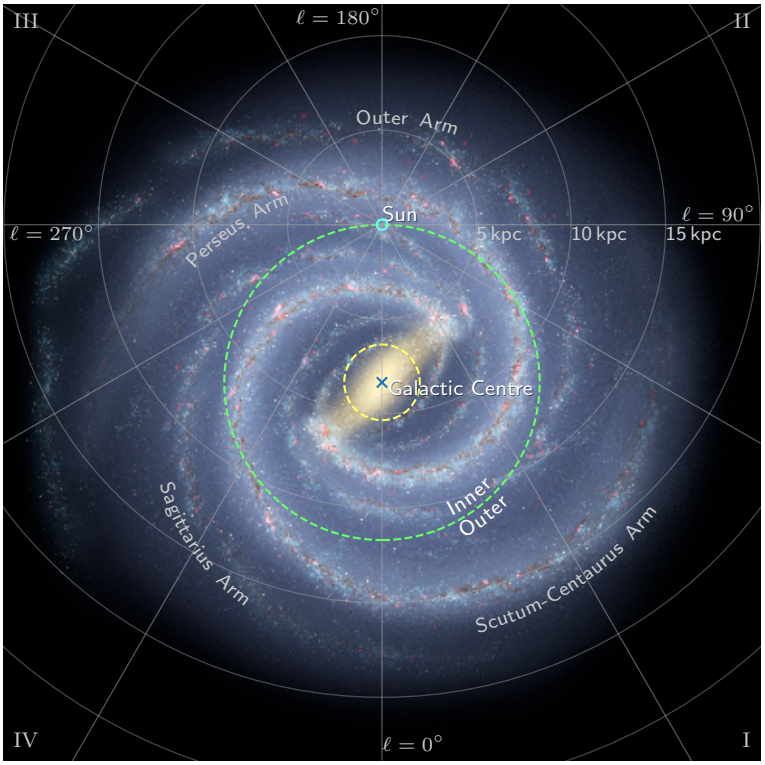

Figure 1.1: Detailed artists impression of the Milky Way visualizing the most important structures. The dashed yellow and green circles mark the Galactic centre region out to 2 kpc and the Solar circle at 8.34 kpc Galactocentric distance. Roman numbers numerate the Galactic quadrants. Image Credit: NASA/JPL-Caltech/ESO/R. Hurt

massive clumps, a great starting point for understanding star formation and the global structure of the Galaxy is available. The aims of this PhD were twofold: on the one hand a primary goal was to substantially contribute to the ATLASGAL project to determine physical properties for a sample in the order of 10,000 sources for the first time, allowing a detailed view on star formation properties in the dense and complex inner part of the Milky Way. On the other hand the goal was to take the research a step further and include an analysis of the outer Galaxy such as to cover the whole Galactocentric distance range and give new insight on star formation throughout the Milky Way in unprecedented detail.

1.2 The Milky Way

In this section we will give a brief overview of the structure and different environments of the Milky Way, our host galaxy, as can be seen in Fig. 1.1. The Milky Way is considered to be a spiral galaxy, with a radius of approximately 20 kpc as seen in CO (Kobayashi et al. 2008) and out to 60 kpc as seem in HI (Diplas & Savage 1991). A super-massive black-hole is located in its centre (Sagittarius A*), around which the Galaxy revolves (e.g. Melia & Falcke 2001). The inner parsec of the Milky Way is referred to as the Galactic centre region. This

part of the Milky Way is highly dynamic and drastically different from the rest of the Galaxy due to the proximity to the central black hole. The most central part is then followed by the central molecular zone, extending out to a few hundred parsec. This region has a density that is several orders of magnitude higher than the average of the disk, is much more turbulent and the molecular gas is on average significantly hotter than the gas found within the disk (Mills 2017). Farther outwards, the region out to the co-rotation radius is then referred to as the inner Galaxy. The co-rotation radius is the distance from the Galactic centre, where the rotation speed of the stars and the rotation speed of the spiral arms are the same (Gerhard 2011). It happens that the co-rotation radius is just outside the orbit of the Sun, also known as the solar circle, which is located at a distance of $R_{\rm gal} = 8.34\,\rm kpc$ (Reid et al. 2014) from the Galactic centre, and hence both terms are often used synonymously. Everything outside the solar circle is referred to as the outer Galaxy, where the stars have a lower orbital velocity than the spiral pattern.

The details of the large-scale structure of the Milky Way are still poorly constrained. Although we know it has four spiral arms (Sagitarius, Scutum-Centaurus, Outer (sometimes Norma), Perseus; see Fig 1.1), the nature and exact locus of these arms is still under debate (Dobbs & Baba 2014). In turn it is not clear whether our host Galaxy is a '*grand-design*' spiral with two density wave arms and the other two being transient features or has to be denominated as a '*flocculent*' Galaxy with four spiral arms.

In the inner Galaxy (including the Galactic centre), 70% of the mass of the whole Galaxy is located, whereas only 30% of the mass are found outside the co-rotation radius (Heyer & Dame 2015). Due to the higher stellar and molecular density, the inner Galaxy in general has higher UV photon flux, higher metallicity, or a lower gas-to-dust ratio.

Although the inner Galaxy contains most of the mass of the Milky Way and thus is of the highest interest for studying star formation, the outer Galaxy comes with an observational advantage. Due to the lower density, line-of-sight confusion is less of an issue and radial velocity distance measurements (see Sect. 2.4.1) do not suffer from the distance ambiguity that is inherent to the inner Galaxy. For these reasons, analysis of the spiral structure and the influence of the spiral arms on star formation is more straight forward in the outer Galaxy.

1.3 Star Formation

As already mentioned above, star formation and the processes involved play an important role for the structure and evolution of our host Galaxy (Kennicutt 2005). This is even more true, when we take a look at the life-cycle of stars and matter in general: clumps within molecular clouds collapse, new stars eventually form, the stars burn their nuclear fuel, and at the end of their lifetime the stars re-inject parts of the processed matter into the interstellar medium. This is depicted in Fig 1.2, sketching the vastly different paths that stars take depending on whether they are high- or low-mass. It becomes clear, that the star formation process taking place in the molecular clouds is an important crossroads for the the fate of a star, essentially deciding whether it will have a long lifetime or a big impact through a supernova explosion, injecting energy and heavy elements into the Galactic environment.

In the next sections we will therefore briefly discuss the differences of high-mass and lower

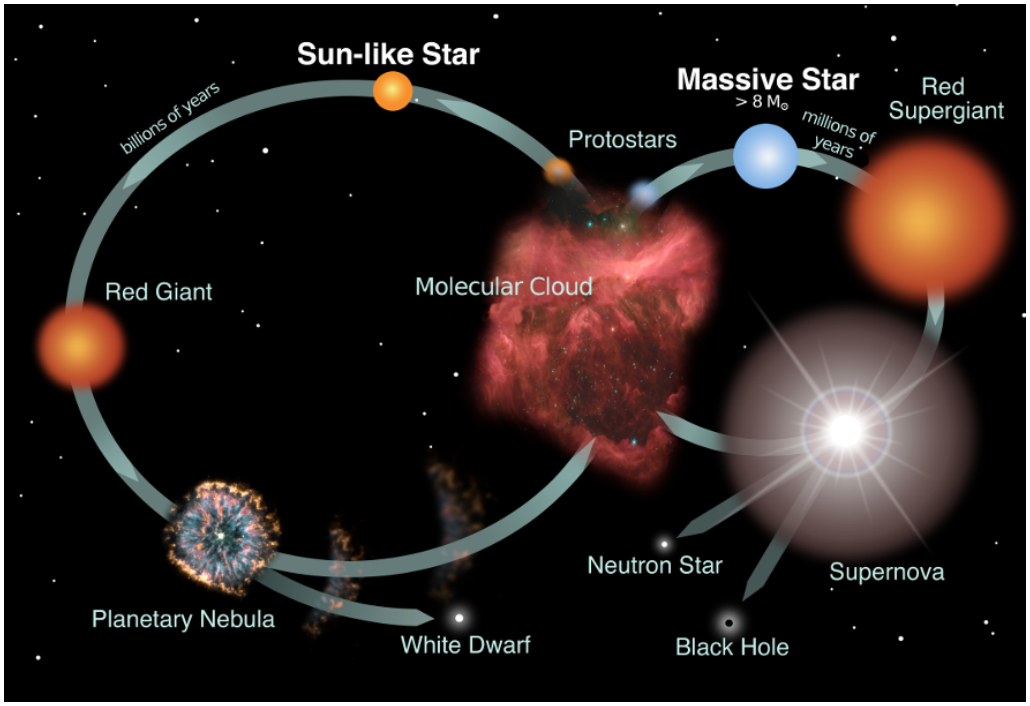

Figure 1.2: The life-cycle of stars: molecular clouds collapse, stars form and evolve, before they finally reach the end of their lifetime, re-injecting molecular material into the interstellar medium to form a new generation of stars. Image Credit: NASA and the Night Sky Network.

mass stars and give an overview of the star formation process.

1.3.1 Low-mass stars

Stars are considered to be 'low-mass' up to about $8\,M_{\odot}$ in our present work. These stars are different from the high-mass stars, as e.g. the UV radiation they produce is comparably low. Furthermore, their formation time-scale as well as their lifetime is rather long when compared to high-mass stars, allowing them to live for several billion years, like our Sun, that is expected to last about 10 billion years. At the end of their lifetime these stars die comparably quietly and eventually end up as white dwarfs ejecting their outer shells back into the interstellar medium, forming planetary nebulae. According to the initial mass function (IMF) (Salpeter 1955, Kroupa 2001) there are supposedly $\sim$ 1000 solar mass stars for every late O-type star ($\sim 20\,M_{\odot}$) - and even more lower mass stars. Although these stars do not have the same impact on the Galactic environment as their high-mass counterparts (see next section), these stars dominate the population of stars throughout the Galaxy.

In general stars form when a cloud becomes unstable and collapses. This is the case, when the mass of a clump exceeds the Jeans mass, causing the clump to collapse. In the most simple case, this is the case when either the temperature is too low, so the thermal pressure is insufficient to support the cloud against gravitational collapse, or the density becomes too high. Once the collapse has started, the angular momentum contained in the gas and dust

in combination with the gravitation will cause the cloud to flatten out into an accretion disk. The material is then channelled through the disk onto the protostar. Angular momentum is removed from the system through outflows, allowing the pre-stellar core to further contract and eventually form a star.

1.3.2 High-mass stars

High-mass stars have a profound impact on their environment and their host Galaxy, in stark contrast to their lower mass counterparts. High UV radiation, strong stellar winds, supernova explosions and the creation of the heavy elements are the four most important effects to mention here (Kennicutt 2005). But their impact comes at a price: due to their higher masses, the high-mass stars form and evolve much more rapidly than the low-mass stars, resulting in significantly shorter lifetimes of millions of years.

This in turn leads to an observational problem, as on the one hand only a fraction of the interstellar medium from which stars are formed form high-mass stars, and on the other hand high-mass stars have a comparably short lifetime. As a result there are much less high-mass stars than low-mass stars to observe, as already mentioned in the previous section. Furthermore, high-mass stars only form in the densest regions of molecular clouds, effectively hiding them from optical observations in the most dusty parts.

Fortunately, radio astronomy comes to the rescue, as the dust is mostly optically thin and the clumps in which massive stars are formed can be observed by powerful mid-infrared to sub-millimetre telescopes.

But despite their importance to the Galaxy, the details of the formation process of high-mass stars are not well understood. Although in general the formation of high-mass stars is believed to be an up-scaled version of low-mass star formation, the Kelvin-Helmholtz timescale to form massive stars through spherical accretion are much shorter than the accretion rates. To make up for this discrepancy two models have been suggested to play an important role in high-mass star formation. In the monolithic collapse model (McKee & Tan 2003), the accretion rates are increased through turbulence, and hence often also referred to as the turbulent core model. For this model strongly peaked cores ($n \propto r^{-1.5}$) are required, that already contain the complete mass for the final stellar mass. The other model is the competitive accretion model (Bonnell et al. 2001), where high-mass stars form depending on their location in the forming cluster and their potential to accrete mass from the whole cloud. In this scenario pre-stellar cores start at similar masses, moving through and competing for the mass of the clump to accrete. Additional effects like magnetic fields, feedback from existing stars or the initial conditions of a pre-stellar clump are likely to also play an important role in the formation of massive stars (e.g. Tan et al. 2014, Motte et al. 2017).

1.3.3 Stages of star formation

Star formation takes place in the densest parts of the interstellar medium. In these dense and dusty regions, molecules form, allowing these molecular clouds to eventually cool down and reduce the thermal pressure that is counteracting gravity. These molecular clouds can be best observed through their molecular line emission as well as through the thermal emission from

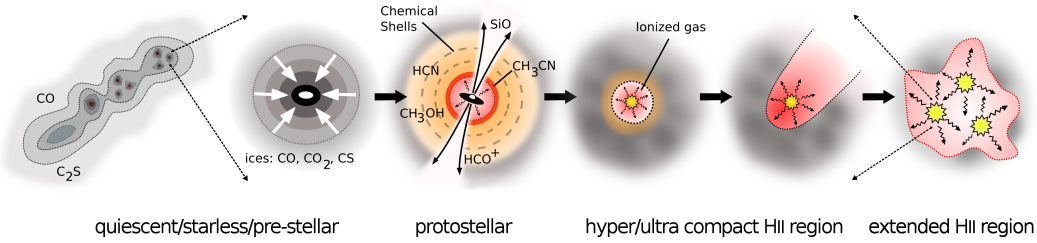

Figure 1.3: Stages of star formation for a high-mass star. Image Credit: Curmac Purcell.

the dust, allowing us to study them in great detail.

In Fig.1.3 the stages of high-mass star formation are depicted as we will describe them in the next sections.

Quiescent/Starless Phase Molecular clouds are rather cold ($T_{\rm dust} \sim 10\,{\rm K}$) and diffuse large structures of the interstellar medium. Within these clouds, local over-densities eventually start collapsing into clumps. While their average temperatures are still considerably low in this early phase ($T_{\rm dust} \lesssim 15\,{\rm K}$), these clumps are only visible in the far-infrared to sub-millimetre continuum regime and in a few molecular transitions of the most abundant molecules.

Pre-stellar Phase Continuuing the process of collapse, pre-stellar cores eventually form inside the clumps. These cores start to considerably heat their host clumps, increasing the average temperatures up to $T_{\rm dust} \lesssim 20\,{\rm K}$, and making them visible in the continuum at wavelengths down to $\sim 70\,\mu{\rm m}$.

Protostellar Phase/Compact HII Regions Further into their evolution, young stellar objects will form, significantly heating their environment ($T_{\rm dust} \lesssim 25-30\,{\rm K}$). Eventually stars will form from the pre-stellar cores, with the most massive ones being able to ionize their environment, and starting to build (ultra-)compact HII regions. With stars formed, the average temperature of the dust can rise above 40 K. These regions are bright at mid-infrared wavelengths, with their mid-infrared luminosity reflecting the evolution and brightness of the embedded stars.

Cleanup Phase/HII Regions As soon as stars have formed, the most massive ones of them will determine the fate of the clump. With their strong stellar winds and UV radiation, they will disrupt their environment, ionize hydrogen forming extended HII regions, and eventually dissolve their natal dust envelope.

1.4 Emission from molecular clouds

Molecular clouds consist of three major constituents: molecular hydrogen, carbon monoxide and dust. Although there are plenty of other elements and molecules found in these clouds that are responsible for the name and allow us to trace different parts of the clouds, these three

constituents (H_2, CO, dust), are responsible for the majority of the mass (H_2), the emission (CO and dust), and enable the grain-based chemistry that is not possible in the gas phase.

Unfortunately, although H_2 is the most abundant molecule, it is hard to observe due to a lacking dipole moment. CO or dust on the other hand are comparably easy to observe, and therefore can be used as a tracer-molecule for H_2 when the abundance ratios are known (Bolatto et al. 2013, Giannetti et al. 2017a).

As we use dust, carbon monoxide, and hydrogen in its three major states throughout the present work, we will briefly introduce them in the following sections. We will put a focus on dust, as determining the physical properties of molecular clouds from dust continuum emission is the main technique.

1.4.1 Dust

Interstellar dust can be modelled as a conglomerate of silicate grains, graphite grains and polycyclic aromatic hydrocarbons (Draine 2003). Interstellar dust grains are small compared to what we refer to as dust on Earth, with grain sizes smaller than a few micron. Coming with or without ice mantles, these grains are the seed on which most molecules form, especially H_2 which can not form in the gas phase. Therefore dust plays an important role in the evolution of molecular clouds and in the formation of stars.

Interstellar dust grains absorb and re-emit the radiation of their environment. The absorbed radiation heats the dust grains, which then emit thermal radiation similar to that of a blackbody. The difference to a blackbody originates from the dust properties (composition and density) and whether or not the dust grains are covered by an ice-mantle (e.g. Draine 2003, Ossenkopf & Henning 1994).

The emission of interstellar dust is therefore best described by a modified black-body, also known as a grey-body (e.g. Dent et al. 1998):

$$F_\lambda(T_{\rm dust}, \tau_{\rm ref}, \beta) = \Omega_{\rm dust} \cdot B_\lambda(T_{\rm dust}) \cdot (1 - e^{-\tau_\lambda}) \tag{1.1}$$

where $\Omega_{\rm dust}$ is the solid angle suspended by the dust clump and $B_\lambda(T_{\rm dust})$ is the emission of the black-body at the average dust temperature $T_{\rm dust}$. The right hand term describes the modification of the black-body, with τ_λ being the optical depth at wavelength λ:

$$\tau_\lambda = \tau_{\rm ref} \cdot \left(\frac{\lambda}{\lambda_{\rm ref}} \right)^{\beta} \tag{1.2}$$

where $\tau_{\rm ref}$ is the optical depth at the reference wavelength $\lambda_{\rm ref}$ and β being the dust spectral index, reflecting the dust properties.

1.4.2 Hydrogen

Hydrogen is the most abundant element in the universe, with a fraction of ∼75% of all (baryonic) matter. In its pure form it comes in three different states.

Atomic Atomic Hydrogen is known as HI, indicating that it is neutral (thus the I). HI can be detected by its emission at ∼21 cm, originating from the spin of the electron occasionally flipping from parallel to the spin of the proton to anti-parallel (i.e. hyperfine transition in the 1s ground state). Although this spin-flip occurs rather seldom for a single hydrogen atom (transition rate of $2.9 \times 10^{-15}\,\mathrm{s}^{-1}$), the emission can be easily detected, as hydrogen is just so abundant.

Ionized Being ionized once, the notation adds another I indicating the ionization level, thus noting ionized hydrogen as HII. As hydrogen consists of a single proton plus a single electron, clouds of ionized hydrogen are a plasma of protons and electrons. To ionize a hydrogen atom from its ground-state, photons with an energy of at least 13.6 eV are needed, corresponding to wavelengths of 91.2 nm or less. As strong UV radiation is emitted by high-mass stars, interstellar HII emission is a great indicator of the presence of these most massive objects. Once an HII region has formed, it can be detected through its thermal bremsstrahlung caused by the electrons moving in the electromagnetic field of the plasma.

Molecular Molecular hydrogen H_2 is the most abundant molecule in the Universe. But as H_2 is a symmetric molecule lacking a dipole moment, only quadrupole transitions can be observed, making H_2 difficult to observe directly. Fortunately, H_2 can be traced by the presence of CO, when the CO-to-H_2 conversion factor X_{CO} is known. In addition, the gas mass, which is dominated by H_2, can be estimated from dust emission, when the gas-to-dust ratio is known. For our Milky Way this factor varies from the inner to the outer parts of our Galaxy, with conversion factors between 100 for the inner Galaxy and 450 at 15 kpc galactocentric radius (Giannetti et al. 2017a).

1.4.3 Carbon

Carbon is the fourth most abundant element in our Galaxy, with a fraction of ∼0.5%, after Hydrogen (∼75%), Helium (∼23%) and Oxygen (∼1%) (Ferrière 2001). Furthermore, carbon monoxide is the second most abundant molecule after H_2, Carbon therefore plays a crucial role in star formation throughout the Galaxy, also as it is found in all complex interstellar molecules found to date (van Dishoeck 2014). Accordingly, as H_2 is difficult to observe (see previous section), CO becomes the most important tracer of molecular gas.

CO In its most abundant form, carbon is bound to a single oxygen atom, forming carbon monoxide (CO). Carbon monoxide is the second most abundant molecule in the Galaxy after molecular Hydrogen H_2. The rotational (J-)transitions of CO are easy to observe with radio telescopes with the CO(J=1–0) and CO(J=2–1) emission lines being the most prominent ones at 2.6 μm (115.3 GHz) and 1.3 μm (230.5 GHz), respectively. CO is most important to estimate the amount of H_2, at least in the inner Galaxy, where the CO-to-H_2 ratio is well correlated. Although large scatter is observed especially on small scales, a conversion factor of $\mathrm{X_{CO}} = 2 \times 10^{20}\,\mathrm{cm}^{-2}\,(\mathrm{K\,km\,s}^{-1})^{-1}$ (Bolatto et al. 2013) with ∼ 30% uncertainty is widely adopted, allowing to derive the total gas mass from the observed CO emission. Unfortunately,

this might not be true for the outer Galaxy, as with decreasing metallicity the ratio between CO and H_2 supposedly drops, leaving the H_2 gas undetectable by observation of CO.

Atomic Atomic carbon, or CI, is found throughout star-forming regions, well mixed with CO (Stutzki & Guesten 1990), or in the lower metallicity environment of the outer Galaxy. CI is most abundant when the shielding is too low so UV radiation can penetrate the clouds such that the CO molecules get dissociated.

Ionized When atomic carbon is not shielded sufficiently, it can become easily ionized with an ionization energy of only 11.3 eV, corresponding to a wavelength of 109.7 nm. [CII] is therefore mostly found in low density environments where the shielding is low or where it is close to an ionizing source.

Others As carbon is so abundant, it plays a role in many other molecules, too. Mostly in combination with Hydrogen and often also with Oxygen, as these are even more abundant. HCN, HNC, HCO^+, H_2CO, CH, are just a few to mention that play important roles in star formation. All complex molecules (i.e. molecules with at least 8 atoms) detected so far in the interstellar medium contain at least one carbon atom, hence classifying them as '*organic*'. Furthermore, carbon plays an important role in building prebiotic molecules that are thought to be the building blocks of more complex organic molecules that are the foundation of life as we know it (Herbst & van Dishoeck 2009).

1.5 Surveys

The Milky Way has never been as accessible for detailed studying as it is now. In recent years several large Galactic surveys have been conducted, mapping the Galactic plane at high sensitivity and resolution over large areas. For the present work we combine the observations of several Galactic plane surveys, which we will introduce here.

1.5.1 ATLASGAL

The APEX Telescope Large Area Survey of the GALaxy (ATLASGAL; Schuller et al. 2009) is a dust continuum survey at 870 μm conducted with LABOCA (Siringo et al. 2009) at the Atacama Pathfinder EXperiment telescope (APEX; Güsten et al. 2006; upper-left in Fig.1.4). It originally covers the Galactic plane between $|\ell| \pm 60$ deg and was later extended to $\ell = -80$ deg (Schuller et al. 2010) at a resolution of 19.2 arcseconds and an rms noise level of 50–70 mJy/beam. With the compact source catalogue (Contreras et al. 2013, Urquhart et al. 2014a, Csengeri et al. 2014) identifying more than 10,000 dense clumps towards the inner Galaxy, ATLASGAL allows for the statistical analysis of star formation properties in an unprecedented way.

Figure 1.4: Telescopes utilized by the surveys used for the present work: APEX (top-left; credit: MPIfR, Bonn), Herschel (top-right; credit: ESA, AOES Medialab), MSX (bottom-left; credit: NASA/JPL, Caltech), WISE (bottom-right; credit: NASA/JPL, Caltech)

1.5.2 Hi-GAL

The Herschel infrared survey of the GALaxy (Hi-GAL; Molinari et al. 2010) is a continuum survey covering the whole Galactic plane in 5 far-infrared bands from 70 μm to 500 μm using the PACS (Poglitsch et al. 2010) and SPIRE (Griffin et al. 2010) instruments aboard the Herschel space telescope (upper-right in Fig.1.4). Depending on wavelength the bands have a resolution between 8.9 and 36.6 arcseconds at sensitivities between 11 and 47 mJy/beam. With dust emission peaking between 70 and 350 micron, this survey is well suited to probe the peak of dust spectral energy distributions, allowing for better temperature estimates than with previous surveys. As Hi-GAL covers the whole Galactic plane following the Galactic warp, it is well suited to also study the outer Galaxy.

1.5.3 MSX

The Midcourse Space eXperiment (MSX; Price et al. 1999; lower-left in Fig.1.4) survey of the Galactic plane (Price et al. 2001) covers the Galactic plane in 4 different bands in the mid-infrared wavelength regime from 8.3 μm to 21.3 μm, using the SPatial InfraRed Imaging Telescope II (SPIRIT III; Bartschi et al. 1996) instrument with a beamwidth of 18 arcseconds. Covering the whole Galactic plane to $|b| \leq \pm 5^{\circ}$, the MSX survey is well suited for studies comparing the inner and outer Galaxy. Although MSX does not reach the sensitivity of modern observatories like WISE, it does almost not suffer from saturation, making it ideal for the brightest regions of any survey.

1.5.4 WISE

The Wide-field Infrared Survey Explorer (WISE; Wright et al. 2010; lower-right in Fig.1.4) observed the whole sky in 4 mid-infrared wavelength bands from 3.4 μm to 22 μm. The AllWISE program combined this data from the WISE cryogenic with the NEOWISE (Mainzer et al. 2011) post-cryogenic survey, covering the whole sky at a resolution between 6.1 and 12 arcseconds. Although the sensitivity is higher than MSX, WISE suffers from saturation at the brightest regions. For these reasons, WISE is preferable for sources with low brightness, whereas MSX is preferable for sources that are saturated in WISE data.

1.5.5 CO Galactic Plane survey

To trace the molecular gas throughout the whole Galactic disc, Dame et al. (2001) combined several CO(1–0) surveys to create the most recent complete view of molecular gas in the Milky Way. With a resolution between $9'$ and $18'$ and an rms noise between 0.1 K and 0.4 K, this survey lacks the resolution and sensitivity of modern surveys, but is the only one that allows for a global view on molecular gas as traced by CO throughout the Galaxy.

1.5.6 HI Galactic All Sky Survey

The Parkes Galactic All Sky Survey (GASS; McClure-Griffiths et al. 2009) covered the whole southern sky south of declination $\delta < 1^\circ$ with a resolution of 16 arcminutes. With a velocity resolution of 0.82 km s^{-1} covering velocities between -400 km s^{-1} and 500 km s^{-1}, and a rms noise level of 57 mK, this survey allows to trace the largest structures out to the farthest edges of the Milky Way.

1.6 Motivation

In the previous sections it became clear that understanding the processes involved in star formation, and in particular those leading to high-mass star formation, are important to understand the dynamics of the Milky Way and the cycle of matter.

To investigate the process of high-mass star formation in more detail, establishing a way to determine the evolutionary phase is crucial. With such an evolutionary sequence established we can then answer questions on how the clumps hosting these massive stars evolve and how their physical properties are affected.

Furthermore, being able to compare the properties and distribution of thousands of dust clumps gives us the opportunity to statistically approach questions of star formation with respect to their Galactic environment. We can investigate how the star forming regions are distributed throughout the Milky Way and where the most massive star-forming regions are located. We can furthermore examine how their physical properties vary depending on their distance to the Galactic centre and how they are influenced by the spiral arms.

With a large number of Galactic plane surveys available for the whole Galaxy, the time is ripe to answer these questions.

1.7 Overview

In Chapter 2 we will explain in detail the three main methods we implemented and used for the present work. We will investigate in detail four evolutionary phases of a well selected sample of the ∼100 brightest, high-mass sources located in the inner Galaxy in Chapter 3, followed by Chapter 4, where we expand this analysis to the full set of sources of the ATLASGAL compact source catalogue. In the following two chapters we will extend the work to the outer Galaxy, applying the methods developed for the inner Galaxy. First we will derive distances in Chapter 5 and discuss the structures that were identified. In Chapter 6 we will then derive the physical properties of dust clumps located in the outer Galaxy and compare their properties to those located in the inner Galaxy, as well as investigate them with respect to their large-scale environment. Finally, in Chapter 7 we will summarize the present work and give an outlook on future research that is already under way.

CHAPTER 2

Methods

2.1 Introduction

In this chapter the three main methods developed and used throughout this work will be introduced in detail: obtaining photometric data from continuum emission maps, fitting a model to the recovered dust continuum spectral energy distributions, and determining line-of-sight velocities from molecular observations to obtain distances. With the model fitted to the continuum data and distances determined from the line of sight velocities, these three methods are the basis of the analysis, as e.g. physical parameters like clump mass and bolometric luminosity can only be determined with proper photometric data and a known distance.

2.2 Photometry

To obtain the dust spectral energy distributions (SEDs) we need to recover the emission in several bands: from the mid-infrared starting at 8 μm to the sub-millimetre wavelengths up to 870 μm. We use an aperture-annulus approach to recover the flux density in each band, essentially calculating the source flux as the difference between the flux measured in an aperture centred on the source peak position and an annulus around the source aperture estimating the background flux.

2.2.1 Normalizing archival data

All continuum data used for the present work is available through different archives. Unfortunately this data is not normalized to a single system. They come in different coordinate systems (equatorial or galactic), different projections (cartesian or gnomonic), and pixel sizes. Furthermore the units are vastly different (Jy/pixel, Jy/beam, Jy/sr, or Digital numbers) or sometimes include correction for the cosmic microwave background and sometimes they do not. In addition, the map making algorithms used to create the archival data also have an impact on the final maps, allowing e.g. to choose from three different data products for the Herschel PACS maps or two different products for the Herschel SPIRE maps, emphasising e.g. either compact or extended emission.

To normalize the continuum emission maps in all 12 possible bands (4 MSX, 2 WISE, 2 Herschel PACS, 3 Herschel SPIRE, 1 ATLASGAL), we had to implement a pipeline starting from the Internet archives and resulting in comparable maps over all wavelengths. This pipeline would start from the downloaded emission maps, and eventually create 3×3 degree tiles that have the same format as the ATLASGAL tiles (centre, extent and projection),

but come in Jy/pixel, as this unit is best suited to extract the photometric data for individual sources.

The first step always was individual for each archive and involved downloading the data and creating a local repository of the original data. This step was semi-automatized, as the Internet interfaces often changed e.g. for Herschel data, and also the available data products evolved during the time of this project. The data for all bands comes as Flexible Image Transport System (FITS) files with the FITS headers containing all necessary information (e.g. astrometry, resolution, projection, observing date, etc.). Taking into account several different standards, interpretations and modifications of the FITS standard, we extracted this information into a local, normalized database which was in turn used by the pipeline.

For bands where the data was not already retrieved as 3×3 degree tiles (i.e. ATLASGAL and MSX), we created them from the downloaded fields. First we selected all downloaded maps that are overlapping for the tile we aim for. This would mean for example that for creating a tile centred at $\ell = 10.5^\circ$ and $b = 0^\circ$, we would use all original fields that overlap into this tile by $\ell \pm 1.5^\circ$ and $b \pm 1.5^\circ$. As we aim to use 5×5 arcminute large cut-outs around each source to process the data, and as we need to make sure that sources located on the edges of the maps are well within the tiles, we added another 0.2 degrees in tile-width and -height as a margin. This process was applied to each of the 12 bands, gathering the maps for a total of 52 tiles between $-60^\circ \leq \ell \leq 60^\circ$ (inner Galaxy) and $225^\circ \leq \ell \leq 260^\circ$ (outer Galaxy), with each tile centred on longitudes that are separated by 3 degrees.

For each tile the downloaded maps were then combined and re-projected to Galactic coordinates using the MONTAGE software package[1]. This process involves multiple steps: re-projecting the images, determining the overlap between the individual maps, adding the images and modelling and correcting for differences in the background between each map. This is a fully automatized process that is performed by the MONTAGE software package and only needs minor configuration. As MONTAGE conserves the flux throughout the process, the co-added and re-projected tiles come out with the same unit as the input files.

At the end of the process all 3×3 degree tiles were converted to Jy/pixel, resulting in tiles with the same coordinate system, projection and physical unit. We chose to keep the original pixel size, as this allows us to still make use of the higher resolution e.g. in the PACS bands, and the varying pixel size has no negative impact on our results due to the aperture photometry approach we use.

To be able to visualize the maps for each source in a convenient way and to make data processing more efficient, we finally extracted 5×5 arcminute cut-outs in each bands. This gave us 129,144 normalized postage-stamps in 12 continuum bands for a total of 10,979 sources of ATLASGAL and the outer Galaxy on which the analysis was performed.

2.2.2 Aperture photometry

We developed a Python code to obtain the flux density in each band using an aperture-annulus approach, where first the flux in an aperture centred on the source position is determined and consecutively is corrected for the background flux obtained from an annulus around the source aperture.

[1] http://montage.ipac.caltech.edu

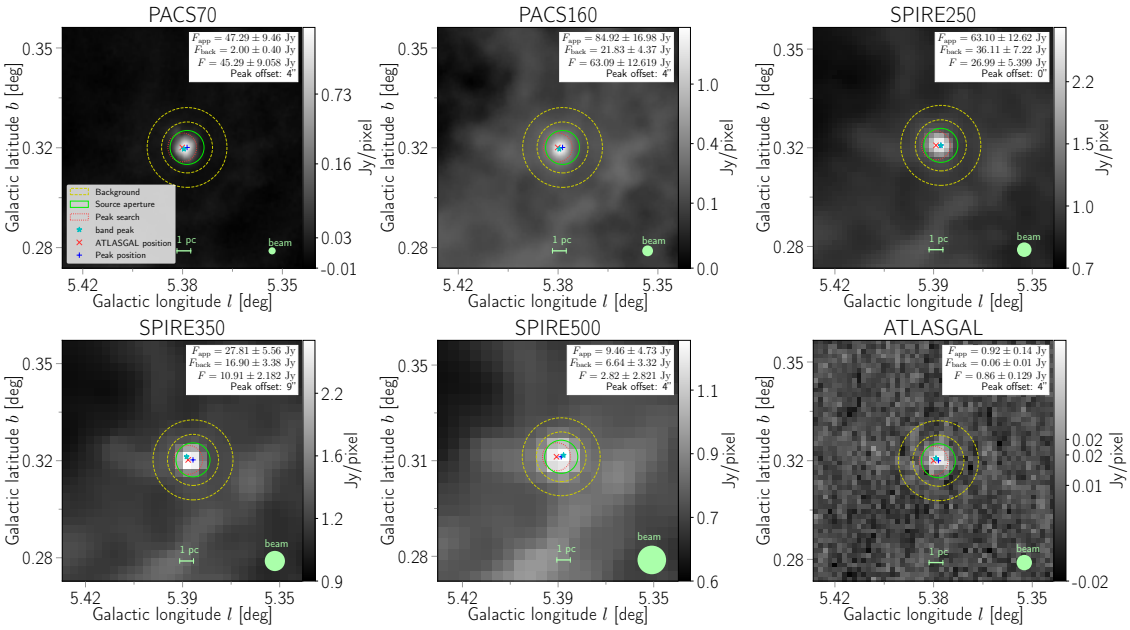

Figure 2.1: Aperture photometry in the mid-infrared to sub-millimetre wavelength regime for AGAL005.371+00.319.

To measure the flux within the aperture, we first re-centre the aperture to a position that is optimal for all bands. We determine this position by searching within a radius of one ATLASGAL beam size (i.e. $r_{\rm search} = 19.2''$) for the peak emission in either the 250, 350, or 870 μm band, using the first band without saturation. After re-centring the aperture to this position, we sum all pixels within the aperture to obtain the aperture-flux $F_{\rm app}(\lambda)$ at wavelength λ in all bands. We use an aperture-size twice as large as found by the source extraction software to make sure that most of the emission of the source is recovered, but still small enough so the aperture does not cut into nearby sources in most cases. Note that due to the aperture-annulus approach the emission considered to be originating from the source would be cut off at the background flux-level. If saturated pixels are found (indicated by NaNs in the maps), the value for these pixels are set to the maximum pixel value within the aperture. The flux for the affected band would then be considered only as a lower limit.

We determine the background flux $F_{\rm back}(\lambda)$ over an annulus around the source-aperture that has an inner radius 1.5 times and and outer radius 2.5 times larger than the aperture. To ensure that a statistical analysis of the background pixels is feasible, the background annulus width was increased to at least $18''$ (i.e. 3 times the ATLASGAL pixel size). Within the background-annulus all pixels above the source-aperture's maximum pixel flux were omitted, assuming that such pixels are likely representing a nearby source contaminating the background annulus. To further reduce the influence of faint sources being present within the background-aperture, we calculate the median pixel flux within the background-annulus rather than the mean. We then obtain the background-flux by normalizing the median background pixel flux to the source-aperture size. Finally, we obtain the background-corrected source flux $F(\lambda)$ by subtracting the normalized background-flux $F_{\rm back}(\lambda)$ from the aperture-flux $F_{\rm app}(\lambda)$.

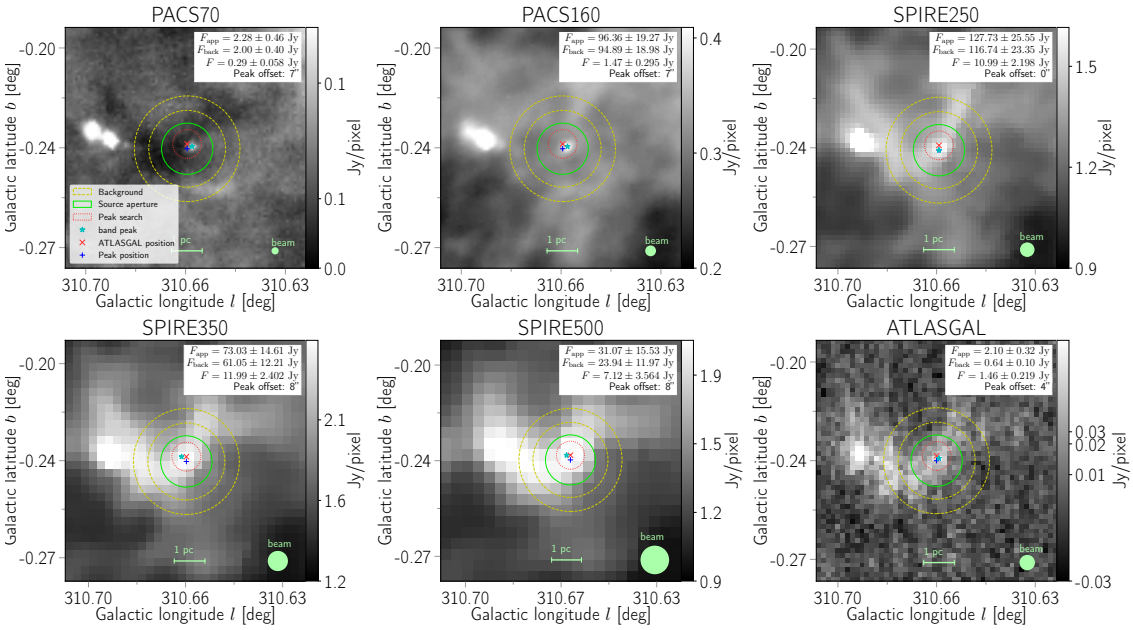

Figure 2.2: Aperture photometry in the mid-infrared to sub-millimetre wavelength regime for AGAL310.648−00.234. The flux in the PACS 70 μm band would have been missed without a dedicated search for a faint point source, which would have led to a wrong evolutionary classification.

This is demonstrated for a single clump (AGAL005.371+00.319) embedded in a much larger cloud in Fig 2.1. As can be seen, the background emission from the host cloud $F_{\rm back}(\lambda)$ dominates the total flux found within the aperture $F_{\rm app}(\lambda)$ for some bands (160–500μm). This example shows the importance of the background correction, as otherwise we would significantly overestimate the source flux density.

In case a negative background-corrected source flux is found ($F(\lambda) < 0$), either the background-flux might be overestimated as the background annulus cuts into some nearby source or the source-flux might suffer from absorption within the source-aperture. To counter the first case we applied the method described in the previous paragraph, omitting pixels above the peak-pixel flux found within the source-aperture and taking the median pixel value rather than the mean. The latter issue might be the case even when a point source is clearly visible, as can be seen in Fig. 2.2 for the 70 μm PACS band (top left). We have empirically determined that a point source can be identified if 80%, 50% and 20% of the pixel-flux in an arbitrary group of connected pixels have a flux above the 1σ, 2σ and 3σ level, respectively. When we were able to identify a point source using this method, we only take those pixels within the source-aperture into account that are above the median pixel-flux in of the background-annulus, thus yielding a positive background-corrected source flux. Applying this method for the ATLASGAL sample, we were able to recover 2,727 flux densities for 1,814 sources, that would otherwise have been missed although clearly having a visible point source, leading e.g. to wrong evolutionary classifications.

To estimate the flux uncertainties we add the pixel-noise-level determined over the whole

image and the general flux measurement uncertainty in quadrature. To determine the pixel-noise-level we use the full $5' \times 5'$ postage-stamps, first blanking out the pixels within a beam-size around local maxima. Consecutively a Gaussian is fit to the histogram of the remaining pixels of the filtered map, yielding the pixel-noise-level as the width (i.e. 1σ) of the Gaussian. For the general flux measurement uncertainty, we assume a rather conservative value, as the uncertainty is not only based on the absolute calibration error, which for most bands is found to be below 10%, but also on the choice and centring of the source-aperture and background-annulus, which might not be optimal for all bands. We estimate the flux measurement uncertainty to be in the order of 15% for ATLASGAL, 20% for the 70, 160, 250, and 350 μm Herschel bands, and a significantly higher uncertainty of 50% for the 500 μm band due to the larger pixel size. For the mid-infrared bands of MSX and WISE ranging from 12 to 22 μm we assign a general measurement uncertainty of 30%, but assign a 50% uncertainty to the 8 μm MSX band due to the possible contamination by emission from PAHs within the band. Take note that the uncertainty of the flux density is usually dominated by the general flux measurement uncertainty, as the pixel-noise-level only contributes a few percent to the total uncertainty.

To constrain the emission in the 70 μm band when no emission was found in this band, we use a conservative 5σ upper limit calculated from the noise determined over an aperture including the background annulus or the point source sensitivity limit as determined for the PACS instrument in this band (i.e. 21 mJy/beam)[2], whichever is higher.

2.3 Dust Spectral Energy Distributions

As a result from the aperture photometry, we are able to recover the emission of the dust clump from the mid-infrared to sub-millimetre wavelength regime. The emission of a clump might not only consist of the dust emission, as the clump undergoes further collapse and stars eventually start forming. The emission of these protostellar objects and young stars, which are deeply embedded in the clump, has to be also taken into account.

The cold dust emission can be described by a blackbody, modified for the dust properties (i.e. a greybody), as explained in Section 1.4.1. The emission from the deeply embedded objects is then added as a hot, optically thick component, described by a blackbody. Therefore the total emission of a dust clump is described by a two component model, consisting of a grey- and blackbody:

$$S_\lambda = \Omega_{\rm hot} \cdot B_\lambda(T_{\rm hot}) + \Omega_{\rm dust} \cdot B_\lambda(T_{\rm dust}) \cdot (1 - e^{-\tau_\lambda(\tau_{\rm ref})}) \tag{2.1}$$

where λ is the wavelength, B the Planck function at temperature T, Ω the solid angles and τ_λ the optical depth at the corresponding wavelength. Note that the optical depth at a given wavelength τ_λ is a function of the optical depth at the reference wavelength $\tau_{\rm ref}$ and the dust spectral index $\tau_\lambda = \tau(\lambda, \tau_{\rm ref}, \beta)$ (compare Eq. 1.2). Therefore the dust spectral index β could in general also be used as a fitting parameter, but as line-of-sight temperature variations as well

[2] herschel.esac.esa.int/Docs/PMODE/html/ch02s03.html

as noise effects influence β (Shetty et al. 2009a;b), we adapted a theoretical value of $\beta = 1.75$ as the mean value for the dust as calculated from Ossenkopf & Henning (1994).

As a result of the SED fitting we obtain two important quantities: the dust temperature $T_{\rm dust}$ as a fitting parameter from the two-component model and an estimate for the integrated mid-infrared to sub-millimetre flux as the integral of the fitted function. Although more sophisticated models are available, we showed for the ATLASGAL Top100 sample (see Chapter 3), that the rather simple two-component model we use is good enough to reproduce the luminosities obtained by more complex models. Furthermore, fitting more sophisticated models to a huge dataset like ATLASGAL is technically difficult.

2.3.1 Technical implementation

The SED fitting is implemented using a least squares minimization algorithm in a Python code. As the blackbody and the greybody of the two component model need to be fitted simultaneously to obtain reasonable fits, some constraints had to be implemented. First we apply some general limits to our fitting parameters. We limit the dust temperature to a maximum of 60 K, and the temperature of the hot component to values below 1000 K – values that are well above the highest values we find from the fitting, so we conclude that these limits do not influence our results, but help the fitting algorithm to find a solution. We furthermore limit the optical depth, as it is supposedly lower than 1 for all sources at 870 μm.

Furthermore, we added some implicit limits that come from having a distinguishable cold and hot component. First, the temperature of the hot component has always to be higher than the temperature of the dust component ($T_{\rm hot} > T_{\rm dust} + 5$ K. We add an arbitrary offset of at least 5 K to the lower limit of the hot components dust temperature, as otherwise both components could be too similar within the uncertainties and cause over-fitting some of the data points. Furthermore, the flux contribution of the hot, embedded component should be lower than the contribution from the dust for the longer wavelengths ($\lambda \geq 160\,\mu$m), whereas the opposite is true for flux densities at wavelengths below 70 μm. Also the solid angle of the embedded hot component $\Omega_{\rm hot}$ has to be smaller than the solid angle calculated from the source size of the dust $\Omega_{\rm dust}$. And finally the peak of the cold dust and hot embedded components should be within the wavelength regime, as otherwise the fit will not be constrained.

Finally, we can only fit a given SED if the flux densities are recovered in at least three bands for the cold, dust component above 20 μm. Similarly, the emission of the embedded and more evolved hot component can only be fitted, if at least two flux measurements are present below 70 μm.

It is also noteworthy that throughout the period of the present work, the SED fitting was slightly adjusted, taking into account the latest research results as the authors became aware of them. For this reason, we take a different approach e.g. for taking into account the emission in the 70 μm PACS band in our latest publication (Urquhart et al. 2018) and the analysis of the outer Galaxy than in our earlier work (König et al. 2017).

As the measured flux in the 70 μm band is considered to be a combination of a cold dust component and a more evolved hot component (e.g. Beuther et al. 2010), the 70 μm flux density was taken as an upper limit, only if no emission was detected for the hot component, assuming it is just not strong enough to be detected in the mid-infrared bands, but still con-

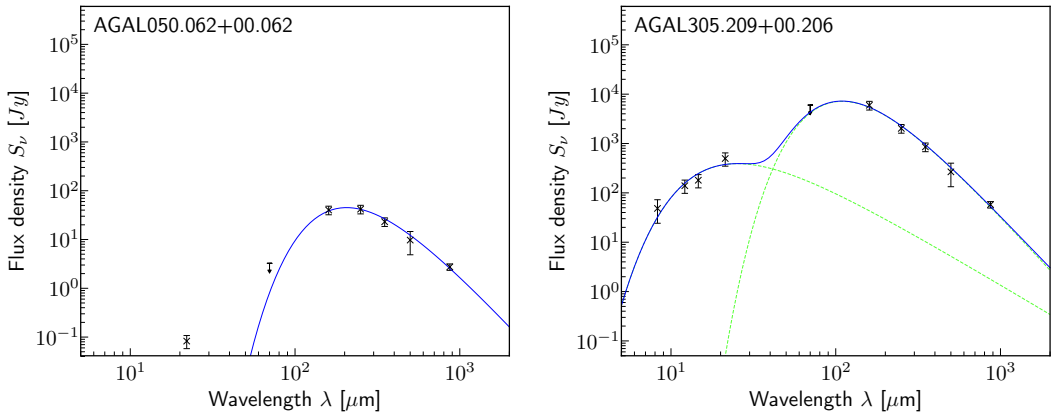

Figure 2.3: Two example SEDs showing the extracted flux densities fitted with a single-component greybody (left) and a two-component model (right). Flux densities are indicated by black crosses, with their uncertainties indicated by vertical bars. In the left panel, the greybody fit to the flux densities is shown in blue. In the right panel, the blue curve indicates the combined fits of the simultaneously fitted grey- and blackbody models, which are shown by the green dashed curves.

tributes to the flux. In addition this band is in general considered to be contaminated by the emission from small grains (Compiégne 2010, Compiègne et al. 2010), likely resulting in an overestimation of the flux, which was not taken into account in our earlier work. This became obvious when comparing our results to recent work by Guzmán et al. (2015) (see Chapter 4 resulting in an over-estimation of the temperatures if a hot component is present. Therefore we adjusted our process, always taking the flux in the 70 μm band as an upper limit for the full ATLASGAL catalogue and the outer Galaxy analysis.

In Fig 2.3 we show the fitted SEDs for two ATLASGAL sources. In the left panel we present a source only showing emission in the far-infrared to sub-millimetre regime, fitting only the cold-component with the greybody. In the right panel we present a much more evolved and luminous source, with a strong hot component that is fitted by the blackbody in combination with the greybody emission which is simultaneously fitted by the greybody. From the fitted SEDs, we most importantly obtained the cold components temperature representative of the average dust temperature of the clump as well as the luminosity which is obtained from the integral under the fitted model. In combination with the distances, these parameters were consecutively used to calculate the physical properties of the ATLASGAL CSC, building the basis for the discussion and findings of this thesis.

2.4 Distances

Distances within the Milky Way can be obtained through several different methods, with parallax measurements being the most direct and precise method (Reid & Honma 2014) and inferring distances from a rotation model of the Galaxy by measuring the line-of-sight velocities being the most commonly used method (Urquhart et al. 2018). There are several other

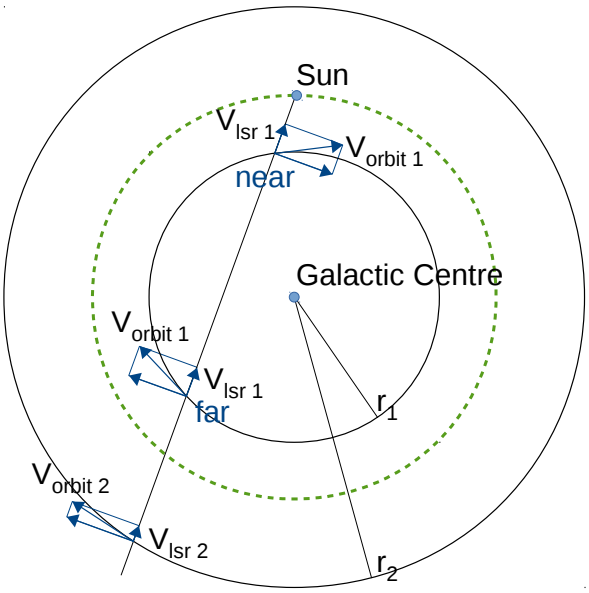

Figure 2.4: Schematic view of rotation around the Galactic centre. There are two solutions for the line-of-sight velocity $v_{\rm lsr1}$ when inside the solar circle (green dashed line) as the line of sight crosses the orbit at the near and far distance. No such ambiguity is found for sources located outside the solar circle.

methods to obtain distances especially to evolved stars (e.g. spectroscopic distance measurement or distances inferred from the light curves of variable stars or supernova), but as these require the stars to be no longer embedded, these do not play a role in the present work as they are not applicable for the early stages of star formation.

But as the sensitivity of the very long baseline interferometry (VLBI) involved in determining parallax distances is rather low (considering the small beam size), this method is only applicable to the brightest objects, preferably masers, at large distances. Furthermore, as parallax measurements require several high precision astrometric measurements at microarcsecond resolution distributed over at least one year to measure the parallax to sufficient precision, these measurements can not be obtained through very long baseline interferometry (VLBI) for a huge number of sources in a short amount of time.

In contrast, line-of-sight velocities can be determined within minutes for a single target or inferred for thousands of sources from spectra extracted from CO surveys like SEDIGISM (Schuller et al. 2017). For these reasons, the bulk of the distances to dust clumps in large samples are inferred from line-of-sight velocities using a rotation model of the Galaxy.

In Fig. 2.4 we show a schematic view of the rotation of the Milky Way. The orbital velocity $v_{\rm orbit}$ at a given radius r can be broken down into two components: one along the line-of-sight and one perpendicular to it. The velocity along the line-of-sight can be directly determined from the Doppler-shift measured for the observed frequency, yielding the velocity measured against the local standard of rest $v_{\rm lsr}$. As the orbital velocity $v_{\rm orbit}$ for a given orbit around the Galactic centre is known from rotation curves measured for the Milky Way, converting the

observed velocity to a distance is straight forward.

Unfortunately, we can not always convert a Galactocentric distance directly to a heliocentric distance as there are always two solutions when the source is located in inner Galaxy (i.e. $R_{\rm gal} < 8.34\,{\rm kpc}$): one that is closer to us and another that is on the other side of the Galaxy. To infer a heliocentric distance we therefore need another indicator if the source is located at the near- or far-distance. For the compact sources of ATLASGAL HI spectra were used to do so, as emission from a source farther away is more likely to show absorption from the medium located between the observer and the source (see Urquhart et al. 2018; for details). Therefore, for the inner Milky Way, the near-far-distance-ambiguity can be broken by taking into account the HI absorption towards a source of interest.

Although distances inferred from line-of-sight velocity measurements are rather quick and easy to obtain they come with a couple of caveats.

First, the rotation curve of the Galaxy itself is suffering from uncertainties as it is based on secondary distance measurements. Depending on the basis on which a rotation curve is derived, one or another might be preferable. In recent years, the model derived by Reid et al. (2014) is considered the most precise one, as it is inferred from parallax distance measurements. But as the measurements only took into account targets visible from the northern hemisphere, we consider the rotation curve from Brand & Blitz (1993) to be more reliable for sources located in the southern outer Galaxy, as it was derived from observations towards the same region of the sky.

Second, the line-of-sight velocity measurements are not only subject to the Galactic rotation, but e.g. also subject to streaming motions, supernovae explosions, or turbulence. These peculiar motions in general add an uncertainty in the order of $\sim \pm 7 - 10\,{\rm km\,s^{-1}}$ with regard to the Galactic rotation. Thus the relative uncertainty of the distance obtained from a Galactic rotation model is inversely proportional to the distance itself. As a consequence, local velocity measurements are dominated by the local streaming motions, whereas distances for sources located farther away are dominated by the Galactic rotation. This leads to the commonly used rule-of-thumb that distances derived from line-of-sight velocities are accurate within $\sim \pm 1$ kpc.

2.4.1 From molecular line observations to distances

As already described in Chapter 1.4.3, CO is the second most abundant molecule in the Milky Way after H_2. It is therefore widely found in molecular clouds, and even more so in the denser parts constituting the dusty clumps we are investigating in this work. Observing the CO emission towards a dust clump therefore allows us to obtain a velocity for a given clump and from this infer a distance to the clump.

For ATLASGAL and the outer Galaxy we used the facility receiver APEX-1 (SHeFI; Vassilev et al. 2008) at the Atacama Pathfinder Experiment telescope (APEX; Güsten et al. 2006) to obtain line-of-sight velocities ($v_{\rm lsr}$) towards the selected sources. For ATLASGAL we aimed at the ^{13}CO(2–1) and C^{18}(2–1) transitions at 219.6 and 220.4 GHz, respectively, as these are considered to be more optically thin when compared to the ^{12}CO(2–1) transition and therefore suffer less from line-of-sight confusion. For the outer Galaxy we targeted the ^{12}CO(2–1) transition at 230.5 GHz, as confusion is not as much an issue for the outer Galaxy than for the

inner Galaxy, and the higher column densities allow for detection of sources at greater distances with similar integration times. Two wide-band Fast Fourier Transform Spectrometers (FFTS; Klein et al. 2012) make up the back-ends, each consisting of 32,768 spectral channels covering an instantaneous bandwidth of 2.5 GHz. With this setup we were able to observe the targeted transitions at a velocity resolution of $\sim 0.1\,\mathrm{km\,s^{-1}}$. (see Chapters 4.2 and 5.1.2 for observational details).

2.4.1.1 Identifying velocity components

The obtained spectra were reduced using the Continuum and Line Analysis Single-dish Software (CLASS[3]). To obtain the velocity components from the observed spectra we first combined all scans for a single observed position into a single spectrum. This was smoothed to a velocity resolution of $1\,\mathrm{km\,s^{-1}}$ and a linear baseline was subtracted. The spectra were then transferred into a Python code, where they were limited to a velocity range of either $-200\,\mathrm{km\,s^{-1}} < v_{lsr} < 200\,\mathrm{km\,s^{-1}}$ for the ATLASGAL sources or $-20\,\mathrm{km\,s^{-1}} < v_{lsr} < 150\,\mathrm{km\,s^{-1}}$ for the outer Galaxy. Coherent groups of emission and absorption likely associated with a single cloud were determined by defining a window where all emission is above the 3σ noise level. These emission groups are then fitted iteratively, starting with the brightest group. First the spectrum is de-spiked, after which the number of peaks in a group is determined and Gaussian profiles are fitted to the peaks, and the resulting fit is subtracted from the original spectrum. The procedure is then repeated until all groups are fitted, i.e. when no residual above 3σ is found. In order to avoid adding too many emission components that are close to each other and are likely associated with the same cloud to be added, we only considered peaks separated by at least twice the width of the fitted Gaussian as major emission components. The same process was repeated for negative emission features, allowing us to identify observations with a contaminated off-position.

In Fig. 2.5 we show example spectra of velocity measurements obtained towards sources located in the outer Galaxy. In the upper left panel a single emission component along the line-of-sight can be fitted with a single Gaussian profile. This allows the velocity to be immediately assigned to the dust clump without further analysis.

The situation becomes more difficult when a cloud is either composed of multiple components or there are multiple clouds located along the line of sight (Fig. 2.5, upper right panel). Furthermore, as CO is the second most abundant molecule in the Milky Way, the reference position used when taking the spectrum might be contaminated, resulting in negative features in the spectrum (Fig. 2.5, lower left panel). Contaminated spectra pose the problem that the emission might be at a similar velocity as the negative feature, thus rendering the velocities less reliable. In extreme cases all these three effects are present in a single spectrum taken (lower right panel).

Although these effects complicate the analysis, in most cases still a velocity can be assigned to the corresponding dust clump. Assuming that the dust emission as seen in the continuum maps is associated mainly with the brightest emission found in CO, only the CO emission with the highest integrated intensity is taken into account. If this CO cloud has an integrated intensity at least twice as high as the rest of the CO emission, we assume that the dust emission

[3]GILDAS/CLASS: https://www.iram.fr/IRAMFR/GILDAS/

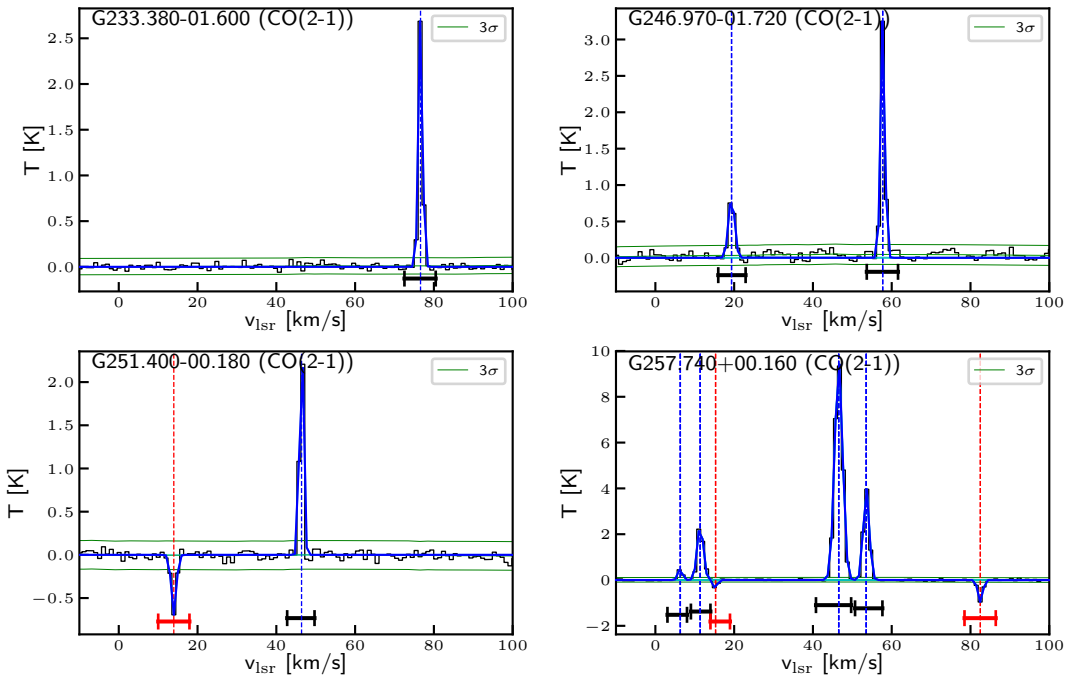

Figure 2.5: CO(2–1) spectra showing different typical profiles: single component (upper left), multiple components (upper right), simple contamination in the off-position (lower left) and a complex spectrum with all features (lower right).

is associated with it. In case a negative feature is located close to it ($dv < 1\,\mathrm{km\,s^{-1}}$), the uncertainty of the velocity measurement is increased by the width of the negative feature from the off-position, considering the velocity measurement still usable but with a higher uncertainty.

With the line-of-sight velocity of a clump known, we can then determine its distance from the rotation curve of the Galaxy. Unfortunately, two solutions are found for the inner Milky Way, either for the far side of the Galaxy or the near side. This is caused by the sources moving from north to south on the far-side, whereas the clumps move from the south to the north at the near-side with identical velocities for a given galactocentric radius. We refer to this problem as the distance ambiguity, and to the distances either as the near- or the far-distance. In Chapter 4 we will briefly explain how this ambiguity was broken for the ATLASGAL sample. For the southern outer Galaxy, such an ambiguity does not exist, as there is only one rotation direction, namely from south to the north, allowing for a direct conversion from the observed line-of-sight velocities to heliocentric distance.

2.5 Summary

In this chapter we introduced the three main methods to infer the physical properties of the targeted dust clumps. First we obtain photometric data through aperture photometry from four different Galactic continuum surveys (ATLASGAL, HiGAL, MSX and WISE). The photometric data in 12 different wavelength-bands, which recovers the spectral energy distribu-

tions from the mid-infrared to submm wavelength regime (8-870 μm), is then fitted by a grey- and blackbody emission model, yielding the dust temperature and the integrated flux of the clumps. Finally we determine kinematic distances for the dust clumps by associating them with velocity components identified from CO(2–1) emission observed at the APEX telescope. Combining the dust temperatures, integrated fluxes, and distances we are then able to estimate physical properties such as bolometric luminosities, clump masses and column densities. Furthermore, by investigating the flux densities in different wavelength bands, we are able to determine the evolutionary phase of a given clump, allowing us to investigate how the physical properties change over the lifetime of a dust clump, as we will see in the next Chapter.

Part II

Inner Galaxy: ATLASGAL

CHAPTER 3

ATLASGAL Top100: An Evolutionary Sample

3.1 Motivation

This chapter was originally published as a paper in A&A called "*ATLASGAL Top100: Dust Characterization of an Evolutionary Sample*" (König et al. 2017). The goal of this paper was to characterize the set of the ∼100 brightest ATLASGAL sources, prove their ability to (mostly) form massive stars, and determine their evolutionary stage. Starting from dust emission maps in 10 different bands ranging from the mid-infrared to the sub-millimetre regime, fluxes were extracted recovering the dust spectral energy distributions. These were subsequently fitted by a two-component model yielding dust temperatures and bolometric luminosities, as well as clump masses and peak H_2 column densities.

The remaining sections of this chapter are taken from the paper published in Astronomy & Astrophysics (König et al. 2017). Changes have been made to fit to the present format of publication. Note that Section 3.6.4 is mainly a contribution from the co-authors of König et al. (2017) who were in charge of the corresponding research.

3.2 Introduction

Massive stars ($>8\,M_\odot$) play an important role in the evolution of their host galaxies (Kennicutt 2005). During the early stages of their formation they drive powerful molecular outflows that inject momentum into the surrounding environment. At their later stages they drive strong stellar winds and emit copious amounts of ionizing radiation that shape their local environments and regulate further star formation. Massive stars are also primarily responsible for the production of nearly all heavy elements, which are returned to the interstellar medium (ISM) through stellar winds and supernovae, leading to an enrichment of the local and global environment and changes to the chemistry. Yet the formation and early evolutionary stages of massive star formation are still not well understood (see Zinnecker & Yorke 2007 for a review).

The main hurdles to an improved understanding are that high-mass stars are rare and are therefore typically found at large distances from the Sun (>2 kpc), and that the earliest stages of their formation take place while they are still deeply embedded in their natal molecular clouds. Consequently, the earliest stages are hidden from more traditional observations at optical and near-infrared wavelengths and therefore observations in the far-infrared and sub-millimeter regimes are required to probe these extremely dense environments. Furthermore, massive stars are known to form almost exclusively in clusters (de Wit et al. 2004) and therefore high-resolution is required to separate individual (proto-)cluster members.

In recent years, a number of Galactic plane surveys have been undertaken that probe large volumes of the Galaxy and provide a straightforward way to identify a large sample of embedded massive stars and clusters that will include examples of sources in all of the important evolutionary stages. These surveys provide almost complete coverage of near-infrared to radio wavelengths (e.g., the UKIRT Infrared Deep Sky Survey Galactic Plane Survey (UKIDSS GPS), Lucas et al. 2008; Galactic Legacy Infrared Mid-Plane Survey Extraordinaire (GLIMPSE), Benjamin et al. & et al. 2003; Midcourse Space Experiment (MSX), Price et al. 2001; Wide-Field Infrared Survey Explorer (WISE) Wright et al. 2010; Multiband Infrared Photometer for Spitzer survey of the inner Galactic Plane (MIPSGAL), Carey et al. 2009; *Herschel* infrared Galactic Plane Survey (Hi-GAL), Molinari et al. 2010; APEX Telescope Large Area Survey of the Galaxy (ATLASGAL), Schuller et al. 2009; Bolocam Galactic Plane Survey (BGPS), Aguirre et al. 2011 and the Co-ordinated Radio and Infrared Survey for High-Mass Star Formation (CORNISH), Purcell et al. 2013 and Hoare et al. 2012).

Dust emission is generally optically thin at submillimeter wavelengths and therefore surveys at these wavelengths are an excellent tracer of column density and total mass. The ATLASGAL survey covers a total area of 420 square degrees, tracing dust throughout the inner Galaxy ($300^\circ < \ell < 60^\circ$ with $|b| \leq 1.5^\circ$ and was subsequently extended to $280^\circ < \ell < 300^\circ$ with $-2^\circ < b < 1^\circ$ (Schuller et al. 2009). The survey was conducted with the Large APEX Bolometer Camera (LABOCA, Siringo et al. 2009) using the Atacama Pathfinder EXperiment 12 m telescope (APEX; Güsten et al. 2006), which is located at a height of ∼5100 m on the Chajnantor plateau in the Atacama desert in Chile. APEX has an angular resolution of $19.2''$ at 870 μm.

Subsequently, the ATLASGAL compact source catalog (CSC; Contreras et al. 2013, Urquhart et al. 2014a) and the ATLASGAL Gaussclumps source catalog (GCSC; Csengeri et al. 2014) were extracted, identifying ∼10,000 dust clumps located throughout the inner Galaxy. These catalogs include large numbers of potential high-mass-star forming regions in different evolutionary stages from massive starless regions to clumps associated with (ultra-) compact HII regions on the verge of destroying their natal environment. In the past, studies into massive-star formation have focused on a single well defined evolutionary stage (e.g., UCHII regions (Wood & Churchwell 1989), high-mass protostellar objects (Sridharan et al. 2002) or Class II methanol masers, which exclusively pinpoint the locations of high-mass protostars (Walsh et al. 1997; 2003)). Although many of these have been successful in parameterising these stages they tell us little about how these various phases are connected, how their properties change as the embedded star evolves or the relative lifetimes of each stage. However, covering the full mid-infrared to submm wavelength regime with unprecedented sensitivity and resolution, the above-mentioned unbiased Galactic plane surveys and in particular the ATLASGAL catalogs provide an excellent starting point to study the complete evolutionary sequence of massive stars in a robust statistical manner (Urquhart et al. 2014c).

We have used the ATLASGAL survey to select a sample of ∼100 massive clumps that likely represent different evolutionary stages (Giannetti et al. 2014). We have also correlated this sample with methanol masers (Urquhart et al. 2013a), young stellar objects (YSOs) and HII regions (Urquhart et al. 2013b; 2014b) to constrain the evolutionary state of the sample's sources. This sample has also been the subject of molecular line follow-up studies to fully characterize the evolutionary sequence and derive the physical properties of different stages.

The results of these studies have been discussed in a series of papers. For example, CO depletion and isotopic ratios have been investigated by Giannetti et al. (2014), SiO emission for the northern sources to trace shocked gas was studied by Csengeri et al. (2016), and NH_3 has been used to investigate infall towards selected sources by Wyrowski et al. (2016) with a number of papers in preparation focusing on their associated outflows (Navarete et al in prep.) and modeling of their chemistry (Giannetti et al. 2017b). Using these spectroscopic and continuum surveys will provide the most detailed view of the evolutionary sequence of massive stars and robust constraints on the physical properties, chemical conditions, and kinematics of this unique sample of high-mass-star forming regions selected from the whole inner Galactic plane.

In this paper we use multi-wavelength dust continuum emission to characterize this sample of candidate massive-star forming regions, in terms of dust temperatures, bolometric luminosities, and clump masses. Together with the latest distances, these quantities are key to the further analysis of the sample. To derive the sources' physical properties from dust continuum spectral energy distributions, we complement the 870 μm ATLASGAL data with publicly available Herschel/Hi-GAL (Molinari et al. 2010), MSX (Egan et al. 2003), and WISE (Wright et al. 2010) data in order to cover a wavelength range from 8 μm to 870 μm. Furthermore, we show that our sample comprises a representative set of sources covering all of the important embedded evolutionary stages of massive-star formation.

This paper is organized as follows: in Section 3.3 we describe how the initial selection was made and briefly discuss how the source classification has evolved as new survey data has become available. In Section 3.4 we explain how the photometry and spectral energy distributions (SEDs) have been obtained. In Section 3.5 we derive physical parameters from the results of the SED modeling, while in Section 3.6 we discuss the assignment of our sources to different stages of development and an evolutionary sequence. In Section 3.7 we summarize our findings and present a brief outlook on future work.

3.3 Sample selection and classification

We selected 110 sources from the ATLASGAL compact source catalog that are likely to be at different evolutionary stages, using ancillary data to trace their star formation activity. We originally selected 102 sources as being the brightest sources at submillimeter wavelengths in four distinct groups as described by Giannetti et al. (2014), using ancillary mid-infrared and radio data. During various ongoing follow-up projects, eight sources were added, and here we investigate the physical properties of this sample of 110 sources as a necessary reference for future studies. In the following sections we refer to this sample as the ATLASGAL "Top100".

3.3.1 Classification

Since the initial classification of the sources by Giannetti et al. (2014), new catalogs have become available, allowing for a refined classification that better reflects the physical properties of the sources in different evolutionary stages. In this paper, we reclassify our sample using four distinct phases of massive-star formation. Three of these phases are drawn from

the scheme originally outlined by Giannetti et al. (2014) and Csengeri et al. (2016) (i.e., mid-infrared weak, mid-infrared bright and HII regions). Here we refine this classification and extend it to include the youngest starless/pre-stellar phase based on the physical properties of the sample.

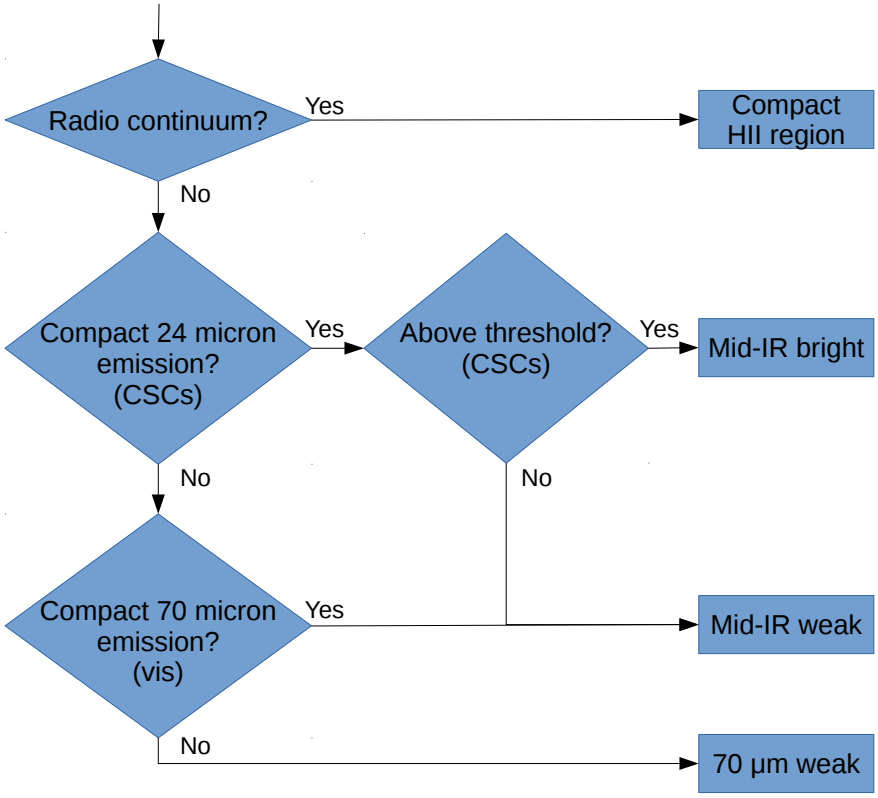

Figure 3.1: Classification process for the Top100 sample.

A schematic diagram of the classification process is shown in Figure 3.1. First, the sources are checked for radio continuum emission using the CORNISH survey (Hoare et al. 2012, Purcell et al. 2013), the RMS survey (Urquhart et al. 2007; 2009), or the targeted observations towards methanol masers reported by Walsh et al. (1998). When radio continuum emission is found at either 4 or 8 GHz within 10″ of the ATLASGAL peak, the source is considered to be a compact HII region. We have adopted the radius of 10″ as our association criterion from Urquhart et al. (2014c), where they compared the angular offsets between the peak of the submillimeter emission and a number of massive-star formation tracers, determining that ∼85 per cent of compact embedded objects were located within 10″ of each other. Furthermore, we refined the distinction between mid-infrared weak and mid-infrared bright sources by inspecting the emission in the 21 μm MSX (Price et al. 2001) and 24 μm MIPSGAL (Carey et al. 2009) images. Looking for signs of star-formation, a source is considered mid-infrared bright if there is a compact mid-infrared source associated with the submm emission peak and the flux reported in the compact source catalogs (Egan et al. 2003, Gutermuth & Heyer 2015) is above 2.6 Jy, corresponding to a 4, 8, or 15 $M_\odot$ star at 1, 4, and 20 kpc, respectively (Heyer

et al. 2016). Accordingly a source is considered to be mid-infrared weak when the compact mid-infrared emission in the 21/24 μm band is below 2.6 Jy or no compact source is associated with the peak. Finally, the sources in the starless/pre-stellar phase are identified from a visual inspection of Hi-GAL PACS 70 μm images. Showing no compact emission at 70 μm within 10$''$ of the submm emission peak, a source is considered 70 μm weak. This means that sources showing diffuse emission at 70 μm or compact 70 μm sources offset from the dust peak are still considered as 70 μm weak clumps.

In Figure 3.2 we show example three color images for each class and below we briefly describe the observed feature of each phase and give the number of sources classified in each:

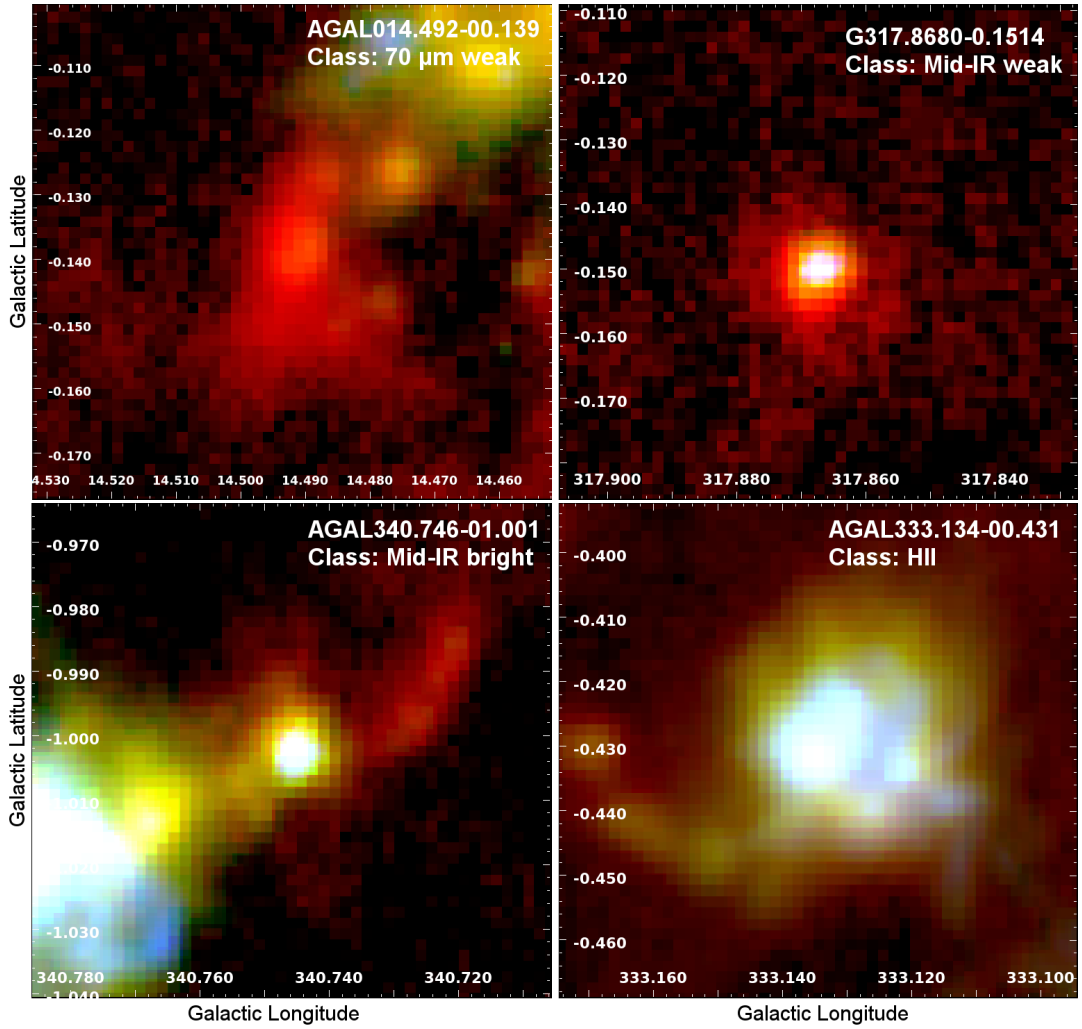

Figure 3.2: Three color images of sample sources for each class sorted from youngest (top) to most evolved (bottom). Size: 5$'\times$5$'$; red: ATLASGAL 870 μm; green: PACS 160 μm; blue: PACS 70 μm.

- Starless/pre-stellar stage (16 sources): a quiescent phase, which represents the earliest

stage of massive-star formation (Fig. 3.2, top panel). These clumps are either mostly devoid of any embedded pointlike sources in the Hi-GAL 70 micron images or only show weak emission. They are likely to be the coldest and least luminous sources of the whole sample, and may already be collapsing, but no protostellar object has yet formed (e.g., Motte et al. 2010, Elia et al. 2013, Traficante et al. 2015). This class is called "70 μm weak" from here on.

- Protostellar stage (33 sources): compact point sources are clearly seen in the 70 μm Hi-GAL image and so protostellar objects are present (Fig. 3.2, second panel). The embedded 70 μm sources are either not associated with any mid-infrared counterparts within 10$''$ of the peak emission or the associated compact emission is below our threshold of 2.6 Jy, which indicates that the star formation is at an early stage and that the clumps are likely to be dominated by cold gas. We call this class "Mid-IR weak" throughout the paper.

- High-mass protostellar stage (36 sources): this phase is characterized by strong compact mid-infrared emission seen in 8 and 24 micron images and is one of the most active stages of massive-star formation (Fig. 3.2, third panel). These clumps are likely undergoing collapse in the absence of a strong magnetic field (Urquhart et al. 2014c; 2015), show signs of infall (Wyrowski et al. 2016) and are likely to be driving strong outflows (Navarete et al. in prep.). Due to the infall, outflows, and already active young stellar objects, these sources are also likely to be significantly hotter than the sources in the quiescent phase, giving rise to the bright emission at mid-IR wavelengths (called "Mid-IR bright" from here on).

- Compact HII region phase (25 sources): in the latest evolutionary phase of massive-star formation we define here, the sources have just begun to disperse their natal envelope and are ionizing their local environment, creating compact HII regions (Fig. 3.2, bottom panel). These sources are associated with bright mid-infrared emission and compact radio continuum emission arising from the ionization of their environment, making them easily distinguishable from the earlier evolutionary phases. We refer to this class as "HII regions" from here on.

3.3.2 Distances

We have determined distances for 109 of the 110 sources of the sample. These distances have been drawn from the literature and supplemented with our own kinematic distances (Wienen et al. 2015). The distances given in Table 3.1 are based on those given by Giannetti et al. (2014) but incorporate the results of the latest maser parallax measurements reported by Reid et al. (2014); this has resulted in the distances for six sources changing by $\sim$2 kpc. For a small number of sources the distances adopted by Giannetti et al. (2014) disagreed with distances reported in the literature. Given that the distances extracted from the literature are kinematic in nature and have been determined using the same HI data and comparable radial velocity measurements these variations likely result from slight differences in the method applied and the sensitivity and transition of the line surveys used in different studies.

There are eight sources where the literature distance and distance adopted by Giannetti et al. (2014) disagree by more than a few kpc. For one source (AGAL330.954−00.182[1].) higher resolution HI data has become available from targeted follow-up observations made toward UC HII regions (Urquhart et al. 2012) and we have adopted the distance obtained from the analysis of this data, which utilizes the presence or non-presence of HI self absorption as a distance indicator. We have examined the mid-infrared images for the other seven sources and find three to be coincident with localized areas of extinction, which would suggest that a near distance is more likely (AGAL008.684−00.367, AGAL008.706−00.414, and AGAL353.066+00.452). Examination of the HI data towards AGAL316.641−00.087 reveals absorption at the source velocity and so we place this source at the near distance. The lack of an absorption feature in the HI data or evidence of extinction would suggest that the three remaining sources are located at the far distance and indeed for three sources this is likely to be the case (AGAL337.704−00.054, AGAL337.176−00.032, and AGAL337.258−00.101; Giannetti et al. 2015). For one source (AGAL008.831−00.027) we did not obtain a distance, as its radial velocity is close to zero ($V_{LSR} = 0.53\,km\,s^{-1}$), hence rendering a kinematic distance unreliable.

In Fig. 3.3 we present the distribution of the Top100 on a schematic diagram of the Milky Way that includes many of the key elements of Galactic structure, such as the location of the spiral arms and the Galactic long and short bars (Churchwell et al. 2009).

In Fig. 3.4 we show the distance distribution of the Top100 sources, which features two distinct peaks at ∼2 kpc and ∼4 kpc. These peaks correlate with the near parts of the Sagittarius and Scutum-Centaurus arms, respectively, as seen in Fig. 3.3. We note that we only show the histogram for the full sample, as the sources in all four phases have a similar distance distribution. This is confirmed by Anderson-Darling tests[2] (Stephens 1974) performed for the different classes yielding p-values higher than 0.02 for all classes, confirming the null hypothesis of two samples being drawn from the same distribution at the 3σ significance level. Furthermore, there is a drop-off in the number of sources beyond a distance of 6 kpc. As the whole sample is selected so that the brightest sources in the ATLASGAL catalog were selected for each category, a general distance bias toward closer distances and being located in the closest spiral arms is not surprising.

3.4 Spectral energy distributions

The evolutionary scheme for high-mass star formation described in Sect. 2 is primarily based on the visual examination of infrared images and the presence or absence of an infrared embedded point source and is therefore largely a phenomenological classification scheme. To robustly test this evolutionary sequence we need to determine the sample members' physical properties and search for trends in these parameters that support this. Key elements are the source temperatures and bolometric luminosities, which can be determined from model fits to the source's spectral energy distributions (SEDs).

[1]We use source names from Contreras et al. (2013)

[2]We chose the Anderson-Darling test over a Kolmogorov-Smirnov test, as it is more sensitive to subtle differences in smaller samples (compare, e.g., Razali 2011).

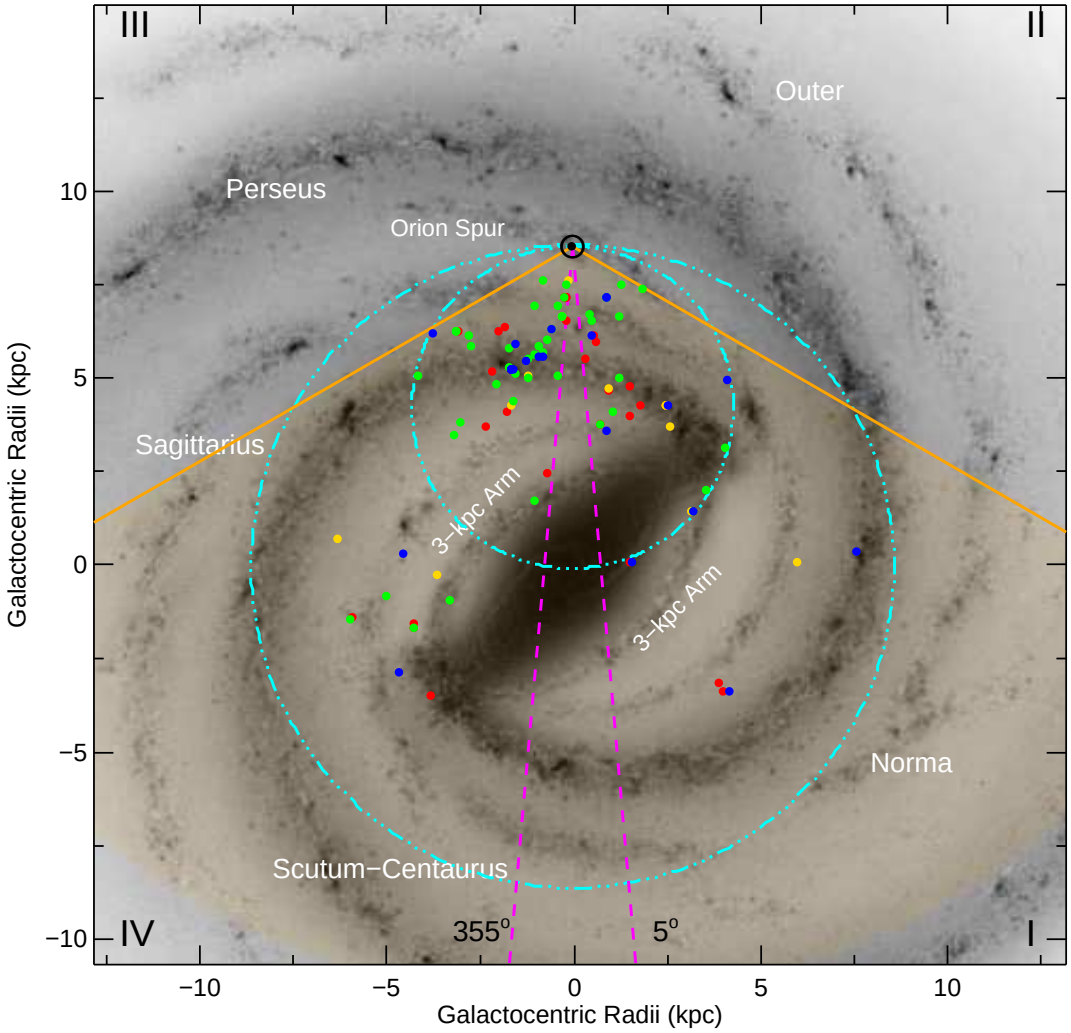

Figure 3.3: Galactic distribution of the ATLASGAL Top100 sample. The positions of the HII regions, mid-infrared bright, mid-infrared weak and 70 μm weak sources are indicated by the blue, green, red, and yellow filled circles, respectively. The orange shaded area indicates the region of the Galactic plane covered by the ATLASGAL survey to a distance of 20 kpc, within which the survey is complete for compact clumps with masses $>1000\,M_{\odot}$. The background image is a schematic of the Galactic disc as viewed from the Northern Galactic Pole (courtesy of NASA/JPL-Caltech/R. Hurt (SSC/Caltech)). The Sun is located at the apex of the wedge and is indicated by the $\odot$ symbol. The smaller of the two cyan dot-dashed circles represents the locus of tangent points, while the larger circle traces the solar circle. The spiral arms are labeled in white and Galactic quadrants are given by the roman numerals in the corners of the image. The magenta line shows the innermost region toward the Galactic center where distances are not reliable.

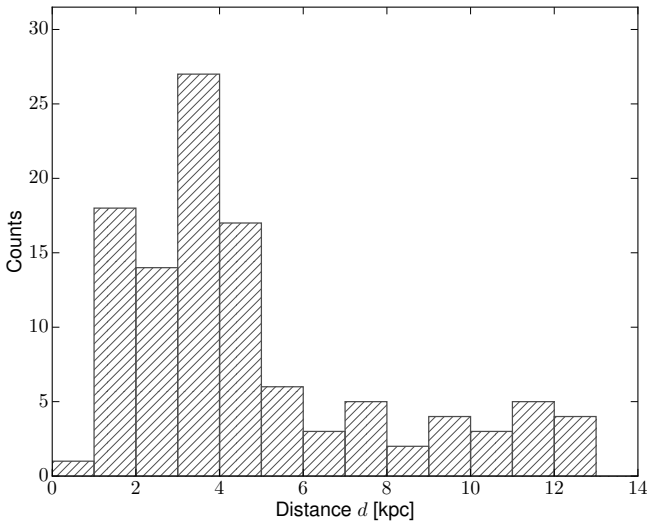

Figure 3.4: Heliocentric distance distribution of all ATLASGAL Top100 sources for which a distance has been unambiguously determined. The bin size is 1 kpc.

To achieve this goal we extracted multi-wavelength continuum data (mid-infrared to submillimeter wavelengths) and performed aperture photometry to reconstruct the dust continuum SEDs. The fluxes obtained from the photometry were fitted with a simple model to derive the dust temperature and integrated flux, which were subsequently used to estimate the bolometric luminosities and total masses. The data used and methods supplied will be described in detail in the following subsections.

3.4.1 Dust continuum surveys

The mid-infrared wavelength regime is covered using archival data from either the MSX (Egan et al. 2003) or the WISE (Wright et al. 2010) surveys. The far-infrared spectrum is covered by the two Herschel (Pilbratt et al. 2010) instruments SPIRE (Griffin et al. 2010) and PACS (Poglitsch et al. 2010), covering the wavelength range from 70 μm up to 500 μm, with five different bands centered at 70, 160, 250, 350, and 500 μm, respectively. These bands are especially well suited to determine the peak of the SED for cool dust. The level 2.5 maps from the Herschel Infrared Galactic Plane Survey (Hi-GAL, Molinari et al. 2010) were retrieved from the Herschel Science Archive (HSA)[3], and were downloaded in version 11 of the Standard Product Generation (SPGv11) pipeline. To obtain the flux for the longest wavelength (submillimeter) entry of the SED, the 870 μm ATLASGAL maps are used.

For all of these data sets we extracted 5×5 arcminute-sized images centered on the source positions. Where necessary the map units were converted to Jy pixel^{-1} while keeping the original resolution. For MSX and WISE images this meant converting from W m^{-2} sr^{-1} and digital numbers (DN) to Jy pixel^{-1}, respectively.[4]

[3] http://herschel.esac.esa.int/Science_Archive.shtml
[4] For more information see http://irsa.ipac.caltech.edu/applications/MSX/MSX/

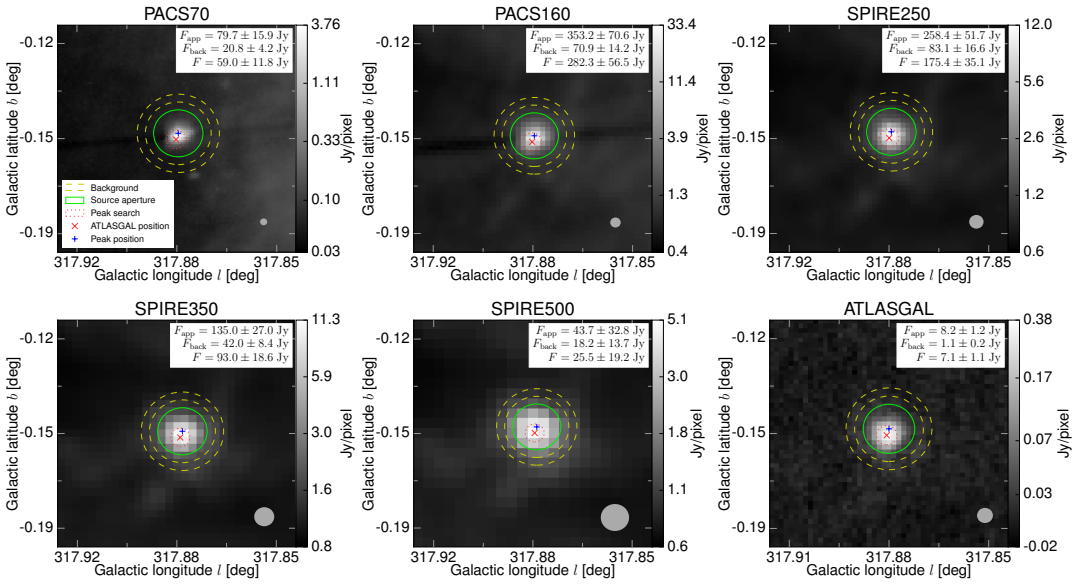

Figure 3.5: Images of a single source (AGAL317.867−00.151) seen in the different bands, showing the aperture (green circle), background annulus (yellow dashed circle), ATLASGAL and peak flux position (red and blue crosses, respectively) and the peak pixel search area (red dotted circle). The beam size is indicated as a gray circle in the lower right.

3.4.2 Aperture photometry

Aperture photometry was used to extract fluxes in a consistent way from the mid-infrared and submillimeter maps. The flux density $F_{\rm aper}$ was integrated over a circular aperture centered on the peak flux pixel position. The peak position was identified in either the 250 μm, 160 μm or the 870 μm band, depending on whether the band was suffering from saturation, following the order of the bands as previously stated. Assuming a Gaussian-shaped source brightness profile with a full width at half maximum size (FWHM) as reported in Csengeri et al. (2014), we use an aperture size for each source with a radius of 3σ, where $\sigma = {\rm FWHM}/(2\sqrt{2\ln 2})$ to obtain most of the flux ($> 99\%$) of a source. With a minimum aperture size of $55.1''$ the apertures were also selected such that they are resolved by the lowest resolution data (i.e. $36.6''$ for SPIRE 500 μm). We performed tests that revealed that smaller aperture sizes underestimate the flux, while a larger aperture size might cut into some other emission nearby, as the source confusion for some of the clumps of our sample is significant, since these are associated with some of the most active star-forming sites in the Galaxy. Subsequently, the background flux density $F_{\rm bg}$ obtained from the median pixel value of a circular annulus around the same center position as the aperture was subtracted from the aperture flux to obtain the background-corrected source flux F.

When fluxes could be successfully extracted from the MSX maps, we preferred these over the WISE fluxes, as the MSX maps have a resolution of $18''$ similar to the longer wavelength bands (e.g., $19.2''$ for ATLASGAL). In addition, MSX suffers less from saturation than the

`imageDescriptions.htm` and `http://wise2.ipac.caltech.edu/docs/release/prelim/expsup/sec2_3f.html#tbl1`

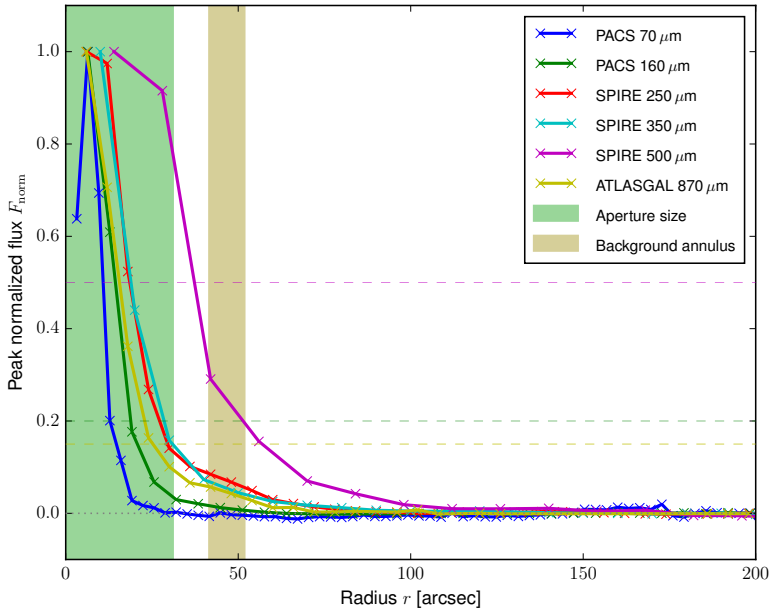

Figure 3.6: Emission profiles of a single source (AGAL317.867−00.151) for the different bands, showing the aperture (green shaded area) and background annulus (ochre shaded area). The horizontal dashed lines shown in yellow, magenta and green indicate the flux uncertainties we assume for the ATLASGAL, SPIRE 500 μm and remaining Herschel bands, respectively. The 500 μm band traces the more extended emission and we therefore assume a measurment uncertainty of 50% in this band when fitting the SEDs.

WISE data (compare, e.g., Cutri et al. 2012, Chapter VI.3, and Robitaille et al. 2007, Table 1). In cases where the photometry extracted from the MSX images is a non-detection we turned to the higher sensitivity WISE data to determine the flux.

An example for the photometry extraction in the far-infrared to submm bands is presented in Fig. 3.5, showing the position and size of the aperture and annulus used to estimate the background contribution for this source. In total, we found one source to be saturated at 70 μm, one source at 160 μm, 39 sources are saturated at 250 μm and 14 sources at 350 μm. When one or more bands in the far-infrared to submm range suffers from saturation, the SPIRE 250 μm band is always one of them. Moreover we note that the fraction of sources being saturated in at least one band increases through the classes: from no source suffering from saturation for the 70 μm weak sample, six sources (i.e., 16%) of the mid-infrared weak class, ten in the mid-infrared bright sample (i.e., 31%), and 23 (i.e., 92%) for the HII regions. For the photometry, the saturated pixels were set to the maximum pixel value of the image, and the flux is only taken as a lower limit for the SED fitting (see Section 3.4.3). To ensure good fitting results we require at least three bands in the far-IR to submm regime to be free from saturation.

In Figure 3.6 we show the emission profiles of the submm bands for a single source (AGAL317.867−00.151). To better emphasize the structure and make it comparable between the different bands, for each wavelength we subtracted the median background emission as determined far away (i.e., five times the aperture size) from the source where the profile gets

flat and then normalized the flux to the peak emission in that band. As can be seen from the plot, the SPIRE 500 μm band traces the more extended emission, falling off to the background plateau level rather slowly compared to the other bands. Conversely, the other bands trace the peak of the emission within the aperture, but the background aperture still cuts into some local plateau associated with the cloud. The contribution of this is lower than 10% for all bands except the SPIRE 500 μm. Accordingly we assume a rather large measurement uncertainty of 50% for the 500 μm band to account for the added uncertainty from the background correction as well as to account for the large pixel size of 15$''$ in this band. For the other Herschel bands we assume a measurement uncertainty of 20% and a measurement uncertainty of 15% for the flux estimate of the ATLASGAL band. Finally, the absolute calibration uncertainties are added to the intrinsic measurement error in quadrature to obtain the uncertainties of the (non-saturated) flux densities.

3.4.3 SED models

The multi-wavelength photometic data obtained was fitted using standard methods to obtain the dust temperature and bolometric luminosity of each source.

For sources for which no mid-infrared emission is detected (or a flux density measurement is available for only one mid-infrared band), we follow the method of Elia et al. (2010) and Motte et al. (2010), fitting a single graybody model to the flux densities measured for the cold dust envelope. When fitting only the cold component, we use the 70 μm flux density as an upper limit for the dust emission. Assuming the measured flux density at 70 μm is always a combination from the cold dust envelope and a young embedded object, taking it as an upper limit for the dust emission avoids overestimating the dust temperature. For the fitting of the graybody we leave the dust spectral index β fixed to a value of 1.75, computed as the mean value from the dust opacities over all dust models of Ossenkopf & Henning (1994) for the submm regime. This also facilitates comparison of the envelope masses calculated here with previous results presented in the literature (e.g., Thompson et al. 2004, Nguyen Luong et al. 2011).

Where at least two flux density measurements are available at the (different) shorter wavelengths, a two-component model consisting of a blackbody and a graybody is fitted to the SED (e.g., Beuther et al. 2010). As the 70 μm flux has a significant influence on the general quality of the fit (Mottram et al. 2011b) and hence on the temperature estimate of the cold dust, the blackbody being added to the model quantitatively constrains the contribution of a deeply embedded, hot component to the 70 μm flux density. For the mid-infrared weak sources a flux density measurement at 21μm might be available, but as at least two measurements are necessary for the hot component to be fitted, only the graybody is taken into account, emphasizing the importance of the 70 μm flux being taken as an upper limit in such cases (compare Figure 3.7, second tile).

We were able to fit the SEDs for all 110 sources in our sample. A single graybody component fit was used to model the emission for 38 of the mid-infrared dark sources while the remaining 73 sources were fitted using the two component fit of a graybody plus the blackbody as described in the previous section. In Fig. 3.7 we show sample SEDs for all four classes and the model fits to the data. The top panels show a single component graybody fit to a 70 μm

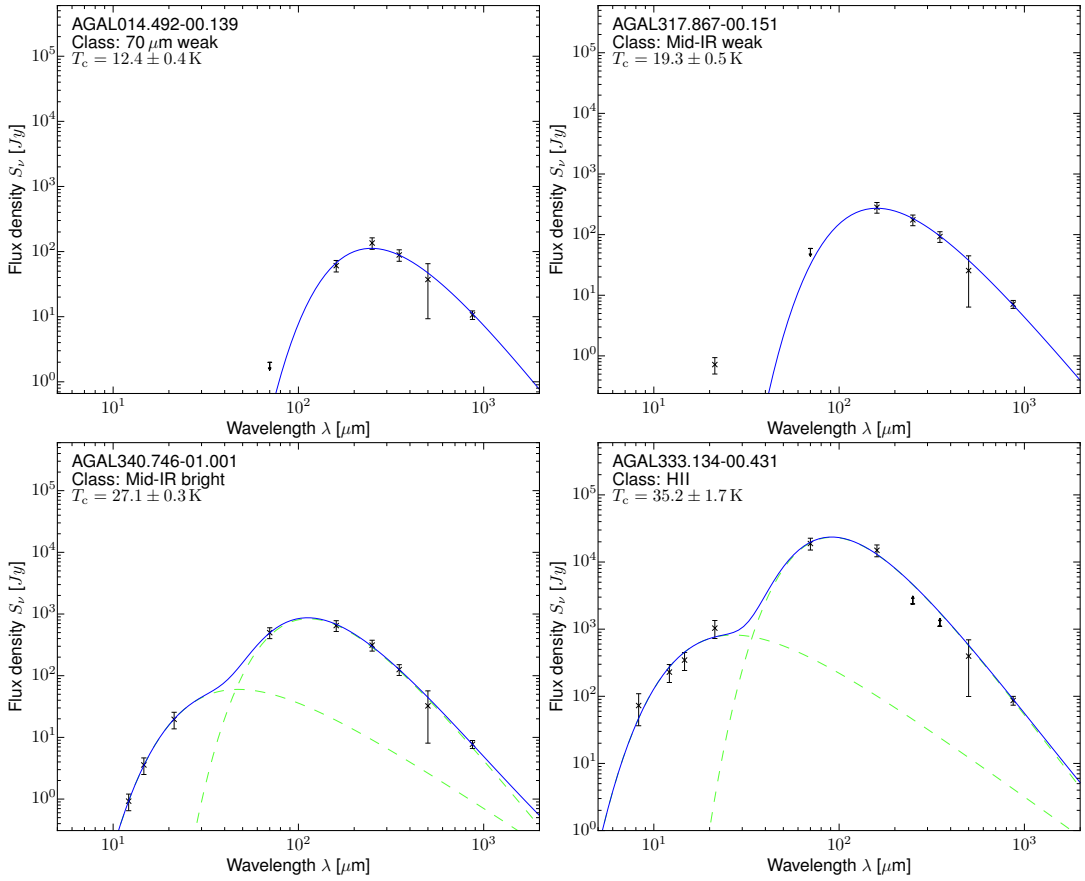

Figure 3.7: Sample SEDs for all four evolutionary classes sorted from youngest to most evolved sources from top to bottom. A single component graybody is fitted for the upper two, whereas a two-component fit is used for the later two sources. The green dashed lines in the lower panels show the graybody and blackbody components of the fit.

weak and to a mid-infrared weak source, whilst the lower panels show the results of a two component fit to sources of the class of mid-infrared weak sources and the HII regions. A comparison of the two-component model with the radiative transfer model used by Robitaille et al. (2007) is presented in Sect. 3.5.1.

3.5 Results

We have obtained estimates for the bolometric dust temperatures and fluxes for the whole sample. Combining these parameters with the distances discussed in Sect. 2, we have calculated the source masses, luminosities and column densities for all but one source. In Tables 3.1 and 3.2 we give the parameters for each source and a summary of the derived parameters for each class, respectively. Figure 3.8 presents cumulative distribution functions for the dust temperatures, bolometric luminosities, masses, linear source sizes, and column densities.

We excluded nine sources from the analysis for which the SEDs or classification were unreliable, as the sources are located in rather complex regions. For four sources (AGAL024.651−00.169, AGAL305.209+00.206, AGAL338.926+00.554, and AGAL354.944−00.537) the aperture is cutting into some nearby source and hence overestimating the background corrected flux. For three sources (AGAL008.706−00.414, AGAL022.376+00.447, and AGAL351.161+00.697) the background aperture is picking up some broad emission, leading the source flux to be underestimated. For AGAL028.564−00.236 the region within the aperture is too complex to be interpreted as a single source and AGAL013.178+00.059 is located on a background with a strong gradient leading to an unreliable flux estimate. This reduces the sample size for the analysis of evolutionary trends to 102 sources.

Comparing the average values of the parameters for the different source classifications and the cumulative distributions presented in Table 3.2 and Fig. 3.8 reveals evidence for evolutionary trends with increases in temperatures, bolometric luminosities, and column densities as a function of the different stages. We also find that the mean masses and linear sizes of the subsamples are similar and so we conclude that the initial conditions were also similar, assuming the clumps not to accrete from a much larger mass reservoir.

3.5.1 Dust temperature and bolometric luminosity

The dust temperature is a fitted parameter of the modified blackbody model. Values range from 11 K for the 70 μm weak sources to 41 K for the HII regions' dust envelopes. The lowest temperatures are close to the temperature expected for quiescent clumps, which is determined by cosmic ray heating ($\sim$10 K; Urban et al. 2009), consistent with the proposed starless nature of the 70 μm weak sources. It is worth bearing in mind that these sources are likely to have even lower temperatures in the inner part of the clumps as indicated by Bernard et al. (2010). The mean temperature of the dust envelope increases through the different categories from 16.4 K for the 70 μm weak sources up to a mean temperature of 31.7 K for the HII regions, with an average dust temperature of 24.7 K for the whole sample. We point out that the dust temperatures for the HII regions should be taken with care (and possibly as lower limits) as the emission might be optically thick for a portion of the SED (see, e.g., Elia & Pezzuto 2016).

Table 3.1: Source parameters for the first 15 sources.

Name	d (kpc)	$d_{\rm ref}$	$V_{\rm lsr}$ (km/s)	$l_{\rm app}$ (deg)	$b_{\rm app}$ (deg)	$D_{\rm app}$ ($''$)	Class	T (K)	ΔT (K)	$L_{\rm bol}$ ($L_\odot$)	$M_{\rm clump}$ ($M_\odot$)	$\alpha_{\rm vir}$
AGAL006.216−00.609	2.9	(22)	18.5	6.216	−0.609	71.6	IRw	16.0	0.2	7.3×10^{2}	4.5×10^{2}	–
AGAL008.671−00.356	4.8	(19)	35.1	8.668	−0.355	69.1	HII	26.3	1.4	8.6×10^{4}	3.0×10^{3}	–
AGAL008.684−00.367	4.8	(19)	38.0	8.682	−0.367	66.1	IRw	24.2	0.2	2.7×10^{4}	1.4×10^{3}	0.69
AGAL008.706−00.414	4.8	(19)	39.4	8.704	−0.412	92.1	IRw	11.8	0.3	5.0×10^{2}	1.6×10^{3}	0.22
AGAL008.831−00.027	–	–	0.5	8.831	−0.027	70.9	IRw	24.1	1.5	–	–	–
AGAL010.444−00.017	8.6	(1)	75.9	10.442	−0.016	65.5	IRw	20.7	0.3	1.1×10^{4}	1.6×10^{3}	0.40
AGAL010.472+00.027	8.6	(1)	67.6	10.472	+0.028	55.1	HII	30.5	2.4	4.6×10^{5}	1.0×10^{4}	0.22
AGAL010.624−00.384	5.0	(1)	−2.9	10.623	−0.382	65.0	HII	34.5	3.6	4.2×10^{5}	3.7×10^{3}	0.42
AGAL012.804−00.199	2.4	(28)	36.2	12.805	−0.197	84.4	HII	35.1	2.3	2.4×10^{5}	1.8×10^{3}	0.78
AGAL013.178+00.059	2.4	(25)	50.4	13.176	+0.062	87.6	70w	24.2	0.8	8.3×10^{3}	3.6×10^{2}	0.96
AGAL013.658−00.599	4.5	(22)	48.4	13.656	−0.596	67.0	IRb	27.4	1.3	2.0×10^{4}	5.6×10^{2}	0.53
AGAL014.114−00.574	2.6	(3)	20.8	14.112	−0.572	81.0	IRw	22.4	0.8	3.1×10^{3}	3.5×10^{2}	0.65
AGAL014.194−00.194	3.9	(3)	39.2	14.194	−0.191	72.0	IRw	18.2	0.6	2.7×10^{3}	8.2×10^{2}	0.50
AGAL014.492−00.139	3.9	(3)	39.5	14.491	−0.137	89.3	70w	12.4	0.4	7.5×10^{2}	1.9×10^{3}	0.55
AGAL014.632−00.577	1.8	(27)	18.5	14.631	−0.576	83.5	IRw	22.5	0.4	2.7×10^{3}	2.5×10^{2}	0.84

Notes: The Columns are as follows: Name: the ATLASGAL catalog source name. d: distance. $d_{\rm ref}$ Distance reference (see list of references below table). $V_{\rm lsr}$: source velocity. $l_{\rm app}$: Galactic longitude of aperture center. $b_{\rm app}$: Galactic latitude of aperture center. $D_{\rm app}$: aperture diameter. Class: class of the source (HII: HII region, IRb: mid-infrared bright, 24d: mid-infrared weak (c: confused within the aperture), 70d: 70 μm weak). T: Dust temperature ΔT: Error of the dust temperature. $L_{\rm bol}$: Bolometric luminosity. $M_{\rm clump}$: Clump mass. $\alpha_{\rm vir}$: virial parameter. All data (including fluxes) will be available in electronic form on the ATLASGAL website (`http://atlasgal.mpifr-bonn.mpg.de/top100`) and the Strasbourg astronomical Data Center (CDS).

Distance references: (1): Sanna et al. (2014); (2): Zhang et al. (2014); (3): Giannetti et al. (2014); (4): Zhang et al. (2013); (5): Brunthaler et al. (2009); (6): Giannetti et al. (2015); (7): Giannetti et al. (2014); (8): Sato et al. (2014); (9): Xu et al. (2011); (10): Sato et al. (2010); (11): Urquhart et al. (2012); (13): Moisés et al. (2011); (14): Busfield et al. (2006); (15): Snell et al. (1990); (16): Davies et al. (2012); (17): Tangent Point; (18): Roman-Duval et al. (2009); (19): Green & McClure-Griffiths (2011); (20): Kurayama et al. (2011); (21): Zhang et al. (2009); (22): Wienen et al. (2015); (23): Urquhart et al. (2014a); (24): Xu et al. (2009); (25): Immer et al. (2013); (26): Caswell et al. (1975); (27): Wu et al. (2014); (28): Immer et al. (2012).

Table 3.2: Overview of the different classes and their parameters. Given are the mean, median, minimum, maximum, standard deviation, and standard error for each parameter.

Class/Parameter	Mean	Median	Min	Max	Standard deviation	Standard error
70 μm weak						
$T_{\rm dust}/{\rm K}$	16.4	16.9	10.7	24.24	3.35	0.8
$L_{\rm bol}/{\rm L}_\odot$	3.2×10^{3}	2.2×10^{3}	4.3×10^{2}	9.1×10^{3}	2.9×10^{3}	7.3×10^{2}
$M_{\rm env}/{\rm M}_\odot$	2.1×10^{3}	1.3×10^{3}	1.2×10^{2}	1.0×10^{4}	2.6×10^{3}	6.4×10^{2}
$L_{\rm bol}/M_{\rm env}\cdot{\rm L}_\odot/{\rm M}_\odot$	3.4	2.6	0.2	22.6	5.1	1.3
$r/{\rm pc}$	1.1	1.0	0.4	2.74	0.63	0.2
$N_{\rm H_2}/{\rm cm}^{-2}$	5.6×10^{22}	4.8×10^{22}	2.4×10^{22}	1.3×10^{23}	2.7×10^{22}	6.8×10^{21}
Mid-IR weak						
$T_{\rm dust}/{\rm K}$	19.9	21.4	11.7	26.18	4.26	0.7
$L_{\rm bol}/{\rm L}_\odot$	2.2×10^{4}	5.7×10^{3}	5.7×10^{1}	2.2×10^{5}	4.1×10^{4}	7.1×10^{3}
$M_{\rm env}/{\rm M}_\odot$	2.2×10^{3}	1.3×10^{3}	1.8×10^{1}	1.1×10^{4}	2.5×10^{3}	4.4×10^{2}
$L_{\rm bol}/M_{\rm env}\cdot{\rm L}_\odot/{\rm M}_\odot$	8.3	7.2	0.3	25.7	7.3	1.3
$r/{\rm pc}$	1.0	0.7	0.2	2.49	0.64	0.1
$N_{\rm H_2}/{\rm cm}^{-2}$	1.1×10^{23}	7.6×10^{22}	3.7×10^{22}	7.6×10^{23}	1.3×10^{23}	2.3×10^{22}
Mid-IR bright						
$T_{\rm dust}/{\rm K}$	28.1	28.2	21.9	34.53	3.65	0.6
$L_{\rm bol}/{\rm L}_\odot$	5.0×10^{4}	2.2×10^{4}	9.9×10^{2}	2.5×10^{5}	5.4×10^{4}	9.1×10^{3}
$M_{\rm env}/{\rm M}_\odot$	1.5×10^{3}	6.0×10^{2}	1.8×10^{1}	9.1×10^{3}	2.3×10^{3}	3.8×10^{2}
$L_{\rm bol}/M_{\rm env}\cdot{\rm L}_\odot/{\rm M}_\odot$	51.2	37.6	7.5	150.0	38.1	6.4
$r/{\rm pc}$	0.6	0.6	0.2	2.45	0.41	0.1
$N_{\rm H_2}/{\rm cm}^{-2}$	1.7×10^{23}	7.4×10^{22}	3.2×10^{22}	7.8×10^{23}	1.8×10^{23}	3.0×10^{22}
HII regions						
$T_{\rm dust}/{\rm K}$	31.7	31.8	22.8	41.12	3.97	0.8
$L_{\rm bol}/{\rm L}_\odot$	4.6×10^{5}	2.0×10^{5}	3.0×10^{3}	3.8×10^{6}	7.7×10^{5}	1.5×10^{5}
$M_{\rm env}/{\rm M}_\odot$	6.0×10^{3}	2.1×10^{3}	2.8×10^{2}	4.3×10^{4}	9.0×10^{3}	1.8×10^{3}
$L_{\rm bol}/M_{\rm env}\cdot{\rm L}_\odot/{\rm M}_\odot$	86.7	75.5	10.8	358.8	67.4	13.5
$r/{\rm pc}$	0.8	0.7	0.2	1.89	0.47	0.1
$N_{\rm H_2}/{\rm cm}^{-2}$	3.6×10^{23}	2.6×10^{23}	1.3×10^{23}	1.1×10^{24}	2.1×10^{23}	4.2×10^{22}
all						
$T_{\rm dust}/{\rm K}$	24.7	24.7	10.7	41.12	6.85	0.7
$L_{\rm bol}/{\rm L}_\odot$	1.3×10^{5}	1.6×10^{4}	5.7×10^{1}	3.8×10^{6}	4.1×10^{5}	3.9×10^{4}
$M_{\rm env}/{\rm M}_\odot$	2.8×10^{3}	1.2×10^{3}	1.8×10^{1}	4.3×10^{4}	5.1×10^{3}	4.9×10^{2}
$L_{\rm bol}/M_{\rm env}\cdot{\rm L}_\odot/{\rm M}_\odot$	39.7	22.5	0.2	358.8	50.7	4.8
$r/{\rm pc}$	0.9	0.7	0.2	2.74	0.56	0.1
$N_{\rm H_2}/{\rm cm}^{-2}$	1.8×10^{23}	8.6×10^{22}	2.4×10^{22}	1.1×10^{24}	1.9×10^{23}	1.8×10^{22}

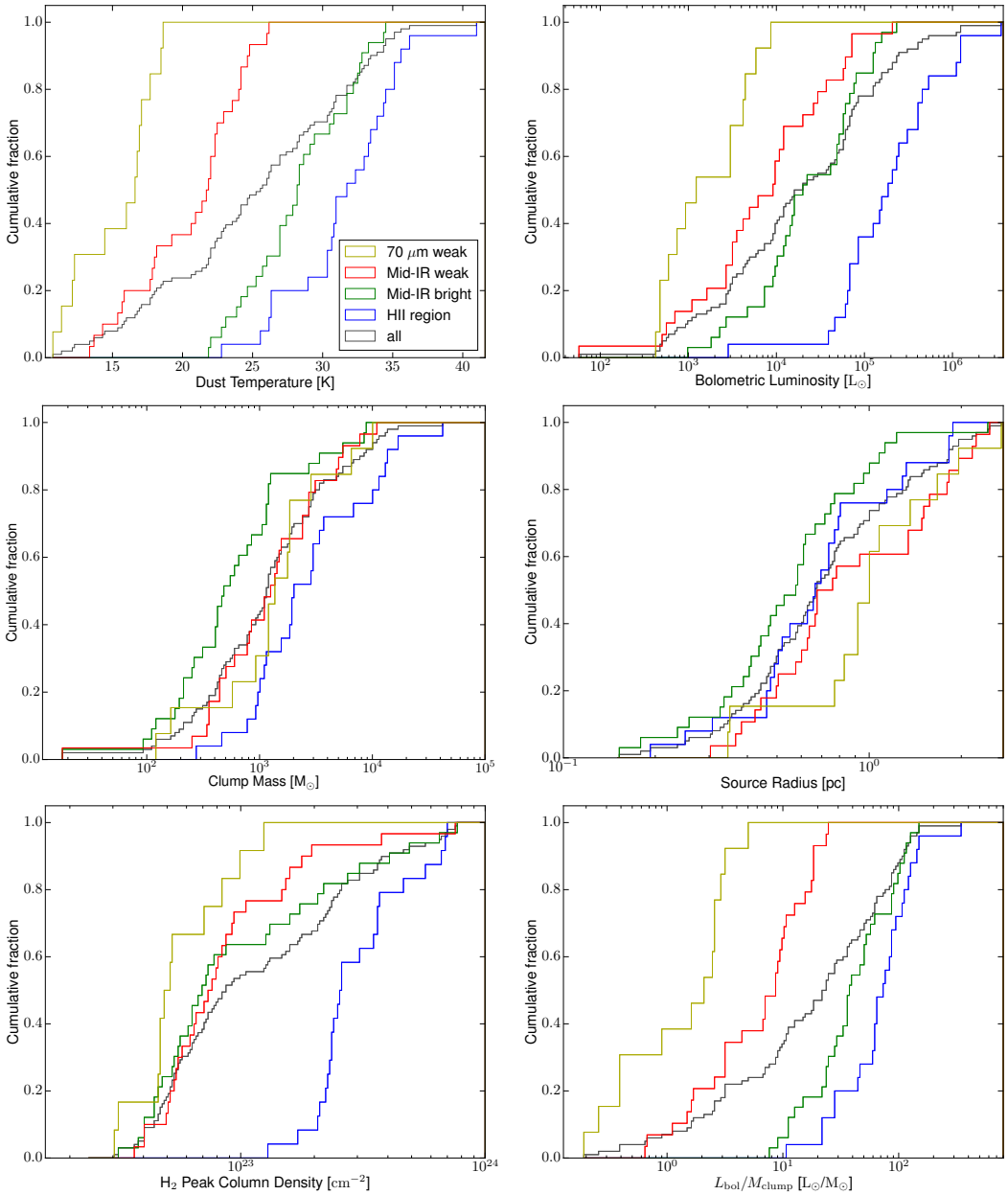

Figure 3.8: Cumulative distribution plots showing the range of values for the derived parameters for the whole sample (grey curve) and the four evolutionary sub-samples (see legend for colours).

As can be seen from the cumulative histogram in Fig. 3.8 (upper left panel), the dust temperature increases with the evolutionary stage and the different classes (and hence evolutionary stages) are well separated with regard to the dust temperature. This is confirmed by Anderson-Darling tests yielding p-values lower than 2.7×10^{-3} for all classes, rejecting the null hypothesis that these are drawn from the same distribution at the 3σ significance level.

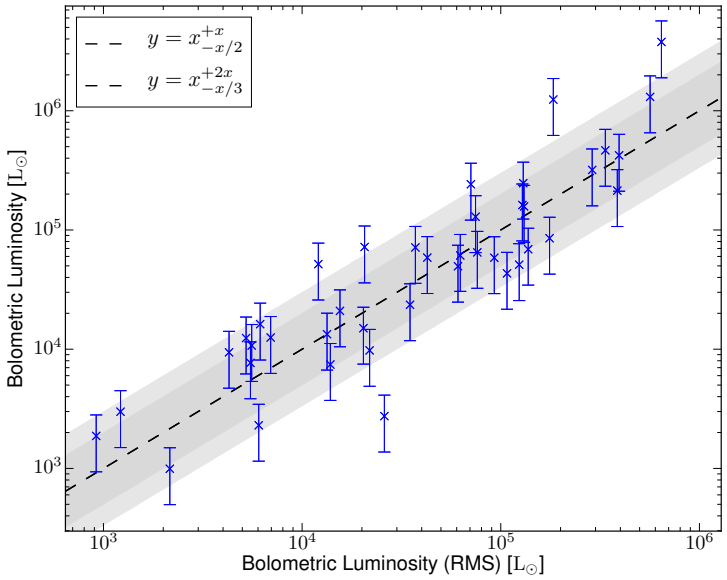

Figure 3.9: Comparison of our luminosities to those of Urquhart et al. (2014b) for sources common in both studies. The gray shaded areas indicate the area of an agreement within a factor of two (dark) and three (light). Most of the luminosities agree within a factor of three, showing that our simplified two-component model is sufficient to get an estimate for the luminosity.

To estimate the bolometric luminosities $L_{\rm bol}$ for each source, we combine the distance and integrated flux determined from the fitted SED model using the equation

$$L_{\rm bol} = 4\pi d^2 \int S_\lambda \, {\rm d}\lambda, \tag{3.1}$$

where d is the distance to the source (Sect. 3.3.2) and $\int S_\lambda \, {\rm d}\lambda$ is the integrated flux. The bolometric luminosities for the whole sample range from 57 $L_\odot$ for the least luminous source to 3.8×10^6 $L_\odot$ for the most luminous HII region, with a mean value of 1.3×10^5 $L_\odot$ and a median value of 1.5×10^4 $L_\odot$. The cumulative distribution function of the luminosities shows that they increase with the evolutionary stage yielding p-values $< 2.4 \times 10^{-5}$ for the Anderson-Darling test. However, these tests reveal no significant difference between the mid-infrared weak and mid-infrared bright samples (p-value = 1.2×10^{-2}) as well as between the mid-infrared weak and the 70 μm weak sources (p-value = 5.6×10^{-3}).

To verify that the extraction of the photometry and the use of a relatively simple two-component model to fit the SED produces reliable results, we compare our derived luminosities with those reported for a subsample of the same sources reported by the RMS team (Urquhart et al. 2014b). This other research has used fluxes drawn from the Hi-GAL point source catalog (Molinari et al. 2016), and the more complex radiative transfer models determined by Whitney et al. (2005) and the fitting tool developed by Robitaille et al. (2007). In Figure 3.9 we show this comparison of the bolometric luminosities for 41 matching sources

of the RMS sample. It is clear from this plot that there is good agreement between these two very different methods.

3.5.2 Clump mass, size, and column density

To estimate the masses of the sources we followed the procedure of Hildebrand (1983) for an optically thin emission and a single temperature, as the derived optical depth at 870 μm is $\tau_{870} \ll 1$ for all sources:

$$M_{\rm clump} = \frac{d^2 S_{870} R}{B_{870}(T_{\rm d})\,\kappa_{870}}, \tag{3.2}$$

where d is the distance to the cloud, S_{870} is the integrated 870 μm flux density obtained from the aperture photometry, R is the gas-to-dust ratio assumed to be 100, $B_{870}(T_{\rm d})$ is the intensity of the blackbody at 870 μm at the dust envelope temperature $T_{\rm d}$, and $\kappa_{870} = 1.85\,{\rm cm^2 g^{-1}}$ is the dust opacity at 870 μm calculated as the average of all dust models from Ossenkopf & Henning (1994) for the dust emissivity index of 1.75 that we use for the fitting of the SEDs.

The derived clump masses range from 18 $M_\odot$ up to 4.3×10^4 $M_\odot$, with a mean value of 2.8×10^3 $M_\odot$ and a median value of 1.2×10^3 $M_\odot$ for the whole sample. Two sources are found to have comparatively low masses (AGAL316.641−00.087 and AGAL353.066+00.452), making them unlikely to form any massive stars. The mass cumulative distribution plot shown in Figure 3.8 (mid-left panel) reveals little variation between the different classes and is therefore relatively independent of the evolutionary phase. This is confirmed by Anderson-Darling tests with only the mid-infrared bright and HII regions yielding a p-value of 1.0×10^{-4} making them unlikely to be drawn from the same distribution. We note that this difference is likely to be an effect of the dust temperatures being lower limits for the compact HII regions (see Section 3.5.1) and hence the envelope masses being upper limits.

The linear size of a source (i.e., its radius r) in pc can be calculated from the distance D in pc and the deconvolved source size $\theta_{\rm deconv}$ as

$$r = d \cdot \tan(\theta_{\rm deconv}/2), \tag{3.3}$$

with the deconvolved size of the source being calculated as

$$\theta_{\rm deconv} = \sqrt{{\rm D}_{\rm ap}^2 - \theta_{\rm beam}^2}, \tag{3.4}$$

where $\rm D_{ap}$ is the source size as used for the aperture and $\theta_{\rm beam}$ is the FWHM size of the beam (i.e., 19.2″). The cumulative distribution of the linear source size is presented in the middle right panel of Fig. 3.8, with a mean value of 0.9 pc and a median value of 0.7 pc over all classes. We find mostly no significant differences between the different evolutionary classes, with Anderson-Darling tests all yielding p-values > 0.003, except between the mid-infrared bright and the 70 μm weak sources (p-value $= 2.6 \times 10^{-3}$).

We also calculate the beam averaged column density according to Schuller et al. (2009), assuming the dust emission at 870 μm is optically thin:

$$N_{\mathrm{H_2}} = \frac{F_{870} R}{B_{870}(T_{\mathrm{d}})\, \Omega_{\mathrm{app}}\, \kappa_{870}\, \mu_{\mathrm{H_2}}\, m_{\mathrm{H}}}, \tag{3.5}$$

where F_{870} being the peak flux density, the beam solid angle Ω_{app}, and $\mu_{\mathrm{H_2}} = 2.8$ as the mean molecular weight of the interstellar medium with respect to a hydrogen molecule according to Kauffmann et al. (2008), and m_{H} the mass of a hydrogen atom. The other parameters are as previously defined.

In Fig. 3.8 (lower left panel) we show the histogram of the beam averaged peak column densities. The mean column density increases from $2.4 \times 10^{22}\,\mathrm{cm^{-2}}$ for the 70 μm weak sources to column densities in excess of $10^{24}\,\mathrm{cm^{-2}}$ for the HII regions. This is to be expected, as the clumps increase their density in the process of collapse. We note that the class of compact HII regions is well distinguished from the other classes, being confirmed by Anderson-Darling tests (p-values $< 2.4 \times 10^{-5}$). We point out that the column densities are effected by the dust temperatures being lower limits for the compact HII regions as discussed in section 3.5.1, hence rendering the column densities upper limits. Furthermore, this nicely shows that the young HII regions have not dispersed the envelope significantly yet, as we would expect for the sources being selected to be the brightest in ATLASGAL, hence making them the densest phase before dispersing the dust envelopes. For the other classes the null-hypothesis of the samples being drawn from the same distribution cannot be rejected with p-values $> 1.1 \times 10^{-2}$. However, taking a closer look at the cumulative distribution of the column density in Fig. 3.8 (lower left plot) and taking into account the small number of only 16 source of the 70 μm weak sample, we speculate that this subclass might be well distinguishable for a larger sample.

3.6 Discussion

3.6.1 Comparison with massive-star formation relations

In Figure 3.10 we present the mass-size relation for the sample. According to Kauffmann et al. (2010a), a lower limit for high-mass star formation is given by $M(r) \geq 580\,\mathrm{M_\odot} \cdot (r/\mathrm{pc})^{1.33}$ when reducing the mass coefficient by a factor of 1.5 from 870 to 580 to match with the dust absorption coefficient used in the present paper. Taking this threshold as the lower limit for massive-star formation, we find that 93 (i.e., 85%) of our sources have the potential to form at least one massive star. Similarly assuming the threshold found by Urquhart et al. (2014c), indicating that sources with surface densities above $0.05\,\mathrm{g\,cm^{-2}}$ can efficiently form high-mass stars, up to 99 sources (i.e., 98% of the sources with good SEDs and classification) have already formed at least one high-mass star or are likely to do so in the future.

To estimate the stability of the clumps, we calculate the virial parameter for the 102 sources of Giannetti et al. (2014), but correct for the revised distances d. Revising the distances affects the linear source sizes r_{FWHM} for the regions for which the velocity dispersion was measured (i.e., approximately the FWHM of the source). We calculate the virial parameter according to Bertoldi & McKee (1992):

$$\alpha_{\mathrm{vir}} = \frac{5}{G} \cdot \left(\frac{\Delta V}{2\sqrt{2\ln 2}} \right)^2 \cdot r_{\mathrm{FWHM}} \cdot M_{\mathrm{clump}}^{-1}, \tag{3.6}$$

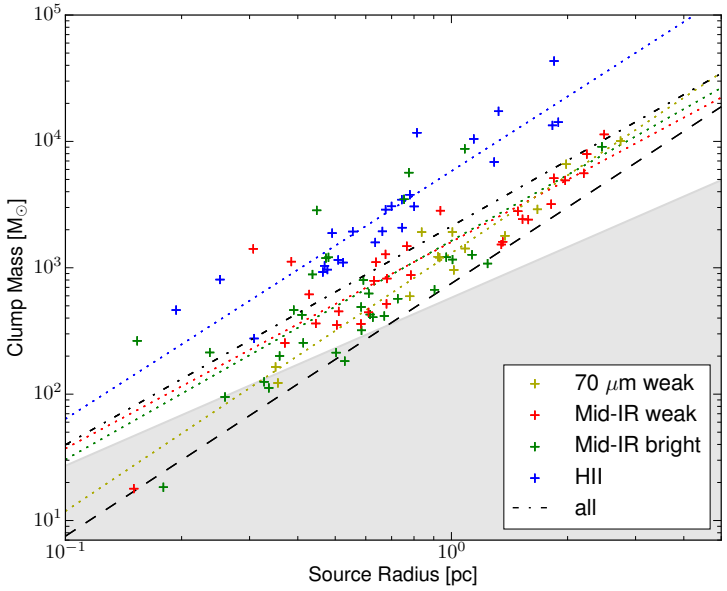

Figure 3.10: Mass-size relationship of the ATLASGAL Top100. The lower right gray shaded area highlights the region where it is unlikely that high-mass stars are formed according to Kauffmann et al. (2010a) and the black dashed line indicates a surface density of 0.05 g cm^{-2} determined as the lower limit for efficient massive-star formation by Urquhart et al. (2014c). The slopes of the linear log-log fits of all classes agree with each other within the margin of error of the fitted power laws.

where we adopted the C^{17}O (3–2) linewidth ΔV in km/s from Giannetti et al. (2014), G the gravitaional constant and $M_{\rm clump}$ the clump mass estimated from the flux given by Csengeri et al. (2014) using Equation 3.2. Here the linewidth and the envelope mass are estimated using the FWHM source sizes. The result is shown in Figure 3.11.

In general, we see a similar anti-correlation of the clump mass with the virial parameter as reported in other works (e.g., Kauffmann et al. 2013, Urquhart et al. 2014c, Giannetti et al. 2014), indicating that stability of clumps decreases as their mass increases. Fitting a power law to the data for all classes, we find the trend of all classes to be very similar to each other, with a general slope of $s = -0.43 \pm 0.04$ for the whole sample (compare Fig. 3.11).

Kauffmann et al. (2013) adopted a critical value of $\alpha_{\rm crit} = 2$ for a Bonnor-Ebert sphere (Bonnor 1955) not being supported by a magnetic field. Under this assumption a clump is likely to be unstable if $\alpha_{\rm vir} < 2$. From this we conclude that at least 99 sources (i.e., 97%) are likely to be unstable.

For the whole sample only three sources show a virial parameter of $\alpha_{\rm vir} > 2$ (AGAL316.641−00.087, AGAL338.066+00.044, and AGAL353.066+00.452) and are therefore unlikely to be collapsing, if external pressure does not confine them. Two of these sources (AGAL316.641−00.087 and AGAL353.066+00.452) with a virial parameter of $\alpha_{\rm vir} \approx 5.4$ and 2.3, respectively, were found to have masses lower than 19 M$_\odot$ making them unlikely to form a massive star.

In case of a magnetic field being present, Bertoldi & McKee (1992) showed that with

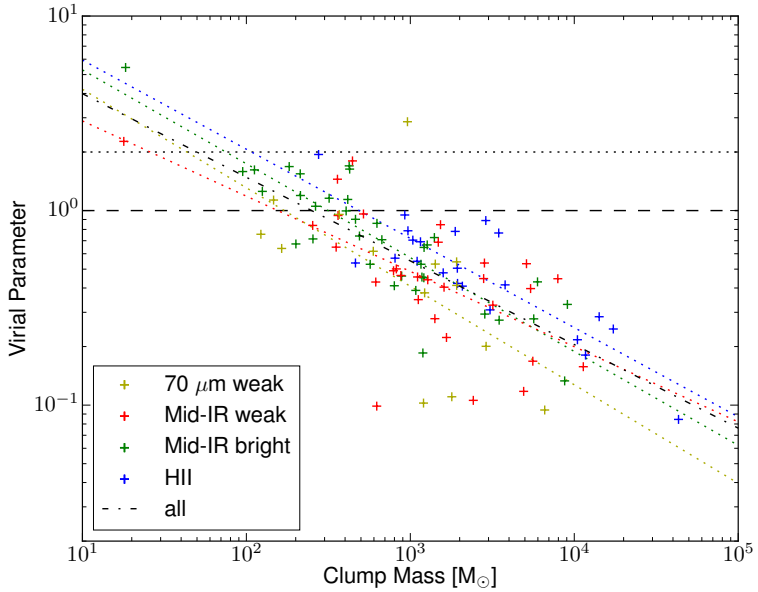

Figure 3.11: Clump mass versus virial parameter $\alpha_{\rm vir}$. The dashed and dotted lines represent $M_{\rm vir} = M_\odot$ and $M_{\rm vir} = 2M_\odot$, respectively. Sources below these lines are likely to be unstable and hence collapsing with and without a magnetic field being present (represented by the dashed and dotted lines, respectively).

the magnetic field and kinetic support being equal, the critical value of the virial parameter is lower ($\alpha_{\rm crit} = 1$). Taking this lower critical parameter as the threshold for collapse, we find that 84 of the sources (i.e., 82%) are gravitationally unstable and in the absence of strong magnetic fields are likely to be collapsing.

To further investigate the minimum magnetic field strength needed to support the clumps against gravitational collapse, we follow the procedure of Kauffmann et al. (2013), calculating the critical field strength as

$$B_{\rm crit} = 81\,\mu{\rm G}\cdot\frac{M_\Phi}{M_{\rm BE}}\left(\frac{\Delta V}{2\sqrt{2\ln 2}}\right)^2\frac{1}{r_{\rm FWHM}}, \tag{3.7}$$

where we substitute

$$\frac{M_\Phi}{M_{\rm BE}} = \frac{2}{\alpha_{\rm vir}} - 1 \tag{3.8}$$

as calculated from the virial parameter $\alpha_{\rm vir}$. We find the median critical field strength to range from 0.8 mG for the 70 μm weak class up to 6.2 mG for the compact HII regions. Crutcher (2012) proposes a density-dependant upper limit for the magnetic field strength in a molecular cloud of

$$B_{\rm max} = 10\,\mu{\rm G}\left(\frac{n_{\rm H_2}}{150\,{\rm cm}^{-3}}\right)^{0.65}, \tag{3.9}$$

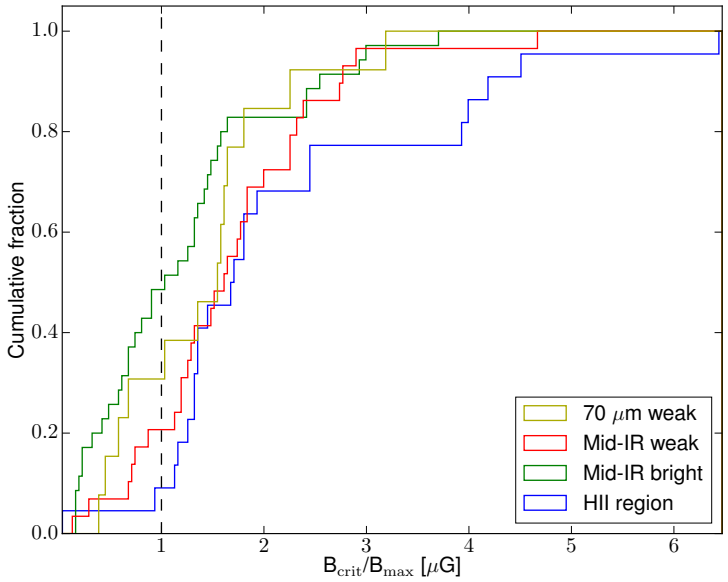

Figure 3.12: Ratio of the minimum critical magnetic field strength needed to stabilize our sources $B_{\rm crit}$ to the upper limit magnetic field strength $B_{\rm max}$ for a cloud as suggested by Crutcher (2012). Sources right of the dashed line ($B_{\rm crit} = B_{\rm max}$) cannot build a magnetic field strong enough to prevent the clumps from collapsing.

implying that if $B_{\rm crit} > B_{\rm max}$ no existing magnetic field can stabilize the cloud. To apply our data, we further transform Equation 3.9 as shown by Kauffmann et al. (2013; C.4) into

$$B_{\rm max} = 336\,\mu{\rm G}\left(\frac{M_{\rm clump}}{10\,{\rm M}_\odot}\right)^{0.65}\left(\frac{r_{\rm FWHM}}{0.1\,{\rm pc}}\right)^{-1.95}. \tag{3.10}$$

Comparing $B_{\rm crit}$ to $B_{\rm max}$ (see Figure 3.12) we find the minimum magnetic field strength needed to stabilize our sources to be higher than the upper limit suggested by Crutcher (2012) for 69% of our sample. From this we conclude that the majority of our sources can either not be stabilized or would need extreme magnetic fields to support them against gravitational collapse.

Our analysis has revealed that there is no significant difference in the global properties of the sample, with similar mass and size distributions found for all of the sub-samples. It is likely therefore, that they had similar initial physical conditions. We have also found that the majority of the sample satisfies the mass-size threshold criterion required for massive-star formation and that they are unstable to gravity and likely to collapse in the absence of a strong magnetic field, clearly confirming that the sources of the ATLASGAL Top100 are a sample of massive-star forming regions.

3.6.2 Evolutionary sequence of the sample

The analysis presented in the previous subsection found little difference in the masses and stability of the various subsamples and revealed them all to be good candidates for massive-star

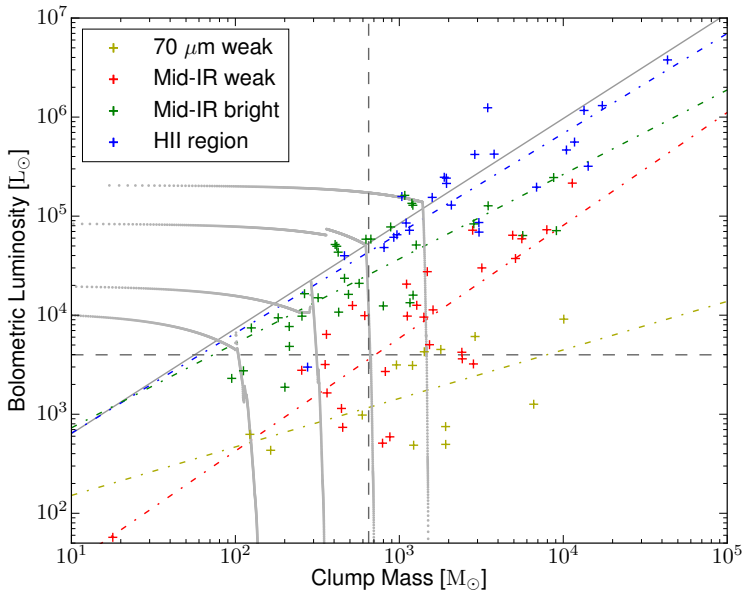

Figure 3.13: Mass-luminosity distribution of the whole sample. The gray tracks are evolutionary models used by Molinari et al. (2008). The dash-dotted colored lines show a linear fit to the corresponding class of sources. The horizontal dashed line shows the luminosity of a B1.5 star as calculated by Mottram et al. (2011a; Table 1), whereas the vertical dashed line shows the threshold of 650 $M_\odot$ beyond which clumps are likely to host massive dense clumps or high-mass protostars (Csengeri et al. 2014).

formation. The results obtained from the SED fitting show trends for increasing temperatures and bolometric luminosity that are consistent with the proposed evolutionary sequence. In this subsection we will extend this analysis in order to robustly test the evolutionary scheme of the ATLASGAL Top100.

Following the procedure of Molinari et al. (2008), we compare here the clump mass versus the bolometric luminosity (Figure 3.13). In such a plot it is expected that clumps first gain luminosity, moving upward in the plot until the embedded stars reach the zero age main sequence (ZAMS, solid diagonal line) and then lose mass, as the dust envelope gets dispersed, moving leftward in the plot (compare with Molinari et al. 2008). It can be seen that the earlier evolutionary stages (i.e., the 70 μm and mid-infrared weak sources) follow this trend clearly toward the zero age main sequence. The later stages (i.e., the mid-infrared bright and HII regions) are not as well separated, making it difficult to distinguish their evolutionary stage from dust emission alone, consistent with the findings of Urquhart et al. (2014c).

Fitting a power law to the data for all four classes, we find that for the HII regions, mid-infrared bright and weak sources the trend is very similar, yielding slopes of $s = 1.01 \pm 0.13$, $s = 0.85 \pm 0.13$ and $s = 1.14 \pm 0.16$, respectively. These values are lower than those reported by Molinari et al. (2008) and Urquhart et al. (2014c), but still in agreement within 3σ. Only the sample of 70 μm weak sources yields a slightly lower slope of $s = 0.49 \pm 0.24$, which, however, is still in agreement with the slopes of the other samples. The low number of sources in this subsample could result in the fit being significantly affected by incomplete sampling

Table 3.3: Overview of different physical parameters and whether or not the Anderson-Darling test is able to distinguish the different classes of sources.

Parameter	HII Mid-IR bright	HII Mid-IR quiet	HII 70 μm weak	Mid-IR bright Mid-IR quiet	Mid-IR bright 70 μm weak	Mid-IR quiet 70 μm weak
T	+	+	+	+	+	+
$L_{\rm bol}$	+	+	+	-	+	-
$M_{\rm env}$	+	-	-	-	-	-
$L_{\rm bol}/M_{\rm env}$	-	+	+	+	+	+
r	-	-	-	-	+	-
$N_{\rm H_2}$	+	+	+	-	-	-

and/or outliers. Nevertheless, the positions of the subsamples seen in the mass-luminosity plot are consistent with the expected evolutionary tracks and nicely illustrate that our sample covers a wide range of evolutionary stages.

Given that early B-type stars have a minimum luminosity of $\sim 10^{3.6}\,L_\odot$ (Mottram et al. 2011a; Table 1), we can see from the mass-luminosity distribution (Fig. 3.13) that a large proportion (80 sources, i.e. 73%) of our sample already has luminosities in excess of this threshold. As the luminosity of a cluster is dominated by the most massive star, it is likely that these clumps have already formed at least one high-mass star. Csengeri et al. (2014) take a mass limit of $650\,M_\odot$ for clumps likely to form high-mass protostars, and 73 sources (i.e., 66%) are found above this limit. Taking into account both aforementioned thresholds ($L_{\rm bol} > 10^{3.6}\,L_\odot$ and $M_{\rm clump} > 650\,M_\odot$,), it is therefore likely that at least 93 sources (i.e., 85% of our sample) have either already formed or will likely go on to form a cluster consisting of at least one massive star in the future.

To further investigate the evolutionary stage of the sources, we present the cumulative histogram of the bolometric luminosity to clump mass ratio in Fig. 3.8 (lower right panel). This ratio is a crude proxy for the evolutionary stage and we would therefore expect this to increase as the embedded objects evolve and become more luminous. This plot clearly shows a trend for increasing $L_{\rm bol}/M_{\rm clump}$ ratio with evolution, increasing continuously from a minimum ratio of 0.2 for the 70 μm weak sources up to a ratio of 358.8 for the HII regions. Performing Anderson-Darling tests, we find that almost all evolutionary stages are clearly distinct from each other, yielding p-values $< 3.6 \times 10^{-4}$, rejecting the null-hypothesis of the samples being drawn from the same distribution at the 3σ significance level. We only find the mid-infrared bright and HII region phases to be similar enough, as to be drawn from the same distribution with a p-value of 2.6×10^{-2}.

3.6.3 Dust continuum emission as evolutionary stage indicator

As we have seen in the previous sections, the physical parameters and derived quantities obtained from dust continuum emission (namely temperature, bolometric luminosity, clump mass, $L_{\rm bol}/M_{\rm env}$, linear source size, or column density) are differently well suited to distinguish between the evolutionary phases of massive-star formation.

In Table 3.3 we give an overview of whether or not the Anderson-Darling tests are able to distinguish two evolutionary stages of our sample using the given parameter. We note that except for the temperature no single parameter is suited to discriminate between all evolutionary stages alone. However, all classes can be well distinguished by a combination of at least two different parameters and the evolutionary sequence is well reflected in the physical parameters obtained from the dust emission. But although there are clear trends seen in the distributions of some of the derived parameters, there is also significant overlap between them (compare Table 3.2). In turn this makes it impossible to assign a given source to a single evolutionary stage just from the dust parameters and further criteria are required.

The optical depth might limit the usability of the dust emission in extreme cases, where the emission being optically thick at far-infrared wavelengths would underestimate the fluxes of the SED. Similarly the estimated dust temperature might be underestimated for sources for which the emission longward of $\lambda > 21\,\mu$m becomes optically thick (Elia & Pezzuto 2016). Both effects likely play an important role for the more evolved sources, making the derived physical parameters less reliable for the densest and most evolved sources.

Comparison of extinction properties of low-mass and high-mass clouds and cores have shown that only modest extinctions are required for a core to manifest as infrared dark (Pillai 2016). In a forthcoming work, we show that at the distance of a few kpc, dust emission alone cannot reveal populations of low-mass protostars (Class 0 and higher) embedded within clouds and line observations are crucial in distinguishing such cores from those that are genuinely quiescent (Pillai et al. in prep.). This is further supported by recent analysis by Feng et al. (2016) and Tan (2016), who have reported a bipolar outflow of a high-mass protostar associated with a 70 μm dark source. As outflows are associated with ongoing star formation, this source as well as the the analysis presented by Pillai (2016) are good examples of the possible limitations of the dust classification when no source is detected at 70 μm.

Accordingly, the ATLASGAL team is investigating a wide range of molecular line tracers as well as different masers for their suitability as evolutionary stage indicators to supplement the rather rough discrimination obtained from the dust continuum parameters. An overview of these projects will be given in the next section.

3.6.4 Complementary molecular observations

Molecular lines can be used to independently derive and investigate the physical and chemical properties of the gas in star-forming regions. In the radio (centimeter to millimeter wavelengths) regime, extinction is in general negligible and it is therefore easier to see directly the effect of protostellar activity (e.g., outflows, gas warm-up and hot cores) in molecular lines. Here we discuss the effects of mechanical and thermal feedback as probed by different tracers available for the Top100 sample, synthesizing the results of various studies of methanol and water masers as well as thermal emission from high density molecular tracers in terms of temperature evolution and probes of star formation activity.

Thermal feedback: CO depletion as a function of evolution was investigated by Giannetti et al. (2014). The abundance of CO is correlated with the evolutionary stages in the low-mass regime (Caselli et al. 1998, Bacmann et al. 2002). In the Top100 we find the same trend:

Table 3.4: Association with Class II methanol and H_2O masers.

Class	Number[a] of sources	MMB assoc.	MMB ratio	HOPS assoc.	HOPS ratio
70 μm weak	16/10	1	0.06	1	0.10
Mid-IR weak	34/27	17	0.50	15	0.56
Mid-IR bright	36/17	28	0.78	14	0.82
HII region	25/17	20	0.80	11	0.65

[a] The first number gives the number of sources within the region covered by the MMB while the second number gives the number of sources covered by HOPS.

CO depletion decreases in more evolved clumps as a function of L/M, indirectly showing that the sources become warmer with time. The revised classification proposed here does not affect these earlier results. We also find that the $C^{17}O(3–2)$ linewidth used in Section 3.6.1 increases with evolutionary stage from a median value of 2.2 km s^{-1} for the 70 μm weak class to 5.3 km s^{-1} for the compact HII regions under the new classification, confirming the earlier results and further bolstering the evolutionary sequence presented here.

Acetonitrile (CH_3CN) and methyl acetylene (CH_3CCH) are reliable thermometers of the gas. Acetonitrile and methyl acetylene, as well as methanol, will be discussed in detail by Giannetti et al. (2017b), where preliminary results give further support for our revised classification scheme.

Furthermore, we searched for Class II methanol maser associations in the MMB survey (Urquhart et al. 2013a). Class II methanol masers are radiatively pumped and therefore trace the radiation field from the central object. We found associations for 66 clumps, with seven clumps being associated with two or more methanol masers. A detailed study of the properties of methanol-maser-associated clumps for the whole ATLASGAL survey is presented in Urquhart et al. (2013a), which includes 55 of the Top100 clumps. The remaining 12 clumps matched with MMB sources are new and have resulted from comparison with the final part of the MMB catalog recently published in Breen et al. (2015). The overall association rate between the Top100 and the MMB catalog is ∼63%, however, the association rate is significantly higher for the more evolved clump classifications as can be seen in Table 3.4. The association ratio is similar for the mid-infrared bright and compact HII region classes but drops to ∼50% for the mid-infrared weak sources and to close to zero for the 70 μm weak sources. We find ∼72% (i.e., 48/66) of all sources associated with a methanol maser to be either mid-infrared bright clumps or compact HII regions. The only 70 μm weak source with maser activity is AGAL013.178+00.059 (Fig. 3.14). This source is removed from the SED analysis as discussed in Section 3.5. AGAL013.178+00.059 is located near the edge of an evolved HII region and is likely being externally heated and undergoing compression on one side. The external heating has resulted in some extended 70 μm emission that has made a definitive classification more difficult. Although care needs to be taken in the interpretation of the association between this clump and the masers, it does suggest that star formation may already be underway in some of these 70 μm weak clumps. This is further supported by the

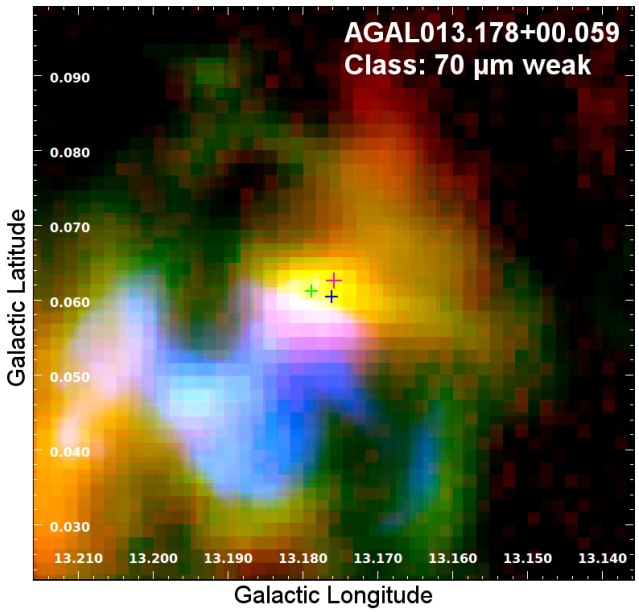

Figure 3.14: Three color image of the 70 μm weak source AGAL013.178+00.059. We note the strong heating from the south east. The magenta, green, and blue crosses mark the positions of the source peak, the associated methanol and water maser, respectively. Size: $\sim 3' \times 3'$; red: ATLASGAL 870 μm; green: PACS 160 μm; blue: PACS 70 μm.

fact that a water maser is detected in the source (see discussion below).

Gallaway et al. (2013) examined the mid-infrared emission towards a larger sample of 776 methanol masers and found a similar fraction associated with mid-infrared emission. This suggests that methanol masers are associated with more evolved stages where the embedded objects are already producing significant luminosity and have started to warm their local environments. This also ties in nicely with a recent study of outflows towards methanol masers (de Villiers et al. 2014; 2015) which found that the dynamical age of outflows associated with methanol masers are older than for the general population of molecular outflows reported in the literature.

Mechanical feedback: Standard tracers of outflow activity are, for example, high-velocity line-wings in CO and SiO lines, as well as water masers.

From the ATLASGAL Top100 sample, 36 sources lie in the Ist Galactic quadrant, and are part of the sources investigated by Csengeri et al. (2016). All of them are detected in the SiO(2–1) and (5–4) transitions except for two mid-infrared weak sources. Line-wings are detected altogether towards 21 sources, including three clumps which are dark at 70 μm, demonstrating that molecular lines can be a more sensitive probe of star formation activity than dust alone. In a forthcoming paper Navarete et al. will extend the analysis on the content of molecular outflows in the Top100 sample, using observations in the Mid-J CO lines to further test the classification scheme.

We have also searched for position coincidences with water masers identified by the H_2O Southern Galactic Plane Survey (HOPS; Walsh et al. 2011; 2014). This survey covers Galactic longitudes $300^\circ < \ell < 30^\circ$ and Galactic latitudes $|b| < 0.5^\circ$ and so only includes 71 of the Top100 sources. In Table 3.4 we give the number of sources, the number of these associated with water masers, and the fractional association rates for each evolutionary type. There is a clear trend for increasing frequency of association with water masers with the first three evolutionary stages. This is in agreement with the evolutionary scheme based on the dust analysis. Comparing the water maser association rates with the methanol maser association rates for the different stages, we find them to be similar for the earliest three stages, but the water maser association rate is noticeably lower for the more evolved HII region stage. As water masers can be collisionally excited and hence are an indicator for shocks and outflows, the H_2O maser found for AGAL013.178+00.059 (Figure 3.14) can either be associated with material ejection or with compression from the south east, making this an interesting source to investigate possibly in more detail.

To summarize, the results of the molecular line observations as well as the associations between Class II methanol and H_2O masers support the evolutionary classification scheme outlined in Sect. 2. In particular, the lack of Class II masers towards the 70 μm-dark sources points to the star formation associated with these clumps being in a very early evolutionary phase, which is supported by the SED analysis. Despite the limited sensitivity of the SED analysis to the distinct evolutionary phases, our comprehensive programme of follow-up molecular line observations will be essential to refine the scheme and derive the physical properties of each stage. The results of these follow-up observations will be fully discussed in a number of forthcoming papers (e.g., Navarete et al. (in prep.), Giannetti et al. (2017b), Urquhart et al. (in prep.)).

3.7 Summary

In this paper we characterize the properties of 110 massive-star forming regions that have been selected to cover important evolutionary stages in the formation of massive stars. This sample includes examples of the coldest pre-stellar stages through to the formation of the ultra-compact HII regions. Using multi-wavelength data, this sample has been classified into four distinct stages: 70 μm weak, mid-infrared weak, mid-infrared bright, and HII regions. Distances for the sources presented in this paper have been revised, incorporating the latest maser parallax measurements.

Exploiting the dust continuum SEDs from mid-infrared to submm wavelengths, we derived dust temperatures and integrated fluxes; these are subsequently used to estimate reliable bolometric luminosities, clump masses, and peak column densities for the whole sample. Comparing the physical properties of the clumps, we found no significant differences between the distances, clump masses, or physical sizes for the different evolutionary phases.

1. The SED analysis provided useful constraints for the dust temperature and integrated emission. We find the dust temperatures to increase from 11 K for the coldest sources to 41 K for the HII regions, with an average value of 24.7 K for the whole sample. A similar trend is seen in the mean bolometric luminosity increasing from 3.2×10^3 $L_\odot$ for

the 70 μm weak sample to 4.6×10^5 $L_\odot$ for the compact HII regions. The classification of the sample is further verified by the continuous increase in the bolometric luminosity to clump mass ratio from an average ratio of 3.4 for the youngest to 86.7 for the most evolved class, all of which is consistent with the proposed evolutionary scheme described in Sect. 2. Although the SED analysis reveals significant differences between the different classes, we also find that there is a large overlap between the different evolutionary phases and additional information is required to confirm and refine the evolutionary scheme.

2. We have found that the majority of the sample satisfy the size-mass criterion for massive-star formation and so have the potential to form massive stars in the future if not already currently doing so. Evaluating the clump stability we find that the vast majority are unstable against gravity and likely to be undergoing global collapse in the absence of significant magnetic support. It therefore seems likely that the majority of the sample will form a cluster that includes at least one massive star. Furthermore, the masses of some clumps exceed 4×10^4 $M_\odot$ and have bolometric luminosities in excess of 3×10^6 $L_\odot$ and are therefore likely to be forming the most massive, earliest O-type stars.

3. We also give an overview of complementary molecular line observations that are being conducted by the ATLASGAL team to classify the source in a more robust way. The association rates of methanol and water masers as well as molecular outflows reveals significant differences between the different phases. In addition thermal emission lines and SiO line profiles are used to discriminate the evolutionary stages. Examining a combination of these molecular line and continuum observation, we have found strong support for the proposed evolutionary scheme and verified that the ATLASGAL Top100 sample represents a statistically significant catalog of massive-star forming clumps covering a range of evolutionary phases from the coldest and youngest 70 μm weak to the most evolved clumps hosting HII regions still embedded in their natal environment.

Using well established standard methods we have investigated the full evolutionary sequence from the earliest pre-stellar to the latest embedded HII region phases on a well-selected sample of (almost) exclusively high-mass-star forming clumps drawn from an unbiased dust survey covering the whole inner Galaxy for the first time. Furthermore, as the properties of this sample have been determined in a consistent way and the majority ($\sim$70 %) is located within 5 kpc these sources are ideal for high resolution follow-up observations to investigate processes such as fragmentation, infall and outflows. This sample therefore provides a solid foundation for more detailed studies to investigate changes of the physical properties and kinematics of the gas through the process of massive-star formation in the future.

CHAPTER 4

The complete ATLASGAL sample

4.1 Introduction and Motivation

In this chapter we will be extending the previous analysis to the whole ATLASGAL sample. As explained in Chapter 1, ATLASGAL is a 870 μm continuum survey of the inner Galactic plane between $-80^\circ \leq \ell \leq 60^\circ$ (Schuller et al. 2009). From this unbiased survey, ~10,000 dust clumps were identified by the ATLASGAL compact source catalogue (CSC; Contreras et al. 2013, Urquhart et al. 2014a), allowing for a statistical analysis of the properties of dust clumps located throughout the inner part of the Milky Way.

This chapter is based on the paper "*ATLASGAL - Properties of a complete sample of Galactic clumps*" (Urquhart et al. 2018), where I was the second author. My main contributions were the measurement and analysis of ~1200 CO spectra (Sect. 4.2), yielding velocities for ~14% of the sample, significantly contributing to the completeness of the distance estimations. Furthermore I did the full photometry and SED analysis (Sect. 4.3), yielding photometric classifications and spectral energy distributions for the full sample, allowing to determine the evolutionary stage and physical properties, such as temperatures, luminosities, masses and column densities. Without these, the detailed conclusions drawn on star formation relations and clump evolution would not have been possible. For completeness I will also give a summary of the main results of the paper, as these will be the basis for our comparison of the inner and outer Galaxy in Chapter 6.

4.2 Velocities and distances

In order to determine physical properties such as bolometric luminosity and clump mass, distances are required. For the 8002 ATLASGAL sources located between $-60^\circ \leq \ell \leq -5^\circ$ and $5^\circ \leq \ell \leq 60^\circ$, the main author of Urquhart et al. (2018) was able to obtain distances to 6694 (84% of the sample) of them from the literature. In order to increase the completeness of the survey, we conducted line-of-sight velocity measurements to obtain distances to the remaining sources. Following the procedures described in Section 2.4.1, we obtained ^{13}CO(2–1) and C^{18}O(2–1) spectra for 1177 dust clumps between June and November 2016. Each source was observed in position-switching mode with an on-source integration time between 1 and 4 minutes at a velocity resolution of 0.1 km s^{-1} and an average precipitable water vapour column of PWV=2.0 $\pm$ 1.2 mm. A summary of the observational parameters can be found in Table 4.1.

We were unable to detect emission towards four sources (AGAL005.476−00.391, AGAL006.461−00.389, AGAL338.306−00.522, and AGAL354.814+00.121), and discarded the spectra for another eight sources as theses were contaminated in the off-position. We were

Table 4.1: Summary of the APEX observational parameters. *Taken from Urquhart et al. (2018).*

Parameter	Value
Galactic longitude range	$5^\circ \leq \lvert\ell\rvert \leq 60^\circ$
Galactic latitude range	$-1.54^\circ < b < 1.58^\circ$
Number of observations	1177
Number of usable spectra	1165
Receiver	SHeFI (APEX-1)
Frequencies	220.4 GHz, 219.6 GHz
Angular resolution	$30''$
Spectral resolution	$0.1\,\mathrm{km\,s^{-1}}$
Smoothed spectral resolution	$1\,\mathrm{km\,s^{-1}}$
Median noise (T_A^*)	$\sim$95 mK channel^{-1}
Median system temperatures (T_{sys})	$\sim$220 K
Integration time (on-source)	1-4 mins

therefore able to obtain usable spectra towards 1165 sources, from which we determined the velocity peaks most likely corresponding to the ATLASGAL clump, and finally determined the corresponding distances.

In general, the kinematic distances were obtained from the velocities using the same procedure as described in Section 2.4, but using the rotation curve from Reid et al. (2014). The distance ambiguity, faced inside the solar circle, was then broken by the co-authors of the paper in a multi-step approach, mainly inspecting HI spectra for self-absorption (Appendix B Urquhart et al. 2018).

4.2.1 Data reduction

Further following the procedures from Section 2.4.1, we extracted the spectra in a velocity range between $\pm 200\,\mathrm{km\,s^{-1}}$ of the rest frequency of each transition. Smoothed to a velocity resolution of $\sim 1\,\mathrm{km\,s^{-1}}$, an average noise level of $\sigma = 95 \pm 50$ mK was achieved, allowing us to search for peaks of emission to identify the major velocity components towards a given source.

In Fig. 4.1 we present three exemplary spectra in ^{13}CO(2–1) and C^{18}O(2–1) (offset by 1 K). In the top panel we show a spectrum representative of the majority of our sources, where a single emission peak allows us to assign a velocity to the corresponding dust clump without ambiguity. In the middle and lower panels we present a spectrum representative of about 40% of our sources, showing multiple emission peaks. In case the strongest peaks (integrated line intensity) overlap within $10\,\mathrm{km\,s^{-1}}$, the strongest component is assigned to the clump. When the peaks are more separated, the strongest component was chosen, if it was at least twice as strong as the second strongest component. In case the ^{13}CO peaks have similar strength, the optical depth (reflected by the ^{13}CO/C^{18}O ratio) was taken into account, selecting the peak with the lowest ratio, assuming it to have the highest column density and thus being

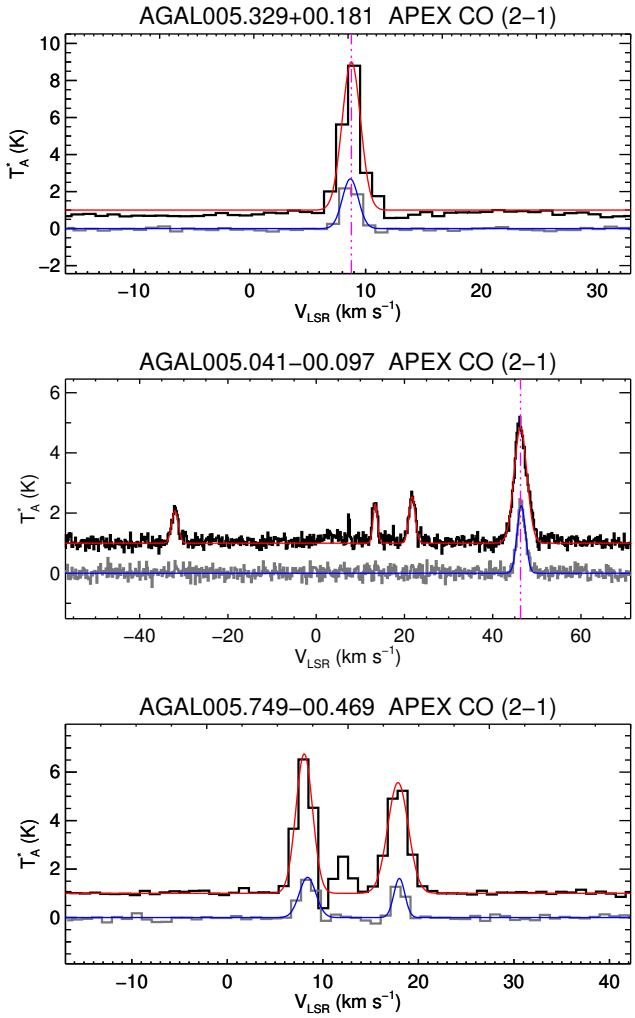

Figure 4.1: Example APEX CO (2–1) spectra towards three sources. The ^{13}CO spectra is offset from the C^{18}O spectra by 1 K and the fits are shown by the red and blue lines, respectively. The vertical dashed lines shown in the upper two panels indicates the preferred source velocity. The two components shown in the lower panel have comparable intensities and optical depths and so no velocity has been assigned to the source. *Taken from Urquhart et al. (2018).*

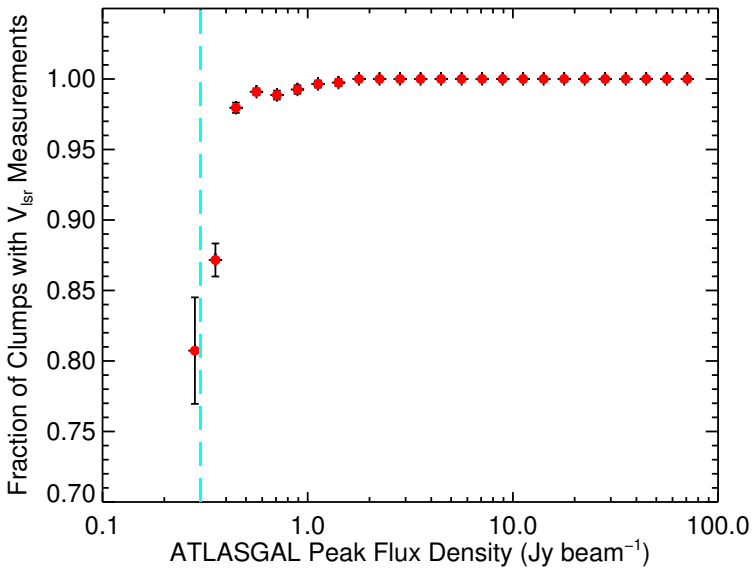

Figure 4.2: Plot of the ratio of sources with velocities as a function of their peak flux densities. The bin size for both plots is 0.1dex. The errors shown have been estimated using binomial statistics. *Taken from Urquhart et al. (2018).*

associated with the dust clump. However, no velocity is assigned in cases where multiple similarly strong emission peaks with similar ^{13}CO/C^{18}O ratios are found, as the contribution to the dust emission from each peak is not clear.

For the 1165 clumps with usable spectra we detected a total of 3142 ^{13}CO and 1271 C^{18}O components. A summary of all fitted components can be found in Table 4.2, also indicating the assigned components to the dust emission. In total, our observations at APEX enabled us to assign velocities to an additional 1115 clumps using the aforementioned criteria. For 50 sources we were unable to assign a velocity, as the spectra showed multiple emission features with similar intensities.

4.2.2 Completeness

With the observations described in the last sections, we were able to add velocities to another 1115 clumps, increasing the number of sources with a known distance from 6694 to at total of 7809 clumps. For the total of 8002 sources in the region between $5^\circ \leq \ell \leq 60^\circ$ and $300^\circ \leq \ell \leq 355^\circ$ (i.e. excluding the Galactic centre region), this means that the targeted CO(2–1) observations at APEX account for ∼14% of the distances of the full sample. In fact the observations increase the fraction of sources with a known velocity from ∼86% to almost 98%, greatly contributing to the completeness of the survey.

In Fig. 4.2 we present the fraction of clumps with a velocity measurement as a function of the ATLASGAL peak flux density to further investigate the completeness of our sample. As can be seen from the plot, we are complete for almost all sources above 0.5 Jy beam^{-1}.

The remaining 193 sources for which we were unable to assign a velocity turned out

Table 4.2: CO components detected by APEX. In this table we indicate the velocity assigned to the source by appending a ⋆ to the source name. We give the noise per channel of the ^{13}CO in Col. 2, however, the ^{13}CO and C^{18}O noise agree to within a few per cent. *Taken from Urquhart et al. (2018).*

		^{13}CO (2-1)				C^{18}O (2-1)				
ATLASGAL CSC name	RMS (mK)	V_{lsr} (km s^{-1})	Peak (K)	Width (km s^{-1})	Intensity (K km s^{-1})	V_{lsr} (km s^{-1})	Peak (K)	Width (km s^{-1})	Intensity (K km s^{-1})	Optical depth
AGAL005.001+00.086⋆	61	2.1	5.8	1.38	20.2	2.0	1.8	0.93	4.2	0.35
AGAL005.041−00.097⋆	118	46.3	3.8	1.53	14.4	46.5	2.1	1.04	5.5	0.82
AGAL005.049−00.192⋆	72	6.1	3.2	1.53	12.4	6.1	0.9	0.97	2.2	0.32
AGAL005.139−00.097⋆	76	44.1	5.0	1.50	18.9	44.2	1.9	1.07	5.1	0.47
AGAL005.184+00.159	168	182.1	1.0	1.26	3.1	...	...	...	...	...
AGAL005.192−00.284⋆	70	8.0	3.4	2.21	18.6	8.6	0.6	1.09	1.7	0.16
AGAL005.202−00.036⋆	68	0.6	4.8	1.99	23.7	0.6	1.4	1.78	6.1	0.32
AGAL005.329+00.181⋆	69	8.8	8.0	0.79	15.9	8.7	2.7	0.69	4.6	0.40
AGAL005.371+00.319⋆	61	18.7	5.7	1.51	21.4	18.7	1.7	1.31	5.6	0.35
AGAL005.387−00.551⋆	92	8.4	1.1	1.61	4.5	...	...	...	...	...
AGAL005.389−00.384	82	21.4	1.1	9.66	26.0	...	...	...	...	...
AGAL005.392−00.409⋆	164	140.8	1.1	7.93	22.8	...	...	...	...	...
AGAL005.399−00.237⋆	53	4.8	1.9	1.34	6.3	5.0	0.4	1.01	1.1	0.24
AGAL005.409−00.302⋆	60	14.2	4.6	0.61	7.1	...	...	...	...	...
AGAL005.437−00.314	74	22.5	1.1	1.35	3.7	22.2	0.4	1.00	1.0	0.43

Notes: Only a small portion of the data is provided here, the full table is available in electronic form at the CDS via anonymous ftp to cdsarc.u-strasbg.fr (130.79.125.5) or via http://cdsweb.u-strasbg.fr/cgi-bin/qcat?J/MNRAS/.

to show the weakest continuum emission of the sample. Inspection of the infrared to sub-millimetre maps revealed that many of these sources are located at the outer parts of larger regions and show a rather wispy structure. Although molecular emission is found for most of these sources, the spectra showed peaks with similar intensity, making it impossible to assign a definite velocity to the dust continuum emission. Besides these clumps that are likely to be less important with regard to their star formation potential, the ATLASGAL compact source catalogue is also sensitive to the emission of the dust envelopes of evolved stars. Although the dust continuum emission of these sources can be detected due to the heating from the star, their column densities are not high enough to emit significant molecular emission. We conclude in the paper that taking into account the possible contamination of the ATLASGAL catalogue by diffuse gas and extended, warm envelopes of evolved stars suggest that the "*sample is likely as complete as possible in terms of velocity determination*" (Urquhart et al. 2018).

4.3 Dust spectral energy distributions

To recover and fit the dust spectral energy distributions (SEDs) we followed the general procedures developed for König et al. (2017) (Chapter 3) and described in detail in Sections 2.2 and 2.3. In total we obtained 120,037 maps in 12 bands for 10,163 sources from the ATLASGAL CSC (Contreras et al. 2013, Urquhart et al. 2014a). These maps were consecutively used to extract the photometric data for each source, which was in turn used to fit the SEDs to obtain the average dust temperature of the clumps. In total we were able to obtain SEDs for 7861 sources of the sample.

4.3.1 Consistency checks and reliability

To show the reliability of our photometric method, in Fig. 4.3 we present a comparison of the flux densities reported in the Hi-GAL compact-source catalogue (Molinari et al. 2016) to the fluxes we recovered as described in Section 2.2 in each band. Note that the Hi-GAL compact source catalogue was obtained using the CUTEX algorithm (CUrvature Thresholding EXtractor; Molinari et al. 2017), vastly different from the aperture-annulus approach we use. There, the sources are first identified individually for each band from the second derivative of the maps (i.e. the curvature maps). Consecutively the source size and flux density are estimated from a 2D Gaussian fitted to the source on the emission map. As a consequence, the Hi-GAL source catalogue traces smaller and less bright structures in the higher resolution bands. To compare the two catalogues, we therefore summed up the fluxes of all Hi-GAL compact sources found within our source aperture. Despite a large scatter (factor $\sim$10) for individual sources, we find a strong correlation between the fluxes in the 160 μm, 250 μm and 350 μm bands that were obtained through two significantly different methods. With a correlation coefficient of $r = 0.86$ and a p-value < 0.0013 for the 250 μm band, we find both photometric methods to be consistent.

However, we find significant differences in the 70 μm and 500 μm bands. This effect is caused by two different effects. For the 70 μm band for example, the source sizes found in the Hi-GAL catalogue are much smaller than for our single aperture approach, as they trace different structures at different wavelengths. As a result, the integrated Hi-GAL flux we

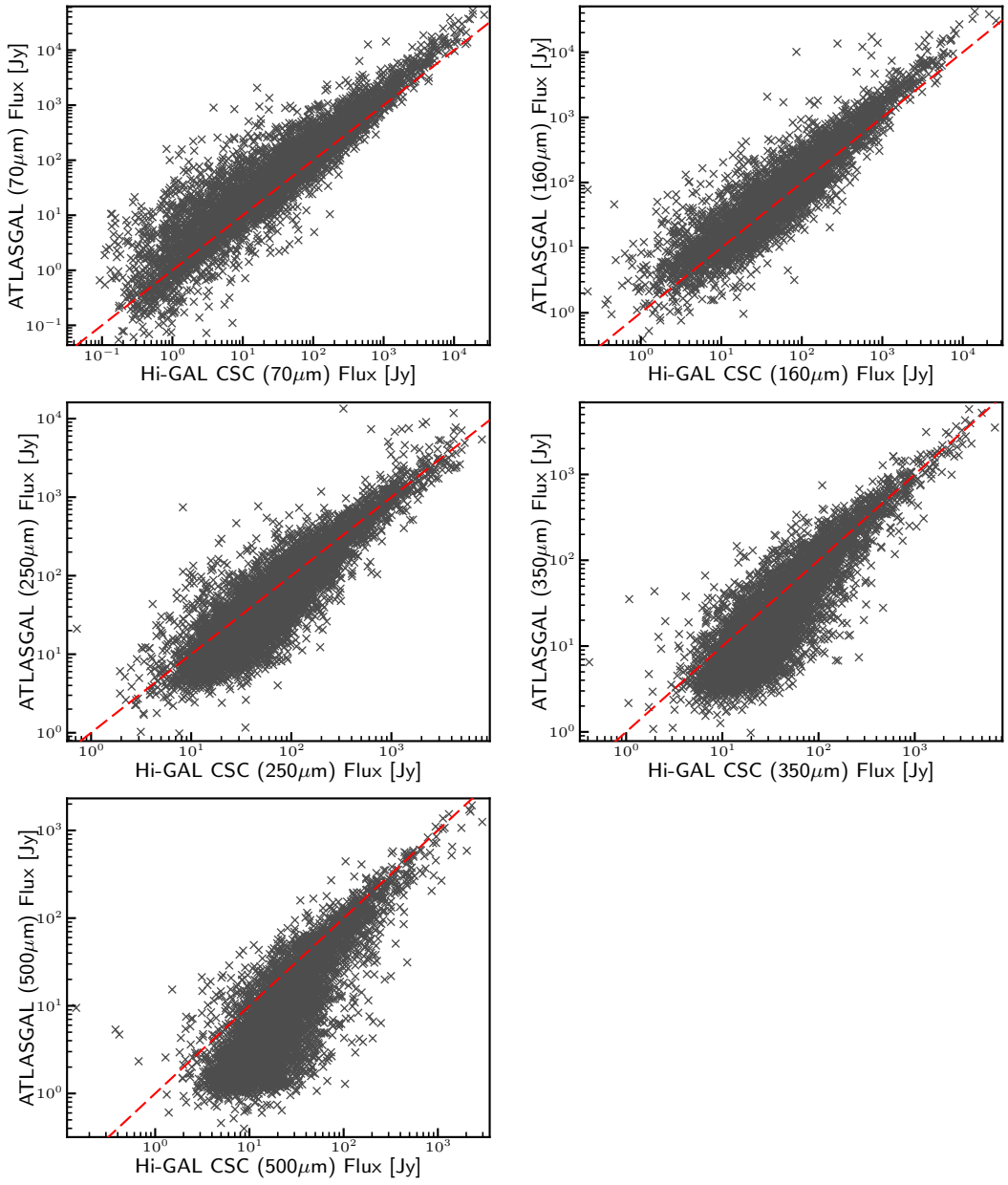

Figure 4.3: Comparison of flux densities obtained from the Hi-GAL compact source catalogue with the fluxes obtained through aperture photometry in the present work. The dashed red line indicates equality between the two sets of measurements.

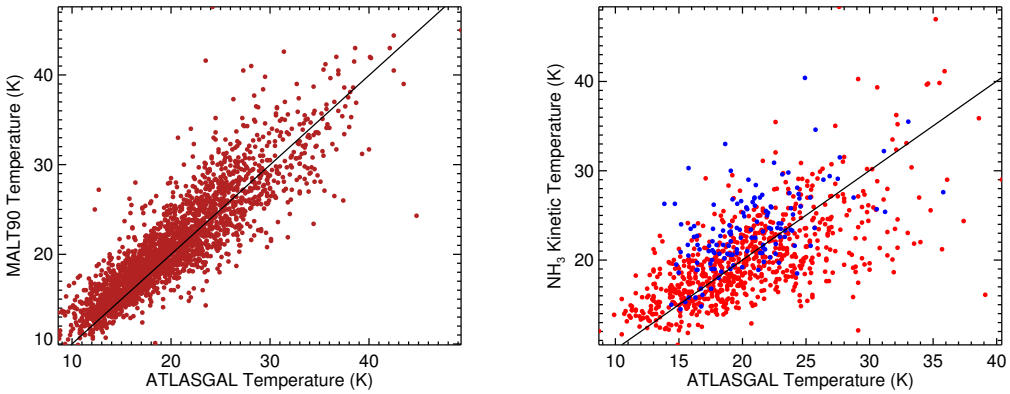

Figure 4.4: Left panel: comparison between dust temperatures derived here and those determined by the MALT90 team (Guzmán et al. 2015). This subsample of ∼2500 includes a significant fraction of all of the sources observed as part of the MALT90 survey (a total of ∼3000 ATLASGAL clumps were observed as part of this programme of follow-up observations). The solid line indicates the line of equality. Right panel: comparison between the dust temperatures and kinematic gas temperatures determined for ∼1500 clumps from NH_3 (1,1) and (2,2) inversion transitions (Wienen et al. 2012, Urquhart et al. 2011, red and blue circles, respectively). Least-square fits to the data presented in both plots result in slopes that are within 1σ of being linear. *Taken from Urquhart et al. (2018).*

calculate for our comparison as the sum of all Hi-GAL sources within our aperture does not sum up to the integrated flux we find. This is caused by the smaller Hi-GAL sources each finding a higher background level resulting in lower background corrected flux levels for the individual Hi-GAL sources found in the 70 μm band.

Similarly, as the 500 μm emission is the most extended one, we miss some flux as we use the aperture size derived from the emission found in the 250 μm band. This effect is more pronounced for weaker sources, as the 250 μm emission is limited to the central region of the clump, tracing a different structure than the extended 500 μm emission picked up by the Hi-GAL compact source catalogue in this band. Nevertheless, we find in general a similar trend and, as seen in the previous paragraph, a good agreement in the 250 μm band which we chose as a reference for recentering the aperture.

To further investigate the consistency of our results with the literature, we compare the derived dust temperatures obtained from the greybody fit with those of Guzmán et al. (2015). As part of the MALT90 survey (Jackson et al. 2013) they used a similar method to obtain the flux densities through aperture photometry, calculating temperatures for a sample of ∼2500 ATLASGAL clumps using a single component greybody model. We find a mean difference of the temperatures of only 0.8 ± 0.1 K and a standard deviation of 2.8 K, proving the good agreement between the temperatures of the cold dust component for the two surveys that can be seen in Fig 4.4 (left panel). In the right panel of Fig 4.4 we also compare our dust temperatures to the kinetic dust temperatures derived from the ammonia (NH_3) (1,1) and (2,2) transitions (Urquhart et al. 2011, Wienen et al. 2012). Although a higher scatter is visible, we still find

a good correlation between the results of the two independent methods with a correlation coefficient of $r = 0.64$ and a p-value lower than 0.01.

We conclude that our method to recover the flux densities through aperture photometry is in good agreement with other methods, as has been shown in detail for the Hi-GAL compact source catalogue. This is further supported by our comparison to the dust temperatures of Guzmán et al. (2015) implicitly requiring similar flux densities to result in the very good agreement of the dust temperatures of the two surveys. Finally the comparison with the ammonia kinetic dust temperatures shows that although comparing the results of two independent methods the results are in good agreement. These three comparisons show the reliability of our results, allowing us to compare the physical properties of 7861 sources of the ATLASGAL compact source catalogue.

4.4 Overview of main findings

In this section I will give an overview of the main results of the analysis conducted in Urquhart et al. (2018), as we will later build on these results, extending the analysis to the outer Galaxy. Note that these conclusions were mostly drawn by the main author of the paper, but would not have been possible without the photometric data and the physical parameters derived from the SEDs which were my main contribution to the paper.

We investigated a complete sample of ∼8000 dense clumps located between $5^\circ \leq |\ell| \leq 60^\circ$. We determined distances to ∼97% of the sample, where the velocity measurements as described in Section 4.2 significantly contributed to the completeness, increasing the fraction of sources with velocity measurements from 84% to almost 98%. Investigating the distribution of the clumps, we find them to be strongly correlated with the spiral arms, with ∼ 90% being located within $10\,\mathrm{km\,s^{-1}}$ of the spiral arm loci.

Furthermore, mid- to sub-millimetre photometry was performed on the whole sample as described in Section 4.3, allowing to determine average dust temperatures, integrated fluxes and column densities for the clumps by fitting a two-component model to the SEDs.

With distances known, bolometric luminosities, clump masses and linear sizes could be derived from the SEDs fitted parameters. We find that the majority of the clumps are capable of forming high-mass stars and are unstable against gravity. Similarly, we find the peak column density strongly correlated with massive star formation, with 100% of clumps at $10^{23}\,\mathrm{cm^{-2}}$ or higher column densities forming high-mass stars.

Table 4.3: Summary of evolutionary types identified from the SED analysis and our previous work (Urquhart et al. 2014c). *Adapted from Urquhart et al. (2018).*

Evolutionary type	Photometric type	Number of sources	Fraction of total			Notes
MSF	mid-IR bright	1222	0.16	}	0.88	Star forming
YSO	mid-IR bright	4053	0.52			
Protostellar	mid-IR weak	1640	0.21			
Quiescent	70 μm weak	946	<0.12	}	<0.12	Non-star forming

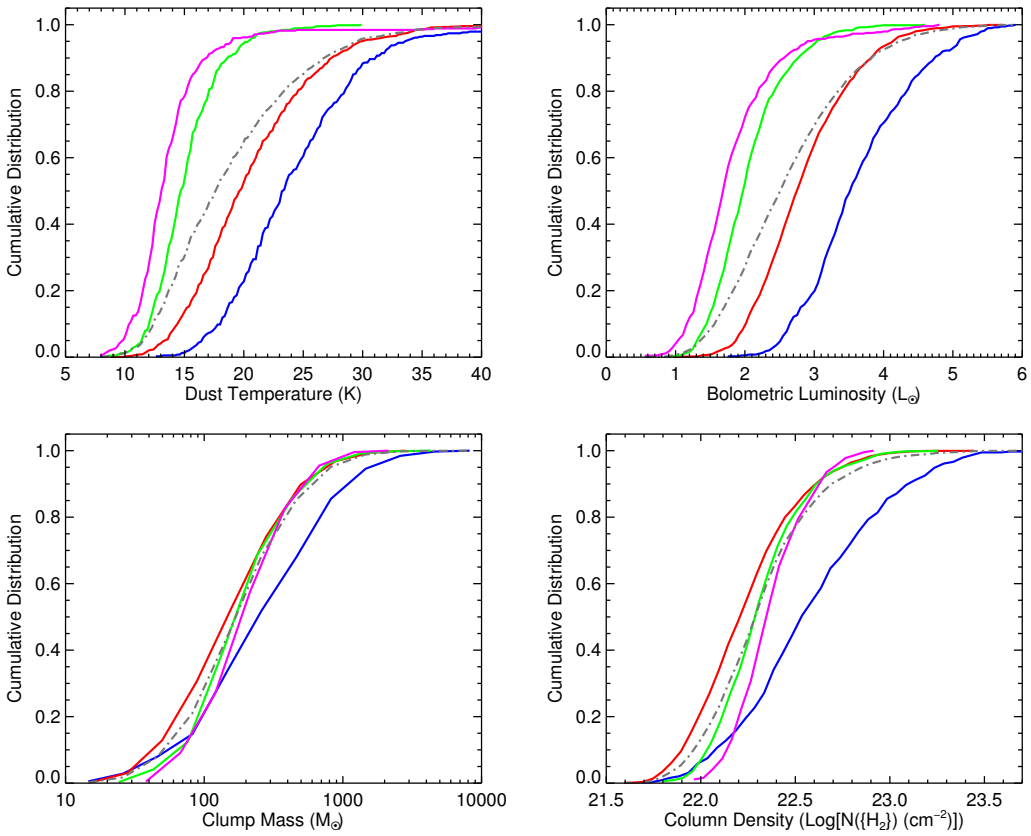

Figure 4.5: Pannels show the distribution of the distance-limited subsamples of the four evolutionary types: Quiescent/pre-stellar (magenta), protostellar (green), YSOs (red) and MSF (blue). *Figures from Urquhart et al. (2018)*

Using the photometric data, the evolutionary stages of the sources could be determined following the classification scheme established in König et al. (2017) (see Sect. 3.3.1), with a slight alteration to the classes of mid-IR bright sources and HII regions. We expand the group previously exclusively associated with HII regions to include all massive star forming clumps (MSF) as identified by Urquhart et al. (2014c). The remaining mid-IR bright sources (i.e. those not associated with a secondary tracer for high-mass star formation) are then referred to as young stellar object (YSO) forming clumps. A summary of sources associated with each class can be found in Table 4.3

With the fractions of clumps in each evolutionary stage known, statistical lifetimes dependent on clump mass are derived. These indicate for the quiescent stage a lifetime of 5×10^4 years for $\sim$1,000 $M_\odot$ clumps down to lifetimes of $\sim 1 \times 10^4$ years for clumps around 10,000 $M_\odot$ and negligible lifetimes in the quiescent stage for even more massive clumps. We conclude that clumps form rapidly and are very unstable in their initial phase, which is followed quickly by star formation.

Furthermore, the evolutionary sequence reveals increasing temperature and luminosity but constant mass and column density (compare Fig 4.5), in agreement with what was found for

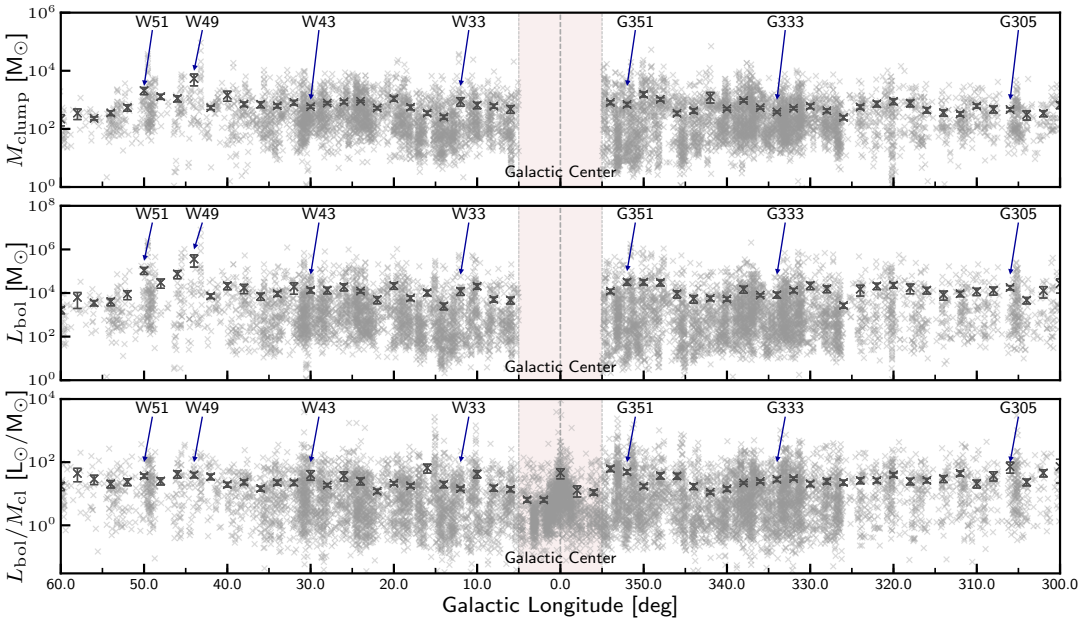

Figure 4.6: Distribution of clump mass, bolometric luminosity and luminosity-to-mass ratio (top to bottom) as a function of galactic longitude. Crosses mark the mean over 2 degree with uncertainties estimated as the standard error of the mean. The red shaded area marks the $|\ell| < 5^\circ$ region towards the Galactic centre not covered by (Urquhart et al. 2018).

the ATLASGAL Top100 sample (Chapter 3). This means that the clumps form already with most of their mass assembled and either no significant amount of mass falls onto the clump during their evolution or infall and outflow cancel out each other. We conclude that once a clump is collapsing, the process is very rapid and almost independent from its larger scale environment.

With the positions and physical parameters known, their properties were investigated on kpc scales with respect to their Galactic environment. No variation was found for the $L_{\rm bol}/M_{\rm clump}$ ratio either with Galactocentric radius nor with respect to the spiral arms, concluding that the arms play an important role in concentrating the material to form clumps, but do not have any impact on the star formation process. Care has to be taken though for the latter, as the small separation of the spiral arms in the inner Galaxy and the high uncertainty in heliocentric distance derived from kinematic distances make an analysis difficult. Similarly, the dust temperature $T_{\rm dust}$ stays about constant in the inner Galaxy, but slightly increases outside the Solar circle, likely due to lower density and hence decreased shielding against the interstellar radiation field.

Furthermore, clusters of star formation have been identified through a friends-of-friends analysis in order compare the properties of these larger scale complexes. We find that the 30 most massive complexes contain only 16% of all clumps, but make up for 36% of the total mass and 52% of the total bolometric luminosity of the sample. Furthermore, we find three outstanding clusters (W49, W51 and G351.598+001.89), that are responsible for almost 25% of the total luminosity of all ATLASGAL sources. These also show a significantly increased

star forming activity, as their integrated $L_{\rm bol}/M_{\rm clump} > 50\,{\rm L}_\odot/{\rm M}_\odot$ ratio is at least twice as high as the remaining clusters, making them the best examples of 'mini-starbursts' within the Milky Way.

Finally, I will give an overview of the distribution of the clump masses, bolometric luminosities and luminosity-to-mass ratio as a function of galactic longitude in Fig. 4.6. As the luminosity-to-mass ratio is a distant independent property, 667 sources located in the $|\ell| < 5^\circ$ region around the Galactic centre are also included here. For the masses and luminosities, we see a rather large scatter, with the bins containing W49 and W51 clearly outstanding. In contrast, the average luminosity-to-mass ratio is found to be rather constant on large scales over the whole inner disk. An exception is the star formation activity (as indicated by $L{\rm bol}/M_{\rm clump}$) for the central $|\ell| < 5$ degree, which we find to be lower on average, with the central 2 degree being on the average level of the disk due to extreme $L{\rm bol}/M_{\rm clump}$ values found for just a hand full of clumps towards the Galactic centre.

4.5 Summary

Using and refining the methods developed for the ATLASGAL Top100 paper, as well as completing the distances needed to derive physical properties, we were able to extend the analysis to a complete sample of massive star-forming clumps above $1000\,{\rm M}_\odot$ throughout the inner Galaxy. With major findings for the inner part of the Milky Way, we can now ask how this compares to the outer Galaxy, where the environment is significantly different. With lower HI density, less intense UV radiation fields, smaller cosmic ray flux, lower metallicity and higher gas-to-dust ratio in the outer Galaxy, changes in the physical properties of star-forming clumps would not be surprising - which we will investigate and compare in the following two Chapters.

Part III

Outer Galaxy

Introduction

In the previous chapters we have investigated the physical properties of star-forming regions in the inner Galaxy based on the ATLASGAL survey. In the next two chapters we are going to extend our view to the outer part of the Milky Way, where the environment changes significantly: in general we find lower HI density (Heyer & Dame 2015) and metallicity (Rudolph et al. 1997), less intense UV radiation fields, a smaller cosmic-ray flux (Bloemen et al. 1984), and a higher gas-to-dust ratio (Giannetti et al. 2017a). Differences between star-formation properties of the outer and inner Galaxy could therefore lead to a better understanding of the influence of the environment on the star-formation processes in general. To find variations of the physical properties with galactocentric radius, we will apply the methods developed for the ATLASGAL sample as described in the last two chapters to the outer Galaxy. For this purpose archival mid-infrared to submm dust continuum data is used in combination with newly obtained kinematic distances from CO(2–1) observations.

As physical properties can only be derived with reliable distances, the main goal of the observations in this part was to obtain these distances, which will be described in detail in Chapter 5. We will then look at how they reveal the structure of the outer Galaxy in unprecedented detail, investigating the large scale structures and the distribution of molecular clouds. We are then able to determine the physical properties of the clumps and investigate these with respect to galactocentric radius, comparing them to the physical properties found for the inner Galaxy sample of ATLASGAL (Chapter 6). At the end of the Chapter we will also briefly look at the influence of large scale structures found in the outer Galaxy on star-formation properties.

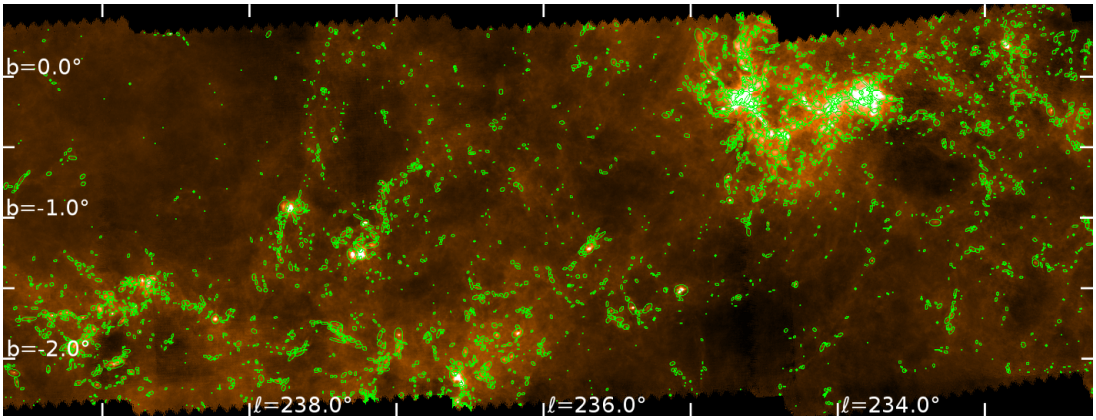

Figure 5.1: Image of SPIRE 250 μm emission showing an example of extracted sources around $\ell = 236°$ and $b = -1°$. The image spans $\sim$7° in longitude and $\sim$3° in latitude. Over-plotted are the sources identified by SExtractor (green ellipses).

CHAPTER 5

Velocities, Distances and Structures

5.1 Observations of ^{12}CO

To determine physical properties of star-forming regions, distances are crucial. These can be obtained through different methods as described in Section 2.4, with kinematic distances being the most widely used (Urquhart et al. 2018). Here, we use radial velocity measurements and a rotation curve of the Milky Way to determine the distance. Although this method is not as accurate as e.g. trigonometric distance measurements, kinematic distances are the key for statistical analysis of large samples as they can be obtained for a large number of sources in a short amount of time. Here we discuss the observations of the ^{12}CO(2–1) line from whose spectrum kinematic distances can be derived.

In this chapter we first describe how we selected a sample of dust clumps in the southern outer Galaxy between $225° \leq \ell \leq 260°$ and how we obtained distances to these clumps. We will then take a look at the structures found in this region of the Milky Way. In Chapter 5 we will then use the obtained distances in combination with the dust spectral energy distributions to calculate physical properties of the clumps in the outer Galaxy and compare these to the properties found in the inner part of the Milky Way.

5.1.1 Source extraction and selection

The region chosen for this survey ($225° \leq \ell \leq 260°$, $-3° \leq b \leq 0.5°$) was selected because there are no kinematic distance ambiguities as the lines-of-sight do not cross the inner Galaxy.

Furthermore the sections of the spiral arms in this region are well separated in velocity, making it relatively straightforward to associate objects with their parent spiral arm. The latitude range was selected as the minimum and maximum latitudes covered by the Herschel Hi-GAL dust continuum emission maps.

The Herschel SPIRE 250 μm emission data obtained by Hi-GAL (Molinari et al. 2010) was used to identify clumps in this region. Note that due to the Galactic warp the latitude range covered by Hi-GAL is centred around $b = -1^\circ$ spanning $\sim$2.5°. Although the authors are aware of the Hi-GAL compact source catalogues that are publicly available for the inner Galaxy (Molinari et al. 2016), their outer Galaxy counterpart is not yet publicly available. Therefore an independent method was chosen to obtain a source catalogue for the targeted area of the outer Galaxy. To identify emission peaks and obtain their source sizes, SExtractor (Bertin & Arnouts 1996) was used, as it was used in a similar way to produce the ATLASGAL compact source catalogue (Contreras et al. 2013, Urquhart et al. 2014c) with great success.

As a general approach we searched for emission peaks of at least 4 pixels (i.e. $\sim$1 beam) above a threshold of $3\sigma_{\rm rms}$ above the local background noise level as determined by SExtractor from an area around any given position defined by a scalable mesh. We used two different mesh sizes to either exclude or include the 6 brightest and most complex regions of emission, as these crowded regions would introduce a bias in the source selection process. As a result we obtained two catalogues: one excluding the brightest regions, which includes 12,783 sources, and a second one that was optimized to identify clumps located in the bright regions, including 15,874 sources. Merging both catalogues and removing duplicate entries, we obtained a full catalogue identifying a total of 23,817 sources in the $225^\circ \leq \ell \leq 260^\circ$ region. The result of the source extraction from the SPIRE 250 μm images can be seen in Fig. 5.1 which includes a variety of bright complexes and dark regions devoid of emission. In Table 5.1 we give the parameters of the extracted sources.

As one major goal of this research is to probe the full distance range from the nearest to the farthest sources, we used the subset excluding the 6 brightest regions to select the majority of our sources. However, in order to characterize these regions, we manually added 34 emission peaks from the full catalogue, so these regions are included but not over-represented (see Table 5.2 and Fig. 5.2 for an overview of these 6 regions). For the observations outside the six brightest and most complex regions, we selected the 100 sources yielding the highest peak flux as well as the 100 sources with the highest integrated flux, accounting for 196 sources with 4 sources being in both categories. Additional 587 sources were finally selected randomly from the brightness limited subset, picking up faint sources which are more likely to be located at farther heliocentric distances. In total 817 sources of the extracted emission peaks were observed.

To show that our source selection procedure does not introduce a strong flux bias, we show in Fig. 5.3 the histogram of the aperture flux at 250 μm of all extracted sources (including the brightest regions) together with the histogram of the aperture flux of the observed sources. As can be seen, our observed sources sample the whole range of the flux distribution of the complete catalogue very well down to the limit of $\sim$2.5 Jy, which was imposed as a selection threshold to ensure the ^{12}CO(2–1) line could be detected at a 3σ level in a reasonable amount of integration time ($\lesssim$ 3 min).

We summarize that we extracted 15,874 sources from the Herschel SPIRE 250 μm emis-

Table 5.1: Astrometric data and integrated flux as determined by SExtractor for the extracted clumps for the first 20 clumps from a total of 23,817 sources. Columns are as follows: name of the source, Galactic longitude, Galactic latitude, full-width-at-half-maximum source size and the 250 μm integrated flux as measured by SExtractor.

Name	ℓ [deg]	b [deg]	FWHM [arcsec]	F_{250} [Jy]
G225.002-00.589	225.002	−0.589	14.4	3.65
G225.003-00.574	225.003	−0.574	21.2	7.78
G225.003-01.113	225.003	−1.113	14.4	3.85
G225.004-00.245	225.004	−0.245	10.1	2.69
G225.004-00.280	225.004	−0.280	12.2	4.43
G225.004-00.281	225.004	−0.281	14.4	2.49
G225.004-01.150	225.004	−1.150	8.6	5.48
G225.013-00.319	225.013	−0.319	15.1	6.79
G225.013-00.570	225.013	−0.570	8.6	6.39
G225.014-00.570	225.014	−0.570	14.4	7.03
G225.014-01.125	225.014	−1.125	14.4	3.65
G225.014-01.126	225.014	−1.126	24.5	5.33
G225.015-01.682	225.015	−1.682	8.3	2.56
G225.015-01.683	225.015	−1.683	10.8	2.64
G225.016-00.586	225.016	−0.586	18.0	5.11
G225.016-01.588	225.016	−1.588	25.2	3.53
G225.017-00.587	225.017	−0.587	22.3	5.03
G225.017-01.588	225.017	−1.588	15.8	3.42
G225.021-00.301	225.021	−0.301	26.3	7.77
G225.022-00.301	225.022	−0.301	18.0	6.46
G225.024-00.178	225.024	−0.178	18.0	2.22
G225.027-00.982	225.027	−0.982	7.2	2.32

Table 5.2: Overview of the 6 dominating bright and complex regions.

ℓ [deg]	b [deg]	# positions	$v_{\rm lsr}$ [km s^{-1}]	$R_{\rm hel}$ [kpc]	$R_{\rm gal}$ [kpc]	extent [deg] ([pc])
259.06	−1.61	7	59.3	6.5	11.5	0.5 (56)
258.06	−1.87	3	44.0	4.9	10.5	0.7 (59)
254.04	−0.22	6	36.1	3.9	10.1	1.5 (100)
234.33	−0.28	7	43.0	3.8	11.0	1.4 (92)
231.78	−1.96	8	47.3	4.2	11.4	0.9 (66)
225.50	−0.40	8	16.0	1.4	9.4	1.1 (25)

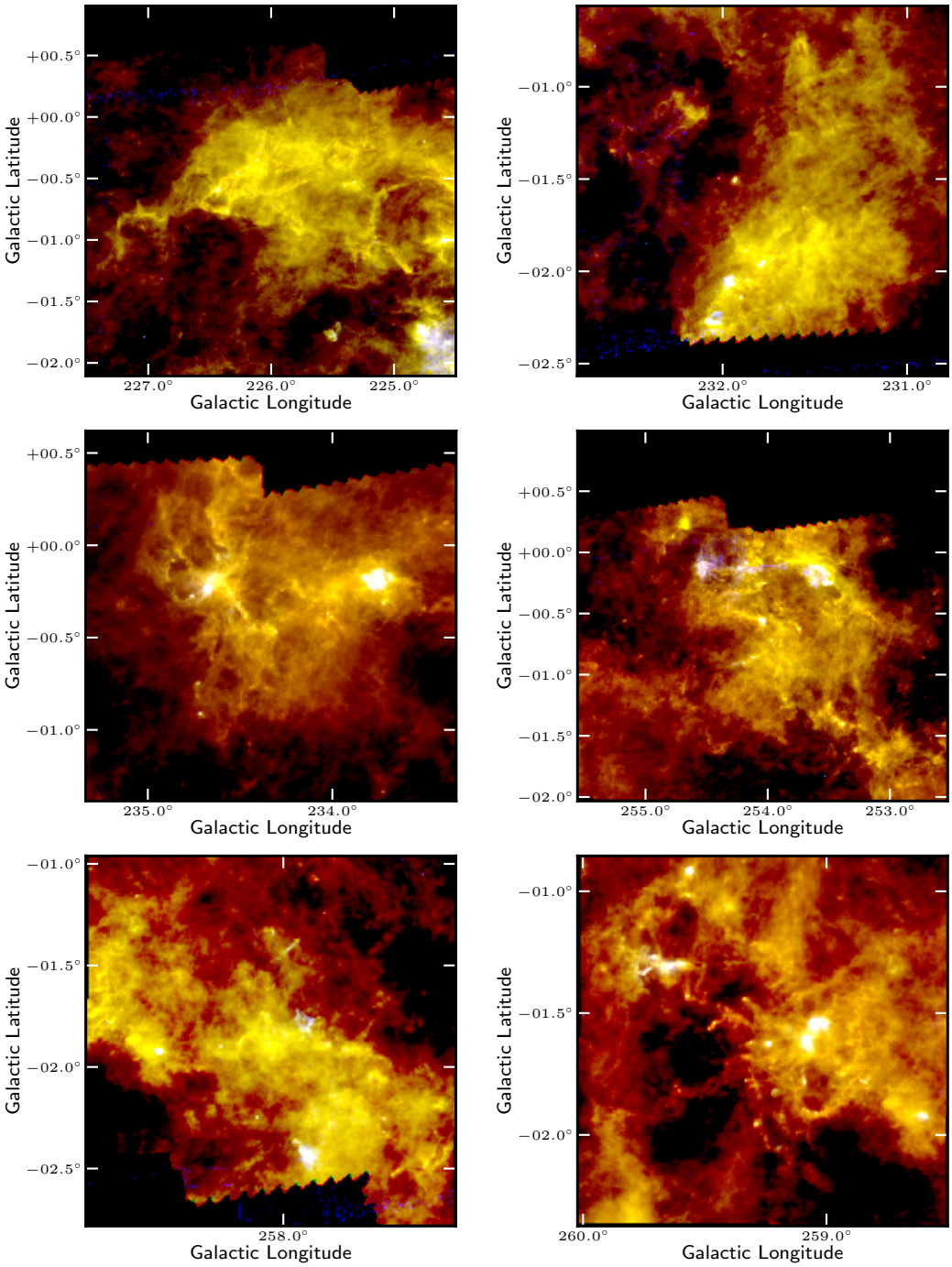

Figure 5.2: RGB images of the six brightest regions in the survey area. These have been excluded from the automated source selection, as not to bias the survey towards these regions. Red: SPIRE 500 μm; Green: SPIRE 250 μm; Blue: PACS 70 μm.

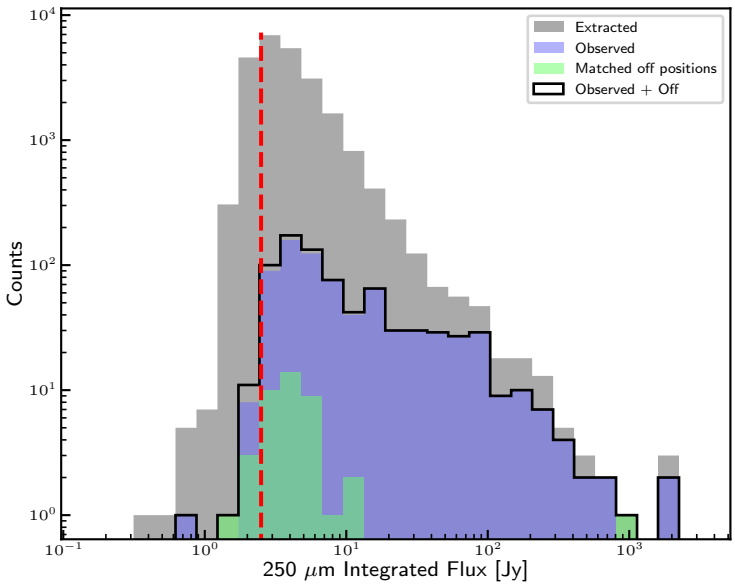

Figure 5.3: Histogram showing the integrated flux for the sources identified by SExtractor (grey) in comparison to those selected for our observations (blue) and those recovered from contaminated off-source positions (green; see Sect. 5.1.3). The red vertical dashed line indicates the limit of ∼2.5 Jy, that was imposed as a selection threshold (see text).

sion maps, selecting 817 sources for pointed ^{12}CO(2–1) observations. The SExtractor catalogue has been constructed to identify observational targets and is not considered sufficiently robust enough to publish. Nevertheless we present the parameters of the first 20 extracted sources in Table 5.1 to give an impression of what was used for the source selection. Therefore we concentrate on presenting the results for the 817 positions we conducted pointed observations towards.

5.1.2 Observations

To obtain CO(2–1) velocity information, we observed the selected clumps according to the method described in Section 2.4.1. For the outer Galaxy, the observations towards 817 sources were conducted between July 2013 and December 2016 as a bad weather backup project at APEX with precipitable water vapour (PWV) up to 6 mm. To reach an rms < 0.1 K per channel each source was observed in position switching mode for 3–6 min, depending on PWV, elevation and line-strength. The off-positions were selected as relative offsets with a separation of 1° roughly perpendicular to the Galactic plane. The pointed ^{12}CO(2–1) observations were obtained with an average PWV of 2.7 mm, resulting in an average RMS of 0.05 K at a smoothed channel resolution of 1 km s^{-1}. A sample spectrum is shown in Fig. 5.4. In total, we found 36 spectra without any emission, leaving 781 (∼96%) spectra for further analysis. A summary of all observational parameters is given in Table 5.3.

Table 5.3: Summary of the APEX observational parameters.

Parameter	Value
Galactic longitude range	$225^\circ < \ell < 260^\circ$
Galactic latitude range	$-2.73^\circ < b < 0.45^\circ$
Number of observations	817
Number of spectra with emission	781
Instrument	SHeFI (APEX-1)
Frequency	230.538 GHz
Angular resolution	$30''$
Spectral resolution	$0.1\,\mathrm{km\,s^{-1}}$
Smoothed spectral resolution	$1\,\mathrm{km\,s^{-1}}$
Mean noise (T_A^*)	$\sim$50 mK channel^{-1}
Average PWV	$\sim$2.7 mm
Integration time (on-source)	1–3 mins

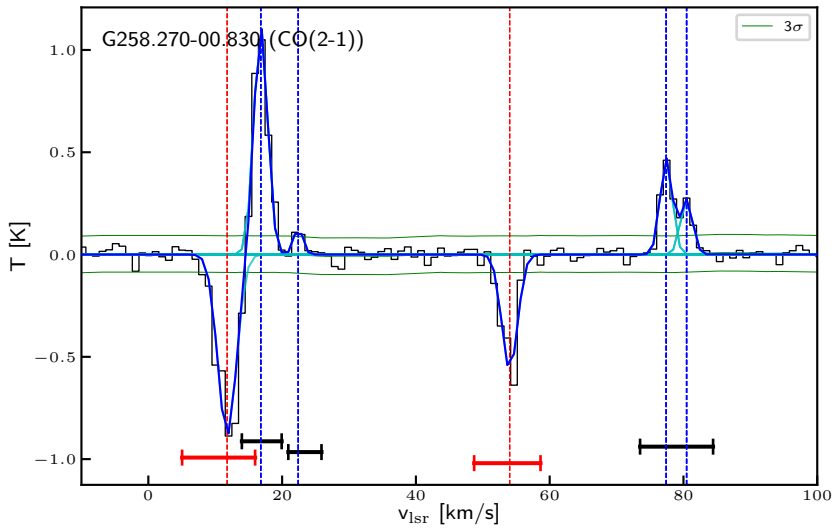

Figure 5.4: Typical ^{12}CO(2–1) spectrum towards a crowded region showing multiple velocity components along the line-of-sight and contamination in the off-position (negative features). The total fitted spectrum is overplotted in blue, single Gaussian profiles in cyan. Coherent velocity complexes are either marked as black (source position) or red (off position) horizontal bars below the spectrum. The vertical dashed blue lines indicate the peak positions of the fitted Gaussian profiles, whereas the vertical red solid line indicates the peak position of the emission found in the off-position.

5.1.3 Data reduction procedures

The data was reduced following the procedure described in Section 2.4.1 We were able to fit spectra for all 781 sources, identifying a total of 1471 velocity components from the CO(2–1) emission. From here on we refer to a single fitted Gaussian as a velocity component and to any coherent group of emission as a cloud, as we assume that these groups of emission are physically connected with similar velocities but distinct components.

We found the source-off reference positions, selected as a relative offset from the target position of ~ 47 arcmin, to be contaminated for 371 sources of the sample (31.9%). As the uncertainty in distances determined from the $v_{\rm lsr}$ are mostly dominated by the uncertainty in the rotation curve used for the calculation rather than from the velocity, we assume that an uncertainty in $v_{\rm lsr}$ of a few km s^{-1} due to contamination in the source-off position, does not pose a serious problem. In fact, we conclude that the CO emission at the source-off position can be used to increase the number of positions for velocity measurements towards the outer Galaxy, but care has to be taken on their usage as discussed in the following paragraph.

Therefore we also analyse the emission at the off positions for the outer Galaxy sample, when a source shows contamination. To do so, we simply invert the baseline corrected spectra and apply the same procedure as for the emission of uncontaminated sources, yielding velocity components for the off-position. Analysing the emission at the off positions for the 371 contaminated spectra, we were able to add another 563 velocity components to our analysis. We want to stress that although these additional velocity components show CO(2–1) emission, they do not necessarily coincide with the peak of any clump or cloud, and rather can be associated with more diffuse emission, rendering these positions less useful for further analysis except for the position-velocity analysis. In order not to bias our results for the physical parameters that are derived from the dust continuum emission, we only take into account off-source positions that are matched with a SExtractor source position within one beam size (i.e. 30″), yielding an additional 40 sources for the SED analysis in Chapter 6. If an absorption feature was found within 10 km s^{-1} of an emission peak, the uncertainties for all derived properties were increased by a factor of two (i.e. velocity, peak temperature and line-width). We choose a rather large range of 10 km s^{-1}, in order to make sure that we also cover cases with broad emission complexes, where the emission between two peaks cancels each other out. We present the results for each position in Table A.1. In total we find 2034 velocity components for a total of 1164 positions (targeted + reference).

As observations were conducted mostly under bad-weather conditions with high and fast varying PWV>5 mm, we calculate the main beam temperature only for sources that have a calibration within a certain time-frame according to the weather conditions[1]. The main beam temperature $T_{\rm mb}$ was then calculated from the antenna temperature $T_{\rm A}^*$ multiplying with a forward efficiency of $\eta_{\rm f} = 95\%$ and dividing by a beam efficiency of $\eta_{\rm mb} = 75\%$. In case no calibration was found within the given time-frame, we do not give a main beam temperature or intensity and add 20% uncertainty to the line width.

For 714 (61.3%) lines-of-sight only a single cloud is found whereas multiple clouds are identified for the remaining 450 (38.7%) lines-of-sight. A total of 1757 clouds are found,

[1] within the last 15, 10, 7 or 5 minutes, for PWV$<1.5, <3, <4, >4$ mm, assuming increasing weather stability with lower PWV

Table 5.4: Velocity components identified from the CO(2–1) observations along 10 lines-of-sight. Source names starting with a '*G*' are measured emission at targeted positions, whereas names starting with an '*O*' indicate emission in the off-position. Uncertainties for $v_{\rm lsr}$ are in the order of 0.5 km s^{-1}, distance uncertainties in the order of 0.3 kpc.

Name	$v_{\rm lsr}$ (km s^{-1})	$\Delta v_{\rm lsr}$ (km s^{-1})	$T_{\rm max}$ (K)	$\int T dv$ (K km s^{-1})	$R_{\rm hel}$ (kpc)	$R_{\rm gal}$ (kpc)
G232.510+00.200	13.8	0.3	0.8 ± 0.2	0.6 ± 0.1	1.3	9.2
	15.9	0.7	1.6 ± 0.2	2.8 ± 0.3	1.4	9.3
	20.9	1.1	1.6 ± 0.2	4.2 ± 0.4	1.8	9.6
G232.590−01.190	22.5	0.6	0.7 ± 0.1	1.1 ± 0.2	1.9	9.6
G232.596−01.352	46.0	1.0	3.0 ± 0.2	7.6 ± 0.5	4.1	11.3
	48.4	0.7	2.3 ± 0.3	4.1 ± 0.6	4.3	11.5
G232.600+00.300	15.7	0.6	4.7 ± 0.1	7.3 ± 0.3	1.4	9.3
G232.600+00.430	16.3	0.6	3.9 ± 0.1	5.7 ± 0.2	1.5	9.3
G232.600+00.100	17.0	1.7	1.9 ± 0.1	8.4 ± 0.5	1.5	9.3
G232.600−01.320	47.1	1.5	2.0 ± 0.1	7.4 ± 0.4	4.2	11.4
G232.630+00.390	16.6	0.6	3.3 ± 0.1	4.7 ± 0.2	1.5	9.3
G232.640−00.420	17.7	1.4	0.4 ± 0.1	1.2 ± 0.3	1.6	9.4
	23.2	0.5	2.7 ± 0.2	3.7 ± 0.3	2.0	9.7
	47.4	0.6	1.0 ± 0.1	1.3 ± 0.2	4.2	11.4
G232.669−01.295	48.9	0.6	0.6 ± 0.1	0.9 ± 0.2	4.4	11.5
	54.4	0.7	0.5 ± 0.1	0.8 ± 0.2	5.0	12.0

yielding an average of 1.5 clouds per line-of-sight. An example of a fitted spectrum with emission at the source-position and at the off-position, as well containing a cloud made up out of two components can be seen in Fig. 5.4.

The results of all velocity and distance measurements can be found in Table A.1. We also give all clouds (i.e. groups of emission) in Table A.2, which we define as continuous emission features above 3σ rms, consisting of one or more fitted Gaussians. An example can be seen in Fig. 5.4 at $\sim$80 km s^{-1}, where 2 components make up 1 complex, indicated by the solid black bar at the lower part of the figure. The velocity found for the strongest velocity complex along a given line-of-sight is later used to assign a distance to the clump as seen in continuum emission, from which then the physical parameters are derived.

5.1.4 Source velocities

In Fig. 5.5 we present the longitude-velocity (ℓ-v) plot covering the observed field. The velocity components above the 5σ rms noise level for all positions are overlaid on the ^{12}CO(1–0) emission data cube from Dame et al. (2001) integrated for $-3\,{\rm deg} \leq b \leq 0.5\,{\rm deg}$.

As can be seen, although we randomly sampled, components obtained for the CO(2–1) line trace all the major structures found in the CO(1–0) emission map very well. In addition, due to the 15 times higher resolution of our pointed observations when compared to the data from Dame et al. (2001; i.e. 7.5′ vs. 30″), we are able to trace small structures that have been previously missed, as these would fall below the detection limit due to beam dilution

Table 5.5: Velocity groups identified from the CO(2–1) observations along a given line-of-sight for 15 complexes. Source names starting with a '*G*' are measured emission at targeted positions, whereas names starting with an '*O*' indicate emission in the off-position.

Name	Group	# components	$v_{\rm lsr}$ (km s^{-1})	$\Delta v_{\rm lsr}$ (km s^{-1})	$T_{\rm max}$ (K)	$\int T dv$ (K km s^{-1})
G232.510+00.200	1/1	3	15.9	11.9	1.6 ± 0.2	7.7 ± 0.8
G232.590−01.190	1/1	1	22.5	6.0	0.7 ± 0.1	1.3 ± 0.2
G232.596−01.352	1/1	2	46.0	10.9	3.0 ± 0.2	11.7 ± 0.8
G232.600+00.300	1/1	1	15.7	8.9	4.7 ± 0.1	7.7 ± 0.3
G232.600+00.430	1/1	1	16.3	6.0	3.9 ± 0.1	5.8 ± 0.2
G232.600+00.100	1/1	1	17.0	13.9	1.9 ± 0.1	8.6 ± 0.5
G232.600−01.320	1/1	1	47.1	9.9	2.0 ± 0.1	7.2 ± 0.4
G232.630+00.390	1/1	1	16.6	6.0	3.3 ± 0.1	5.1 ± 0.3
G232.640−00.420	3/3	1	17.7	6.9	0.4 ± 0.1	1.2 ± 0.3
	1/3	1	23.2	6.9	2.7 ± 0.2	3.9 ± 0.3
	2/3	1	47.4	6.9	1.0 ± 0.1	1.5 ± 0.2
G232.669−01.295	1/3	1	48.9	5.0	0.6 ± 0.1	1.0 ± 0.2
	2/3	1	54.4	4.0	0.5 ± 0.1	0.9 ± 0.2

or blending with other clumps within the beam. For example, the structures with the highest velocity components at any given longitude would trace the most distant arm. The structure traced by our pointed observations from $\ell \approx 242°$, $V_{\rm lsr} \approx 60\,{\rm km\,s^{-1}}$ to $\ell \approx 252°$, $V_{\rm lsr} \approx 40\,{\rm km\,s^{-1}}$ is completely missed by the lower sensitivity CO(1–0) map. Additional features can be identified, indicating the structure between the spiral arms towards this region of the outer Galaxy to be more complex than indicated by the data from Dame et al. (2001). We will discuss this in more detail in Section 5.2.

5.1.5 Kinematic distances and Galactic distribution

We determined distances for all velocity components by applying the Brand & Blitz (1993) rotation curve, assuming a distance to the Galactic centre of $R_0 = 8.34\,{\rm kpc}$ and an orbital velocity of $\theta_0 = 240\,{\rm km\,s^{-1}}$, as derived by Reid et al. (2014) and used by Urquhart et al. (2018). We prefer the rotation curve from Brand & Blitz (1993) over the more recent one from Reid et al. (2014), as the latter is derived from paralactic distances to objects visible from the northern hemisphere and does not include measurements for the southern outer Galaxy.

In Fig. 5.6 we show the histogram of Galactocentric (left panel) and heliocentric (right panel) distances for all velocity components above the 5σ rms noise level. The peaks are not only tracing the spiral arms, but also result from complexes lying at similar Galactocentric distances. This can also be seen in Fig. 5.5, where the 4 peaks are marked by the coloured dashed lines in the same way as in Fig. 5.6. We find that the peak located at $r_{\rm gal} \sim 9\,{\rm kpc}$ traces local gas including emission from the Vela molecular ridge. The peak at ∼11 kpc would trace the Perseus arm, if it were present in the area (see discussion in Sect. 5.2). The peaks around $r_{\rm gal} \sim 12.5$ (cyan dashed line) trace emission not associated with a spiral arms, being dominated by the huge complex at ℓ∼242° at $v_{\rm lsr}$∼70 km s^{-1} (i.e. behind the supershell; see

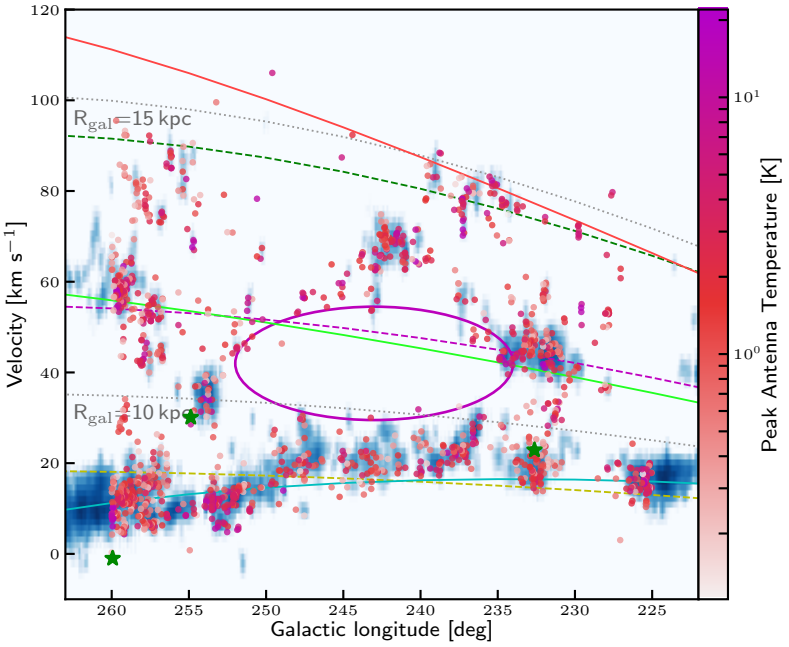

Figure 5.5: Galactic longitude vs. radial velocity. The dots mark all velocity components found above 5σ rms between $260° \leq \ell \leq 225°$, with the peak antenna temperature colour coded. Background image: CO(1–0) emission from Dame et al. (2001). Dashed yellow, magenta, and green lines: peaks at 9, 11, and 14.0 kpc, respectively, as found in Fig. 5.6. The spiral arms and the position of the local emission as determined from HI emission are marked by the coloured solid lines. Cyan: local emission; green: Perseus arm; red: Outer arm. The solid magenta ellipse marks the rim of the Galactic supershell GSH 242-3+77. Grey dashed lines: Galactocentric radii at 10 and 15 kpc. The green stars mark the positions of the 3 sources from the Methanol Multibeam (MMB; Green et al. 2012) survey found in the region.

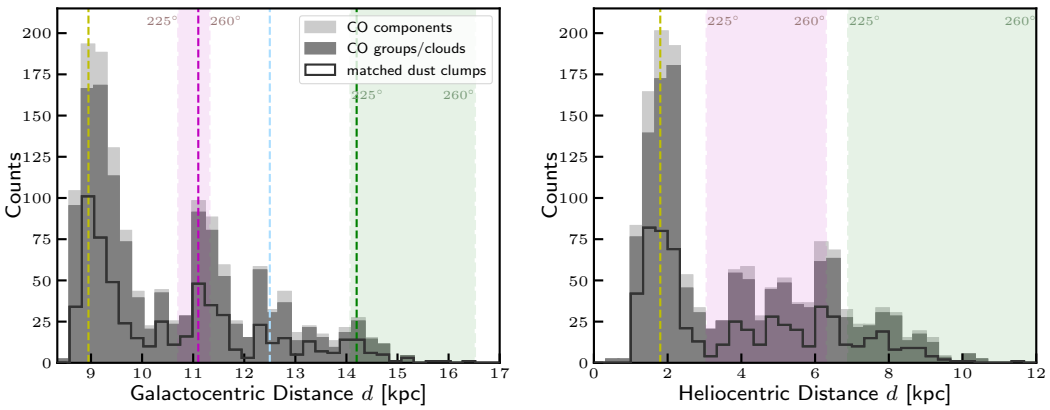

Figure 5.6: Histograms showing CO velocity components above 5σ (light grey), CO emission groups/clouds (dark grey) and matched dust clumps (black outline) by Galactocentric (left) and heliocentric (right) distance. The vertical dashed yellow line indicates the peak associated with local emission. The magenta and green shaded areas mark the distance range between $225° \leq \ell \leq 260°$ of the loci of the Perseus and Outer arms, respectively. The two peaks between $r_{\rm gal} \sim 12$ and ~ 13 kpc correspond to complexes between the Perseus and Outer arm.

Chapter 5.2.2). The peak found at $r_{\rm gal} \sim 14$ kpc partially arises from emission from the distant arm as well as from structures between the near and the distant arm located at $\ell{\sim}255°$. Similarly, we see a number of peaks in the heliocentric distance histogram, but due to the projection these cannot be assigned to the arms, as the arms are spread out over a larger heliocentric distance range between $225° \leq \ell \leq 260°$ than with regard to Galactocentric distance.

In Fig. 5.7 we show the distribution of our sources in the 3rd Galactic quadrant as viewed from the Galactic north pole. We find the closest source to be located at a heliocentric distance of $\mathrm{R_{hel}} = 0.40$ kpc and the most distant sources at $\mathrm{R_{hel}} \sim 12$ kpc. This results in the sources spanning a range of Galactocentric distances between $\mathrm{R_{gal}} = 8.50$ kpc and $\mathrm{R_{gal}} \sim 16.5$ kpc. Note that the distances are not only affected by the uncertainty of the velocity measurement, but also by the spread due to streaming motions ($\lesssim$10 km s^{-1}; Reid et al. 2014), the expanding supershell ($\sim$7 km s^{-1}; McClure-Griffiths et al. 2006), and the accuracy of the rotation curve, which can change the distance of any given source as determined from the rotation curve significantly ($\sim\pm$1 kpc), effectively dominating the uncertainty of the distance estimates.

5.2 Structure of the outer Galaxy

In this section we use the distance information as derived from the radial velocities to give an overview of the structure of the area investigated in this work. We will briefly investigate the spiral structure as found toward the 3rd Galactic quadrant, the influence of a Galactic supershell known to exist in the observed region, and we look into larger scale structures as found through a clustering analysis.

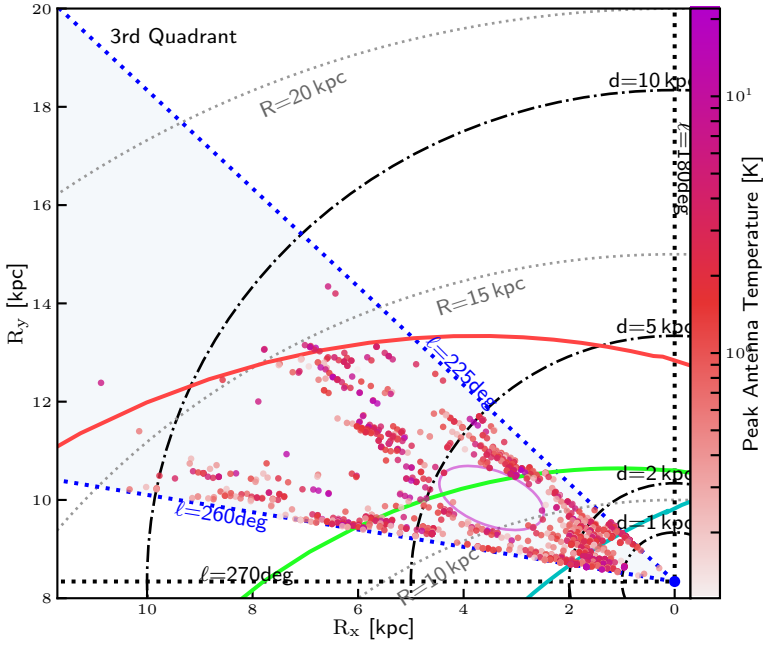

Figure 5.7: Third Quadrant of the Milky Way. The dots mark all velocity components above 5σ rms, using the same colour coding as Fig. 5.5. The observed region ($225° < \ell < 260°$) is highlighted in light blue. Heliocentric distances d and Galactocentric radii R are indicated as dash-dotted black and dotted grey circles, respectively. Positions of arms and local emission are indicated by solid lines in the same colors as in Fig. 5.5. The position of the supershell is indicated by the magenta ellipse. From the observed V_{lsr} we calculated the Heliocentric distances for each component using the Brand & Blitz (1993) rotation curve to obtain Galactic positions for all components.

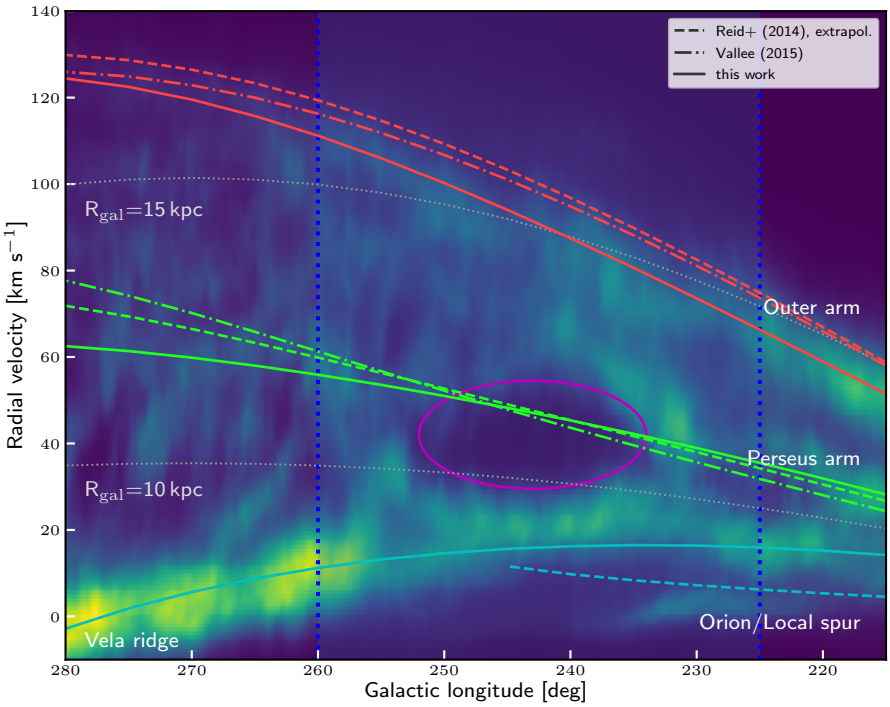

Figure 5.8: HI emission from the GASS survey (McClure-Griffiths et al. 2009) for a larger region of the outer Galaxy covering $215^\circ < \ell < 280^\circ$ indicating the integrated brightness temperature between $-5^\circ < b < 1.5^\circ$. Overplotted are the positions of the spiral arms from Reid et al. (2014) and Vallée (2015) as dashed and dash-dotted lines, respectively. The spiral arms and local emission as determined in the present work are marked by the solid lines. The dotted grey lines mark Galactocentric radii at 10 and 15 kpc. the solid magenta ellipse marks the position of the Galactic supershell GSH 242-3+37. The light blue area framed by the blue dotted lines marks the area of the present work.

5.2.1 Spiral arms and inter-arm regions

The nature of the structure of the Milky Way is still under debate (Dobbs & Baba 2014), and it is unclear weather it is a '*flocculent*' or '*grand-design*' spiral galaxy. The existence of four spiral arms would denominate it as a flocculent galaxy, whereas an interpretation as grand-design would leave the Galaxy with two density wave arms (Perseus and Scutum-Centaurus) and the others being transient features. For this reason, the location and visibility of the spiral arms towards the observed Galactic quadrant is also still under debate with either a single arm or two arms visible (compare e.g. Reid et al. 2014; 2016, Koo et al. 2017). Here we will focus on a model where both, the Perseus arm and the Outer arm, are found in the southern outer Galaxy. However, the location of the arms in the 3rd Galactic quadrant is not well constrained, as their loci are extrapolated from the northern hemisphere, where the measurements of spiral arm positions were throughout the 1st and 2nd Galactic quadrants.

We show a larger region towards the outer Galaxy in Fig. 5.8, covering Galactic longitudes $215^\circ < \ell < 280^\circ$ as mapped in HI by the GASS survey (McClure-Griffiths et al. 2009). To plot the loci of the spiral arms, we use the equation for a log-periodic spiral as described in Reid et al. (2014):

$$\ln(R_{\rm gal}/R_{\rm ref}) = -(\beta - \beta_{\rm ref}) \tan \Psi \tag{5.1}$$

where $R_{\rm gal}$ is the Galactocentric radius, $R_{\rm ref}$ the Galactocentric radius at the reference Galactocentric azimuth $\beta_{\rm ref}$ (with $\beta_{\rm ref} = 0$ towards the sun, increasing with Galactic longitude), and the pitch angle Ψ.

In Fig. 5.8 we indicate the spiral arms and Orion/Local spur as determined by Reid et al. (2014) from trigonometric parallax measurements for the northern hemisphere as dashed lines. This includes (from low to high $V_{\rm lsr}$) the Orion/Local spur, the Perseus arm and the Outer arm. Furthermore, we plot the two arms visible in the 3rd Galactic quadrant from the 4-arm model as determined as the average from several publications by Vallée (2015) as dash-dotted lines. We also plot our own estimates as solid lines for the 3 main features (from low $V_{\rm lsr}$ to high $V_{\rm lsr}$): the Vela molecular ridge (lower left) and Orion/Local spur (lower right), the Perseus arm (middle) and the Outer arm (upper). As a detailed analysis of the position of the spiral arms is out of the scope of this work, we manually modified the spiral arm parameters such as to visually match the densest emission as seen in the HI integrated intensity map.

Note that the local emission (Vela molecular ridge and Orion/Local spur) is an inter-arm feature between the Sagitarius spiral arm located in the inner Galaxy at $R_{\rm gal} \sim 7$ kpc and $\ell = 0^\circ$ (not visible here) and the outer Galaxy. The position indicated here by the solid cyan line therefore does not represent an arm that is part of the spiral pattern but just a fit to the local emission. In case of the Vela molecular ridge the emission distribution bends inwards with increasing Galactic azimuth with a large negative pitch angle, in contrast to the spiral arms extending outwards with increasing Galactic azimuth and a comparably smaller pitch angle. The parameters used for the spiral arms and the local emission are summarized in Table 5.6.

To give an overview and explore the three dimensional structure of the observed region, we present longitude-velocity ($\ell - v$) plots for different slices of Galactic latitude in Fig. 5.9 and latitude-velocity ($b - v$) plots for different slices of Galactic longitude in Figs. 5.10 and 5.11. We show the HI integrated intensity as a background image (McClure-Griffiths et al. 2009), the CO(1–0) emission from Dame et al. (2001) as black contours, and mark the positions of

Table 5.6: Spiral arm parameters. See text for a detailed description.

Name	$R_{\rm ref}$ (kpc)	$\beta_{\rm ref}$ (deg)	Ψ (deg)
Reid et al. (2014)			
Orion/Local	8.4	8.9	12.8
Perseus	9.9	14.2	9.9
Outer	13.0	18.6	13.8
Vallée (2015)			
Perseus	7.0	90.0	13.0
Outer	7.0	180.0	13.0
This work			
Vela/Orion/Local spur	9.8	-0.5	-24.0
Perseus	10.9	-16.6	5.7
Outer	14.4	-23.56	15.8

our sources observed in CO(2–1) as small crosses with those associated with dust clumps as coloured dots. We will now discuss the different features present in the area.

We find that our sources as detected in ^{12}CO(2–1) are mostly well correlated with the brightest features of the HI emission. They are tracing the local emission very well, but except for the region of the brightest HI emission located at $\ell \sim 233^\circ$, are poorly tracing the Perseus arm. We conclude that this is not a sensitivity issue, as plenty of sources at $V_{\rm lsr}$ ∼80-90 km s^{-1} are well detected in the $\ell \sim 258^\circ$ region, and therefore we find no reason why such sources should not be detected in the Perseus arm between $225^\circ < \ell < 250^\circ$. Similarly, we find the CO(1–0) emission to be poorly correlated with the Perseus arm for some slices of longitude ($\ell \sim 254^\circ$ and $\ell \sim 227^\circ$, Fig. 5.10, right panels). We rather conclude that the poor coherence of the observed source velocities with the locus of the Perseus arm in $\ell - v$ and $b - v$ plots is a consequence of the presence of the expanding Galactic supershell G 242-03+37, which we will investigate further in Sect. 5.2.2.

Several larger features can be identified spanning between the local emission and the suspected positions of the spiral arms (compare Fig. 5.9): In the region south of the supershell ($250^\circ < \ell < 260^\circ$) a network of blobs, bridges or spurs can be seen, with large clusters of clumps correlated with the brightest HI emission. At least four such complexes can be identified by eye from the $\ell - v$ maps ($\ell \sim 254^\circ$, $v_{\rm lsr} \sim 38$ km s^{-1}; $\ell \sim 257.5^\circ$, $v_{\rm lsr} \sim 50$ km s^{-1}; $\ell \sim 258^\circ$, $v_{\rm lsr} \sim 80$ km s^{-1}; $\ell \sim 259^\circ$, $v_{\rm lsr} \sim 60$ km s^{-1}), with more isolated clumps along the bridges. These bridges are also well visible in the $b - v$ plot around $\ell \sim 285.5^\circ$ (Fig. 5.10, upper right panel). Note that these bridges might not be visible in CO(1–0) (black contours), as the sensitivity is rather poor (Chapter 1.5.5). Unfortunately, due to the limited number of observed sources we are not able to give a complete summary of all complexes, but are only able to identify the largest structures (see Sect. 5.2.3).

Between $225^\circ < \ell < 240^\circ$ (i.e. north of the supershell) we find at the lower latitudes (see right hand column of Fig. 5.9) a feature in HI that is aligned perpendicular to the line-of-sight, indicating the continuation of the Perseus arm from the north. But for higher latitudes (right hand column of Fig. 5.9) this structure becomes more complex with a network of bridges

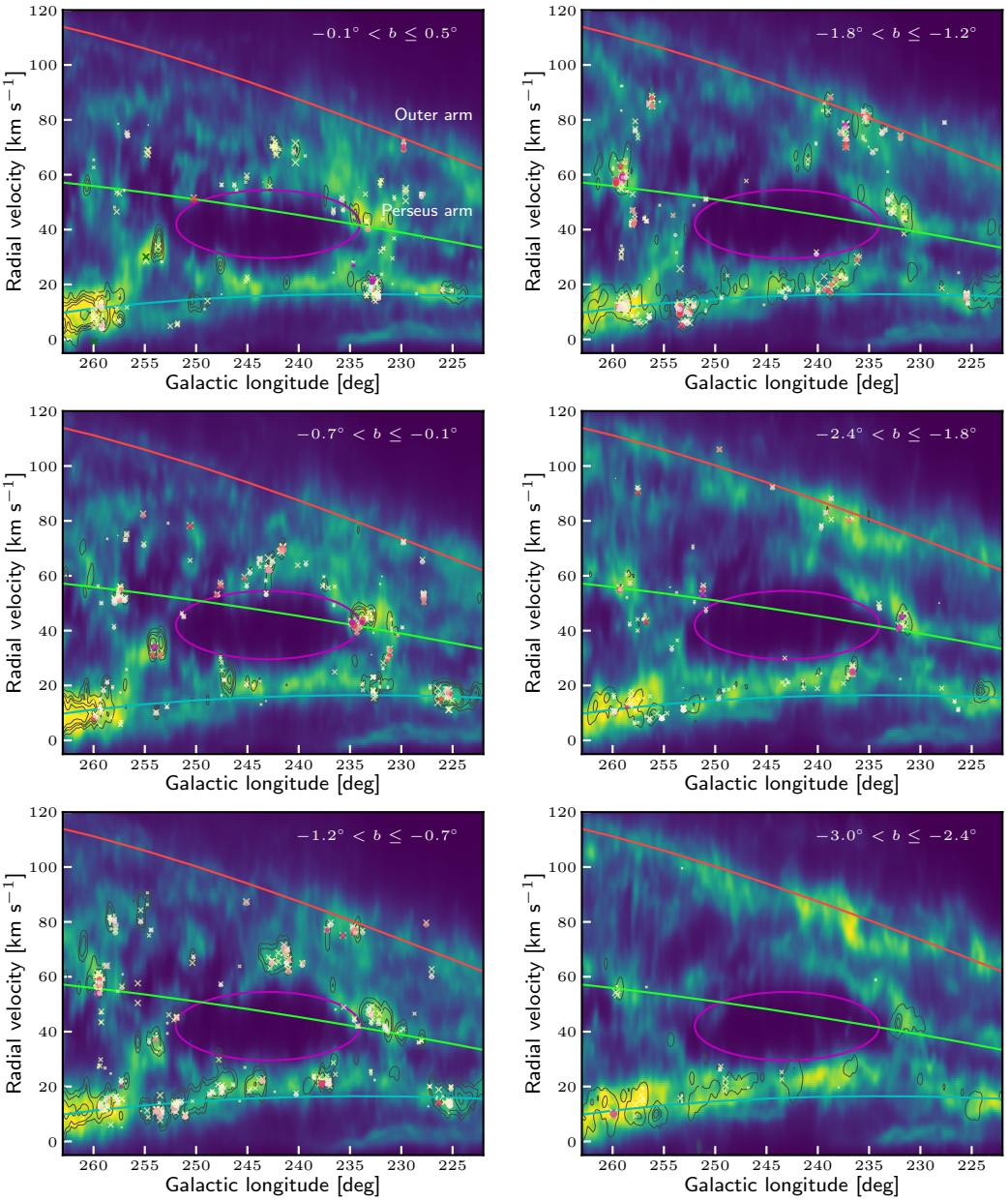

Figure 5.9: Galactic longitude vs. radial velocity integrated for slices of Galactic latitude. Latitude ranges from $b = +0.5°$ (top left panel) to $b = -3.0°$ (lower right panel). Crosses mark the CO(2–1) velocity components along a line-of-sight, with coloured dots indicating associated dust clumps. Sizes correspond to the integrated line intensity and the colours for the dust clumps to the 22 μm WISE emission being indicative of ongoing star formation. The background image shows the corresponding HI integrated intensity from the GASS survey (McClure-Griffiths et al. 2004). The contours mark the CO(1–0) emission from Dame et al. (2001) at levels of 3σ, 5σ, 7σ and the 10th, 30th, 50th and 70th percentile. The spiral arms as determined in the present work and the position of the local emission are marked by the coloured solid lines. Cyan: local emission; green: Perseus arm; red: Outer arm. The solid magenta ellipse marks the position of the Galactic supershell GSH 242-3+37.

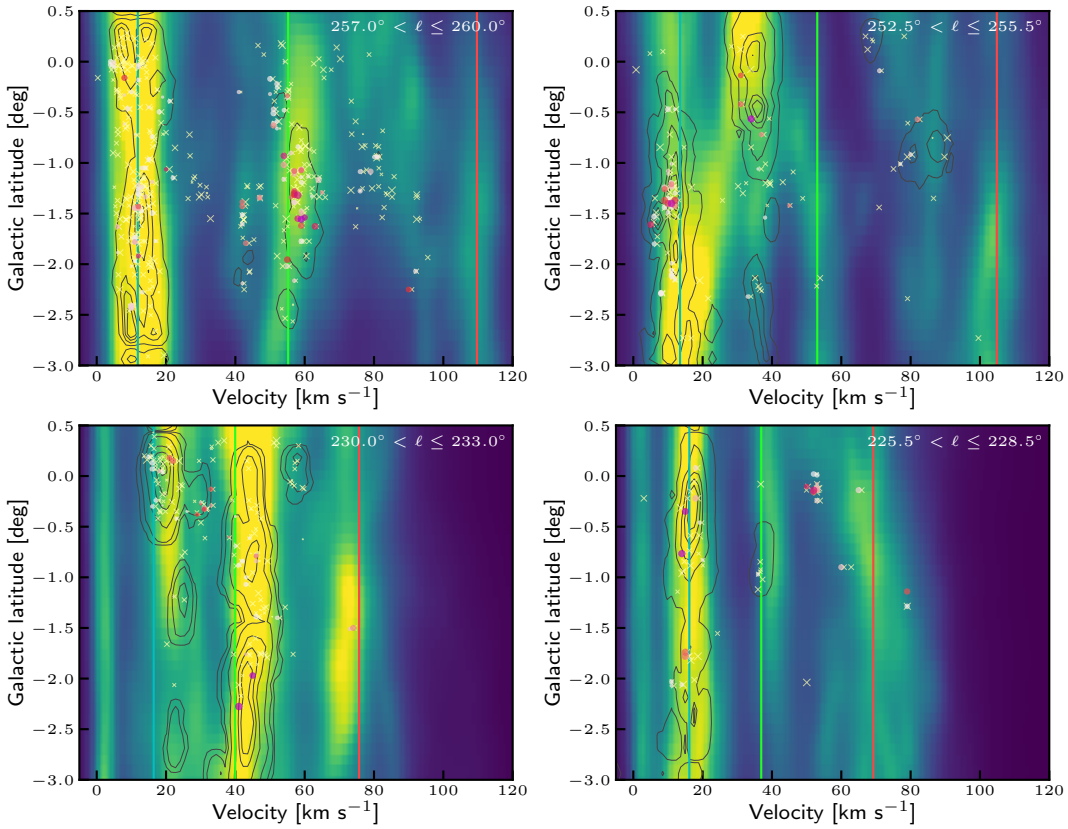

Figure 5.10: Selected slices of Galactic latitude vs. radial velocity integrated over 3° in Galactic longitude away from the Galactic supershell. Crosses mark the CO(2–1) velocity components along a line-of-sight, with coloured dots indicating associated dust clumps. Sizes correspond to the integrated line intensity and the colours for the dust clumps to the 22 μm WISE emission being indicative of ongoing star formation. The background image shows the corresponding HI integrated intensity from the GASS survey (McClure-Griffiths et al. 2004). The contours mark the CO(1–0) emission from Dame et al. (2001) at levels of 5σ, 7σ and the 10th, 30th, 50th and 70th percentile. The spiral arms as determined in the present work and the position of the local emission are marked by the coloured solid lines. Cyan: local emission; green: Perseus arm; red: Outer arm.

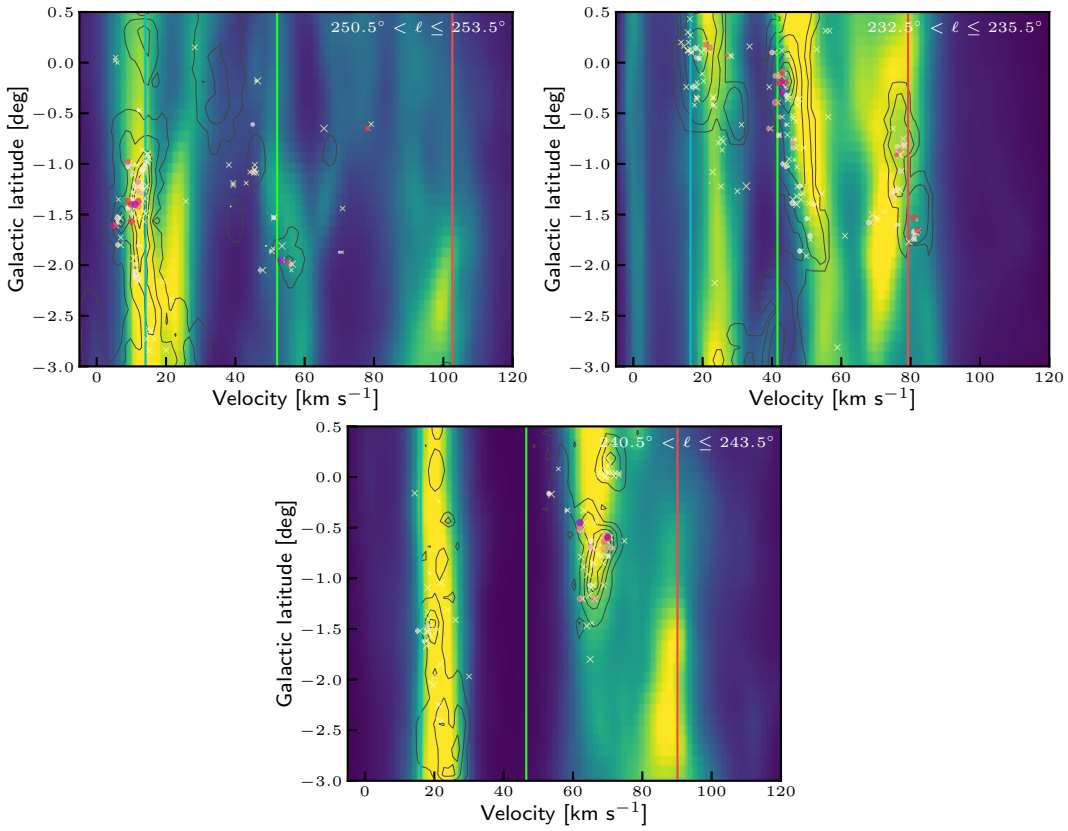

Figure 5.11: Slices of Galactic latitude vs. radial velocity integrated over 3° in Galactic longitude at the edges (top) and the center (bottom) of the Galactic supershell. Coloured dots mark the positions of the dust clumps, white crosses mark the positions of clouds identified by the CO(2–1) pointed observations that are not associated with the dust clump. The background image shows the corresponding HI integrated intensity from the GASS survey (McClure-Griffiths et al. 2004). The contours mark the CO(1–0) emission from Dame et al. (2001) at levels of 5σ, 7σ and the 10th, 30th, 50th and 70th percentile. The spiral arms as determined in the present work and the position of the local emission are marked by the coloured solid lines. Cyan: local emission; green: Perseus arm; red: Outer arm.

spanning between the Orion/Local spur and the Outer arm more parallel to the line-of-sight. This can also be seen in the $b-v$ plot in Fig. 5.10, lower left panel, where the CO emission at $b \sim 0°$ is spanning from $v_{\rm lsr} \sim 20\,{\rm km\,s^{-1}}$ out to $v_{\rm lsr} \sim 60\,{\rm km\,s^{-1}}$, whereas the local emission and the Perseus and Outer arm are more clearly separated at lower latitudes. This change in morphology and orientation in dependence on the Galactic latitude could be either interpreted as the Perseus arm being disrupted or this structure not being a spiral arm at all. In contrast to the web located south of the supershell between 250° and 260°, we only find one larger star forming complex in this area ($\ell \sim 232°$, $v_{\rm lsr} \sim 50\,{\rm km\,s^{-1}}$), located at the rim of the supershell (Fig. 5.11).

In general, we find the three-dimensional structure of the Galactic disk towards the outer Galaxy in the third quadrant to be rather complex; not only with respect to longitude and velocity/distance but also with respect to the vertical structure of the thin disc. The structures found in the observed region change rather dramatically with Galactic latitude, showing that the thin disk is rather a complex three-dimensional web-like structure than a flat pan-cake-like structure.

5.2.2 The Galactic supershell GSH 242–03+37

One of the most striking features towards the observed region is the void located at $\ell \sim 242°$ and $V_{\rm lsr} \sim 40\,{\rm km\,s^{-1}}$. This structure is known to be the Galactic supershell GSH 242–03+37 first identified by Heiles (1979) and more recently investigated by McClure-Griffiths et al. (2006). It has a diameter of the order of a kiloparsec and an expansion velocity of $\sim 7\,{\rm km\,s^{-1}}$. With the shell spanning about 15° in Galactic longitude, $25\,{\rm km\,s^{-1}}$ in velocity and centred -1.6° below the Galactic plane, we find that our observed region spans roughly a band around the equator of that supershell.

As this structure has a profound impact on this region, we will briefly discuss the possible origin of this supershell. McClure-Griffiths et al. (2006) calculate the energy needed to form such an expanding supershell to be in the order of 10^{53} ergs, which is about two orders of magnitude higher than the expected energy input from a single Type II supernova (Woltjer 1974). This would therefore require in the order of hundreds of Type II supernovae to drive this shell, which is rather unlikely, especially as there is no strong x-ray source at the centre of the shell indicating the origin of hundreds of supernova remnants. A more suitable explanation might be the passage of a high velocity cloud (HVC) through the Galactic disk, like the one observed by Park et al. (2016) for the Galactic shell GS040.2+00.6-70 in the northern hemisphere. Furthermore, HVCs are known to punch holes through galactic discs (e.g. Schulman 1996, Boomsma et al. 2008). Preliminary literature research further bolsters this hypothesis (compare e.g. Galyardt & Shelton 2016, McClure-Griffiths et al. 2006, Planck Collaboration et al. 2015), but as an investigation of the origin of this shell is out of the scope of this work, we will instead continue with its impact on the region.

A consequence of the existence of this huge expanding supershell is a low reliability of kinematic distances for sources within its vicinity. This needs to be taken into account when interpreting structures and especially spiral arms in this region of the Milky Way. Furthermore, the supershell is coincident with the extrapolation of the Perseus arm, which might be the main reason why the Perseus arm cannot be traced clearly in this part of the outer Galaxy. If a large

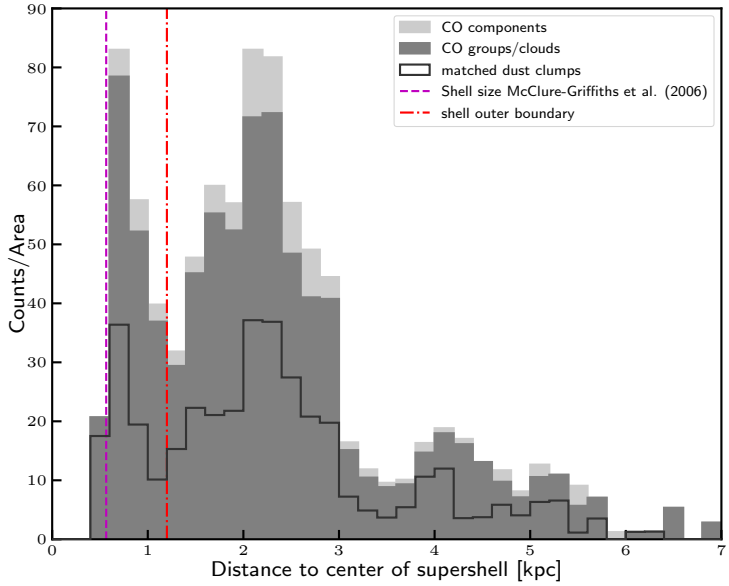

Figure 5.12: Histogram for the distance of all clouds identified in CO to the centre of the supershell. The edge of the supershell is clearly distinguishable from the other sources. Note the void at $R < 0.565$ kpc.

high-velocity cloud has hit the Perseus arm in the past, such an event might simply have lead to its local destruction, pushing the material of the arm away. Indeed, we see a ring of sources identified in CO emission around this supershell.

In Fig. 5.12 we present a histogram of the distance of the CO components, clouds and associated dust clumps to the centre of the supershell normalized by the area. With the Galactic plane being coincident with the rim around the equator GSH 242–03+37, we find the central region ($r_{\rm GSH} \leq 0.4$ kpc) void of any clumps. However, we find that the number-density of sources is increased in the wall of this supershell between 0.6 kpc$\leq r_{\rm GSH} \leq$1.2 kpc, which we estimate to be $\sim$0.6 kpc wide. There seems to be a sharp increase in number-density of clumps from the inner void to the wall, which then gradually falls off again[2]. This is in agreement with McClure-Griffiths et al. (2006), finding a sharp increase in HI from the inner region to the wall of the shell, interpreting it as an indication of compression and and being associated with a shock. We will have a more detailed look into the physical properties of the clumps located in the walls of the shell in Section 6.4.

5.2.3 Complexes and notable regions

As mentioned in Section 5.1.1 we excluded the 6 dominant bright regions located in the survey area from the automated source extraction. As can be seen from Table 5.2, these complexes are all located in a rather narrow band between Galactocentric distances from $R_{\rm gal} = 9.4$ kpc at $\ell \sim 226^\circ$ to $R_{\rm gal} = 11.5$ kpc at $\ell \sim 226^\circ$. This places most of these complexes slightly inward

[2]The broad peak between 1.4 and 3.2 kpc in Fig. 5.12 is not associated with the shell, but the superposition of different clusters of clumps in the observed region.

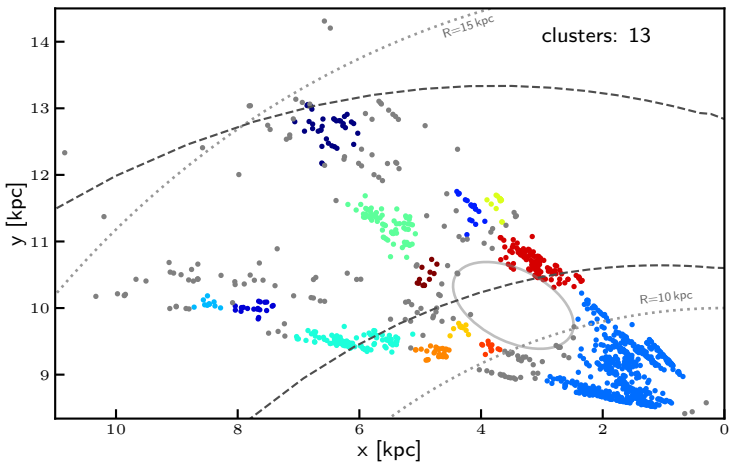

Figure 5.13: Identified clusters of CO clouds, in different colours, grey dots are not assigned to any cluster. The dashed lines indicate the loci of the Perseus and Outer arm, the dotted grey lines indicate Galactocentric radii of 10 and 15 kpc. The solid grey ellipse indicates the edge of the supershell. Be aware as projection effects sometimes make two close-by clusters appear to be one, although separated along the z-axis.

of the locus of the Perseus spiral arm. As these are located in the outer Galaxy, a density wave manifested in the Perseus spiral arm would travel faster than the rotation of the interstellar medium around the Galaxy. Being located slightly inward of the locus of the Perseus arm therefore means that these complexes would just have passed through the arm or are in the process of leaving it. With these complexes being the brightest in the survey area, and them just leaving the density wave of the spiral arm, it is possible that the activity of the regions is triggered by the passage through the arm. Such an effect is observed in M51, where the clouds after passing through the spiral arms are the brightest and most active observed (Colombo et al. 2014).

Unfortunately a detailed clustering analysis of clumps on the cloud size scale of $\sim$30 pc (Miville-Deschênes et al. 2017) is not possible with our dataset, as the incompleteness of the survey would render the number of clusters as well as the clumps per cluster and all derived properties would be lower limits.

But as much larger structures are clearly visible above the cloud-scale, we first identified those by eye, and consecutively tried to identify them in a robust way using the DBSCAN algorithm (Density-Based Spatial Clustering of Applications with Noise; Ester et al. 1996) with a minimum density of 1, effectively implementing a friends-of-friends analysis. We find that these large structures are best represented with a distance threshold of 250 pc and a minimum cluster size of 10 clouds per cluster. In total we are able to identify 13 large clusters. The results can be seen in Fig. 5.13 and a summary is given in Table 5.7. The local emission is identified as a single cluster made out of 693 CO clouds, whereas the remaining clusters are comprised of 11 to 119 CO clouds. Excluding the local emission, we find these clusters to range in size from a few hundred parsec to more than a kiloparsec, constituting the largest structures in the Galaxy after the spiral arms.

Table 5.7: Summary of the clusters identified.

Label	ℓ [deg]	b [deg]	$v_{\rm lsr}$ [km s^{-1}]	$R_{\rm gal}$ [kpc]	# clouds	$\Delta\ell$ [deg]	Δb [deg]	$\Delta v_{\rm lsr}$ [km s^{-1}]
1	251.05	−1.11	15.3	9.2	636	34.98	3.34	30.7
2	259.15	−1.14	57.5	11.3	115	4.31	2.75	15.9
3	232.76	−0.73	44.5	11.2	112	8.82	2.63	15.2
4	242.19	−0.61	66.4	12.5	72	6.46	1.99	11.4
5	235.48	−1.53	78.7	14.3	39	6.28	1.56	8.0
6	257.96	−1.63	43.2	10.5	32	2.59	2.61	5.6
7	257.63	−0.72	74.7	12.6	21	2.04	1.59	4.8
8	232.06	−0.08	56.8	12.3	18	4.75	2.07	5.4
9	227.92	−0.08	53.0	12.2	15	2.90	0.59	3.2
10	246.97	−0.21	57.3	11.6	13	4.44	2.06	2.5
11	251.90	−1.08	45.4	10.7	11	2.91	1.24	3.3
12	253.87	−1.21	37.7	10.2	11	2.89	1.70	3.4

5.2.4 Summary

In order to extend our previous analysis to the outer Galaxy between $225^\circ \leq \ell \leq 260^\circ$ we used Herschel/Hi-GAL 250 μm SPIRE continuum emission maps to select a representative sample of more than 800 sources from a rudimentary source catalogue of more than 25,000 extracted clumps using SExtracor (Bertin & Arnouts 1996), giving positions and source sizes for these clumps. To derive physical properties such as clump masses and bolometric luminosities, which require a known distance, we observed these sources in ^{12}CO(2–1) in order to obtain velocities and eventually determine distances to these dust clumps.

In the CO(2–1) emission spectra we identified 1757 clouds that consist of a total of 2034 individual velocity components, for a total of 1164 positions, including the recovered off-positions. 714 (61.3%) lines-of-sight were found with a single velocity component, whereas two or more clouds were found towards 450 (38.7%) lines-of sight, yielding on average 1.5 clouds per line of sight. Consecutively, distances were calculated using a rotation model of the Galaxy, applying the rotation curve from Brand & Blitz (1993) for all clouds and velocity components. For every line-of-sight, we finally associated the cloud with the highest integrated intensity to the according dust clump.

Combining our velocity measurements with HI emission maps from the GASS survey (McClure-Griffiths et al. 2004) and CO(1–0) maps from Dame et al. (2001), we were able investigate the structure of the southern outer Galaxy. In order to be able to investigate star formation with respect to the spiral arms, the position of the latter was discussed. We focus on the model where both, the Perseus and the Outer arm, are continued from the 2nd Galactic quadrant. The Sagittarius arm is not located in the observed region but is located further inwards within the Solar circle. In general, we find the positions of the identified CO clouds to be strongly correlated with the dense parts of the HI emission. On the other hand, we were also able to identify a web of bridges, spurs and blobs of star forming regions spanning

between the larger star forming regions, unveiling the complex three-dimensional structure of the outer Galaxy in unprecedented detail. Although the latter might be an indication of the outer Galaxy to be of a flucculent nature, a definite answer is difficult due to the influence of a large, expanding supershell in the survey area.

The Galactic supershell G242-03+37 as first identified by Heiles (1979) adds to the complexity of the structure in the outer Galaxy. In case there are indeed two arms present in the 3rd Galactic quadrant, the first one (Perseus) would have a large hole in between ($\sim 234^\circ \leq \ell \leq \sim 253$). Reviewing the literature, we hypothesize that this supershell was caused by a high-velocity cloud passing through the Galactic disc, disrupting the Perseus arm in the 3rd Galactic quadrant, and causing the observed expanding supershell. Investigating the impact of the supershell on the distribution of the CO clouds and dust clumps, we find the number-density of the sources increased within the walls of the shell. We find this to be in agreement with McClure-Griffiths et al. (2006), interpreting the steep walls of the shell as an indication of compression and being associated with a shock.

Finally large scale complexes were identified using a friends-of-friends analysis towards the outer Galaxy, hinting at a hierarchical structure at the largest scales reaching sizes up to the order of 250 pc. These complexes seem not to be necessarily associated with the spiral arms, and therefore future study of much larger regions is necessary to understand these structures.

With the distances and positions known for the selected dust clumps, we can now investigate their physical properties and compare these to the results of the previous work, in order to get a view on star formation throughout the whole Milky Way.

CHAPTER 6

Physical Properties

6.1 Introduction

In this chapter we are going to investigate the physical properties that can be derived from archival mid-infrared to sub-millimetre continuum emission data in combination with the distances obtained in Chapter 5. First we will discuss how we obtained the dust spectral energy distributions for the outer Galaxy. We will then present the derived physical properties and investigate how consistent they are, followed by a detailed look at the results in the following sections. Here we will mainly investigate the dependence on the distance to the Galactic centre (Galactocentric radius) and differences found in the physical parameters of star-forming clumps between the environments of the inner and outer Galaxy. For this purpose we use the properties derived for ATLASGAL by Urquhart et al. (2018; reviewed in Chapter 4) as a sample for the inner Galaxy and the sources of the present work for the outer Galaxy. At the end of this chapter, we will briefly look at how the spiral arms and the supershell, that happens to be located in the survey area, influence the properties of the observed clumps.

6.2 Physical Properties

6.2.1 Dust spectral energy distributions

To obtain and fit the dust spectral energy distributions (SEDs) we follow the procedures described in detail in Chapter 2 that were already used for the work described in Chapters 3 (König et al. 2017) and 4 (Urquhart et al. 2018), hence we only give a brief overview here.

We use archival mid-infrared to sub-millimetre continuum maps to obtain the SEDs in 9 different bands at 8, 12, 14, 21/22, 70, 160, 250, 350 and 500 micron. In contrast to our previous work, there is no ATLASGAL data available at 870 μm for the outer Galaxy, so we use the 250 μm positions and source sizes obtained from the source extraction process as described in Chapter 5 for the photometry. In the far-infrared to submm regime we use Herschel/Hi-GAL (Molinari et al. 2010) PACS (Poglitsch et al. 2010) and SPIRE (Griffin et al. 2010) emission maps, covering the cold dust emission from 70 μm to 500 μm. This data is complemented by mid-infrared maps from WISE (Wright et al. 2010) and MSX (Price et al. 2001) covering the wavelength regime between 8 μm and 22 μm that is mostly dominated by the emission of a hot embedded component of (proto-)stars. The fluxes for each band are obtained through aperture photometry as described in detail in our previous work (Urquhart et al. 2018), reconstructing the SED of each source. Whenever a flux was measured in the WISE emission maps at the 12 or 22 micron bands, it was preferred over the corresponding fluxes at 12 or 21 micron determined for the MSX bands due to the lower noise level and moderately better resolution

Table 6.1: Source parameters obtained from the SEDs for the first 15 sources: Galactic longitude ℓ and latitude b, heliocentric distance $R_{\rm hel}$, aperture diameter $D_{\rm app}$, linear size $D_{\rm lin}$, evolutionary class, dust temperature $T_{\rm dust}$, and optical depth τ_{350}. Full table in Appendix (Tab. A.4).

Name	$\ell_{\rm app}$ (deg)	$b_{\rm app}$ (deg)	$R_{\rm hel}$ (kpc)	$D_{\rm app}$ ($''$)	$D_{\rm lin}$ (pc)	Class	$T_{\rm dust}$ (K)	τ_{350}
G225.020–00.590	225.017	–0.588	1.3	88.9	0.13	Quiescent	10.3 ± 0.7	$(20.6 \pm 8.4) \times 10^{-5}$
G225.030+00.060	225.029	0.058	1.6	68.3	0.11	Protostellar	15.8 ± 0.2	$(126.6 \pm 6.4) \times 10^{-7}$
G225.080+00.060	225.082	0.060	1.6	63.3	0.10	YSO	14.6 ± 0.6	$(41.1 \pm 7.8) \times 10^{-6}$
G225.160–00.830	225.160	–0.835	1.7	69.6	0.12	YSO	19.9 ± 1.4	$(19.7 \pm 4.9) \times 10^{-6}$
G225.160–00.840	225.163	–0.841	1.7	65.9	0.11	Protostellar	16.5 ± 2.0	$(16.0 \pm 7.9) \times 10^{-6}$
G225.170–00.750	225.167	–0.746	1.3	53.1	0.06	YSO	16.5 ± 1.9	$(2.5 \pm 1.2) \times 10^{-5}$
G225.210–01.110	225.215	–1.110	1.3	200.0	0.31	Quiescent	12.0 ± 0.1	$(32.1 \pm 1.9) \times 10^{-5}$
G225.220–01.200	225.220	–1.195	1.2	59.3	0.07	Quiescent	17.7 ± 0.6	$(26.9 \pm 3.6) \times 10^{-6}$
G225.230–00.960	225.228	–0.961	1.3	89.5	0.13	Quiescent	16.1 ± 0.5	$(51.4 \pm 7.0) \times 10^{-6}$
G225.240–01.110	225.243	–1.106	1.2	42.5	0.03	Quiescent	15.3 ± 0.2	$(48.7 \pm 2.4) \times 10^{-6}$
G225.300–01.090	225.300	–1.093	1.3	55.3	0.07	YSO	12.7 ± 1.8	$(10.7 \pm 7.7) \times 10^{-5}$
G225.320–00.280	225.319	–0.277	1.3	90.5	0.13	Quiescent	13.1 ± 0.6	$(25.6 \pm 5.3) \times 10^{-5}$
G225.320–01.100	225.323	–1.103	1.3	85.7	0.12	Quiescent	9.7 ± 0.9	$(4.8 \pm 3.0) \times 10^{-4}$
G225.320–01.170	225.315	–1.170	1.2	51.8	0.05	Protostellar	14.8 ± 2.0	$(11.9 \pm 7.0) \times 10^{-5}$
G225.330–00.540	225.330	–0.535	1.6	42.5	0.04	YSO	21.0 ± 3.4	$(4.9 \pm 2.6) \times 10^{-4}$

of the WISE images. In this way we obtained SEDs for all observed positions as well as for off-positions that were matched with the extracted sources (see Table A.3).

We have fitted the SEDs using a single component grey-body or two component model, depending on the emission in the mid-infrared bands. In contrast to our previous work we use the emission found in the 350 μm SPIRE band as the reference wavelength due to the absence of a flux measurement at 870 μm. In total we were able to fit 611 SEDs ($\sim$77%) of the 791 sources. The SEDs for 180 sources were either not recovered completely due to sensitivity, the source being located in a crowded region, the SED being irregular or the source was too close to the edge of the Hi-GAL area (or a combination of those). We summarize the parameters used to obtain the SEDs and the fitted parameters (dust temperature and opacity) in Table 6.1 alongside the evolutionary classes as determined from the SEDs (see Chapter 6.3.2).

6.2.2 Deriving physical properties

Using the dust temperatures from the fitted SEDs and assigning distances as determined in Chapter 5.1.5, we calculate the physical properties ($L_{\rm bol}$, $M_{\rm clump}$, $N_{\rm H_2}$) from the SEDs as described in detail in Chapter 3 and König et al. (2017). As the gas-to-dust ratio increases with Galactocentric distance due to the decreasing metallicity in the outer Galaxy, we apply a correction factor according to the recently determined trend by Giannetti et al. (2017a; Eq. 2):

$$\log \gamma = 0.087 \cdot \frac{R_{\rm gal}}{[\rm kpc]} + 1.44 \tag{6.1}$$

Here a linear slope is applied to the logarithm of the gas-to-dust ratio γ, increasing the

Table 6.2: Physical parameters derived from the dust SEDs for the first 15 sources: bolometric luminosity L, clump mass M, peak column density N_{H_2}, and luminosity-to-mass ratio L/M. Full table in Appendix (Tab. A.5).

Name	L ($L_\odot$)	M ($M_\odot$)	N_{H_2} (cm^{-2})	L/M ($L_\odot/M_\odot$)
G225.020–00.590	$(49.5\pm3.2)\times10^{-2}$	$(5.3\pm1.7)\times10^{+0}$	$(31.8\pm1.6)\times10^{20}$	$(9.3\pm3.0)\times10^{-2}$
G225.030+00.060	$(383.5\pm4.7)\times10^{-3}$	$(31.6\pm8.7)\times10^{-2}$	$(22.1\pm1.8)\times10^{19}$	$(12.1\pm3.3)\times10^{-1}$
G225.080+00.060	$(58.0\pm2.5)\times10^{-2}$	$(9.0\pm2.5)\times10^{-1}$	$(54.8\pm5.3)\times10^{19}$	$(6.4\pm1.8)\times10^{-1}$
G225.160–00.830	$(29.1\pm2.1)\times10^{-1}$	$(6.2\pm1.7)\times10^{-1}$	$(27.6\pm2.4)\times10^{19}$	$(4.7\pm1.3)\times10^{+0}$
G225.160–00.840	$(56.5\pm6.9)\times10^{-2}$	$(3.6\pm1.1)\times10^{-1}$	$(28.0\pm2.9)\times10^{19}$	$(15.8\pm5.1)\times10^{-1}$
G225.170–00.750	$(64.5\pm7.6)\times10^{-2}$	$(24.4\pm8.0)\times10^{-2}$	$(33.8\pm5.7)\times10^{19}$	$(26.4\pm9.2)\times10^{-1}$
G225.210–01.110	$(97.8\pm1.1)\times10^{-1}$	$(4.4\pm1.3)\times10^{+1}$	$(146.0\pm1.4)\times10^{20}$	$(22.4\pm6.8)\times10^{-2}$
G225.220–01.200	$(56.7\pm2.0)\times10^{-2}$	$(28.7\pm9.2)\times10^{-2}$	$(34.6\pm3.8)\times10^{19}$	$(19.8\pm6.4)\times10^{-1}$
G225.230–00.960	$(166.7\pm5.5)\times10^{-2}$	$(14.9\pm4.6)\times10^{-1}$	$(79.0\pm3.8)\times10^{19}$	$(11.2\pm3.5)\times10^{-1}$
G225.240–01.110	$(223.8\pm2.6)\times10^{-3}$	$(26.0\pm8.4)\times10^{-2}$	$(6.1\pm1.5)\times10^{20}$	$(8.6\pm2.8)\times10^{-1}$
G225.300–01.090	$(37.7\pm5.3)\times10^{-2}$	$(11.9\pm4.0)\times10^{-1}$	$(15.0\pm2.3)\times10^{20}$	$(3.2\pm1.2)\times10^{-1}$
G225.320–00.280	$(75.1\pm3.2)\times10^{-1}$	$(7.3\pm2.3)\times10^{+0}$	$(40.6\pm2.0)\times10^{20}$	$(10.2\pm3.2)\times10^{-1}$
G225.320–01.100	$(17.3\pm1.6)\times10^{+0}$	$(11.4\pm3.6)\times10^{+0}$	$(71.9\pm4.2)\times10^{20}$	$(15.1\pm5.0)\times10^{-1}$
G225.320–01.170	$(7.9\pm1.1)\times10^{-1}$	$(8.4\pm2.9)\times10^{-1}$	$(15.1\pm2.7)\times10^{20}$	$(9.4\pm3.5)\times10^{-1}$
G225.330–00.540	$(55.4\pm9.0)\times10^{+0}$	$(5.0\pm1.6)\times10^{+0}$	$(8.0\pm2.2)\times10^{21}$	$(11.0\pm3.9)\times10^{+0}$

factor from $\gamma\sim150$ near the solar circle to $\gamma\sim550$ at 15 kpc Galactocentric radius. We point out that without this correction the clump masses in the outer Galaxy would be underestimated by up to a factor of five compared to masses calculated using the widely adopted value of 100 for the gas-to-dust ratio for the inner Galaxy. We summarize the physical properties derived from the dust emission for each source in Table 6.2. A summary of the dust properties, also taking into account their evolutionary stage (Chapter 6.3.2), can be found in Table 6.3. We will discuss the physical properties in detail and put them into context of their Galactic environment in the following sections.

6.2.3 Consistency checks

To check the consistency of our method, we compare the N_{H_2} column densities derived from the SEDs with column densities derived from the ^{12}CO(2–1) emission. To obtain the column densities from ^{12}CO(2–1), we calculate them as

$$N_{H_2} = X_{^{12}\mathrm{CO}(1-0)} \cdot \frac{1}{0.7} \cdot I(^{12}\mathrm{CO}(2-1)), \tag{6.2}$$

where we use the H_2-to-CO conversion factor of $X_{^{12}\mathrm{CO}(2-1)} = 2.3\times10^{20}\,\mathrm{cm^{-2}}\,(\mathrm{km\,s^{-1}})^{-1}$ obtained by Brand & Wouterloot (1995) for the outer Galaxy, and the integrated line intensity $I(^{12}\mathrm{CO}(2-1))$ as measured from the observed spectra with a line ratio of ^{12}CO(2–1)/^{12}CO(1–0)= 0.7 (Sandstrom et al. 2013). In the left panel of Fig. 6.1 we show the comparison of the column densities derived from dust and CO, finding both quantities to be in good agreement (p-value of 0.0155) although a large scatter is observed.

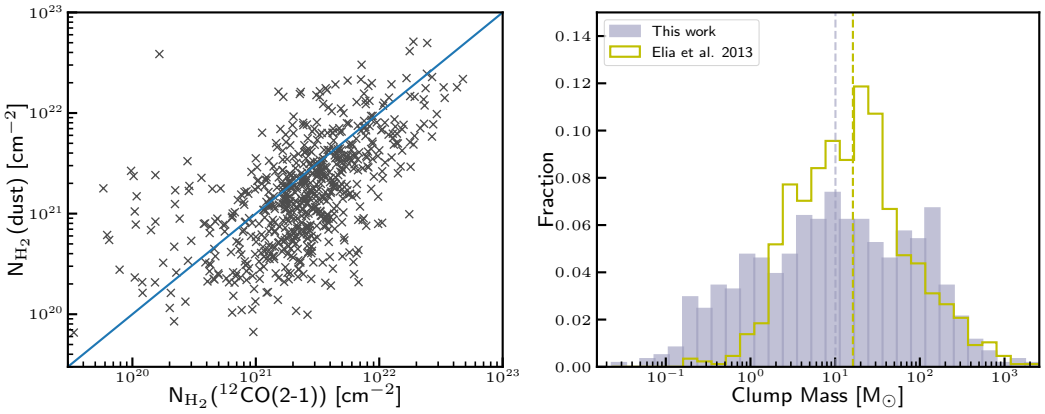

Figure 6.1: Consistency checks. Left: Comparing peak N_{H_2} column densities derived from dust and ^{12}CO(2–1). Equality of both quantities is marked by the solid line. Right: Clump masses as calculated for the present work (blue) and from Elia et al. (2013; yellow outline) for $216.5° < \ell < 225.5°$ from the dust SEDs.

We also compare our results to a similar sample of southern outer Galaxy sources from Elia et al. (2013) obtained for an adjacent area of the southern sky ($216.5° < \ell < 225.5°$). In the right panel of Fig. 6.1 we compare the clump masses of both samples. Similar to the masses calculated for our sample, we apply a correction factor for the varying gas-to-dust ratio found by Giannetti et al. (2017a) to the masses calculated by Elia et al. (2013). We find the distribution to be slightly different (p-value of 5.3×10^{-4}) with the sample of the present work picking up significantly more lower mass sources. This is reflected by the mean values to be almost identical with values of 58.2 ± 6.0 and $56.8 \pm 5.4\,M_\odot$ for our sample and the Elia et al. (2013) sample, respectively, but the median values to differ by a factor of 1.6 (10.1 and $16.2\,M_\odot$, respectively). The difference for these two samples is likely caused by a combination of two effects. First, the areas are non-overlapping, so the differences might reflect intrinsic differences of the two areas covered in the outer Galaxy, especially when taking into account the Galactic supershell GSH242-03+37 covered in the present work (see Section 5.2.2). Furthermore, the distances for the sample by Elia et al. (2013) were obtained with the NANTEN 4m telescope with a beamsize of 2.6′ (Kim et al. 2004), only allowing to assign distances to the brighter sources within the beam.

From the comparison with the column densities derived from ^{12}CO as well as with the clump masses from Elia et al. (2013), we conclude that our methods can be considered reliable, as either the distributions are similar as shown by an Anderson-Darling test or agree on average within the margin of error.

6.2.4 Distance biases

Some physical properties suffer from observational distance biases, such as the bolometric luminosity, clump mass and linear source size. These biases are caused by the fixed sensitivity and resolution of the telescope/instrument used. Due to the limited sensitivity, only the brightest and most massive sources can be observed at the farthest distances. Similarly the

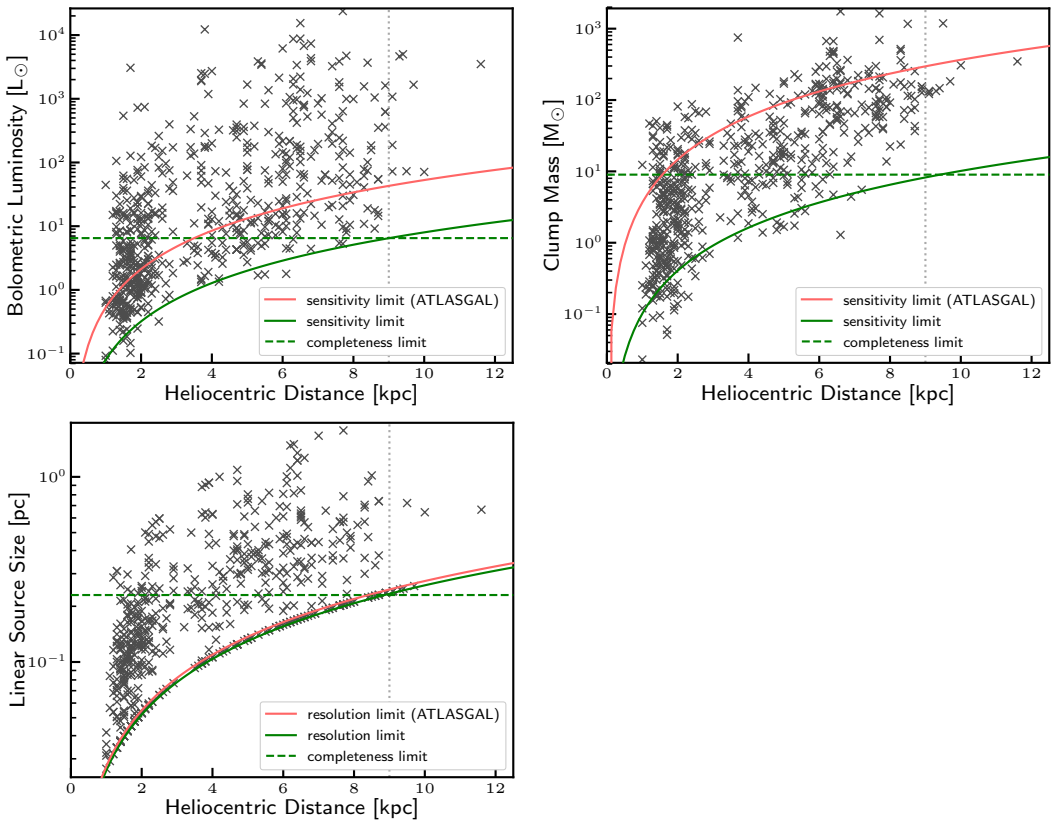

Figure 6.2: Observational distance biases. Bolometric luminosity (top-left), clump mass (top right), and linear source size (lower left) versus Heliocentric distance. The solid lines mark the distance dependent sensitivity/resolution limit for the outer Galaxy sample (green) and ATLASGAL (red). The horizontally dashed green lines mark the limit above which our survey is not suffering from a distance bias up to 9 kpc (vertical dotted line).

limited angular resolution allows us only to observe sources down to this apparent size, which at farther distances translates to larger linear source sizes. To avoid misleading trends that are introduced due to theses sensitivity and resolution based selection biases, we determine the the completeness limit, above which the survey does not suffer from these selection effect up to the given distance.

First we need to distinguish between distance independent parameters and distance dependent parameters. The dust temperature, peak column density and L/M are distance independent, as they are either intrinsic to the sources or cancel out the distance dependence. As mentioned in the last paragraph, the bolometric luminosity and clump mass are directly scaled by the distance squared, and hence are highly dependent on correct distances and are prone to distance dependent observational biases. The same is true for the linear source size, which is linearly dependent on the distance. The CO line-width is indirectly dependent on the distance, as it is known that the line-width is correlated with the size of a source (Larson 1981).

To determine in which mass and luminosity range our survey is not suffering from distance biases, we show the distribution of luminosities, masses and linear source sizes with respect to

heliocentric distance in Fig. 6.2. We calculate the theoretical sensitivity according to Equations 3.1 and 3.2 for the bolometric luminosity and clump mass from the minimum values found for each survey as input parameters, varying the distance. Similarly we calculate the resolution limit from Equation 3.3 but use the beam sizes for ATLASGAL (19.2″) and SPIRE 250 (18.2″) as input parameters. The theoretical sensitivity and resolution limits are plotted as green (outer Galaxy) and red (ATLASGAL) solid lines in Fig. 6.2.

As the source density of our sample drops significantly after 9 kpc we estimate the completeness limit up to this distance as the value of the theoretical sensitivity or resolution limit at 9 kpc. For the bolometric luminosity we find that sources out to ∼9 kpc distance are strongly affected by the sensitivity of this survey for luminosities below 6.5 $L_\odot$. Masses of 9 $M_\odot$ are found to be the completeness limit for clump mass, whereas for the linear source size, sources smaller than 0.23 pc suffer from the distance bias. We will filter our samples according to these completeness limits when analysing the distance dependent physical properties.

We also added the sensitivity limits as derived for the ATLASGAL compact source catalogue (Urquhart et al. 2018) as red solid lines. As can be seen, the two surveys are different by about two orders of magnitude in clump mass and one order of magnitude in bolometric luminosity. No significant difference is found for the resolution limit. The difference in sensitivity is a result of the two source catalogues being extracted from maps with different sensitivity. The outer Galaxy catalogue was selected from Herschel Hi-GAL 250 μm SPIRE maps, whereas the ATLASGAL compact source catalogue is based on the ATLASGAL 870 μm LABOCA maps.

6.3 Discussion and dependence on Galactocentric radius

In this section we will discuss the physical properties derived in the previous section. We put a focus on the analysis of the properties with respect to the distance to the Galactic centre, comparing the results for the outer Galaxy sample of the present work to the sources located in the inner Galaxy as characterized in Urquhart et al. (2018).

6.3.1 Sample adaptation: inner and outer Galaxy

To compare our sample of outer Galaxy clumps to the inner Galaxy sample identified by ATLASGAL, we need to make sure that both samples are comparable. To mitigate the influence of observational biases, we will work on sensitivity matched and distance limited samples.

In the left panel of Fig. 6.3 we show the 250 μm peak fluxes of both samples for those sources where we obtained a distance. In the right panel we show the histograms of the 250μm peak fluxes, but extend the outer Galaxy sample to all sources we extracted, that have a complete SED, to a total of 17,782 sources.

As the source selection was done using different starting points, the sensitivity of the Herschel Hi-GAL 250 μm SPIRE selected sample for the outer Galaxy (blue) is about 2 orders of magnitudes higher than the sensitivity of the ATLASGAL 870 μm LABOCA selected sample (red). This SPIRE 250 μm band has a sensitivity limit of ∼13 mJy/beam[1]. Comparing this

[1] http://herschel.esac.esa.int/Docs/PMODE/html/ch02s03.html

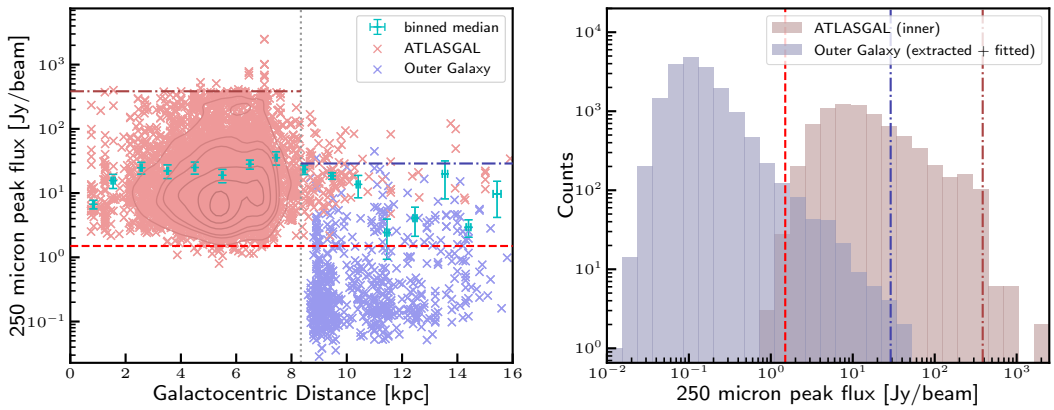

Figure 6.3: Left panel: 250 μm peak fluxes as function of Galactocentric distance. Right: Histogram of 250 μm peak fluxes including all extracted sources for the outer Galaxy. The red dashed line marks the sensitivity limit for ATLASGAL at 250 μm of $\sim$ 1.5 Jy. The dash-dotted lines mark the 3σ (i.e. 99.73%) percentiles, approximately indicating upper limits for the inner and outer Galaxy samples. The vertical dotted grey line in the left panel indicates the position of the Sun at 8.34 kpc.

value to the 3σ sensitivity of 180 mJy/beam for the 870 μm band of ATLASGAL and scaling the sensitivity limit to 250 μm using the relation $S_{250} = S_{870} \cdot (\frac{870}{250})^{1.75}$, we find the sensitivity of the 250 μm SPIRE band to be about 109 times higher than the sensitivity found for the 870 μm band used for ATLASGAL. This introduces a strong observational bias, as a survey based on the 250 μm SPIRE band will pick up objects two orders of magnitude less luminous compared to the objects with the lowest luminosity in ATLASGAL. Therefore we use a peak flux threshold of 1.5 Jy/beam at 250 μm as calculated from ATLASGAL at a heliocentric distance of $\sim$9 kpc as a lower filtering limit for both samples (indicated by the red dashed lines in Fig. 6.3), reducing the sample size for the outer Galaxy to 126 sources.

In Fig. 6.3 we can already see a peculiarity of the outer Galaxy: the highest peak flux densities reached by any given source are about an order of magnitude lower than the highest peak flux densities found in the inner Galaxy. This can also be seen from the 3σ percentiles of the two distributions, as indicated by the dash-dotted lines for the inner (385 $M_\odot$) and outer Galaxy (29 $M_\odot$). We interpret this not to be an observational bias, as the ATLASGAL sources in the outer Galaxy are located on the far-side of the Galaxy, therefore picking up the brightest sources at these extreme heliocentric distances. We conclude that the lower upper limit of flux densities when compared to the inner Galaxy is therefore an intrinsic property of sources located in the outer Galaxy.

Furthermore, as the number of sources drops significantly beyond 9 kpc heliocentric distance for the outer Galaxy sample (compare e.g. Fig. 6.2), we limit both samples (ATLASGAL and outer Galaxy) to sources no farther away than 9 kpc when comparing both samples. We also exclude all remaining ATLASGAL sources that are located in the outer Galaxy, as these would be biased to higher masses and luminosities due to their large heliocentric distance as compared to the average distance of the present work. This also allows us to simply refer to the ATLASGAL sample as the *inner Galaxy sample* and the sources of the present work as the

Table 6.3: Summary of physical properties of the whole population of clumps and the three evolutionary sub-samples identified.

Parameter	#	$\bar{x}$	$\frac{\sigma}{\sqrt{(N)}}$	σ	$x_{\rm med}$	$x_{\rm min}$	$x_{\rm max}$
Temperature (K)	611	17.29	0.20	4.94	15.88	9.65	41.31
YSO	259	20.18	0.35	5.62	19.10	10.57	41.31
Protostellar	197	15.76	0.22	3.02	15.12	9.88	25.97
Quiescent	155	14.39	0.21	2.55	14.00	9.65	24.60
Radius (pc)	611	0.40	0.02	0.46	0.30	0.06	6.21
YSO	259	0.49	0.03	0.55	0.39	0.07	6.21
Protostellar	197	0.34	0.03	0.38	0.25	0.06	4.65
Quiescent	155	0.34	0.03	0.36	0.24	0.06	3.14
Log[Luminosity ($L_\odot$)]	611	1.16	0.04	1.10	1.03	−1.10	4.38
YSO	259	1.88	0.07	1.09	1.88	−0.54	4.38
Protostellar	197	0.75	0.05	0.75	0.71	−1.03	2.39
Quiescent	155	0.48	0.06	0.71	0.41	−1.10	2.80
Log[Clump Mass ($M_\odot$)]	611	0.99	0.04	0.93	1.00	−1.64	3.24
YSO	259	1.31	0.06	0.92	1.45	−1.05	3.24
Protostellar	197	0.78	0.06	0.89	0.79	−1.22	2.71
Quiescent	155	0.71	0.07	0.82	0.70	−1.64	3.21
Log[L/M ($L_\odot/M_\odot$)]	611	0.17	0.03	0.67	0.10	−1.21	2.17
YSO	259	0.57	0.04	0.66	0.59	−1.21	2.17
Protostellar	197	−0.04	0.04	0.50	−0.06	−1.18	1.67
Quiescent	155	−0.23	0.04	0.47	−0.26	−1.19	1.44
Log[Peak N_{H_2} (cm^{-2})]	611	21.26	0.02	0.55	21.28	19.80	22.61
YSO	259	21.46	0.03	0.56	21.56	19.90	22.61
Protostellar	197	21.12	0.04	0.50	21.12	19.92	22.39
Quiescent	155	21.10	0.04	0.49	21.16	19.80	22.16

filtered outer Galaxy sample.

6.3.2 Evolutionary Sequence

Based on the flux densities obtained for the SEDs we determine the evolutionary state of the sources, following the classification scheme introduced in König et al. (2017; Chapter 3), which was also used by Urquhart et al. (2018; Chapter 4) for the entire ATLASGAL sample. For the mid-infrared bright sources we follow here the naming scheme of our latest paper and refer to these as young-stellar-objects (YSOs), well aware, that these might also include some compact HII regions, which we did not identify individually. We will therefore refer to the following three classes:

- Quiescent sources, which are dark at 70 μm (no compact emission at 70 μm) and represent the earliest phase of star-formation in our sample. These sources might or might not be collapsing.
- Protostellar sources, which are bright at far-infrared and submm wavelengths but are

not sufficiently evolved to produce significant emission at mid-infrared wavelengths ($F_{20} \leq 0.1$ Jy). These sources are in the process of collapse and are internally heated.

- Young-stellar-objects (YSOs) which are bright at mid-infrared wavelengths ($F_{20} > 0.1$ Jy). This group of sources is significantly evolved to produce strong emission at mid-infrared wavelengths by an internal heating source.

This classification scheme has been proven to be reliable as shown by Giannetti et al. (2017b) using molecular line data. It was further bolstered by our recent work on the ATLASGAL sample (Urquhart et al. 2018), showing clear trends for increasing dust temperature and the bolometric luminosity to clump mass ratio, proving this evolutionary sequence.

Cumulative histograms for the dust properties and the three evolutionary phases of all sources are shown in Fig. 6.4. Again we find the evolutionary stages to be well characterized by the dust temperature, the bolometric luminosity and the luminosity-to-mass ratio as found in König et al. (2017) for the Top100 sample all with p-values below 5.8×10^{-4}. These three properties are therefore excellent indicators of the evolutionary phase of a clump. Care has to be taken though, as there is a large overlap between the different phases, and therefore we can not simply read of the evolutionary phase of a single clump by only taking into account these numbers. However, they can be used to determine statistical properties and identify significant trends in the data.

For the remaining three physical properties (clump mass, linear source size and H_2 column density), the quiescent and protostellar evolutionary stages are indistinguishable with a p-value of 0.1. Only the clumps in the YSO phase show, on average, slightly higher values of these properties than the two earlier phases with p-values below 1.8×10^{-4}. This indicates that the classification scheme tends to identify the larger, more massive clumps as being more evolved, indicating that the more massive clumps evolve significantly faster than their low-mass counterparts.

6.3.3 Dust temperatures

First we take a look at the dust temperature and optical depth, as these are determined as fit parameters from the SEDs and are distance independent. We find that the dust temperatures range from 9.65 K to 41.31 K with a mean value of 17.29 K. For the optical depth we find that all our sources are optically thin ($\tau \ll 1$) at 350 μm, as the optical depths range from 1.9×10^{-6} up to a maximum of 2.9×10^{-3}.

In Fig. 6.5, upper left panel, we investigate the correlation of the dust temperatures with Galactocentric radius. For this purpose we calculate the slope and correlation coefficient through linear regression as well as the two-sided p-value testing the null-hypothesis that the our sample is equivalent to a distribution with a slope of zero[2]. Taking into account the given uncertainties by Monte-Carlo sampling our data, we find a significant correlation between the dust temperature and Galactocentric distance with a correlation coefficient of 0.78, and a two-sided p-value of $9.0 \pm 0.1 \times 10^{-4}$, rejecting the null-hypothesis. We determine the slope of the dust temperature to be $\Delta t = 0.58 \pm 0.07$ K per kiloparsec Galactocentric radius, which is

[2]Finding a p-value below 3σ (i.e. 0.0027) would imply the slope to be significantly different from zero.

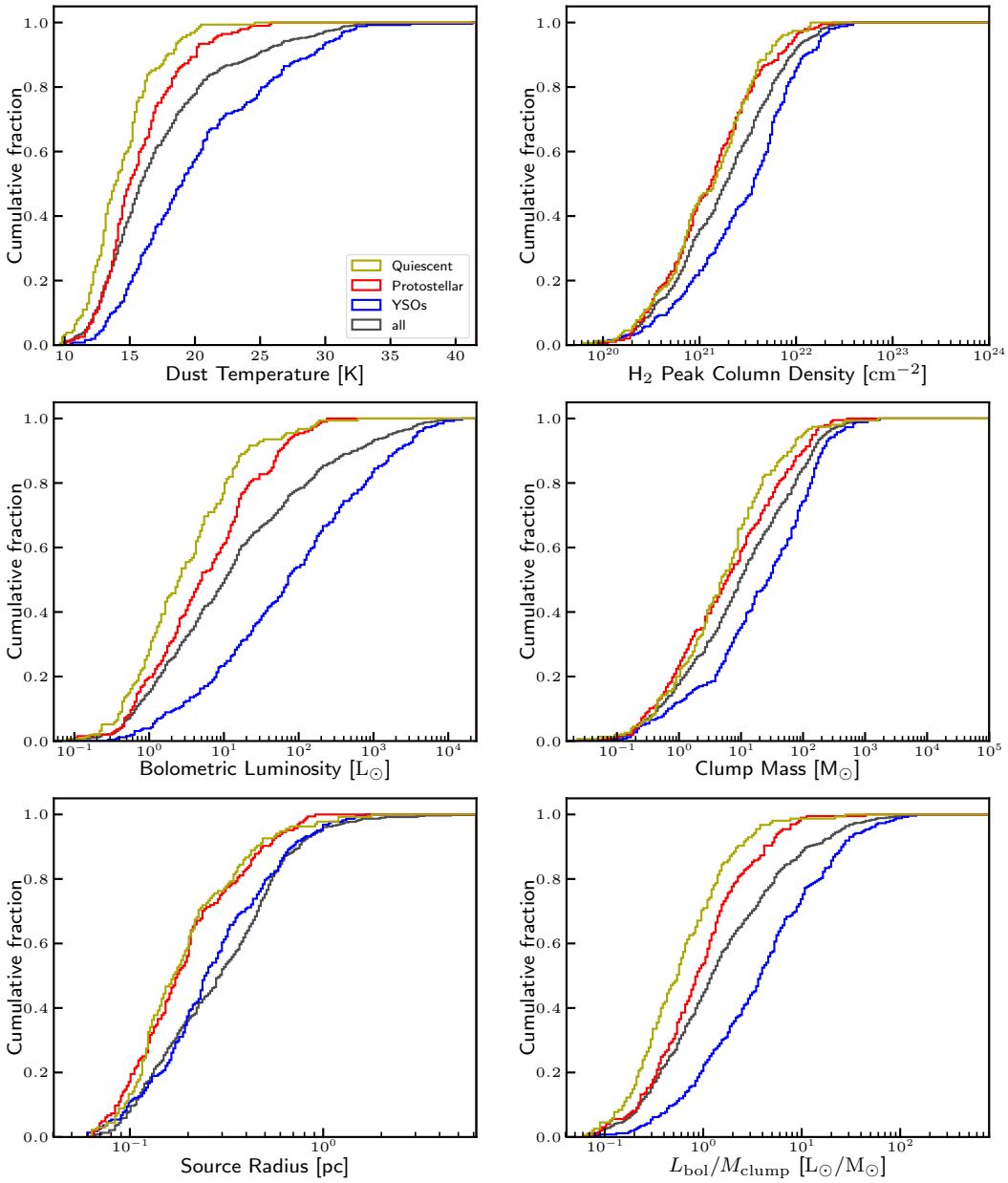

Figure 6.4: Cumulative distributions for the derived parameters of this survey. Coloured lines indicate the distribution for the different evolutionary phases, whereas the dark grey line represents the full sample.

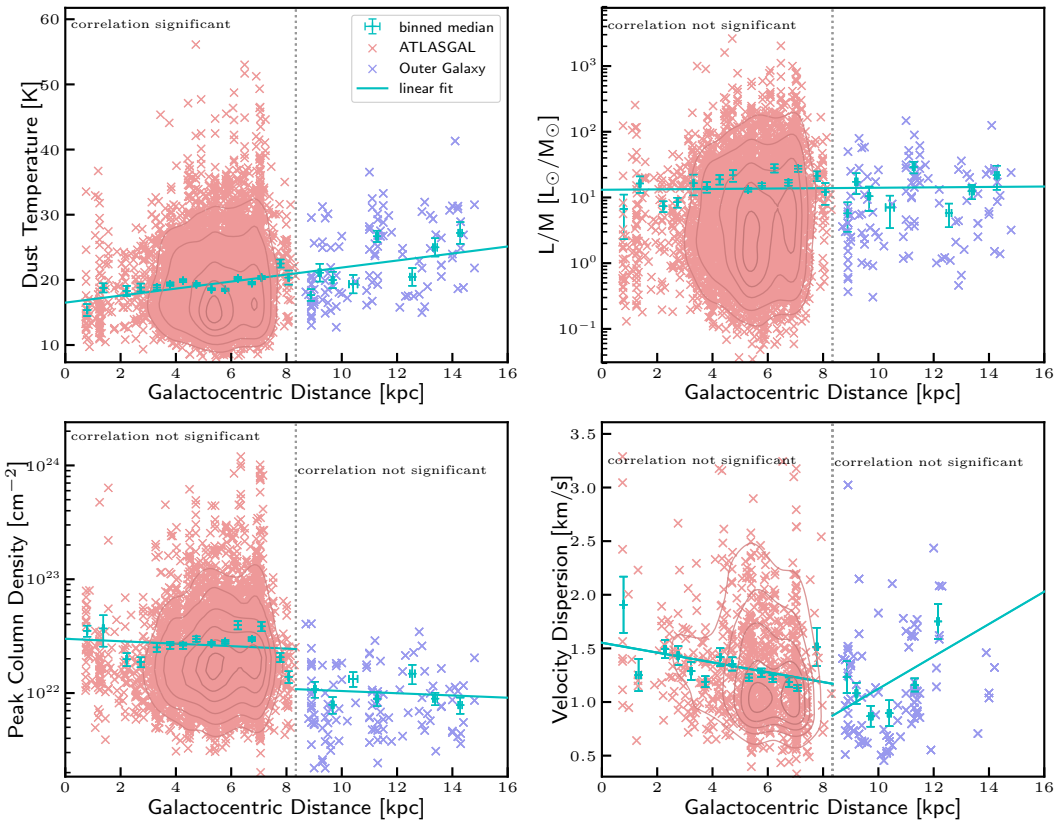

Figure 6.5: Dependence of physical parameters on Galactocentric radius for distance independent properties (filtered for 250μm flux).

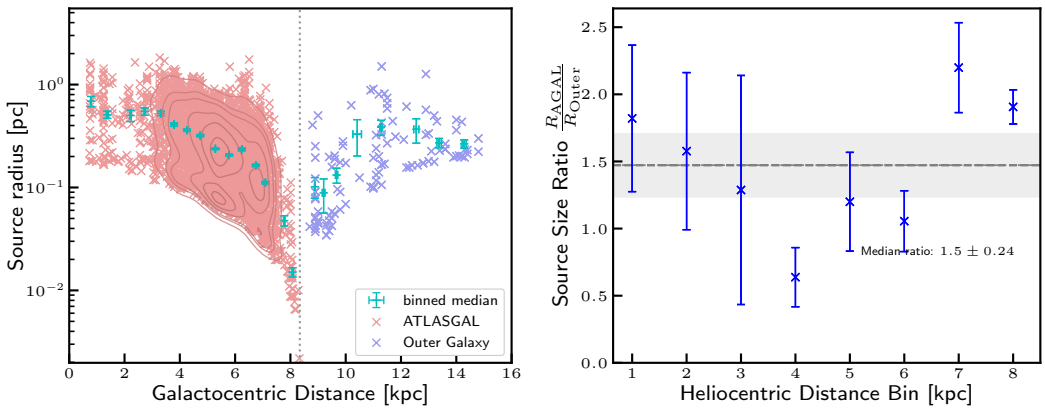

Figure 6.6: Left: dependence of linear source size on Galactocentric distance. Right: ratio of source sizes for similar heliocentric distance bins. The horizontal dashed line marks the median value for all bins and the grey-shaded area the standard deviation from the median.

consistent within 3σ with the value of 0.44 determined by Urquhart et al. (2018). We interpret this as a combined effect of less cooling due to the increasing gas-to-dust ratio, making cooling through the gas less efficient in the clumps of the outer Galaxy, as well as an effect of less shielding from the interstellar radiation field due to the lower densities. We find no trend with Galactocentric radius for the optical depth.

6.3.4 Source sizes

In Fig. 6.4, lower-left panel, we show the distribution of linear source sizes for our sample. Linear source sizes derived from the apparent full-width at half maximum source size vary between 0.06 pc and 6.21 pc yielding a mean source size of 0.40 pc. This is almost identical to the value of 0.48 pc for the ATLASGAL sample in the 1st and 4th Galactic quadrant (Urquhart et al. 2018), showing that both samples trace structures of similar scale, allowing for a detailed comparison of the different samples.

The linear source sizes are highly correlated with the distance to the observer due to the limited resolution of the maps as described in Chapter 6.2.4. This can be nicely seen in Fig. 6.6, left panel, showing that sources found near the solar circle at 8.34 kpc are on average smaller than those located far away due to the limited resolution. Unfortunately, this makes it impossible to find any trend with Galactocentric radius using a correlation test.

To mitigate this observational bias, we compare sources in similar heliocentric distance bins, which are then subject to similar distance biases, cancelling out the effects. This is shown in Fig. 6.6, right panel, where the ratio of the linear source size in the inner Galaxy distance bin to the value found in the corresponding outer Galaxy bin is plotted for bins containing at least 10 sources. From this we find that the sources located in the inner Galaxy are on average larger (factor ~ 1.5) than those found in the outer Galaxy.

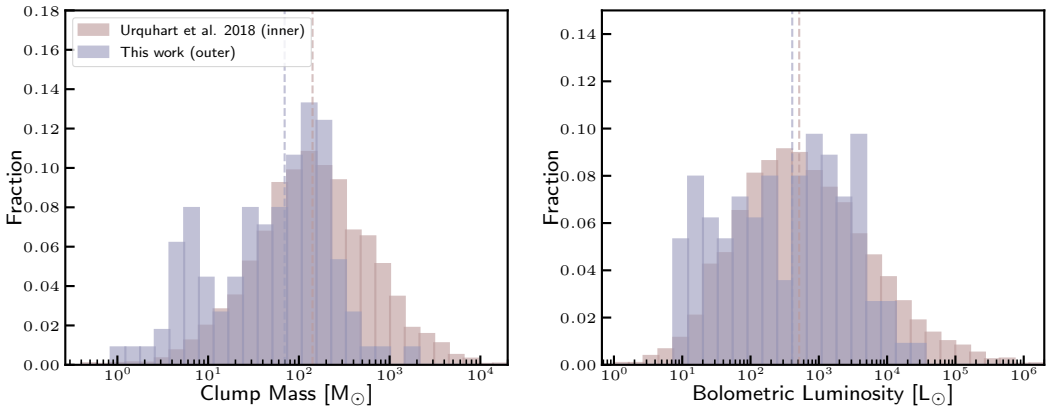

Figure 6.7: Clump mass (left) and bolometric luminosity (right) histograms for inner and outer Galaxy comparing the samples of the present work and Urquhart et al. (2018) (filtered for 250 μm flux). Vertical dashed lines indicate the median of the corresponding sample.

6.3.5 H_2 Column Density

The peak H_2 column density is found to range between 6.3×10^{19} cm^{-2} and 4.1×10^{22} cm^{-2} with a mean value of 3.8×10^{21} cm^{-2} in the outer Galaxy. In Fig. 6.5, lower left, we show the peak H_2 column density as a function of Galactocentric distance. We find a significant drop by a factor of ~ 3 in peak H_2 column density from the inner to the outer Galaxy between $r_{\rm gal} \approx 7.5$ kpc and $r_{\rm gal} \approx 9$ kpc. This is not surprising, as the H_2 surface density drops of by up to an order of magnitude from the inner Galaxy to the outer Galaxy (e.g. Heyer & Dame 2015) within just a few kiloparsec. We fail to find any further correlation with Galactocentric radius for either the inner and outer Galaxy, although W49 (at $r_{\rm gal} \approx 7.6$ kpc) and W51 ($r_{\rm gal} \approx 6.3$ kpc) are clearly increasing the average peak column density.

6.3.6 Bolometric luminosity and clump mass

The bolometric luminosities for the outer Galaxy sample range between 8.0×10^{-2} L$_\odot$ and 2.4×10^4 L$_\odot$ with a mean value of 3.6×10^2 L$_\odot$. Clump masses range from 2.3×10^{-2} M$_\odot$ to 1.7×10^3 M$_\odot$ with a mean value of 58 M$_\odot$. These values are on average one and two orders of magnitude lower than the values for the inner Milky Way found by Urquhart et al. (2018). The difference in average clump masses and bolometric luminosities between the two surveys are caused mainly by two effects: an observational bias and a physical change of the environment.

As discussed in Chapter 6.3.1, both the sensitivities of the ATLASGAL survey and the present work differ significantly, introducing an observational bias. From Equations 3.1 and 3.2 in Chapter 3.5 can be seen that the luminosities and masses are directly tied to the measured fluxes, and therefore the difference in sensitivity is the major cause for the observed difference in average luminosities and masses found by the two surveys. To counter this effect, we apply a sensitivity threshold for the 250 μm emission of 1.5 Jy, at which both surveys are cut to compare them (‘*filtered samples*’ from here on, see Chapter 6.3.1).

We show the histograms of the clump masses and bolometric luminosities for the filtered

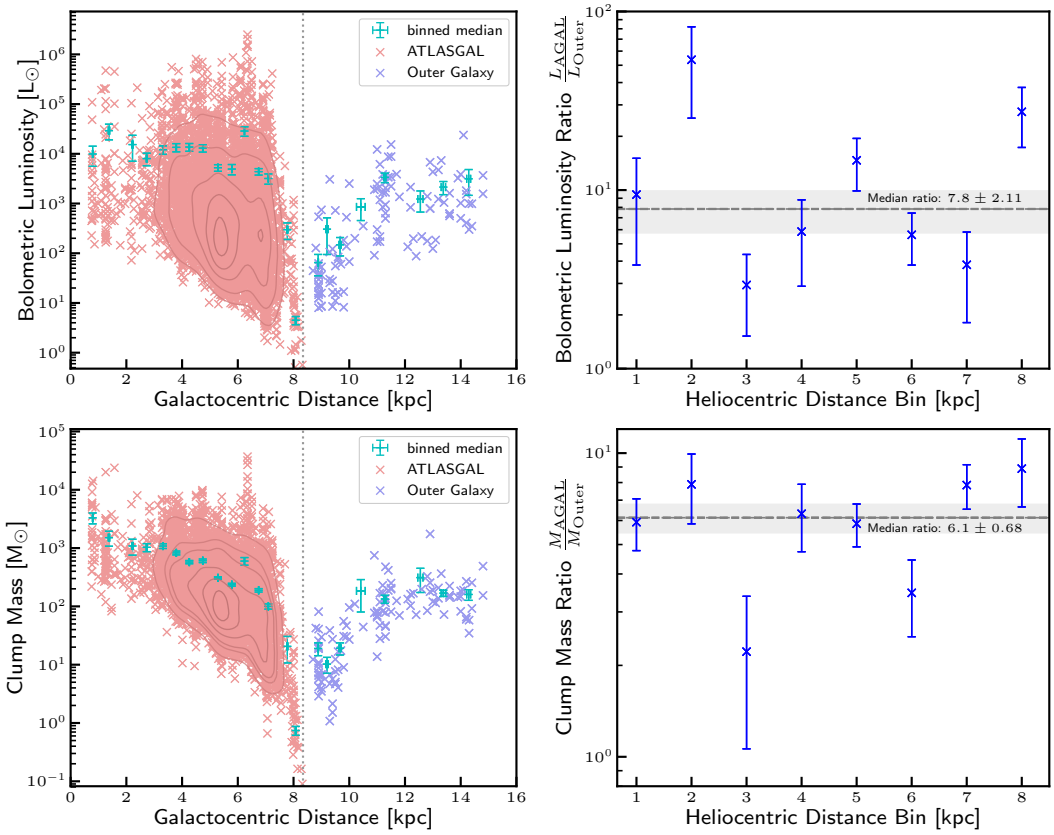

Figure 6.8: Dependence of bolometric luminosity (top) and clump mass (bottom) on Galactocentric distance (left column). On the right hand column the inner-to-outer Galaxy ratio of equal heliocentric distance bins are calculated for luminosity (top) and mass (bottom). The horizontal dashed line marks the median value for all bins and the grey-shaded area the standard deviation from the median.

samples in Fig. 6.7. We find the median of the masses and luminosity to differ by a factor of 2.0 and 1.3, respectively. The poor similarity of the outer Galaxy sample to a Gaussian distribution is caused by the small sample size and is not a physical effect. However, we find the most extreme ATLASGAL sources to be an order of magnitude more massive and luminous than those found in the outer Galaxy, and see an excess in mass and luminosity at the high-end tails of the distributions for the ATLASGAL sample.

We conclude that this excess in high-mass (and luminosity) sources reflects an underlying physical difference between the inner and outer Galaxy. As the mean mass surface density decreases with Galactocentric radius, the available mass to form a clump is significantly reduced. In fact, the mass surface density drops an order of magnitude between the inner and the outer Galaxy (Heyer & Dame 2015).

In Fig. 6.8, left column, we show the dependence of the bolometric luminosity (top) and clump mass (bottom) on Galactocentric distance for the filtered samples. Similar to the linear source size (Chapter 6.3.4), these properties are biased with heliocentric distance: the farther

away, the brighter a clump needs to be to get detected, biasing the detected sources towards more luminous and massive clumps. This selection effect prevents that the correlation with Galactocentric distance can be calculated like we did for the dust temperature (Chapter 6.3.3).

However, the upper limits for masses and luminosities are not prone to this selection effect. In fact, we observe the same steep drop of the maximum masses and luminosities from the inner to the outer Galaxy as we have seen for the peak flux densities in Chapter 6.3.1, which is expected, as the flux densities, masses and luminosities are directly correlated, as discussed before. We find that the drop in clump mass is about an order of magnitude, similar to the drop found in sensitivity, and similar to the drop of the mass surface density (Heyer & Dame 2015). From this we conclude, that the maximum mass of clumps formed is directly correlated to (and therefore limited by) the mass surface density of the Milky Way. This also implies, that the fragmentation of the interstellar medium into clumps is independent of the mass surface density, as otherwise we would find either more clumps with even lower maximum masses or less clumps with higher masses (e.g. comparable to the inner Galaxy) in the outer Galaxy.

To further investigate the masses and luminosities as a function of Galactocentric radius, we can follow the procedure we used for the linear source size. Therefore, we calculate the ratio for equal bins of heliocentric distance between inner and outer Galaxy, cancelling out the distance bias and taking into account the uncertainties. This is shown in Fig. 6.8, right column. We find the values for the bolometric luminosity on average to be higher for the inner Galaxy than for the outer Galaxy with a median ratio of 7.9 ± 2.1. Similarly we find the clump masses in the inner Galaxy to be significantly higher on average than those found in the outer Galaxy, with a median ratio of 6.1 ± 0.67. As for the H_2 column density, this is to be expected taking into account the steep drop of the mass surface density from the inner to the outer Galaxy (e.g. Heyer & Dame 2015), thus reducing the available matter to form clumps and high-mass stars.

The ratio of the bolometric luminosity to the clump mass is a measure of star-formation efficiency, as shown by Eden et al. (2015). In Fig. 6.5 (upper right panel) we plot the luminosity-to-mass ratio as a function of Galactocentric distance, extending the analysis of Urquhart et al. (2018; Chapter 4) to the outer Galaxy. Taking into account uncertainties, we find the luminosity-to-mass ratio to be on average constant ($0.0 \pm 0.02\,L_\odot/M_\odot$ kpc^{-1}) throughout the Milky Way with a p-value of 0.5, accepting the null-hypothesis of the sample being equivalent to a distribution with a slope of zero. We conclude that although the masses and luminosities are on average lower in the outer Galaxy, the underlying physical processes of star-formation are the same throughout the Milky Way.

6.3.7 Star formation relations

In Fig. 6.9 we show the bolometric luminosity plotted versus the clump mass. For a given clump one expects the luminosity to increase during the contraction phase, hence moving upwards in the figure until stars reach the zero age main sequence (diagonal solid line). When star formation has started, the clump gets dispersed, decreasing its mass, hence moving left in the diagram. These evolutionary paths through the diagram are indicated by the grey tracks, as calculated by Molinari et al. (2008). In order to visualize the differences between the evolutionary phases as described in Chapter 6.3.2, we show the linear fits to the evolutionary classes as dash-dotted lines in the left panel. As can be seen, the sources of the different classes

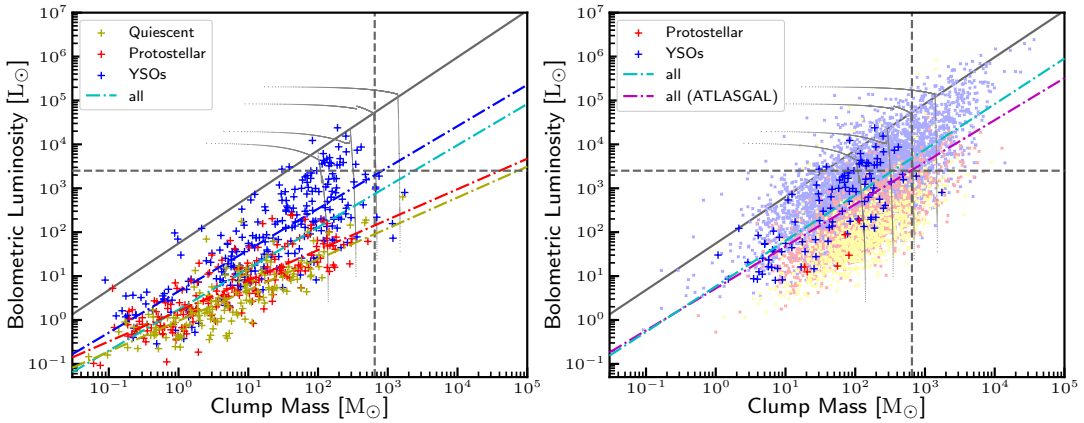

Figure 6.9: Bolometric luminosity versus clump mass. Left: all outer Galaxy sources. Right: ATLASGAL (light colour) and outer Galaxy sources filtered for the 250 μm sensitivity threshold. The grey tracks indicate the evolutionary path through the diagram for the given initial masses as calculated by Molinari et al. (2008). The diagonal solid line marks the expected luminosity for a given mass for a zero age main sequence (ZAMS) star. The horizontal dashed line indicates the expected luminosity for a B2 star ($\sim 8\,M_\odot$) as calculated by Mottram et al. (2011a). The vertical dashed line marks the threshold calculated by Csengeri et al. (2014) above which the clumps are likely to host massive dense cores or a high-mass protostar. The dash-dotted lines are linear fits to the three evolutionary classes. The light coloured crosses are the same evolutionary stages but from Urquhart et al. (2018).

move up in the plot as expected from the evolutionary scheme described in Chapter 6.3.2. This trend is consistent with the cumulative histogram of the bolometric luminosity-to-clump mass ratio $L_\odot/M_\odot$ shown in the lower right panel of Fig. 6.4. There we find the three classes to be well separated with all p-values below 5.5×10^{-5}, following the expected evolutionary trend.

Further we indicate the expected luminosity for a B2 star ($\sim 8\,M_\odot$) as calculated by Mottram et al. (2011a) as dashed horizontal dashed line. Above this threshold we assume that at least one massive star has formed in the clump being responsible for most of its luminosity. The vertical dashed line marks the clump mass threshold above which it is likely that the clumps host massive dense cores or a high-mass protostar (Csengeri et al. 2014). From these thresholds we see that only the minority of the sources in the outer Galaxy are able to form a high-mass star (32 sources) and the majority of these have already done so (24 sources).

In the right panel of Fig. 6.9, we compare the sensitivity and distance filtered outer Galaxy and ATLASGAL samples, with a linear fit to each shown as cyan and magenta dash-dotted lines, respectively. We find the trends for both samples to be in good agreement, with slopes of 0.96 ± 0.01 and 1.04 ± 0.09 for ATLASGAL and the outer Galaxy, respectively. This similarity is also reflected in the constant luminosity-to-mass ratio we find with respect to Galactocentric radius, as can be seen in Fig. 6.8 (upper right panel). There we find a slope of $0.4 \pm 2.3 \times 10^{-2}\,L_\odot/M_\odot$/kpc with a p-value of 0.48 ± 0.001, being consistent with the null-hypothesis of the sample being drawn from a distribution with a slope of zero. This shows that although the clump masses and bolometric luminosities differ significantly for the inner

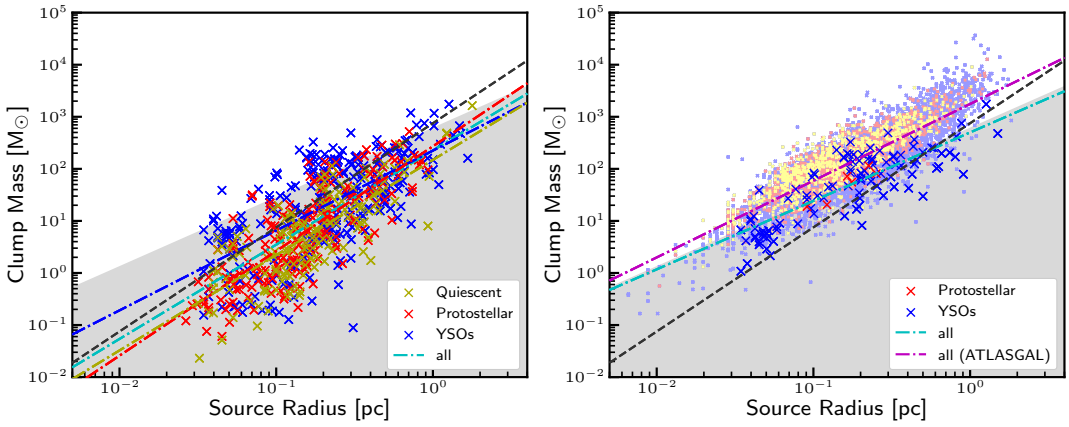

Figure 6.10: Clump mass versus source radius. Left: all outer Galaxy sources. Right: ATLASGAL (light colour) and outer Galaxy sources (both filtered for the 250 μm sensitivity threshold). The shaded area marks the regime where only low-mass stars form as determined by Kauffmann et al. (2010b). The black dashed line marks the lower limit for effective high-mass star formation as determined by Urquhart et al. (2014c), indicating a surface density threshold of 0.05 g cm^{-2}. The coloured dotted lines are a linear fit to the corresponding sub-samples and the black dash-dotted line a fit to the full sample. The light coloured crosses are the same evolutionary stages but from Urquhart et al. (2018).

and outer Galaxy, the star formation processes on clump scales are the same independent of Galactocentric radius, as the luminosity-to-mass ratio is invariant to location. These results are consistent with Urquhart et al. (2014c), finding that although the environment affects how clumps form and and determines their initial properties, however, they collapse independent from their large scale environment once formed.

6.3.8 Mass-size relation

In Fig. 6.10 we show the clump mass plotted versus the source radius with the full outer Galaxy sample in the left hand panel, and the sensitivity and distance filtered inner(ATLASGAL) and outer Galaxy samples in the right hand panel.

The grey shaded area marks the regime where supposedly only low-mass stars form as determined by Kauffmann et al. (2010b), with 86 sources (21%) of the full outer Galaxy sample above the threshold. The black dashed line marks the lower limit for effective high-mass star formation as determined by Urquhart et al. (2014c) indicating a surface density threshold of 0.05 g cm^{-2} found for the inner Galaxy using the ATLASGAL, where 174 sources (i.e. 28%) are found above this threshold. Although we find the majority of the clumps to be able to only form low-mass stars, as we did in the last section, we find a significantly higher fraction to potentially form high-mass stars according to the used thresholds. Taking also into account our findings on the number of methanol masers and HII regions present in the survey area for the outer Galaxy, we conclude that the thresholds based on mass surface density are likely to be different in the inner and outer Galaxy, as the mass surface density drops significantly according to the review by Heyer & Dame (2015).

For the full outer Galaxy sample (left), we compare the evolutionary phases (colour-coded), no trend with regard to the evolutionary state of the clumps, as can be seen from the linear fits to the individual classes (coloured dash-dotted lines). This is in agreement to no trends being found with evolutionary stage for either the clump masses or the sizes individually, as we have seen in Fig. 6.4, centre right and lower left panels. In the right hand panel of Fig. 6.10 we show the sensitivity filtered inner (ATLASGAL) and outer Galaxy samples. Linear fits to both samples show no significant difference with regard to the slopes of $1.47 \pm 0.05\,M_{\odot}$/pc and $1.31 \pm 0.11\,M_{\odot}$/pc for the inner and outer Galaxy, respectively, but with offsets of $17.6 \pm 0.3 \times 10^2\,M_{\odot}$ and $5.0 \pm 0.2 \times 10^2\,M_{\odot}$ reflect the difference in the average clump mass found in the previous section.

6.3.9 Independent high-mass star formation tracers

To further identify high-mass star forming clumps, we have also investigated the presence of methanol Class II masers as identified by the Methanol MultiBeam survey (MMB; Green et al. 2012), which are thought to be exclusively associated with high-mass star formation (Urquhart et al. 2015). In the whole area of our survey, only 2 methanol Class II masers are found (G254.880+0.451 and G259.939-0.041), indicating either a lower rate of high-mass star formation, or being the result of the lower metallicity towards the outer Galaxy, and thus reducing the amount of methanol available, or a combination of both effects.

Therefore we also investigated the number of HII regions in the survey area as identified by the Red MSX Survey (Lumsden et al. 2013) and the WISE catalogue of Galactic HII regions (Anderson et al. 2014), as the formation of HII regions is independent of the metallicity. Merging both catalogues we find 10 known HII regions in our survey area (3 from the RMS survey, 8 from the WISE catalogue with one source in both), as well as another 24 candidate HII regions from the WISE catalogue. These are about a factor 20–30 less sources per unit-area as compared to the inner Milky Way. We therefore conclude that indeed the rate of high-mass star formation is significantly lower in the outer Galaxy than in the inner Galaxy.

At the same time we see a clear drop of the highest masses, luminosities, column densities and 250 μm peak flux densities between $\sim 7.5\,\mathrm{kpc} \leq R_{\mathrm{gal}} \leq 9\,\mathrm{kpc}$ from the inner to the outer Galaxy (compare Figs. 6.3, 6.5 and 6.8). As also the H_2 mass surface density drops by an order of magnitude from the inner to the outer Galaxy (compare Fig. 7; Heyer & Dame 2015), we speculate that these are connected.

In Table 6.4 we present the mean of the maximum values found in bins of 0.5 kpc for

Table 6.4: Comparison of inner and outer Galaxy averaged maximum values for different physical properties.

Parameter	Inner Galaxy	Outer Galaxy	Ratio
H_2 surface density	$3.9\,M_{\odot}\,\mathrm{pc}^{-2}$	$0.39\,M_{\odot}\,\mathrm{pc}^{-2}$	9.8
Clump mass	$3.4 \times 10^4\,M_{\odot}$	$5.0 \times 10^3\,M_{\odot}$	6.8
Bolometric Luminosity	$1.9 \times 10^6\,L_{\odot}$	$1.9 \times 10^5\,L_{\odot}$	10.2
Peak H_2 column density	$6.6 \times 10^{23}\,\mathrm{cm}^{-2}$	$3.1 \times 10^{22}\,\mathrm{cm}^{-2}$	21.4
250 μm peak flux density	692.6 Jy/beam	47.6 Jy/beam	14.6

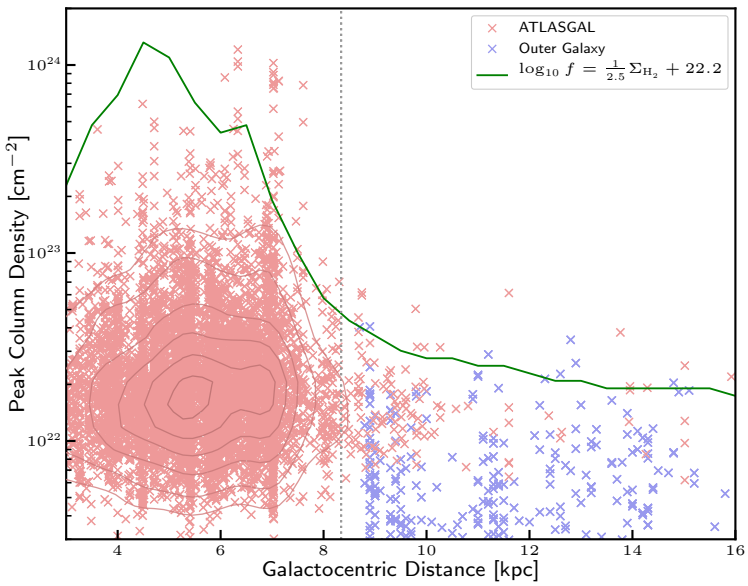

Figure 6.11: N_{H_2} peak column density for the unfiltered samples of ATLASGAL and the outer Galaxy. The green curve is the mean of the surface densities as found in Heyer & Dame (2015), Fig. 7, manually scaled to the column density in order to illustrate the similarity.

physical properties of clumps in the inner and outer Galaxy. We excluded the transition region between $\sim 7.5\,\mathrm{kpc} \leq R_{\mathrm{gal}} \leq 9\,\mathrm{kpc}$ in order to clearly separate both regions, and use the unfiltered samples in order to include the most extreme sources found throughout the Milky Way. We find that the four physical properties follow a similar general trend as the H_2 surface density, with the masses and column densities deviating on the average by up to a factor of two. Moreover, we find the drop in column density to be also similar to the drop in number density of high-mass star forming regions as found in the previous paragraphs.

In Fig. 6.11 we therefore plot the distribution of the N_{H_2} peak column density for the unfiltered ATLASGAL and outer Galaxy samples as red and blue crosses, respectively, including the most extreme sources as before. To illustrate the similarity between the distributions we determine the mean H_2 mass surface density per 0.5 kpc bin from Heyer & Dame (2015), and manually scale it to the N_{H_2} peak column density (green curve). Although a more detailed analysis including a more complete sample of sources for the outer Galaxy is needed, we find the similarity between the upper limit of the N_{H_2} peak column density and the Galactic H_2 mass surface density striking enough to draw the conclusion that these, as well as the other physical properties of the clumps, which show a similar profile, are indeed connected to the Galactic H_2 mass surface density.

We therefore suggest that the H_2 mass surface density of the Galaxy determines the mass distribution of the clumps, effectively limiting the maximum clump masses and column densities – similar to the initial mass function (IMF) that determines the distribution of stars forming from a given mass reservoir. This hypothesis is further supported by the observed decrease in number density of high-mass star forming clumps from the inner to the outer Galaxy, dropping by a factor of 20-30 as discussed in the previous paragraph, which is in line with the trends of

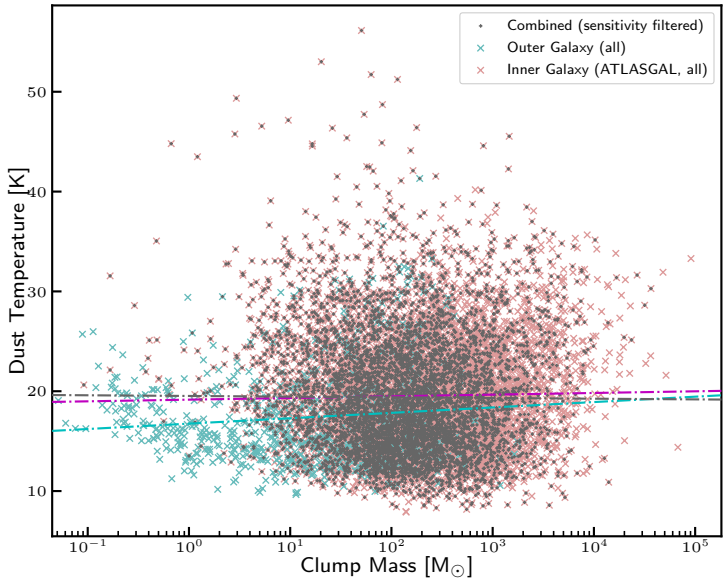

Figure 6.12: Dust temperature versus clump mass. The cyan, magenta and grey dash-dotted lines are linear fits to the data, showing no significant correlation between clump mass and dust temperature for the individual samples or the combined, sensitivity filtered sample.

the clump properties.

Following these arguments, we conclude that the lower H_2 surface density found in the outer Galaxy favours the formation of lower mass clumps. And as mostly lower mass clumps are formed, predominantly lower mass stars can be formed according to the IMF. Hence we find much less high-mass star formation in the outer Galaxy.

6.3.10 Temperature-mass relation

As we have seen in Section 3.6.2, the dust temperature is a good indicator of evolutionary phase. In Fig. 6.12 we plot the dust temperature as a function of clump mass for the ATLASGAL inner Galaxy sample (red) and the full outer Galaxy sample (cyan), as well as for the combined, sensitivity filtered sample for the inner and outer Galaxy. As found by Urquhart et al. (2018) for the full ATLASGAL sample, we find that there is no significant correlation between the evolutionary phase (as indicated by the dust temperature) and the clump mass for the outer Galaxy. We find all slopes to be smaller than 0.23 K/M$_\odot$ with a correlation coefficients below 0.097 and p-values above 0.02, in agreement with the null-hypothesis of the samples being equivalent to a distribution with a slope of zero.

These results imply that after the clump-collapse has started, the total clump mass does not change significantly, in agreement with the evolutionary tracks derived by Molinari et al. (2008). This either indicates that infall and outflow cancel each other out or both are not significant with respect to the total mass of the clumps, i.e. star-formation is fast compared to the clump accretion and infall time scale. Furthermore it means that the sources of the sample have not yet started to significantly clean up their envelope towards the end of their evolution,

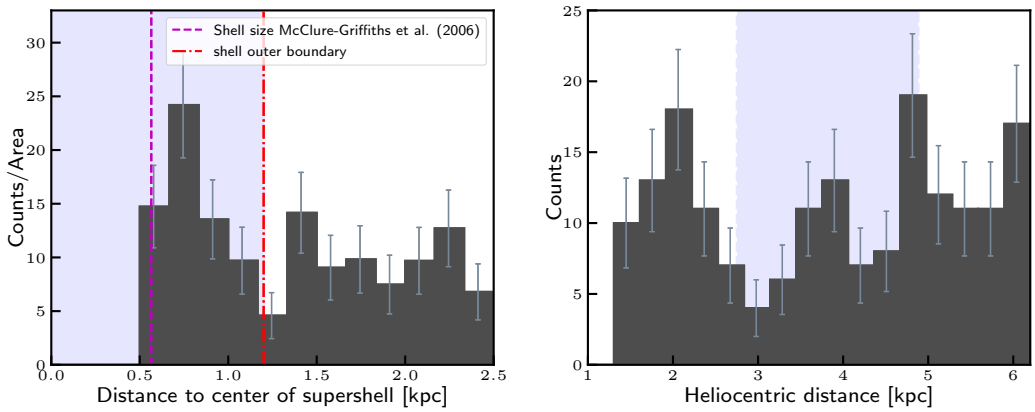

Figure 6.13: Histograms of the sensitivity filtered sources (see text) for the distance to the centre of the supershell (left) and Heliocentric distance of this subsample. The blue shaded area marks the distance range spanned by the shell.

as otherwise a trend for the higher temperature sources would be observed. Finally, as there is no correlation for either the inner or outer Galaxy sample, it also shows that the underlying mechanism is independent of the Galactic environment.

6.4 Physical Properties with respect to the Galactic Supershell

In Section 5.2.2 we had a look at the distribution of clumps around the supershell. In this section we will take a look at the impact of the supershell on its environment.

To avoid observational and selection biases, we limit our sample to only include sources that are symmetrically distributed around the shell with a maximum distance of 2.5 kpc to its centre, reducing our sample size to 429 sources. Furthermore, we need to filter our sample for sensitivity and resolution thresholds, with the farthest source in this sub-sample is located at 6.2 kpc Heliocentric distance. For this distance we limit our sample to sources with $L_{\rm bol} > 2\,{\rm L}_{\odot}$, $M_{\rm clump} > 3\,{\rm M}_{\odot}$, and $r_{\rm src} > 0.15$ pc according to Fig. 6.2, reducing our sample to 178 sources.

In Fig. 6.13 we show two histograms for this subsample. First we show the distribution of sources per unit area with respect to the distance to the shells centre (left). Again we are able to identify the central void of the supershell extending up to ~ 0.5 kpc as well as the the enhanced number of sources located in the shells wall. In the right panel, we show the histogram of heliocentric distances, with the range covered by the supershell marked as blue shaded area. We find no bias to any heliocentric distance, although peaks from local clusters are clearly visible. These are either from local emission (at ~ 2 kpc), the edge of the shell (at ~ 4 kpc), the rear wall (at ~ 5 kpc) or farther out (at 6 kpc).

In Fig. 6.14 we investigate the influence of the Galactic supershell on the physical properties of the clumps, as well as for the $F_{70\mu{\rm m}}/F_{500\mu{\rm m}}$ flux ratio as an indicator for star-formation activity. For all properties we are unable to find any significant correlation with the distance to the centre of the supershell, with all p-values well below the 3σ level, accepting the null-

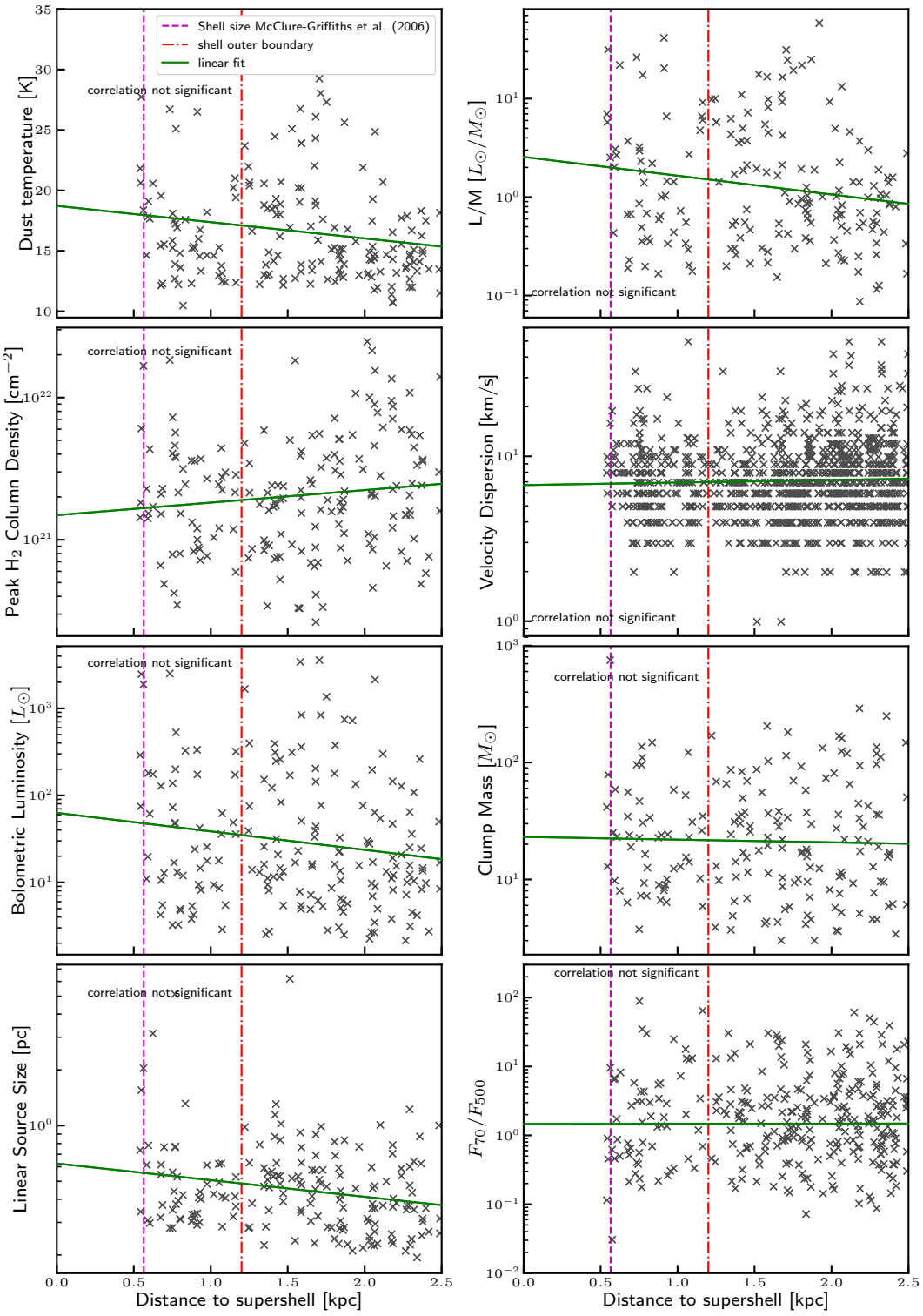

Figure 6.14: Dependence of physical parameters on distance to the Galactic supershell. The vertical lines indicate the inner and outer boundary of the shell walls. The green line indicates a linear fit to the data taking into account uncertainties. We also show the flux ratio $F_{70\mu m}/F_{500\mu m}$ in the lower right panel, indicating star-formation activity.

hypothesis of the sample being equivalent to a distribution with a slope of zero. Care has to be taken though, as the distances to the shell are determined from kinematic distances, and these are affected by the supershells expansion velocity of $\sim$7 km s^{-1} and thus might have a strong impact on distance dependent properties like the masses, luminosities and linear source sizes. But as this would influence sources in the near and far wall, and thus equally decrease and increase the distances and thus the physical properties, we conclude that the average values in the shells walls are statistically unaffected.

In summary, we find an increase in the number-density of sources in the walls of the supershell, but find their physical properties or the star-formation activity unaffected. In fact, we find the increased number-density of clumps to be consistent with the hypothesis of McClure-Griffiths et al. (2006), finding that the material in the walls of the supershell might be shocked and compressed. Furthermore, the increased source count per unit area fits perfectly into the picture of Izumi et al. (2014), who found star formation to be possibly induced by the passage of a high-velocity cloud through the disc in the outer Galaxy in the 2nd Quadrant.

6.5 Physical properties with respect to the spiral arms

In this final section we want to try to quantitatively compare the properties of the clumps located in or near the spiral arms and those located in the inter-arm regions, we calculate the distance to each spiral arm. Here we concentrate on the four-arm model, taking into account the presence of the Perseus arm and the Outer arm in the region we observed (compare Fig. 5.8). In addition the Sagittarius arm further inward towards the Galactic centre has to be taken into account (not shown in Fig. 5.8). This places the sources of our survey in or between three spiral arms: the Sagittarius arm, the Perseus arm, and the Outer arm.

As the kinematic distances determined for the region around the supershell are less reliable, a correct determination of the position relative to the spiral arms is difficult. Therefore we exclude the region in the direction of the Galactic supershell ($252^\circ < \ell < 233^\circ$) from the analysis, reducing our sample to 399 sources. Care has to be taken as some properties suffer significantly from distance biases (Section 6.2.4). The sub-sample is therefore further filtered for the completeness limits determined up to 9 kpc heliocentric distance for the distance dependent physical properties such as bolometric luminosity, clump mass, and linear source size, reducing the sample size to 88 sources.

In Fig. 6.15 we show the derived physical parameters with respect to the distance to the nearest spiral arm. A linear fit taking into account the uncertainties of the physical parameters is added as a green line. Furthermore we indicate the result of a correlation test determining if the slope differs significantly from a constant distribution. We find no correlation between any of the physical parameters derived from the dust SEDs and the location relative to the spiral arms.

The width of the spiral arms as determined by Reid et al. (2014) are indicated by the vertical lines. As can be seen, some of the highest values are found inside or very close to the spiral arms (e.g. for the temperature, luminosities and masses), but we fail to find any significant difference between the sources located in the spiral arms and the inter-arm regions.

In summary, we fail to find any significant correlation of the eight investigated physical

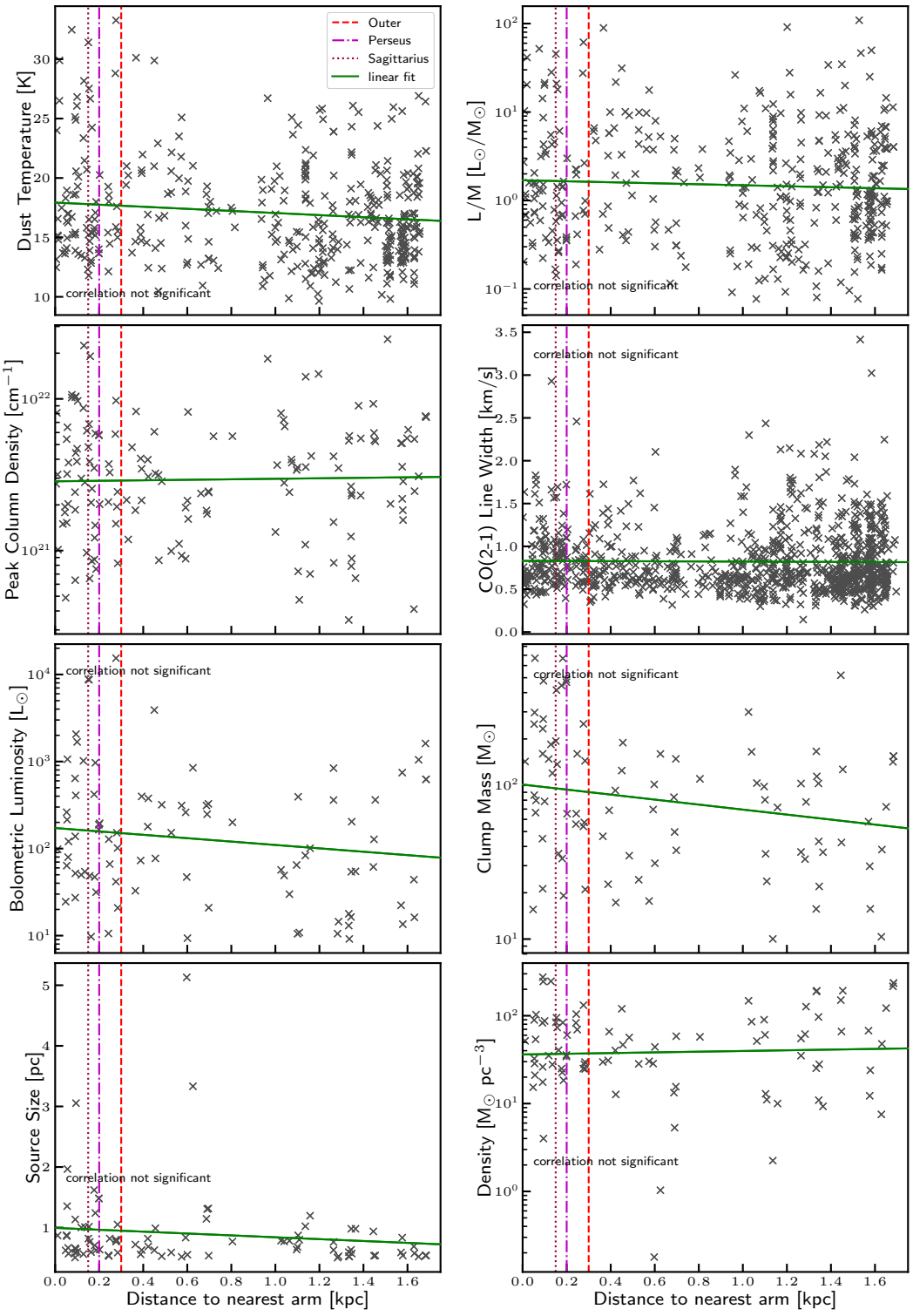

Figure 6.15: Physical properties as function of the distance to the locii of the spiral arms. Vertical lines indicate the width of the spiral arms as reported by Reid et al. (2014). The green line indicates a linear fit to the data taking into account uncertainties.

properties with the position relative to the spiral arms for the outer Galaxy. This can be interpreted as either star-formation being independent of the spiral arms or the spiral structure of the Galaxy not being prominent in the investigated region. The latter is supported by our discussion in Section 5.2, indicating a more flocculent structure of the Milky Way in the outer Galaxy. The former on the other hand is in agreement with Urquhart et al. (2018) (Chapter 4), where we find the star-formation efficiency in the inner Galaxy not to be enhanced by the spiral arms.

In general, this comes a bit as a surprise, as we might have expected that the spiral arms not only increase the number density of molecular clouds, as we have shown for the much larger ATLASGAL sample in Urquhart et al. (2018) (Chapter 4), but also increase the star-formation efficiency e.g. through the increased feedback from preceding star formation that would be more common in the crowded regions of the spiral arms. Likewise, Roman-Duval et al. (2010) speculate that the longer lifetime observed for clouds located in the spiral arms allows for longer star-formation timescales and hence would increase the star-formation efficiency. On the other hand no variation for either the star-formation efficiency, clump-formation efficiency, or star-formation fraction is found in several recent studies (Moore et al. 2012, Eden et al. 2013; 2015, Ragan et al. 2018). Our results for the inner and outer Galaxy are therefore in line with these results, showing no increase in the star-formation efficiency, although we see a clear increase in the number density at the location of the spiral arms.

This means that although the spiral arms are responsible for organizing the interstellar material on large scales, they have no effect on the star formation properties. Indeed, this is consistent with our finding in Chapter 6.3.10 and Urquhart et al. (2018) (Chapter 4), that once a clump collapses, its mass remains about throughout its evolution, indicating a decoupling from larger scale structures. We therefore come to the conclusion that once star formation is initiated, it is independent of the large-scale environment in general.

6.6 Summary and Outlook

In order to determine the physical properties of the selected dust clumps, we recovered the dust spectral energy distributions from Hi-GAL, MSX and WISE continuum emission maps. The SEDs were consecutively fitted with a simple two-component model as described in Chapter 2 yielding dust temperatures, integrated fluxes and H_2 column densities. Combining the results with the kinematic distances determined from the CO emission as described in Chapter 5 allows us to calculate physical properties such as bolometric luminosities and clump masses.

To guarantee the consistency of our data with other studies, we compare the peak N_{H_2} column densities obtained from dust continuum emission against the column density derived from the ^{12}CO(2–1) emission. Although deviations of up to an order of magnitude are found for individual clumps, we find a good agreement for the general trend, and allot the deviations to local variations in the gas-to-dust ratio and CO-to-H_2 conversion factor. Furthermore, we compare the clump masses of our sample to a similar sample from (Elia et al. 2013), finding the mean values to be almost identical, showing our methods to be reliable.

In order to compare the outer Galaxy sample to the inner Galaxy sample of ATLASGAL, we compared their sensitivities. We find the sensitivity of ATLASGAL for the peak flux

density in the 250 μm band to be two orders of magnitude lower than the sensitivity of the outer Galaxy sample due to the different bands used for the source extraction. Therefore we adjust the sensitivity of both surveys by filtering both samples to peak flux densities above 1.5 Jy/beam and a heliocentric distance of 9 kpc, which we determined as the distance limit for the outer Galaxy sample.

We investigate the physical properties of our sample with respect to their evolutionary phase. We find the evolutionary stages to be well separated by the dust temperature, bolometric luminosity and luminosity-to-mass ratio, consistent with our results in Chapter 3 (König et al. 2017) and Chapter 4 (Urquhart et al. 2018). However, we find the clump masses and peak column densities to be similar in the starless and protostellar phase, but find these quantities to be significantly higher for the YSO phase, indicating that the more massive clumps evolve significantly faster than their lower mass counterparts.

We find that our sources span all evolutionary phases, and in general follow similar evolutionary trends as found for clumps the inner Galaxy. On the other hand we find the masses to be on average lower than those in the inner Galaxy and only a few clumps of our sample being able to form high-mass stars, indicating a significant difference to the inner Galaxy.

To investigate the influence of Galactocentric radius on the physical properties, we combine our sample with the one from Urquhart et al. (2018). We find significant differences for sources located inside and outside the solar circle. The dust temperature increases with Galactocentric distance at a slope of $\Delta t = 0.58 \pm 0.07$ K per kiloparsec Galactocentric radius. In contrast, the bolometric luminosity, clump mass, and H_2 column density drop on average by a factor of ~ 8, ~ 6, and ~ 3, respectively, from the inner to the outer Galaxy within just a few kiloparsec around the solar circle. This leads us to the conclusion that the lower column density found in the outer Galaxy reduces the shielding from the interstellar radiation field, and effectively allows for an increase in average dust temperature in combination with the reduced cooling due to the lower metallicity found in the outer Galaxy,

Comparing high-mass star formation in the inner and outer Galaxy, we find significantly less massive clumps in the outer Galaxy. We find only 24 sources above the luminosity of an early B-Type star ($\sim 8\,M_\odot$ Mottram et al. 2011a), the masses of only 8 sources above the threshold where it would be likely to host a massive dense core or high-mass protostar according to Csengeri et al. (2014) or at most 86 sources above the threshold for high-mass star formation as determined by (Kauffmann et al. 2010b). Even more so, we only find 2 methanol Class II masers, and 10 known as well as 24 candidate HII regions in the whole survey area of the outer Galaxy. Comparing the number density of HII regions to the inner Galaxy, we find that there are at least a factor of 20-30 less HII regions per unit area in the outer Galaxy than in the inner Milky Way, indicating a significant drop in high-mass star formation.

To further explore the origin of this deficiency in high-mass star forming clumps that is observed for the outer Galaxy, we investigate the ratio of the highest masses, luminosities peak column densities and 250 μm fluxes between the inner and outer Galaxy. We find a general trend of these values to drop between a factor of 6.7 for the clump masses to a factor of 20 for the peak column densities. As also the Galactic H_2 mass surface density drops by an order of magnitude from the inner to the outer Galaxy, and the distribution is similar to the upper boundary of the peak column densities, we speculate that these are connected. We suggest that the Galactic H_2 mass surface density determines the distribution of clump masses

and column densities, effectively limiting the maximum clump mass – similar to the initial mass function (IMF), which determines the distribution of stars forming from a given mass reservoir. We conclude that the lower H_2 mass surface density found in the outer Galaxy favours the formation of lower-mass clumps and hence predominantly lower mass stars are formed according to the IMF. As a consequence we find much less high-mass star formation in the outer Galaxy than in the inner Galaxy.

We find star formation to be independent of the large scale environment. The star formation activity as indicated by the luminosity-to-mass ratio is found to be constant over kiloparsec scales throughout the whole Milky Way. Similarly, we find the clump mass to be independent of the evolutionary stage as indicated by the dust temperature, showing that once a clump started to collapse, it effectively 'decouples' from its environment. This means that just the initial mass of a clump determines their fate, whereas the large-scale environment (like spiral arms) has no influence.

Investigating the influence of the expanding Galactic supershell GSH 242–03+37 in detail, we find the physical properties and star formation activity of sources located within the walls to be not statistically different from sources located farther away. Nevertheless, as we have seen in Chapter 5 we find the number-density of sources increased within the walls of the supershell, leading us to the conclusion that the expanding supershell supports the formation of clumps, but once they collapse has no further influence.

Similarly, we find the spiral arms in the outer Galaxy to have no influence on the physical properties and star formation activity, but point out that this might be related to the incomplete sampling and the small longitude range covered of the spiral arms due to the supershell complicating the analysis. Comparison with the literature and the inner Galaxy (Chapter 4 Urquhart et al. 2018) though show our findings to be consistent with the global trends, and thus we conclude that the spiral arms support the formation of clumps as seen in the increase in number density for the inner Galaxy, but have no further influence on the clumps once they collapse.

Part IV

Summary and Outlook

CHAPTER 7

Summary and Outlook

7.1 Summary

In this thesis we have investigated star formation properties throughout the Milky Way - from the inner parts to the far outer Galaxy, ranging from a small, well selected sub-sample up to a complete sample of massive star-forming regions. We were able to find the following:

- We developed methods to compile the spectral energy distributions of dust clumps from continuum emission maps from the ATLASGAL, Hi-GAL, MSX and WISE surveys, and characterize their emission by a two-component model in order to determine their dust temperature, integrated flux and column density. We furthermore developed a method to identify emission peaks in CO spectra, in order to assign a velocity to a dust clump, allowing us to determine the distance of a given clump from a rotation model. Using the distances and fitted parameters, we were then able to determine further physical properties like clump masses, bolometric luminosities or linear source sizes.

- We established an evolutionary sequence based on the recovered dust spectral energy distributions for a sample of 110 brightness selected high-mass star forming clumps. We have shown in Chapter 3 (König et al. 2017) that either the dust temperature or the luminosity-to-mass ratio are best suited to distinguish the different evolutionary stages. Adding radio continuum emission allows to further separate the most evolved stage of high-mass star formation when compact HII regions are formed. In contrast, tracers like methanol or water masers are found to spread over several evolutionary phases, only indicating sources to be in one of their later stages. In general, we find the more evolved sources to have higher average dust temperatures, bolometric luminosities, and luminosity-to-mass ratio than sources in an earlier phase.

- We applied the methods developed for König et al. (2017; Chapter 3) to the sources of the ATLASGAL compact source catalogue in Urquhart et al. (2018; Chapter 4). We obtained the photometry and distances for $\sim$ 8000 dense dust clumps located between $5^\circ \leq |\ell| \leq 60^\circ$, determining their evolutionary phase and physical parameters, in order to investigate general star forming relations and extended the analysis to this complete sample of star-forming clumps throughout the inner Galaxy.

- We find the majority of the clumps located in the inner Galaxy to be able to form high-mass stars, reaching a 100% probability for clumps with a peak column density higher than 10^{23} cm^{-2}.

- With a complete sample of star forming clumps, and the fraction of clumps in each evolutionary stage known, we were able to determine statistical lifetimes. In the quiescent stage we find lifetimes of 5×10^4 years for $\sim$1,000 $M_\odot$ clumps, down to $\sim 1 \times 10^4$ years for $\sim$10,000 $M_\odot$ clumps, and negligible lifetimes for even more massive clumps. We conclude that clumps form rapidly and are very unstable in their earliest phase, which is quickly followed by star formation.

- Larger entities, star formation complexes, have been identified through a friends-of-friends analysis, allowing us to compare their properties. We find the 30 most massive complexes to contain only 16% of all clumps, but make up for 36% of the total mass and 52% of the total luminosity of all sources. We furthermore identified three compelxes (W49, W51 and G351) that are responsible for almost 25% of all ATLASGAL sources. As their integrated luminosity-to-mass ratio is at least twice as high as the remaining clusters, these three clusters are the best examples of 'mini-starbursts' within our own Galaxy.

- Finally, we further extended our research to a region of the outer Galaxy between $225^\circ \leq \ell \leq 260^\circ$. After extracting positions and source sizes for $\sim 25,000$ emission peaks from Herschel Hi-GAL 250 μm emission maps, we selected a representative sample of 817 sources for further study. For these sources we determined distances from CO(2–1) emission observed with the APEX telescope, recovered their SEDs with aperture photometry of Hi-GAL, MSX and WISE dust continuum maps and determined their physical parameters and evolutionary stages from in the same way as for König et al. (2017; Chapter 3) and Urquhart et al. (2018; Chapter 4).

- Identifying 2034 velocity components that are grouped into 1757 clouds, and associated to 857 dust clumps, we were able to probe the molecular gas structure of the southern outer Galaxy in unprecedented detail. We found the CO clumps not only to be well correlated with the bright HI emission, but also found bridges, spurs and blobs of star forming regions between the large scale structures, that the thin disk is a rather complex three-dimensional web-like structure, than a flat, pancake-like structure.

- Comparing the inner and the outer Galaxy, we find a significant trend for increasing dust temperature with increasing Galactocentric distance. Furthermore, we see a drop of a factor ~ 3, ~ 6, and ~ 8 in average H_2 column density, clump mass and bolometric luminosity, respectively, from the inner to the outer Galaxy within just a few kiloparsec around the solar circle. This leads us to the conclusion that the lower column density found for the outer Galaxy clumps reduces the shielding from the interstellar radiation field, and effectively allows for an increase in average dust temperature in combination with the reduced cooling due to the lower metallicity found in the outer Galaxy,

- Comparing the most massive clumps of the inner and outer Galaxy, we find that there is considerable less high-mass star formation taking place in the outer Galaxy. This can be inferred from our data either through the luminosities, finding only 24 sources above the luminosity of an early B-Type star ($\sim 8\,M_\odot$; Mottram et al. 2011b), the masses of only 8 sources above the threshold from where it would be likely to host a massive dense core

or high-mass protostar according to Csengeri et al. (2014), or at most 86 sources found above the threshold for high-mass star formation as determined by Kauffmann et al. (2010b). Furthermore, we also find only 2 methanol Class II masers, as well as only 10 known and 24 candidate HII regions towards the outer Galaxy, which are considered to be uniquely associated with high-mass star formation. Moreover, comparing the number density of HII regions in the outer Galaxy to the inner Galaxy (including all candidate HII regions as found by Anderson et al. (2014)), we find high mass-star formation to be at least a factor of 20-30 lower per unit area in the outer than in the inner Galaxy.

- Furthermore, we find the highest masses, luminosities, peak column densities and 250 μm peak flux densities to differ by about an order of magnitude between the inner and outer Galaxy. As also the H_2 mass surface density drops by a factor of ~ 20 from $\sim 4\,M_\odot$ pc^{-2} in the inner Galaxy to $\sim 0.2\,M_\odot$ pc^{-2} in the outer Galaxy (Heyer & Dame 2015), we speculate that these are connected. We therefore suggest that the H_2 mass surface density of the Galaxy determines the distribution of clump masses and column densities, effectively limiting the maximum clump mass – similar to the initial mass function (IMF) that determines the distribution of stars forming from a given mass reservoir. Following these arguments, we conclude that the lower H_2 surface density found in the outer Galaxy favours the formation of lower mass clumps. And as mostly lower mass clumps are formed, predominantly lower mass stars can be formed according to the IMF. Hence we find much less high-mass star formation in the outer Galaxy.

- We find star formation to be independent of its large scale environment. The star formation efficiency, as indicated by the luminosity-to-mass ratio $L_{\rm bol}/M_{\rm clump}$, is found to be constant on average on kiloparsec scales. Furthermore, we find the clump mass to be independent of the evolutionary phase as indicated by the dust temperature, showing that once a clump has started to collapse, the net mass infall and outflow cancel each other out. This implies that once a clump has started to collapse, the clump effectively 'decouples' from its environment, with just the initial mass determining their fate and the large-scale environment (like spiral arms) having no influence.

- We investigated the influence of the expanding Galactic supershell GSH 242-3+37 on star-formation in the outer Galaxy. We find an increased number density in the shell of the bubble, but fail to find any other influence on the physical properties of these clumps. This leads us to the conclusion that clump formation and their collapse is triggered through the expansion of the shell, but does not have any influence on the star-formation processes with the clumps. This is in fact consistent with both, the dependency of star formation on the spiral arms, as well as with our observation of the clumps 'decoupling' from their environment, once collapsing.

- Although we fail to find any significant direct influence of the spiral arms or the supershell on the physical properties of the clumps, we find an increased number density of clumps close to the loci of the spiral arms or in the rim of the expanding supershell. From this we conclude that the spiral arms, but also structures like the supershell, are efficient in organizing the interstellar material into clumps, but have no further influence once the clumps start to collapse.

7.2 Outlook

In the present thesis, we have approached several topics, such as the structure of the Galaxy, where and under which conditions high-mass stars form, or the impact of the large scale structures on star formation. Although we were able to investigate these questions in unprecedented detail, it also has become clear, that further, more detailed study of the outer Galaxy is required in order to obtain a complete view and get definite answers. In this section we will discuss possible future projects that either have already been started or that are noteworthy.

In the future, a selected sub-sample of sources from the outer Galaxy could be investigated in more detail. Different isotopologues and higher transitions, atomic and ionized carbon are only a few avenues we have already started to pursue for a more in-depth analysis of selected sources. For the ATLASGAL Top100 sample (König et al. 2017) such follow-up observations are ongoing or have already been undertaken and could be compared to the outer Galaxy, e.g. by investigating CO depletion (Giannetti et al. 2014) or the temperature structure and evolution of clumps (Giannetti et al. 2017b). Investigating the atomic-to-molecular carbon ratio alongside ionized carbon will allow us to constrain the contribution of 'CO-dark' H_2 gas, which can not be traced by CO as the CO-to-H_2 conversion factor increases due to the lower metallicity (Pineda et al. 2013).

As has become clear throughout this thesis a much larger view on the outer Galaxy and a complete sample of star forming regions is needed in order to approach questions like the loci and influence of the spiral arms, the total amount of high-mass star formation in the outer Galaxy or how the star formation regions in the outer Galaxy compare to the dominating complexes found in the inner Milky Way. Therefore mapping the outer Galaxy in the 3rd Galactic quadrant in CO will help us to obtain a complete view on star formation towards the southern outer Galaxy. This will not only allow for a more robust investigation of the physical properties, but will also allow an unprecedented view on the hierarchical structure of the Milky Way e.g. using SCIMES (Spectral Clustering for Molecular Emission Segmentation, Colombo et al. 2015). Furthermore, comparing the outer Galaxy in the 2nd and 3rd Galactic quadrants might be of interest, as the leading arms of the Magelanic stream are possibly interacting with the Galactic disc in the southern, far outer Galaxy. This could possibly open up a new chapter of galaxy-companion interaction research. With first pilot studies already on the way, a complete view of our Galaxy seems closer than ever.

7.2.1 Atomic and ionized carbon

As mentioned in the introduction, carbon is the fourth most abundant element in the universe. Usually carbon monoxide is used to determine the total mass in a given volume by using a CO-to-H_2 conversion factor, commonly known as the X_{CO} factor. But as this factor changes with Galactocentric distance and the molecular fraction of the gas decreases, the conversion factor increases, up to a point where CO is no longer detected. At this point, where the interstellar medium becomes '*CO-dark*', the atomic carbon would be a better tracer of the total gas mass. Therefore knowing the atomic-to-molecular carbon ratio helps us understand the interplay of CO, atomic carbon and H_2. Furthermore, as the shielding in dust clumps in the far outer Galaxy is reduced, the total mass of star forming clumps might be underestimated, as not

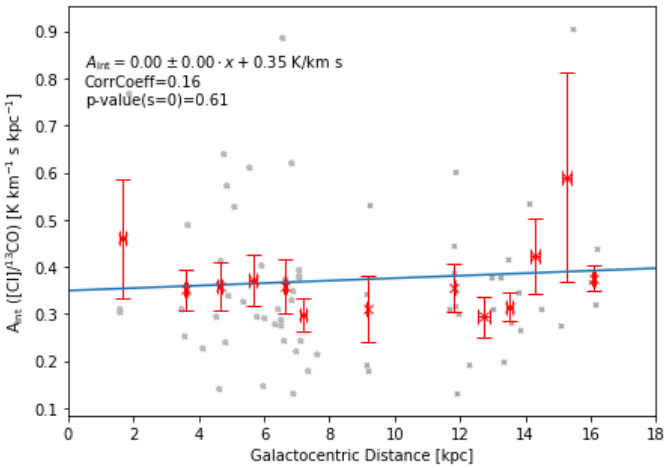

Figure 7.1: [CI]-to-^{13}CO emissivity ratio as a function of Galactocentric distance. Red crosses mark the mean values of 1 kpc wide bins and the blue line is a linear fit to the data, taking into account uncertainties. The preliminary analysis shows no significant trend.

only the molecular fraction decreases, but atomic carbon will be ionized due to the lower shielding and the therefore higher impact of the interstellar radiation field. Thus studying the fraction of molecular, atomic and ionized carbon is not only important to understand the changed morphology of individual star-forming regions, but also to estimate the total mass of the Galaxy in the far outer fringes of the Galactic disc.

To answer these questions, we started a project in order to observe selected sources in [CI] with the FLASH$^+$ receiver at the APEX telescope(Güsten et al. 2006), as well as [CII] using the upGreat(Risacher et al. 2016) receiver array on board the 'Stratospheric Observatory for Infrared Astronomy' (SOFIA; Young et al. 2012). We show preliminary results from our [CI] observations in Fig. 7.1, where plot the [CI]-to^{13}CO ratio as a function of Galactocentric distance. So far, our preliminary analysis indicates the atomic-to-molecular carbon ratio to be constant throughout the Galaxy, finding no significant correlation with the distance to the Galactic centre within the uncertainties out to $R_{\rm gal} \sim 16$ kpc. In addition, first observations of [CII] have been conducted with SOFIA, enabling us to study the ionized carbon content of these clumps and compare it to the already measured CO and atomic carbon. This will enable us to investigate their relative abundance under the changing physical conditions of the outer Galaxy, but will also allow us to study their impact on the CO-dark H_2 gas fraction, which is poorly constrained towards the outer Galaxy and is completly unknown for Galactocentric distances above 11 kpc (Pineda et al. 2013).

7.2.2 OGHReS

Although we were able to gain new insights into the dependence of the properties of star-forming clumps on their Galactic environment in Chapters 5 and 6, it also became clear, that a much larger and complete view on the outer Galaxy is necessary to give definitive answers. The positions of the spiral arms, large scale structures like GMCs and clusters, the 3D structure

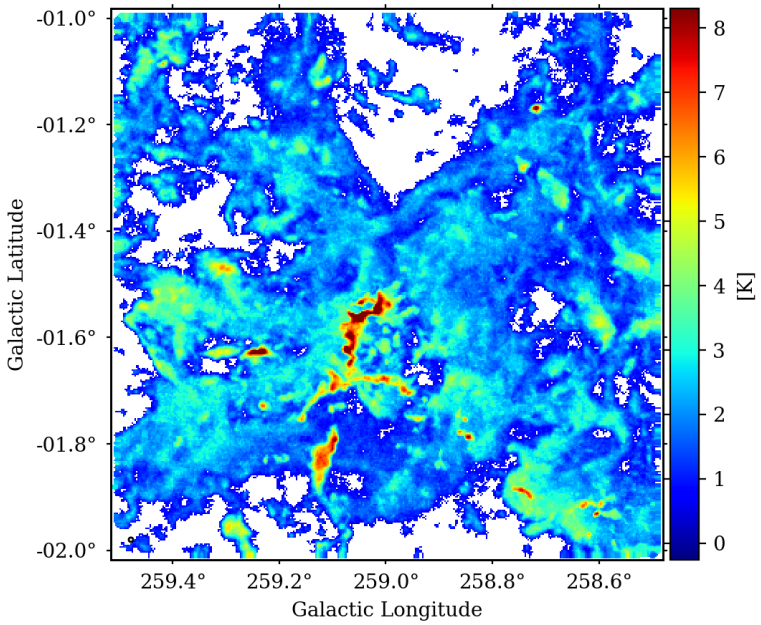

Figure 7.2: Integrated intensity map of the first 1×1 degree field observed for the Outer Galaxy High Resolution Survey (OGHReS, König et al.) in ^{12}CO(2–1) with a beam width of $27''$. When OGHReS is finished, it will cover 100 square degrees between $180° \leq \ell \leq 280°$, mapping the southern outer Galaxy in unprecedented detail.

of the ISM out to the edge of the Galaxy, or the dynamics of the ISM, or the very nature of our host Galaxy ('flocculent' vs 'grand design') are just a few topics that should be extended to a much larger region.

For this purpose the Outer Galaxy High Resolution Survey (OGHReS, PI C. König) is under way to map 100 square degrees between $180° \leq \ell \leq 280°$. Several molecular transitions are targeted by this survey, focusing on ^{12}CO(2–1), ^{13}CO(2–1), and C^{18}O(2–1) in order to get a complete census of thousands of highly resolved clouds and filaments, forming under drastically different conditions than those in the inner Galaxy e.g. idendified by SEDIGISM ('Structure, Excitation and Dynamics for the Inner Galactic InterStellar Medium'; Schuller et al. 2017) or the Galactic Ring survey (GRS; Jackson et al. 2006).

In Fig. 7.2 we present an integrated intensity map of the first 1×1 degree field observed for OGHReS of the ^{12}CO(2–1) emission, showing a complex located close to the locus of the Perseus spiral arm. With a beamsize of 27 arcseconds, the resolution of this survey is almost a factor 18 better than the ~ 8 arcmin resolution of Dame et al. (2001), which is the only other CO survey to date, covering the whole southern outer Galaxy.

The OGHReS CO survey will therefore lead to dramatic improvements in our understanding of the Galactic structure, and give new insights into the connection between the large-scale Galactic dynamics and star formation in the Milky Way. The results from OGHReS will also provide the basis that is needed for studies of Galactic structure and to investigate the impact of different environments on the structure and evolution of giant molecular filaments (GMF) and giant molecular clouds (GMC) and their star formation properties. Finally, the results

found for the low-metallicity environment of the outer Galaxy will also provide a template for understanding star formation in low metallicity galaxies, such as nearby dwarf galaxies.

7.3 Closing remarks

In the present thesis we were able to shed some light on the questions raised in the introduction on how and where low or high-mass stars form. Although high-mass star formation is common in the inner Galaxy, it is comparably rare in the outer Galaxy. We found that the spiral arms, although organizing the molecular material into clumps, have no influence on how massive these are or how they evolve. Instead, we found that the star formation efficiency is on average independent of the large-scale environment, in the sense that once the initial mass of a clump is gathered and the clumps start to collapse, it will be independent of the environment. In this sense, the global environment as defined by the mass surface density might only determine the initial mass of the clumps, which in turn determines the size of the stars that can be formed. Future surveys will allow us to determine robust limits to the number of high-mass star forming clumps and the mass distribution of clumps in the outer Galaxy. They will also enable us to understand the large scale structure and nature of our host Galaxy. With the present work, we therefore did not only answer questions on star formation throughout the Milky Way, we also opened the door to a plethora of new questions that hopefully can be answered in the coming years.

Part V

Appendix

APPENDIX A

Data

Table A.1: Velocity components identified from the CO(2–1) observations along 10 lines-of-sight. Source names starting with a '*G*' are measured emission at targeted positions, whereas names starting with an '*O*' indicate emission in the off-position. Uncertainties for $v_{\rm lsr}$ are in the order of 0.5 km s^{-1}, distance uncertainties in the order of 0.3 kpc.

Name	$v_{\rm lsr}$ (km s^{-1})	$\Delta v_{\rm lsr}$ (km s^{-1})	$T_{\rm max}$ (K)	$\int T dv$ (K km s^{-1})	$R_{\rm hel}$ (kpc)	$R_{\rm gal}$ (kpc)
G225.020−00.590	14.6	1.1	3.6 ± 0.1	9.6 ± 0.4	1.3	9.3
G225.030+00.060	17.9	0.8	0.8 ± 0.1	1.6 ± 0.2	1.6	9.5
G225.080+00.060	17.8	0.8	3.0 ± 0.1	5.7 ± 0.2	1.6	9.5
G225.160−00.830	14.3	0.7	0.2 ± 0.1	0.4 ± 0.2	1.3	9.3
G225.160−00.840	14.8	0.5	0.4 ± 0.1	0.5 ± 0.1	1.3	9.3
	19.9	0.5	4.0 ± 0.1	4.5 ± 0.2	1.7	9.6
	20.0	0.4	2.9 ± 0.1	3.0 ± 0.1	1.7	9.6
G225.170−00.750	19.5	0.6	2.6 ± 0.6	3.8 ± 0.8	1.7	9.6
G225.210−01.110	13.9	0.7	5.1 ± 0.1	9.0 ± 0.4	1.2	9.3
	19.4	0.6	0.4 ± 0.2	0.6 ± 0.2	1.7	9.6
G225.220−01.200	13.5	0.7	2.2 ± 0.1	3.7 ± 0.2	1.2	9.2
G225.230−00.960	14.7	0.7	5.6 ± 0.1	10.5 ± 0.4	1.3	9.3
G225.240−01.110	13.8	1.0	4.8 ± 0.1	12.2 ± 0.5	1.2	9.2
G225.300−01.090	14.0	0.8	3.7 ± 0.1	7.5 ± 0.3	1.2	9.3
G225.320−01.170	13.7	0.8	3.7 ± 0.1	7.2 ± 0.3	1.2	9.2
G225.320−01.100	14.2	0.8	4.3 ± 0.1	8.6 ± 0.4	1.3	9.3
G225.320−00.280	15.2	0.8	1.8 ± 0.1	3.9 ± 0.2	1.3	9.3
G225.330−00.866	14.4	0.6	1.5 ± 0.1	2.4 ± 0.2	1.3	9.3
G225.330−00.540	11.2	0.7	0.7 ± 0.6	1.2 ± 1.0	1.0	9.1
G225.330−01.120	14.4	0.6	4.5 ± 0.1	6.8 ± 0.3	1.3	9.3
	17.3	1.6	8.7 ± 0.1	34.6 ± 1.1	1.5	9.5
G225.350−00.540	11.6	0.6	0.5 ± 0.1	0.8 ± 0.2	1.1	9.1
	16.8	0.6	6.1 ± 2.8	9.3 ± 4.3	1.5	9.4
	18.6	0.5	6.7 ± 2.9	8.6 ± 3.8	1.6	9.6
G225.370−01.380	13.3	0.7	1.9 ± 0.1	3.1 ± 0.2	1.2	9.2
G225.380−00.540	11.7	0.5	1.6 ± 0.2	2.0 ± 0.2	1.1	9.1
	17.0	0.7	4.5 ± 0.1	8.3 ± 0.4	1.5	9.4
G225.390−01.370	13.3	0.5	–	–	1.2	9.2
G225.390−00.990	15.0	0.8	2.5 ± 0.1	4.7 ± 0.2	1.3	9.3
G225.400−01.020	10.3	0.5	0.8 ± 0.1	1.1 ± 0.1	1.0	9.0
G225.400−00.560	11.0	0.6	1.0 ± 0.5	1.6 ± 0.8	1.0	9.1
	14.8	0.6	3.1 ± 0.1	4.4 ± 0.2	1.3	9.3
	16.2	1.0	7.1 ± 0.1	17.9 ± 0.6	1.4	9.4
G225.440−00.390	15.9	1.2	1.7 ± 0.5	5.2 ± 1.6	1.4	9.4
	18.5	0.6	4.5 ± 0.3	7.1 ± 0.5	1.6	9.5
G225.460−01.680	15.7	0.6	9.5 ± 0.1	15.1 ± 0.5	1.4	9.4

Table A.1: continued

Name	$v_{\rm lsr}$ (km s^{-1})	$\Delta v_{\rm lsr}$ (km s^{-1})	$T_{\rm max}$ (K)	$\int T dv$ (K km s^{-1})	$R_{\rm hel}$ (kpc)	$R_{\rm gal}$ (kpc)
G225.470−01.680	16.0	0.6	10.7 ± 0.1	16.7 ± 0.5	1.4	9.4
G225.472−01.674	16.7	0.4	5.2 ± 0.2	5.8 ± 0.2	1.5	9.4
G225.480−00.230	16.0	1.4	1.7 ± 0.1	6.2 ± 0.4	1.4	9.4
G225.480−01.790	16.7	0.7	11.8 ± 0.1	19.9 ± 0.6	1.5	9.4
G225.480−01.800	16.9	0.8	4.9 ± 0.1	9.6 ± 0.3	1.5	9.4
G225.490−01.780	16.2	0.7	10.7 ± 0.1	18.4 ± 0.6	1.4	9.4
G225.490−00.400	16.4	1.0	3.3 ± 0.7	8.5 ± 1.8	1.4	9.4
G225.490−01.810	16.9	0.8	5.1 ± 0.1	10.0 ± 0.4	1.5	9.4
	18.6	0.6	4.1 ± 0.8	5.7 ± 1.1	1.6	9.5
G225.500−01.800	16.2	1.1	0.7 ± 0.1	1.9 ± 0.3	1.4	9.4
G225.500−01.770	16.2	0.8	13.5 ± 0.1	27.3 ± 0.9	1.4	9.4
G225.510−01.740	15.5	0.7	12.6 ± 0.1	22.5 ± 0.7	1.4	9.3
G225.510−01.780	16.0	0.6	14.7 ± 0.1	23.1 ± 0.7	1.4	9.4
G225.530−01.780	16.1	0.6	12.9 ± 0.1	20.5 ± 0.7	1.4	9.4
G225.604−02.013	17.6	0.5	0.1 ± 0.1	0.1 ± 0.1	1.5	9.5
G225.660−00.220	15.6	0.9	1.3 ± 0.5	3.1 ± 1.2	1.4	9.4
	18.7	0.6	6.4 ± 0.1	10.0 ± 0.3	1.6	9.5
G225.770−00.960	14.1	0.6	3.3 ± 0.1	4.7 ± 0.2	1.2	9.3
G225.780−00.940	14.4	0.6	2.7 ± 0.1	4.1 ± 0.2	1.3	9.3
G225.954−00.884	16.5	0.7	1.0 ± 0.1	1.7 ± 0.2	1.4	9.4
G225.980+00.080	18.5	0.7	4.0 ± 0.1	6.8 ± 0.2	1.6	9.5
G226.065−00.056	17.6	0.5	0.9 ± 0.1	1.2 ± 0.1	1.5	9.5
G226.095−00.316	13.7	0.5	0.3 ± 0.2	0.3 ± 0.2	1.2	9.2
G226.117−00.349	15.1	2.1	3.1 ± 0.1	16.9 ± 0.8	1.3	9.3
G226.150−00.150	16.5	0.7	4.5 ± 0.1	7.9 ± 0.3	1.4	9.4
G226.273−01.554	24.3	0.6	1.2 ± 0.1	1.8 ± 0.2	2.1	9.9
G226.279−00.844	14.7	0.4	0.3 ± 0.2	0.3 ± 0.2	1.3	9.3
G226.280−02.070	11.7	0.5	1.9 ± 0.1	2.4 ± 0.2	1.1	9.1
G226.330−02.030	11.1	0.7	2.1 ± 0.1	3.6 ± 0.2	1.0	9.1
G226.353−00.766	14.6	1.6	3.3 ± 0.2	13.4 ± 1.0	1.3	9.3
	18.9	2.3	1.6 ± 0.4	9.2 ± 2.1	1.6	9.5
G226.430−00.588	13.8	1.2	6.3 ± 0.5	18.4 ± 1.7	1.2	9.2
	16.5	0.4	7.9 ± 0.6	8.3 ± 0.7	1.4	9.4
	19.0	1.9	3.7 ± 0.6	17.6 ± 2.8	1.7	9.6
G226.514−00.736	16.2	0.4	1.3 ± 0.8	1.1 ± 0.7	1.4	9.4
G226.670−02.060	14.4	0.7	2.2 ± 0.1	3.7 ± 0.2	1.3	9.3
G227.040−00.900	60.8	0.9	2.4 ± 0.2	5.4 ± 0.4	6.0	13.2
	62.9	0.7	1.8 ± 0.3	3.2 ± 0.5	6.3	13.4
G227.070−00.220	3.0	0.6	0.4 ± 0.1	0.6 ± 0.2	0.4	8.6
G227.180−00.460	19.8	0.6	1.6 ± 0.1	2.5 ± 0.2	1.7	9.6
G227.230−00.830	20.1	0.6	1.4 ± 0.1	2.2 ± 0.2	1.7	9.6
G227.242−00.883	20.1	0.6	3.8 ± 0.1	5.8 ± 0.2	1.7	9.6
G227.343−01.821	16.6	0.6	0.7 ± 0.1	1.0 ± 0.2	1.5	9.4
G227.370−01.142	12.8	0.7	0.6 ± 0.1	1.1 ± 0.2	1.1	9.2
G227.570−01.140	79.7	0.8	5.6 ± 0.1	10.7 ± 0.2	8.9	15.8
G227.650−01.286	79.0	0.7	3.3 ± 0.1	5.7 ± 0.2	8.8	15.6
G227.792−00.104	50.4	2.4	1.1 ± 0.1	6.9 ± 0.6	4.7	12.0
G227.800−00.080	36.7	0.5	0.8 ± 0.1	0.9 ± 0.1	3.2	10.8
	53.0	0.9	1.1 ± 0.1	2.6 ± 0.2	5.0	12.2

Table A.1: continued

Name	$v_{\rm lsr}$ (km s^{-1})	$\Delta v_{\rm lsr}$ (km s^{-1})	$T_{\rm max}$ (K)	$\int T dv$ (K km s^{-1})	$R_{\rm hel}$ (kpc)	$R_{\rm gal}$ (kpc)
G227.800−00.140	53.1	1.8	1.2 ± 0.1	5.5 ± 0.5	5.0	12.3
G227.810−00.120	53.6	1.5	1.8 ± 0.1	6.7 ± 0.4	5.0	12.3
G227.815−00.129	53.2	2.2	2.9 ± 0.1	16.2 ± 0.6	5.0	12.3
G227.820−00.140	52.8	2.1	5.6 ± 0.1	29.2 ± 0.6	4.9	12.2
G227.820−00.160	52.9	1.6	2.5 ± 0.1	10.0 ± 0.4	5.0	12.2
G227.862−00.243	53.8	1.1	2.1 ± 0.1	5.7 ± 0.3	5.1	12.3
G227.870−01.120	36.0	0.7	0.4 ± 0.1	0.6 ± 0.2	3.2	10.7
G227.880−01.780	18.6	0.7	3.8 ± 0.1	7.0 ± 0.3	1.6	9.5
G227.910−01.880	19.0	0.5	4.7 ± 0.1	5.6 ± 0.2	1.7	9.5
G227.924−00.241	53.0	0.7	0.3 ± 0.1	0.5 ± 0.2	5.0	12.2
G227.940−00.139	50.0	0.4	0.2 ± 0.2	0.2 ± 0.2	4.6	11.9
	65.9	1.1	3.2 ± 0.1	8.6 ± 0.3	6.6	13.7
G227.969−00.847	36.6	0.6	0.3 ± 0.1	0.4 ± 0.2	3.2	10.8
G228.026−00.946	36.6	0.6	2.3 ± 0.1	3.2 ± 0.1	3.2	10.8
G228.027−00.924	36.7	0.6	2.1 ± 0.1	3.0 ± 0.1	3.2	10.8
G228.030+00.020	53.0	0.7	3.6 ± 0.1	6.3 ± 0.2	5.0	12.2
G228.030+00.010	53.0	0.6	3.3 ± 0.1	5.0 ± 0.2	5.0	12.2
G228.059−01.021	37.3	0.6	0.2 ± 0.1	0.3 ± 0.2	3.3	10.8
G228.173−02.039	50.0	0.6	0.7 ± 0.1	1.0 ± 0.2	4.6	11.9
G228.300−00.970	36.1	0.5	2.6 ± 0.1	3.1 ± 0.1	3.2	10.7
G228.520+00.240	16.6	1.0	0.8 ± 0.1	1.9 ± 0.2	1.5	9.4
G228.710−00.910	46.5	0.4	2.5 ± 0.1	2.7 ± 0.1	4.2	11.6
G229.570+00.150	50.4	1.7	6.0 ± 0.8	25.5 ± 3.5	4.6	11.9
	55.1	2.1	8.8 ± 0.5	45.9 ± 2.7	5.1	12.3
G229.590+00.160	53.3	1.3	13.4 ± 0.1	44.1 ± 0.5	4.9	12.1
G229.600+00.150	54.3	1.5	14.5 ± 0.1	56.1 ± 0.7	5.0	12.2
G229.740+00.120	70.2	0.6	3.4 ± 0.1	5.2 ± 0.2	7.1	14.0
G229.750+00.030	71.2	0.5	3.8 ± 0.2	4.9 ± 0.3	7.2	14.1
G229.760−00.440	72.6	0.7	2.6 ± 0.1	4.4 ± 0.2	7.4	14.3
G229.770+00.040	69.8	0.8	5.2 ± 0.1	9.7 ± 0.2	7.0	13.9
G229.770+00.060	70.6	1.0	6.0 ± 0.1	15.7 ± 0.3	7.1	14.0
G229.780+00.050	72.4	0.5	2.0 ± 0.1	2.4 ± 0.1	7.4	14.3
G229.790−00.680	41.0	0.6	2.5 ± 0.1	3.5 ± 0.1	3.6	11.0
G229.800−00.360	72.3	0.9	4.6 ± 0.1	10.7 ± 0.2	7.4	14.3
G229.900−00.650	41.3	0.7	1.6 ± 0.1	2.8 ± 0.2	3.6	11.0
G230.047−00.888	40.2	0.7	0.8 ± 0.1	1.6 ± 0.2	3.5	10.9
G230.340−00.610	38.3	0.7	0.7 ± 0.1	1.3 ± 0.2	3.3	10.8
G230.390−00.780	39.7	0.5	1.0 ± 0.1	1.1 ± 0.1	3.5	10.9
G230.660+00.330	35.0	0.5	0.5 ± 0.1	0.6 ± 0.1	3.0	10.5
	51.1	0.6	2.0 ± 0.1	3.0 ± 0.2	4.6	11.8
G230.680+00.300	51.8	0.7	0.5 ± 0.1	0.8 ± 0.2	4.7	11.9
G230.700+00.350	36.8	0.7	2.0 ± 0.1	3.3 ± 0.2	3.2	10.7
	51.9	0.8	2.0 ± 0.1	3.9 ± 0.2	4.7	11.9
G230.860+00.150	20.2	0.6	0.8 ± 0.1	1.2 ± 0.2	1.8	9.5
	29.5	0.5	3.7 ± 0.2	4.9 ± 0.3	2.5	10.1
	43.3	0.6	0.3 ± 0.1	0.4 ± 0.2	3.8	11.2
G230.940−00.400	40.9	0.7	1.3 ± 0.1	2.1 ± 0.2	3.6	11.0
G230.955−00.587	44.4	0.6	0.8 ± 0.1	1.1 ± 0.2	3.9	11.2
G230.976−00.617	44.0	0.7	0.9 ± 0.1	1.6 ± 0.2	3.9	11.2

Table A.1: continued

Name	$v_{\rm lsr}$ (km s^{-1})	$\Delta v_{\rm lsr}$ (km s^{-1})	$T_{\rm max}$ (K)	$\int T dv$ (K km s^{-1})	$R_{\rm hel}$ (kpc)	$R_{\rm gal}$ (kpc)
G230.995−00.567	45.5	0.6	0.6 ± 0.1	0.8 ± 0.1	4.0	11.3
G231.010−00.180	19.0	0.6	0.3 ± 0.1	0.5 ± 0.2	1.7	9.5
	33.4	0.7	0.4 ± 0.1	0.7 ± 0.2	2.9	10.4
G231.070−00.130	33.5	0.5	6.1 ± 0.3	8.3 ± 0.5	2.9	10.4
G231.130−00.320	32.0	0.5	9.8 ± 0.1	13.4 ± 0.2	2.8	10.3
	44.5	0.6	0.2 ± 0.1	0.4 ± 0.2	3.9	11.2
G231.140−00.330	31.7	0.5	5.6 ± 0.1	7.3 ± 0.2	2.7	10.3
	44.6	0.6	0.7 ± 0.1	0.9 ± 0.1	3.9	11.2
G231.250−00.330	31.7	0.5	0.3 ± 0.1	0.3 ± 0.1	2.7	10.3
G231.260−00.290	17.6	0.5	0.3 ± 0.2	0.4 ± 0.2	1.5	9.4
	20.2	0.4	0.2 ± 0.1	0.2 ± 0.1	1.8	9.5
	30.7	0.6	0.7 ± 0.2	1.2 ± 0.2	2.6	10.2
	33.6	0.5	1.5 ± 0.1	2.0 ± 0.2	2.9	10.4
	46.2	0.7	0.6 ± 0.1	0.9 ± 0.2	4.1	11.4
G231.280−00.260	30.4	0.6	1.8 ± 0.2	2.9 ± 0.3	2.6	10.2
G231.280−00.280	31.0	0.5	1.5 ± 0.1	1.7 ± 0.1	2.7	10.2
G231.290−00.360	28.9	0.5	0.2 ± 0.1	0.3 ± 0.1	2.5	10.1
	46.4	0.5	0.5 ± 0.1	0.7 ± 0.1	4.1	11.4
G231.310−00.290	19.5	0.7	1.1 ± 0.1	1.9 ± 0.2	1.7	9.5
G231.330−00.380	29.6	0.5	4.5 ± 0.2	5.7 ± 0.3	2.5	10.1
G231.330−00.690	40.5	0.6	2.3 ± 1.0	3.3 ± 1.4	3.5	10.9
G231.390−00.460	30.0	0.6	4.8 ± 0.1	7.4 ± 0.2	2.6	10.2
G231.470−01.860	41.8	0.9	4.6 ± 0.3	10.5 ± 0.7	3.7	11.0
	44.3	0.3	2.0 ± 0.7	1.8 ± 0.6	3.9	11.2
	46.4	1.6	1.2 ± 0.7	4.9 ± 2.7	4.1	11.4
G231.490−01.770	44.3	1.6	2.5 ± 0.2	10.2 ± 0.6	3.9	11.2
	48.6	1.0	2.1 ± 0.2	5.3 ± 0.6	4.4	11.6
G231.540−00.880	41.3	1.6	2.0 ± 0.1	7.8 ± 0.4	3.6	11.0
G231.540−00.840	41.7	1.2	3.1 ± 0.1	9.3 ± 0.3	3.7	11.0
G231.560−01.660	20.3	0.5	0.4 ± 0.2	0.5 ± 0.2	1.8	9.5
	44.1	1.2	3.9 ± 0.1	11.4 ± 0.3	3.9	11.2
G231.590−00.840	42.2	1.0	3.1 ± 0.1	8.0 ± 0.3	3.7	11.0
G231.610−01.260	38.4	0.7	4.0 ± 0.3	7.5 ± 0.6	3.3	10.7
	45.0	0.4	1.3 ± 0.3	1.3 ± 0.3	4.0	11.3
G231.630−01.603	45.8	0.7	0.4 ± 0.1	0.7 ± 0.2	4.1	11.3
G231.730+00.270	33.1	0.7	2.8 ± 0.1	4.7 ± 0.2	2.9	10.4
G231.740−01.760	39.5	0.4	0.3 ± 0.3	0.3 ± 0.3	3.4	10.8
	44.0	0.6	0.8 ± 0.1	1.2 ± 0.2	3.9	11.2
	47.4	1.5	0.4 ± 0.1	1.5 ± 0.4	4.2	11.5
	56.7	0.8	0.3 ± 0.1	0.6 ± 0.2	5.2	12.3
G231.750+00.290	20.8	0.6	0.2 ± 0.1	0.3 ± 0.1	1.8	9.6
	33.2	0.7	2.5 ± 0.1	4.3 ± 0.2	2.9	10.4
G231.760−00.250	19.3	0.5	0.5 ± 0.1	0.6 ± 0.2	1.7	9.5
	28.3	0.7	5.3 ± 0.1	10.0 ± 0.3	2.4	10.0
G231.770−00.350	19.9	0.5	0.2 ± 0.1	0.3 ± 0.1	1.7	9.5
	26.5	0.6	1.5 ± 0.1	2.1 ± 0.2	2.3	9.9
G231.793−01.970	42.1	1.6	3.6 ± 1.2	14.2 ± 4.5	3.7	11.0
	45.5	1.7	4.2 ± 0.9	18.3 ± 4.1	4.0	11.3
G231.812+00.075	19.0	0.9	0.2 ± 0.1	0.4 ± 0.2	1.7	9.5

Table A.1: continued

Name	$v_{\rm lsr}$ (km s^{-1})	$\Delta v_{\rm lsr}$ (km s^{-1})	$T_{\rm max}$ (K)	$\int T dv$ (K km s^{-1})	$R_{\rm hel}$ (kpc)	$R_{\rm gal}$ (kpc)
	43.8	0.8	2.5 ± 0.1	5.0 ± 0.2	3.9	11.2
G231.841−01.752	48.4	0.6	0.7 ± 0.1	1.1 ± 0.2	4.3	11.5
G231.841−01.792	49.2	0.9	0.5 ± 0.1	1.1 ± 0.2	4.4	11.6
G231.872−00.115	59.4	0.7	0.5 ± 0.1	0.9 ± 0.2	5.5	12.5
G231.882−00.125	59.8	0.5	0.9 ± 0.1	1.1 ± 0.1	5.6	12.6
G231.891−01.752	47.1	0.6	0.3 ± 0.1	0.4 ± 0.2	4.2	11.4
G231.910+00.150	23.7	0.5	2.2 ± 0.1	2.8 ± 0.1	2.0	9.7
	57.9	1.1	2.8 ± 0.1	7.3 ± 0.4	5.4	12.4
G231.913−02.171	41.7	1.0	3.8 ± 0.1	9.0 ± 0.3	3.7	11.0
G231.930−01.500	74.3	1.3	6.4 ± 0.1	21.1 ± 0.4	7.5	14.2
G231.931−01.512	74.1	0.8	2.2 ± 0.2	4.7 ± 0.4	7.5	14.2
G231.940−01.510	73.3	0.9	2.2 ± 0.1	4.8 ± 0.2	7.4	14.1
G231.959−02.064	22.4	0.7	0.9 ± 0.1	1.6 ± 0.2	1.9	9.7
	41.0	1.8	14.3 ± 0.2	63.7 ± 1.2	3.6	10.9
G231.992−00.125	23.9	0.7	0.2 ± 0.1	0.3 ± 0.2	2.1	9.7
G232.000+00.300	32.1	0.8	5.3 ± 0.1	10.2 ± 0.2	2.8	10.3
	58.2	0.6	1.3 ± 0.1	2.2 ± 0.2	5.4	12.4
G232.022−00.076	17.7	0.4	0.8 ± 0.7	0.8 ± 0.6	1.6	9.4
G232.022−00.056	55.8	0.5	1.5 ± 0.1	1.9 ± 0.1	5.1	12.2
G232.040+00.070	57.1	1.0	4.9 ± 0.2	11.9 ± 0.5	5.3	12.3
G232.045−00.625	59.4	1.0	0.2 ± 0.1	0.6 ± 0.2	5.5	12.5
G232.052−00.086	24.2	0.5	0.4 ± 0.1	0.6 ± 0.1	2.1	9.8
	56.9	0.5	0.6 ± 0.2	0.7 ± 0.2	5.3	12.3
G232.057−01.163	45.7	1.1	0.2 ± 0.1	0.5 ± 0.3	4.1	11.3
G232.062−00.126	19.2	0.4	1.0 ± 0.2	1.2 ± 0.2	1.7	9.5
G232.062−00.096	24.7	0.7	0.3 ± 0.1	0.5 ± 0.2	2.1	9.8
	57.0	0.5	0.9 ± 0.1	1.3 ± 0.1	5.3	12.3
G232.062−00.076	56.4	0.6	1.1 ± 0.1	1.7 ± 0.2	5.2	12.2
G232.071−00.176	19.7	0.4	1.1 ± 0.8	1.0 ± 0.8	1.7	9.5
G232.075−02.276	41.8	1.7	22.0 ± 0.2	91.5 ± 1.5	3.7	11.0
G232.080+00.130	57.2	0.9	2.4 ± 0.1	5.1 ± 0.2	5.3	12.3
G232.082−00.046	13.9	0.5	0.7 ± 0.1	0.9 ± 0.1	1.3	9.2
	56.3	0.7	0.6 ± 0.1	1.0 ± 0.2	5.2	12.2
G232.111−01.158	46.7	1.8	2.9 ± 0.1	12.8 ± 0.5	4.1	11.4
G232.131−00.256	21.7	0.6	0.7 ± 0.1	1.0 ± 0.1	1.9	9.6
G232.205−00.764	44.4	0.5	1.0 ± 0.1	1.2 ± 0.1	3.9	11.2
G232.220+00.190	15.3	0.6	2.9 ± 0.1	4.1 ± 0.2	1.4	9.2
	19.2	0.9	1.1 ± 0.2	2.3 ± 0.4	1.7	9.5
G232.220−01.070	43.7	1.7	1.7 ± 0.1	7.3 ± 0.4	3.8	11.1
G232.230+00.180	15.6	0.4	1.4 ± 0.2	1.3 ± 0.2	1.4	9.3
	18.2	1.0	2.0 ± 0.1	5.2 ± 0.3	1.6	9.4
	21.7	0.6	0.3 ± 0.2	0.5 ± 0.3	1.9	9.6
G232.240+00.130	16.9	1.8	2.6 ± 0.1	11.7 ± 0.6	1.5	9.3
G232.250+00.070	16.9	1.8	2.4 ± 0.1	10.5 ± 0.5	1.5	9.3
G232.250+00.060	17.0	1.7	2.3 ± 0.1	9.6 ± 0.5	1.5	9.3
G232.420+00.240	20.6	1.0	1.9 ± 0.1	4.7 ± 0.3	1.8	9.5
G232.490−00.300	17.0	0.9	2.1 ± 0.1	4.5 ± 0.3	1.5	9.3
G232.500−00.040	17.3	0.9	2.2 ± 0.1	5.3 ± 0.3	1.5	9.3
	20.2	0.7	0.9 ± 0.2	1.6 ± 0.4	1.8	9.5

Table A.1: continued

Name	$v_{\rm lsr}$ (km s^{-1})	$\Delta v_{\rm lsr}$ (km s^{-1})	$T_{\rm max}$ (K)	$\int T dv$ (K km s^{-1})	$R_{\rm hel}$ (kpc)	$R_{\rm gal}$ (kpc)
G232.504−01.223	25.3	0.6	0.4 ± 0.1	0.6 ± 0.2	2.2	9.8
	47.3	0.6	0.3 ± 0.1	0.4 ± 0.2	4.2	11.4
G232.510+00.200	13.8	0.3	0.8 ± 0.2	0.6 ± 0.1	1.3	9.2
	15.9	0.7	1.6 ± 0.2	2.8 ± 0.3	1.4	9.3
	20.9	1.1	1.6 ± 0.2	4.2 ± 0.4	1.8	9.6
G232.590−01.190	22.5	0.6	0.7 ± 0.1	1.1 ± 0.2	1.9	9.6
G232.596−01.352	46.0	1.0	3.0 ± 0.2	7.6 ± 0.5	4.1	11.3
	48.4	0.7	2.3 ± 0.3	4.1 ± 0.6	4.3	11.5
G232.600+00.300	15.7	0.6	4.7 ± 0.1	7.3 ± 0.3	1.4	9.3
G232.600+00.430	16.3	0.6	3.9 ± 0.1	5.7 ± 0.2	1.5	9.3
G232.600+00.100	17.0	1.7	1.9 ± 0.1	8.4 ± 0.5	1.5	9.3
G232.600−01.320	47.1	1.5	2.0 ± 0.1	7.4 ± 0.4	4.2	11.4
G232.630+00.390	16.6	0.6	3.3 ± 0.1	4.7 ± 0.2	1.5	9.3
G232.640−00.420	17.7	1.4	0.4 ± 0.1	1.2 ± 0.3	1.6	9.4
	23.2	0.5	2.7 ± 0.2	3.7 ± 0.3	2.0	9.7
	47.4	0.6	1.0 ± 0.1	1.3 ± 0.2	4.2	11.4
G232.669−01.295	48.9	0.6	0.6 ± 0.1	0.9 ± 0.2	4.4	11.5
	54.4	0.7	0.5 ± 0.1	0.8 ± 0.2	5.0	12.0
G232.679−01.305	48.2	0.9	0.4 ± 0.1	1.0 ± 0.2	4.3	11.5
G232.680+00.160	14.5	0.4	3.4 ± 0.3	3.5 ± 0.3	1.3	9.2
	16.6	1.6	1.9 ± 0.3	7.5 ± 1.1	1.5	9.3
	21.6	0.8	1.7 ± 0.3	3.5 ± 0.7	1.9	9.6
	33.5	0.7	0.3 ± 0.2	0.6 ± 0.4	2.9	10.4
G232.710−00.240	15.3	0.8	1.3 ± 0.2	2.5 ± 0.4	1.4	9.2
	18.2	0.8	2.3 ± 0.1	4.9 ± 0.3	1.6	9.4
	39.2	0.6	0.7 ± 0.1	1.0 ± 0.1	3.4	10.8
G232.760−00.240	17.8	1.1	1.8 ± 0.1	5.0 ± 0.3	1.6	9.4
G232.760+00.050	18.5	2.1	0.9 ± 0.1	4.5 ± 0.5	1.6	9.4
	39.2	0.8	0.4 ± 0.1	0.7 ± 0.2	3.4	10.8
	43.9	0.6	0.7 ± 0.1	1.0 ± 0.2	3.9	11.1
G232.770−00.340	18.1	1.0	0.5 ± 0.1	1.2 ± 0.2	1.6	9.4
G232.770−00.350	18.3	1.0	0.7 ± 0.2	1.9 ± 0.6	1.6	9.4
G232.770−00.360	18.4	1.0	0.5 ± 0.2	1.2 ± 0.5	1.6	9.4
	22.8	0.6	3.2 ± 0.1	4.8 ± 0.2	2.0	9.7
	23.0	0.7	3.5 ± 0.1	5.8 ± 0.2	2.0	9.7
	23.1	0.6	2.9 ± 0.1	4.4 ± 0.2	2.0	9.7
	45.2	0.7	0.6 ± 0.1	1.1 ± 0.2	4.0	11.2
	47.9	0.7	0.2 ± 0.1	0.4 ± 0.2	4.3	11.4
G232.782+00.271	16.5	1.8	1.8 ± 0.1	8.0 ± 0.5	1.5	9.3
G232.790+00.150	18.4	1.3	2.8 ± 0.3	9.3 ± 1.0	1.6	9.4
	22.8	1.1	3.9 ± 0.2	10.5 ± 0.7	2.0	9.7
G232.790−01.400	47.1	1.2	1.0 ± 0.1	3.0 ± 0.3	4.2	11.4
	52.9	0.6	1.1 ± 0.1	1.7 ± 0.2	4.8	11.9
G232.796−00.952	45.0	0.5	0.9 ± 0.1	1.2 ± 0.1	4.0	11.2
G232.805−00.713	44.5	1.2	1.4 ± 0.1	4.4 ± 0.3	3.9	11.2
G232.820−00.840	46.9	0.8	1.5 ± 0.5	3.2 ± 1.0	4.2	11.4
	49.3	0.5	1.0 ± 0.7	1.3 ± 0.9	4.4	11.5
G232.894−01.389	46.8	1.3	3.2 ± 0.1	10.7 ± 0.4	4.1	11.3
	50.6	0.8	0.5 ± 0.3	1.0 ± 0.6	4.5	11.7

Table A.1: continued

Name	$v_{\rm lsr}$ (km s^{-1})	$\Delta v_{\rm lsr}$ (km s^{-1})	$T_{\rm max}$ (K)	$\int T dv$ (K km s^{-1})	$R_{\rm hel}$ (kpc)	$R_{\rm gal}$ (kpc)
G232.894−00.613	31.2	0.6	0.7 ± 0.1	1.0 ± 0.2	2.7	10.2
	44.4	0.7	1.1 ± 0.1	1.9 ± 0.2	3.9	11.1
G232.900+00.120	19.1	1.2	1.5 ± 0.4	4.4 ± 1.2	1.7	9.4
	21.6	0.5	1.8 ± 0.5	2.2 ± 0.7	1.9	9.6
G232.923−00.523	45.9	0.8	0.4 ± 0.1	0.9 ± 0.2	4.1	11.3
G232.930+00.040	19.2	1.4	1.6 ± 0.1	5.7 ± 0.4	1.7	9.4
G232.940−01.000	43.7	0.8	2.0 ± 0.1	4.2 ± 0.2	3.8	11.1
G232.950−00.790	24.5	1.0	0.7 ± 0.1	1.8 ± 0.3	2.1	9.8
	46.3	1.4	2.2 ± 0.1	7.9 ± 0.4	4.1	11.3
G232.970−00.780	25.8	0.5	1.4 ± 0.1	1.8 ± 0.1	2.2	9.8
	46.3	1.0	2.3 ± 0.1	5.8 ± 0.3	4.1	11.3
G232.975−00.752	25.4	1.1	0.9 ± 0.1	2.6 ± 0.3	2.2	9.8
	46.6	1.3	1.8 ± 0.1	5.8 ± 0.3	4.1	11.3
G233.025−00.580	47.0	0.9	1.1 ± 0.1	2.7 ± 0.2	4.2	11.3
G233.045−00.550	46.1	0.7	0.8 ± 0.1	1.5 ± 0.2	4.1	11.3
G233.120−01.749	51.1	0.6	0.8 ± 0.1	1.2 ± 0.1	4.6	11.7
G233.140−01.220	32.6	0.6	0.3 ± 0.1	0.5 ± 0.2	2.8	10.3
	48.8	0.9	3.1 ± 0.1	6.9 ± 0.2	4.4	11.5
G233.140−01.540	50.5	1.1	1.6 ± 0.1	4.5 ± 0.3	4.5	11.6
G233.180−01.710	51.2	1.3	2.9 ± 0.1	9.4 ± 0.3	4.6	11.7
	61.1	0.7	0.9 ± 0.1	1.6 ± 0.2	5.7	12.6
G233.200−00.960	46.5	1.4	1.2 ± 0.1	4.1 ± 0.3	4.1	11.3
G233.208−01.340	47.6	1.0	0.9 ± 0.1	2.3 ± 0.3	4.2	11.4
G233.241−01.908	46.0	0.5	0.4 ± 0.2	0.5 ± 0.2	4.1	11.3
G233.250+00.100	16.7	0.5	0.4 ± 0.1	0.4 ± 0.1	1.5	9.3
	19.6	0.7	1.4 ± 0.1	2.6 ± 0.2	1.7	9.5
	40.7	1.3	2.5 ± 0.1	8.2 ± 0.3	3.6	10.8
G233.250−00.360	47.0	0.7	0.5 ± 0.1	0.9 ± 0.2	4.2	11.3
G233.250−01.030	47.2	0.8	3.5 ± 0.1	7.1 ± 0.2	4.2	11.4
G233.290−00.310	45.9	0.8	0.5 ± 0.1	1.1 ± 0.2	4.1	11.2
G233.320−00.330	44.6	0.6	1.7 ± 0.1	2.8 ± 0.2	3.9	11.1
G233.320−00.320	44.8	0.6	2.4 ± 0.1	3.9 ± 0.2	3.9	11.2
G233.380+00.120	15.8	1.0	2.2 ± 0.1	5.7 ± 0.3	1.4	9.3
	42.9	1.0	4.1 ± 0.2	10.5 ± 0.4	3.8	11.0
G233.380−01.600	76.6	0.5	2.8 ± 0.1	3.6 ± 0.1	7.7	14.4
G233.390+00.120	15.7	0.9	2.1 ± 0.1	4.8 ± 0.3	1.4	9.2
	43.2	1.2	3.7 ± 0.1	11.4 ± 0.4	3.8	11.0
G233.460−00.360	44.4	0.8	2.2 ± 0.1	4.2 ± 0.2	3.9	11.1
G233.480−00.360	44.7	0.5	2.5 ± 0.1	3.1 ± 0.1	3.9	11.1
G233.500+00.130	16.6	0.9	1.4 ± 0.1	3.1 ± 0.2	1.5	9.3
	20.3	0.9	1.2 ± 0.1	2.7 ± 0.2	1.8	9.5
	52.9	0.8	4.8 ± 0.1	9.8 ± 0.3	4.8	11.8
G233.730−01.330	75.6	0.9	2.6 ± 0.1	5.5 ± 0.2	7.6	14.2
G233.736−00.197	18.3	0.6	0.3 ± 0.2	0.5 ± 0.3	1.6	9.4
	20.7	0.5	1.9 ± 0.1	2.4 ± 0.1	1.8	9.5
	44.2	1.3	6.2 ± 0.1	20.6 ± 0.5	3.9	11.1
G233.750−01.270	75.9	1.4	3.7 ± 0.1	13.2 ± 0.5	7.6	14.2
G233.757−01.269	30.0	0.5	0.4 ± 0.1	0.5 ± 0.1	2.6	10.1
G233.760−01.250	76.9	0.9	2.2 ± 0.1	5.0 ± 0.2	7.7	14.3

Table A.1: continued

Name	$v_{\rm lsr}$ (km s^{-1})	$\Delta v_{\rm lsr}$ (km s^{-1})	$T_{\rm max}$ (K)	$\int T dv$ (K km s^{-1})	$R_{\rm hel}$ (kpc)	$R_{\rm gal}$ (kpc)
G233.777−01.269	23.7	0.5	0.6 ± 0.1	0.8 ± 0.1	2.1	9.7
G233.810−00.110	19.9	1.2	0.2 ± 0.1	0.6 ± 0.3	1.7	9.5
	43.7	1.0	2.7 ± 0.1	6.6 ± 0.3	3.8	11.1
G233.840−00.183	20.3	0.5	1.8 ± 0.1	2.4 ± 0.1	1.8	9.5
	43.3	0.6	6.2 ± 0.2	9.6 ± 0.3	3.8	11.0
G233.980−01.860	48.5	1.0	3.2 ± 0.1	8.3 ± 0.3	4.3	11.4
G234.033−00.537	43.0	0.6	2.5 ± 0.1	3.9 ± 0.2	3.8	11.0
	56.2	0.6	0.2 ± 0.1	0.4 ± 0.2	5.1	12.1
G234.050−00.130	41.6	0.8	5.7 ± 0.1	11.6 ± 0.2	3.6	10.9
G234.050−01.910	49.9	1.0	4.4 ± 0.1	10.8 ± 0.3	4.5	11.5
G234.052−02.176	23.5	0.7	0.4 ± 0.1	0.7 ± 0.2	2.0	9.7
	48.9	0.5	2.6 ± 0.1	3.3 ± 0.1	4.4	11.5
G234.121+00.315	55.5	0.5	0.7 ± 0.1	0.9 ± 0.1	5.0	12.0
G234.131+00.315	56.6	0.7	0.3 ± 0.1	0.5 ± 0.2	5.2	12.1
G234.234−00.717	42.1	0.5	6.3 ± 0.3	8.1 ± 0.4	3.7	10.9
G234.260−01.490	69.1	0.6	1.0 ± 0.1	1.7 ± 0.2	6.7	13.4
G234.270−01.500	69.0	0.6	0.2 ± 0.1	0.4 ± 0.2	6.6	13.3
G234.333−00.651	39.6	0.7	3.6 ± 0.1	6.4 ± 0.2	3.4	10.7
	74.9	1.0	0.1 ± 0.1	0.3 ± 0.3	7.4	14.0
G234.356−02.813	58.9	0.4	1.3 ± 0.4	1.4 ± 0.4	5.4	12.3
G234.450−01.070	77.3	0.9	4.3 ± 0.1	9.3 ± 0.2	7.8	14.3
G234.468−00.393	41.8	1.6	12.4 ± 0.1	51.0 ± 0.7	3.7	10.9
G234.493−00.829	76.9	1.1	2.2 ± 0.1	5.8 ± 0.3	7.7	14.3
G234.501−00.863	25.6	0.4	0.3 ± 0.3	0.3 ± 0.3	2.2	9.8
	77.5	1.3	4.0 ± 0.1	12.6 ± 0.3	7.8	14.3
G234.570−01.003	44.5	0.6	2.9 ± 0.1	4.5 ± 0.2	3.9	11.1
G234.580−01.030	44.8	0.6	3.0 ± 0.1	4.6 ± 0.2	3.9	11.1
G234.590−01.080	22.9	0.6	0.4 ± 0.1	0.5 ± 0.1	2.0	9.6
G234.620−00.197	42.6	1.8	11.4 ± 8.5	52.3 ± 39.1	3.7	10.9
G234.650−01.580	68.5	1.2	5.7 ± 0.1	16.4 ± 0.3	6.6	13.3
G234.660+00.070	27.9	0.5	3.0 ± 0.1	3.9 ± 0.1	2.4	9.9
	44.7	0.9	1.0 ± 0.1	2.2 ± 0.2	3.9	11.1
G234.710−00.910	76.6	0.7	1.6 ± 0.1	2.7 ± 0.2	7.6	14.2
G234.715−00.911	77.0	0.8	4.3 ± 0.1	8.9 ± 0.2	7.7	14.2
G234.720−00.820	78.1	0.6	0.3 ± 0.1	0.5 ± 0.1	7.8	14.4
G234.730−00.750	77.9	0.7	2.2 ± 0.1	3.7 ± 0.2	7.8	14.3
G234.730−00.810	78.2	0.8	4.7 ± 0.1	9.5 ± 0.2	7.9	14.4
G234.764−00.282	43.3	0.7	21.2 ± 0.1	35.7 ± 0.4	3.8	11.0
G234.790+00.062	28.4	0.7	0.5 ± 0.1	1.0 ± 0.2	2.5	10.0
G234.860−00.090	43.4	1.0	8.4 ± 0.1	21.9 ± 0.4	3.8	11.0
G234.880−00.130	42.8	0.5	5.3 ± 0.1	7.1 ± 0.2	3.8	10.9
G234.890−00.180	43.0	0.6	3.9 ± 0.1	5.7 ± 0.2	3.8	11.0
G235.050−01.530	70.2	0.6	0.7 ± 0.1	1.1 ± 0.1	6.8	13.4
	81.4	1.2	13.5 ± 0.1	39.8 ± 0.4	8.3	14.8
G235.060−01.550	70.5	0.5	0.5 ± 0.1	0.6 ± 0.1	6.8	13.4
	81.7	1.4	6.8 ± 0.1	23.7 ± 0.4	8.4	14.8
G235.150−01.530	81.2	1.0	2.5 ± 0.1	6.4 ± 0.3	8.3	14.7
G235.220−01.670	79.4	0.8	2.7 ± 0.3	5.6 ± 0.7	8.0	14.5
	81.6	1.0	2.8 ± 0.3	7.4 ± 0.7	8.3	14.8

Table A.1: continued

Name	$v_{\rm lsr}$ (km s^{-1})	$\Delta v_{\rm lsr}$ (km s^{-1})	$T_{\rm max}$ (K)	$\int T dv$ (K km s^{-1})	$R_{\rm hel}$ (kpc)	$R_{\rm gal}$ (kpc)
G235.347−01.740	81.1	1.2	3.1 ± 0.1	9.3 ± 0.3	8.2	14.7
G235.348−01.687	81.7	0.9	3.9 ± 0.1	8.5 ± 0.2	8.3	14.8
G235.360−01.470	72.5	0.5	1.4 ± 0.1	1.8 ± 0.1	7.0	13.6
G235.389−01.655	82.3	1.1	10.9 ± 0.1	30.3 ± 0.3	8.4	14.8
G235.477−01.769	23.5	0.6	0.3 ± 0.1	0.5 ± 0.1	2.1	9.7
	79.5	1.2	2.1 ± 0.1	6.2 ± 0.3	8.0	14.5
G235.532−01.675	83.2	1.7	4.7 ± 0.1	20.0 ± 0.4	8.5	14.9
G235.590−01.520	74.0	0.7	1.5 ± 0.1	2.6 ± 0.2	7.2	13.8
G235.610−00.710	48.9	1.2	2.2 ± 0.2	6.6 ± 0.5	4.4	11.4
G235.680−00.030	47.4	0.7	1.9 ± 0.1	3.3 ± 0.2	4.2	11.3
G235.690−01.240	75.1	0.8	7.9 ± 0.1	15.1 ± 0.2	7.4	13.9
G235.780+00.010	51.6	1.0	4.7 ± 0.1	12.0 ± 0.3	4.6	11.6
G235.907−01.613	30.1	0.5	3.6 ± 0.1	4.1 ± 0.2	2.6	10.1
	53.0	0.5	0.2 ± 0.1	0.2 ± 0.1	4.8	11.7
G236.180−01.830	28.0	0.1	2.2 ± 0.5	0.8 ± 0.2	2.4	9.9
	30.3	0.9	6.5 ± 0.2	15.1 ± 0.5	2.6	10.1
	79.5	1.3	0.2 ± 0.1	0.8 ± 0.3	8.0	14.4
G236.420−00.710	24.5	0.7	3.3 ± 0.1	5.4 ± 0.2	2.2	9.7
	48.0	0.6	0.9 ± 0.1	1.3 ± 0.2	4.3	11.3
G236.490−00.590	25.0	1.1	3.0 ± 0.1	8.1 ± 0.4	2.2	9.7
	56.0	0.6	2.2 ± 0.1	3.2 ± 0.1	5.1	11.9
G236.570−00.460	49.5	0.8	1.0 ± 0.1	2.0 ± 0.2	4.4	11.4
G236.600−02.130	25.6	2.4	10.7 ± 0.1	63.8 ± 1.4	2.3	9.8
G236.600−02.290	26.8	1.3	6.7 ± 0.1	22.7 ± 0.5	2.4	9.8
G236.600−02.310	26.9	1.8	4.2 ± 0.1	18.9 ± 0.6	2.4	9.8
	79.5	0.9	0.2 ± 0.1	0.5 ± 0.2	7.9	14.3
	80.6	1.2	0.8 ± 0.1	2.5 ± 0.3	8.1	14.5
	81.1	0.8	0.8 ± 0.1	1.7 ± 0.2	8.2	14.5
G236.610−02.110	24.2	1.3	5.5 ± 0.2	18.4 ± 0.9	2.1	9.7
G236.610+00.010	24.3	0.7	0.7 ± 0.1	1.3 ± 0.2	2.1	9.7
	27.5	0.7	2.7 ± 0.6	4.5 ± 1.1	2.4	9.9
	47.4	0.8	3.6 ± 0.1	7.3 ± 0.2	4.2	11.2
	79.5	0.6	0.2 ± 0.1	0.3 ± 0.1	7.9	14.3
G236.620+00.000	46.9	0.6	2.9 ± 0.1	4.7 ± 0.2	4.2	11.2
G236.630−01.150	28.7	0.6	3.2 ± 0.1	4.5 ± 0.2	2.5	9.9
G236.717−01.611	18.8	0.4	0.7 ± 0.1	0.8 ± 0.1	1.7	9.4
G236.880−01.010	79.9	0.7	6.1 ± 0.2	10.4 ± 0.3	8.0	14.3
G236.950−00.780	20.2	1.0	2.2 ± 0.1	5.5 ± 0.3	1.8	9.5
G237.000−01.840	23.9	0.7	1.3 ± 0.1	2.2 ± 0.2	2.1	9.7
	80.6	1.1	10.8 ± 0.1	29.4 ± 0.3	8.1	14.4
G237.050−00.770	22.1	0.9	3.3 ± 0.1	7.2 ± 0.3	2.0	9.6
	78.7	0.5	1.6 ± 0.1	2.1 ± 0.1	7.8	14.2
G237.100−00.820	21.3	1.6	3.3 ± 0.1	13.2 ± 0.5	1.9	9.5
G237.110−00.990	21.4	1.3	3.5 ± 0.1	11.8 ± 0.4	1.9	9.5
G237.110−00.790	22.2	0.7	2.9 ± 0.1	5.4 ± 0.2	2.0	9.6
G237.110−00.300	55.7	1.0	2.7 ± 0.1	6.6 ± 0.3	5.0	11.9
G237.170−00.960	21.9	1.0	4.2 ± 0.1	11.1 ± 0.4	2.0	9.5
G237.178−01.909	22.8	0.9	1.8 ± 0.1	4.1 ± 0.2	2.0	9.6
G237.180−01.470	22.5	0.7	1.0 ± 0.1	1.7 ± 0.2	2.0	9.6

Table A.1: continued

Name	$v_{\rm lsr}$ (km s^{-1})	$\Delta v_{\rm lsr}$ (km s^{-1})	$T_{\rm max}$ (K)	$\int T dv$ (K km s^{-1})	$R_{\rm hel}$ (kpc)	$R_{\rm gal}$ (kpc)
	70.8	0.8	2.0 ± 0.1	4.1 ± 0.2	6.8	13.3
G237.210−01.440	73.9	0.6	5.2 ± 0.4	7.4 ± 0.6	7.1	13.6
G237.230−01.060	24.0	0.8	1.2 ± 0.1	2.5 ± 0.2	2.1	9.7
	77.1	0.7	2.9 ± 0.1	5.1 ± 0.2	7.6	14.0
G237.240−01.080	22.8	0.6	3.1 ± 0.1	4.9 ± 0.2	2.0	9.6
	77.4	0.8	4.4 ± 0.2	9.2 ± 0.4	7.6	14.0
G237.243−02.556	26.1	0.4	0.5 ± 0.5	0.4 ± 0.5	2.3	9.8
G237.247−01.679	23.9	0.6	0.3 ± 0.1	0.4 ± 0.1	2.1	9.7
G237.260−01.280	21.9	0.6	1.4 ± 0.1	2.1 ± 0.2	2.0	9.5
G237.260−01.300	22.0	0.6	0.8 ± 0.1	1.3 ± 0.2	2.0	9.5
G237.260−01.260	22.1	0.5	2.5 ± 0.1	3.3 ± 0.1	2.0	9.6
	70.2	1.0	14.0 ± 0.3	36.5 ± 0.8	6.7	13.2
	71.5	1.2	16.6 ± 0.3	49.9 ± 1.1	6.8	13.3
	73.4	1.4	11.3 ± 0.4	40.5 ± 1.4	7.1	13.6
	76.5	2.6	3.7 ± 0.8	24.2 ± 5.3	7.5	13.9
	78.3	1.1	3.7 ± 1.0	10.0 ± 2.7	7.7	14.1
	78.5	1.7	2.0 ± 0.9	8.5 ± 3.8	7.8	14.1
G237.320−01.280	22.7	0.7	0.5 ± 0.1	0.8 ± 0.2	2.0	9.6
	78.3	1.2	17.5 ± 0.1	51.7 ± 0.5	7.7	14.1
G237.330−01.260	74.9	0.9	2.5 ± 0.2	5.3 ± 0.5	7.3	13.7
	77.8	0.8	3.2 ± 0.2	6.4 ± 0.4	7.7	14.0
G237.347−01.669	83.1	1.2	0.3 ± 0.1	1.0 ± 0.3	8.4	14.7
G237.460−01.790	22.9	0.9	3.4 ± 0.1	7.5 ± 0.3	2.0	9.6
G237.499−01.978	32.5	0.5	0.2 ± 0.2	0.2 ± 0.2	2.9	10.2
G237.500−02.018	82.8	0.6	0.2 ± 0.1	0.3 ± 0.1	8.4	14.6
G237.511−02.336	20.7	0.7	2.8 ± 0.1	5.3 ± 0.2	1.9	9.5
G237.530−01.380	75.9	0.6	1.2 ± 0.1	1.9 ± 0.2	7.4	13.8
G237.540−00.660	57.0	0.6	0.3 ± 0.1	0.4 ± 0.1	5.2	11.9
	59.6	0.6	0.5 ± 0.1	0.7 ± 0.1	5.5	12.2
G237.550−00.640	56.9	0.5	1.2 ± 0.1	1.5 ± 0.1	5.2	11.9
	59.7	0.5	0.4 ± 0.1	0.5 ± 0.1	5.5	12.2
G237.660−01.790	23.4	0.9	0.9 ± 0.1	2.0 ± 0.2	2.1	9.6
G237.661−00.514	56.2	0.8	2.6 ± 0.1	5.5 ± 0.2	5.1	11.9
G237.740−00.970	21.7	1.5	11.9 ± 0.2	45.3 ± 1.3	1.9	9.5
G237.740−00.960	22.0	1.4	14.2 ± 0.2	48.1 ± 1.4	2.0	9.5
	81.5	0.6	0.2 ± 0.1	0.3 ± 0.2	8.2	14.4
G237.763−02.684	62.5	0.6	0.5 ± 0.1	0.8 ± 0.2	5.8	12.4
G237.770−01.010	22.2	0.8	4.2 ± 0.1	8.5 ± 0.3	2.0	9.6
G237.820−01.280	23.6	0.8	1.7 ± 0.1	3.6 ± 0.2	2.1	9.6
	75.8	1.1	5.8 ± 0.1	15.3 ± 0.3	7.4	13.8
G237.836−01.558	22.6	0.6	0.9 ± 0.1	1.3 ± 0.1	2.0	9.6
G237.845−01.538	22.5	0.7	0.9 ± 0.1	1.5 ± 0.2	2.0	9.6
G237.940−01.170	21.1	0.4	3.2 ± 0.2	3.4 ± 0.3	1.9	9.5
	23.5	0.8	3.0 ± 0.2	6.0 ± 0.4	2.1	9.6
G237.963−02.684	19.7	0.3	1.3 ± 1.2	1.1 ± 1.1	1.8	9.4
G238.038−01.867	78.9	0.7	0.4 ± 0.1	0.7 ± 0.2	7.8	14.1
G238.260−01.720	20.1	1.1	3.3 ± 2.6	8.8 ± 6.8	1.8	9.4
	22.3	0.6	11.7 ± 1.0	16.7 ± 1.5	2.0	9.6
G238.511−00.885	23.7	0.6	2.5 ± 0.1	3.8 ± 0.2	2.1	9.6

Table A.1: continued

Name	$v_{\rm lsr}$ (km s^{-1})	$\Delta v_{\rm lsr}$ (km s^{-1})	$T_{\rm max}$ (K)	$\int T dv$ (K km s^{-1})	$R_{\rm hel}$ (kpc)	$R_{\rm gal}$ (kpc)
G238.540−00.920	24.0	0.5	1.6 ± 0.1	1.9 ± 0.1	2.2	9.6
G238.560+00.240	22.2	0.8	0.5 ± 0.1	0.9 ± 0.2	2.0	9.5
G238.670−01.440	20.3	1.1	4.5 ± 0.1	12.8 ± 0.4	1.9	9.4
G238.690−01.860	80.5	0.7	0.6 ± 0.2	1.2 ± 0.4	8.0	14.2
	88.3	1.2	3.2 ± 0.1	9.4 ± 0.3	9.1	15.2
G238.700−01.270	20.2	0.5	2.2 ± 0.1	2.8 ± 0.2	1.9	9.4
G238.750−01.460	18.4	2.3	3.5 ± 0.1	20.5 ± 0.8	1.7	9.3
G238.770−01.810	19.6	0.5	0.6 ± 0.1	0.7 ± 0.1	1.8	9.4
	88.4	1.6	5.9 ± 0.1	24.0 ± 0.4	9.1	15.2
G238.800−01.630	17.3	1.0	2.8 ± 0.4	7.3 ± 1.0	1.6	9.3
	19.9	1.8	2.0 ± 0.4	9.2 ± 1.9	1.8	9.4
G238.830−02.080	81.1	1.5	–	–	8.1	14.3
G238.960−01.680	18.5	0.8	4.0 ± 0.1	8.3 ± 0.3	1.7	9.3
	83.1	1.2	3.2 ± 0.2	9.8 ± 0.7	8.3	14.5
G238.970−02.030	81.2	0.7	4.4 ± 0.1	7.5 ± 0.2	8.1	14.3
G239.190−01.960	83.0	1.2	4.3 ± 0.1	12.9 ± 0.3	8.3	14.5
G239.300−00.630	64.7	0.7	2.6 ± 0.1	4.7 ± 0.2	6.0	12.5
G239.370−01.690	18.8	1.2	6.8 ± 0.1	20.9 ± 0.7	1.8	9.4
	22.9	1.8	0.6 ± 0.4	2.6 ± 2.0	2.1	9.6
G239.370−00.080	66.9	0.7	1.6 ± 0.1	2.6 ± 0.2	6.3	12.7
	85.9	0.8	0.8 ± 0.1	1.7 ± 0.2	8.7	14.8
G239.524−00.711	65.3	0.6	1.6 ± 0.1	2.4 ± 0.2	6.1	12.6
G239.533−01.457	83.4	0.9	0.9 ± 0.1	2.2 ± 0.2	8.3	14.5
G239.594−01.524	19.9	1.8	0.2 ± 0.1	0.9 ± 0.5	1.8	9.4
	85.5	0.7	0.2 ± 0.1	0.4 ± 0.2	8.7	14.7
G239.630−02.090	78.4	1.3	1.7 ± 0.1	5.5 ± 0.3	7.7	13.9
G239.650−00.810	64.6	0.7	2.6 ± 0.2	4.5 ± 0.3	6.0	12.5
G239.660−02.040	24.1	0.5	0.5 ± 0.1	0.6 ± 0.1	2.2	9.6
	78.3	1.1	1.2 ± 0.1	3.4 ± 0.3	7.7	13.9
G239.678−00.802	65.1	1.4	2.7 ± 0.1	9.4 ± 0.4	6.1	12.5
G239.680−02.040	24.4	0.7	0.8 ± 0.1	1.4 ± 0.2	2.2	9.7
	77.9	0.9	1.6 ± 0.1	3.7 ± 0.2	7.6	13.8
G239.945−01.702	18.2	0.5	3.5 ± 0.1	4.7 ± 0.2	1.7	9.3
G239.950−01.810	17.9	1.0	6.8 ± 0.1	16.6 ± 0.5	1.7	9.3
	24.3	0.6	0.2 ± 0.1	0.3 ± 0.1	2.2	9.6
	27.0	0.5	0.6 ± 0.1	0.8 ± 0.1	2.4	9.8
G239.990−01.730	17.2	0.5	1.3 ± 0.4	1.6 ± 0.5	1.6	9.3
	20.4	0.7	4.3 ± 0.1	7.5 ± 0.3	1.9	9.4
G240.040−01.840	18.9	0.7	4.5 ± 0.1	8.0 ± 0.3	1.8	9.4
	23.6	0.6	0.6 ± 0.1	0.8 ± 0.1	2.2	9.6
G240.095−00.180	63.8	0.5	5.8 ± 0.1	8.0 ± 0.2	5.9	12.4
G240.140−01.540	31.9	0.5	7.0 ± 0.1	9.5 ± 0.2	2.9	10.1
G240.170−01.590	25.2	0.5	0.5 ± 0.1	0.7 ± 0.2	2.3	9.7
	64.1	0.7	0.4 ± 0.1	0.7 ± 0.2	5.9	12.4
	71.5	0.8	1.1 ± 0.1	2.3 ± 0.2	6.8	13.1
G240.250−00.910	17.6	0.7	3.6 ± 0.1	6.0 ± 0.2	1.7	9.3
G240.320+00.070	64.5	2.9	17.0 ± 0.9	123.0 ± 6.2	6.0	12.4
	71.5	1.9	10.1 ± 1.7	49.3 ± 8.1	6.8	13.1
G240.440−02.428	25.6	0.5	0.8 ± 0.1	0.9 ± 0.1	2.3	9.7

Table A.1: continued

Name	$v_{\rm lsr}$ (km s^{-1})	$\Delta v_{\rm lsr}$ (km s^{-1})	$T_{\rm max}$ (K)	$\int T dv$ (K km s^{-1})	$R_{\rm hel}$ (kpc)	$R_{\rm gal}$ (kpc)
G240.490−00.070	68.8	0.5	3.9 ± 0.1	4.5 ± 0.1	6.5	12.8
G240.545−01.800	65.0	0.7	0.3 ± 0.1	0.5 ± 0.2	6.0	12.5
G240.940−01.440	65.5	1.1	2.7 ± 0.1	7.2 ± 0.3	6.1	12.5
G240.990−01.470	19.0	0.8	2.7 ± 0.1	5.6 ± 0.3	1.8	9.3
	64.0	0.7	1.1 ± 0.1	1.8 ± 0.2	5.9	12.4
G241.003−01.203	62.8	1.2	4.4 ± 0.2	13.6 ± 0.6	5.8	12.3
	66.3	1.2	2.8 ± 0.3	8.0 ± 1.0	6.2	12.6
G241.010−01.200	62.7	0.9	2.8 ± 0.2	6.7 ± 0.6	5.8	12.2
	66.4	1.6	3.3 ± 0.2	13.3 ± 0.7	6.2	12.6
G241.121−00.781	70.1	1.1	3.8 ± 0.1	10.1 ± 0.3	6.6	12.9
G241.140−01.170	64.7	1.4	3.0 ± 0.1	10.5 ± 0.4	6.0	12.4
G241.160−00.960	64.4	1.4	1.0 ± 0.1	3.5 ± 0.3	6.0	12.4
G241.180−01.070	65.9	1.0	2.8 ± 0.2	7.1 ± 0.4	6.2	12.5
	68.8	0.8	1.3 ± 0.3	2.5 ± 0.5	6.5	12.8
G241.190−00.780	68.3	1.2	4.0 ± 0.1	11.9 ± 0.3	6.4	12.7
G241.290−00.710	69.2	3.1	–	–	6.5	12.8
G241.390−02.030	18.9	1.1	2.2 ± 0.1	5.9 ± 0.3	1.8	9.3
G241.420−00.700	68.7	0.8	2.4 ± 0.3	5.0 ± 0.6	6.5	12.8
	71.6	1.6	3.6 ± 0.1	14.6 ± 0.6	6.8	13.0
G241.436−02.056	19.7	1.2	0.5 ± 0.1	1.6 ± 0.3	1.9	9.4
G241.454−01.847	21.7	0.5	1.7 ± 0.1	2.2 ± 0.1	2.0	9.5
G241.483−01.668	17.8	0.5	1.4 ± 0.1	1.8 ± 0.1	1.7	9.3
G241.530−00.600	70.8	1.4	10.9 ± 0.1	39.2 ± 0.5	6.7	13.0
G241.538−00.594	70.5	1.3	11.9 ± 0.1	37.8 ± 0.4	6.7	12.9
G241.560−00.590	70.5	0.9	10.2 ± 0.1	23.0 ± 0.3	6.7	12.9
G241.570−00.640	70.0	1.6	8.0 ± 0.1	31.1 ± 0.4	6.6	12.9
G241.640−00.650	68.4	1.3	6.3 ± 0.1	21.1 ± 0.4	6.4	12.7
G241.653−01.410	26.1	0.7	0.2 ± 0.1	0.4 ± 0.2	2.4	9.7
G241.680−00.580	69.3	1.6	8.2 ± 0.1	33.6 ± 0.5	6.5	12.8
G241.762−01.310	23.9	0.5	0.4 ± 0.1	0.5 ± 0.1	2.2	9.6
G241.815−00.627	69.0	1.4	3.4 ± 0.1	12.5 ± 0.4	6.5	12.8
G241.820−00.620	68.9	1.4	4.6 ± 0.1	15.8 ± 0.4	6.5	12.8
G241.820+00.000	69.2	1.0	1.3 ± 0.1	3.3 ± 0.2	6.5	12.8
G241.867−00.563	68.9	0.8	2.8 ± 0.1	5.8 ± 0.2	6.5	12.8
G241.971−00.848	65.5	0.9	2.7 ± 0.2	6.4 ± 0.5	6.1	12.4
	68.7	1.4	2.6 ± 0.2	9.0 ± 0.6	6.5	12.7
G242.020+00.190	69.7	1.0	1.6 ± 0.1	4.1 ± 0.3	6.6	12.8
G242.111−01.507	20.9	0.6	0.2 ± 0.1	0.3 ± 0.1	2.0	9.4
G242.190+00.010	67.2	1.8	5.3 ± 0.1	23.4 ± 0.5	6.3	12.6
G242.190−00.780	67.3	0.7	0.5 ± 0.1	0.8 ± 0.2	6.3	12.6
	70.3	0.5	0.3 ± 0.1	0.4 ± 0.1	6.7	12.9
G242.210+00.040	67.6	1.2	1.2 ± 0.1	3.6 ± 0.3	6.3	12.6
	71.1	0.9	1.0 ± 0.1	2.2 ± 0.3	6.7	12.9
G242.250+00.020	68.5	0.5	0.6 ± 0.2	0.7 ± 0.2	6.4	12.7
	73.2	0.6	0.3 ± 0.2	0.5 ± 0.4	7.0	13.1
G242.260+00.040	70.2	1.4	1.5 ± 0.1	5.0 ± 0.5	6.6	12.9
G242.310+00.070	68.0	0.7	1.5 ± 0.1	2.6 ± 0.2	6.4	12.7
	70.7	1.6	1.6 ± 0.1	6.1 ± 0.4	6.7	12.9
G242.320+00.040	69.6	0.9	1.8 ± 0.1	4.1 ± 0.3	6.6	12.8

Table A.1: continued

Name	$v_{\rm lsr}$ (km s^{-1})	$\Delta v_{\rm lsr}$ (km s^{-1})	$T_{\rm max}$ (K)	$\int T dv$ (K km s^{-1})	$R_{\rm hel}$ (kpc)	$R_{\rm gal}$ (kpc)
G242.320+00.100	70.1	1.1	2.7 ± 0.1	7.4 ± 0.3	6.6	12.8
	72.1	0.7	1.4 ± 0.2	2.5 ± 0.4	6.9	13.0
G242.337−01.093	18.1	0.5	1.0 ± 0.1	1.4 ± 0.1	1.8	9.3
	65.2	1.4	2.8 ± 0.1	9.6 ± 0.3	6.1	12.4
G242.340+00.010	69.4	0.5	1.2 ± 0.1	1.5 ± 0.2	6.6	12.8
	71.8	1.2	1.7 ± 0.1	5.0 ± 0.3	6.8	13.0
G242.482−01.665	18.4	0.7	0.3 ± 0.1	0.5 ± 0.2	1.8	9.3
G242.490+00.000	69.2	0.8	1.1 ± 0.1	2.4 ± 0.3	6.5	12.8
G242.540+00.040	70.2	0.8	2.2 ± 0.1	4.6 ± 0.2	6.6	12.8
	73.3	0.7	0.5 ± 0.2	0.8 ± 0.3	7.0	13.1
G242.545−00.848	65.9	0.8	2.6 ± 0.1	5.2 ± 0.2	6.2	12.4
G242.560−00.630	65.6	1.4	4.0 ± 0.1	13.7 ± 0.4	6.1	12.4
	74.8	0.8	0.4 ± 0.1	0.8 ± 0.2	7.2	13.3
G242.590−00.240	21.3	0.5	0.3 ± 0.1	0.4 ± 0.2	2.0	9.4
G242.604−00.789	62.3	0.7	0.3 ± 0.1	0.5 ± 0.2	5.8	12.1
G242.610+00.070	70.3	0.9	2.4 ± 0.1	5.4 ± 0.2	6.7	12.8
G242.620−00.690	65.8	1.1	5.3 ± 0.1	14.9 ± 0.3	6.2	12.4
G242.625−00.878	65.6	0.9	0.3 ± 0.1	0.6 ± 0.2	6.1	12.4
G242.640−00.700	65.7	1.1	5.2 ± 0.1	13.9 ± 0.3	6.1	12.4
G242.660+00.130	70.5	0.9	1.4 ± 0.1	3.1 ± 0.3	6.7	12.9
G242.770−01.530	18.0	0.7	–	–	1.8	9.3
G242.775−00.888	63.1	1.5	1.2 ± 0.1	4.5 ± 0.4	5.9	12.2
G242.810+00.080	55.8	1.0	4.6 ± 0.1	11.6 ± 0.3	5.1	11.6
G242.819−00.949	18.6	0.5	0.4 ± 0.1	0.5 ± 0.2	1.8	9.3
G242.850−01.515	17.8	0.5	0.9 ± 0.1	1.0 ± 0.1	1.8	9.3
G242.880−02.250	21.3	1.0	–	–	2.0	9.4
G242.910−01.574	19.1	0.5	1.3 ± 0.1	1.7 ± 0.1	1.9	9.3
G242.920−00.520	62.7	1.8	7.0 ± 0.1	30.9 ± 0.5	5.8	12.2
G242.920−00.450	63.4	1.2	6.7 ± 0.1	19.7 ± 0.3	5.9	12.2
G242.940−00.500	62.5	2.0	5.4 ± 0.1	27.3 ± 0.5	5.8	12.1
G242.940−00.450	62.6	1.8	7.7 ± 1.9	35.6 ± 8.9	5.8	12.2
	66.5	1.7	7.0 ± 2.2	29.5 ± 9.4	6.2	12.5
G242.944−00.758	67.2	0.6	2.4 ± 0.1	3.8 ± 0.2	6.3	12.5
G243.067−02.410	22.2	0.5	–	–	2.1	9.5
G243.150−00.170	53.8	1.0	1.5 ± 0.1	3.9 ± 0.3	4.9	11.4
G243.160−01.520	15.9	1.0	1.2 ± 1.0	3.1 ± 2.6	1.6	9.2
	18.4	0.5	1.2 ± 1.1	1.6 ± 1.5	1.8	9.3
G243.190−00.160	14.3	0.6	0.8 ± 0.2	1.1 ± 0.3	1.5	9.1
	53.6	0.6	3.3 ± 0.1	5.1 ± 0.2	4.9	11.4
G243.200−00.330	58.4	0.5	1.9 ± 0.2	2.4 ± 0.2	5.4	11.8
	63.1	0.8	1.3 ± 0.1	2.8 ± 0.2	5.9	12.2
G243.208−01.334	18.1	0.5	0.7 ± 0.1	0.8 ± 0.1	1.8	9.3
G243.209−01.404	18.3	0.6	1.3 ± 0.1	1.8 ± 0.2	1.8	9.3
G243.220−01.970	20.1	0.6	1.6 ± 0.1	2.4 ± 0.2	2.0	9.4
	30.0	0.8	2.7 ± 0.1	5.4 ± 0.3	2.8	9.9
G243.450−01.620	17.7	0.7	2.0 ± 0.1	3.4 ± 0.2	1.8	9.3
G243.457−02.399	21.1	0.9	2.0 ± 0.1	4.4 ± 0.2	2.0	9.4
G243.470+00.340	57.3	1.0	0.4 ± 0.1	1.0 ± 0.3	5.3	11.7
G243.475−01.045	21.8	0.7	1.6 ± 0.1	2.9 ± 0.2	2.1	9.5

Table A.1: continued

Name	$v_{\rm lsr}$ (km s^{-1})	$\Delta v_{\rm lsr}$ (km s^{-1})	$T_{\rm max}$ (K)	$\int T dv$ (K km s^{-1})	$R_{\rm hel}$ (kpc)	$R_{\rm gal}$ (kpc)
G243.521−02.846	22.6	0.4	0.5 ± 0.1	0.5 ± 0.1	2.2	9.5
	25.2	0.9	1.0 ± 0.1	2.3 ± 0.2	2.4	9.6
G243.540−00.810	22.7	1.6	4.3 ± 0.1	16.9 ± 0.5	2.2	9.5
G243.670−00.355	13.1	0.6	0.7 ± 0.6	1.2 ± 0.9	1.4	9.0
G243.751−00.536	66.5	0.7	1.9 ± 0.1	3.1 ± 0.2	6.2	12.4
G243.751−00.546	66.4	0.7	0.6 ± 0.1	1.0 ± 0.2	6.2	12.4
G243.770−01.420	17.3	0.6	3.2 ± 0.1	4.9 ± 0.2	1.7	9.2
G243.771−00.596	21.5	0.7	1.2 ± 0.1	2.0 ± 0.2	2.1	9.4
	63.2	0.7	1.3 ± 0.1	2.3 ± 0.2	5.9	12.2
G243.780−00.240	15.3	0.6	0.5 ± 0.1	0.8 ± 0.2	1.6	9.1
	66.0	1.0	7.1 ± 0.1	17.0 ± 0.3	6.2	12.4
G243.820−00.350	65.7	1.0	4.1 ± 0.1	10.3 ± 0.3	6.2	12.4
G243.860−00.870	22.4	0.8	2.3 ± 0.1	4.5 ± 0.2	2.2	9.5
G243.950−00.200	15.9	0.7	0.1 ± 0.1	0.3 ± 0.3	1.6	9.2
	64.6	0.5	1.6 ± 0.2	1.9 ± 0.2	6.1	12.3
G244.235−01.083	19.4	0.9	1.9 ± 0.1	4.0 ± 0.2	1.9	9.3
G244.410−01.970	92.4	1.6	1.9 ± 0.1	7.5 ± 0.4	9.5	15.1
G244.460−00.540	20.1	0.7	1.1 ± 0.1	1.9 ± 0.2	2.0	9.4
G244.680−00.840	19.3	1.0	1.3 ± 0.1	3.1 ± 0.3	1.9	9.3
	22.7	0.5	0.2 ± 0.1	0.2 ± 0.1	2.2	9.5
G244.747−01.419	14.7	0.4	0.3 ± 0.3	0.4 ± 0.4	1.5	9.1
G244.760−00.320	19.9	0.6	0.2 ± 0.1	0.3 ± 0.1	2.0	9.4
	61.8	0.9	3.9 ± 0.1	8.7 ± 0.2	5.8	12.0
G244.830−00.960	18.3	0.6	3.0 ± 0.1	4.5 ± 0.2	1.9	9.3
G244.960−00.060	21.9	0.4	4.3 ± 0.1	4.6 ± 0.1	2.2	9.5
G245.040−00.050	22.7	0.6	5.2 ± 0.1	7.4 ± 0.2	2.2	9.5
G245.044−01.200	16.2	0.5	0.3 ± 0.1	0.3 ± 0.1	1.7	9.2
G245.060+00.060	58.8	0.6	2.8 ± 0.1	4.3 ± 0.2	5.5	11.8
G245.060+00.080	59.7	0.7	10.9 ± 0.1	19.2 ± 0.2	5.6	11.8
G245.070−00.210	56.6	0.6	3.4 ± 0.1	4.7 ± 0.1	5.3	11.6
G245.080−00.180	20.7	0.6	3.9 ± 0.1	6.1 ± 0.2	2.1	9.4
G245.100−00.990	87.4	1.4	–	–	8.8	14.4
G245.170−00.050	21.1	0.5	2.8 ± 0.2	3.3 ± 0.2	2.1	9.4
	57.3	0.6	1.5 ± 0.1	2.3 ± 0.2	5.3	11.6
G245.240−01.390	12.6	0.6	1.1 ± 0.1	1.7 ± 0.2	1.4	9.0
G245.242−00.940	26.9	0.6	1.0 ± 0.1	1.7 ± 0.2	2.6	9.7
G245.300−00.300	59.7	0.7	7.1 ± 0.1	13.1 ± 0.2	5.6	11.8
G245.760−00.670	14.7	0.5	0.6 ± 0.6	0.7 ± 0.6	1.6	9.1
	63.8	0.6	1.6 ± 0.1	2.2 ± 0.2	6.0	12.1
G246.060+00.090	54.4	0.4	2.3 ± 0.2	2.6 ± 0.2	5.1	11.4
G246.270−00.070	56.5	0.9	2.0 ± 0.1	4.2 ± 0.2	5.3	11.5
G246.360−00.750	20.4	0.9	0.8 ± 0.1	1.7 ± 0.2	2.1	9.4
G246.410−00.680	20.9	1.2	0.9 ± 0.1	2.6 ± 0.3	2.1	9.4
G246.790−02.430	19.6	0.5	1.1 ± 0.2	1.5 ± 0.3	2.0	9.3
G246.970−01.720	19.3	0.8	0.9 ± 0.1	1.6 ± 0.2	2.0	9.3
	57.7	0.5	3.3 ± 0.1	4.4 ± 0.1	5.4	11.6
G247.240−01.120	19.5	0.6	3.5 ± 0.1	5.2 ± 0.2	2.0	9.3
G247.270−00.570	22.0	1.2	1.3 ± 0.1	4.0 ± 0.3	2.3	9.4
G247.280−00.560	22.2	1.4	0.9 ± 0.1	3.2 ± 0.4	2.3	9.5

Table A.1: continued

Name	$v_{\rm lsr}$ (km s^{-1})	$\Delta v_{\rm lsr}$ (km s^{-1})	$T_{\rm max}$ (K)	$\int T dv$ (K km s^{-1})	$R_{\rm hel}$ (kpc)	$R_{\rm gal}$ (kpc)
G247.440−00.930	18.1	0.7	3.6 ± 0.1	6.6 ± 0.3	1.9	9.3
G247.460−00.820	20.5	0.7	3.8 ± 0.1	6.4 ± 0.2	2.1	9.4
G247.510+00.060	16.4	0.7	0.5 ± 0.1	1.0 ± 0.2	1.8	9.2
G247.510−00.570	25.5	0.8	1.2 ± 0.1	2.3 ± 0.2	2.6	9.6
	28.3	0.6	0.4 ± 0.2	0.7 ± 0.3	2.8	9.8
	56.4	0.6	1.7 ± 0.1	2.6 ± 0.2	5.3	11.5
	56.5	0.6	2.0 ± 0.1	3.1 ± 0.2	5.3	11.5
G247.520+00.050	16.1	0.6	0.5 ± 0.1	0.8 ± 0.2	1.8	9.2
G247.520−00.240	16.5	0.7	0.7 ± 0.1	1.2 ± 0.2	1.8	9.2
	56.4	0.5	4.7 ± 0.2	5.7 ± 0.2	5.3	11.5
G247.528−01.988	8.4	0.6	0.2 ± 0.1	0.3 ± 0.2	1.1	8.8
	21.6	0.6	0.3 ± 0.1	0.5 ± 0.1	2.2	9.4
G247.590−00.820	20.0	0.8	2.8 ± 0.1	5.7 ± 0.2	2.1	9.3
	57.4	0.5	4.1 ± 1.0	4.7 ± 1.2	5.4	11.6
G247.610−00.830	17.4	0.7	1.2 ± 0.1	2.1 ± 0.2	1.9	9.2
	20.0	0.5	1.7 ± 0.1	2.3 ± 0.1	2.1	9.3
G247.630−00.550	29.6	0.6	1.5 ± 0.1	2.5 ± 0.2	2.9	9.8
	56.5	0.6	13.5 ± 0.1	19.9 ± 0.2	5.4	11.5
G247.640−00.530	30.4	0.7	1.2 ± 0.1	2.0 ± 0.2	3.0	9.9
	57.6	0.7	4.2 ± 0.1	7.8 ± 0.2	5.5	11.6
G247.786−00.813	29.8	0.5	0.3 ± 0.1	0.4 ± 0.1	2.9	9.8
G247.790−00.840	20.9	1.0	0.3 ± 0.1	0.8 ± 0.3	2.2	9.4
	29.8	0.8	3.9 ± 0.1	7.7 ± 0.2	2.9	9.8
G247.796−00.823	18.3	0.5	0.2 ± 0.1	0.2 ± 0.2	2.0	9.3
G247.865−01.226	19.7	0.5	0.7 ± 0.1	0.9 ± 0.1	2.1	9.3
G247.890−00.990	20.7	0.7	4.0 ± 0.1	7.3 ± 0.3	2.2	9.4
	24.6	0.4	0.3 ± 0.1	0.3 ± 0.1	2.5	9.6
G247.930−00.440	53.4	1.0	4.9 ± 0.1	12.1 ± 0.3	5.1	11.3
G248.000−00.430	53.1	0.7	3.2 ± 0.1	5.3 ± 0.2	5.0	11.2
G248.074−01.708	9.7	0.4	0.7 ± 0.2	0.7 ± 0.2	1.2	8.9
G248.150−02.210	19.7	0.5	1.2 ± 0.3	1.4 ± 0.3	2.1	9.3
G248.223−01.126	17.4	0.7	1.2 ± 0.1	2.0 ± 0.2	1.9	9.2
G248.440−00.910	18.1	0.8	3.5 ± 0.1	6.7 ± 0.3	2.0	9.2
G248.690−01.930	18.6	0.5	1.9 ± 1.6	2.3 ± 1.9	2.0	9.3
G248.700−01.010	17.4	0.7	3.4 ± 0.1	5.8 ± 0.2	1.9	9.2
G248.810−01.770	23.2	0.8	1.5 ± 0.1	3.0 ± 0.3	2.4	9.5
G248.890−00.010	14.0	0.8	14.8 ± 0.1	30.8 ± 1.1	1.6	9.1
G248.984−02.789	20.3	0.6	2.6 ± 0.2	3.6 ± 0.2	2.2	9.3
	22.7	0.8	2.0 ± 0.2	4.1 ± 0.3	2.4	9.5
	46.4	0.6	0.5 ± 0.1	0.7 ± 0.1	4.5	10.8
G249.102−02.629	18.4	0.7	1.7 ± 0.1	2.7 ± 0.2	2.0	9.3
G249.170+00.110	11.0	0.5	1.1 ± 0.1	1.4 ± 0.1	1.4	8.9
G249.170−02.020	18.4	0.8	1.3 ± 0.1	2.6 ± 0.2	2.0	9.3
	22.9	0.6	0.3 ± 0.1	0.4 ± 0.1	2.4	9.5
G249.390−01.410	15.4	0.7	1.9 ± 0.1	3.4 ± 0.3	1.8	9.1
G249.450−02.420	22.2	0.5	0.5 ± 0.1	0.6 ± 0.2	2.4	9.4
	27.3	0.8	2.3 ± 0.1	4.5 ± 0.2	2.8	9.7
G249.530−02.500	26.3	0.9	1.1 ± 0.1	2.5 ± 0.2	2.7	9.6
G249.600−02.080	16.0	0.8	2.0 ± 0.1	4.2 ± 0.2	1.8	9.1

Table A.1: continued

Name	$v_{\rm lsr}$ (km s^{-1})	$\Delta v_{\rm lsr}$ (km s^{-1})	$T_{\rm max}$ (K)	$\int T dv$ (K km s^{-1})	$R_{\rm hel}$ (kpc)	$R_{\rm gal}$ (kpc)
	106.0	0.9	6.3 ± 0.1	13.7 ± 0.3	11.6	16.4
G249.680−02.100	15.3	0.6	3.7 ± 0.2	5.1 ± 0.3	1.8	9.1
G250.230−00.040	51.7	1.7	7.2 ± 0.1	31.6 ± 0.5	5.0	11.1
G250.270−00.980	14.6	0.6	0.2 ± 0.1	0.4 ± 0.2	1.7	9.1
	67.4	0.6	2.0 ± 0.1	3.1 ± 0.2	6.6	12.2
G250.360−00.980	14.7	0.9	0.9 ± 0.1	2.0 ± 0.2	1.8	9.1
	65.1	0.9	6.0 ± 2.2	13.0 ± 4.7	6.3	12.1
G250.590−00.650	65.6	1.4	1.5 ± 0.1	5.3 ± 0.3	6.4	12.1
	78.3	1.3	11.9 ± 0.1	39.4 ± 0.5	7.8	13.2
G250.811−01.338	13.8	0.6	0.9 ± 0.1	1.3 ± 0.2	1.7	9.0
G250.900−01.530	11.3	0.4	1.0 ± 0.6	1.0 ± 0.6	1.5	8.9
G250.900−02.050	47.9	0.8	1.8 ± 0.1	3.6 ± 0.2	4.7	10.8
	51.1	0.7	5.3 ± 0.2	8.7 ± 0.3	5.0	11.0
	56.2	0.7	0.3 ± 0.1	0.6 ± 0.2	5.5	11.4
G250.910−01.280	10.5	0.7	0.9 ± 0.1	1.5 ± 0.2	1.4	8.9
G251.040−01.030	9.3	1.0	3.4 ± 0.1	8.4 ± 0.5	1.3	8.8
G251.070−01.000	9.7	1.1	4.5 ± 0.1	12.2 ± 0.7	1.3	8.9
G251.070−00.980	10.0	1.1	4.7 ± 0.1	12.7 ± 0.7	1.4	8.9
G251.080−00.990	9.4	0.9	4.1 ± 0.1	9.0 ± 0.5	1.3	8.9
G251.160−01.990	56.4	0.7	7.2 ± 0.1	11.8 ± 0.2	5.5	11.4
G251.186−02.384	15.2	0.6	1.1 ± 0.1	1.6 ± 0.1	1.8	9.1
G251.190−01.970	55.3	0.7	6.9 ± 0.1	12.5 ± 0.2	5.4	11.3
G251.210−00.610	45.2	0.7	3.6 ± 0.1	6.4 ± 0.2	4.5	10.7
G251.230−01.950	53.6	1.8	9.7 ± 0.1	44.3 ± 0.7	5.3	11.2
G251.400−00.180	46.4	0.5	2.6 ± 0.2	3.3 ± 0.3	4.6	10.7
G251.410−00.980	14.8	0.8	2.0 ± 0.1	3.8 ± 0.2	1.8	9.1
G251.421−02.651	15.4	0.6	0.1 ± 0.1	0.2 ± 0.2	1.9	9.1
G251.450−02.840	15.1	0.4	0.4 ± 0.1	0.5 ± 0.1	1.8	9.1
	20.0	0.7	0.2 ± 0.1	0.4 ± 0.2	2.3	9.3
G251.461−02.631	14.9	0.9	0.2 ± 0.1	0.6 ± 0.2	1.8	9.1
G251.485−01.468	13.7	0.6	0.2 ± 0.1	0.4 ± 0.1	1.7	9.0
G251.670−01.040	14.0	0.6	0.7 ± 0.1	1.1 ± 0.2	1.8	9.0
G251.689−01.835	50.8	0.7	0.3 ± 0.1	0.5 ± 0.2	5.0	11.0
G251.750−01.010	14.0	1.1	2.0 ± 0.1	5.5 ± 0.3	1.8	9.0
G251.750−00.900	14.6	0.6	1.5 ± 0.3	2.1 ± 0.5	1.8	9.1
	45.6	0.5	0.2 ± 0.1	0.2 ± 0.1	4.6	10.7
G251.756−00.942	15.0	0.5	0.7 ± 0.1	0.9 ± 0.1	1.9	9.1
G251.786−00.913	14.8	0.7	1.1 ± 0.1	1.8 ± 0.2	1.8	9.1
G251.796−00.903	14.6	0.6	1.8 ± 0.1	2.8 ± 0.2	1.8	9.1
G251.800+00.050	5.5	0.6	5.3 ± 0.1	8.0 ± 0.8	1.0	8.7
G251.800+00.000	6.0	0.5	6.0 ± 0.1	6.9 ± 0.6	1.0	8.7
G251.870+00.020	5.3	0.4	9.5 ± 0.3	9.8 ± 1.0	0.9	8.7
G251.880−01.060	13.7	0.8	3.7 ± 0.1	7.1 ± 0.3	1.7	9.0
	45.7	0.5	1.0 ± 0.1	1.3 ± 0.1	4.6	10.7
G251.900−01.080	13.5	0.7	3.5 ± 0.1	6.1 ± 0.3	1.7	9.0
G251.900−01.060	13.5	0.7	4.0 ± 0.1	7.0 ± 0.3	1.7	9.0
	45.1	0.9	4.8 ± 0.2	10.8 ± 0.6	4.5	10.6
	45.5	0.8	3.5 ± 0.3	6.9 ± 0.6	4.6	10.7
G251.920−01.090	13.0	1.0	3.7 ± 0.2	9.1 ± 0.6	1.7	9.0

Table A.1: continued

Name	$v_{\rm lsr}$ (km s^{-1})	$\Delta v_{\rm lsr}$ (km s^{-1})	$T_{\rm max}$ (K)	$\int T dv$ (K km s^{-1})	$R_{\rm hel}$ (kpc)	$R_{\rm gal}$ (kpc)
	45.4	0.6	3.7 ± 0.1	6.1 ± 0.2	4.5	10.7
G251.940−01.170	12.4	1.0	4.3 ± 0.1	10.3 ± 0.5	1.6	9.0
G251.950−01.190	10.7	0.4	2.6 ± 1.0	2.6 ± 1.0	1.5	8.9
	12.8	0.8	2.7 ± 0.7	5.3 ± 1.4	1.7	9.0
G252.029−01.864	50.6	0.7	1.1 ± 0.1	1.9 ± 0.2	5.0	11.0
G252.068−00.860	13.1	0.9	0.6 ± 0.1	1.3 ± 0.2	1.7	9.0
G252.080−01.810	12.6	0.8	3.3 ± 0.4	6.2 ± 0.8	1.6	9.0
G252.080−01.290	13.0	1.0	3.7 ± 0.1	9.5 ± 0.4	1.7	9.0
	48.9	0.7	1.0 ± 0.4	1.8 ± 0.6	4.9	10.9
	53.5	1.1	0.3 ± 0.3	0.8 ± 0.8	5.3	11.2
G252.090−01.270	12.8	1.0	4.1 ± 0.1	9.9 ± 0.5	1.7	9.0
G252.100−01.220	11.9	0.7	2.5 ± 0.2	4.6 ± 0.4	1.6	9.0
	14.5	0.8	1.8 ± 0.2	3.4 ± 0.4	1.8	9.1
G252.110−01.270	12.8	1.2	3.3 ± 0.1	9.7 ± 0.5	1.7	9.0
G252.120−01.170	12.9	1.3	4.5 ± 0.1	14.8 ± 0.7	1.7	9.0
G252.133−01.175	12.5	1.5	3.4 ± 0.1	12.9 ± 0.6	1.6	9.0
G252.159−01.913	10.8	0.4	0.7 ± 0.8	0.6 ± 0.7	1.5	8.9
G252.173−01.872	70.8	1.5	0.6 ± 0.1	2.2 ± 0.4	7.1	12.5
G252.179−01.933	10.8	0.4	1.5 ± 0.5	1.5 ± 0.4	1.5	8.9
G252.180−01.250	11.3	0.6	–	–	1.5	8.9
	13.7	0.8	–	–	1.8	9.0
G252.180−01.080	44.2	0.7	2.6 ± 0.1	4.3 ± 0.2	4.5	10.6
G252.480−01.570	6.0	1.8	1.8 ± 1.2	8.1 ± 5.3	1.0	8.7
	10.4	1.0	14.6 ± 0.5	37.0 ± 2.3	1.5	8.9
	13.7	1.1	6.9 ± 1.1	19.0 ± 3.0	1.8	9.0
G252.510−01.440	9.2	0.3	7.9 ± 0.3	5.2 ± 0.3	1.4	8.8
	10.8	1.4	2.5 ± 0.4	8.5 ± 1.5	1.5	8.9
	70.9	0.7	0.2 ± 0.1	0.4 ± 0.2	7.1	12.5
G252.520+00.080	4.8	0.6	9.3 ± 0.2	13.0 ± 1.4	0.9	8.7
G252.654−01.089	46.1	1.3	1.5 ± 0.1	4.7 ± 0.3	4.7	10.7
G252.680−01.530	6.7	0.6	6.7 ± 0.5	10.8 ± 1.1	1.1	8.7
	10.0	0.5	5.1 ± 0.6	5.7 ± 0.8	1.4	8.9
	12.6	0.7	0.9 ± 0.8	1.6 ± 1.3	1.7	9.0
G252.700−01.490	6.6	0.6	2.0 ± 0.1	3.3 ± 0.3	1.1	8.7
	10.4	0.6	2.2 ± 0.1	3.3 ± 0.3	1.5	8.9
	14.1	1.2	0.9 ± 0.2	2.9 ± 0.5	1.8	9.0
G252.731−00.607	79.2	0.5	1.4 ± 0.1	1.6 ± 0.2	8.0	13.2
G252.792−01.727	6.9	0.6	5.5 ± 0.1	8.8 ± 0.7	1.1	8.7
G252.793−01.210	39.4	0.6	0.6 ± 0.1	0.9 ± 0.2	4.1	10.3
G252.803−01.190	39.3	0.8	0.2 ± 0.1	0.3 ± 0.2	4.1	10.3
	43.1	0.8	0.6 ± 0.1	1.2 ± 0.2	4.4	10.5
G252.840−00.470	12.4	0.6	4.9 ± 0.6	6.8 ± 0.8	1.7	9.0
G252.982−02.338	21.6	0.7	0.3 ± 0.1	0.5 ± 0.2	2.5	9.4
G253.030−01.990	11.6	0.6	4.1 ± 0.1	6.2 ± 0.3	1.6	8.9
G253.080−02.100	11.5	0.7	6.0 ± 0.1	10.3 ± 0.5	1.6	8.9
G253.100−01.350	6.3	0.6	1.7 ± 0.1	2.6 ± 0.3	1.1	8.7
	10.6	0.6	4.4 ± 0.2	7.1 ± 0.4	1.5	8.9
G253.110−01.800	6.9	0.5	5.6 ± 0.3	6.9 ± 0.6	1.1	8.7
G253.110−02.120	11.7	0.5	9.4 ± 0.1	11.9 ± 0.5	1.6	8.9

Table A.1: continued

Name	$v_{\rm lsr}$ (km s^{-1})	$\Delta v_{\rm lsr}$ (km s^{-1})	$T_{\rm max}$ (K)	$\int T dv$ (K km s^{-1})	$R_{\rm hel}$ (kpc)	$R_{\rm gal}$ (kpc)
G253.110−02.150	12.1	0.4	4.8 ± 0.1	5.2 ± 0.2	1.6	9.0
G253.120−02.060	11.4	0.7	5.8 ± 0.1	9.5 ± 0.4	1.6	8.9
G253.123−01.582	5.9	0.6	11.3 ± 0.1	16.3 ± 1.4	1.1	8.7
G253.130−02.160	12.1	0.4	4.2 ± 0.1	4.2 ± 0.2	1.6	9.0
	19.1	0.6	0.5 ± 0.1	0.8 ± 0.2	2.3	9.3
G253.230−01.350	10.8	1.0	0.3 ± 0.1	0.9 ± 0.3	1.5	8.9
G253.230−02.730	14.4	0.6	0.6 ± 0.1	0.9 ± 0.1	1.9	9.1
	16.7	0.5	0.2 ± 0.1	0.3 ± 0.2	2.1	9.2
	99.6	0.7	0.6 ± 0.1	1.1 ± 0.2	10.6	15.3
G253.270−01.110	10.7	0.7	1.4 ± 0.1	2.4 ± 0.2	1.5	8.9
G253.290−01.610	5.6	1.4	11.0 ± 0.2	38.8 ± 3.5	1.0	8.7
G253.290−01.010	11.6	0.6	2.0 ± 0.1	3.0 ± 0.2	1.6	8.9
	38.1	0.6	0.6 ± 0.1	0.9 ± 0.1	4.0	10.2
G253.300−01.080	10.7	0.6	3.0 ± 0.1	4.3 ± 0.2	1.5	8.9
G253.340+00.150	28.3	0.9	0.9 ± 0.1	2.0 ± 0.2	3.1	9.7
G253.395−02.645	15.8	0.8	2.7 ± 0.1	5.1 ± 0.3	2.0	9.1
G253.400−01.420	10.0	0.8	6.5 ± 0.6	13.8 ± 1.5	1.5	8.9
G253.400−01.400	11.8	3.0	15.6 ± 0.3	118.0 ± 5.6	1.6	8.9
	12.5	1.4	6.9 ± 0.5	24.0 ± 1.9	1.7	9.0
	38.6	0.6	0.3 ± 0.1	0.4 ± 0.2	4.0	10.3
G253.420−01.400	10.3	1.2	8.3 ± 0.4	26.0 ± 1.7	1.5	8.9
G253.430−01.370	9.8	1.0	6.7 ± 0.7	15.9 ± 1.8	1.4	8.9
	12.3	1.1	7.4 ± 0.6	20.4 ± 1.8	1.7	9.0
	25.7	1.9	0.9 ± 0.9	4.4 ± 4.1	2.9	9.6
G253.450−01.370	10.0	1.1	10.5 ± 0.4	29.0 ± 1.9	1.5	8.9
	13.3	1.3	7.9 ± 0.5	25.7 ± 2.0	1.8	9.0
G253.460−01.410	11.0	1.4	7.7 ± 0.1	26.4 ± 1.2	1.6	8.9
G253.470−01.360	10.5	1.4	9.3 ± 0.1	31.9 ± 1.6	1.5	8.9
G253.470−01.420	11.3	1.0	8.3 ± 0.1	20.0 ± 0.9	1.6	8.9
G253.480−01.370	10.6	1.2	8.7 ± 0.1	26.4 ± 1.3	1.5	8.9
G253.480−01.290	10.6	1.2	3.8 ± 0.1	11.7 ± 0.6	1.5	8.9
G253.503−01.237	11.6	1.5	4.0 ± 0.1	15.1 ± 0.8	1.6	8.9
G253.504−00.846	7.7	0.7	5.1 ± 0.2	9.5 ± 0.7	1.2	8.8
	14.7	0.8	0.3 ± 0.1	0.5 ± 0.2	1.9	9.1
	34.0	0.4	2.5 ± 0.3	2.4 ± 0.3	3.6	10.0
G253.510−01.240	9.7	0.4	5.4 ± 0.3	5.4 ± 0.4	1.4	8.9
G253.510−01.260	9.8	1.1	–	–	1.4	8.9
	11.7	0.9	5.2 ± 0.2	11.5 ± 0.7	1.6	8.9
	12.4	1.3	–	–	1.7	9.0
	16.8	1.1	0.7 ± 0.4	2.1 ± 1.2	2.1	9.2
G253.520−01.370	10.7	0.7	4.0 ± 0.1	7.3 ± 0.4	1.5	8.9
G253.530−00.420	31.3	1.1	6.4 ± 0.1	18.1 ± 0.4	3.4	9.9
G253.602−00.706	14.1	0.4	1.7 ± 0.1	1.8 ± 0.1	1.9	9.0
G253.630−01.310	10.3	0.6	3.2 ± 0.1	4.5 ± 0.3	1.5	8.9
G253.630−01.440	11.9	0.7	3.8 ± 0.1	6.3 ± 0.3	1.7	9.0
G253.695−00.077	33.9	1.1	16.6 ± 0.1	45.4 ± 0.7	3.6	10.0
G253.699−02.246	36.5	0.5	2.0 ± 0.1	2.6 ± 0.2	3.9	10.1
G253.758−02.137	35.1	0.5	0.3 ± 0.1	0.4 ± 0.1	3.8	10.1
	53.9	0.5	1.4 ± 0.1	1.7 ± 0.1	5.5	11.2

Table A.1: continued

Name	$v_{\rm lsr}$ (km s^{-1})	$\Delta v_{\rm lsr}$ (km s^{-1})	$T_{\rm max}$ (K)	$\int T dv$ (K km s^{-1})	$R_{\rm hel}$ (kpc)	$R_{\rm gal}$ (kpc)
G253.759−02.216	36.1	0.5	0.6 ± 0.2	0.7 ± 0.2	3.8	10.1
	52.9	0.6	0.2 ± 0.1	0.3 ± 0.1	5.4	11.1
G253.770−01.300	12.7	0.5	4.4 ± 0.2	5.8 ± 0.4	1.7	9.0
	31.6	0.9	1.0 ± 0.1	2.1 ± 0.2	3.4	9.9
G253.860−01.230	11.9	0.5	6.7 ± 0.1	8.9 ± 0.4	1.7	8.9
	30.2	0.6	0.2 ± 0.1	0.3 ± 0.1	3.3	9.8
G253.870−01.210	11.5	0.7	11.8 ± 0.1	20.4 ± 0.9	1.6	8.9
G253.870−01.200	11.5	0.7	12.4 ± 0.1	23.2 ± 1.0	1.6	8.9
	32.5	0.5	0.9 ± 0.1	1.1 ± 0.1	3.5	9.9
	38.1	0.6	0.2 ± 0.1	0.3 ± 0.2	4.0	10.2
	39.5	0.6	0.7 ± 0.1	1.1 ± 0.2	4.2	10.3
G253.890−00.470	10.2	0.8	10.2 ± 0.1	20.2 ± 1.0	1.5	8.9
G253.950−00.563	39.2	0.7	0.4 ± 0.1	0.6 ± 0.2	4.1	10.3
G253.980−00.720	10.5	0.7	3.4 ± 0.1	5.8 ± 0.3	1.5	8.9
	37.7	0.7	6.3 ± 0.2	11.7 ± 0.5	4.0	10.2
G254.052−00.566	34.3	1.8	19.3 ± 0.2	88.6 ± 1.6	3.7	10.0
G254.120−01.420	45.2	0.8	2.2 ± 0.1	4.4 ± 0.2	4.7	10.6
G254.230−02.320	33.9	0.7	2.8 ± 0.1	4.9 ± 0.2	3.7	10.0
G254.232−00.136	31.3	0.9	7.3 ± 0.1	16.1 ± 0.3	3.5	9.9
G254.270−02.340	79.1	0.6	0.2 ± 0.2	0.3 ± 0.2	8.1	13.1
G254.390−01.010	77.1	0.8	2.1 ± 0.1	4.3 ± 0.2	7.9	12.9
G254.398−02.264	37.0	0.7	0.5 ± 0.1	0.7 ± 0.2	4.0	10.2
	55.8	0.5	0.7 ± 0.1	1.0 ± 0.1	5.7	11.3
G254.490+00.100	8.5	0.6	0.2 ± 0.1	0.3 ± 0.2	1.4	8.8
G254.590−01.060	36.9	0.6	1.8 ± 0.1	2.7 ± 0.2	4.0	10.1
	75.1	1.1	1.0 ± 0.1	2.9 ± 0.3	7.7	12.7
G254.660−01.250	8.9	0.6	2.4 ± 0.1	3.7 ± 0.3	1.4	8.8
G254.670+00.250	31.6	0.4	–	–	3.5	9.9
	67.0	0.8	–	–	6.8	12.1
	78.2	1.2	–	–	8.0	13.0
G254.680−01.890	9.9	0.6	3.4 ± 0.1	5.1 ± 0.3	1.5	8.9
G254.680+00.220	68.8	1.6	12.7 ± 0.1	50.3 ± 0.5	7.0	12.2
G254.710+00.200	69.2	0.7	10.0 ± 0.1	18.8 ± 0.2	7.0	12.3
G254.750−00.752	86.3	1.1	0.4 ± 0.1	1.1 ± 0.3	9.0	13.8
	90.6	0.9	0.2 ± 0.1	0.6 ± 0.2	9.5	14.2
G254.760−01.240	11.2	1.4	3.5 ± 0.1	12.1 ± 0.6	1.7	8.9
G254.780+00.120	31.0	0.6	0.3 ± 0.1	0.4 ± 0.1	3.5	9.8
	67.6	1.1	15.7 ± 0.1	44.9 ± 0.4	6.9	12.1
G254.880+00.451	28.6	1.3	8.3 ± 0.2	27.7 ± 0.8	3.3	9.7
G254.943−00.080	0.8	0.5	0.5 ± 0.2	0.6 ± 0.4	0.5	8.5
G255.100−00.090	71.6	1.1	2.8 ± 0.1	7.3 ± 0.3	7.3	12.4
G255.170−00.570	82.6	0.8	8.7 ± 0.1	17.2 ± 0.2	8.6	13.4
G255.190−02.280	8.5	0.8	5.6 ± 0.1	11.6 ± 0.7	1.4	8.8
G255.200−02.290	8.5	0.9	7.7 ± 0.1	17.3 ± 1.0	1.4	8.8
G255.210−02.290	8.4	0.9	8.4 ± 0.1	19.0 ± 1.2	1.4	8.8
G255.360−00.939	11.0	0.9	0.4 ± 0.1	1.0 ± 0.2	1.7	8.9
	79.0	0.6	0.3 ± 0.2	0.5 ± 0.3	8.2	13.1
	89.8	0.7	0.4 ± 0.1	0.7 ± 0.2	9.4	14.1
G255.401−00.918	80.4	1.1	1.2 ± 0.1	3.4 ± 0.3	8.3	13.2

Table A.1: continued

Name	$v_{\rm lsr}$ (km s^{-1})	$\Delta v_{\rm lsr}$ (km s^{-1})	$T_{\rm max}$ (K)	$\int T dv$ (K km s^{-1})	$R_{\rm hel}$ (kpc)	$R_{\rm gal}$ (kpc)
	84.3	1.1	1.2 ± 0.1	3.2 ± 0.3	8.8	13.5
G255.410−01.350	48.9	0.6	1.3 ± 0.4	1.9 ± 0.6	5.1	10.8
	86.6	1.8	0.3 ± 0.3	1.3 ± 1.1	9.0	13.8
G255.680−01.220	36.9	0.6	0.6 ± 0.1	0.9 ± 0.2	4.1	10.1
	50.4	1.0	5.1 ± 0.1	12.5 ± 0.3	5.3	10.9
	57.6	2.5	0.3 ± 0.2	1.8 ± 1.5	6.0	11.4
	80.1	0.7	0.4 ± 0.1	0.7 ± 0.2	8.3	13.1
G255.684−02.190	9.8	0.8	5.3 ± 0.1	10.2 ± 0.6	1.6	8.9
G256.130−01.470	85.1	0.7	4.3 ± 0.9	7.7 ± 1.6	8.9	13.6
	87.7	0.6	2.8 ± 1.1	4.3 ± 1.7	9.2	13.8
G256.150−01.370	85.0	0.8	7.8 ± 0.8	15.7 ± 1.6	8.9	13.6
G256.150−01.380	85.1	1.0	5.4 ± 2.2	13.8 ± 5.5	8.9	13.6
	87.7	0.7	6.6 ± 0.9	10.9 ± 1.5	9.2	13.8
	87.7	0.5	4.5 ± 3.7	5.4 ± 4.5	9.2	13.8
G256.156−01.456	87.4	1.5	1.0 ± 0.1	3.6 ± 0.5	9.2	13.8
G256.187−01.547	88.9	1.1	4.4 ± 0.1	12.0 ± 0.3	9.4	14.0
G256.190−01.540	88.5	1.5	1.5 ± 0.2	5.6 ± 0.6	9.3	13.9
G256.348−02.140	7.9	1.3	3.2 ± 0.1	10.1 ± 0.8	1.4	8.8
	16.1	0.6	2.4 ± 0.1	3.5 ± 0.2	2.2	9.1
G256.409−02.210	8.0	1.0	1.8 ± 0.1	4.5 ± 0.4	1.4	8.8
	15.5	0.7	2.5 ± 0.2	4.4 ± 0.4	2.2	9.1
G256.422−02.208	8.0	0.7	3.5 ± 0.1	6.2 ± 0.4	1.4	8.8
	15.0	0.6	0.5 ± 0.1	0.8 ± 0.2	2.1	9.1
	18.9	0.4	0.8 ± 0.1	0.8 ± 0.1	2.5	9.2
G256.430−01.640	8.4	0.6	5.9 ± 0.1	9.2 ± 0.6	1.5	8.8
G256.430−01.630	8.6	0.7	5.5 ± 0.1	9.9 ± 0.6	1.5	8.8
	19.8	1.2	0.2 ± 0.1	0.6 ± 0.3	2.6	9.3
	21.4	0.9	0.2 ± 0.1	0.4 ± 0.2	2.7	9.4
G256.440−01.610	8.8	0.7	5.2 ± 0.2	9.1 ± 0.7	1.5	8.8
	22.0	1.0	0.4 ± 0.1	1.1 ± 0.3	2.8	9.4
	85.4	1.0	2.8 ± 0.1	6.8 ± 0.2	9.0	13.6
G256.450−01.608	8.7	0.6	3.7 ± 0.1	5.9 ± 0.4	1.5	8.8
	86.1	1.2	4.6 ± 0.2	14.4 ± 0.6	9.1	13.7
G256.620−00.050	17.3	0.5	0.5 ± 0.1	0.6 ± 0.2	2.3	9.2
	74.3	1.0	2.0 ± 0.1	4.9 ± 0.2	7.7	12.6
G256.670−00.040	11.8	0.6	–	–	1.8	8.9
	74.7	1.1	–	–	7.8	12.6
G256.680−00.100	17.4	1.1	0.4 ± 0.1	1.1 ± 0.3	2.4	9.2
	74.2	1.0	2.3 ± 0.1	5.7 ± 0.3	7.7	12.6
G256.682−01.627	43.1	0.8	2.8 ± 0.1	5.6 ± 0.2	4.7	10.5
G256.690−00.040	74.5	0.8	2.3 ± 0.1	4.8 ± 0.2	7.8	12.6
G256.705−02.465	56.3	0.6	1.0 ± 0.1	1.5 ± 0.2	5.9	11.3
G256.705−02.475	56.1	1.0	0.2 ± 0.1	0.6 ± 0.3	5.9	11.3
G256.715−02.445	15.8	0.6	0.6 ± 0.1	0.9 ± 0.2	2.2	9.1
	42.5	0.5	0.4 ± 0.1	0.5 ± 0.1	4.6	10.4
G256.720−01.930	43.7	2.1	3.7 ± 0.1	19.3 ± 0.6	4.8	10.5
G256.730−01.670	6.3	0.6	1.6 ± 0.1	2.3 ± 0.3	1.2	8.7
	43.2	0.9	2.3 ± 0.1	5.0 ± 0.3	4.7	10.5
G256.740−01.580	13.0	0.6	0.4 ± 0.1	0.6 ± 0.2	1.9	9.0

Table A.1: continued

Name	$v_{\rm lsr}$ (km s^{-1})	$\Delta v_{\rm lsr}$ (km s^{-1})	$T_{\rm max}$ (K)	$\int T dv$ (K km s^{-1})	$R_{\rm hel}$ (kpc)	$R_{\rm gal}$ (kpc)
G256.750−00.060	11.6	0.7	3.0 ± 0.1	5.1 ± 0.3	1.8	8.9
	75.4	0.8	3.2 ± 0.2	6.6 ± 0.4	7.9	12.7
G256.780−02.070	8.7	0.5	1.7 ± 0.8	1.9 ± 0.9	1.5	8.8
G256.780−00.130	25.8	0.8	1.0 ± 0.1	1.8 ± 0.2	3.2	9.6
	44.9	0.9	1.3 ± 0.1	2.8 ± 0.3	4.9	10.6
	75.2	1.0	6.0 ± 0.1	14.5 ± 0.3	7.8	12.7
G256.810−00.510	23.5	0.5	0.2 ± 0.2	0.3 ± 0.3	2.9	9.5
	52.2	0.9	1.6 ± 0.1	3.5 ± 0.2	5.5	11.0
	73.1	0.6	1.9 ± 0.2	2.9 ± 0.4	7.6	12.5
G256.822−01.879	45.9	0.6	1.3 ± 0.1	2.1 ± 0.2	5.0	10.6
	53.4	0.5	0.3 ± 0.2	0.4 ± 0.2	5.7	11.1
G256.858−01.786	13.4	0.7	0.9 ± 0.1	1.7 ± 0.2	2.0	9.0
	44.7	0.7	1.0 ± 0.1	1.7 ± 0.2	4.9	10.6
G256.875−00.895	22.1	0.6	0.6 ± 0.1	1.0 ± 0.2	2.8	9.4
G256.910−00.280	73.1	1.2	1.9 ± 0.1	5.4 ± 0.3	7.6	12.5
G256.920−01.830	44.0	0.8	2.1 ± 0.1	4.1 ± 0.3	4.8	10.5
G256.942−02.596	14.8	0.7	1.5 ± 0.1	2.5 ± 0.2	2.1	9.1
G256.945−00.885	17.7	0.9	0.2 ± 0.1	0.5 ± 0.2	2.4	9.2
G256.950−00.530	51.7	1.2	3.9 ± 0.3	11.4 ± 0.8	5.5	11.0
G256.990−02.130	44.5	0.9	0.7 ± 0.1	1.5 ± 0.2	4.9	10.6
G256.990−00.570	51.7	1.1	2.6 ± 0.1	7.0 ± 0.3	5.5	11.0
G257.005−02.504	15.6	0.8	1.1 ± 0.1	2.2 ± 0.2	2.2	9.1
G257.010+00.000	54.4	0.6	1.0 ± 0.1	1.5 ± 0.2	5.8	11.2
G257.014−02.414	9.7	0.5	0.3 ± 0.2	0.4 ± 0.2	1.6	8.8
	15.4	0.6	0.9 ± 0.1	1.4 ± 0.2	2.2	9.1
G257.036−00.974	14.8	0.6	0.7 ± 0.1	1.1 ± 0.2	2.1	9.1
G257.060−02.901	19.4	0.7	1.9 ± 0.1	3.2 ± 0.2	2.6	9.3
G257.060−02.080	44.0	0.7	0.7 ± 0.7	1.1 ± 1.2	4.8	10.5
G257.070−01.351	26.4	1.5	0.2 ± 0.1	0.9 ± 0.4	3.2	9.6
G257.080+00.240	7.1	0.6	0.2 ± 0.1	0.4 ± 0.2	1.4	8.7
G257.167−01.123	60.9	0.5	0.9 ± 0.1	1.2 ± 0.1	6.4	11.6
G257.196−02.662	16.9	1.2	1.5 ± 0.1	4.6 ± 0.3	2.4	9.2
G257.210−01.371	6.0	0.7	4.6 ± 0.1	8.3 ± 0.7	1.2	8.7
G257.227−00.902	4.7	0.5	0.3 ± 0.2	0.3 ± 0.3	1.1	8.7
	56.5	0.7	3.5 ± 0.1	6.4 ± 0.2	6.0	11.3
G257.240−00.700	15.5	0.8	2.9 ± 0.1	6.0 ± 0.3	2.2	9.1
	20.0	0.6	0.4 ± 0.1	0.6 ± 0.2	2.7	9.3
G257.250−01.410	7.3	0.6	0.6 ± 0.1	1.0 ± 0.2	1.4	8.8
G257.261−01.240	5.1	0.5	0.9 ± 0.1	1.0 ± 0.2	1.1	8.7
G257.282−00.336	6.8	0.6	2.2 ± 0.1	3.1 ± 0.3	1.3	8.7
	55.1	0.8	3.4 ± 0.1	6.9 ± 0.3	5.9	11.2
G257.298−01.147	22.4	1.0	2.4 ± 0.1	6.1 ± 0.3	2.9	9.4
G257.320−01.063	21.0	0.7	2.6 ± 0.1	4.6 ± 0.2	2.7	9.3
G257.330−00.258	52.5	0.8	2.3 ± 0.1	4.8 ± 0.2	5.6	11.0
G257.330−00.605	18.6	1.1	0.2 ± 0.1	0.7 ± 0.3	2.5	9.2
G257.339−02.910	14.8	1.0	4.8 ± 0.1	12.5 ± 0.5	2.2	9.1
G257.340−00.360	6.9	0.5	1.4 ± 0.1	1.6 ± 0.2	1.3	8.7
	55.4	0.6	2.0 ± 0.1	3.3 ± 0.2	5.9	11.2
G257.354−00.220	11.8	0.6	0.2 ± 0.1	0.3 ± 0.1	1.9	8.9

Table A.1: continued

Name	$v_{\rm lsr}$ (km s^{-1})	$\Delta v_{\rm lsr}$ (km s^{-1})	$T_{\rm max}$ (K)	$\int T dv$ (K km s^{-1})	$R_{\rm hel}$ (kpc)	$R_{\rm gal}$ (kpc)
	52.4	0.8	3.6 ± 0.2	6.8 ± 0.4	5.6	11.0
	56.1	0.7	2.3 ± 0.3	3.9 ± 0.6	6.0	11.3
G257.374−00.276	5.8	0.5	2.4 ± 0.1	2.9 ± 0.3	1.2	8.7
	17.5	0.7	0.7 ± 0.1	1.2 ± 0.2	2.4	9.2
	55.5	0.9	2.2 ± 0.1	5.0 ± 0.3	5.9	11.2
G257.380−00.280	5.8	0.4	4.1 ± 0.9	4.6 ± 1.1	1.2	8.7
	17.4	0.6	0.8 ± 0.1	1.1 ± 0.2	2.4	9.2
	55.4	0.8	2.5 ± 0.1	5.4 ± 0.2	5.9	11.2
G257.410−00.300	6.5	0.9	0.3 ± 0.1	0.7 ± 0.2	1.3	8.7
	55.2	1.0	2.3 ± 0.1	5.9 ± 0.3	5.9	11.2
G257.424−00.300	5.9	0.5	1.1 ± 0.1	1.4 ± 0.2	1.2	8.7
	56.0	1.2	3.3 ± 0.1	10.0 ± 0.3	6.0	11.3
G257.460−00.610	51.3	0.7	4.5 ± 0.1	7.3 ± 0.2	5.5	11.0
G257.470−00.630	51.4	1.1	9.0 ± 0.1	24.3 ± 0.4	5.5	11.0
G257.480−00.610	51.4	0.8	3.8 ± 0.1	7.6 ± 0.2	5.5	11.0
G257.490+00.180	6.4	0.7	3.0 ± 0.1	5.3 ± 0.4	1.3	8.7
	16.0	0.5	1.1 ± 0.1	1.3 ± 0.1	2.3	9.1
	53.2	0.8	8.3 ± 0.2	16.7 ± 0.5	5.7	11.1
G257.501−01.539	6.8	0.6	0.6 ± 0.1	0.8 ± 0.2	1.3	8.7
	9.6	0.6	0.5 ± 0.1	0.8 ± 0.2	1.6	8.8
	82.4	0.7	0.2 ± 0.1	0.4 ± 0.2	8.7	13.3
G257.510−02.250	6.6	0.8	–	–	1.3	8.7
	15.3	0.8	–	–	2.2	9.1
	42.5	0.8	–	–	4.7	10.4
	90.9	1.9	–	–	9.7	14.1
G257.540−01.630	6.4	0.7	4.3 ± 0.3	8.0 ± 0.9	1.3	8.7
G257.540−01.270	73.3	0.8	2.6 ± 0.1	5.2 ± 0.2	7.7	12.5
	74.7	0.8	1.2 ± 0.3	2.4 ± 0.5	7.8	12.6
G257.560−00.480	54.8	0.7	2.9 ± 0.1	5.1 ± 0.2	5.9	11.2
G257.570−02.070	18.2	1.0	0.2 ± 0.1	0.6 ± 0.2	2.5	9.2
	40.0	0.9	0.4 ± 0.1	1.0 ± 0.2	4.5	10.3
	44.1	0.9	1.0 ± 0.1	2.2 ± 0.2	4.9	10.5
	92.2	1.2	2.2 ± 0.1	6.9 ± 0.3	9.9	14.2
G257.580+00.070	6.9	1.0	2.7 ± 0.1	6.9 ± 0.6	1.4	8.7
	78.6	0.6	0.7 ± 0.1	1.2 ± 0.2	8.3	13.0
G257.597−01.201	17.1	0.6	0.7 ± 0.1	1.0 ± 0.2	2.4	9.2
G257.610−00.660	52.9	0.7	1.9 ± 0.1	3.1 ± 0.2	5.7	11.1
G257.617−01.772	17.2	1.2	1.0 ± 0.1	3.0 ± 0.3	2.4	9.2
G257.630−01.050	14.2	0.9	3.5 ± 0.1	8.0 ± 0.4	2.1	9.0
G257.630−00.590	52.5	0.7	3.2 ± 0.1	5.4 ± 0.2	5.6	11.0
	74.7	0.6	0.6 ± 0.1	1.0 ± 0.2	7.9	12.6
G257.636−01.121	74.3	0.6	0.3 ± 0.1	0.4 ± 0.1	7.8	12.6
G257.640−00.959	15.4	0.6	2.1 ± 0.2	3.2 ± 0.3	2.2	9.1
	54.7	0.6	1.4 ± 0.1	2.1 ± 0.2	5.9	11.2
G257.649−01.360	8.7	0.6	0.8 ± 0.1	1.1 ± 0.2	1.6	8.8
	12.0	1.0	0.7 ± 0.1	1.6 ± 0.2	1.9	8.9
G257.655−01.250	14.6	0.6	0.2 ± 0.1	0.3 ± 0.2	2.2	9.1
	56.9	0.5	0.3 ± 0.2	0.4 ± 0.2	6.1	11.3
G257.719−01.449	75.1	0.6	0.5 ± 0.1	0.8 ± 0.2	7.9	12.7

Table A.1: continued

Name	$v_{\rm lsr}$ (km s^{-1})	$\Delta v_{\rm lsr}$ (km s^{-1})	$T_{\rm max}$ (K)	$\int T dv$ (K km s^{-1})	$R_{\rm hel}$ (kpc)	$R_{\rm gal}$ (kpc)
G257.740+00.160	6.3	0.5	0.5 ± 0.2	0.7 ± 0.2	1.3	8.7
	11.4	0.8	2.4 ± 0.1	4.7 ± 0.3	1.9	8.9
	46.5	1.0	9.6 ± 0.3	24.0 ± 0.8	5.1	10.7
	53.5	0.7	4.0 ± 0.2	7.5 ± 0.4	5.8	11.1
G257.798−01.252	76.7	1.0	3.2 ± 0.2	7.8 ± 0.5	8.1	12.8
	79.4	1.0	2.3 ± 0.2	5.8 ± 0.6	8.4	13.0
G257.807−02.104	6.3	0.5	0.8 ± 0.1	1.1 ± 0.2	1.3	8.7
	11.0	3.4	0.3 ± 0.1	2.4 ± 0.9	1.8	8.9
	13.5	0.8	0.6 ± 0.1	1.3 ± 0.2	2.1	9.0
G257.808−01.277	76.0	1.4	2.1 ± 0.1	7.5 ± 0.4	8.0	12.7
G257.812−02.462	9.3	0.5	2.4 ± 0.1	3.2 ± 0.2	1.6	8.8
	13.4	0.6	3.5 ± 0.2	5.6 ± 0.4	2.1	9.0
G257.830−00.740	16.4	0.7	4.5 ± 0.1	8.0 ± 0.3	2.4	9.1
G257.831−00.773	16.6	0.6	0.9 ± 0.1	1.3 ± 0.2	2.4	9.1
G257.831−01.758	45.4	0.6	3.7 ± 0.1	5.6 ± 0.2	5.0	10.6
G257.850−01.070	77.9	0.8	2.5 ± 0.1	5.1 ± 0.2	8.2	12.9
G257.864−01.086	10.5	0.7	0.7 ± 0.1	1.2 ± 0.2	1.8	8.9
	76.9	0.9	3.0 ± 0.1	6.6 ± 0.2	8.1	12.8
G257.865−01.495	16.7	1.6	4.3 ± 0.1	17.0 ± 0.6	2.4	9.1
G257.867−01.793	44.0	0.6	9.0 ± 0.1	13.5 ± 0.2	4.9	10.5
G257.870−01.498	5.7	0.6	0.4 ± 0.1	0.5 ± 0.1	1.2	8.7
G257.879−01.729	7.1	1.2	0.5 ± 0.1	1.4 ± 0.3	1.4	8.7
G257.889−01.428	5.4	1.4	0.4 ± 0.1	1.2 ± 0.4	1.2	8.7
	15.0	0.5	0.4 ± 0.1	0.6 ± 0.1	2.2	9.1
G257.894−01.885	6.8	0.9	1.0 ± 0.1	2.1 ± 0.3	1.4	8.7
G257.920−00.470	51.6	0.9	4.4 ± 0.1	10.4 ± 0.3	5.6	11.0
G257.932−01.387	42.9	0.6	8.3 ± 0.1	13.1 ± 0.2	4.8	10.4
G257.940−00.942	81.0	1.2	1.2 ± 0.1	3.6 ± 0.3	8.6	13.2
G257.950+00.070	48.2	0.8	0.8 ± 0.1	1.6 ± 0.2	5.3	10.8
G257.950−00.170	50.8	1.0	5.5 ± 0.1	13.2 ± 0.3	5.5	10.9
G257.950−00.510	51.9	0.8	9.1 ± 0.1	19.0 ± 0.3	5.6	11.0
G257.960−00.940	81.5	1.2	1.9 ± 0.6	5.6 ± 1.8	8.6	13.2
G257.978−01.428	42.9	0.7	9.4 ± 0.1	15.8 ± 0.2	4.8	10.4
G257.982−00.951	80.7	1.2	1.8 ± 0.1	5.4 ± 0.3	8.6	13.1
G257.989−00.683	15.3	0.5	0.4 ± 0.1	0.5 ± 0.2	2.3	9.1
	82.5	0.6	1.0 ± 0.1	1.5 ± 0.2	8.8	13.3
G258.000−00.010	7.3	0.5	1.5 ± 0.1	1.8 ± 0.2	1.4	8.8
G258.000−00.300	41.6	0.6	2.6 ± 0.2	4.0 ± 0.3	4.7	10.4
	51.7	1.4	1.8 ± 0.1	6.4 ± 0.4	5.6	11.0
G258.047−01.604	42.0	0.8	3.1 ± 0.1	6.2 ± 0.2	4.7	10.4
G258.050−01.341	47.1	0.8	6.1 ± 0.1	12.6 ± 0.2	5.2	10.7
	52.9	2.9	0.3 ± 0.2	2.4 ± 1.8	5.7	11.0
G258.080−01.563	8.4	0.6	1.3 ± 0.1	2.2 ± 0.2	1.6	8.8
	42.4	0.7	3.8 ± 0.1	6.8 ± 0.2	4.8	10.4
G258.080−01.561	8.5	0.7	1.3 ± 0.1	2.2 ± 0.2	1.6	8.8
	42.4	0.7	3.8 ± 0.1	6.7 ± 0.2	4.8	10.4
G258.080−01.350	47.1	0.6	2.5 ± 0.1	3.9 ± 0.2	5.2	10.7
G258.081−01.558	8.5	0.7	1.3 ± 0.1	2.2 ± 0.2	1.6	8.8
G258.081−01.561	8.5	0.7	1.3 ± 0.1	2.3 ± 0.2	1.6	8.8

Table A.1: continued

Name	$v_{\rm lsr}$ (km s^{-1})	$\Delta v_{\rm lsr}$ (km s^{-1})	$T_{\rm max}$ (K)	$\int T dv$ (K km s^{-1})	$R_{\rm hel}$ (kpc)	$R_{\rm gal}$ (kpc)
	42.4	0.6	4.1 ± 0.2	6.4 ± 0.3	4.8	10.4
	42.4	0.7	3.9 ± 0.1	6.6 ± 0.2	4.8	10.4
G258.082−01.626	41.5	1.0	2.9 ± 0.1	7.2 ± 0.3	4.7	10.4
G258.107−01.740	9.9	0.8	0.4 ± 0.1	0.7 ± 0.2	1.7	8.9
	42.1	1.1	6.3 ± 0.1	17.3 ± 0.3	4.7	10.4
G258.114−01.904	12.1	0.7	0.6 ± 0.1	1.1 ± 0.2	2.0	8.9
G258.130−00.390	51.3	0.8	0.2 ± 0.1	0.5 ± 0.2	5.6	10.9
G258.140−00.350	19.5	0.8	0.9 ± 0.1	1.8 ± 0.2	2.7	9.3
G258.156−01.517	42.0	1.1	3.2 ± 0.1	8.7 ± 0.3	4.7	10.4
G258.182−01.512	42.5	1.1	2.9 ± 0.1	7.7 ± 0.3	4.8	10.4
G258.190−02.277	13.9	1.0	1.5 ± 0.1	3.7 ± 0.3	2.1	9.0
	17.9	1.2	0.2 ± 0.1	0.6 ± 0.3	2.5	9.2
G258.194−02.221	16.2	2.2	5.0 ± 0.1	28.0 ± 1.0	2.4	9.1
G258.207−01.348	8.3	0.5	0.2 ± 0.2	0.2 ± 0.2	1.6	8.8
G258.222−01.775	9.3	1.0	4.7 ± 0.1	11.7 ± 0.7	1.7	8.8
	59.2	0.7	1.0 ± 0.1	1.9 ± 0.2	6.3	11.5
G258.250−00.851	22.6	0.6	0.2 ± 0.1	0.3 ± 0.1	3.0	9.4
G258.255−01.233	81.3	0.7	0.3 ± 0.1	0.5 ± 0.2	8.6	13.2
G258.257−01.052	81.4	1.5	0.2 ± 0.1	0.9 ± 0.4	8.7	13.2
G258.260−00.840	16.1	0.7	0.4 ± 0.1	0.7 ± 0.2	2.4	9.1
	76.6	0.6	0.5 ± 0.1	0.8 ± 0.2	8.1	12.8
	81.3	0.5	0.3 ± 0.1	0.3 ± 0.2	8.6	13.2
G258.270−00.830	16.8	1.0	1.1 ± 0.1	2.9 ± 0.3	2.4	9.1
	77.4	0.9	0.5 ± 0.1	1.1 ± 0.2	8.2	12.8
	80.5	0.9	0.3 ± 0.1	0.6 ± 0.2	8.5	13.1
G258.289−00.457	8.3	0.9	1.2 ± 0.1	2.6 ± 0.3	1.6	8.8
	15.8	0.5	0.2 ± 0.1	0.3 ± 0.1	2.3	9.1
G258.300−02.163	15.5	1.1	1.5 ± 0.1	4.0 ± 0.3	2.3	9.1
	57.5	0.7	2.4 ± 0.1	4.2 ± 0.2	6.2	11.3
G258.319−00.920	6.1	0.9	4.3 ± 0.1	9.9 ± 0.8	1.3	8.7
	24.7	0.6	0.7 ± 0.1	1.1 ± 0.2	3.2	9.5
	80.4	1.4	0.9 ± 0.1	3.1 ± 0.4	8.6	13.1
G258.340−02.190	42.6	0.6	2.2 ± 0.2	3.3 ± 0.2	4.8	10.4
G258.384−01.113	79.5	0.6	0.6 ± 0.2	0.9 ± 0.3	8.5	13.0
	82.1	0.5	0.2 ± 0.2	0.3 ± 0.3	8.7	13.2
G258.420−00.940	81.5	1.4	0.9 ± 0.2	2.9 ± 0.6	8.7	13.2
G258.427−01.444	12.0	0.7	1.6 ± 0.1	2.9 ± 0.2	2.0	8.9
G258.430−00.940	81.9	1.3	1.1 ± 0.3	3.5 ± 1.2	8.7	13.2
G258.495−00.716	19.1	0.9	0.2 ± 0.1	0.5 ± 0.2	2.7	9.2
	73.6	0.6	0.3 ± 0.1	0.5 ± 0.2	7.8	12.5
	76.8	0.6	0.2 ± 0.1	0.4 ± 0.2	8.2	12.8
G258.520−01.704	10.5	1.0	2.4 ± 0.9	6.2 ± 2.4	1.8	8.9
	13.4	0.5	1.9 ± 1.6	2.4 ± 2.0	2.1	9.0
G258.530−01.665	11.8	1.4	0.9 ± 0.1	3.1 ± 0.4	1.9	8.9
	54.0	1.2	0.6 ± 0.1	1.7 ± 0.3	5.9	11.1
G258.532−01.188	12.3	1.1	0.4 ± 0.1	1.1 ± 0.3	2.0	9.0
	16.0	1.4	0.6 ± 0.1	2.3 ± 0.4	2.4	9.1
G258.610−01.920	13.0	1.4	2.6 ± 0.2	9.0 ± 0.6	2.1	9.0
	52.1	0.6	1.0 ± 0.1	1.5 ± 0.1	5.7	11.0

Table A.1: continued

Name	$v_{\rm lsr}$ (km s^{-1})	$\Delta v_{\rm lsr}$ (km s^{-1})	$T_{\rm max}$ (K)	$\int T dv$ (K km s^{-1})	$R_{\rm hel}$ (kpc)	$R_{\rm gal}$ (kpc)
	60.5	0.6	2.4 ± 0.1	3.5 ± 0.1	6.5	11.5
G258.660−00.390	21.3	0.7	2.8 ± 0.1	5.0 ± 0.3	2.9	9.3
	73.5	1.1	0.5 ± 0.1	1.4 ± 0.3	7.8	12.5
G258.667−01.050	14.0	0.9	2.2 ± 0.2	5.1 ± 0.6	2.2	9.0
G258.681−01.774	10.7	0.5	1.1 ± 0.1	1.2 ± 0.2	1.8	8.9
	13.9	1.1	1.7 ± 0.1	4.7 ± 0.3	2.2	9.0
	61.3	0.6	2.8 ± 0.2	4.3 ± 0.4	6.6	11.6
G258.691−01.773	11.0	1.5	1.0 ± 0.8	3.7 ± 2.9	1.9	8.9
	13.3	0.9	2.1 ± 0.5	4.6 ± 1.2	2.1	9.0
	53.9	0.6	0.8 ± 0.1	1.3 ± 0.2	5.9	11.1
	59.8	0.8	5.6 ± 0.2	10.8 ± 0.4	6.4	11.5
G258.718−01.168	10.7	0.5	0.7 ± 0.4	0.9 ± 0.5	1.9	8.9
	12.7	0.5	0.8 ± 0.4	1.1 ± 0.5	2.1	9.0
	64.0	0.7	11.2 ± 0.1	20.0 ± 0.3	6.9	11.8
G258.733−01.335	9.8	1.0	0.2 ± 0.2	0.5 ± 0.5	1.8	8.9
	14.9	1.2	2.2 ± 0.1	6.5 ± 0.4	2.3	9.1
	64.2	0.6	1.4 ± 0.1	2.1 ± 0.1	6.9	11.8
G258.743−01.291	65.3	0.6	3.4 ± 0.2	4.7 ± 0.3	7.0	11.9
G258.790−00.970	15.9	0.5	4.0 ± 0.1	5.1 ± 0.2	2.4	9.1
G258.792−01.422	9.3	0.8	0.7 ± 0.2	1.5 ± 0.4	1.7	8.8
	12.7	1.5	2.6 ± 0.1	9.6 ± 0.5	2.1	9.0
	51.6	0.5	0.7 ± 0.1	0.9 ± 0.1	5.7	11.0
G258.822−01.402	12.4	1.3	2.6 ± 0.1	8.9 ± 0.6	2.0	9.0
	16.2	0.7	1.5 ± 0.3	2.5 ± 0.5	2.4	9.1
G258.842−01.446	11.5	1.2	2.6 ± 0.1	7.7 ± 0.5	1.9	8.9
	60.7	0.6	0.3 ± 0.1	0.5 ± 0.1	6.5	11.5
G258.860−01.397	11.1	0.9	3.2 ± 0.1	7.2 ± 0.4	1.9	8.9
G258.870−01.475	11.0	1.0	1.4 ± 0.2	3.5 ± 0.4	1.9	8.9
	13.3	0.7	1.5 ± 0.2	2.7 ± 0.3	2.1	9.0
G258.878−01.440	11.3	1.1	2.5 ± 0.1	6.5 ± 0.4	1.9	8.9
	82.9	0.7	0.4 ± 0.1	0.8 ± 0.2	8.9	13.3
G258.880−00.720	11.6	0.6	4.5 ± 0.8	6.3 ± 1.2	2.0	8.9
	26.8	0.5	1.4 ± 0.4	1.8 ± 0.5	3.4	9.6
G258.885−01.498	12.0	1.2	1.4 ± 0.1	4.3 ± 0.3	2.0	8.9
	60.5	1.0	0.4 ± 0.1	1.1 ± 0.3	6.5	11.5
G258.910−01.450	11.6	1.5	1.8 ± 0.1	6.7 ± 0.5	2.0	8.9
G258.930−00.730	11.7	0.7	4.2 ± 0.1	6.9 ± 0.3	2.0	8.9
G258.960−00.720	11.4	0.7	0.8 ± 0.1	1.5 ± 0.2	1.9	8.9
G258.965−01.475	11.1	1.3	2.1 ± 0.1	7.0 ± 0.5	1.9	8.9
	59.6	0.8	3.8 ± 0.2	7.8 ± 0.4	6.4	11.5
G259.002−01.498	12.5	1.0	1.7 ± 0.1	4.2 ± 0.3	2.1	9.0
	56.1	0.6	1.3 ± 0.2	2.1 ± 0.4	6.1	11.2
	59.9	0.9	2.5 ± 0.2	5.4 ± 0.4	6.5	11.5
G259.018−01.550	12.7	1.4	2.4 ± 0.1	8.6 ± 0.5	2.1	9.0
	32.8	0.5	1.8 ± 0.1	2.4 ± 0.1	4.0	9.9
	58.3	1.0	14.8 ± 0.2	37.8 ± 0.7	6.3	11.4
G259.031−00.496	18.7	1.2	2.9 ± 0.1	8.3 ± 0.4	2.7	9.2
G259.045−01.557	12.2	1.0	2.6 ± 0.1	6.3 ± 0.4	2.0	9.0
	59.3	1.1	21.5 ± 0.2	58.3 ± 0.7	6.4	11.4

Table A.1: continued

Name	$v_{\rm lsr}$ (km s^{-1})	$\Delta v_{\rm lsr}$ (km s^{-1})	$T_{\rm max}$ (K)	$\int T dv$ (K km s^{-1})	$R_{\rm hel}$ (kpc)	$R_{\rm gal}$ (kpc)
	92.3	0.6	0.7 ± 0.1	1.0 ± 0.1	10.0	14.2
G259.050−01.802	12.2	0.7	1.2 ± 0.1	2.1 ± 0.2	2.0	9.0
G259.050−01.538	12.7	1.3	2.0 ± 0.1	6.4 ± 0.4	2.1	9.0
	58.3	0.9	5.4 ± 1.0	12.2 ± 2.3	6.3	11.4
	60.4	0.8	5.8 ± 1.0	11.8 ± 2.0	6.5	11.5
G259.052−01.140	13.7	0.5	0.5 ± 0.3	0.6 ± 0.3	2.2	9.0
	59.3	0.7	1.8 ± 0.1	3.1 ± 0.2	6.4	11.5
	64.3	0.4	1.4 ± 0.4	1.5 ± 0.5	6.9	11.8
G259.078−01.620	12.8	1.2	2.3 ± 0.1	7.0 ± 0.4	2.1	9.0
	59.3	0.9	12.0 ± 0.2	25.8 ± 0.5	6.4	11.4
G259.080−00.050	6.0	0.5	2.6 ± 0.1	3.3 ± 0.3	1.4	8.7
	14.0	0.6	1.0 ± 0.1	1.3 ± 0.1	2.2	9.0
G259.115+00.229	8.9	0.5	1.4 ± 0.3	1.7 ± 0.4	1.7	8.8
	11.1	0.6	0.6 ± 0.5	0.8 ± 0.8	1.9	8.9
G259.133−01.426	15.1	0.7	1.7 ± 0.1	3.0 ± 0.2	2.3	9.1
	34.1	1.0	0.7 ± 0.1	1.6 ± 0.2	4.1	10.0
G259.136−01.554	6.7	0.6	0.2 ± 0.1	0.4 ± 0.2	1.4	8.7
	54.6	1.0	0.6 ± 0.4	1.4 ± 1.1	6.0	11.1
	58.4	0.6	5.6 ± 0.1	8.5 ± 0.2	6.3	11.4
	93.3	0.7	0.2 ± 0.1	0.4 ± 0.2	10.2	14.3
G259.150−01.298	12.7	0.5	2.8 ± 0.9	3.3 ± 1.0	2.1	9.0
	15.3	0.5	1.1 ± 0.2	1.4 ± 0.3	2.4	9.1
	31.8	1.1	2.0 ± 0.1	5.5 ± 0.3	3.9	9.8
	58.8	1.2	2.7 ± 0.2	8.0 ± 0.6	6.4	11.4
	83.4	0.7	0.7 ± 0.1	1.3 ± 0.2	9.0	13.3
G259.153−01.337	12.4	1.5	2.5 ± 0.2	9.1 ± 0.8	2.1	9.0
	29.6	1.2	1.7 ± 0.2	5.2 ± 0.7	3.7	9.7
	32.0	0.7	1.1 ± 0.3	2.0 ± 0.6	3.9	9.9
	57.1	0.7	2.3 ± 0.3	4.0 ± 0.5	6.2	11.3
	85.2	0.6	0.5 ± 0.1	0.8 ± 0.1	9.2	13.5
	92.3	0.6	1.1 ± 0.1	1.7 ± 0.1	10.0	14.2
G259.165−01.217	12.2	0.9	2.1 ± 0.1	4.6 ± 0.3	2.0	9.0
	57.4	0.8	0.4 ± 0.1	0.7 ± 0.2	6.2	11.3
	59.4	0.6	0.4 ± 0.1	0.6 ± 0.2	6.4	11.5
G259.167−01.313	12.8	0.6	3.3 ± 0.3	5.1 ± 0.6	2.1	9.0
	15.5	0.8	1.6 ± 0.4	2.9 ± 0.8	2.4	9.1
	30.2	1.4	2.2 ± 0.1	7.8 ± 0.4	3.8	9.8
	57.9	0.8	1.8 ± 0.1	3.5 ± 0.2	6.3	11.4
	83.8	0.6	0.3 ± 0.1	0.5 ± 0.2	9.0	13.4
	92.3	0.7	0.3 ± 0.1	0.5 ± 0.2	10.0	14.2
G259.172−01.253	12.5	1.3	3.2 ± 0.1	10.0 ± 0.5	2.1	9.0
	57.9	0.9	0.4 ± 0.1	0.9 ± 0.2	6.3	11.4
	62.1	0.9	0.2 ± 0.1	0.5 ± 0.2	6.7	11.6
G259.178−00.717	6.2	1.0	0.2 ± 0.1	0.5 ± 0.3	1.4	8.7
G259.188−00.673	6.0	0.5	0.7 ± 0.1	1.0 ± 0.2	1.4	8.7
G259.190−00.030	4.3	0.4	8.8 ± 0.3	9.8 ± 1.2	1.2	8.6
	12.7	0.6	4.4 ± 0.1	6.1 ± 0.3	2.1	9.0
G259.198−01.272	13.0	1.4	2.7 ± 0.1	9.3 ± 0.5	2.1	9.0
	57.4	0.8	1.5 ± 0.1	2.9 ± 0.2	6.3	11.3

Table A.1: continued

Name	$v_{\rm lsr}$ (km s^{-1})	$\Delta v_{\rm lsr}$ (km s^{-1})	$T_{\rm max}$ (K)	$\int T dv$ (K km s^{-1})	$R_{\rm hel}$ (kpc)	$R_{\rm gal}$ (kpc)
	85.2	0.8	0.4 ± 0.1	0.8 ± 0.2	9.2	13.5
G259.200+00.000	4.9	0.6	6.1 ± 0.2	9.4 ± 1.0	1.2	8.7
G259.200−00.010	5.0	0.6	5.0 ± 0.3	6.9 ± 0.8	1.2	8.7
	12.8	0.5	3.1 ± 0.3	4.2 ± 0.4	2.1	9.0
	13.2	0.4	3.0 ± 0.6	3.3 ± 0.6	2.1	9.0
G259.215−01.389	57.9	1.1	4.0 ± 0.1	10.9 ± 0.3	6.3	11.4
G259.217−01.390	57.9	1.1	3.6 ± 0.1	10.0 ± 0.3	6.3	11.4
G259.230−00.030	4.6	0.7	1.2 ± 0.2	2.1 ± 0.4	1.2	8.6
G259.230−00.300	10.8	0.7	3.0 ± 0.1	4.9 ± 0.3	1.9	8.9
	12.6	0.6	3.0 ± 0.3	4.5 ± 0.5	2.1	9.0
G259.236−00.804	5.7	0.5	0.4 ± 0.4	0.5 ± 0.5	1.3	8.7
G259.237−01.627	10.9	0.3	0.7 ± 0.1	0.6 ± 0.1	1.9	8.9
	55.1	0.8	2.0 ± 0.7	4.3 ± 1.5	6.0	11.2
	63.4	0.9	14.0 ± 0.1	32.8 ± 0.4	6.8	11.7
G259.240−00.320	11.1	0.5	1.4 ± 0.1	1.8 ± 0.2	1.9	8.9
	50.0	0.8	2.0 ± 0.1	3.8 ± 0.3	5.6	10.9
G259.245−01.227	11.2	0.3	1.4 ± 0.2	1.0 ± 0.2	1.9	8.9
	13.9	1.0	2.5 ± 0.1	6.1 ± 0.4	2.2	9.0
	43.4	0.6	3.1 ± 0.3	4.8 ± 0.5	5.0	10.5
	47.3	0.7	2.8 ± 0.3	5.3 ± 0.6	5.3	10.7
G259.250−00.050	4.8	0.5	0.9 ± 0.3	1.0 ± 0.4	1.2	8.7
	7.5	0.9	0.3 ± 0.3	0.7 ± 0.6	1.5	8.8
	12.5	1.1	3.4 ± 0.2	9.2 ± 0.6	2.1	9.0
G259.250−02.020	55.5	0.7	5.3 ± 0.1	9.5 ± 0.2	6.1	11.2
G259.270−00.330	11.7	0.6	0.7 ± 0.1	1.0 ± 0.2	2.0	8.9
G259.272−01.238	13.9	1.3	2.2 ± 0.1	7.4 ± 0.4	2.2	9.0
	31.7	0.7	0.2 ± 0.1	0.4 ± 0.2	3.9	9.8
	43.5	0.8	0.8 ± 0.1	1.5 ± 0.2	5.0	10.5
	46.8	0.7	0.2 ± 0.1	0.4 ± 0.2	5.3	10.7
G259.284−01.331	12.1	0.7	1.6 ± 0.1	2.6 ± 0.2	2.0	8.9
G259.292−01.955	55.6	1.6	6.7 ± 0.1	27.4 ± 0.5	6.1	11.2
G259.300+00.030	12.8	0.9	–	–	2.1	9.0
G259.302−01.220	13.5	0.7	2.8 ± 0.2	4.7 ± 0.4	2.2	9.0
	29.8	0.9	1.7 ± 0.1	4.0 ± 0.2	3.7	9.7
G259.320−01.740	11.1	0.8	3.6 ± 0.1	6.9 ± 0.4	1.9	8.9
G259.320−01.780	11.9	2.0	2.5 ± 0.1	12.8 ± 0.7	2.0	8.9
G259.320+00.220	14.1	0.5	5.4 ± 0.1	7.5 ± 0.3	2.2	9.0
G259.327−00.888	62.7	0.7	0.4 ± 0.1	0.6 ± 0.2	6.8	11.7
G259.330−01.780	11.9	1.7	3.0 ± 0.4	13.2 ± 1.8	2.0	8.9
G259.338−01.445	11.5	1.2	3.8 ± 0.5	12.0 ± 1.7	2.0	8.9
	14.2	1.1	2.4 ± 0.7	6.5 ± 2.0	2.3	9.0
G259.340−01.444	12.1	1.5	4.0 ± 0.2	15.3 ± 0.9	2.0	8.9
G259.340−00.450	12.6	0.7	0.7 ± 0.1	1.2 ± 0.2	2.1	9.0
	15.1	0.6	0.9 ± 0.1	1.2 ± 0.2	2.3	9.1
G259.360−01.740	11.8	1.2	3.7 ± 0.1	11.2 ± 0.6	2.0	8.9
G259.368−01.192	27.5	1.0	1.8 ± 0.1	4.4 ± 0.3	3.5	9.6
	59.9	1.0	2.7 ± 0.1	6.7 ± 0.3	6.5	11.5
G259.370−00.090	5.4	0.5	1.8 ± 0.5	2.3 ± 0.6	1.3	8.7
G259.383−01.083	57.6	1.7	2.8 ± 0.2	11.9 ± 1.0	6.3	11.3

Table A.1: continued

Name	$v_{\rm lsr}$ (km s^{-1})	$\Delta v_{\rm lsr}$ (km s^{-1})	$T_{\rm max}$ (K)	$\int T dv$ (K km s^{-1})	$R_{\rm hel}$ (kpc)	$R_{\rm gal}$ (kpc)
G259.390−00.180	4.8	0.7	0.5 ± 0.1	0.8 ± 0.2	1.2	8.7
G259.390−01.710	11.4	1.1	3.1 ± 0.1	8.8 ± 0.5	2.0	8.9
	12.3	0.5	4.0 ± 0.2	5.3 ± 0.3	2.1	9.0
G259.400−01.075	55.7	1.3	0.5 ± 0.5	1.5 ± 1.7	6.1	11.2
	59.3	0.9	5.0 ± 0.4	11.1 ± 0.8	6.5	11.4
G259.405−01.162	13.6	0.6	0.7 ± 0.3	0.9 ± 0.4	2.2	9.0
	54.2	0.4	2.5 ± 0.2	2.7 ± 0.2	6.0	11.1
	56.6	1.8	1.1 ± 0.2	5.1 ± 0.8	6.2	11.3
G259.409−01.302	12.5	0.7	2.6 ± 0.1	4.9 ± 0.3	2.1	9.0
	43.6	0.6	0.2 ± 0.1	0.3 ± 0.1	5.0	10.5
	61.7	0.8	0.3 ± 0.1	0.5 ± 0.2	6.7	11.6
G259.410−01.488	12.4	1.0	3.5 ± 0.1	8.9 ± 0.4	2.1	9.0
G259.410−01.710	11.5	0.9	4.0 ± 0.9	8.5 ± 1.9	2.0	8.9
G259.411−00.105	14.4	0.6	0.7 ± 0.1	1.2 ± 0.2	2.3	9.0
G259.417−01.065	57.3	1.0	3.4 ± 0.3	8.6 ± 0.8	6.3	11.3
	59.9	1.0	3.8 ± 0.3	9.2 ± 0.7	6.5	11.5
G259.420−01.037	58.1	0.9	5.3 ± 0.1	12.0 ± 0.3	6.3	11.4
G259.437−00.867	29.0	0.6	0.6 ± 0.1	0.9 ± 0.1	3.7	9.7
	59.1	1.2	0.3 ± 0.1	1.0 ± 0.3	6.4	11.4
G259.440−01.080	57.7	1.6	4.0 ± 0.1	16.2 ± 0.4	6.3	11.3
G259.446−00.838	58.7	1.0	1.9 ± 0.1	4.7 ± 0.3	6.4	11.4
G259.446−00.847	58.8	1.1	2.6 ± 0.1	6.9 ± 0.3	6.4	11.4
G259.457−01.110	12.4	0.6	1.0 ± 0.1	1.4 ± 0.2	2.1	9.0
	57.4	1.2	3.1 ± 0.1	9.2 ± 0.3	6.3	11.3
G259.463−01.065	59.0	0.9	3.8 ± 0.1	8.7 ± 0.2	6.4	11.4
G259.476−00.867	58.1	0.6	1.6 ± 0.1	2.6 ± 0.2	6.3	11.4
	61.5	1.4	0.7 ± 0.1	2.5 ± 0.3	6.7	11.6
G259.480−01.135	28.3	0.8	0.5 ± 0.1	0.9 ± 0.2	3.6	9.7
	61.2	0.7	1.1 ± 0.1	2.0 ± 0.2	6.6	11.6
	85.8	0.6	0.4 ± 0.1	0.6 ± 0.2	9.3	13.6
G259.487−00.651	58.4	0.9	3.5 ± 0.1	7.5 ± 0.2	6.4	11.4
G259.490−01.155	13.5	0.7	1.1 ± 0.1	2.0 ± 0.2	2.2	9.0
	27.9	0.6	1.0 ± 0.1	1.6 ± 0.2	3.6	9.7
G259.497−00.887	58.9	0.9	2.4 ± 0.1	5.3 ± 0.2	6.4	11.4
G259.520−00.300	9.4	1.1	1.3 ± 0.1	3.6 ± 0.3	1.8	8.8
G259.544−02.440	53.4	0.7	6.1 ± 0.1	10.9 ± 0.2	5.9	11.1
G259.560−00.930	26.9	0.5	1.2 ± 0.1	1.4 ± 0.1	3.5	9.6
	54.8	1.5	8.2 ± 0.1	31.2 ± 0.5	6.0	11.1
G259.563−00.619	56.3	0.6	1.5 ± 0.1	2.5 ± 0.2	6.2	11.2
G259.570−01.020	9.1	0.8	–	–	1.7	8.8
G259.570−01.430	12.7	0.8	4.9 ± 0.3	9.8 ± 0.7	2.1	9.0
	54.8	1.3	–	–	6.0	11.1
	56.8	1.1	3.4 ± 0.1	9.6 ± 0.3	6.2	11.3
	61.3	0.9	–	–	6.7	11.6
G259.580+00.140	5.2	0.5	0.3 ± 0.1	0.3 ± 0.1	1.3	8.7
	7.8	0.6	0.9 ± 0.1	1.4 ± 0.2	1.6	8.8
	69.2	0.5	0.2 ± 0.1	0.3 ± 0.1	7.5	12.2
G259.588−02.565	56.5	0.5	1.0 ± 0.1	1.2 ± 0.1	6.2	11.3
G259.593−01.302	57.2	1.1	16.6 ± 0.1	46.5 ± 0.5	6.3	11.3

Table A.1: continued

Name	$v_{\rm lsr}$ (km s^{-1})	$\Delta v_{\rm lsr}$ (km s^{-1})	$T_{\rm max}$ (K)	$\int T dv$ (K km s^{-1})	$R_{\rm hel}$ (kpc)	$R_{\rm gal}$ (kpc)
G259.610−01.300	57.0	0.9	14.6 ± 0.1	34.5 ± 0.4	6.3	11.3
G259.613−01.684	11.9	0.8	1.9 ± 0.1	3.9 ± 0.3	2.0	8.9
G259.617−00.640	8.8	0.4	0.9 ± 0.9	0.8 ± 0.8	1.7	8.8
G259.620+00.060	12.0	1.3	–	–	2.0	8.9
G259.638−01.016	59.9	0.9	0.5 ± 0.1	1.2 ± 0.2	6.5	11.5
G259.640−01.320	57.7	0.8	3.1 ± 0.1	6.5 ± 0.2	6.3	11.3
G259.643−00.659	8.4	0.6	0.8 ± 0.1	1.2 ± 0.2	1.7	8.8
G259.652−01.313	57.6	1.0	19.3 ± 0.1	48.2 ± 0.5	6.3	11.3
G259.668−01.318	58.2	1.7	18.3 ± 0.2	77.8 ± 1.1	6.4	11.4
G259.678−02.535	54.3	0.8	12.2 ± 0.1	24.2 ± 0.3	6.0	11.1
G259.680+00.040	6.0	0.6	–	–	1.4	8.7
	13.4	0.7	–	–	2.2	9.0
	17.0	1.5	–	–	2.6	9.2
G259.691−00.614	8.4	0.6	1.6 ± 0.1	2.3 ± 0.2	1.7	8.8
G259.699−01.165	57.9	1.0	16.4 ± 0.1	41.5 ± 0.4	6.3	11.3
G259.700−01.280	57.2	1.2	–	–	6.3	11.3
G259.711−01.934	10.7	0.9	2.7 ± 0.1	5.8 ± 0.3	1.9	8.9
	95.5	0.5	0.7 ± 0.1	0.9 ± 0.1	10.5	14.5
G259.726+00.282	8.7	0.5	1.0 ± 0.2	1.3 ± 0.2	1.7	8.8
G259.750−01.340	57.0	1.1	1.6 ± 0.1	4.5 ± 0.3	6.3	11.3
	65.9	0.6	0.7 ± 0.1	1.0 ± 0.1	7.1	11.9
G259.769−01.135	62.7	0.8	0.7 ± 0.1	1.4 ± 0.2	6.8	11.7
G259.781−00.834	60.3	0.6	2.9 ± 0.1	4.2 ± 0.2	6.6	11.5
G259.783−00.833	60.2	0.6	3.0 ± 0.1	4.3 ± 0.2	6.6	11.5
G259.830−01.099	56.6	1.1	0.6 ± 0.1	1.6 ± 0.3	6.2	11.3
G259.830−00.473	9.5	0.6	5.2 ± 0.1	8.3 ± 0.5	1.8	8.8
G259.847−00.465	9.5	0.7	5.4 ± 0.1	8.8 ± 0.5	1.8	8.8
G259.849−01.982	8.8	0.7	0.2 ± 0.1	0.4 ± 0.2	1.7	8.8
	15.4	0.6	0.7 ± 0.1	1.1 ± 0.2	2.4	9.1
G259.851−00.551	9.2	0.5	2.3 ± 0.1	2.9 ± 0.2	1.8	8.8
G259.860−02.030	15.9	0.8	1.9 ± 0.3	3.7 ± 0.5	2.5	9.1
G259.864−00.777	59.0	0.6	–	–	6.5	11.4
G259.870−02.400	10.5	1.3	6.1 ± 0.1	19.6 ± 1.0	1.9	8.9
	56.6	0.5	0.3 ± 0.2	0.3 ± 0.2	6.2	11.3
G259.880−02.020	10.2	0.7	0.9 ± 0.1	1.4 ± 0.2	1.9	8.9
G259.880−02.410	10.6	1.4	6.5 ± 0.2	22.1 ± 1.2	1.9	8.9
	15.5	1.1	0.2 ± 0.1	0.6 ± 0.3	2.4	9.1
	53.7	0.6	0.3 ± 0.1	0.4 ± 0.1	6.0	11.1
G259.890−02.420	10.3	1.5	7.9 ± 0.2	29.3 ± 1.5	1.9	8.9
G259.900+00.010	7.8	0.9	–	–	1.6	8.8
G259.900−02.430	10.3	1.4	8.7 ± 0.2	29.9 ± 1.6	1.9	8.9
G259.900−01.970	11.1	0.9	0.9 ± 0.1	2.0 ± 0.3	2.0	8.9
	14.5	0.8	–	–	2.3	9.0
	16.7	1.5	0.4 ± 0.1	1.4 ± 0.5	2.5	9.1
G259.908−01.942	15.9	0.6	–	–	2.5	9.1
G259.910−00.050	7.8	1.3	17.2 ± 0.1	58.2 ± 3.8	1.6	8.8
G259.920−00.010	7.9	1.0	15.1 ± 0.1	36.6 ± 2.3	1.6	8.8
G259.939−00.042	5.2	2.7	11.2 ± 3.4	76.3 ± 24.2	1.3	8.7
	10.3	2.1	12.9 ± 3.4	66.8 ± 17.9	1.9	8.9

Table A.1: continued

Name	$v_{\rm lsr}$ (km s^{-1})	$\Delta v_{\rm lsr}$ (km s^{-1})	$T_{\rm max}$ (K)	$\int T dv$ (K km s^{-1})	$R_{\rm hel}$ (kpc)	$R_{\rm gal}$ (kpc)
G259.940−00.040	6.1	1.4	16.9 ± 4.4	58.1 ± 15.8	1.4	8.7
	10.1	1.5	20.3 ± 3.5	74.8 ± 13.5	1.9	8.9
G259.950−01.330	62.7	0.8	0.5 ± 0.1	1.1 ± 0.2	6.8	11.7
G259.958−02.002	11.8	0.5	0.2 ± 0.1	0.3 ± 0.1	2.1	8.9
	14.9	0.6	0.6 ± 0.1	0.9 ± 0.2	2.4	9.1
G259.960−00.080	7.4	0.8	16.0 ± 0.1	32.4 ± 2.2	1.6	8.8
	11.4	0.8	1.3 ± 1.2	2.5 ± 2.4	2.0	8.9
	67.7	1.1	0.3 ± 0.1	0.9 ± 0.3	7.3	12.0
G259.980−00.080	4.3	0.5	0.5 ± 0.1	0.7 ± 0.2	1.2	8.6
	8.9	1.4	0.9 ± 0.1	3.1 ± 0.4	1.7	8.8
	65.4	0.6	1.2 ± 0.1	1.8 ± 0.2	7.1	11.9
G259.987+00.027	8.0	0.9	12.8 ± 0.1	27.6 ± 1.7	1.6	8.8
	64.1	0.7	0.4 ± 0.1	0.6 ± 0.2	7.0	11.8
	70.3	1.1	0.1 ± 0.1	0.4 ± 0.3	7.6	12.2
G259.990−00.020	8.9	0.5	13.6 ± 0.1	17.3 ± 1.0	1.7	8.8
	13.6	0.5	0.4 ± 0.3	0.5 ± 0.3	2.2	9.0
	62.6	1.4	0.8 ± 0.1	2.7 ± 0.4	6.8	11.7
G260.000−00.160	0.3	0.5	0.2 ± 0.1	0.3 ± 0.4	0.7	8.5
	8.3	0.7	12.3 ± 0.1	22.7 ± 1.4	1.7	8.8
	14.4	0.7	0.8 ± 0.1	1.2 ± 0.2	2.3	9.0
	65.6	0.4	0.1 ± 0.1	0.1 ± 0.1	7.1	11.9

Table A.2: Velocity groups identified from the CO(2–1) observations along a given line-of-sight for 15 complexes. Source names starting with a '*G*' are measured emission at targeted positions, whereas names starting with an '*O*' indicate emission in the off-position.

Name	Group	# components	$v_{\rm lsr}$ (km s^{-1})	$\Delta v_{\rm lsr}$ (km s^{-1})	$T_{\rm max}$ (K)	$\int T dv$ (K km s^{-1})
G225.020−00.590	1/1	1	14.6	8.9	3.6 ± 0.1	9.5 ± 0.4
G225.030+00.060	1/1	1	17.9	4.0	0.8 ± 0.1	1.9 ± 0.2
G225.080+00.060	1/1	1	17.8	6.0	3.0 ± 0.1	5.8 ± 0.3
G225.160−00.830	2/2	1	14.3	4.0	0.2 ± 0.1	0.4 ± 0.2
G225.160−00.840	2/2	1	14.8	3.0	0.4 ± 0.1	0.5 ± 0.1
	1/2	1	19.9	5.0	4.0 ± 0.1	4.7 ± 0.2
	1/2	1	20.0	4.0	2.9 ± 0.1	3.2 ± 0.1
G225.170−00.750	2/2	1	19.5	4.0	2.6 ± 0.6	3.7 ± 0.8
G225.210−01.110	1/2	1	13.9	4.0	5.1 ± 0.1	9.0 ± 0.4
	2/2	1	19.4	4.0	0.4 ± 0.2	0.7 ± 0.3
G225.220−01.200	1/1	1	13.5	5.0	2.2 ± 0.1	3.6 ± 0.2
G225.230−00.960	1/1	1	14.7	7.9	5.6 ± 0.1	10.6 ± 0.4
G225.240−01.110	1/1	1	13.8	10.9	4.8 ± 0.1	11.9 ± 0.5
G225.300−01.090	1/2	1	14.0	7.9	3.7 ± 0.1	7.7 ± 0.3
G225.320−01.170	1/1	1	13.7	9.9	3.7 ± 0.1	7.5 ± 0.3
G225.320−01.100	1/1	1	14.2	6.0	4.3 ± 0.1	8.5 ± 0.4
G225.320−00.280	1/1	1	15.2	5.0	1.8 ± 0.1	4.0 ± 0.3
G225.330−00.866	1/1	1	14.4	6.9	1.5 ± 0.1	2.4 ± 0.2
G225.330−01.120	1/1	1	14.4	7.9	4.5 ± 0.1	6.9 ± 0.3
G225.330−00.540	1/1	2	17.3	18.9	8.7 ± 0.1	36.2 ± 1.1
G225.350−00.540	2/2	1	11.6	4.0	0.5 ± 0.1	0.9 ± 0.2
	1/2	2	18.6	7.9	6.7 ± 2.9	18.0 ± 7.9
G225.370−01.380	1/2	1	13.3	7.9	1.9 ± 0.1	3.2 ± 0.2
G225.380−00.540	2/2	1	11.7	3.0	1.6 ± 0.2	2.0 ± 0.2
	1/2	1	17.0	5.0	4.5 ± 0.1	8.6 ± 0.4
G225.390−01.370	1/2	1	13.3	5.0	–	–
G225.390−00.990	1/2	1	15.0	6.9	2.5 ± 0.1	4.7 ± 0.2
G225.400−01.020	2/2	1	10.3	4.0	0.8 ± 0.1	1.1 ± 0.1
	1/2	1	14.8	6.9	3.1 ± 0.1	4.5 ± 0.2
G225.400−00.560	1/1	2	16.2	19.8	7.1 ± 0.1	22.0 ± 0.7
G225.440−00.390	1/1	2	18.5	11.9	4.5 ± 0.3	12.2 ± 0.8
G225.460−01.680	1/1	1	15.7	7.9	9.5 ± 0.1	15.6 ± 0.5
G225.470−01.680	1/1	1	16.0	7.9	10.7 ± 0.1	16.8 ± 0.5
G225.472−01.674	1/1	1	16.7	2.0	5.2 ± 0.2	5.8 ± 0.2
G225.480−00.230	1/1	1	16.0	9.9	1.7 ± 0.1	6.2 ± 0.4
G225.480−01.790	1/1	1	16.7	6.0	11.8 ± 0.1	19.9 ± 0.6
G225.480−01.800	1/1	1	16.9	8.9	4.9 ± 0.1	9.8 ± 0.4
G225.490−01.780	1/1	1	16.2	6.9	10.7 ± 0.1	18.4 ± 0.6
G225.490−01.810	1/2	1	16.9	9.9	5.1 ± 0.1	10.2 ± 0.4
G225.490−00.400	1/2	2	18.6	9.9	4.1 ± 0.8	14.2 ± 2.6
G225.500−01.800	1/1	1	16.2	6.9	0.7 ± 0.1	1.9 ± 0.3
G225.500−01.770	1/1	1	16.2	7.9	13.5 ± 0.1	26.7 ± 0.8
G225.510−01.740	1/1	1	15.5	8.9	12.6 ± 0.1	22.4 ± 0.7
G225.510−01.780	1/1	1	16.0	6.9	14.7 ± 0.1	23.4 ± 0.8
G225.530−01.780	1/1	1	16.1	7.9	12.9 ± 0.1	20.5 ± 0.7
G225.604−02.013	1/1	1	17.6	3.0	0.1 ± 0.1	0.1 ± 0.1

Table A.2: continued

Name	Group	# components	$v_{\rm lsr}$ (km s^{-1})	$\Delta v_{\rm lsr}$ (km s^{-1})	$T_{\rm max}$ (K)	$\int T dv$ (K km s^{-1})
G225.660−00.220	1/3	2	18.7	9.9	6.4±0.1	13.2±0.4
G225.770−00.960	1/1	1	14.1	4.0	3.3±0.1	4.8±0.2
G225.780−00.940	1/1	1	14.4	4.0	2.7±0.1	4.2±0.2
G225.954−00.884	1/1	1	16.5	2.0	1.0±0.1	1.7±0.2
G225.980+00.080	1/1	1	18.5	4.0	4.0±0.1	6.6±0.2
G226.065−00.056	1/1	1	17.6	2.0	0.9±0.1	1.2±0.1
G226.095−00.316	1/1	1	13.7	2.0	0.3±0.2	0.3±0.2
G226.117−00.349	1/1	1	15.1	14.9	3.1±0.1	16.9±0.8
G226.150−00.150	1/1	1	16.5	10.9	4.5±0.1	8.6±0.3
G226.273−01.554	1/1	1	24.3	6.9	1.2±0.1	1.8±0.2
G226.279−00.844	1/3	1	14.7	2.0	0.3±0.2	0.3±0.2
G226.280−02.070	1/1	1	11.7	5.0	1.9±0.1	2.3±0.2
G226.330−02.030	1/1	1	11.1	6.9	2.1±0.1	3.7±0.2
G226.353−00.766	1/1	2	14.6	21.8	3.3±0.2	23.7±1.8
G226.430−00.588	1/1	3	16.5	25.8	7.9±0.6	48.0±4.0
G226.514−00.736	1/1	1	16.2	4.0	1.3±0.8	1.3±0.8
G226.670−02.060	1/1	1	14.4	8.9	2.2±0.1	3.8±0.2
G227.040−00.900	1/2	2	60.8	13.9	2.4±0.2	9.2±0.7
G227.070−00.220	1/1	1	3.0	3.0	0.4±0.1	0.6±0.2
G227.180−00.460	1/1	1	19.8	5.0	1.6±0.1	2.6±0.2
G227.230−00.830	1/1	1	20.1	5.0	1.4±0.1	2.3±0.2
G227.242−00.883	1/1	1	20.1	3.0	3.8±0.1	5.8±0.2
G227.343−01.821	1/1	1	16.6	6.0	0.7±0.1	1.0±0.2
G227.370−01.142	1/2	1	12.8	6.9	0.6±0.1	1.2±0.2
G227.570−01.140	1/1	1	79.7	9.9	5.6±0.1	11.0±0.2
G227.650−01.286	1/1	1	79.0	6.9	3.3±0.1	5.9±0.2
G227.792−00.104	1/1	1	50.4	15.9	1.1±0.1	7.1±0.6
G227.800−00.080	2/2	1	36.7	5.0	0.8±0.1	1.0±0.1
	1/2	1	53.0	6.0	1.1±0.1	2.7±0.2
G227.800−00.140	1/1	1	53.1	11.9	1.2±0.1	5.4±0.5
G227.810−00.120	1/1	1	53.6	11.9	1.8±0.1	6.8±0.4
G227.815−00.129	1/1	1	53.2	16.9	2.9±0.1	16.4±0.6
G227.820−00.140	1/1	1	52.8	15.9	5.6±0.1	28.8±0.6
G227.820−00.160	1/1	1	52.9	12.9	2.5±0.1	10.3±0.4
G227.862−00.243	1/1	1	53.8	9.9	2.1±0.1	5.8±0.3
G227.870−01.120	1/1	1	36.0	6.0	0.4±0.1	0.6±0.2
G227.880−01.780	1/1	1	18.6	6.9	3.8±0.1	6.9±0.3
G227.910−01.880	1/2	1	19.0	5.0	4.7±0.1	5.7±0.2
G227.924−00.241	1/1	1	53.0	3.0	0.3±0.1	0.5±0.2
G227.940−00.139	2/2	1	50.0	3.0	0.2±0.2	0.2±0.2
	1/2	1	65.9	11.9	3.2±0.1	9.3±0.3
G227.969−00.847	1/1	1	36.6	5.0	0.3±0.1	0.4±0.2
G228.026−00.946	1/1	1	36.6	6.9	2.3±0.1	3.3±0.1
G228.027−00.924	1/1	1	36.7	7.9	2.1±0.1	3.2±0.2
G228.030+00.020	1/1	1	53.0	6.9	3.6±0.1	6.4±0.2
G228.030+00.010	1/1	1	53.0	6.9	3.3±0.1	5.1±0.2
G228.059−01.021	1/1	1	37.3	4.0	0.2±0.1	0.4±0.2
G228.173−02.039	1/1	1	50.0	5.0	0.7±0.1	1.1±0.2
G228.300−00.970	1/1	1	36.1	4.0	2.6±0.1	3.2±0.1

Table A.2: continued

Name	Group	# components	$v_{\rm lsr}$ (km s^{-1})	$\Delta v_{\rm lsr}$ (km s^{-1})	$T_{\rm max}$ (K)	$\int T dv$ (K km s^{-1})
G228.520+00.240	1/1	1	16.6	8.9	0.8 ± 0.1	2.0 ± 0.3
G228.710−00.910	1/1	1	46.5	4.0	2.5 ± 0.1	2.8 ± 0.1
G229.570+00.150	1/1	2	55.1	32.7	8.8 ± 0.5	78.0 ± 4.6
G229.590+00.160	1/1	1	53.3	13.9	13.4 ± 0.1	44.7 ± 0.5
G229.600+00.150	1/1	1	54.3	14.9	14.5 ± 0.1	55.5 ± 0.7
G229.740+00.120	1/1	1	70.2	6.9	3.4 ± 0.1	5.2 ± 0.2
G229.750+00.030	1/1	1	71.2	6.0	3.8 ± 0.2	5.7 ± 0.4
G229.760−00.440	1/2	1	72.6	7.9	2.6 ± 0.1	4.4 ± 0.2
G229.770+00.040	1/1	1	69.8	9.9	5.2 ± 0.1	10.1 ± 0.2
G229.770+00.060	1/1	1	70.6	10.9	6.0 ± 0.1	15.2 ± 0.3
G229.780+00.050	1/1	1	72.4	7.9	2.0 ± 0.1	2.8 ± 0.1
G229.790−00.680	1/1	1	41.0	4.0	2.5 ± 0.1	3.5 ± 0.1
G229.800−00.360	1/1	1	72.3	8.9	4.6 ± 0.1	10.7 ± 0.2
G229.900−00.650	1/1	1	41.3	6.0	1.6 ± 0.1	2.8 ± 0.2
G230.047−00.888	1/1	1	40.2	5.0	0.8 ± 0.1	1.6 ± 0.2
G230.340−00.610	1/1	1	38.3	4.0	0.7 ± 0.1	1.3 ± 0.2
G230.390−00.780	1/2	1	39.7	4.0	1.0 ± 0.1	1.2 ± 0.1
G230.660+00.330	2/2	1	35.0	6.9	0.5 ± 0.1	0.7 ± 0.2
	1/2	1	51.1	6.0	2.0 ± 0.1	3.0 ± 0.2
G230.680+00.300	1/1	1	51.8	6.9	0.5 ± 0.1	1.0 ± 0.2
G230.700+00.350	1/3	1	36.8	9.9	2.0 ± 0.1	3.6 ± 0.3
	2/3	1	51.9	6.9	2.0 ± 0.1	4.0 ± 0.2
G230.860+00.150	2/3	1	20.2	4.0	0.8 ± 0.1	1.2 ± 0.2
	1/3	1	29.5	3.0	3.7 ± 0.2	4.8 ± 0.2
	3/3	1	43.3	3.0	0.3 ± 0.1	0.4 ± 0.2
G230.940−00.400	1/1	1	40.9	5.0	1.3 ± 0.1	2.2 ± 0.2
G230.955−00.587	1/1	1	44.4	5.0	0.8 ± 0.1	1.2 ± 0.2
G230.976−00.617	1/1	1	44.0	6.0	0.9 ± 0.1	1.8 ± 0.2
G230.995−00.567	1/1	1	45.5	3.0	0.6 ± 0.1	0.8 ± 0.1
G231.010−00.180	2/2	1	19.0	4.0	0.3 ± 0.1	0.6 ± 0.2
	1/2	1	33.4	5.0	0.4 ± 0.1	0.8 ± 0.2
G231.070−00.130	1/1	1	33.5	7.9	6.1 ± 0.3	8.5 ± 0.5
G231.130−00.320	1/2	1	32.0	6.9	9.8 ± 0.1	13.5 ± 0.3
	2/2	1	44.5	4.0	0.2 ± 0.1	0.4 ± 0.2
G231.140−00.330	1/2	1	31.7	7.9	5.6 ± 0.1	7.5 ± 0.2
	2/2	1	44.6	4.0	0.7 ± 0.1	0.9 ± 0.1
G231.250−00.330	1/2	1	31.7	5.0	0.3 ± 0.1	0.4 ± 0.1
G231.260−00.290	3/4	1	17.6	2.0	0.3 ± 0.2	0.4 ± 0.3
	4/4	1	20.2	3.0	0.2 ± 0.1	0.2 ± 0.1
	1/4	2	33.6	9.9	1.5 ± 0.1	3.3 ± 0.3
	2/4	1	46.2	5.0	0.6 ± 0.1	1.0 ± 0.2
G231.280−00.260	1/3	1	30.4	6.0	1.8 ± 0.2	2.9 ± 0.3
G231.280−00.280	1/2	1	31.0	5.0	1.5 ± 0.1	1.8 ± 0.1
G231.290−00.360	3/3	1	28.9	4.0	0.2 ± 0.1	0.3 ± 0.1
	1/3	1	46.4	6.9	0.5 ± 0.1	0.8 ± 0.2
G231.310−00.290	1/2	1	19.5	6.0	1.1 ± 0.1	1.9 ± 0.2
G231.330−00.380	1/1	1	29.6	7.9	4.5 ± 0.2	5.9 ± 0.3
G231.330−00.690	1/1	1	40.5	7.9	2.3 ± 1.0	3.9 ± 1.7
G231.390−00.460	1/2	1	30.0	6.9	4.8 ± 0.1	7.6 ± 0.2

Table A.2: continued

Name	Group	# components	$v_{\rm lsr}$ (km s^{-1})	$\Delta v_{\rm lsr}$ (km s^{-1})	$T_{\rm max}$ (K)	$\int T dv$ (K km s^{-1})
G231.470−01.860	1/1	3	41.8	16.9	4.6 ± 0.3	17.2 ± 1.2
G231.490−01.770	1/1	2	44.3	15.9	2.5 ± 0.2	15.3 ± 1.0
G231.540−00.880	1/1	1	41.3	6.9	2.0 ± 0.1	7.7 ± 0.4
G231.540−00.840	1/1	1	41.7	10.9	3.1 ± 0.1	9.3 ± 0.3
G231.560−01.660	2/2	1	20.3	3.0	0.4 ± 0.2	0.5 ± 0.2
	1/2	1	44.1	9.9	3.9 ± 0.1	11.5 ± 0.3
G231.590−00.840	1/1	1	42.2	5.0	3.1 ± 0.1	7.7 ± 0.3
G231.610−01.260	1/4	1	38.4	6.0	4.0 ± 0.3	7.9 ± 0.7
	2/4	1	45.0	6.9	1.3 ± 0.3	2.0 ± 0.5
G231.630−01.603	1/3	1	45.8	7.9	0.4 ± 0.1	1.0 ± 0.3
G231.730+00.270	1/1	1	33.1	6.0	2.8 ± 0.1	4.9 ± 0.2
G231.740−01.760	3/3	1	39.5	4.0	0.3 ± 0.3	0.4 ± 0.3
	1/3	2	44.0	9.9	0.8 ± 0.1	2.7 ± 0.4
	2/3	1	56.7	4.0	0.3 ± 0.1	0.5 ± 0.2
G231.750+00.290	2/2	1	20.8	6.0	0.2 ± 0.1	0.4 ± 0.2
	1/2	1	33.2	6.0	2.5 ± 0.1	4.4 ± 0.2
G231.760−00.250	2/2	1	19.3	3.0	0.5 ± 0.1	0.6 ± 0.2
	1/2	1	28.3	6.9	5.3 ± 0.1	10.0 ± 0.3
G231.770−00.350	2/3	1	19.9	4.0	0.2 ± 0.1	0.3 ± 0.1
	1/3	1	26.5	5.0	1.5 ± 0.1	2.1 ± 0.2
G231.793−01.970	1/1	2	45.5	25.8	4.2 ± 0.9	37.9 ± 8.5
G231.812+00.075	2/2	1	19.0	6.0	0.2 ± 0.1	0.5 ± 0.2
	1/2	1	43.8	4.0	2.5 ± 0.1	4.8 ± 0.2
G231.841−01.752	1/1	1	48.4	3.0	0.7 ± 0.1	1.2 ± 0.2
G231.841−01.792	1/2	1	49.2	6.0	0.5 ± 0.1	1.1 ± 0.2
G231.872−00.115	1/1	1	59.4	5.0	0.5 ± 0.1	0.9 ± 0.2
G231.882−00.125	1/2	1	59.8	4.0	0.9 ± 0.1	1.1 ± 0.1
G231.891−01.752	1/1	1	47.1	4.0	0.3 ± 0.1	0.4 ± 0.2
G231.910+00.150	2/2	1	23.7	6.9	2.2 ± 0.1	2.9 ± 0.1
	1/2	1	57.9	6.0	2.8 ± 0.1	7.1 ± 0.3
G231.913−02.171	1/2	1	41.7	3.0	3.8 ± 0.1	8.5 ± 0.2
G231.930−01.500	1/2	1	74.3	17.9	6.4 ± 0.1	23.4 ± 0.4
G231.931−01.512	1/1	1	74.1	5.0	2.2 ± 0.2	4.7 ± 0.4
G231.940−01.510	1/1	1	73.3	7.9	2.2 ± 0.1	4.7 ± 0.2
G231.959−02.064	2/2	1	22.4	5.0	0.9 ± 0.1	1.5 ± 0.2
	1/2	1	41.0	18.9	14.3 ± 0.2	66.2 ± 1.2
G231.992−00.125	1/3	1	23.9	3.0	0.2 ± 0.1	0.3 ± 0.2
G232.000+00.300	1/3	1	32.1	8.9	5.3 ± 0.1	10.1 ± 0.2
	2/3	1	58.2	7.9	1.3 ± 0.1	2.4 ± 0.2
G232.022−00.076	1/1	1	17.7	5.0	0.8 ± 0.7	0.9 ± 0.7
G232.022−00.056	1/4	1	55.8	5.0	1.5 ± 0.1	2.0 ± 0.1
G232.040+00.070	1/2	1	57.1	7.9	4.9 ± 0.2	12.2 ± 0.5
G232.045−00.625	1/1	1	59.4	6.9	0.2 ± 0.1	0.6 ± 0.3
G232.052−00.086	2/3	1	24.2	2.0	0.4 ± 0.1	0.6 ± 0.1
	1/3	1	56.9	6.0	0.6 ± 0.2	0.8 ± 0.2
G232.057−01.163	1/1	1	45.7	5.0	0.2 ± 0.1	0.5 ± 0.3
G232.062−00.126	1/3	1	19.2	2.0	1.0 ± 0.2	1.2 ± 0.2
G232.062−00.096	2/2	1	24.7	5.0	0.3 ± 0.1	0.6 ± 0.2
	1/2	1	57.0	6.0	0.9 ± 0.1	1.3 ± 0.1

Table A.2: continued

Name	Group	# components	$v_{\rm lsr}$ (km s^{-1})	$\Delta v_{\rm lsr}$ (km s^{-1})	$T_{\rm max}$ (K)	$\int T dv$ (K km s^{-1})
G232.062−00.076	2/3	1	56.4	5.0	1.1 ± 0.1	1.8 ± 0.2
G232.071−00.176	1/2	1	19.7	10.9	1.1 ± 0.8	1.9 ± 1.4
G232.075−02.276	1/1	1	41.8	32.7	22.0 ± 0.2	116.1 ± 1.8
G232.080+00.130	1/1	1	57.2	7.9	2.4 ± 0.1	5.4 ± 0.2
G232.082−00.046	1/3	1	13.9	4.0	0.7 ± 0.1	0.9 ± 0.1
	2/3	1	56.3	6.0	0.6 ± 0.1	1.1 ± 0.2
G232.111−01.158	1/1	1	46.7	9.9	2.9 ± 0.1	12.4 ± 0.5
G232.131−00.256	1/1	1	21.7	6.0	0.7 ± 0.1	1.1 ± 0.2
G232.205−00.764	1/1	1	44.4	6.0	1.0 ± 0.1	1.3 ± 0.1
G232.220+00.190	1/1	2	15.3	9.9	2.9 ± 0.1	6.6 ± 0.3
G232.220−01.070	1/1	1	43.7	8.9	1.7 ± 0.1	7.1 ± 0.4
G232.230+00.180	1/1	3	18.2	10.9	2.0 ± 0.1	7.1 ± 0.4
G232.240+00.130	1/1	1	16.9	13.9	2.6 ± 0.1	11.6 ± 0.6
G232.250+00.070	1/1	1	16.9	11.9	2.4 ± 0.1	10.4 ± 0.5
G232.250+00.060	1/1	1	17.0	9.9	2.3 ± 0.1	10.6 ± 0.6
G232.420+00.240	1/1	1	20.6	6.9	1.9 ± 0.1	4.6 ± 0.3
G232.490−00.300	1/1	1	17.0	5.0	2.1 ± 0.1	4.5 ± 0.3
G232.500−00.040	1/1	2	17.3	8.9	2.2 ± 0.1	6.9 ± 0.4
G232.504−01.223	1/2	1	25.3	4.0	0.4 ± 0.1	0.7 ± 0.2
	2/2	1	47.3	4.0	0.3 ± 0.1	0.5 ± 0.2
G232.510+00.200	1/1	3	15.9	11.9	1.6 ± 0.2	7.7 ± 0.8
G232.590−01.190	1/1	1	22.5	6.0	0.7 ± 0.1	1.3 ± 0.2
G232.596−01.352	1/1	2	46.0	10.9	3.0 ± 0.2	11.7 ± 0.8
G232.600+00.300	1/1	1	15.7	8.9	4.7 ± 0.1	7.7 ± 0.3
G232.600+00.430	1/1	1	16.3	6.0	3.9 ± 0.1	5.8 ± 0.2
G232.600+00.100	1/1	1	17.0	13.9	1.9 ± 0.1	8.6 ± 0.5
G232.600−01.320	1/1	1	47.1	9.9	2.0 ± 0.1	7.2 ± 0.4
G232.630+00.390	1/1	1	16.6	6.0	3.3 ± 0.1	5.1 ± 0.3
G232.640−00.420	3/3	1	17.7	6.9	0.4 ± 0.1	1.2 ± 0.3
	1/3	1	23.2	6.9	2.7 ± 0.2	3.9 ± 0.3
	2/3	1	47.4	6.9	1.0 ± 0.1	1.5 ± 0.2
G232.669−01.295	1/3	1	48.9	5.0	0.6 ± 0.1	1.0 ± 0.2
	2/3	1	54.4	4.0	0.5 ± 0.1	0.9 ± 0.2
G232.679−01.305	1/1	1	48.2	7.9	0.4 ± 0.1	1.0 ± 0.3
G232.680+00.160	1/5	3	14.5	11.9	3.4 ± 0.3	14.2 ± 1.4
	2/5	1	33.5	7.9	0.3 ± 0.2	0.8 ± 0.5
G232.710−00.240	1/2	2	18.2	12.9	2.3 ± 0.1	7.5 ± 0.4
	2/2	1	39.2	6.9	0.7 ± 0.1	1.2 ± 0.2
G232.760−00.240	1/3	1	17.8	10.9	1.8 ± 0.1	5.2 ± 0.3
G232.760+00.050	1/1	1	18.5	11.9	0.9 ± 0.1	4.5 ± 0.5
	3/3	1	39.2	5.0	0.4 ± 0.1	0.8 ± 0.2
	2/3	1	43.9	5.0	0.7 ± 0.1	1.1 ± 0.2
G232.770−00.340	3/3	1	18.1	6.0	0.5 ± 0.1	1.1 ± 0.2
G232.770−00.360	1/3	2	22.8	9.9	3.2 ± 0.1	6.0 ± 0.2
G232.770−00.350	1/1	2	23.0	10.9	3.5 ± 0.1	7.6 ± 0.3
	1/3	1	23.1	4.0	2.9 ± 0.1	4.5 ± 0.2
	2/3	1	45.2	4.0	0.6 ± 0.1	1.2 ± 0.2
	3/3	1	47.9	5.0	0.2 ± 0.1	0.5 ± 0.2
G232.782+00.271	1/1	1	16.5	7.9	1.8 ± 0.1	7.7 ± 0.5

Table A.2: continued

Name	Group	# components	$v_{\rm lsr}$ (km s^{-1})	$\Delta v_{\rm lsr}$ (km s^{-1})	$T_{\rm max}$ (K)	$\int T dv$ (K km s^{-1})
G232.790+00.150	1/1	2	22.8	17.9	3.9 ± 0.2	21.2 ± 1.4
G232.790−01.400	1/2	2	52.9	10.9	1.1 ± 0.1	4.8 ± 0.4
G232.796−00.952	1/1	1	45.0	3.0	0.9 ± 0.1	1.2 ± 0.1
G232.805−00.713	1/2	1	44.5	9.9	1.4 ± 0.1	4.6 ± 0.3
G232.820−00.840	1/1	2	46.9	8.9	1.5 ± 0.5	5.8 ± 1.8
G232.894−01.389	1/1	2	46.8	12.9	3.2 ± 0.1	11.7 ± 0.4
G232.894−00.613	2/2	1	31.2	4.0	0.7 ± 0.1	1.0 ± 0.2
	1/2	1	44.4	6.0	1.1 ± 0.1	2.2 ± 0.2
G232.900+00.120	1/1	2	21.6	8.9	1.8 ± 0.5	6.6 ± 2.0
G232.923−00.523	1/1	1	45.9	7.9	0.4 ± 0.1	1.2 ± 0.3
G232.930+00.040	1/1	1	19.2	10.9	1.6 ± 0.1	5.7 ± 0.4
G232.940−01.000	1/1	1	43.7	4.0	2.0 ± 0.1	4.2 ± 0.2
G232.950−00.790	2/2	1	24.5	5.0	0.7 ± 0.1	1.8 ± 0.2
	1/2	1	46.3	13.9	2.2 ± 0.1	8.6 ± 0.4
G232.970−00.780	2/2	1	25.8	7.9	1.4 ± 0.1	1.9 ± 0.1
	1/2	1	46.3	6.0	2.3 ± 0.1	5.8 ± 0.3
G232.975−00.752	2/2	1	25.4	5.0	0.9 ± 0.1	2.5 ± 0.3
	1/2	1	46.6	9.9	1.8 ± 0.1	5.7 ± 0.3
G233.025−00.580	1/3	1	47.0	6.9	1.1 ± 0.1	2.7 ± 0.2
G233.045−00.550	1/1	1	46.1	6.9	0.8 ± 0.1	1.5 ± 0.2
G233.120−01.749	1/1	1	51.1	3.0	0.8 ± 0.1	1.2 ± 0.2
G233.140−01.220	2/3	1	32.6	5.0	0.3 ± 0.1	0.5 ± 0.2
	1/3	1	48.8	7.9	3.1 ± 0.1	7.7 ± 0.3
G233.140−01.540	1/1	1	50.5	10.9	1.6 ± 0.1	4.7 ± 0.3
G233.180−01.710	1/2	1	51.2	9.9	2.9 ± 0.1	9.3 ± 0.3
	2/2	1	61.1	6.0	0.9 ± 0.1	1.7 ± 0.2
G233.200−00.960	1/1	1	46.5	11.9	1.2 ± 0.1	4.1 ± 0.3
G233.208−01.340	1/1	1	47.6	6.0	0.9 ± 0.1	2.3 ± 0.3
G233.241−01.908	1/1	1	46.0	6.0	0.4 ± 0.2	0.5 ± 0.2
G233.250+00.100	2/3	2	19.6	9.9	1.4 ± 0.1	3.3 ± 0.3
	1/3	1	40.7	11.9	2.5 ± 0.1	8.5 ± 0.4
G233.250−00.360	1/2	1	47.0	6.9	0.5 ± 0.1	1.1 ± 0.2
G233.250−01.030	1/2	1	47.2	9.9	3.5 ± 0.1	7.4 ± 0.2
G233.290−00.310	1/1	1	45.9	7.9	0.5 ± 0.1	1.2 ± 0.2
G233.320−00.330	1/1	1	44.6	7.9	1.7 ± 0.1	3.0 ± 0.2
G233.320−00.320	1/1	1	44.8	5.0	2.4 ± 0.1	3.9 ± 0.2
G233.380+00.120	2/2	1	15.8	5.0	2.2 ± 0.1	5.5 ± 0.3
	1/2	1	42.9	7.9	4.1 ± 0.2	10.4 ± 0.4
G233.380−01.600	1/1	1	76.6	5.0	2.8 ± 0.1	3.7 ± 0.1
G233.390+00.120	2/3	1	15.7	5.0	2.1 ± 0.1	4.7 ± 0.3
	1/3	1	43.2	8.9	3.7 ± 0.1	11.2 ± 0.4
G233.460−00.360	1/1	1	44.4	5.0	2.2 ± 0.1	4.2 ± 0.2
G233.480−00.360	1/1	1	44.7	6.0	2.5 ± 0.1	3.5 ± 0.1
G233.500+00.130	2/2	2	16.6	8.9	1.4 ± 0.1	5.7 ± 0.4
	1/2	1	52.9	6.9	4.8 ± 0.1	9.8 ± 0.3
G233.730−01.330	1/1	1	75.6	8.9	2.6 ± 0.1	5.8 ± 0.2
G233.736−00.197	2/2	2	20.7	6.9	1.9 ± 0.1	3.0 ± 0.2
	1/2	1	44.2	11.9	6.2 ± 0.1	21.3 ± 0.5
G233.750−01.270	1/1	1	75.9	17.9	3.7 ± 0.1	15.0 ± 0.5

Table A.2: continued

Name	Group	# components	$v_{\rm lsr}$ (km s^{-1})	$\Delta v_{\rm lsr}$ (km s^{-1})	$T_{\rm max}$ (K)	$\int T dv$ (K km s^{-1})
G233.757−01.269	1/2	1	30.0	4.0	0.4 ± 0.1	0.5 ± 0.1
G233.760−01.250	1/1	1	76.9	8.9	2.2 ± 0.1	5.3 ± 0.2
G233.777−01.269	1/1	1	23.7	4.0	0.6 ± 0.1	0.9 ± 0.1
G233.810−00.110	2/2	1	19.9	6.0	0.2 ± 0.1	0.7 ± 0.3
	1/2	1	43.7	7.9	2.7 ± 0.1	6.8 ± 0.3
G233.840−00.183	2/2	1	20.3	7.9	1.8 ± 0.1	2.4 ± 0.1
	1/2	1	43.3	6.0	6.2 ± 0.2	10.0 ± 0.4
G233.980−01.860	1/1	1	48.5	8.9	3.2 ± 0.1	8.2 ± 0.3
G234.033−00.537	1/2	1	43.0	9.9	2.5 ± 0.1	4.2 ± 0.2
	2/2	1	56.2	6.9	0.2 ± 0.1	0.5 ± 0.2
G234.050−00.130	1/1	1	41.6	11.9	5.7 ± 0.1	12.0 ± 0.3
G234.050−01.910	1/1	1	49.9	9.9	4.4 ± 0.1	10.8 ± 0.3
G234.052−02.176	2/2	1	23.5	6.0	0.4 ± 0.1	0.9 ± 0.2
	1/2	1	48.9	3.0	2.6 ± 0.1	3.3 ± 0.1
G234.121+00.315	1/1	1	55.5	5.0	0.7 ± 0.1	1.0 ± 0.1
G234.131+00.315	1/2	1	56.6	4.0	0.3 ± 0.1	0.5 ± 0.2
G234.234−00.717	1/2	1	42.1	8.9	6.3 ± 0.3	8.3 ± 0.4
G234.260−01.490	1/1	1	69.1	6.9	1.0 ± 0.1	1.8 ± 0.2
G234.270−01.500	1/3	1	69.0	4.0	0.2 ± 0.1	0.4 ± 0.2
G234.333−00.651	1/3	1	39.6	11.9	3.6 ± 0.1	7.1 ± 0.2
	2/3	1	74.9	6.0	0.1 ± 0.1	0.3 ± 0.3
G234.356−02.813	1/1	1	58.9	4.0	1.3 ± 0.4	1.5 ± 0.4
G234.450−01.070	1/1	1	77.3	7.9	4.3 ± 0.1	9.5 ± 0.2
G234.468−00.393	1/1	1	41.8	18.9	12.4 ± 0.1	52.7 ± 0.8
G234.493−00.829	1/3	1	76.9	9.9	2.2 ± 0.1	5.9 ± 0.3
G234.501−00.863	2/2	1	25.6	4.0	0.3 ± 0.3	0.4 ± 0.4
	1/2	1	77.5	12.9	4.0 ± 0.1	12.6 ± 0.3
G234.570−01.003	1/1	1	44.5	10.9	2.9 ± 0.1	4.9 ± 0.2
G234.580−01.030	1/1	1	44.8	7.9	3.0 ± 0.1	4.7 ± 0.2
G234.590−01.080	1/1	1	22.9	5.0	0.4 ± 0.1	0.6 ± 0.2
G234.620−00.197	1/1	1	42.6	15.9	11.4 ± 8.5	62.3 ± 46.6
G234.650−01.580	1/1	1	68.5	12.9	5.7 ± 0.1	16.6 ± 0.3
G234.660+00.070	1/2	1	27.9	4.0	3.0 ± 0.1	4.0 ± 0.1
	2/2	1	44.7	9.9	1.0 ± 0.1	2.5 ± 0.2
G234.710−00.910	1/2	1	76.6	6.0	1.6 ± 0.1	2.7 ± 0.2
G234.715−00.911	1/1	1	77.0	7.9	4.3 ± 0.1	8.8 ± 0.2
G234.720−00.820	1/1	1	78.1	5.0	0.3 ± 0.1	0.5 ± 0.2
G234.730−00.750	1/1	1	77.9	6.0	2.2 ± 0.1	3.8 ± 0.2
G234.730−00.810	1/1	1	78.2	8.9	4.7 ± 0.1	10.0 ± 0.2
G234.764−00.282	1/1	1	43.3	8.9	21.2 ± 0.1	35.8 ± 0.4
G234.790+00.062	1/1	1	28.4	6.9	0.5 ± 0.1	1.1 ± 0.2
G234.860−00.090	1/1	1	43.4	9.9	8.4 ± 0.1	21.9 ± 0.4
G234.880−00.130	1/1	1	42.8	6.0	5.3 ± 0.1	7.2 ± 0.2
G234.890−00.180	1/1	1	43.0	7.9	3.9 ± 0.1	5.8 ± 0.2
G235.050−01.530	2/2	1	70.2	5.0	0.7 ± 0.1	1.2 ± 0.2
	1/2	1	81.4	15.9	13.5 ± 0.1	42.9 ± 0.4
G235.060−01.550	2/2	1	70.5	6.0	0.5 ± 0.1	0.9 ± 0.2
	1/2	1	81.7	13.9	6.8 ± 0.1	24.3 ± 0.4
G235.150−01.530	1/1	1	81.2	8.9	2.5 ± 0.1	6.4 ± 0.3

Table A.2: continued

Name	Group	# components	$v_{\rm lsr}$ (km s^{-1})	$\Delta v_{\rm lsr}$ (km s^{-1})	$T_{\rm max}$ (K)	$\int T dv$ (K km s^{-1})
G235.220−01.670	1/1	2	81.6	12.9	2.8 ± 0.3	13.2 ± 1.3
G235.347−01.740	1/2	1	81.1	15.9	3.1 ± 0.1	10.7 ± 0.4
G235.348−01.687	1/1	1	81.7	9.9	3.9 ± 0.1	9.1 ± 0.2
G235.360−01.470	1/2	1	72.5	6.9	1.4 ± 0.1	2.0 ± 0.1
G235.389−01.655	1/2	1	82.3	10.9	10.9 ± 0.1	30.4 ± 0.3
G235.477−01.769	2/2	1	23.5	4.0	0.3 ± 0.1	0.5 ± 0.2
	1/2	1	79.5	12.9	2.1 ± 0.1	8.6 ± 0.4
G235.532−01.675	1/1	1	83.2	7.9	4.7 ± 0.1	19.5 ± 0.4
G235.590−01.520	1/1	1	74.0	5.0	1.5 ± 0.1	2.6 ± 0.2
G235.610−00.710	1/1	1	48.9	7.9	2.2 ± 0.2	6.4 ± 0.5
G235.680−00.030	1/1	1	47.4	7.9	1.9 ± 0.1	3.5 ± 0.2
G235.690−01.240	1/1	1	75.1	9.9	7.9 ± 0.1	15.5 ± 0.2
G235.780+00.010	1/1	1	51.6	8.9	4.7 ± 0.1	11.9 ± 0.3
G235.907−01.613	1/2	1	30.1	6.0	3.6 ± 0.1	4.2 ± 0.2
	2/2	1	53.0	3.0	0.2 ± 0.1	0.3 ± 0.1
G236.180−01.830	1/3	2	30.3	8.9	6.5 ± 0.2	17.9 ± 0.6
	2/3	1	79.5	8.9	0.2 ± 0.1	0.9 ± 0.4
G236.420−00.710	1/2	1	24.5	3.0	3.3 ± 0.1	5.2 ± 0.2
	2/2	1	48.0	6.0	0.9 ± 0.1	1.3 ± 0.2
G236.490−00.590	1/2	1	25.0	7.9	3.0 ± 0.1	8.0 ± 0.4
	2/2	1	56.0	6.9	2.2 ± 0.1	3.3 ± 0.2
G236.570−00.460	1/1	1	49.5	6.9	1.0 ± 0.1	2.1 ± 0.2
G236.600−02.130	1/2	1	25.6	22.8	10.7 ± 0.1	64.7 ± 1.4
G236.600−02.290	1/2	1	26.8	11.9	6.7 ± 0.1	22.2 ± 0.5
G236.600−02.310	1/2	1	26.9	18.9	4.2 ± 0.1	21.1 ± 0.6
	2/2	1	79.5	8.9	0.2 ± 0.1	0.7 ± 0.3
	2/2	1	80.6	7.9	0.8 ± 0.1	2.6 ± 0.3
	2/2	1	81.1	8.9	0.8 ± 0.1	1.9 ± 0.2
G236.610−02.110	1/3	2	24.2	18.9	5.5 ± 0.2	23.6 ± 1.1
G236.610+00.010	2/2	1	24.3	6.9	0.7 ± 0.1	1.3 ± 0.2
	1/2	1	47.4	7.9	3.6 ± 0.1	7.3 ± 0.2
	2/3	1	79.5	6.0	0.2 ± 0.1	0.4 ± 0.2
G236.620+00.000	1/2	1	46.9	5.0	2.9 ± 0.1	4.7 ± 0.2
G236.630−01.150	1/3	1	28.7	6.9	3.2 ± 0.1	4.6 ± 0.2
G236.717−01.611	1/2	1	18.8	6.0	0.7 ± 0.1	0.9 ± 0.1
G236.880−01.010	1/1	1	79.9	6.9	6.1 ± 0.2	10.6 ± 0.3
G236.950−00.780	1/1	1	20.2	6.0	2.2 ± 0.1	5.4 ± 0.3
G237.000−01.840	2/2	1	23.9	6.9	1.3 ± 0.1	2.5 ± 0.2
	1/2	1	80.6	11.9	10.8 ± 0.1	29.1 ± 0.3
G237.050−00.770	1/2	1	22.1	6.0	3.3 ± 0.1	7.2 ± 0.3
	2/2	1	78.7	5.0	1.6 ± 0.1	2.1 ± 0.1
G237.100−00.820	1/1	1	21.3	9.9	3.3 ± 0.1	13.1 ± 0.5
G237.110−00.990	1/1	1	21.4	8.9	3.5 ± 0.1	11.7 ± 0.4
G237.110−00.790	1/1	1	22.2	6.0	2.9 ± 0.1	5.4 ± 0.2
G237.110−00.300	1/1	1	55.7	6.0	2.7 ± 0.1	6.4 ± 0.2
G237.170−00.960	1/1	1	21.9	10.9	4.2 ± 0.1	11.1 ± 0.4
G237.178−01.909	1/1	1	22.8	6.0	1.8 ± 0.1	4.1 ± 0.2
G237.180−01.470	2/2	1	22.5	6.9	1.0 ± 0.1	1.8 ± 0.2
	1/2	1	70.8	8.9	2.0 ± 0.1	4.4 ± 0.2

Table A.2: continued

Name	Group	# components	$v_{\rm lsr}$ (km s^{-1})	$\Delta v_{\rm lsr}$ (km s^{-1})	$T_{\rm max}$ (K)	$\int T dv$ (K km s^{-1})
G237.210−01.440	1/1	1	73.9	5.0	5.2 ± 0.4	7.4 ± 0.6
G237.230−01.060	2/2	1	24.0	6.9	1.2 ± 0.1	2.6 ± 0.2
	1/2	1	77.1	5.0	2.9 ± 0.1	5.1 ± 0.2
G237.240−01.080	2/2	1	22.8	6.0	3.1 ± 0.1	5.0 ± 0.2
	1/2	1	77.4	9.9	4.4 ± 0.2	9.2 ± 0.4
G237.243−02.556	1/1	1	26.1	1.0	0.5 ± 0.5	0.4 ± 0.4
G237.247−01.679	1/2	1	23.9	5.0	0.3 ± 0.1	0.4 ± 0.2
G237.260−01.280	2/2	1	21.9	7.9	1.4 ± 0.1	2.2 ± 0.2
G237.260−01.300	2/2	1	22.0	7.9	0.8 ± 0.1	1.4 ± 0.2
G237.260−01.260	2/2	1	22.1	6.9	2.5 ± 0.1	3.5 ± 0.2
	1/2	2	70.2	15.9	14.0 ± 0.3	48.4 ± 1.0
	1/2	2	71.5	17.9	16.6 ± 0.3	72.8 ± 1.6
	1/2	2	73.4	20.8	11.3 ± 0.4	62.8 ± 2.1
G237.320−01.280	2/2	1	22.7	6.0	0.5 ± 0.1	0.9 ± 0.2
	1/2	1	78.3	14.9	17.5 ± 0.1	51.6 ± 0.5
G237.330−01.260	1/1	2	77.8	8.9	3.2 ± 0.2	11.7 ± 0.7
G237.347−01.669	1/1	1	83.1	6.0	0.3 ± 0.1	1.0 ± 0.3
G237.460−01.790	1/1	1	22.9	9.9	3.4 ± 0.1	7.7 ± 0.3
G237.499−01.978	1/3	1	32.5	4.0	0.2 ± 0.2	0.2 ± 0.2
G237.500−02.018	1/1	1	82.8	2.0	0.2 ± 0.1	0.3 ± 0.1
G237.511−02.336	1/1	1	20.7	6.9	2.8 ± 0.1	5.3 ± 0.2
G237.530−01.380	1/2	1	75.9	6.9	1.2 ± 0.1	1.9 ± 0.2
G237.540−00.660	1/1	2	59.6	6.9	0.5 ± 0.1	1.1 ± 0.2
G237.550−00.640	1/1	2	56.9	7.9	1.2 ± 0.1	2.0 ± 0.2
G237.660−01.790	1/1	1	23.4	6.0	0.9 ± 0.1	2.2 ± 0.3
G237.661−00.514	1/1	1	56.2	7.9	2.6 ± 0.1	5.6 ± 0.2
G237.740−00.970	1/2	1	21.7	14.9	11.9 ± 0.2	47.7 ± 1.3
G237.740−00.960	1/1	1	22.0	13.9	14.2 ± 0.2	52.6 ± 1.5
	2/2	1	81.5	3.0	0.2 ± 0.1	0.3 ± 0.2
G237.763−02.684	1/2	1	62.5	5.0	0.5 ± 0.1	0.9 ± 0.2
G237.770−01.010	1/1	1	22.2	6.9	4.2 ± 0.1	8.9 ± 0.3
G237.820−01.280	2/2	1	23.6	6.9	1.7 ± 0.1	3.7 ± 0.2
	1/2	1	75.8	12.9	5.8 ± 0.1	15.4 ± 0.3
G237.836−01.558	1/1	1	22.6	6.9	0.9 ± 0.1	1.4 ± 0.2
G237.845−01.538	1/1	1	22.5	5.0	0.9 ± 0.1	1.5 ± 0.2
G237.940−01.170	1/1	2	21.1	8.9	3.2 ± 0.2	9.5 ± 0.8
G237.963−02.684	1/1	1	19.7	3.0	1.3 ± 1.2	1.1 ± 1.1
G238.038−01.867	1/1	1	78.9	3.0	0.4 ± 0.1	0.7 ± 0.2
G238.260−01.720	1/1	2	22.3	13.9	11.7 ± 1.0	26.6 ± 2.4
G238.511−00.885	1/1	1	23.7	5.0	2.5 ± 0.1	3.9 ± 0.2
G238.540−00.920	1/1	1	24.0	4.0	1.6 ± 0.1	1.9 ± 0.1
G238.560+00.240	1/1	1	22.2	7.9	0.5 ± 0.1	1.0 ± 0.2
G238.670−01.440	1/1	1	20.3	11.9	4.5 ± 0.1	13.3 ± 0.4
G238.690−01.860	1/1	2	88.3	14.9	3.2 ± 0.1	10.9 ± 0.3
G238.700−01.270	1/1	1	20.2	6.9	2.2 ± 0.1	3.2 ± 0.2
G238.750−01.460	1/1	1	18.4	18.9	3.5 ± 0.1	21.2 ± 0.8
G238.770−01.810	2/4	1	19.6	3.0	0.6 ± 0.1	0.8 ± 0.2
	1/4	1	88.4	13.9	5.9 ± 0.1	24.6 ± 0.4
G238.800−01.630	1/1	2	17.3	16.9	2.8 ± 0.4	17.7 ± 2.5

Table A.2: continued

Name	Group	# components	$v_{\rm lsr}$ (km s^{-1})	$\Delta v_{\rm lsr}$ (km s^{-1})	$T_{\rm max}$ (K)	$\int T dv$ (K km s^{-1})
G238.830−02.080	1/2	1	81.1	9.9	–	–
G238.960−01.680	2/2	1	18.5	8.9	4.0±0.1	8.3±0.3
	1/2	1	83.1	10.9	3.2±0.2	10.0±0.8
G238.970−02.030	1/1	1	81.2	8.9	4.4±0.1	8.5±0.2
G239.190−01.960	1/2	1	83.0	12.9	4.3±0.1	13.7±0.3
G239.300−00.630	1/1	1	64.7	8.9	2.6±0.1	4.8±0.2
G239.370−01.690	1/2	2	18.8	21.8	6.8±0.1	28.3±0.9
G239.370−00.080	1/1	1	66.9	5.0	1.6±0.1	2.7±0.2
	2/2	1	85.9	7.9	0.8±0.1	1.9±0.2
G239.524−00.711	1/1	1	65.3	5.0	1.6±0.1	2.5±0.2
G239.533−01.457	1/1	1	83.4	5.0	0.9±0.1	2.1±0.2
G239.594−01.524	2/2	1	19.9	7.9	0.2±0.1	0.9±0.5
	1/2	1	85.5	3.0	0.2±0.1	0.4±0.2
G239.630−02.090	1/1	1	78.4	8.9	1.7±0.1	5.5±0.3
G239.650−00.810	1/1	1	64.6	6.0	2.6±0.2	4.5±0.4
G239.660−02.040	2/2	1	24.1	7.9	0.5±0.1	1.0±0.2
	1/2	1	78.3	7.9	1.2±0.1	3.5±0.3
G239.678−00.802	1/1	1	65.1	11.9	2.7±0.1	9.7±0.4
G239.680−02.040	2/2	1	24.4	5.0	0.8±0.1	1.5±0.2
	1/2	1	77.9	9.9	1.6±0.1	3.8±0.2
G239.945−01.702	1/1	1	18.2	6.0	3.5±0.1	4.9±0.2
G239.950−01.810	1/3	1	17.9	8.9	6.8±0.1	16.1±0.5
	3/3	1	24.3	1.0	0.2±0.1	0.2±0.1
	2/3	1	27.0	6.0	0.6±0.1	1.0±0.2
G239.990−01.730	1/1	2	20.4	13.9	4.3±0.1	9.6±0.4
G240.040−01.840	1/2	1	18.9	4.0	4.5±0.1	7.9±0.3
	2/2	1	23.6	7.9	0.6±0.1	1.2±0.2
G240.095−00.180	1/1	1	63.8	7.9	5.8±0.1	8.3±0.2
G240.140−01.540	1/2	1	31.9	6.9	7.0±0.1	9.6±0.2
G240.170−01.590	2/3	1	25.2	6.0	0.5±0.1	0.7±0.2
	3/3	1	64.1	4.0	0.4±0.1	0.7±0.2
	1/3	1	71.5	6.0	1.1±0.1	2.3±0.2
G240.250−00.910	1/1	1	17.6	7.9	3.6±0.1	6.0±0.2
G240.320+00.070	1/1	2	64.5	40.7	17.0±0.9	194.7±9.8
G240.440−02.428	1/2	1	25.6	3.0	0.8±0.1	0.9±0.1
G240.490−00.070	1/1	1	68.8	5.0	3.9±0.1	4.6±0.1
G240.545−01.800	1/2	1	65.0	6.9	0.3±0.1	0.6±0.2
G240.940−01.440	1/1	1	65.5	7.9	2.7±0.1	7.0±0.3
G240.990−01.470	1/2	1	19.0	8.9	2.7±0.1	5.8±0.3
	2/2	1	64.0	6.0	1.1±0.1	2.1±0.2
G241.003−01.203	1/1	2	62.8	17.9	4.4±0.2	22.7±1.1
G241.010−01.200	1/1	2	66.4	17.9	3.3±0.2	21.0±1.1
G241.121−00.781	1/1	1	70.1	10.9	3.8±0.1	10.4±0.3
G241.140−01.170	1/1	1	64.7	9.9	3.0±0.1	10.4±0.4
G241.160−00.960	1/1	1	64.4	6.9	1.0±0.1	3.5±0.3
G241.180−01.070	1/1	2	65.9	8.9	2.8±0.2	9.4±0.5
G241.190−00.780	1/1	1	68.3	8.9	4.0±0.1	11.6±0.3
G241.290−00.710	1/1	1	69.2	23.8	–	–
G241.390−02.030	1/1	1	18.9	8.9	2.2±0.1	5.9±0.3

Table A.2: continued

Name	Group	# components	$v_{\rm lsr}$ (km s^{-1})	$\Delta v_{\rm lsr}$ (km s^{-1})	$T_{\rm max}$ (K)	$\int T dv$ (K km s^{-1})
G241.420−00.700	1/1	2	71.6	13.9	3.6 ± 0.1	20.5 ± 0.8
G241.436−02.056	1/2	1	19.7	6.0	0.5 ± 0.1	1.6 ± 0.3
G241.454−01.847	1/1	1	21.7	6.0	1.7 ± 0.1	2.4 ± 0.1
G241.483−01.668	1/1	1	17.8	6.9	1.4 ± 0.1	1.9 ± 0.1
G241.530−00.600	1/1	1	70.8	11.9	10.9 ± 0.1	38.6 ± 0.5
G241.538−00.594	1/1	1	70.5	15.9	11.9 ± 0.1	38.5 ± 0.4
G241.560−00.590	1/1	1	70.5	8.9	10.2 ± 0.1	22.2 ± 0.3
G241.570−00.640	1/1	1	70.0	17.9	8.0 ± 0.1	32.7 ± 0.5
G241.640−00.650	1/1	1	68.4	9.9	6.3 ± 0.1	21.0 ± 0.4
G241.653−01.410	1/1	1	26.1	4.0	0.2 ± 0.1	0.4 ± 0.2
G241.680−00.580	1/3	1	69.3	16.9	8.2 ± 0.1	34.2 ± 0.5
G241.762−01.310	1/1	1	23.9	5.0	0.4 ± 0.1	0.6 ± 0.2
G241.815−00.627	1/1	1	69.0	13.9	3.4 ± 0.1	12.9 ± 0.4
G241.820−00.620	1/1	1	68.9	11.9	4.6 ± 0.1	15.4 ± 0.4
G241.820+00.000	1/1	1	69.2	5.0	1.3 ± 0.1	3.3 ± 0.2
G241.867−00.563	1/1	1	68.9	6.0	2.8 ± 0.1	5.8 ± 0.2
G241.971−00.848	1/1	2	65.5	12.9	2.7 ± 0.2	15.2 ± 1.1
G242.020+00.190	1/2	1	69.7	7.9	1.6 ± 0.1	4.1 ± 0.3
G242.111−01.507	1/1	1	20.9	4.0	0.2 ± 0.1	0.3 ± 0.2
G242.190+00.010	1/1	1	67.2	26.8	5.3 ± 0.1	28.1 ± 0.6
G242.190−00.780	1/2	1	67.3	6.0	0.5 ± 0.1	1.1 ± 0.2
	2/2	1	70.3	4.0	0.3 ± 0.1	0.4 ± 0.2
G242.210+00.040	1/1	2	67.6	7.9	1.2 ± 0.1	5.7 ± 0.5
G242.250+00.020	1/2	1	68.5	2.0	0.6 ± 0.2	0.7 ± 0.2
	2/2	1	73.2	3.0	0.3 ± 0.2	0.5 ± 0.4
G242.260+00.040	1/1	1	70.2	6.9	1.5 ± 0.1	5.5 ± 0.6
G242.310+00.070	1/1	2	70.7	8.9	1.6 ± 0.1	8.5 ± 0.6
G242.320+00.040	1/1	2	69.6	6.9	1.8 ± 0.1	6.6 ± 0.5
G242.320+00.100	1/1	1	70.1	10.9	2.7 ± 0.1	7.6 ± 0.3
G242.337−01.093	2/2	1	18.1	5.0	1.0 ± 0.1	1.4 ± 0.1
	1/2	1	65.2	12.9	2.8 ± 0.1	9.6 ± 0.3
G242.340+00.010	1/1	2	71.8	7.9	1.7 ± 0.1	6.5 ± 0.4
G242.482−01.665	1/1	1	18.4	6.9	0.3 ± 0.1	0.5 ± 0.2
G242.490+00.000	1/1	1	69.2	6.0	1.1 ± 0.1	2.4 ± 0.3
G242.540+00.040	1/2	2	70.2	8.9	2.2 ± 0.1	5.5 ± 0.3
G242.545−00.848	1/1	1	65.9	7.9	2.6 ± 0.1	5.2 ± 0.2
G242.560−00.630	1/2	1	65.6	12.9	4.0 ± 0.1	13.9 ± 0.4
	2/2	1	74.8	6.9	0.4 ± 0.1	0.8 ± 0.2
G242.590−00.240	1/1	1	21.3	3.0	0.3 ± 0.1	0.4 ± 0.2
G242.604−00.789	1/1	1	62.3	4.0	0.3 ± 0.1	0.5 ± 0.2
G242.610+00.070	1/2	1	70.3	7.9	2.4 ± 0.1	5.9 ± 0.3
G242.620−00.690	1/1	1	65.8	11.9	5.3 ± 0.1	14.7 ± 0.3
G242.625−00.878	1/1	1	65.6	5.0	0.3 ± 0.1	0.6 ± 0.2
G242.640−00.700	1/1	1	65.7	8.9	5.2 ± 0.1	13.5 ± 0.3
G242.660+00.130	1/1	1	70.5	6.9	1.4 ± 0.1	3.4 ± 0.4
G242.770−01.530	1/1	1	18.0	7.9	–	–
G242.775−00.888	1/1	1	63.1	10.9	1.2 ± 0.1	4.5 ± 0.4
G242.810+00.080	1/1	1	55.8	9.9	4.6 ± 0.1	11.5 ± 0.3
G242.819−00.949	1/1	1	18.6	7.9	0.4 ± 0.1	0.6 ± 0.2

Table A.2: continued

Name	Group	# components	$v_{\rm lsr}$ (km s^{-1})	$\Delta v_{\rm lsr}$ (km s^{-1})	$T_{\rm max}$ (K)	$\int T dv$ (K km s^{-1})
G242.850−01.515	1/1	1	17.8	6.0	0.9 ± 0.1	1.1 ± 0.1
G242.880−02.250	1/1	1	21.3	4.0	–	–
G242.910−01.574	1/1	1	19.1	8.9	1.3 ± 0.1	1.9 ± 0.2
G242.920−00.520	1/1	1	62.7	24.8	7.0 ± 0.1	35.3 ± 0.6
G242.920−00.450	1/1	1	63.4	13.9	6.7 ± 0.1	20.5 ± 0.3
G242.940−00.500	1/2	1	62.5	18.9	5.4 ± 0.1	28.9 ± 0.6
G242.940−00.450	1/2	2	62.6	26.8	7.7 ± 1.9	79.7 ± 20.0
G242.944−00.758	1/1	1	67.2	6.9	2.4 ± 0.1	4.8 ± 0.2
G243.067−02.410	1/1	1	22.2	3.0	–	–
G243.150−00.170	1/1	1	53.8	9.9	1.5 ± 0.1	4.0 ± 0.3
G243.160−01.520	1/1	2	15.9	7.9	1.2 ± 1.0	5.0 ± 4.1
G243.190−00.160	2/2	1	14.3	6.9	0.8 ± 0.2	1.2 ± 0.3
	1/2	1	53.6	8.9	3.3 ± 0.1	5.6 ± 0.2
G243.200−00.330	1/2	1	58.4	5.0	1.9 ± 0.2	2.4 ± 0.2
	2/2	1	63.1	7.9	1.3 ± 0.1	2.9 ± 0.2
G243.208−01.334	1/1	1	18.1	6.0	0.7 ± 0.1	0.9 ± 0.1
G243.209−01.404	1/2	1	18.3	6.0	1.3 ± 0.1	1.9 ± 0.2
G243.220−01.970	2/2	1	20.1	5.0	1.6 ± 0.1	2.4 ± 0.2
	1/2	1	30.0	5.0	2.7 ± 0.1	5.3 ± 0.3
G243.450−01.620	1/1	1	17.7	7.9	2.0 ± 0.1	3.7 ± 0.2
G243.457−02.399	1/1	1	21.1	6.0	2.0 ± 0.1	4.3 ± 0.2
G243.470+00.340	1/2	1	57.3	7.9	0.4 ± 0.1	1.0 ± 0.3
G243.475−01.045	1/1	1	21.8	6.9	1.6 ± 0.1	3.2 ± 0.2
G243.521−02.846	1/1	2	25.2	6.0	1.0 ± 0.1	2.7 ± 0.3
G243.540−00.810	1/1	1	22.7	16.9	4.3 ± 0.1	18.2 ± 0.6
G243.670−00.355	1/2	1	13.1	6.9	0.7 ± 0.6	1.6 ± 1.2
G243.751−00.536	1/1	1	66.5	6.9	1.9 ± 0.1	3.1 ± 0.2
G243.751−00.546	1/1	1	66.4	6.0	0.6 ± 0.1	1.0 ± 0.2
G243.770−01.420	1/2	1	17.3	6.9	3.2 ± 0.1	4.9 ± 0.2
G243.771−00.596	2/2	1	21.5	6.0	1.2 ± 0.1	2.1 ± 0.2
	1/2	1	63.2	5.0	1.3 ± 0.1	2.4 ± 0.2
G243.780−00.240	2/2	1	15.3	6.0	0.5 ± 0.1	0.8 ± 0.2
	1/2	1	66.0	14.9	7.1 ± 0.1	18.7 ± 0.3
G243.820−00.350	1/1	1	65.7	8.9	4.1 ± 0.1	10.3 ± 0.3
G243.860−00.870	1/2	1	22.4	6.9	2.3 ± 0.1	4.9 ± 0.2
G243.950−00.200	2/2	1	15.9	5.0	0.1 ± 0.1	0.3 ± 0.3
	1/2	1	64.6	5.0	1.6 ± 0.2	2.0 ± 0.2
G244.235−01.083	1/2	1	19.4	9.9	1.9 ± 0.1	4.2 ± 0.2
G244.410−01.970	1/1	1	92.4	11.9	1.9 ± 0.1	7.8 ± 0.4
G244.460−00.540	1/1	1	20.1	6.0	1.1 ± 0.1	2.1 ± 0.2
G244.680−00.840	1/3	1	19.3	6.0	1.3 ± 0.1	2.9 ± 0.2
	2/3	1	22.7	5.0	0.2 ± 0.1	0.3 ± 0.2
G244.747−01.419	1/1	1	14.7	2.0	0.3 ± 0.3	0.4 ± 0.4
G244.760−00.320	2/2	1	19.9	5.0	0.2 ± 0.1	0.4 ± 0.2
	1/2	1	61.8	7.9	3.9 ± 0.1	8.6 ± 0.2
G244.830−00.960	1/1	1	18.3	6.9	3.0 ± 0.1	4.7 ± 0.2
G244.960−00.060	1/1	1	21.9	4.0	4.3 ± 0.1	4.8 ± 0.2
G245.040−00.050	1/1	1	22.7	6.9	5.2 ± 0.1	7.4 ± 0.2
G245.044−01.200	1/1	1	16.2	5.0	0.3 ± 0.1	0.4 ± 0.1

Table A.2: continued

Name	Group	# components	$v_{\rm lsr}$ (km s^{-1})	$\Delta v_{\rm lsr}$ (km s^{-1})	$T_{\rm max}$ (K)	$\int T dv$ (K km s^{-1})
G245.060+00.060	1/1	1	58.8	6.0	2.8 ± 0.1	4.4 ± 0.2
G245.060+00.080	1/1	1	59.7	6.0	10.9 ± 0.1	18.9 ± 0.2
G245.070−00.210	1/2	1	56.6	7.9	3.4 ± 0.1	4.9 ± 0.1
G245.080−00.180	1/1	1	20.7	5.0	3.9 ± 0.1	6.0 ± 0.2
G245.100−00.990	1/1	1	87.4	9.9	–	–
G245.170−00.050	1/2	1	21.1	7.9	2.8 ± 0.2	3.5 ± 0.2
	2/2	1	57.3	3.0	1.5 ± 0.1	2.3 ± 0.2
G245.240−01.390	1/1	1	12.6	6.0	1.1 ± 0.1	1.7 ± 0.2
G245.242−00.940	1/1	1	26.9	5.0	1.0 ± 0.1	1.7 ± 0.2
G245.300−00.300	1/1	1	59.7	8.9	7.1 ± 0.1	13.5 ± 0.2
G245.760−00.670	2/2	1	14.7	6.0	0.6 ± 0.6	1.4 ± 1.4
	1/2	1	63.8	3.0	1.6 ± 0.1	2.2 ± 0.2
G246.060+00.090	1/1	1	54.4	4.0	2.3 ± 0.2	2.6 ± 0.2
G246.270−00.070	1/1	1	56.5	7.9	2.0 ± 0.1	4.3 ± 0.2
G246.360−00.750	1/1	1	20.4	6.9	0.8 ± 0.1	1.8 ± 0.2
G246.410−00.680	1/1	1	20.9	8.9	0.9 ± 0.1	2.7 ± 0.3
G246.790−02.430	1/1	1	19.6	3.0	1.1 ± 0.2	1.5 ± 0.3
G246.970−01.720	2/2	1	19.3	5.0	0.9 ± 0.1	1.6 ± 0.2
	1/2	1	57.7	6.9	3.3 ± 0.1	4.8 ± 0.2
G247.240−01.120	1/1	1	19.5	2.0	3.5 ± 0.1	5.3 ± 0.2
G247.270−00.570	1/1	1	22.0	7.9	1.3 ± 0.1	3.9 ± 0.3
G247.280−00.560	1/1	1	22.2	9.9	0.9 ± 0.1	3.3 ± 0.4
G247.440−00.930	1/1	1	18.1	6.9	3.6 ± 0.1	7.0 ± 0.3
G247.460−00.820	1/1	1	20.5	4.0	3.8 ± 0.1	6.6 ± 0.2
G247.510+00.060	2/2	1	16.4	6.0	0.5 ± 0.1	1.1 ± 0.2
G247.510−00.570	2/2	2	25.5	10.9	1.2 ± 0.1	3.3 ± 0.3
	1/2	1	56.4	3.0	1.7 ± 0.1	2.6 ± 0.2
	1/2	1	56.5	6.9	2.0 ± 0.1	3.2 ± 0.2
G247.520+00.050	2/2	1	16.1	6.9	0.5 ± 0.1	1.0 ± 0.2
G247.520−00.240	1/1	1	16.5	6.0	0.7 ± 0.1	1.3 ± 0.2
	1/2	1	56.4	5.0	4.7 ± 0.2	5.8 ± 0.2
G247.528−01.988	2/2	1	8.4	2.0	0.2 ± 0.1	0.3 ± 0.2
	1/2	1	21.6	3.0	0.3 ± 0.1	0.5 ± 0.1
G247.590−00.820	2/2	1	20.0	6.9	2.8 ± 0.1	5.6 ± 0.2
	1/2	1	57.4	6.0	4.1 ± 1.0	4.7 ± 1.2
G247.610−00.830	1/1	2	20.0	6.9	1.7 ± 0.1	4.5 ± 0.3
G247.630−00.550	2/2	1	29.6	6.0	1.5 ± 0.1	2.5 ± 0.2
	1/2	1	56.5	6.0	13.5 ± 0.1	20.0 ± 0.2
G247.640−00.530	2/2	1	30.4	6.0	1.2 ± 0.1	2.1 ± 0.2
	1/2	1	57.6	6.0	4.2 ± 0.1	7.7 ± 0.2
G247.786−00.813	1/1	1	29.8	2.0	0.3 ± 0.1	0.3 ± 0.1
G247.790−00.840	2/2	1	20.9	8.9	0.3 ± 0.1	1.1 ± 0.4
	1/2	1	29.8	8.9	3.9 ± 0.1	7.7 ± 0.2
G247.796−00.823	1/2	1	18.3	4.0	0.2 ± 0.1	0.3 ± 0.2
G247.865−01.226	1/1	1	19.7	4.0	0.7 ± 0.1	0.9 ± 0.1
G247.890−00.990	1/2	1	20.7	4.0	4.0 ± 0.1	7.1 ± 0.3
	2/2	1	24.6	7.9	0.3 ± 0.1	0.9 ± 0.4
G247.930−00.440	1/1	1	53.4	13.9	4.9 ± 0.1	13.1 ± 0.3
G248.000−00.430	1/1	1	53.1	8.9	3.2 ± 0.1	5.5 ± 0.2

Table A.2: continued

Name	Group	# components	$v_{\rm lsr}$ (km s^{-1})	$\Delta v_{\rm lsr}$ (km s^{-1})	$T_{\rm max}$ (K)	$\int T dv$ (K km s^{-1})
G248.074−01.708	1/1	1	9.7	4.0	0.7±0.2	0.7±0.2
G248.150−02.210	1/1	1	19.7	5.0	1.2±0.3	1.4±0.3
G248.223−01.126	1/1	1	17.4	7.9	1.2±0.1	2.0±0.2
G248.440−00.910	1/2	1	18.1	6.9	3.5±0.1	6.7±0.3
G248.690−01.930	1/2	1	18.6	6.0	1.9±1.6	2.9±2.4
G248.700−01.010	1/1	1	17.4	8.9	3.4±0.1	6.0±0.2
G248.810−01.770	1/1	1	23.2	3.0	1.5±0.1	2.9±0.3
G248.890−00.010	1/1	1	14.0	4.0	14.8±0.1	29.6±1.1
G248.984−02.789	1/2	2	20.3	6.0	2.6±0.2	7.7±0.5
	2/2	1	46.4	3.0	0.5±0.1	0.7±0.1
G249.102−02.629	1/1	1	18.4	5.0	1.7±0.1	2.9±0.3
G249.170+00.110	1/1	1	11.0	5.0	1.1±0.1	1.4±0.1
G249.170−02.020	1/2	1	18.4	6.0	1.3±0.1	2.5±0.2
	2/2	1	22.9	5.0	0.3±0.1	0.6±0.2
G249.390−01.410	1/2	1	15.4	5.0	1.9±0.1	3.5±0.3
G249.450−02.420	2/2	1	22.2	3.0	0.5±0.1	0.7±0.2
	1/2	1	27.3	6.9	2.3±0.1	4.5±0.2
G249.530−02.500	1/1	1	26.3	6.9	1.1±0.1	2.5±0.2
G249.600−02.080	2/2	1	16.0	6.0	2.0±0.1	4.2±0.3
	1/2	1	106.0	6.0	6.3±0.1	13.8±0.3
G249.680−02.100	1/1	1	15.3	6.9	3.7±0.2	5.5±0.3
G250.230−00.040	1/1	1	51.7	15.9	7.2±0.1	32.4±0.5
G250.270−00.980	2/2	1	14.6	6.0	0.2±0.1	0.5±0.2
	1/2	1	67.4	7.9	2.0±0.1	3.4±0.2
G250.360−00.980	2/2	1	14.7	7.9	0.9±0.1	2.2±0.3
	1/2	1	65.1	10.9	6.0±2.2	13.0±4.7
G250.590−00.650	2/2	1	65.6	9.9	1.5±0.1	5.4±0.4
	1/2	1	78.3	14.9	11.9±0.1	40.6±0.6
G250.811−01.338	1/2	1	13.8	5.0	0.9±0.1	1.4±0.2
G250.900−01.530	2/2	1	11.3	4.0	1.0±0.6	1.0±0.6
G250.900−02.050	1/3	1	47.9	6.9	1.8±0.1	3.7±0.2
	1/2	1	51.1	4.0	5.3±0.2	8.4±0.3
	2/3	1	56.2	5.0	0.3±0.1	0.6±0.2
G250.910−01.280	1/2	1	10.5	5.0	0.9±0.1	1.7±0.3
G251.040−01.030	1/1	1	9.3	6.9	3.4±0.1	8.4±0.5
G251.070−01.000	1/1	1	9.7	6.9	4.5±0.1	12.0±0.7
G251.070−00.980	1/1	1	10.0	11.9	4.7±0.1	14.0±0.8
G251.080−00.990	1/1	1	9.4	6.9	4.1±0.1	9.0±0.5
G251.160−01.990	1/2	1	56.4	7.9	7.2±0.1	12.3±0.2
G251.186−02.384	1/1	1	15.2	4.0	1.1±0.1	1.6±0.1
G251.190−01.970	1/2	1	55.3	8.9	6.9±0.1	12.7±0.2
G251.210−00.610	1/1	1	45.2	6.0	3.6±0.1	6.4±0.2
G251.230−01.950	1/1	1	53.6	17.9	9.7±0.1	45.3±0.7
G251.400−00.180	1/1	1	46.4	3.0	2.6±0.2	3.3±0.3
G251.410−00.980	1/1	1	14.8	6.9	2.0±0.1	3.9±0.2
G251.421−02.651	1/2	1	15.4	6.9	0.1±0.1	0.3±0.2
G251.450−02.840	1/1	2	15.1	11.9	0.4±0.1	1.0±0.2
G251.461−02.631	1/1	1	14.9	6.9	0.2±0.1	0.7±0.3
G251.485−01.468	1/1	1	13.7	4.0	0.2±0.1	0.4±0.2

Table A.2: continued

Name	Group	# components	$v_{\rm lsr}$ (km s^{-1})	$\Delta v_{\rm lsr}$ (km s^{-1})	$T_{\rm max}$ (K)	$\int T dv$ (K km s^{-1})
G251.670−01.040	1/1	1	14.0	5.0	0.7 ± 0.1	1.2 ± 0.2
G251.689−01.835	1/1	1	50.8	4.0	0.3 ± 0.1	0.5 ± 0.2
G251.750−01.010	1/2	1	14.0	6.9	2.0 ± 0.1	5.5 ± 0.3
G251.750−00.900	1/1	1	14.6	4.0	1.5 ± 0.3	2.3 ± 0.5
	2/2	1	45.6	6.9	0.2 ± 0.1	0.3 ± 0.2
G251.756−00.942	1/1	1	15.0	2.0	0.7 ± 0.1	0.8 ± 0.1
G251.786−00.913	1/1	1	14.8	5.0	1.1 ± 0.1	1.8 ± 0.2
G251.796−00.903	1/1	1	14.6	3.0	1.8 ± 0.1	2.7 ± 0.2
G251.800+00.050	1/2	1	5.5	4.0	5.3 ± 0.1	8.0 ± 0.7
G251.800+00.000	1/1	1	6.0	6.0	6.0 ± 0.1	7.2 ± 0.6
G251.870+00.020	1/1	1	5.3	4.0	9.5 ± 0.3	9.7 ± 1.0
G251.880−01.060	1/2	1	13.7	5.0	3.7 ± 0.1	7.1 ± 0.3
	2/2	1	45.7	6.9	1.0 ± 0.1	1.4 ± 0.1
G251.900−01.080	2/2	1	13.5	6.0	3.5 ± 0.1	6.1 ± 0.3
G251.900−01.060	2/2	1	13.5	6.0	4.0 ± 0.1	7.5 ± 0.3
	1/2	1	45.1	12.9	4.8 ± 0.2	11.5 ± 0.6
	1/2	1	45.5	6.9	3.5 ± 0.3	7.1 ± 0.6
G251.920−01.090	1/2	1	13.0	6.9	3.7 ± 0.2	9.2 ± 0.6
	2/2	1	45.4	4.0	3.7 ± 0.1	6.0 ± 0.2
G251.940−01.170	1/1	1	12.4	7.9	4.3 ± 0.1	10.2 ± 0.5
G251.950−01.190	1/1	2	12.8	9.9	2.7 ± 0.7	8.0 ± 2.1
G252.029−01.864	1/1	1	50.6	3.0	1.1 ± 0.1	1.8 ± 0.2
G252.068−00.860	1/1	1	13.1	5.0	0.6 ± 0.1	1.3 ± 0.2
G252.080−01.810	1/3	1	12.6	6.0	3.3 ± 0.4	6.3 ± 0.8
G252.080−01.290	1/1	1	13.0	8.9	3.7 ± 0.1	9.3 ± 0.4
	2/3	1	48.9	5.0	1.0 ± 0.4	1.9 ± 0.7
	3/3	1	53.5	6.0	0.3 ± 0.3	0.9 ± 0.9
G252.090−01.270	1/4	1	12.8	12.9	4.1 ± 0.1	10.6 ± 0.5
G252.100−01.220	1/1	2	11.9	10.9	2.5 ± 0.2	8.2 ± 0.6
G252.110−01.270	1/1	1	12.8	9.9	3.3 ± 0.1	9.7 ± 0.5
G252.120−01.170	1/1	1	12.9	13.9	4.5 ± 0.1	14.9 ± 0.7
G252.133−01.175	1/1	1	12.5	12.9	3.4 ± 0.1	13.0 ± 0.6
G252.159−01.913	1/1	1	10.8	4.0	0.7 ± 0.8	0.7 ± 0.8
G252.173−01.872	1/1	1	70.8	8.9	0.6 ± 0.1	2.2 ± 0.4
G252.179−01.933	1/2	1	10.8	5.0	1.5 ± 0.5	1.6 ± 0.5
G252.180−01.250	1/1	2	11.3	14.9	–	–
G252.180−01.080	1/1	1	44.2	6.0	2.6 ± 0.1	4.2 ± 0.2
G252.480−01.570	1/1	3	10.4	25.8	14.6 ± 0.5	66.6 ± 4.1
G252.510−01.440	1/2	2	9.2	9.9	7.9 ± 0.3	14.1 ± 0.9
	2/2	1	70.9	6.9	0.2 ± 0.1	0.4 ± 0.2
G252.520+00.080	1/1	1	4.8	14.9	9.3 ± 0.2	14.6 ± 1.5
G252.654−01.089	1/1	1	46.1	11.9	1.5 ± 0.1	4.8 ± 0.3
G252.680−01.530	1/1	3	6.7	11.9	6.7 ± 0.5	18.5 ± 1.9
G252.700−01.490	2/2	1	6.6	4.0	2.0 ± 0.1	3.2 ± 0.3
	1/2	2	10.4	8.9	2.2 ± 0.1	6.1 ± 0.5
G252.731−00.607	1/2	1	79.2	4.0	1.4 ± 0.1	1.7 ± 0.2
G252.792−01.727	1/1	1	6.9	6.0	5.5 ± 0.1	8.9 ± 0.7
G252.793−01.210	1/1	1	39.4	5.0	0.6 ± 0.1	1.0 ± 0.2
G252.803−01.190	1/1	2	43.1	7.9	0.6 ± 0.1	1.5 ± 0.3

Table A.2: continued

Name	Group	# components	$v_{\rm lsr}$ (km s^{-1})	$\Delta v_{\rm lsr}$ (km s^{-1})	$T_{\rm max}$ (K)	$\int T dv$ (K km s^{-1})
G252.840−00.470	1/1	1	12.4	6.0	4.9±0.6	7.2±0.9
G252.982−02.338	1/1	1	21.6	6.9	0.3±0.1	0.6±0.2
G253.030−01.990	1/1	1	11.6	6.0	4.1±0.1	6.2±0.3
G253.080−02.100	1/1	1	11.5	5.0	6.0±0.1	10.1±0.5
G253.100−01.350	2/2	1	6.3	5.0	1.7±0.1	2.7±0.3
	1/2	1	10.6	4.0	4.4±0.2	6.8±0.4
G253.110−01.800	1/1	1	6.9	6.9	5.6±0.3	7.1±0.6
G253.110−02.120	1/1	1	11.7	5.0	9.4±0.1	11.9±0.5
G253.110−02.150	1/1	1	12.1	4.0	4.8±0.1	5.4±0.2
G253.120−02.060	1/1	1	11.4	4.0	5.8±0.1	9.2±0.4
G253.123−01.582	1/2	1	5.9	5.0	11.3±0.1	16.3±1.4
G253.130−02.160	1/2	1	12.1	8.9	4.2±0.1	4.7±0.2
	2/2	1	19.1	7.9	0.5±0.1	1.0±0.2
G253.230−01.350	1/1	1	10.8	8.9	0.3±0.1	1.1±0.3
G253.230−02.730	2/2	2	14.4	6.9	0.6±0.1	1.3±0.2
	1/2	1	99.6	6.0	0.6±0.1	1.3±0.2
G253.270−01.110	1/1	1	10.7	5.0	1.4±0.1	2.4±0.2
G253.290−01.610	1/1	1	5.6	31.8	11.0±0.2	51.5±4.7
G253.290−01.010	1/2	1	11.6	4.0	2.0±0.1	3.1±0.2
	2/2	1	38.1	4.0	0.6±0.1	0.8±0.1
G253.300−01.080	1/1	1	10.7	7.9	3.0±0.1	4.4±0.3
G253.340+00.150	1/1	1	28.3	8.9	0.9±0.1	2.1±0.2
G253.395−02.645	1/1	1	15.8	6.0	2.7±0.1	5.1±0.3
G253.400−01.400	1/1	1	11.8	31.8	15.6±0.3	129.7±6.1
G253.400−01.420	1/2	2	12.5	18.9	6.9±0.5	41.7±3.3
	2/2	1	38.6	5.0	0.3±0.1	0.5±0.2
G253.420−01.400	1/1	1	10.3	33.7	8.3±0.4	63.5±4.3
G253.430−01.370	1/1	3	12.3	49.6	7.4±0.6	74.6±6.7
G253.450−01.370	1/2	2	10.0	35.7	10.5±0.4	72.9±4.7
G253.460−01.410	1/1	1	11.0	14.9	7.7±0.1	26.7±1.3
G253.470−01.360	1/2	1	10.5	12.9	9.3±0.1	31.2±1.5
G253.470−01.420	1/1	1	11.3	11.9	8.3±0.1	20.4±0.9
G253.480−01.370	1/1	1	10.6	12.9	8.7±0.1	26.0±1.3
G253.480−01.290	1/1	1	10.6	8.9	3.8±0.1	11.4±0.6
G253.503−01.237	1/1	1	11.6	11.9	4.0±0.1	15.1±0.8
G253.504−00.846	1/3	1	7.7	6.9	5.1±0.2	9.5±0.7
	3/3	1	14.7	3.0	0.3±0.1	0.5±0.2
	2/3	1	34.0	3.0	2.5±0.3	2.5±0.3
G253.510−01.240	1/1	3	9.7	14.9	5.4±0.3	19.4±1.6
G253.510−01.260	1/2	2	9.8	16.9	–	–
G253.520−01.370	1/1	1	10.7	6.9	4.0±0.1	7.4±0.4
G253.530−00.420	1/1	1	31.3	11.9	6.4±0.1	20.3±0.5
G253.602−00.706	1/1	1	14.1	6.9	1.7±0.1	2.0±0.1
G253.630−01.310	1/1	1	10.3	7.9	3.2±0.1	4.6±0.3
G253.630−01.440	1/2	1	11.9	7.9	3.8±0.1	7.0±0.3
G253.695−00.077	1/1	1	33.9	15.9	16.6±0.1	51.5±0.8
G253.699−02.246	1/1	1	36.5	3.0	2.0±0.1	2.6±0.2
G253.758−02.137	2/2	1	35.1	3.0	0.3±0.1	0.4±0.1
	1/2	1	53.9	4.0	1.4±0.1	1.8±0.1

Table A.2: continued

Name	Group	# components	$v_{\rm lsr}$ (km s^{-1})	$\Delta v_{\rm lsr}$ (km s^{-1})	$T_{\rm max}$ (K)	$\int T dv$ (K km s^{-1})
G253.759−02.216	1/2	1	36.1	2.0	0.6 ± 0.2	0.7 ± 0.2
	2/2	1	52.9	6.0	0.2 ± 0.1	0.4 ± 0.2
G253.770−01.300	1/2	1	12.7	6.9	4.4 ± 0.2	6.0 ± 0.4
	2/2	1	31.6	5.0	1.0 ± 0.1	2.1 ± 0.2
G253.860−01.230	1/2	1	11.9	6.0	6.7 ± 0.1	9.1 ± 0.4
	2/2	1	30.2	6.0	0.2 ± 0.1	0.4 ± 0.2
G253.870−01.210	1/2	1	11.5	10.9	11.8 ± 0.1	21.3 ± 0.9
G253.870−01.200	1/2	1	11.5	8.9	12.4 ± 0.1	24.0 ± 1.1
	2/2	2	32.5	7.9	0.9 ± 0.1	1.4 ± 0.2
	2/2	1	39.5	5.0	0.7 ± 0.1	1.2 ± 0.2
G253.890−00.470	1/1	1	10.2	9.9	10.2 ± 0.1	20.5 ± 1.0
G253.950−00.563	1/1	1	39.2	7.9	0.4 ± 0.1	1.0 ± 0.3
G253.980−00.720	2/4	1	10.5	7.9	3.4 ± 0.1	5.9 ± 0.3
	1/4	1	37.7	6.0	6.3 ± 0.2	11.6 ± 0.5
G254.052−00.566	1/1	1	34.3	17.9	19.3 ± 0.2	90.5 ± 1.7
G254.120−01.420	1/1	1	45.2	9.9	2.2 ± 0.1	5.2 ± 0.2
G254.230−02.320	1/1	1	33.9	8.9	2.8 ± 0.1	5.1 ± 0.2
G254.232−00.136	1/2	1	31.3	10.9	7.3 ± 0.1	16.7 ± 0.4
G254.270−02.340	2/2	1	79.1	4.0	0.2 ± 0.2	0.4 ± 0.3
G254.390−01.010	1/1	1	77.1	7.9	2.1 ± 0.1	4.5 ± 0.2
G254.398−02.264	2/2	1	37.0	5.0	0.5 ± 0.1	0.9 ± 0.2
	1/2	1	55.8	6.9	0.7 ± 0.1	1.1 ± 0.2
G254.490+00.100	1/2	1	8.5	3.0	0.2 ± 0.1	0.3 ± 0.2
G254.590−01.060	1/2	1	36.9	6.0	1.8 ± 0.1	2.7 ± 0.2
	2/2	1	75.1	7.9	1.0 ± 0.1	2.9 ± 0.3
G254.660−01.250	1/1	1	8.9	3.0	2.4 ± 0.1	3.7 ± 0.3
G254.670+00.250	2/3	1	31.6	3.0	–	–
	1/3	1	67.0	10.9	–	–
	3/3	1	78.2	8.9	–	–
G254.680−01.890	1/1	1	9.9	6.9	3.4 ± 0.1	5.1 ± 0.3
G254.680+00.220	1/1	1	68.8	18.9	12.7 ± 0.1	51.3 ± 0.6
G254.710+00.200	1/1	1	69.2	8.9	10.0 ± 0.1	18.9 ± 0.2
G254.750−00.752	1/2	2	86.3	9.9	0.4 ± 0.1	1.7 ± 0.4
G254.760−01.240	1/1	1	11.2	7.9	3.5 ± 0.1	11.7 ± 0.6
G254.780+00.120	2/2	1	31.0	6.0	0.3 ± 0.1	0.5 ± 0.2
	1/2	1	67.6	16.9	15.7 ± 0.1	46.7 ± 0.5
G254.880+00.451	1/1	1	28.6	22.8	8.3 ± 0.2	37.2 ± 1.0
G254.943−00.080	1/1	1	0.8	5.0	0.5 ± 0.2	0.6 ± 0.5
G255.100−00.090	1/1	1	71.6	12.9	2.8 ± 0.1	7.9 ± 0.3
G255.170−00.570	1/1	1	82.6	9.9	8.7 ± 0.1	17.8 ± 0.2
G255.190−02.280	1/1	1	8.5	4.0	5.6 ± 0.1	11.5 ± 0.7
G255.200−02.290	1/1	1	8.5	6.9	7.7 ± 0.1	17.0 ± 1.0
G255.210−02.290	1/2	1	8.4	6.9	8.4 ± 0.1	18.5 ± 1.1
G255.360−00.939	1/3	1	11.0	6.0	0.4 ± 0.1	1.1 ± 0.3
	3/3	1	79.0	5.0	0.3 ± 0.2	0.7 ± 0.4
	2/3	1	89.8	5.0	0.4 ± 0.1	0.9 ± 0.3
G255.401−00.918	1/1	2	80.4	11.9	1.2 ± 0.1	6.7 ± 0.5
G255.410−01.350	1/3	1	48.9	5.0	1.3 ± 0.4	2.1 ± 0.7
	2/3	1	86.6	8.9	0.3 ± 0.3	1.4 ± 1.2

Table A.2: continued

Name	Group	# components	$v_{\rm lsr}$ (km s^{-1})	$\Delta v_{\rm lsr}$ (km s^{-1})	$T_{\rm max}$ (K)	$\int T dv$ (K km s^{-1})
G255.680−01.220	2/3	1	36.9	6.0	0.6 ± 0.1	1.0 ± 0.2
	1/3	2	50.4	15.9	5.1 ± 0.1	14.8 ± 0.3
	3/3	1	80.1	6.0	0.4 ± 0.1	0.8 ± 0.2
G255.684−02.190	1/1	1	9.8	4.0	5.3 ± 0.1	10.0 ± 0.5
G256.130−01.470	1/3	2	85.1	10.9	4.3 ± 0.9	12.4 ± 2.6
G256.150−01.370	1/3	2	85.0	23.8	7.8 ± 0.8	34.3 ± 3.4
G256.150−01.380	1/1	2	85.1	16.9	5.4 ± 2.2	21.6 ± 8.6
G256.156−01.456	1/1	1	87.4	9.9	1.0 ± 0.1	3.7 ± 0.5
G256.187−01.547	1/1	1	88.9	10.9	4.4 ± 0.1	12.7 ± 0.3
G256.190−01.540	1/1	1	88.5	8.9	1.5 ± 0.2	5.6 ± 0.6
G256.348−02.140	1/2	1	7.9	5.0	3.2 ± 0.1	9.7 ± 0.7
	2/2	1	16.1	5.0	2.4 ± 0.1	3.5 ± 0.2
G256.409−02.210	2/3	1	8.0	5.0	1.8 ± 0.1	4.3 ± 0.4
	1/3	1	15.5	6.0	2.5 ± 0.2	4.4 ± 0.4
G256.422−02.208	1/3	1	8.0	7.9	3.5 ± 0.1	6.4 ± 0.4
	3/3	1	15.0	3.0	0.5 ± 0.1	0.8 ± 0.2
	2/3	1	18.9	5.0	0.8 ± 0.1	0.9 ± 0.1
G256.430−01.640	1/2	1	8.4	7.9	5.9 ± 0.1	9.3 ± 0.6
G256.430−01.630	1/2	1	8.6	6.9	5.5 ± 0.1	10.0 ± 0.6
	2/2	1	19.8	6.0	0.2 ± 0.1	0.6 ± 0.3
	2/2	1	21.4	5.0	0.2 ± 0.1	0.5 ± 0.3
G256.440−01.610	1/3	1	8.8	6.0	5.2 ± 0.2	8.9 ± 0.7
	3/3	1	22.0	6.0	0.4 ± 0.1	1.1 ± 0.3
	2/3	1	85.4	8.9	2.8 ± 0.1	6.9 ± 0.3
G256.450−01.608	2/2	1	8.7	4.0	3.7 ± 0.1	5.8 ± 0.4
	1/2	1	86.1	12.9	4.6 ± 0.2	14.7 ± 0.6
G256.620−00.050	2/2	1	17.3	3.0	0.5 ± 0.1	0.6 ± 0.2
	1/2	1	74.3	7.9	2.0 ± 0.1	4.9 ± 0.2
G256.670−00.040	2/2	1	11.8	4.0	–	–
	1/2	1	74.7	6.9	–	–
G256.680−00.100	2/2	1	17.4	6.0	0.4 ± 0.1	1.1 ± 0.3
	1/2	1	74.2	9.9	2.3 ± 0.1	6.0 ± 0.3
G256.682−01.627	1/1	1	43.1	8.9	2.8 ± 0.1	5.6 ± 0.2
G256.690−00.040	1/1	1	74.5	6.0	2.3 ± 0.1	4.7 ± 0.2
G256.705−02.465	1/1	1	56.3	3.0	1.0 ± 0.1	1.4 ± 0.1
G256.705−02.475	1/1	1	56.1	6.9	0.2 ± 0.1	0.7 ± 0.3
G256.715−02.445	1/3	1	15.8	3.0	0.6 ± 0.1	0.9 ± 0.2
	2/3	1	42.5	5.0	0.4 ± 0.1	0.5 ± 0.1
G256.720−01.930	1/1	1	43.7	18.9	3.7 ± 0.1	21.0 ± 0.6
G256.730−01.670	2/2	1	6.3	6.9	1.6 ± 0.1	2.5 ± 0.3
	1/2	1	43.2	4.0	2.3 ± 0.1	5.0 ± 0.3
G256.740−01.580	2/2	1	13.0	2.0	0.4 ± 0.1	0.5 ± 0.1
G256.750−00.060	2/2	1	11.6	6.0	3.0 ± 0.1	5.1 ± 0.3
	1/2	1	75.4	9.9	3.2 ± 0.2	6.9 ± 0.4
G256.780−02.070	1/2	1	8.7	6.9	1.7 ± 0.8	2.0 ± 1.0
G256.780−00.130	2/3	1	25.8	6.9	1.0 ± 0.1	2.0 ± 0.2
	2/2	1	44.9	5.0	1.3 ± 0.1	2.7 ± 0.3
	1/3	1	75.2	12.9	6.0 ± 0.1	14.8 ± 0.3
G256.810−00.510	3/3	1	23.5	4.0	0.2 ± 0.2	0.5 ± 0.5

Table A.2: continued

Name	Group	# components	$v_{\rm lsr}$ (km s^{-1})	$\Delta v_{\rm lsr}$ (km s^{-1})	$T_{\rm max}$ (K)	$\int T dv$ (K km s^{-1})
	2/3	1	52.2	7.9	1.6 ± 0.1	3.6 ± 0.2
	1/3	1	73.1	5.0	1.9 ± 0.2	2.9 ± 0.4
G256.822−01.879	1/4	1	45.9	6.0	1.3 ± 0.1	2.2 ± 0.2
	3/4	1	53.4	4.0	0.3 ± 0.2	0.5 ± 0.2
G256.858−01.786	2/2	1	13.4	6.9	0.9 ± 0.1	1.8 ± 0.2
	1/2	1	44.7	6.0	1.0 ± 0.1	1.8 ± 0.2
G256.875−00.895	1/1	1	22.1	5.0	0.6 ± 0.1	1.1 ± 0.2
G256.910−00.280	1/3	1	73.1	6.9	1.9 ± 0.1	5.2 ± 0.3
G256.920−01.830	1/1	1	44.0	6.9	2.1 ± 0.1	4.1 ± 0.3
G256.942−02.596	1/1	1	14.8	6.9	1.5 ± 0.1	2.8 ± 0.2
G256.945−00.885	1/1	1	17.7	6.0	0.2 ± 0.1	0.6 ± 0.2
G256.950−00.530	1/2	1	51.7	11.9	3.9 ± 0.3	11.1 ± 0.8
G256.990−02.130	1/2	1	44.5	7.9	0.7 ± 0.1	1.6 ± 0.2
G256.990−00.570	1/1	1	51.7	11.9	2.6 ± 0.1	7.4 ± 0.3
G257.005−02.504	1/1	1	15.6	6.9	1.1 ± 0.1	2.2 ± 0.2
G257.010+00.000	1/1	1	54.4	4.0	1.0 ± 0.1	1.5 ± 0.2
G257.014−02.414	2/2	1	9.7	2.0	0.3 ± 0.2	0.4 ± 0.2
	1/2	1	15.4	3.0	0.9 ± 0.1	1.6 ± 0.2
G257.036−00.974	1/1	1	14.8	6.0	0.7 ± 0.1	1.3 ± 0.2
G257.060−02.901	1/1	1	19.4	3.0	1.9 ± 0.1	3.1 ± 0.2
G257.060−02.080	1/1	1	44.0	6.9	0.7 ± 0.7	1.8 ± 1.9
G257.070−01.351	1/1	1	26.4	6.9	0.2 ± 0.1	0.9 ± 0.4
G257.080+00.240	1/1	1	7.1	6.0	0.2 ± 0.1	0.4 ± 0.2
G257.167−01.123	1/2	1	60.9	5.0	0.9 ± 0.1	1.3 ± 0.1
G257.196−02.662	1/2	1	16.9	8.9	1.5 ± 0.1	4.6 ± 0.3
G257.210−01.371	1/1	1	6.0	8.9	4.6 ± 0.1	8.3 ± 0.7
G257.227−00.902	2/3	1	4.7	3.0	0.3 ± 0.2	0.3 ± 0.3
	1/3	1	56.5	8.9	3.5 ± 0.1	6.6 ± 0.2
G257.240−00.700	1/3	1	15.5	4.0	2.9 ± 0.1	5.9 ± 0.3
	2/3	1	20.0	6.9	0.4 ± 0.1	0.8 ± 0.2
G257.250−01.410	1/2	1	7.3	6.0	0.6 ± 0.1	1.1 ± 0.2
G257.261−01.240	1/2	1	5.1	5.0	0.9 ± 0.1	1.2 ± 0.2
G257.282−00.336	2/2	1	6.8	6.0	2.2 ± 0.1	3.2 ± 0.3
	1/2	1	55.1	5.0	3.4 ± 0.1	7.0 ± 0.3
G257.298−01.147	1/1	1	22.4	8.9	2.4 ± 0.1	6.2 ± 0.3
G257.320−01.063	1/1	1	21.0	6.9	2.6 ± 0.1	4.7 ± 0.2
G257.330−00.258	1/1	1	52.5	8.9	2.3 ± 0.1	5.0 ± 0.2
G257.330−00.605	1/1	1	18.6	6.0	0.2 ± 0.1	0.8 ± 0.3
G257.339−02.910	1/1	1	14.8	8.9	4.8 ± 0.1	12.5 ± 0.5
G257.340−00.360	2/2	1	6.9	3.0	1.4 ± 0.1	1.6 ± 0.2
	1/2	1	55.4	5.0	2.0 ± 0.1	3.8 ± 0.3
G257.354−00.220	2/2	1	11.8	5.0	0.2 ± 0.1	0.4 ± 0.2
	1/2	2	52.4	11.9	3.6 ± 0.2	11.0 ± 0.7
G257.374−00.276	2/3	1	5.8	4.0	2.4 ± 0.1	3.1 ± 0.3
	3/3	1	17.5	3.0	0.7 ± 0.1	1.2 ± 0.2
	1/3	1	55.5	6.0	2.2 ± 0.1	5.1 ± 0.3
G257.380−00.280	1/3	1	5.8	6.9	4.1 ± 0.9	4.7 ± 1.1
	3/3	1	17.4	3.0	0.8 ± 0.1	1.2 ± 0.2
	2/3	1	55.4	7.9	2.5 ± 0.1	5.4 ± 0.2

Table A.2: continued

Name	Group	# components	$v_{\rm lsr}$ (km s^{-1})	$\Delta v_{\rm lsr}$ (km s^{-1})	$T_{\rm max}$ (K)	$\int T dv$ (K km s^{-1})
G257.410−00.300	2/2	1	6.5	6.0	0.3 ± 0.1	0.7 ± 0.2
	1/2	1	55.2	6.0	2.3 ± 0.1	5.8 ± 0.3
G257.424−00.300	2/2	1	5.9	5.0	1.1 ± 0.1	1.4 ± 0.2
	1/2	1	56.0	6.9	3.3 ± 0.1	9.8 ± 0.3
G257.460−00.610	1/1	1	51.3	10.9	4.5 ± 0.1	7.5 ± 0.2
G257.470−00.630	1/1	1	51.4	9.9	9.0 ± 0.1	24.1 ± 0.4
G257.480−00.610	1/1	1	51.4	9.9	3.8 ± 0.1	7.7 ± 0.2
G257.490+00.180	2/3	1	6.4	4.0	3.0 ± 0.1	5.2 ± 0.4
	3/3	1	16.0	6.0	1.1 ± 0.1	1.4 ± 0.1
	1/3	1	53.2	6.9	8.3 ± 0.2	16.7 ± 0.5
G257.501−01.539	1/2	2	6.8	7.9	0.6 ± 0.1	1.6 ± 0.3
	2/2	1	82.4	5.0	0.2 ± 0.1	0.4 ± 0.2
G257.510−02.250	3/4	1	6.6	5.0	–	–
	2/4	1	15.3	5.0	–	–
	4/4	1	42.5	6.0	–	–
	1/4	1	90.9	14.9	–	–
G257.540−01.630	1/2	1	6.4	3.0	4.3 ± 0.3	8.0 ± 0.9
G257.540−01.270	1/2	1	73.3	5.0	2.6 ± 0.1	5.2 ± 0.2
	2/2	1	74.7	6.9	1.2 ± 0.3	2.4 ± 0.5
G257.560−00.480	1/1	1	54.8	8.9	2.9 ± 0.1	5.2 ± 0.2
G257.570−02.070	3/3	1	18.2	5.0	0.2 ± 0.1	0.6 ± 0.3
	2/3	2	44.1	10.9	1.0 ± 0.1	3.2 ± 0.3
	1/3	1	92.2	6.9	2.2 ± 0.1	6.8 ± 0.3
G257.580+00.070	1/3	1	6.9	6.9	2.7 ± 0.1	6.7 ± 0.5
	2/3	1	78.6	5.0	0.7 ± 0.1	1.2 ± 0.2
G257.597−01.201	1/1	1	17.1	5.0	0.7 ± 0.1	1.1 ± 0.2
G257.610−00.660	1/2	1	52.9	8.9	1.9 ± 0.1	3.5 ± 0.2
G257.617−01.772	1/1	1	17.2	9.9	1.0 ± 0.1	3.1 ± 0.3
G257.630−01.050	1/1	1	14.2	7.9	3.5 ± 0.1	8.1 ± 0.4
G257.630−00.590	1/3	1	52.5	6.0	3.2 ± 0.1	5.4 ± 0.2
	2/3	1	74.7	6.0	0.6 ± 0.1	1.0 ± 0.2
G257.636−01.121	1/1	1	74.3	6.9	0.3 ± 0.1	0.5 ± 0.2
G257.640−00.959	1/2	1	15.4	4.0	2.1 ± 0.2	3.2 ± 0.3
	2/2	1	54.7	5.0	1.4 ± 0.1	2.1 ± 0.2
G257.649−01.360	1/2	2	8.7	7.9	0.8 ± 0.1	2.7 ± 0.4
G257.655−01.250	2/2	1	14.6	5.0	0.2 ± 0.1	0.3 ± 0.2
	1/2	1	56.9	6.0	0.3 ± 0.2	0.6 ± 0.3
G257.719−01.449	1/1	1	75.1	3.0	0.5 ± 0.1	0.8 ± 0.2
G257.740+00.160	4/4	1	6.3	4.0	0.5 ± 0.2	0.7 ± 0.2
	3/4	1	11.4	5.0	2.4 ± 0.1	4.7 ± 0.3
	1/4	1	46.5	6.9	9.6 ± 0.3	23.8 ± 0.8
	2/4	1	53.5	6.9	4.0 ± 0.2	7.5 ± 0.4
G257.798−01.252	1/1	2	76.7	14.9	3.2 ± 0.2	14.1 ± 0.8
G257.807−02.104	1/3	2	6.3	6.0	0.8 ± 0.1	2.1 ± 0.3
	2/3	1	13.5	6.9	0.6 ± 0.1	1.4 ± 0.2
G257.808−01.277	1/2	1	76.0	13.9	2.1 ± 0.1	8.5 ± 0.4
G257.812−02.462	2/2	1	9.3	6.0	2.4 ± 0.1	3.2 ± 0.2
	1/2	1	13.4	4.0	3.5 ± 0.2	5.4 ± 0.4
G257.830−00.740	1/2	1	16.4	4.0	4.5 ± 0.1	7.8 ± 0.3

Table A.2: continued

Name	Group	# components	$v_{\rm lsr}$ (km s^{-1})	$\Delta v_{\rm lsr}$ (km s^{-1})	$T_{\rm max}$ (K)	$\int T dv$ (K km s^{-1})
G257.831−00.773	1/1	1	16.6	3.0	0.9 ± 0.1	1.3 ± 0.2
G257.831−01.758	1/1	1	45.4	7.9	3.7 ± 0.1	5.7 ± 0.2
G257.850−01.070	1/2	1	77.9	7.9	2.5 ± 0.1	5.6 ± 0.2
G257.864−01.086	2/2	1	10.5	5.0	0.7 ± 0.1	1.2 ± 0.2
	1/2	1	76.9	11.9	3.0 ± 0.1	7.1 ± 0.2
G257.865−01.495	1/1	1	16.7	14.9	4.3 ± 0.1	17.9 ± 0.7
G257.867−01.793	1/2	1	44.0	6.0	9.0 ± 0.1	13.6 ± 0.2
G257.870−01.498	1/1	1	5.7	5.0	0.4 ± 0.1	0.6 ± 0.2
G257.879−01.729	1/1	1	7.1	7.9	0.5 ± 0.1	1.5 ± 0.4
G257.889−01.428	2/3	1	5.4	6.9	0.4 ± 0.1	1.1 ± 0.3
	1/3	1	15.0	4.0	0.4 ± 0.1	0.6 ± 0.1
G257.894−01.885	1/2	1	6.8	6.9	1.0 ± 0.1	2.2 ± 0.3
G257.920−00.470	1/1	1	51.6	6.9	4.4 ± 0.1	10.4 ± 0.3
G257.932−01.387	1/1	1	42.9	5.0	8.3 ± 0.1	13.1 ± 0.2
G257.940−00.942	1/1	1	81.0	10.9	1.2 ± 0.1	3.8 ± 0.3
G257.950+00.070	1/1	1	48.2	8.9	0.8 ± 0.1	1.8 ± 0.2
G257.950−00.170	1/1	1	50.8	9.9	5.5 ± 0.1	13.7 ± 0.3
G257.950−00.510	1/1	1	51.9	9.9	9.1 ± 0.1	19.0 ± 0.3
G257.960−00.940	1/1	1	81.5	12.9	1.9 ± 0.6	7.4 ± 2.4
G257.978−01.428	1/1	1	42.9	8.9	9.4 ± 0.1	15.8 ± 0.2
G257.982−00.951	1/1	1	80.7	10.9	1.8 ± 0.1	5.6 ± 0.3
G257.989−00.683	2/2	1	15.3	2.0	0.4 ± 0.1	0.5 ± 0.2
	1/2	1	82.5	4.0	1.0 ± 0.1	1.5 ± 0.2
G258.000−00.010	1/1	1	7.3	5.0	1.5 ± 0.1	1.9 ± 0.2
G258.000−00.300	1/2	1	41.6	6.9	2.6 ± 0.2	4.1 ± 0.3
	2/2	1	51.7	6.9	1.8 ± 0.1	6.3 ± 0.4
G258.047−01.604	1/1	1	42.0	8.9	3.1 ± 0.1	6.5 ± 0.2
G258.050−01.341	1/1	2	47.1	19.8	6.1 ± 0.1	16.3 ± 0.3
G258.080−01.563	2/2	1	8.4	7.9	1.3 ± 0.1	2.7 ± 0.3
	1/2	1	42.4	6.0	3.8 ± 0.1	6.7 ± 0.2
G258.080−01.561	2/2	1	8.5	6.0	1.3 ± 0.1	2.1 ± 0.2
	1/2	1	42.4	6.9	3.8 ± 0.1	6.8 ± 0.2
G258.080−01.350	1/1	1	47.1	6.0	2.5 ± 0.1	3.9 ± 0.2
G258.081−01.558	2/2	1	8.5	7.9	1.3 ± 0.1	2.2 ± 0.2
G258.081−01.561	2/2	1	8.5	6.0	1.3 ± 0.1	2.3 ± 0.2
	1/2	1	42.4	4.0	4.1 ± 0.2	6.4 ± 0.3
	1/2	1	42.4	5.0	3.9 ± 0.1	6.6 ± 0.2
G258.082−01.626	1/1	1	41.5	8.9	2.9 ± 0.1	7.1 ± 0.3
G258.107−01.740	2/2	1	9.9	9.9	0.4 ± 0.1	1.0 ± 0.3
	1/2	1	42.1	8.9	6.3 ± 0.1	17.4 ± 0.3
G258.114−01.904	1/1	1	12.1	6.9	0.6 ± 0.1	1.3 ± 0.2
G258.130−00.390	1/2	1	51.3	6.0	0.2 ± 0.1	0.5 ± 0.2
G258.140−00.350	1/1	1	19.5	7.9	0.9 ± 0.1	2.3 ± 0.3
G258.156−01.517	1/1	1	42.0	10.9	3.2 ± 0.1	9.1 ± 0.3
G258.182−01.512	1/1	1	42.5	8.9	2.9 ± 0.1	7.7 ± 0.3
G258.190−02.277	1/1	2	13.9	12.9	1.5 ± 0.1	4.5 ± 0.3
G258.194−02.221	1/1	1	16.2	17.9	5.0 ± 0.1	28.7 ± 1.1
G258.207−01.348	1/1	1	8.3	3.0	0.2 ± 0.2	0.3 ± 0.2
G258.222−01.775	1/2	1	9.3	7.9	4.7 ± 0.1	11.7 ± 0.7

Table A.2: continued

Name	Group	# components	$v_{\rm lsr}$ (km s^{-1})	$\Delta v_{\rm lsr}$ (km s^{-1})	$T_{\rm max}$ (K)	$\int T dv$ (K km s^{-1})
	2/2	1	59.2	6.0	1.0 ± 0.1	2.0 ± 0.2
G258.250−00.851	1/1	1	22.6	6.0	0.2 ± 0.1	0.3 ± 0.2
G258.255−01.233	1/1	1	81.3	7.9	0.3 ± 0.1	0.8 ± 0.3
G258.257−01.052	1/1	1	81.4	9.9	0.2 ± 0.1	1.0 ± 0.4
G258.260−00.840	2/3	1	16.1	4.0	0.4 ± 0.1	0.8 ± 0.2
	1/3	1	76.6	5.0	0.5 ± 0.1	0.7 ± 0.1
	3/3	1	81.3	7.9	0.3 ± 0.1	1.2 ± 0.6
G258.270−00.830	1/3	1	16.8	5.0	1.1 ± 0.1	2.9 ± 0.3
	2/3	2	77.4	9.9	0.5 ± 0.1	1.7 ± 0.4
G258.289−00.457	1/2	1	8.3	5.0	1.2 ± 0.1	2.6 ± 0.3
	2/2	1	15.8	3.0	0.2 ± 0.1	0.3 ± 0.1
G258.300−02.163	2/2	1	15.5	8.9	1.5 ± 0.1	4.1 ± 0.3
	1/2	1	57.5	10.9	2.4 ± 0.1	4.8 ± 0.2
G258.319−00.920	1/4	1	6.1	8.9	4.3 ± 0.1	9.7 ± 0.8
	3/4	1	24.7	6.0	0.7 ± 0.1	1.4 ± 0.2
	2/4	1	80.4	8.9	0.9 ± 0.1	3.3 ± 0.4
G258.340−02.190	1/1	1	42.6	5.0	2.2 ± 0.2	3.3 ± 0.2
G258.384−01.113	1/2	2	79.5	6.9	0.6 ± 0.2	1.3 ± 0.4
G258.420−00.940	1/2	1	81.5	7.9	0.9 ± 0.2	3.0 ± 0.6
G258.427−01.444	1/1	1	12.0	7.9	1.6 ± 0.1	3.1 ± 0.2
G258.430−00.940	1/2	1	81.9	9.9	1.1 ± 0.3	3.6 ± 1.2
G258.495−00.716	2/3	1	19.1	6.0	0.2 ± 0.1	0.6 ± 0.2
	1/3	2	73.6	6.9	0.3 ± 0.1	0.8 ± 0.3
G258.520−01.704	1/1	2	10.5	9.9	2.4 ± 0.9	8.7 ± 3.4
G258.530−01.665	1/2	1	11.8	6.9	0.9 ± 0.1	3.1 ± 0.4
	2/2	1	54.0	6.9	0.6 ± 0.1	1.7 ± 0.3
G258.532−01.188	1/1	2	16.0	10.9	0.6 ± 0.1	3.5 ± 0.5
G258.610−01.920	1/3	1	13.0	7.9	2.6 ± 0.2	9.2 ± 0.6
	3/3	1	52.1	5.0	1.0 ± 0.1	1.6 ± 0.2
	2/3	1	60.5	5.0	2.4 ± 0.1	3.7 ± 0.2
G258.660−00.390	1/3	1	21.3	6.9	2.8 ± 0.1	5.1 ± 0.3
	2/3	1	73.5	8.9	0.5 ± 0.1	1.5 ± 0.3
G258.667−01.050	1/1	1	14.0	7.9	2.2 ± 0.2	5.2 ± 0.6
G258.681−01.774	2/2	2	13.9	7.9	1.7 ± 0.1	5.9 ± 0.4
	1/2	1	61.3	5.0	2.8 ± 0.2	4.4 ± 0.4
G258.691−01.773	2/3	2	13.3	9.9	2.1 ± 0.5	8.2 ± 2.1
	3/3	1	53.9	7.9	0.8 ± 0.1	1.4 ± 0.2
	1/3	1	59.8	6.9	5.6 ± 0.2	10.6 ± 0.4
G258.718−01.168	2/2	2	12.7	6.9	0.8 ± 0.4	2.1 ± 1.0
	1/2	1	64.0	9.9	11.2 ± 0.1	21.4 ± 0.3
G258.733−01.335	1/3	2	14.9	11.9	2.2 ± 0.1	7.1 ± 0.4
	2/3	1	64.2	6.9	1.4 ± 0.1	2.2 ± 0.2
G258.743−01.291	1/2	1	65.3	6.0	3.4 ± 0.2	4.9 ± 0.3
G258.790−00.970	1/1	1	15.9	4.0	4.0 ± 0.1	5.2 ± 0.2
G258.792−01.422	1/2	2	12.7	11.9	2.6 ± 0.1	12.1 ± 0.7
	2/2	1	51.6	4.0	0.7 ± 0.1	1.0 ± 0.1
G258.822−01.402	1/1	2	12.4	12.9	2.6 ± 0.1	11.6 ± 0.8
G258.842−01.446	1/3	1	11.5	10.9	2.6 ± 0.1	7.8 ± 0.5
	2/3	1	60.7	3.0	0.3 ± 0.1	0.5 ± 0.2

Table A.2: continued

Name	Group	# components	$v_{\rm lsr}$ (km s^{-1})	$\Delta v_{\rm lsr}$ (km s^{-1})	$T_{\rm max}$ (K)	$\int T dv$ (K km s^{-1})
G258.860−01.397	1/1	1	11.1	6.0	3.2 ± 0.1	7.1 ± 0.4
G258.870−01.475	1/1	2	13.3	9.9	1.5 ± 0.2	6.4 ± 0.8
G258.878−01.440	1/2	1	11.3	8.9	2.5 ± 0.1	6.8 ± 0.4
	2/2	1	82.9	5.0	0.4 ± 0.1	0.9 ± 0.2
G258.880−00.720	1/4	1	11.6	3.0	4.5 ± 0.8	6.4 ± 1.2
	2/4	1	26.8	6.9	1.4 ± 0.4	1.9 ± 0.6
G258.885−01.498	1/2	1	12.0	6.0	1.4 ± 0.1	4.3 ± 0.3
	2/2	1	60.5	6.9	0.4 ± 0.1	1.2 ± 0.3
G258.910−01.450	1/1	1	11.6	7.9	1.8 ± 0.1	6.6 ± 0.5
G258.930−00.730	1/1	1	11.7	4.0	4.2 ± 0.1	7.2 ± 0.4
G258.960−00.720	1/1	1	11.4	4.0	0.8 ± 0.1	1.5 ± 0.2
G258.965−01.475	2/2	1	11.1	10.9	2.1 ± 0.1	7.6 ± 0.5
	1/2	1	59.6	6.9	3.8 ± 0.2	8.0 ± 0.4
G259.002−01.498	2/2	1	12.5	6.9	1.7 ± 0.1	4.5 ± 0.3
	1/2	2	59.9	10.9	2.5 ± 0.2	7.4 ± 0.5
G259.018−01.550	2/3	1	12.7	12.9	2.4 ± 0.1	8.7 ± 0.5
	3/3	1	32.8	5.0	1.8 ± 0.1	2.6 ± 0.1
	1/3	1	58.3	10.9	14.8 ± 0.2	37.6 ± 0.7
G259.031−00.496	1/1	1	18.7	8.9	2.9 ± 0.1	8.2 ± 0.4
G259.045−01.557	2/3	1	12.2	10.9	2.6 ± 0.1	7.9 ± 0.4
	1/3	1	59.3	10.9	21.5 ± 0.2	58.5 ± 0.7
	3/3	1	92.3	7.9	0.7 ± 0.1	1.2 ± 0.2
G259.050−01.802	1/1	1	12.2	5.0	1.2 ± 0.1	2.1 ± 0.2
G259.050−01.538	2/2	1	12.7	11.9	2.0 ± 0.1	6.5 ± 0.4
	1/2	2	60.4	10.9	5.8 ± 1.0	24.1 ± 4.1
G259.052−01.140	3/3	1	13.7	3.0	0.5 ± 0.3	0.6 ± 0.3
	1/3	1	59.3	6.0	1.8 ± 0.1	3.2 ± 0.2
	2/3	1	64.3	6.0	1.4 ± 0.4	1.7 ± 0.5
G259.078−01.620	2/2	1	12.8	11.9	2.3 ± 0.1	7.5 ± 0.4
	1/2	1	59.3	11.9	12.0 ± 0.2	27.3 ± 0.6
G259.080−00.050	1/2	1	6.0	6.9	2.6 ± 0.1	3.5 ± 0.3
	2/2	1	14.0	6.0	1.0 ± 0.1	1.5 ± 0.2
G259.115+00.229	1/1	2	8.9	10.9	1.4 ± 0.3	3.0 ± 0.7
G259.133−01.426	1/3	1	15.1	5.0	1.7 ± 0.1	3.1 ± 0.2
	2/3	1	34.1	6.9	0.7 ± 0.1	1.7 ± 0.3
G259.136−01.554	3/3	1	6.7	4.0	0.2 ± 0.1	0.4 ± 0.2
	1/3	2	58.4	9.9	5.6 ± 0.1	9.9 ± 0.2
	2/3	1	93.3	6.0	0.2 ± 0.1	0.4 ± 0.2
G259.150−01.298	2/5	1	12.7	3.0	2.8 ± 0.9	3.4 ± 1.0
	4/5	1	15.3	5.0	1.1 ± 0.2	1.5 ± 0.3
	3/5	1	31.8	8.9	2.0 ± 0.1	5.5 ± 0.3
	1/5	1	58.8	15.9	2.7 ± 0.2	9.4 ± 0.7
	5/5	1	83.4	7.9	0.7 ± 0.1	1.4 ± 0.2
G259.153−01.337	1/5	1	12.4	9.9	2.5 ± 0.2	9.0 ± 0.8
	3/5	2	29.6	12.9	1.7 ± 0.2	8.0 ± 1.0
	2/5	1	57.1	7.9	2.3 ± 0.3	4.1 ± 0.5
	5/5	1	85.2	6.0	0.5 ± 0.1	0.9 ± 0.2
	4/5	1	92.3	5.0	1.1 ± 0.1	1.7 ± 0.2
G259.165−01.217	1/2	1	12.2	6.0	2.1 ± 0.1	4.5 ± 0.3

Table A.2: continued

Name	Group	# components	$v_{\rm lsr}$ (km s^{-1})	$\Delta v_{\rm lsr}$ (km s^{-1})	$T_{\rm max}$ (K)	$\int T dv$ (K km s^{-1})
	2/2	2	59.4	9.9	0.4 ± 0.1	1.4 ± 0.4
G259.167−01.313	1/5	2	12.8	10.9	3.3 ± 0.3	8.3 ± 0.9
	2/5	1	30.2	11.9	2.2 ± 0.1	7.9 ± 0.4
	3/5	1	57.9	7.9	1.8 ± 0.1	3.8 ± 0.2
	5/5	1	83.8	6.0	0.3 ± 0.1	0.6 ± 0.2
	4/5	1	92.3	4.0	0.3 ± 0.1	0.6 ± 0.2
G259.172−01.253	1/3	1	12.5	6.9	3.2 ± 0.1	10.4 ± 0.5
	2/3	1	57.9	8.9	0.4 ± 0.1	1.3 ± 0.3
	3/3	1	62.1	5.0	0.2 ± 0.1	0.6 ± 0.3
G259.178−00.717	1/4	1	6.2	3.0	0.2 ± 0.1	0.5 ± 0.2
G259.188−00.673	1/1	1	6.0	4.0	0.7 ± 0.1	1.0 ± 0.2
G259.190−00.030	1/2	1	4.3	8.9	8.8 ± 0.3	10.2 ± 1.2
	2/2	1	12.7	6.9	4.4 ± 0.1	6.2 ± 0.3
G259.198−01.272	1/3	1	13.0	6.9	2.7 ± 0.1	9.3 ± 0.5
	2/3	1	57.4	7.9	1.5 ± 0.1	3.2 ± 0.2
	3/3	1	85.2	5.0	0.4 ± 0.1	0.8 ± 0.2
G259.200+00.000	1/2	1	4.9	6.9	6.1 ± 0.2	9.6 ± 1.0
G259.200−00.010	1/2	1	5.0	5.0	5.0 ± 0.3	6.9 ± 0.8
	2/2	1	12.8	4.0	3.1 ± 0.3	4.3 ± 0.4
	2/2	1	13.2	6.9	3.0 ± 0.6	3.5 ± 0.7
G259.215−01.389	1/3	1	57.9	6.9	4.0 ± 0.1	10.7 ± 0.3
G259.217−01.390	1/2	1	57.9	9.9	3.6 ± 0.1	9.8 ± 0.3
G259.230−00.030	2/2	1	4.6	9.9	1.2 ± 0.2	2.5 ± 0.5
G259.230−00.300	1/1	1	10.8	5.0	3.0 ± 0.1	4.9 ± 0.3
	1/2	1	12.6	7.9	3.0 ± 0.3	4.9 ± 0.5
G259.236−00.804	1/1	1	5.7	2.0	0.4 ± 0.4	0.5 ± 0.5
G259.237−01.627	2/2	1	10.9	7.9	0.7 ± 0.1	1.4 ± 0.2
	1/2	2	63.4	21.8	14.0 ± 0.1	41.7 ± 0.5
G259.240−00.320	2/3	1	11.1	6.0	1.4 ± 0.1	1.9 ± 0.2
	1/3	1	50.0	6.0	2.0 ± 0.1	3.9 ± 0.3
G259.245−01.227	2/2	2	13.9	6.0	2.5 ± 0.1	7.1 ± 0.4
	1/2	2	43.4	13.9	3.1 ± 0.3	10.2 ± 1.1
G259.250−00.050	1/1	3	12.5	16.9	3.4 ± 0.2	11.2 ± 0.7
G259.250−02.020	1/1	1	55.5	7.9	5.3 ± 0.1	9.8 ± 0.2
G259.270−00.330	1/1	1	11.7	5.0	0.7 ± 0.1	1.1 ± 0.2
G259.272−01.238	1/3	1	13.9	7.9	2.2 ± 0.1	7.4 ± 0.4
	3/3	1	31.7	4.0	0.2 ± 0.1	0.4 ± 0.2
	2/3	2	43.5	9.9	0.8 ± 0.1	2.0 ± 0.3
G259.284−01.331	1/1	1	12.1	5.0	1.6 ± 0.1	2.6 ± 0.2
G259.292−01.955	1/1	1	55.6	21.8	6.7 ± 0.1	35.1 ± 0.7
G259.300+00.030	1/1	1	12.8	6.9	–	–
G259.302−01.220	1/2	1	13.5	6.0	2.8 ± 0.2	4.8 ± 0.4
	2/2	1	29.8	7.9	1.7 ± 0.1	4.0 ± 0.2
G259.320−01.740	1/2	1	11.1	7.9	3.6 ± 0.1	7.1 ± 0.4
G259.320−01.780	1/1	1	11.9	15.9	2.5 ± 0.1	13.1 ± 0.8
G259.320+00.220	1/2	1	14.1	4.0	5.4 ± 0.1	7.5 ± 0.3
G259.327−00.888	1/2	1	62.7	7.9	0.4 ± 0.1	0.8 ± 0.2
G259.330−01.780	1/1	1	11.9	13.9	3.0 ± 0.4	13.5 ± 1.8
G259.338−01.445	1/1	2	11.5	20.8	3.8 ± 0.5	23.4 ± 3.4

Table A.2: continued

Name	Group	# components	$v_{\rm lsr}$ (km s^{-1})	$\Delta v_{\rm lsr}$ (km s^{-1})	$T_{\rm max}$ (K)	$\int T dv$ (K km s^{-1})
G259.340−01.444	1/1	1	12.1	24.8	4.0 ± 0.2	24.0 ± 1.4
G259.340−00.450	1/3	2	15.1	8.9	0.9 ± 0.1	2.5 ± 0.3
G259.360−01.740	1/2	1	11.8	7.9	3.7 ± 0.1	11.1 ± 0.6
G259.368−01.192	2/3	1	27.5	8.9	1.8 ± 0.1	4.5 ± 0.3
	1/3	1	59.9	7.9	2.7 ± 0.1	6.6 ± 0.3
G259.370−00.090	1/2	1	5.4	3.0	1.8 ± 0.5	2.4 ± 0.6
G259.383−01.083	1/1	1	57.6	11.9	2.8 ± 0.2	13.5 ± 1.2
G259.390−00.180	2/2	1	4.8	6.9	0.5 ± 0.1	0.9 ± 0.2
G259.390−01.710	1/1	1	11.4	6.0	3.1 ± 0.1	8.5 ± 0.5
	1/2	1	12.3	7.9	4.0 ± 0.2	5.4 ± 0.3
G259.400−01.075	1/2	2	59.3	8.9	5.0 ± 0.4	12.6 ± 0.9
G259.405−01.162	2/2	1	13.6	4.0	0.7 ± 0.3	1.1 ± 0.5
	1/2	2	54.2	10.9	2.5 ± 0.2	7.7 ± 0.6
G259.409−01.302	1/3	1	12.5	8.9	2.6 ± 0.1	4.9 ± 0.3
	3/3	1	43.6	6.0	0.2 ± 0.1	0.4 ± 0.2
	2/3	1	61.7	9.9	0.3 ± 0.1	1.0 ± 0.4
G259.410−01.488	1/1	1	12.4	7.9	3.5 ± 0.1	8.9 ± 0.4
G259.410−01.710	1/2	1	11.5	7.9	4.0 ± 0.9	8.5 ± 1.9
G259.411−00.105	1/1	1	14.4	6.9	0.7 ± 0.1	1.2 ± 0.2
G259.417−01.065	1/1	2	59.9	13.9	3.8 ± 0.3	18.3 ± 1.4
G259.420−01.037	1/1	1	58.1	9.9	5.3 ± 0.1	12.4 ± 0.3
G259.437−00.867	1/2	1	29.0	6.9	0.6 ± 0.1	1.0 ± 0.2
	2/2	1	59.1	9.9	0.3 ± 0.1	1.4 ± 0.4
G259.440−01.080	1/2	1	57.7	12.9	4.0 ± 0.1	16.1 ± 0.4
G259.446−00.838	1/1	1	58.7	8.9	1.9 ± 0.1	5.0 ± 0.3
G259.446−00.847	1/1	1	58.8	8.9	2.6 ± 0.1	6.9 ± 0.3
G259.457−01.110	2/2	1	12.4	6.0	1.0 ± 0.1	1.5 ± 0.2
	1/2	1	57.4	9.9	3.1 ± 0.1	9.3 ± 0.3
G259.463−01.065	1/1	1	59.0	9.9	3.8 ± 0.1	9.0 ± 0.3
G259.476−00.867	1/2	2	58.1	11.9	1.6 ± 0.1	5.2 ± 0.3
G259.480−01.135	2/3	1	28.3	5.0	0.5 ± 0.1	1.0 ± 0.2
	1/3	1	61.2	6.9	1.1 ± 0.1	2.2 ± 0.2
	3/3	1	85.8	6.0	0.4 ± 0.1	0.7 ± 0.2
G259.487−00.651	1/1	1	58.4	6.0	3.5 ± 0.1	7.7 ± 0.2
G259.490−01.155	2/2	1	13.5	6.9	1.1 ± 0.1	2.0 ± 0.2
	1/2	1	27.9	5.0	1.0 ± 0.1	1.6 ± 0.2
G259.497−00.887	1/1	1	58.9	10.9	2.4 ± 0.1	5.8 ± 0.2
G259.520−00.300	1/1	1	9.4	7.9	1.3 ± 0.1	3.7 ± 0.4
G259.544−02.440	1/1	1	53.4	6.9	6.1 ± 0.1	10.9 ± 0.2
G259.560−00.930	2/2	1	26.9	6.0	1.2 ± 0.1	1.5 ± 0.1
	1/2	1	54.8	8.9	8.2 ± 0.1	30.3 ± 0.5
G259.563−00.619	1/1	1	56.3	6.9	1.5 ± 0.1	2.5 ± 0.2
G259.570−01.020	2/2	1	9.1	5.0	–	–
G259.570−01.430	1/2	1	12.7	13.9	4.9 ± 0.3	11.4 ± 0.8
	1/2	2	54.8	18.9	–	–
	2/2	1	56.8	5.0	3.4 ± 0.1	9.3 ± 0.3
G259.580+00.140	1/2	2	7.8	6.9	0.9 ± 0.1	1.7 ± 0.2
	2/2	1	69.2	5.0	0.2 ± 0.1	0.4 ± 0.2
G259.588−02.565	1/1	1	56.5	6.9	1.0 ± 0.1	1.3 ± 0.1

Table A.2: continued

Name	Group	# components	$v_{\rm lsr}$ (km s^{-1})	$\Delta v_{\rm lsr}$ (km s^{-1})	$T_{\rm max}$ (K)	$\int T dv$ (K km s^{-1})
G259.593−01.302	1/2	1	57.2	17.9	16.6 ± 0.1	48.5 ± 0.5
G259.610−01.300	1/1	1	57.0	15.9	14.6 ± 0.1	36.8 ± 0.4
G259.613−01.684	1/1	1	11.9	6.0	1.9 ± 0.1	3.8 ± 0.3
G259.617−00.640	1/1	1	8.8	2.0	0.9 ± 0.9	0.9 ± 0.9
G259.620+00.060	1/2	1	12.0	10.9	–	–
G259.638−01.016	1/1	1	59.9	8.9	0.5 ± 0.1	1.3 ± 0.2
G259.640−01.320	1/2	1	57.7	8.9	3.1 ± 0.1	6.9 ± 0.2
G259.643−00.659	1/1	1	8.4	5.0	0.8 ± 0.1	1.3 ± 0.2
G259.652−01.313	1/2	1	57.6	12.9	19.3 ± 0.1	48.9 ± 0.5
G259.668−01.318	1/1	1	58.2	28.8	18.3 ± 0.2	92.3 ± 1.3
G259.678−02.535	1/1	1	54.3	11.9	12.2 ± 0.1	24.7 ± 0.3
G259.680+00.040	1/2	1	6.0	6.9	–	–
	2/2	2	13.4	11.9	–	–
G259.691−00.614	1/2	1	8.4	3.0	1.6 ± 0.1	2.2 ± 0.2
G259.699−01.165	1/2	1	57.9	9.9	16.4 ± 0.1	42.8 ± 0.5
G259.700−01.280	1/1	1	57.2	15.9	–	–
G259.711−01.934	1/2	1	10.7	8.9	2.7 ± 0.1	5.7 ± 0.3
	2/2	1	95.5	6.0	0.7 ± 0.1	1.0 ± 0.2
G259.726+00.282	1/1	1	8.7	6.0	1.0 ± 0.2	1.5 ± 0.3
G259.750−01.340	1/2	1	57.0	9.9	1.6 ± 0.1	4.6 ± 0.3
	2/2	1	65.9	5.0	0.7 ± 0.1	1.0 ± 0.2
G259.769−01.135	1/2	1	62.7	6.0	0.7 ± 0.1	1.5 ± 0.2
G259.781−00.834	1/1	1	60.3	4.0	2.9 ± 0.1	4.1 ± 0.2
G259.783−00.833	1/1	1	60.2	6.0	3.0 ± 0.1	4.4 ± 0.2
G259.830−01.099	1/1	1	56.6	7.9	0.6 ± 0.1	1.7 ± 0.3
G259.830−00.473	1/1	1	9.5	6.0	5.2 ± 0.1	8.0 ± 0.5
G259.847−00.465	1/1	1	9.5	6.9	5.4 ± 0.1	8.6 ± 0.5
G259.849−01.982	2/2	1	8.8	6.0	0.2 ± 0.1	0.5 ± 0.2
	1/2	1	15.4	7.9	0.7 ± 0.1	1.2 ± 0.2
G259.851−00.551	1/1	1	9.2	5.0	2.3 ± 0.1	2.9 ± 0.2
G259.860−02.030	1/2	1	15.9	6.9	1.9 ± 0.3	4.2 ± 0.6
G259.864−00.777	1/1	1	59.0	3.0	–	–
G259.870−02.400	1/2	1	10.5	8.9	6.1 ± 0.1	19.6 ± 1.0
	2/2	1	56.6	6.0	0.3 ± 0.2	0.5 ± 0.3
G259.880−02.020	1/4	1	10.2	6.0	0.9 ± 0.1	1.7 ± 0.2
G259.880−02.410	1/2	1	10.6	9.9	6.5 ± 0.2	21.9 ± 1.2
	3/4	1	15.5	4.0	0.2 ± 0.1	0.6 ± 0.3
	2/4	1	53.7	6.9	0.3 ± 0.1	0.6 ± 0.2
G259.890−02.420	1/1	1	10.3	9.9	7.9 ± 0.2	29.9 ± 1.6
G259.900+00.010	1/2	1	7.8	7.9	–	–
G259.900−02.430	1/1	1	10.3	8.9	8.7 ± 0.2	29.2 ± 1.6
G259.900−01.970	1/2	2	11.1	11.9	0.9 ± 0.1	3.4 ± 0.5
	2/2	1	14.5	4.0	–	–
G259.908−01.942	1/3	1	15.9	7.9	–	–
G259.910−00.050	1/1	1	7.8	12.9	17.2 ± 0.1	59.9 ± 3.9
G259.920−00.010	1/3	1	7.9	11.9	15.1 ± 0.1	37.2 ± 2.4
G259.939−00.042	1/1	2	10.3	31.7	12.9 ± 3.4	154.2 ± 41.3
G259.940−00.040	1/1	2	10.1	41.7	20.3 ± 3.5	172.4 ± 31.1
G259.950−01.330	1/2	1	62.7	6.0	0.5 ± 0.1	1.4 ± 0.3

Table A.2: continued

Name	Group	# components	$v_{\rm lsr}$ (km s^{-1})	$\Delta v_{\rm lsr}$ (km s^{-1})	$T_{\rm max}$ (K)	$\int T dv$ (K km s^{-1})
G259.958−02.002	1/1	2	14.9	9.9	0.6 ± 0.1	1.3 ± 0.2
G259.960−00.080	1/3	2	7.4	10.9	16.0 ± 0.1	34.8 ± 2.4
	2/3	1	67.7	6.0	0.3 ± 0.1	0.9 ± 0.3
G259.980−00.080	2/2	2	8.9	11.9	0.9 ± 0.1	3.9 ± 0.5
	1/2	1	65.4	5.0	1.2 ± 0.1	1.9 ± 0.2
G259.987+00.027	1/3	1	8.0	6.0	12.8 ± 0.1	27.0 ± 1.7
	2/3	1	64.1	6.0	0.4 ± 0.1	0.7 ± 0.2
	3/3	1	70.3	6.0	0.1 ± 0.1	0.4 ± 0.3
G259.990−00.020	1/3	1	8.9	7.9	13.6 ± 0.1	18.5 ± 1.0
	3/3	1	13.6	4.0	0.4 ± 0.3	0.7 ± 0.5
	2/3	1	62.6	7.9	0.8 ± 0.1	2.8 ± 0.4
G260.000−00.160	3/4	1	0.3	7.9	0.2 ± 0.1	0.4 ± 0.7
	1/4	1	8.3	8.9	12.3 ± 0.1	22.7 ± 1.4
	2/4	1	14.4	4.0	0.8 ± 0.1	1.2 ± 0.2
	4/4	1	65.6	5.0	0.1 ± 0.1	0.2 ± 0.2

Table A.3: Photometric data for all outer Galaxy sources.

Name	F_{70} (Jy)	F_{160} (Jy)	F_{250} (Jy)	F_{350} (Jy)	F_{500} (Jy)	F_{8} (Jy)	$F_{12.1}$ (Jy)	$F_{14.7}$ (Jy)	F_{21} (Jy)	F_{14} (Jy)	F_{22} (Jy)
G225.020–00.590	–	$(23.5\pm4.7)\times10^{-2}$	$(9.3\pm1.9)\times10^{-1}$	$(7.0\pm1.4)\times10^{-1}$	$(2.9\pm1.5)\times10^{-1}$	–	–	$(5.7\pm1.7)\times10^{-1}$	$(9.9\pm3.0)\times10^{-1}$	$(4.1\pm1.2)\times10^{-3}$	–
G225.030+00.060	$(20.5\pm4.1)\times10^{-2}$	$(20.5\pm4.1)\times10^{-2}$	$(20.1\pm4.0)\times10^{-2}$	$(11.5\pm2.3)\times10^{-2}$	$(5.3\pm2.7)\times10^{-2}$	–	$(4.7\pm1.4)\times10^{-1}$	–	–	$(16.2\pm4.9)\times10^{-4}$	$(32.1\pm9.6)\times10^{-4}$
G225.080+00.060	$(34.0\pm7.1)\times10^{-3}$	$(34.4\pm6.9)\times10^{-2}$	$(43.3\pm8.7)\times10^{-2}$	$(26.0\pm5.2)\times10^{-2}$	$(9.1\pm4.5)\times10^{-2}$	$(5.3\pm2.6)\times10^{-2}$	–	–	$(5.5\pm1.7)\times10^{-1}$	$(30.6\pm9.2)\times10^{-4}$	–
G225.160–00.830	$(6.5\pm1.3)\times10^{-1}$	$(10.8\pm2.2)\times10^{-1}$	$(6.5\pm1.3)\times10^{-1}$	$(35.1\pm7.0)\times10^{-2}$	$(13.4\pm6.7)\times10^{-2}$	$(2.3\pm1.1)\times10^{-2}$	$(17.1\pm5.4)\times10^{-2}$	–	$(5.0\pm1.5)\times10^{-1}$	$(12.7\pm3.8)\times10^{-3}$	$(9.3\pm2.8)\times10^{-3}$
G225.160–00.840	$(33.4\pm6.7)\times10^{-2}$	$(31.0\pm6.2)\times10^{-2}$	$(29.4\pm5.9)\times10^{-2}$	$(12.7\pm2.6)\times10^{-2}$	$(13.8\pm6.9)\times10^{-2}$	–	$(31.1\pm9.4)\times10^{-2}$	$(16.0\pm5.0)\times10^{-2}$	–	$(22.9\pm6.9)\times10^{-4}$	–
G225.170–00.750	$(20.0\pm4.0)\times10^{-2}$	$(29.9\pm6.0)\times10^{-2}$	$(29.1\pm5.8)\times10^{-2}$	$(15.6\pm3.1)\times10^{-2}$	$(5.5\pm2.7)\times10^{-2}$	$(2.8\pm1.4)\times10^{-2}$	$(3.5\pm1.1)\times10^{-1}$	–	$(4.6\pm1.4)\times10^{-1}$	$(8.4\pm2.5)\times10^{-3}$	$(7.2\pm2.2)\times10^{-3}$
G225.210–01.110	–	$(7.3\pm1.5)\times10^{+0}$	$(13.8\pm2.8)\times10^{+0}$	$(10.5\pm2.1)\times10^{+0}$	$(5.8\pm2.9)\times10^{+0}$	$(7.5\pm3.8)\times10^{-2}$	–	–	–	–	–
G225.220–01.200	–	$(6.0\pm1.2)\times10^{-1}$	$(46.8\pm9.4)\times10^{-2}$	$(26.6\pm5.3)\times10^{-2}$	$(8.5\pm4.2)\times10^{-2}$	–	$(24.8\pm7.8)\times10^{-2}$	$(5.1\pm1.5)\times10^{-1}$	–	$(11.7\pm3.5)\times10^{-3}$	$(7.7\pm2.3)\times10^{-3}$
G225.230–00.960	–	$(15.6\pm3.1)\times10^{-1}$	$(14.6\pm2.9)\times10^{-1}$	$(8.9\pm1.8)\times10^{-1}$	$(3.0\pm1.5)\times10^{-1}$	–	–	$(5.0\pm1.5)\times10^{-1}$	$(22.9\pm6.9)\times10^{-1}$	$(25.2\pm7.6)\times10^{-3}$	$(20.2\pm6.1)\times10^{-3}$
G225.240–01.110	–	$(25.0\pm5.0)\times10^{-2}$	$(24.8\pm5.0)\times10^{-2}$	$(16.1\pm3.3)\times10^{-2}$	$(6.5\pm6.5)\times10^{-2}$	$(2.1\pm1.1)\times10^{-2}$	–	$(15.8\pm4.9)\times10^{-2}$	–	$(4.6\pm1.4)\times10^{-3}$	$(14.1\pm4.2)\times10^{-4}$
G225.300–01.090	$(14.4\pm2.9)\times10^{-2}$	$(27.0\pm5.4)\times10^{-2}$	$(46.7\pm9.4)\times10^{-2}$	$(34.6\pm7.0)\times10^{-2}$	$(10.8\pm5.5)\times10^{-2}$	–	–	–	$(6.9\pm2.1)\times10^{-1}$	$(3.6\pm1.1)\times10^{-3}$	$(12.0\pm3.6)\times10^{-4}$
G225.320–00.280	–	$(23.5\pm4.7)\times10^{-1}$	$(33.2\pm6.6)\times10^{-1}$	$(23.8\pm4.8)\times10^{-1}$	$(10.5\pm5.3)\times10^{-1}$	$(3.8\pm1.9)\times10^{-2}$	–	–	$(5.7\pm1.7)\times10^{-1}$	–	–
G225.320–01.100	–	$(32.5\pm6.5)\times10^{-2}$	$(15.5\pm3.1)\times10^{-1}$	$(11.6\pm2.3)\times10^{-1}$	$(4.9\pm2.4)\times10^{-1}$	–	$(12.6\pm3.8)\times10^{-1}$	–	$(10.1\pm3.0)\times10^{-1}$	–	–
G225.320–01.170	$(24.2\pm5.1)\times10^{-3}$	$(7.1\pm1.4)\times10^{-1}$	$(9.8\pm2.0)\times10^{-1}$	$(47.9\pm9.6)\times10^{-2}$	$(2.1\pm1.1)\times10^{-1}$	–	–	–	–	$(10.6\pm3.2)\times10^{-3}$	$(4.6\pm1.4)\times10^{-3}$
G225.330–00.540	$(10.2\pm2.0)\times10^{+0}$	$(12.6\pm2.5)\times10^{+0}$	$(7.2\pm1.4)\times10^{+0}$	$(37.2\pm7.4)\times10^{-1}$	$(9.4\pm9.4)\times10^{-1}$	$(9.4\pm4.7)\times10^{-1}$	$(11.7\pm3.5)\times10^{-1}$	$(15.7\pm4.7)\times10^{-1}$	$(28.0\pm8.4)\times10^{-1}$	$(6.4\pm1.9)\times10^{-1}$	$(17.0\pm5.1)\times10^{-1}$
G225.330–01.120	$(6.9\pm1.4)\times10^{-2}$	$(48.2\pm9.6)\times10^{-2}$	$(5.2\pm1.0)\times10^{-1}$	$(36.6\pm7.4)\times10^{-2}$	$(1.5\pm1.5)\times10^{-1}$	–	–	$(15.9\pm5.0)\times10^{-2}$	–	$(23.2\pm7.0)\times10^{-4}$	$(12.1\pm3.6)\times10^{-4}$
G225.370–01.380	$(10.2\pm2.0)\times10^{-2}$	$(40.3\pm8.1)\times10^{-2}$	$(31.5\pm6.3)\times10^{-2}$	$(19.2\pm3.9)\times10^{-2}$	$(6.5\pm3.3)\times10^{-2}$	–	–	–	$(8.8\pm2.7)\times10^{-1}$	$(17.8\pm5.3)\times10^{-4}$	$(31.3\pm9.4)\times10^{-4}$
G225.380–00.540	–	$(17.1\pm3.4)\times10^{-1}$	$(27.9\pm5.6)\times10^{-1}$	$(19.8\pm4.0)\times10^{-1}$	$(9.3\pm4.7)\times10^{-1}$	$(4.9\pm2.5)\times10^{-2}$	$(24.8\pm7.6)\times10^{-2}$	–	–	–	–
G225.390–00.990	$(10.2\pm2.1)\times10^{-2}$	$(5.4\pm1.1)\times10^{-1}$	$(6.6\pm1.3)\times10^{-1}$	$(37.2\pm7.5)\times10^{-2}$	$(15.1\pm7.6)\times10^{-2}$	–	$(19.5\pm6.1)\times10^{-2}$	$(29.4\pm9.0)\times10^{-2}$	–	–	$(3.9\pm1.2)\times10^{-4}$
G225.390–01.370	$(6.6\pm1.3)\times10^{-2}$	$(48.4\pm9.7)\times10^{-2}$	$(7.7\pm1.5)\times10^{-1}$	$(38.1\pm7.6)\times10^{-2}$	$(16.3\pm8.1)\times10^{-2}$	$(2.6\pm1.3)\times10^{-1}$	$(6.6\pm2.0)\times10^{-1}$	–	–	$(8.5\pm2.6)\times10^{-2}$	$(27.3\pm8.2)\times10^{-3}$
G225.400–00.560	$(32.3\pm6.5)\times10^{-1}$	$(40.2\pm8.0)\times10^{-1}$	$(24.3\pm4.9)\times10^{-1}$	$(13.1\pm2.6)\times10^{-1}$	$(4.9\pm4.9)\times10^{-1}$	–	–	$(21.8\pm6.7)\times10^{-2}$	–	–	$(13.0\pm3.9)\times10^{-2}$
G225.440–00.390	$(5.7\pm1.1)\times10^{-1}$	$(7.2\pm1.4)\times10^{+0}$	$(7.3\pm1.5)\times10^{+0}$	$(5.1\pm1.0)\times10^{+0}$	$(2.4\pm1.2)\times10^{+0}$	$(8.2\pm4.1)\times10^{-2}$	$(10.1\pm3.0)\times10^{-1}$	–	–	$(10.3\pm3.1)\times10^{-2}$	$(12.8\pm3.9)\times10^{-2}$
G225.460–01.680	$(23.4\pm4.7)\times10^{-2}$	$(6.0\pm1.2)\times10^{-1}$	$(42.2\pm8.4)\times10^{-2}$	$(22.6\pm4.5)\times10^{-2}$	$(8.4\pm8.4)\times10^{-2}$	–	–	–	–	–	–
G225.470–01.680	$(15.9\pm3.2)\times10^{-2}$	$(5.4\pm1.1)\times10^{-1}$	$(32.5\pm6.5)\times10^{-2}$	$(16.9\pm3.4)\times10^{-2}$	$(5.9\pm5.9)\times10^{-2}$	–	–	–	–	$(5.4\pm1.6)\times10^{-4}$	–
G225.480–00.230	–	$(5.0\pm1.0)\times10^{+0}$	$(10.5\pm2.1)\times10^{+0}$	$(8.8\pm1.8)\times10^{+0}$	$(4.7\pm2.4)\times10^{+0}$	$(3.6\pm1.8)\times10^{-2}$	$(5.1\pm1.5)\times10^{-1}$	$(9.8\pm3.0)\times10^{-1}$	$(19.9\pm6.0)\times10^{-1}$	$(16.4\pm4.9)\times10^{-3}$	$(14.6\pm4.4)\times10^{-3}$
G225.480–01.790	$(6.3\pm1.3)\times10^{-1}$	$(20.5\pm4.1)\times10^{-1}$	$(12.4\pm2.5)\times10^{-1}$	$(6.2\pm1.2)\times10^{-1}$	$(16.7\pm8.4)\times10^{-2}$	–	–	–	$(8.1\pm2.5)\times10^{-1}$	$(4.0\pm1.2)\times10^{-2}$	$(4.1\pm1.2)\times10^{-2}$
G225.480–01.800	$(49.6\pm9.9)\times10^{-2}$	$(17.0\pm3.4)\times10^{-1}$	$(10.4\pm2.1)\times10^{-1}$	$(39.8\pm8.0)\times10^{-2}$	$(1.2\pm1.2)\times10^{-1}$	–	–	$(24.8\pm7.6)\times10^{-2}$	$(6.6\pm2.0)\times10^{-1}$	$(31.0\pm9.3)\times10^{-3}$	$(30.9\pm9.3)\times10^{-3}$
G225.490–00.400	$(8.3\pm1.7)\times10^{-1}$	$(10.0\pm2.0)\times10^{+0}$	$(10.4\pm2.1)\times10^{+0}$	$(6.6\pm1.3)\times10^{+0}$	$(3.2\pm1.6)\times10^{+0}$	–	–	–	$(9.6\pm2.9)\times10^{-1}$	$(6.2\pm1.9)\times10^{-2}$	$(7.0\pm2.1)\times10^{-2}$
G225.490–01.780	$(10.0\pm2.0)\times10^{-1}$	$(33.4\pm6.7)\times10^{-1}$	$(22.7\pm4.5)\times10^{-1}$	$(9.1\pm1.8)\times10^{-1}$	$(3.3\pm1.6)\times10^{-1}$	$(3.0\pm1.5)\times10^{-2}$	–	–	–	$(8.4\pm2.5)\times10^{-2}$	$(9.2\pm2.8)\times10^{-2}$
G225.490–01.810	$(23.5\pm4.7)\times10^{-1}$	$(8.9\pm1.8)\times10^{+0}$	$(5.1\pm1.0)\times10^{+0}$	$(24.9\pm5.0)\times10^{-1}$	$(10.2\pm5.1)\times10^{-1}$	$(18.8\pm9.4)\times10^{-2}$	$(11.7\pm3.5)\times10^{-1}$	$(10.0\pm3.0)\times10^{-1}$	$(13.9\pm4.2)\times10^{-1}$	$(30.9\pm9.3)\times10^{-2}$	$(3.3\pm1.0)\times10^{-1}$
G225.500–01.230	–	$(11.5\pm2.3)\times10^{-2}$	$(7.1\pm1.4)\times10^{-2}$	$(39.6\pm8.6)\times10^{-3}$	–	$(3.0\pm1.5)\times10^{-2}$	–	$(31.6\pm9.6)\times10^{-2}$	–	$(18.0\pm5.4)\times10^{-4}$	–
G225.500–01.770	$(34.2\pm6.8)\times10^{-2}$	$(14.2\pm2.8)\times10^{-1}$	$(9.3\pm1.9)\times10^{-1}$	$(43.8\pm9.0)\times10^{-2}$	$(1.5\pm1.5)\times10^{-1}$	–	–	–	–	$(26.1\pm7.8)\times10^{-3}$	$(27.7\pm8.3)\times10^{-3}$
G225.510–01.230	$(13.5\pm2.7)\times10^{-2}$	$(14.5\pm2.9)\times10^{-2}$	$(13.4\pm2.7)\times10^{-2}$	$(8.2\pm1.7)\times10^{-2}$	$(2.4\pm1.2)\times10^{-2}$	$(3.9\pm2.0)\times10^{-2}$	–	$(3.4\pm1.0)\times10^{-1}$	–	$(22.7\pm6.8)\times10^{-4}$	$(3.9\pm1.2)\times10^{-3}$
G225.510–01.740	$(13.6\pm2.7)\times10^{-1}$	$(33.3\pm6.7)\times10^{-1}$	$(17.8\pm3.6)\times10^{-1}$	$(16.0\pm3.6)\times10^{-2}$	$(4.8\pm2.4)\times10^{-1}$	–	$(23.1\pm6.9)\times10^{-1}$	–	$(19.9\pm6.0)\times10^{-1}$	$(22.2\pm6.7)\times10^{-2}$	$(18.3\pm5.5)\times10^{-2}$
G225.510–01.780	$(20.0\pm4.0)\times10^{-1}$	$(10.7\pm2.1)\times10^{+0}$	$(7.9\pm1.6)\times10^{+0}$	$(42.4\pm8.5)\times10^{-1}$	$(16.9\pm8.5)\times10^{-1}$	–	–	–	–	$(15.5\pm4.7)\times10^{-2}$	$(14.9\pm4.5)\times10^{-2}$
G225.660–00.220	$(6.9\pm1.4)\times10^{-1}$	$(42.3\pm8.5)\times10^{-1}$	$(36.3\pm7.3)\times10^{-1}$	$(23.0\pm4.6)\times10^{-1}$	$(9.2\pm4.6)\times10^{-1}$	–	$(6.6\pm2.0)\times10^{-1}$	–	–	$(5.9\pm1.8)\times10^{-2}$	$(6.1\pm1.8)\times10^{-2}$
G225.780–00.940	–	$(38.6\pm7.7)\times10^{-1}$	$(6.9\pm1.4)\times10^{+0}$	$(5.2\pm1.0)\times10^{+0}$	$(2.4\pm1.2)\times10^{+0}$	–	–	–	–	–	–
G225.980+00.080	$(23.2\pm4.7)\times10^{-2}$	$(9.6\pm1.9)\times10^{-1}$	$(6.3\pm1.3)\times10^{-1}$	$(30.4\pm6.1)\times10^{-2}$	$(10.1\pm5.1)\times10^{-2}$	$(3.1\pm1.6)\times10^{-2}$	–	–	–	$(19.4\pm5.8)\times10^{-3}$	$(17.5\pm5.2)\times10^{-3}$
G226.117–00.349	$(6.6\pm1.3)\times10^{+0}$	$(9.8\pm2.0)\times10^{+0}$	$(44.5\pm8.9)\times10^{-1}$	$(19.6\pm3.9)\times10^{-1}$	$(4.8\pm4.8)\times10^{-1}$	$(16.3\pm8.1)\times10^{-2}$	–	$(7.2\pm2.2)\times10^{-1}$	$(8.2\pm2.5)\times10^{-1}$	$(4.5\pm1.3)\times10^{-1}$	$(12.1\pm3.6)\times10^{-1}$
G226.280–02.070	$(25.1\pm5.0)\times10^{-2}$	$(5.4\pm1.1)\times10^{-1}$	$(40.7\pm8.1)\times10^{-2}$	$(22.1\pm4.4)\times10^{-2}$	$(8.1\pm4.1)\times10^{-2}$	–	–	$(5.7\pm1.7)\times10^{-1}$	–	$(5.4\pm1.6)\times10^{-3}$	$(4.4\pm1.3)\times10^{-3}$
G226.330–02.030	–	$(7.7\pm1.5)\times10^{-1}$	$(7.1\pm1.4)\times10^{-1}$	$(42.9\pm8.6)\times10^{-2}$	$(14.6\pm7.3)\times10^{-2}$	$(7.2\pm3.6)\times10^{-2}$	–	$(4.3\pm1.3)\times10^{-1}$	$(11.5\pm3.5)\times10^{-1}$	$(32.1\pm9.6)\times10^{-4}$	$(3.8\pm1.1)\times10^{-3}$
G226.353–00.766	$(33.0\pm6.6)\times10^{+0}$	$(5.4\pm1.1)\times10^{+1}$	$(26.0\pm5.2)\times10^{+0}$	$(11.4\pm2.3)\times10^{+0}$	$(3.4\pm3.4)\times10^{+0}$	$(6.3\pm3.2)\times10^{-2}$	$(26.1\pm8.0)\times10^{-2}$	–	–	$(12.3\pm3.7)\times10^{-2}$	$(14.2\pm4.3)\times10^{-1}$

Table A.3: continued

Name	F_{70} (Jy)	F_{160} (Jy)	F_{250} (Jy)	F_{350} (Jy)	F_{500} (Jy)	F_{8} (Jy)	$F_{12.1}$ (Jy)	$F_{14.7}$ (Jy)	F_{21} (Jy)	F_{14} (Jy)	F_{22} (Jy)
G226.670–02.060	–	$(5.3\pm1.1)\times10^{-1}$	$(5.6\pm1.1)\times10^{-1}$	$(28.5\pm5.7)\times10^{-2}$	$(11.4\pm5.7)\times10^{-2}$	–	–	–	–	$(5.4\pm1.6)\times10^{-3}$	$(4.5\pm1.4)\times10^{-3}$
G227.040–00.900	$(15.6\pm3.1)\times10^{-2}$	$(5.4\pm1.1)\times10^{-1}$	$(7.6\pm1.5)\times10^{-1}$	$(6.0\pm1.2)\times10^{-1}$	$(2.4\pm1.2)\times10^{-1}$	–	–	–	$(4.3\pm1.3)\times10^{-1}$	$(13.9\pm4.2)\times10^{-3}$	$(3.4\pm1.0)\times10^{-2}$
G227.180–00.460	–	$(7.4\pm1.5)\times10^{-2}$	$(47.7\pm9.6)\times10^{-3}$	$(26.3\pm5.5)\times10^{-3}$	$(1.3\pm1.3)\times10^{-2}$	–	–	–	–	–	$(7.1\pm2.1)\times10^{-4}$
G227.230–00.830	–	$(6.6\pm1.3)\times10^{-1}$	$(7.0\pm1.4)\times10^{-1}$	$(44.3\pm8.9)\times10^{-2}$	$(16.0\pm8.0)\times10^{-2}$	–	–	–	$(14.4\pm4.3)\times10^{-1}$	$(7.6\pm2.3)\times10^{-3}$	$(5.7\pm1.7)\times10^{-3}$
G227.570–01.140	$(9.3\pm1.9)\times10^{-1}$	$(27.6\pm5.5)\times10^{-1}$	$(16.0\pm3.2)\times10^{-1}$	$(8.3\pm1.7)\times10^{-1}$	$(2.9\pm2.9)\times10^{-1}$	$(14.2\pm7.1)\times10^{-2}$	$(4.9\pm1.5)\times10^{-1}$	$(3.8\pm1.2)\times10^{-1}$	–	$(18.2\pm5.5)\times10^{-2}$	$(21.4\pm6.4)\times10^{-2}$
G227.650–01.286	–	$(30.3\pm6.1)\times10^{-2}$	$(33.0\pm6.6)\times10^{-2}$	$(22.4\pm4.5)\times10^{-2}$	$(9.1\pm9.1)\times10^{-2}$	–	–	$(24.9\pm7.6)\times10^{-2}$	–	$(29.8\pm8.9)\times10^{-4}$	$(28.9\pm8.7)\times10^{-4}$
G227.689–00.121	$(21.1\pm4.2)\times10^{-1}$	$(31.3\pm6.3)\times10^{-1}$	$(15.3\pm3.1)\times10^{-1}$	$(6.0\pm1.2)\times10^{-1}$	$(2.0\pm1.0)\times10^{-1}$	$(4.3\pm2.2)\times10^{-2}$	–	$(4.4\pm1.3)\times10^{-1}$	$(11.6\pm3.5)\times10^{-1}$	$(23.1\pm6.9)\times10^{-2}$	$(14.7\pm4.4)\times10^{-2}$
G227.792–00.104	$(7.9\pm1.6)\times10^{+0}$	$(12.1\pm2.4)\times10^{+0}$	$(5.6\pm1.1)\times10^{+0}$	$(25.9\pm5.2)\times10^{-1}$	$(9.9\pm4.9)\times10^{-1}$	$(19.4\pm9.7)\times10^{-2}$	$(15.1\pm4.5)\times10^{-1}$	$(8.0\pm2.4)\times10^{-1}$	$(7.4\pm2.3)\times10^{-1}$	$(6.2\pm1.9)\times10^{-1}$	$(5.0\pm1.5)\times10^{-1}$
G227.800–00.080	$(6.1\pm1.2)\times10^{-1}$	$(15.7\pm3.1)\times10^{-1}$	$(9.5\pm1.9)\times10^{-1}$	$(47.5\pm9.5)\times10^{-2}$	$(2.1\pm1.0)\times10^{-1}$	–	–	$(21.8\pm6.7)\times10^{-2}$	$(4.1\pm1.3)\times10^{-1}$	$(5.7\pm1.7)\times10^{-2}$	$(5.7\pm1.7)\times10^{-2}$
G227.800–00.140	$(29.4\pm5.9)\times10^{-1}$	$(6.0\pm1.2)\times10^{+0}$	$(29.8\pm6.0)\times10^{-1}$	$(13.1\pm2.6)\times10^{-1}$	$(4.4\pm2.2)\times10^{-1}$	$(6.2\pm3.1)\times10^{-2}$	$(31.7\pm9.6)\times10^{-2}$	$(3.9\pm1.2)\times10^{-1}$	–	$(23.3\pm7.0)\times10^{-2}$	$(9.2\pm2.8)\times10^{-2}$
G227.810–00.120	$(13.1\pm2.6)\times10^{-1}$	$(29.9\pm6.0)\times10^{-1}$	$(17.8\pm3.6)\times10^{-1}$	$(7.8\pm1.6)\times10^{-1}$	$(2.2\pm2.2)\times10^{-1}$	–	–	–	$(12.1\pm3.6)\times10^{-1}$	$(5.1\pm1.5)\times10^{-2}$	$(5.3\pm1.6)\times10^{-2}$
G227.815–00.129	$(13.4\pm2.7)\times10^{-1}$	$(35.0\pm7.0)\times10^{-1}$	$(20.1\pm4.0)\times10^{-1}$	$(8.9\pm1.8)\times10^{-1}$	$(2.8\pm2.8)\times10^{-1}$	$(15.4\pm7.8)\times10^{-3}$	–	–	$(10.1\pm3.1)\times10^{-1}$	$(6.2\pm1.9)\times10^{-2}$	$(5.3\pm1.6)\times10^{-2}$
G227.820–00.140	$(12.8\pm2.6)\times10^{+0}$	$(27.8\pm5.6)\times10^{+0}$	$(14.1\pm2.8)\times10^{+0}$	$(6.3\pm1.3)\times10^{+0}$	$(2.1\pm1.1)\times10^{+0}$	$(4.4\pm2.2)\times10^{-1}$	–	–	$(15.5\pm4.7)\times10^{-1}$	$(8.1\pm2.4)\times10^{-1}$	$(6.2\pm1.9)\times10^{-1}$
G227.820–00.160	$(42.9\pm8.6)\times10^{-1}$	$(13.0\pm2.6)\times10^{+0}$	$(5.2\pm1.0)\times10^{+0}$	$(22.4\pm4.5)\times10^{-1}$	$(7.1\pm3.6)\times10^{-1}$	$(2.2\pm1.1)\times10^{-1}$	$(5.0\pm1.5)\times10^{-1}$	$(6.9\pm2.1)\times10^{-1}$	–	$(3.6\pm1.1)\times10^{-1}$	$(20.9\pm6.3)\times10^{-2}$
G227.862–00.243	$(38.8\pm7.8)\times10^{-2}$	$(18.3\pm3.7)\times10^{-1}$	$(13.6\pm2.7)\times10^{-1}$	$(6.4\pm1.3)\times10^{-1}$	$(2.3\pm1.1)\times10^{-1}$	–	$(15.4\pm4.8)\times10^{-2}$	–	$(30.3\pm9.5)\times10^{-2}$	$(32.9\pm9.9)\times10^{-3}$	$(21.3\pm6.4)\times10^{-3}$
G227.880–01.780	–	$(10.2\pm2.0)\times10^{-2}$	$(5.5\pm1.1)\times10^{-1}$	$(35.6\pm7.1)\times10^{-2}$	$(15.1\pm7.6)\times10^{-2}$	$(2.6\pm1.3)\times10^{-2}$	–	–	–	–	–
G227.910–01.880	–	$(18.9\pm3.8)\times10^{-1}$	$(22.5\pm4.5)\times10^{-1}$	$(13.4\pm2.7)\times10^{-1}$	$(5.8\pm2.9)\times10^{-1}$	$(8.6\pm4.3)\times10^{-2}$	–	$(3.6\pm1.1)\times10^{-1}$	–	–	–
G227.940–00.139	$(12.5\pm2.5)\times10^{-2}$	$(38.8\pm7.8)\times10^{-2}$	$(49.2\pm9.8)\times10^{-2}$	$(35.1\pm7.0)\times10^{-2}$	$(1.3\pm1.3)\times10^{-1}$	–	–	–	–	$(5.6\pm1.7)\times10^{-3}$	$(21.2\pm6.4)\times10^{-3}$
G228.030+00.010	–	$(33.2\pm6.6)\times10^{-2}$	$(48.4\pm9.7)\times10^{-2}$	$(29.7\pm5.9)\times10^{-2}$	$(10.8\pm5.4)\times10^{-2}$	–	–	–	–	–	$(3.9\pm1.2)\times10^{-4}$
G228.030+00.020	–	$(29.9\pm6.0)\times10^{-2}$	$(43.5\pm8.7)\times10^{-2}$	$(30.4\pm6.1)\times10^{-2}$	$(9.7\pm9.7)\times10^{-2}$	–	–	–	–	–	$(19.9\pm6.0)\times10^{-4}$
G228.027–00.924	–	$(34.2\pm6.8)\times10^{-2}$	$(6.6\pm1.3)\times10^{-1}$	$(44.3\pm8.9)\times10^{-2}$	$(17.9\pm9.0)\times10^{-2}$	–	–	–	–	$(11.5\pm3.4)\times10^{-4}$	–
G228.026–00.946	–	$(8.4\pm1.7)\times10^{-1}$	$(11.4\pm2.3)\times10^{-1}$	$(8.6\pm1.7)\times10^{-1}$	$(4.1\pm2.0)\times10^{-1}$	–	–	$(6.1\pm1.8)\times10^{-1}$	$(5.5\pm1.7)\times10^{-1}$	–	–
G228.300–00.970	$(18.5\pm4.2)\times10^{-3}$	$(39.9\pm8.0)\times10^{-2}$	$(35.1\pm7.0)\times10^{-2}$	$(18.3\pm3.7)\times10^{-2}$	$(7.7\pm3.9)\times10^{-2}$	–	–	–	–	$(22.3\pm6.7)\times10^{-4}$	$(16.1\pm4.8)\times10^{-4}$
G228.710–00.910	$(16.1\pm3.2)\times10^{-2}$	$(37.1\pm7.4)\times10^{-2}$	$(8.0\pm1.6)\times10^{-1}$	$(48.1\pm9.6)\times10^{-2}$	$(19.4\pm9.7)\times10^{-2}$	–	$(6.9\pm2.1)\times10^{-1}$	$(4.9\pm1.5)\times10^{-1}$	$(4.2\pm1.3)\times10^{-1}$	$(7.3\pm2.2)\times10^{-4}$	–
G229.750+00.030	–	$(13.5\pm2.7)\times10^{-1}$	$(13.0\pm2.6)\times10^{-1}$	$(6.8\pm1.4)\times10^{-1}$	$(3.2\pm1.6)\times10^{-1}$	–	–	–	–	$(4.2\pm1.3)\times10^{-2}$	$(28.4\pm8.5)\times10^{-3}$
G229.770+00.040	$(9.3\pm1.9)\times10^{-1}$	$(31.0\pm6.2)\times10^{-1}$	$(18.4\pm3.7)\times10^{-1}$	$(9.6\pm1.9)\times10^{-1}$	$(3.7\pm1.9)\times10^{-1}$	–	–	$(30.2\pm9.2)\times10^{-2}$	–	$(10.7\pm3.2)\times10^{-2}$	$(8.3\pm2.5)\times10^{-2}$
G229.770+00.060	$(6.0\pm1.2)\times10^{+0}$	$(15.4\pm3.1)\times10^{+0}$	$(8.1\pm1.6)\times10^{+0}$	$(35.6\pm7.1)\times10^{-1}$	$(12.8\pm6.4)\times10^{-1}$	$(3.7\pm1.9)\times10^{-1}$	$(6.5\pm2.0)\times10^{-1}$	$(3.9\pm1.2)\times10^{-1}$	$(8.7\pm2.6)\times10^{-1}$	$(5.3\pm1.6)\times10^{-1}$	$(3.4\pm1.0)\times10^{-1}$
G229.780+00.050	$(16.0\pm3.2)\times10^{-1}$	$(37.3\pm7.5)\times10^{-1}$	$(15.6\pm3.1)\times10^{-1}$	$(6.6\pm1.3)\times10^{-1}$	$(2.8\pm2.8)\times10^{-1}$	$(12.9\pm6.5)\times10^{-2}$	–	–	$(7.0\pm2.1)\times10^{-1}$	$(13.2\pm4.0)\times10^{-2}$	$(6.9\pm2.1)\times10^{-2}$
G229.790–00.680	–	$(22.8\pm4.6)\times10^{-2}$	$(46.3\pm9.3)\times10^{-2}$	$(35.7\pm7.1)\times10^{-2}$	$(1.6\pm1.6)\times10^{-1}$	–	–	–	–	$(3.5\pm1.0)\times10^{-4}$	–
G229.800–00.360	$(19.7\pm3.9)\times10^{-2}$	$(11.6\pm2.3)\times10^{-1}$	$(14.2\pm2.8)\times10^{-1}$	$(10.3\pm2.1)\times10^{-1}$	$(4.4\pm2.2)\times10^{-1}$	$(2.6\pm1.3)\times10^{-2}$	–	–	–	$(9.3\pm2.8)\times10^{-3}$	$(24.7\pm7.4)\times10^{-3}$
G229.900–00.650	$(5.8\pm1.2)\times10^{-2}$	$(39.2\pm7.8)\times10^{-2}$	$(6.3\pm1.3)\times10^{-1}$	$(5.5\pm1.1)\times10^{-1}$	$(2.3\pm1.1)\times10^{-1}$	–	–	–	$(12.0\pm3.6)\times10^{-1}$	–	$(30.9\pm9.3)\times10^{-5}$
G230.340–00.610	$(6.4\pm1.3)\times10^{+0}$	$(11.9\pm2.4)\times10^{+0}$	$(46.4\pm9.3)\times10^{-1}$	$(17.6\pm3.5)\times10^{-1}$	$(5.3\pm2.7)\times10^{-1}$	$(15.2\pm7.6)\times10^{-2}$	–	–	–	$(27.7\pm8.3)\times10^{-2}$	$(16.6\pm5.0)\times10^{-2}$
G230.350–00.600	$(14.4\pm2.9)\times10^{+0}$	$(16.7\pm3.3)\times10^{+0}$	$(5.6\pm1.1)\times10^{+0}$	$(21.0\pm4.2)\times10^{-1}$	$(6.2\pm3.1)\times10^{-1}$	$(4.3\pm2.1)\times10^{-1}$	$(5.2\pm1.6)\times10^{-1}$	$(25.0\pm7.6)\times10^{-2}$	$(6.6\pm2.0)\times10^{-1}$	$(6.3\pm1.9)\times10^{-1}$	$(4.2\pm1.3)\times10^{-1}$
G230.390–00.780	–	$(5.0\pm1.0)\times10^{-1}$	$(32.1\pm6.4)\times10^{-2}$	$(18.5\pm3.7)\times10^{-2}$	$(6.5\pm3.3)\times10^{-2}$	$(4.0\pm2.0)\times10^{-2}$	–	$(4.7\pm1.4)\times10^{-1}$	$(8.7\pm2.6)\times10^{-1}$	$(4.2\pm1.3)\times10^{-3}$	$(21.2\pm6.4)\times10^{-4}$
G230.940–00.400	$(16.5\pm3.3)\times10^{-2}$	$(45.8\pm9.2)\times10^{-2}$	$(6.6\pm1.3)\times10^{-1}$	$(42.5\pm8.5)\times10^{-2}$	$(18.2\pm9.1)\times10^{-2}$	–	$(3.8\pm1.1)\times10^{-1}$	–	–	$(20.0\pm6.0)\times10^{-4}$	$(9.7\pm2.9)\times10^{-3}$
G231.010–00.180	$(40.5\pm8.1)\times10^{-2}$	$(31.8\pm6.4)\times10^{-1}$	$(20.6\pm4.1)\times10^{-1}$	$(9.2\pm1.8)\times10^{-1}$	$(3.1\pm1.6)\times10^{-1}$	$(14.1\pm7.1)\times10^{-2}$	–	–	–	$(18.1\pm5.4)\times10^{-2}$	$(13.0\pm3.9)\times10^{-2}$
G231.070–00.130	$(5.4\pm1.1)\times10^{+0}$	$(17.3\pm3.5)\times10^{+0}$	$(10.2\pm2.0)\times10^{+0}$	$(49.3\pm9.9)\times10^{-1}$	$(18.9\pm9.4)\times10^{-1}$	$(5.7\pm2.9)\times10^{-1}$	$(5.6\pm1.7)\times10^{-1}$	$(20.8\pm6.4)\times10^{-2}$	–	$(8.3\pm2.5)\times10^{-1}$	$(6.3\pm1.9)\times10^{-1}$
G231.130–00.320	$(20.0\pm4.0)\times10^{-1}$	$(8.6\pm1.7)\times10^{+0}$	$(5.3\pm1.1)\times10^{+0}$	$(25.8\pm5.2)\times10^{-1}$	$(8.9\pm4.4)\times10^{-1}$	$(13.6\pm6.8)\times10^{-2}$	$(17.5\pm5.5)\times10^{-2}$	$(3.6\pm1.1)\times10^{-1}$	$(4.7\pm1.4)\times10^{-1}$	$(31.0\pm9.3)\times10^{-2}$	$(24.3\pm7.3)\times10^{-2}$
G231.140–00.330	$(9.8\pm2.0)\times10^{+0}$	$(44.1\pm8.8)\times10^{+0}$	$(27.3\pm5.5)\times10^{+0}$	$(13.2\pm2.6)\times10^{+0}$	$(5.3\pm2.7)\times10^{+0}$	$(10.2\pm5.1)\times10^{-1}$	$(29.6\pm8.9)\times10^{-1}$	$(14.4\pm4.3)\times10^{-1}$	–	$(17.9\pm5.4)\times10^{-1}$	$(12.8\pm3.8)\times10^{-1}$
G231.240–00.390	$(5.2\pm1.0)\times10^{+0}$	$(28.4\pm5.7)\times10^{+0}$	$(16.6\pm3.3)\times10^{+0}$	$(7.3\pm1.5)\times10^{+0}$	$(3.4\pm1.7)\times10^{+0}$	$(5.2\pm2.6)\times10^{-1}$	$(22.8\pm6.9)\times10^{-1}$	$(24.5\pm7.4)\times10^{-1}$	–	$(9.0\pm2.7)\times10^{-1}$	$(6.2\pm1.9)\times10^{-1}$
G231.250–00.330	$(11.1\pm2.2)\times10^{-1}$	$(34.5\pm6.9)\times10^{-1}$	$(18.5\pm3.7)\times10^{-1}$	$(8.9\pm1.8)\times10^{-1}$	$(3.5\pm1.8)\times10^{-1}$	$(11.1\pm5.6)\times10^{-2}$	$(4.5\pm1.4)\times10^{-1}$	–	–	$(19.4\pm5.8)\times10^{-2}$	$(23.3\pm7.0)\times10^{-2}$
G231.260–00.290	$(14.3\pm2.9)\times10^{-1}$	$(5.8\pm1.2)\times10^{+0}$	$(36.8\pm7.4)\times10^{-1}$	$(17.6\pm3.5)\times10^{-1}$	$(6.9\pm3.4)\times10^{-1}$	$(4.5\pm2.3)\times10^{-2}$	–	–	–	$(17.2\pm5.2)\times10^{-2}$	$(16.8\pm5.0)\times10^{-2}$
G231.280–00.260	$(38.5\pm7.7)\times10^{-2}$	$(18.3\pm3.7)\times10^{-1}$	$(13.1\pm2.6)\times10^{-1}$	$(6.9\pm1.4)\times10^{-1}$	$(2.2\pm1.1)\times10^{-1}$	$(3.6\pm1.8)\times10^{-2}$	–	$(28.8\pm8.7)\times10^{-2}$	–	$(8.0\pm2.4)\times10^{-2}$	$(8.5\pm2.5)\times10^{-2}$

Table A.3: continued

Name	F_{70} (Jy)	F_{160} (Jy)	F_{250} (Jy)	F_{350} (Jy)	F_{500} (Jy)	F_{8} (Jy)	$F_{12.1}$ (Jy)	$F_{14.7}$ (Jy)	F_{21} (Jy)	F_{14} (Jy)	F_{22} (Jy)
G231.280–00.280	$(5.7\pm1.1)\times10^{+0}$	$(19.2\pm3.8)\times10^{+0}$	$(11.7\pm2.3)\times10^{+0}$	$(5.7\pm1.1)\times10^{+0}$	$(2.3\pm1.1)\times10^{+0}$	$(2.5\pm1.3)\times10^{-1}$	$(19.2\pm5.9)\times10^{-2}$	$(20.3\pm6.1)\times10^{-1}$	$(10.1\pm3.0)\times10^{-1}$	$(6.1\pm1.8)\times10^{-1}$	$(5.8\pm1.7)\times10^{-1}$
G231.290–00.360	$(45.9\pm9.2)\times10^{-2}$	$(14.3\pm2.9)\times10^{-1}$	$(6.9\pm1.4)\times10^{-1}$	$(28.0\pm5.7)\times10^{-2}$	$(13.0\pm6.5)\times10^{-2}$	–	–	$(3.5\pm1.1)\times10^{-1}$	–	$(15.3\pm4.6)\times10^{-3}$	$(5.6\pm1.7)\times10^{-2}$
G231.300–00.310	$(6.3\pm1.3)\times10^{-1}$	$(11.4\pm2.3)\times10^{-1}$	$(18.9\pm3.8)\times10^{-1}$	$(9.7\pm1.9)\times10^{-1}$	$(3.5\pm1.7)\times10^{-1}$	$(2.1\pm1.0)\times10^{-2}$	$(21.4\pm6.6)\times10^{-2}$	–	–	$(4.1\pm1.2)\times10^{-2}$	$(4.5\pm1.3)\times10^{-2}$
G231.310–00.290	$(34.5\pm6.9)\times10^{-2}$	$(10.5\pm2.1)\times10^{-1}$	$(46.0\pm9.2)\times10^{-2}$	$(18.9\pm3.9)\times10^{-2}$	–	$(4.0\pm2.0)\times10^{-2}$	–	–	$(7.0\pm2.1)\times10^{-1}$	$(22.0\pm6.6)\times10^{-3}$	$(24.0\pm7.2)\times10^{-3}$
G231.320–00.280	$(6.4\pm1.3)\times10^{-1}$	$(27.7\pm5.5)\times10^{-1}$	$(13.2\pm2.6)\times10^{-1}$	$(5.4\pm1.1)\times10^{-1}$	$(16.9\pm8.5)\times10^{-2}$	$(7.1\pm3.6)\times10^{-2}$	$(26.8\pm8.2)\times10^{-2}$	–	–	$(7.0\pm2.1)\times10^{-2}$	$(6.7\pm2.0)\times10^{-2}$
G231.330–00.380	$(9.5\pm1.9)\times10^{+0}$	$(39.9\pm8.0)\times10^{+0}$	$(25.4\pm5.1)\times10^{+0}$	$(14.5\pm2.9)\times10^{+0}$	$(6.0\pm3.0)\times10^{+0}$	$(8.7\pm4.4)\times10^{-1}$	$(7.8\pm2.3)\times10^{-1}$	$(10.5\pm3.1)\times10^{-1}$	–	$(15.0\pm4.5)\times10^{-1}$	$(9.4\pm2.8)\times10^{-1}$
G231.330–00.690	$(11.7\pm2.4)\times10^{-2}$	$(48.8\pm9.8)\times10^{-2}$	$(6.2\pm1.2)\times10^{-1}$	$(34.1\pm6.8)\times10^{-2}$	$(13.8\pm6.9)\times10^{-2}$	–	–	–	$(7.2\pm2.2)\times10^{-1}$	$(11.5\pm3.4)\times10^{-3}$	$(5.4\pm1.6)\times10^{-3}$
G231.470–01.860	$(9.5\pm1.9)\times10^{-1}$	$(5.4\pm1.1)\times10^{+0}$	$(6.9\pm1.4)\times10^{+0}$	$(46.8\pm9.4)\times10^{-1}$	$(2.1\pm1.0)\times10^{+0}$	–	–	–	–	–	–
G231.540–00.880	$(33.5\pm7.0)\times10^{-3}$	$(13.3\pm2.7)\times10^{-2}$	$(11.8\pm2.4)\times10^{-2}$	$(6.6\pm1.4)\times10^{-2}$	$(3.7\pm3.7)\times10^{-2}$	–	$(31.0\pm9.4)\times10^{-2}$	–	–	$(14.8\pm4.5)\times10^{-4}$	$(11.1\pm3.3)\times10^{-4}$
G231.590–00.840	–	$(18.0\pm3.6)\times10^{-2}$	$(16.4\pm3.3)\times10^{-2}$	$(11.6\pm2.4)\times10^{-2}$	$(8.0\pm8.0)\times10^{-2}$	–	$(27.5\pm8.4)\times10^{-2}$	$(19.1\pm5.9)\times10^{-2}$	$(6.9\pm2.1)\times10^{-1}$	–	$(15.0\pm4.5)\times10^{-4}$
G231.610–01.260	–	$(8.0\pm1.6)\times10^{-1}$	$(7.5\pm1.5)\times10^{-1}$	$(5.4\pm1.1)\times10^{-1}$	$(2.0\pm1.0)\times10^{-1}$	–	–	–	–	$(14.8\pm4.4)\times10^{-4}$	–
G231.740–01.760	$(49.1\pm9.8)\times10^{-2}$	$(14.7\pm2.9)\times10^{-1}$	$(25.5\pm5.1)\times10^{-1}$	$(17.3\pm3.5)\times10^{-1}$	$(8.4\pm4.2)\times10^{-1}$	$(7.1\pm3.5)\times10^{-2}$	–	–	–	$(15.5\pm4.6)\times10^{-2}$	$(8.5\pm2.6)\times10^{-2}$
G231.760–00.250	–	$(18.4\pm3.7)\times10^{-2}$	$(49.3\pm9.9)\times10^{-2}$	$(39.1\pm7.8)\times10^{-2}$	$(2.2\pm1.1)\times10^{-1}$	$(4.0\pm2.0)\times10^{-2}$	–	–	$(4.5\pm1.4)\times10^{-1}$	$(5.3\pm1.6)\times10^{-3}$	–
G231.770–00.350	$(35.2\pm7.0)\times10^{-2}$	$(6.2\pm1.2)\times10^{-1}$	$(49.1\pm9.8)\times10^{-2}$	$(28.4\pm5.7)\times10^{-2}$	$(11.5\pm5.8)\times10^{-2}$	–	–	–	–	$(4.2\pm1.3)\times10^{-3}$	$(13.9\pm4.2)\times10^{-4}$
G231.793–01.970	$(48.9\pm9.8)\times10^{+0}$	$(32.8\pm6.6)\times10^{+0}$	$(12.1\pm2.4)\times10^{+0}$	$(5.2\pm1.0)\times10^{+0}$	$(1.9\pm1.9)\times10^{+0}$	$(7.0\pm3.5)\times10^{+0}$	$(10.2\pm3.1)\times10^{+0}$	$(12.8\pm3.8)\times10^{+0}$	$(18.1\pm5.4)\times10^{+0}$	$(28.2\pm8.4)\times10^{-1}$	$(10.8\pm3.2)\times10^{+0}$
G231.930–01.500	$(28.9\pm5.8)\times10^{-1}$	$(7.2\pm1.4)\times10^{+0}$	$(5.1\pm1.0)\times10^{+0}$	$(27.3\pm5.5)\times10^{-1}$	$(9.8\pm4.9)\times10^{-1}$	$(12.1\pm6.1)\times10^{-2}$	$(28.7\pm8.9)\times10^{-2}$	$(25.3\pm7.8)\times10^{-2}$	–	$(26.6\pm8.0)\times10^{-2}$	$(27.8\pm8.3)\times10^{-2}$
G231.940–01.510	$(16.1\pm3.2)\times10^{-1}$	$(39.3\pm7.9)\times10^{-1}$	$(19.3\pm3.9)\times10^{-1}$	$(7.8\pm1.6)\times10^{-1}$	$(2.7\pm2.7)\times10^{-1}$	$(3.6\pm1.8)\times10^{-2}$	–	–	–	$(10.1\pm3.0)\times10^{-2}$	$(7.8\pm2.3)\times10^{-2}$
G232.075–02.276	$(6.4\pm1.3)\times10^{+1}$	$(7.8\pm1.6)\times10^{+1}$	$(33.7\pm6.7)\times10^{+0}$	$(13.2\pm2.6)\times10^{+0}$	$(3.6\pm3.6)\times10^{+0}$	$(17.7\pm8.8)\times10^{-1}$	$(22.2\pm6.7)\times10^{-1}$	$(25.4\pm7.6)\times10^{-1}$	$(8.1\pm2.4)\times10^{+0}$	$(26.1\pm7.8)\times10^{-1}$	$(8.7\pm2.6)\times10^{+0}$
G232.220+00.190	$(12.7\pm2.5)\times10^{-2}$	$(6.8\pm1.4)\times10^{-1}$	$(6.1\pm1.2)\times10^{-1}$	$(5.4\pm1.1)\times10^{-1}$	$(2.5\pm1.3)\times10^{-1}$	–	–	–	$(8.8\pm2.7)\times10^{-1}$	–	$(3.7\pm1.1)\times10^{-3}$
G232.220–01.070	–	$(17.1\pm3.4)\times10^{-2}$	$(23.2\pm4.7)\times10^{-2}$	$(14.8\pm3.0)\times10^{-2}$	$(5.6\pm2.8)\times10^{-2}$	$(4.5\pm2.2)\times10^{-2}$	$(5.5\pm1.6)\times10^{-1}$	$(30.2\pm9.2)\times10^{-2}$	–	$(6.4\pm1.9)\times10^{-3}$	$(5.0\pm1.5)\times10^{-3}$
G232.230+00.180	–	$(13.9\pm2.8)\times10^{-2}$	$(39.3\pm7.9)\times10^{-2}$	$(30.0\pm6.1)\times10^{-2}$	$(1.1\pm1.1)\times10^{-1}$	–	–	–	–	–	–
G232.240+00.130	$(12.9\pm2.6)\times10^{-2}$	$(38.6\pm7.7)\times10^{-2}$	$(44.4\pm8.9)\times10^{-2}$	$(34.4\pm6.9)\times10^{-2}$	$(17.8\pm8.9)\times10^{-2}$	$(3.8\pm1.9)\times10^{-2}$	$(28.0\pm8.6)\times10^{-2}$	–	–	–	$(16.5\pm4.9)\times10^{-4}$
G232.250+00.060	–	$(32.6\pm6.5)\times10^{-2}$	$(33.7\pm6.8)\times10^{-2}$	$(19.6\pm4.0)\times10^{-2}$	$(6.0\pm6.0)\times10^{-2}$	–	–	–	–	–	–
G232.250+00.070	–	$(25.0\pm5.0)\times10^{-2}$	$(32.8\pm6.6)\times10^{-2}$	$(20.2\pm4.2)\times10^{-2}$	$(7.9\pm7.9)\times10^{-2}$	–	–	–	–	$(6.2\pm1.9)\times10^{-4}$	$(19.6\pm5.9)\times10^{-4}$
G232.490–00.300	$(24.7\pm5.0)\times10^{-2}$	$(25.4\pm5.1)\times10^{-1}$	$(39.5\pm7.9)\times10^{-1}$	$(28.7\pm5.7)\times10^{-1}$	$(15.1\pm7.5)\times10^{-1}$	–	–	–	–	–	$(6.3\pm1.9)\times10^{-3}$
G232.500–00.040	–	$(24.2\pm4.8)\times10^{-2}$	$(41.7\pm8.3)\times10^{-2}$	$(26.2\pm5.3)\times10^{-2}$	$(7.7\pm7.7)\times10^{-2}$	$(17.0\pm8.6)\times10^{-3}$	–	–	–	–	–
G232.504–01.223	$(21.9\pm4.4)\times10^{-2}$	$(41.7\pm8.3)\times10^{-2}$	$(43.0\pm8.6)\times10^{-2}$	$(23.7\pm4.7)\times10^{-2}$	$(7.0\pm7.0)\times10^{-2}$	$(4.7\pm2.3)\times10^{-2}$	–	$(15.4\pm4.9)\times10^{-2}$	$(8.2\pm2.5)\times10^{-1}$	$(4.6\pm1.4)\times10^{-2}$	$(5.8\pm1.7)\times10^{-2}$
G232.590–01.190	$(18.0\pm3.6)\times10^{-2}$	$(32.8\pm6.6)\times10^{-2}$	$(26.2\pm5.2)\times10^{-2}$	$(9.7\pm1.9)\times10^{-2}$	$(5.1\pm2.6)\times10^{-2}$	–	–	–	–	$(24.6\pm7.4)\times10^{-3}$	$(18.7\pm5.6)\times10^{-3}$
G232.600+00.100	–	$(32.9\pm6.6)\times10^{-2}$	$(7.5\pm1.5)\times10^{-1}$	$(5.3\pm1.1)\times10^{-1}$	$(2.0\pm1.0)\times10^{-1}$	–	–	–	–	–	–
G232.600–01.320	–	$(11.8\pm2.4)\times10^{-2}$	$(14.3\pm2.9)\times10^{-2}$	$(8.6\pm1.7)\times10^{-2}$	–	–	–	$(5.0\pm1.5)\times10^{-1}$	–	$(3.5\pm1.0)\times10^{-3}$	–
G232.640–00.420	–	$(41.1\pm8.2)\times10^{-2}$	$(30.7\pm6.1)\times10^{-2}$	$(17.4\pm3.5)\times10^{-2}$	$(6.1\pm3.1)\times10^{-2}$	–	–	–	–	–	$(12.6\pm3.8)\times10^{-4}$
G232.680+00.160	$(13.6\pm2.8)\times10^{-2}$	$(41.3\pm8.3)\times10^{-2}$	$(22.7\pm4.6)\times10^{-2}$	$(16.8\pm3.4)\times10^{-2}$	$(6.8\pm6.8)\times10^{-2}$	–	–	–	–	–	–
G232.710–00.240	–	$(11.6\pm2.3)\times10^{-2}$	$(24.3\pm4.9)\times10^{-2}$	$(16.5\pm3.4)\times10^{-2}$	$(6.8\pm6.8)\times10^{-2}$	–	–	–	$(3.4\pm1.1)\times10^{-1}$	–	–
G232.760+00.050	$(33.4\pm6.7)\times10^{-2}$	$(8.8\pm1.8)\times10^{-1}$	$(9.6\pm1.9)\times10^{-1}$	$(7.4\pm1.5)\times10^{-1}$	$(3.1\pm3.1)\times10^{-1}$	$(2.7\pm1.3)\times10^{-2}$	–	–	–	$(5.1\pm1.5)\times10^{-2}$	$(9.3\pm2.8)\times10^{-2}$
G232.760–00.240	$(6.0\pm1.2)\times10^{-2}$	$(9.2\pm1.8)\times10^{-1}$	$(8.9\pm1.8)\times10^{-1}$	$(5.2\pm1.0)\times10^{-1}$	$(2.3\pm1.1)\times10^{-1}$	–	$(4.1\pm1.2)\times10^{-1}$	–	–	$(17.4\pm5.2)\times10^{-4}$	$(13.2\pm4.0)\times10^{-4}$
G232.770–00.340	$(8.9\pm1.8)\times10^{-2}$	$(32.0\pm6.4)\times10^{-2}$	$(5.3\pm1.1)\times10^{-1}$	$(38.3\pm7.7)\times10^{-2}$	$(1.3\pm1.3)\times10^{-1}$	–	–	–	–	–	–
G232.770–00.350	–	$(30.4\pm6.1)\times10^{-2}$	$(5.2\pm1.0)\times10^{-1}$	$(38.5\pm7.7)\times10^{-2}$	$(1.6\pm1.6)\times10^{-1}$	–	–	–	–	–	–
G232.770–00.360	–	$(23.7\pm4.7)\times10^{-2}$	$(7.0\pm1.4)\times10^{-1}$	$(46.6\pm9.4)\times10^{-2}$	$(2.3\pm1.2)\times10^{-1}$	–	–	$(3.5\pm1.1)\times10^{-1}$	$(4.4\pm1.3)\times10^{-1}$	–	–
G232.790+00.150	$(10.7\pm2.1)\times10^{+0}$	$(17.5\pm3.5)\times10^{+0}$	$(12.1\pm2.4)\times10^{+0}$	$(6.3\pm1.3)\times10^{+0}$	$(2.4\pm1.2)\times10^{+0}$	–	–	–	$(5.2\pm1.6)\times10^{-1}$	$(11.0\pm3.3)\times10^{-2}$	$(5.4\pm1.6)\times10^{-1}$
G232.790–01.400	$(39.7\pm8.2)\times10^{-3}$	$(8.2\pm1.6)\times10^{-1}$	$(7.3\pm1.5)\times10^{-1}$	$(36.6\pm7.3)\times10^{-2}$	$(14.3\pm7.1)\times10^{-2}$	$(5.9\pm2.9)\times10^{-2}$	–	–	–	$(12.5\pm3.8)\times10^{-3}$	$(11.1\pm3.3)\times10^{-3}$
G232.810+00.180	$(16.6\pm3.3)\times10^{+0}$	$(24.2\pm4.8)\times10^{+0}$	$(12.4\pm2.5)\times10^{+0}$	$(6.5\pm1.3)\times10^{+0}$	$(2.7\pm1.4)\times10^{+0}$	$(7.1\pm3.6)\times10^{-1}$	$(6.8\pm2.0)\times10^{-1}$	$(5.6\pm1.7)\times10^{-1}$	$(8.9\pm2.7)\times10^{-1}$	$(8.6\pm2.6)\times10^{-1}$	$(6.5\pm1.9)\times10^{-1}$
G232.820–00.840	$(25.0\pm5.0)\times10^{-2}$	$(11.2\pm2.2)\times10^{-2}$	$(41.1\pm8.2)\times10^{-2}$	$(30.4\pm6.1)\times10^{-2}$	$(10.2\pm5.1)\times10^{-2}$	$(2.5\pm1.2)\times10^{-2}$	–	–	–	$(4.4\pm1.3)\times10^{-2}$	$(7.3\pm2.2)\times10^{-2}$
G232.894–01.389	$(20.0\pm4.4)\times10^{-3}$	$(33.2\pm6.6)\times10^{-2}$	$(41.8\pm8.4)\times10^{-2}$	$(23.3\pm4.7)\times10^{-2}$	$(7.4\pm7.4)\times10^{-2}$	–	–	$(20.4\pm6.3)\times10^{-2}$	–	$(4.0\pm1.2)\times10^{-3}$	$(12.5\pm3.7)\times10^{-4}$

Table A.3: continued

Name	F_{70} (Jy)	F_{160} (Jy)	F_{250} (Jy)	F_{350} (Jy)	F_{500} (Jy)	F_{8} (Jy)	$F_{12.1}$ (Jy)	$F_{14.7}$ (Jy)	F_{21} (Jy)	F_{14} (Jy)	F_{22} (Jy)
G232.930+00.040	–	$(5.4\pm1.1)\times10^{-1}$	$(10.5\pm2.1)\times10^{-1}$	$(7.1\pm1.4)\times10^{-1}$	$(3.0\pm1.5)\times10^{-1}$	–	–	$(3.5\pm1.1)\times10^{-1}$	$(3.4\pm1.1)\times10^{-1}$	$(26.3\pm7.9)\times10^{-4}$	$(3.8\pm1.1)\times10^{-3}$
G232.940–01.000	$(14.8\pm3.0)\times10^{-2}$	$(40.5\pm8.1)\times10^{-2}$	$(38.5\pm7.7)\times10^{-2}$	$(26.1\pm5.2)\times10^{-2}$	$(10.0\pm5.0)\times10^{-2}$	–	–	–	–	$(29.7\pm8.9)\times10^{-4}$	$(24.1\pm7.2)\times10^{-4}$
G232.950–00.790	$(5.2\pm1.0)\times10^{-1}$	$(12.8\pm2.6)\times10^{-1}$	$(11.2\pm2.2)\times10^{-1}$	$(7.9\pm1.6)\times10^{-1}$	$(4.6\pm2.3)\times10^{-1}$	$(16.9\pm8.4)\times10^{-2}$	$(28.0\pm8.6)\times10^{-2}$	$(5.4\pm1.6)\times10^{-1}$	–	$(25.2\pm7.6)\times10^{-2}$	$(4.1\pm1.2)\times10^{-1}$
G232.970–00.780	–	$(23.8\pm4.8)\times10^{-2}$	$(25.7\pm5.1)\times10^{-2}$	$(14.4\pm2.9)\times10^{-2}$	$(4.0\pm2.1)\times10^{-2}$	–	$(29.5\pm9.0)\times10^{-2}$	–	$(5.5\pm1.7)\times10^{-1}$	$(6.9\pm2.1)\times10^{-4}$	$(6.1\pm1.8)\times10^{-3}$
G233.030+00.140	–	$(12.2\pm2.5)\times10^{-2}$	$(5.0\pm1.0)\times10^{-1}$	$(37.7\pm7.6)\times10^{-2}$	$(1.2\pm1.2)\times10^{-1}$	–	–	–	$(5.1\pm1.6)\times10^{-1}$	$(14.7\pm4.4)\times10^{-4}$	$(8.2\pm2.5)\times10^{-4}$
G233.100–00.380	$(44.8\pm9.0)\times10^{-2}$	$(10.1\pm2.0)\times10^{-1}$	$(8.2\pm1.6)\times10^{-1}$	$(48.3\pm9.7)\times10^{-2}$	$(1.7\pm1.7)\times10^{-1}$	–	–	$(28.0\pm8.5)\times10^{-2}$	–	$(11.1\pm3.3)\times10^{-4}$	$(10.4\pm3.1)\times10^{-3}$
G233.140–01.220	–	$(31.6\pm6.3)\times10^{-2}$	$(37.4\pm7.5)\times10^{-2}$	$(19.7\pm4.0)\times10^{-2}$	$(7.7\pm3.8)\times10^{-2}$	–	$(3.3\pm1.0)\times10^{-1}$	–	–	$(14.7\pm4.4)\times10^{-4}$	$(11.2\pm3.4)\times10^{-4}$
G233.140–01.540	$(26.2\pm5.2)\times10^{-2}$	$(13.3\pm2.7)\times10^{-1}$	$(9.5\pm1.9)\times10^{-1}$	$(5.4\pm1.1)\times10^{-1}$	$(19.5\pm9.7)\times10^{-2}$	$(2.8\pm1.4)\times10^{-2}$	–	$(26.8\pm8.2)\times10^{-2}$	$(10.4\pm3.1)\times10^{-1}$	$(18.8\pm5.6)\times10^{-3}$	$(8.8\pm2.6)\times10^{-3}$
G233.180–01.710	–	$(25.4\pm5.1)\times10^{-1}$	$(34.3\pm6.9)\times10^{-1}$	$(22.8\pm4.6)\times10^{-1}$	$(10.2\pm5.1)\times10^{-1}$	–	–	$(5.9\pm1.8)\times10^{-1}$	$(11.8\pm3.6)\times10^{-1}$	–	$(29.9\pm9.0)\times10^{-5}$
G233.250+00.100	$(28.0\pm5.6)\times10^{-2}$	$(9.0\pm1.8)\times10^{-1}$	$(7.6\pm1.5)\times10^{-1}$	$(49.3\pm9.9)\times10^{-2}$	$(2.0\pm2.0)\times10^{-1}$	–	–	–	–	$(8.0\pm2.4)\times10^{-3}$	$(6.0\pm1.8)\times10^{-2}$
G233.250–00.360	–	$(15.9\pm3.2)\times10^{-2}$	$(14.8\pm3.0)\times10^{-2}$	$(9.5\pm1.9)\times10^{-2}$	$(5.6\pm2.8)\times10^{-2}$	$(3.6\pm1.8)\times10^{-2}$	–	–	–	$(5.1\pm1.5)\times10^{-3}$	$(3.7\pm1.1)\times10^{-3}$
G233.290–00.310	–	$(32.8\pm6.6)\times10^{-2}$	$(6.8\pm1.4)\times10^{-1}$	$(45.0\pm9.0)\times10^{-2}$	$(17.5\pm8.8)\times10^{-2}$	–	$(4.5\pm1.4)\times10^{-1}$	–	–	$(7.6\pm2.3)\times10^{-3}$	$(9.2\pm2.8)\times10^{-3}$
G233.320–00.320	$(39.2\pm8.1)\times10^{-3}$	$(33.9\pm6.8)\times10^{-2}$	$(32.9\pm6.6)\times10^{-2}$	$(18.9\pm4.0)\times10^{-2}$	–	–	$(28.2\pm8.6)\times10^{-2}$	–	–	$(21.4\pm6.4)\times10^{-4}$	$(3.6\pm1.1)\times10^{-3}$
G233.380–01.600	$(23.4\pm4.7)\times10^{-2}$	$(23.5\pm4.7)\times10^{-2}$	$(26.3\pm5.3)\times10^{-2}$	$(17.5\pm3.5)\times10^{-2}$	$(7.8\pm3.9)\times10^{-2}$	–	–	$(29.8\pm9.1)\times10^{-2}$	–	$(6.0\pm1.8)\times10^{-3}$	$(14.4\pm4.3)\times10^{-3}$
G233.730–01.330	$(11.4\pm2.3)\times10^{-1}$	$(32.5\pm6.5)\times10^{-1}$	$(16.7\pm3.4)\times10^{-1}$	$(7.0\pm1.4)\times10^{-1}$	$(2.6\pm2.6)\times10^{-1}$	$(7.0\pm3.5)\times10^{-2}$	–	–	–	$(12.6\pm3.8)\times10^{-2}$	$(8.1\pm2.4)\times10^{-2}$
G233.736–00.197	$(44.5\pm8.9)\times10^{+0}$	$(39.1\pm7.8)\times10^{+0}$	$(14.9\pm3.0)\times10^{+0}$	$(5.6\pm1.1)\times10^{+0}$	$(1.5\pm1.5)\times10^{+0}$	$(8.0\pm4.0)\times10^{-1}$	$(12.0\pm3.6)\times10^{-1}$	$(5.5\pm1.6)\times10^{-1}$	$(12.6\pm3.8)\times10^{-1}$	$(11.5\pm3.4)\times10^{-1}$	$(17.7\pm5.3)\times10^{-1}$
G233.750–01.270	$(14.8\pm3.0)\times10^{-2}$	$(29.1\pm5.8)\times10^{-2}$	$(49.5\pm9.9)\times10^{-2}$	$(40.7\pm8.2)\times10^{-2}$	$(19.2\pm9.6)\times10^{-2}$	$(3.3\pm1.7)\times10^{-2}$	–	$(3.4\pm1.0)\times10^{-1}$	–	$(11.1\pm3.3)\times10^{-3}$	$(8.1\pm2.4)\times10^{-3}$
G233.760–01.250	$(9.9\pm2.0)\times10^{-2}$	$(27.8\pm5.6)\times10^{-2}$	$(38.1\pm7.6)\times10^{-2}$	$(32.1\pm6.4)\times10^{-2}$	$(12.6\pm6.3)\times10^{-2}$	–	–	–	–	$(13.8\pm4.1)\times10^{-3}$	$(22.2\pm6.7)\times10^{-3}$
G233.810–00.110	–	$(32.7\pm6.5)\times10^{-1}$	$(19.7\pm3.9)\times10^{-1}$	$(6.9\pm1.4)\times10^{-1}$	$(5.5\pm2.8)\times10^{-1}$	–	–	–	–	$(8.6\pm2.6)\times10^{-1}$	$(11.6\pm3.5)\times10^{-1}$
G233.980–01.860	–	$(18.4\pm3.7)\times10^{-2}$	$(48.2\pm9.7)\times10^{-2}$	$(25.1\pm5.1)\times10^{-2}$	$(9.5\pm4.7)\times10^{-2}$	–	–	–	–	$(18.0\pm5.4)\times10^{-4}$	$(21.0\pm6.3)\times10^{-4}$
G234.033–00.537	$(27.0\pm5.4)\times10^{-1}$	$(13.1\pm2.6)\times10^{+0}$	$(8.1\pm1.6)\times10^{+0}$	$(45.7\pm9.1)\times10^{-1}$	$(2.1\pm1.0)\times10^{+0}$	$(2.2\pm1.1)\times10^{-1}$	–	$(27.7\pm8.4)\times10^{-2}$	$(10.8\pm3.2)\times10^{-1}$	$(31.4\pm9.4)\times10^{-2}$	$(19.3\pm5.8)\times10^{-2}$
G234.050–00.130	$(13.6\pm2.7)\times10^{-1}$	$(36.3\pm7.3)\times10^{-1}$	$(29.3\pm5.9)\times10^{-1}$	$(15.8\pm3.2)\times10^{-1}$	$(5.5\pm2.7)\times10^{-1}$	$(14.0\pm7.0)\times10^{-2}$	–	–	–	$(17.8\pm5.3)\times10^{-2}$	$(17.0\pm5.1)\times10^{-2}$
G234.050–01.910	–	$(24.9\pm5.0)\times10^{-2}$	$(14.0\pm2.8)\times10^{-2}$	$(10.4\pm2.1)\times10^{-2}$	$(2.7\pm2.7)\times10^{-2}$	$(3.9\pm2.0)\times10^{-2}$	$(4.4\pm1.3)\times10^{-1}$	$(3.3\pm1.0)\times10^{-1}$	$(5.2\pm1.6)\times10^{-1}$	–	–
G234.234–00.717	$(25.8\pm5.2)\times10^{-2}$	$(16.2\pm3.2)\times10^{-1}$	$(12.2\pm2.4)\times10^{-1}$	$(6.9\pm1.4)\times10^{-1}$	$(2.6\pm1.3)\times10^{-1}$	$(2.5\pm1.2)\times10^{-2}$	–	–	–	$(32.9\pm9.9)\times10^{-3}$	$(32.9\pm9.9)\times10^{-3}$
G234.260–01.490	$(5.4\pm1.1)\times10^{+0}$	$(8.5\pm1.7)\times10^{+0}$	$(34.1\pm6.8)\times10^{-1}$	$(11.8\pm2.4)\times10^{-1}$	$(3.3\pm1.7)\times10^{-1}$	$(13.0\pm6.5)\times10^{-2}$	$(5.3\pm1.6)\times10^{-1}$	$(13.7\pm4.3)\times10^{-2}$	–	$(20.2\pm6.1)\times10^{-2}$	$(12.5\pm3.7)\times10^{-2}$
G234.270–01.500	$(21.2\pm4.2)\times10^{-1}$	$(43.4\pm8.7)\times10^{-1}$	$(16.7\pm3.3)\times10^{-1}$	$(6.7\pm1.3)\times10^{-1}$	$(1.7\pm1.7)\times10^{-1}$	$(4.3\pm2.1)\times10^{-2}$	–	–	$(14.9\pm4.5)\times10^{-1}$	$(10.0\pm3.0)\times10^{-2}$	$(5.8\pm1.7)\times10^{-2}$
G234.333–00.651	$(18.9\pm3.8)\times10^{-1}$	$(11.2\pm2.2)\times10^{+0}$	$(7.5\pm1.5)\times10^{+0}$	$(37.7\pm7.5)\times10^{-1}$	$(13.7\pm6.8)\times10^{-1}$	$(16.9\pm8.5)\times10^{-2}$	–	$(21.9\pm6.7)\times10^{-2}$	–	$(3.6\pm1.1)\times10^{-1}$	$(29.7\pm8.9)\times10^{-2}$
G234.450–01.070	$(6.5\pm1.3)\times10^{-1}$	$(21.9\pm4.4)\times10^{-1}$	$(18.0\pm3.6)\times10^{-1}$	$(10.1\pm2.0)\times10^{-1}$	$(3.9\pm3.9)\times10^{-1}$	$(6.0\pm3.0)\times10^{-2}$	$(32.5\pm9.9)\times10^{-2}$	$(21.8\pm6.7)\times10^{-2}$	–	$(9.7\pm2.9)\times10^{-2}$	$(8.1\pm2.4)\times10^{-2}$
G234.468–00.393	$(22.7\pm4.5)\times10^{-1}$	$(7.5\pm1.5)\times10^{+0}$	$(6.7\pm1.3)\times10^{+0}$	$(41.7\pm8.4)\times10^{-1}$	$(1.4\pm1.4)\times10^{+0}$	$(7.8\pm3.9)\times10^{-2}$	–	$(28.8\pm8.7)\times10^{-2}$	$(11.6\pm3.5)\times10^{-1}$	$(11.0\pm3.3)\times10^{-2}$	$(29.7\pm8.9)\times10^{-2}$
G234.493–00.829	$(19.1\pm3.8)\times10^{-2}$	$(7.0\pm1.4)\times10^{-1}$	$(7.0\pm1.4)\times10^{-1}$	$(41.5\pm8.3)\times10^{-2}$	$(17.5\pm8.8)\times10^{-2}$	$(8.1\pm4.0)\times10^{-2}$	–	–	–	$(5.9\pm1.8)\times10^{-2}$	$(3.4\pm1.0)\times10^{-2}$
G234.501–00.863	–	$(8.4\pm1.7)\times10^{+0}$	$(8.4\pm1.7)\times10^{+0}$	$(6.4\pm1.3)\times10^{+0}$	$(3.0\pm1.5)\times10^{+0}$	–	–	–	$(24.2\pm7.3)\times10^{-1}$	$(9.8\pm2.9)\times10^{-1}$	$(3.8\pm1.1)\times10^{-1}$
G234.570–01.003	$(27.9\pm5.6)\times10^{-2}$	$(12.0\pm2.4)\times10^{-1}$	$(10.8\pm2.2)\times10^{-1}$	$(8.9\pm1.8)\times10^{-1}$	$(4.4\pm2.2)\times10^{-1}$	–	$(7.3\pm2.2)\times10^{-1}$	–	–	–	–
G234.580–01.030	$(10.3\pm2.1)\times10^{-2}$	$(19.4\pm3.9)\times10^{-2}$	$(23.6\pm4.7)\times10^{-2}$	$(16.5\pm3.3)\times10^{-2}$	–	$(2.1\pm1.1)\times10^{-2}$	–	$(18.5\pm5.8)\times10^{-2}$	–	$(31.8\pm9.5)\times10^{-4}$	$(25.0\pm7.5)\times10^{-4}$
G234.590–01.080	$(11.6\pm2.3)\times10^{-2}$	$(5.2\pm1.0)\times10^{-1}$	$(22.1\pm4.4)\times10^{-2}$	$(7.7\pm1.7)\times10^{-2}$	–	–	–	$(3.3\pm1.0)\times10^{-1}$	$(5.9\pm1.8)\times10^{-1}$	$(5.1\pm1.5)\times10^{-3}$	$(4.8\pm1.4)\times10^{-3}$
G234.620–00.197	$(33.6\pm6.7)\times10^{+0}$	$(15.0\pm3.0)\times10^{+1}$	$(10.4\pm2.1)\times10^{+1}$	$(5.7\pm1.1)\times10^{+1}$	$(2.6\pm1.3)\times10^{+1}$	$(19.4\pm9.7)\times10^{-1}$	$(27.1\pm8.1)\times10^{-1}$	$(4.4\pm1.3)\times10^{+0}$	–	$(3.8\pm1.2)\times10^{+0}$	$(29.5\pm8.9)\times10^{-1}$
G234.650–01.580	$(18.3\pm3.7)\times10^{-2}$	$(18.4\pm3.7)\times10^{-1}$	$(21.3\pm4.3)\times10^{-1}$	$(13.4\pm2.7)\times10^{-1}$	$(6.0\pm3.0)\times10^{-1}$	–	$(5.4\pm1.6)\times10^{-1}$	–	$(6.3\pm1.9)\times10^{-1}$	$(26.2\pm7.9)\times10^{-3}$	$(4.6\pm1.4)\times10^{-2}$
G234.660+00.070	$(43.4\pm8.7)\times10^{-1}$	$(33.3\pm6.7)\times10^{+0}$	$(29.1\pm5.8)\times10^{+0}$	$(15.6\pm3.1)\times10^{+0}$	$(6.8\pm3.4)\times10^{+0}$	$(3.9\pm1.9)\times10^{-1}$	$(8.7\pm2.6)\times10^{-1}$	–	–	$(8.5\pm2.6)\times10^{-1}$	$(6.9\pm2.1)\times10^{-1}$
G234.710–00.910	$(14.0\pm2.8)\times10^{+0}$	$(13.5\pm2.7)\times10^{+0}$	$(49.5\pm9.9)\times10^{-1}$	$(16.7\pm3.3)\times10^{-1}$	$(4.9\pm4.9)\times10^{-1}$	$(3.4\pm1.7)\times10^{-1}$	$(5.3\pm1.6)\times10^{-1}$	$(3.6\pm1.1)\times10^{-1}$	$(6.9\pm2.1)\times10^{-1}$	$(6.0\pm1.8)\times10^{-1}$	$(5.7\pm1.7)\times10^{-1}$
G234.720–00.820	$(25.4\pm5.1)\times10^{-2}$	$(6.3\pm1.3)\times10^{-1}$	$(36.9\pm7.4)\times10^{-2}$	$(16.9\pm3.4)\times10^{-2}$	$(5.5\pm5.5)\times10^{-2}$	–	$(20.1\pm6.3)\times10^{-2}$	–	–	$(23.2\pm7.0)\times10^{-3}$	$(16.3\pm4.9)\times10^{-3}$
G234.715–00.911	$(16.4\pm3.3)\times10^{+0}$	$(15.8\pm3.2)\times10^{+0}$	$(5.2\pm1.0)\times10^{+0}$	$(18.8\pm3.8)\times10^{-1}$	$(4.7\pm4.7)\times10^{-1}$	$(4.3\pm2.1)\times10^{-1}$	$(9.0\pm2.7)\times10^{-1}$	$(4.6\pm1.4)\times10^{-1}$	$(5.2\pm1.6)\times10^{-1}$	$(7.4\pm2.2)\times10^{-1}$	$(6.7\pm2.0)\times10^{-1}$
G234.730–00.750	$(8.1\pm1.6)\times10^{+0}$	$(10.0\pm2.0)\times10^{+0}$	$(39.5\pm7.9)\times10^{-1}$	$(13.4\pm2.7)\times10^{-1}$	$(3.9\pm3.9)\times10^{-1}$	$(16.8\pm8.4)\times10^{-2}$	$(6.3\pm1.9)\times10^{-1}$	–	$(7.1\pm2.1)\times10^{-1}$	$(28.9\pm8.7)\times10^{-2}$	$(18.0\pm5.4)\times10^{-2}$
G234.730–00.810	$(9.3\pm1.9)\times10^{-1}$	$(24.7\pm4.9)\times10^{-1}$	$(16.7\pm3.3)\times10^{-1}$	$(7.8\pm1.6)\times10^{-1}$	$(3.7\pm1.8)\times10^{-1}$	$(3.1\pm1.6)\times10^{-2}$	–	–	–	$(4.4\pm1.3)\times10^{-2}$	$(5.0\pm1.5)\times10^{-2}$
G234.764–00.282	$(7.6\pm1.5)\times10^{+1}$	$(7.8\pm1.6)\times10^{+1}$	$(32.0\pm6.4)\times10^{+0}$	$(13.7\pm2.7)\times10^{+0}$	$(5.1\pm2.5)\times10^{+0}$	$(3.4\pm1.7)\times10^{+0}$	$(6.4\pm1.9)\times10^{+0}$	$(4.0\pm1.2)\times10^{+0}$	$(12.1\pm3.6)\times10^{+0}$	$(5.8\pm1.7)\times10^{+0}$	$(16.7\pm5.0)\times10^{+0}$

Table A.3: continued

Name	F_{70} (Jy)	F_{160} (Jy)	F_{250} (Jy)	F_{350} (Jy)	F_{500} (Jy)	F_{8} (Jy)	$F_{12.1}$ (Jy)	$F_{14.7}$ (Jy)	F_{21} (Jy)	F_{14} (Jy)	F_{22} (Jy)
G234.860–00.090	$(5.2\pm1.0)\times10^{+0}$	$(9.1\pm1.8)\times10^{+0}$	$(46.4\pm9.3)\times10^{-1}$	$(18.9\pm3.8)\times10^{-1}$	$(6.4\pm6.4)\times10^{-1}$	$(7.7\pm3.9)\times10^{-2}$	$(4.6\pm1.4)\times10^{-1}$	$(17.8\pm5.5)\times10^{-2}$	$(11.0\pm3.3)\times10^{-1}$	$(17.2\pm5.2)\times10^{-2}$	$(5.3\pm1.6)\times10^{-1}$
G234.880–00.130	$(9.2\pm1.8)\times10^{-1}$	$(43.2\pm8.6)\times10^{-1}$	$(29.3\pm5.9)\times10^{-1}$	$(13.0\pm2.6)\times10^{-1}$	$(4.1\pm2.1)\times10^{-1}$	$(14.4\pm7.2)\times10^{-2}$	–	$(21.9\pm6.7)\times10^{-2}$	–	$(15.0\pm4.5)\times10^{-2}$	$(12.6\pm3.8)\times10^{-2}$
G234.890–00.180	$(6.0\pm1.2)\times10^{+0}$	$(16.9\pm3.4)\times10^{+0}$	$(9.4\pm1.9)\times10^{+0}$	$(44.1\pm8.8)\times10^{-1}$	$(17.4\pm8.7)\times10^{-1}$	$(2.7\pm1.3)\times10^{-1}$	$(3.7\pm1.1)\times10^{-1}$	–	$(6.2\pm1.9)\times10^{-1}$	$(6.4\pm1.9)\times10^{-1}$	$(6.5\pm2.0)\times10^{-1}$
G235.050–01.530	$(9.4\pm1.9)\times10^{+0}$	$(19.6\pm3.9)\times10^{+0}$	$(11.7\pm2.3)\times10^{+0}$	$(5.1\pm1.0)\times10^{+0}$	$(19.4\pm9.7)\times10^{-1}$	$(19.3\pm9.7)\times10^{-2}$	$(3.4\pm1.0)\times10^{-1}$	$(8.9\pm2.7)\times10^{-1}$	$(8.0\pm2.4)\times10^{-1}$	$(4.3\pm1.3)\times10^{-1}$	$(9.2\pm2.8)\times10^{-1}$
G235.220–01.670	$(25.2\pm5.0)\times10^{-2}$	$(34.4\pm6.9)\times10^{-2}$	$(6.0\pm1.2)\times10^{-1}$	$(5.3\pm1.1)\times10^{-1}$	$(2.7\pm1.4)\times10^{-1}$	$(18.9\pm9.6)\times10^{-3}$	–	$(4.5\pm1.4)\times10^{-1}$	–	$(27.2\pm8.2)\times10^{-4}$	$(13.2\pm4.0)\times10^{-3}$
G235.348–01.687	$(11.0\pm2.2)\times10^{-1}$	$(14.5\pm2.9)\times10^{-1}$	$(8.3\pm1.7)\times10^{-1}$	$(46.4\pm9.3)\times10^{-2}$	$(1.5\pm1.5)\times10^{-1}$	–	–	$(25.8\pm8.0)\times10^{-2}$	–	$(4.8\pm1.5)\times10^{-3}$	$(5.9\pm1.8)\times10^{-2}$
G235.347–01.740	$(12.6\pm2.5)\times10^{-2}$	$(6.9\pm1.4)\times10^{-1}$	$(8.3\pm1.7)\times10^{-1}$	$(5.8\pm1.2)\times10^{-1}$	$(2.7\pm1.4)\times10^{-1}$	–	–	–	–	$(6.3\pm1.9)\times10^{-3}$	$(25.8\pm7.7)\times10^{-3}$
G235.389–01.655	$(28.5\pm5.7)\times10^{+0}$	$(25.0\pm5.0)\times10^{+0}$	$(8.9\pm1.8)\times10^{+0}$	$(32.5\pm6.5)\times10^{-1}$	$(9.4\pm9.4)\times10^{-1}$	$(6.5\pm3.3)\times10^{-1}$	$(7.0\pm2.1)\times10^{-1}$	$(5.4\pm1.6)\times10^{-1}$	–	$(10.3\pm3.1)\times10^{-1}$	$(16.8\pm5.0)\times10^{-1}$
G235.532–01.675	$(26.3\pm5.3)\times10^{-2}$	$(28.0\pm5.6)\times10^{-1}$	$(37.3\pm7.5)\times10^{-1}$	$(29.3\pm5.9)\times10^{-1}$	$(14.2\pm7.1)\times10^{-1}$	$(3.6\pm1.8)\times10^{-2}$	–	–	$(5.9\pm1.8)\times10^{-1}$	$(14.1\pm4.2)\times10^{-3}$	$(3.6\pm1.1)\times10^{-2}$
G235.590–01.520	$(37.4\pm7.5)\times10^{-2}$	$(7.3\pm1.5)\times10^{-1}$	$(29.5\pm5.9)\times10^{-2}$	$(13.2\pm2.7)\times10^{-2}$	$(3.0\pm3.0)\times10^{-2}$	$(9.6\pm4.8)\times10^{-2}$	$(4.9\pm1.5)\times10^{-1}$	–	–	$(27.4\pm8.2)\times10^{-3}$	$(13.7\pm4.1)\times10^{-3}$
G235.680–00.030	–	$(17.8\pm3.6)\times10^{-2}$	$(39.2\pm7.8)\times10^{-2}$	$(19.8\pm4.0)\times10^{-2}$	$(6.4\pm6.4)\times10^{-2}$	$(6.2\pm3.1)\times10^{-2}$	$(3.4\pm1.0)\times10^{-1}$	$(24.7\pm7.5)\times10^{-2}$	–	$(6.7\pm2.0)\times10^{-3}$	$(27.1\pm8.1)\times10^{-4}$
G235.690–01.240	$(33.2\pm6.6)\times10^{+0}$	$(31.5\pm6.3)\times10^{+0}$	$(11.5\pm2.3)\times10^{+0}$	$(44.4\pm8.9)\times10^{-1}$	$(1.3\pm1.3)\times10^{+0}$	$(4.9\pm2.4)\times10^{-1}$	$(7.2\pm2.2)\times10^{-1}$	$(5.0\pm1.5)\times10^{-1}$	$(8.7\pm2.6)\times10^{-1}$	$(8.5\pm2.5)\times10^{-1}$	$(16.4\pm4.9)\times10^{-1}$
G235.780+00.010	$(18.1\pm3.6)\times10^{-2}$	$(18.6\pm3.7)\times10^{-1}$	$(22.9\pm4.6)\times10^{-1}$	$(13.4\pm2.7)\times10^{-1}$	$(5.8\pm2.9)\times10^{-1}$	$(8.3\pm4.2)\times10^{-2}$	$(3.8\pm1.1)\times10^{-1}$	$(6.9\pm2.1)\times10^{-1}$	$(10.5\pm3.2)\times10^{-1}$	$(23.7\pm7.1)\times10^{-3}$	$(20.0\pm6.0)\times10^{-3}$
G236.180–01.830	$(5.2\pm1.0)\times10^{+0}$	$(11.1\pm2.2)\times10^{+0}$	$(8.1\pm1.6)\times10^{+0}$	$(46.5\pm9.3)\times10^{-1}$	$(18.4\pm9.2)\times10^{-1}$	$(5.5\pm2.7)\times10^{-2}$	$(21.7\pm6.8)\times10^{-2}$	–	$(6.2\pm1.9)\times10^{-1}$	$(15.7\pm4.7)\times10^{-2}$	$(5.1\pm1.5)\times10^{-1}$
G236.420–00.710	–	$(45.3\pm9.1)\times10^{-2}$	$(5.5\pm1.1)\times10^{-1}$	$(34.1\pm6.8)\times10^{-2}$	$(1.1\pm1.1)\times10^{-1}$	$(2.4\pm1.2)\times10^{-2}$	–	–	–	–	–
G236.490–00.590	–	$(46.6\pm9.3)\times10^{-2}$	$(9.7\pm1.9)\times10^{-1}$	$(6.6\pm1.3)\times10^{-1}$	$(3.0\pm1.5)\times10^{-1}$	$(6.7\pm3.3)\times10^{-2}$	$(5.2\pm1.6)\times10^{-1}$	–	–	$(25.2\pm7.6)\times10^{-4}$	–
G236.570–00.460	$(21.6\pm4.3)\times10^{-1}$	$(44.4\pm8.9)\times10^{-2}$	$(17.7\pm3.5)\times10^{-2}$	$(11.5\pm2.3)\times10^{-2}$	$(3.3\pm1.7)\times10^{-2}$	–	$(4.2\pm1.3)\times10^{-1}$	–	$(4.1\pm1.3)\times10^{-1}$	$(19.5\pm5.8)\times10^{-4}$	$(9.4\pm2.8)\times10^{-4}$
G236.600–02.130	$(18.2\pm3.6)\times10^{+0}$	$(32.3\pm6.5)\times10^{+0}$	$(18.2\pm3.6)\times10^{+0}$	$(10.0\pm2.0)\times10^{+0}$	$(3.1\pm1.6)\times10^{+0}$	$(2.2\pm1.1)\times10^{-1}$	$(4.5\pm1.4)\times10^{-1}$	$(4.6\pm1.4)\times10^{-1}$	$(19.2\pm5.8)\times10^{-1}$	$(8.4\pm2.5)\times10^{-1}$	$(29.6\pm8.9)\times10^{-1}$
G236.600–02.290	$(6.2\pm1.2)\times10^{-1}$	$(39.8\pm8.0)\times10^{-1}$	$(5.9\pm1.2)\times10^{+0}$	$(47.0\pm9.4)\times10^{-1}$	$(2.4\pm1.2)\times10^{+0}$	$(4.3\pm2.1)\times10^{-2}$	–	–	–	$(19.2\pm5.8)\times10^{-3}$	$(5.8\pm1.7)\times10^{-2}$
G236.600–02.310	$(26.1\pm5.2)\times10^{-1}$	$(25.6\pm5.1)\times10^{-1}$	$(20.9\pm4.2)\times10^{-1}$	$(15.1\pm3.0)\times10^{-1}$	$(5.6\pm5.6)\times10^{-1}$	$(4.2\pm2.1)\times10^{-2}$	–	–	$(12.2\pm3.7)\times10^{-1}$	$(24.4\pm7.4)\times10^{-5}$	$(4.5\pm1.4)\times10^{-2}$
G236.610–02.110	$(10.4\pm2.1)\times10^{-1}$	$(27.1\pm5.4)\times10^{-1}$	$(27.3\pm5.5)\times10^{-1}$	$(19.3\pm3.9)\times10^{-1}$	$(6.6\pm6.6)\times10^{-1}$	$(6.2\pm3.1)\times10^{-2}$	–	–	$(7.5\pm2.3)\times10^{-1}$	$(7.5\pm2.3)\times10^{-2}$	$(12.9\pm3.9)\times10^{-2}$
G236.620+00.000	–	$(11.7\pm2.3)\times10^{-2}$	$(20.8\pm4.2)\times10^{-2}$	$(12.2\pm2.5)\times10^{-2}$	$(6.1\pm6.1)\times10^{-2}$	–	–	–	–	–	$(22.5\pm6.7)\times10^{-4}$
G236.630–01.150	$(8.5\pm1.7)\times10^{-2}$	$(5.0\pm1.0)\times10^{-1}$	$(6.9\pm1.4)\times10^{-1}$	$(49.6\pm9.9)\times10^{-2}$	$(2.1\pm1.1)\times10^{-1}$	–	–	$(6.0\pm1.8)\times10^{-1}$	–	–	–
G236.880–01.010	$(10.7\pm2.1)\times10^{-2}$	$(6.5\pm1.3)\times10^{-1}$	$(7.2\pm1.4)\times10^{-1}$	$(47.8\pm9.6)\times10^{-2}$	$(2.4\pm1.2)\times10^{-1}$	–	–	$(30.9\pm9.4)\times10^{-2}$	–	$(9.1\pm2.7)\times10^{-3}$	$(10.5\pm3.1)\times10^{-3}$
G237.000–01.840	$(7.5\pm1.5)\times10^{+0}$	$(9.3\pm1.9)\times10^{+0}$	$(40.7\pm8.1)\times10^{-1}$	$(17.2\pm3.4)\times10^{-1}$	$(5.7\pm5.7)\times10^{-1}$	$(19.1\pm9.5)\times10^{-2}$	$(26.1\pm8.0)\times10^{-2}$	$(4.8\pm1.4)\times10^{-1}$	–	$(3.7\pm1.1)\times10^{-1}$	$(3.6\pm1.1)\times10^{-1}$
G237.050–00.770	–	$(6.6\pm1.3)\times10^{-1}$	$(6.3\pm1.3)\times10^{-1}$	$(41.0\pm8.2)\times10^{-2}$	$(15.6\pm7.8)\times10^{-2}$	$(2.8\pm1.4)\times10^{-2}$	–	–	–	$(13.8\pm4.2)\times10^{-3}$	$(4.5\pm1.4)\times10^{-3}$
G237.100–00.820	–	$(6.4\pm1.3)\times10^{-1}$	$(8.3\pm1.7)\times10^{-1}$	$(5.2\pm1.1)\times10^{-1}$	$(2.1\pm1.1)\times10^{-1}$	$(6.8\pm3.4)\times10^{-2}$	–	–	$(6.7\pm2.0)\times10^{-1}$	$(26.2\pm7.9)\times10^{-4}$	–
G237.110–00.300	–	$(27.5\pm5.5)\times10^{-2}$	$(29.8\pm6.0)\times10^{-2}$	$(17.9\pm3.6)\times10^{-2}$	$(7.3\pm7.3)\times10^{-2}$	–	–	–	$(4.6\pm1.4)\times10^{-1}$	$(17.9\pm5.4)\times10^{-5}$	–
G237.110–00.790	$(15.8\pm3.2)\times10^{-1}$	$(5.3\pm1.1)\times10^{+0}$	$(5.5\pm1.1)\times10^{+0}$	$(34.4\pm6.9)\times10^{-1}$	$(13.0\pm6.5)\times10^{-1}$	–	$(3.3\pm1.0)\times10^{-1}$	–	–	$(4.1\pm1.2)\times10^{-2}$	$(12.1\pm3.6)\times10^{-2}$
G237.110–00.990	$(28.8\pm6.1)\times10^{-3}$	$(7.3\pm1.5)\times10^{-1}$	$(7.2\pm1.4)\times10^{-1}$	$(44.2\pm8.9)\times10^{-2}$	$(17.0\pm8.5)\times10^{-2}$	$(17.8\pm9.1)\times10^{-3}$	$(25.1\pm7.8)\times10^{-2}$	–	$(4.2\pm1.3)\times10^{-1}$	–	$(3.9\pm1.2)\times10^{-4}$
G237.170–00.960	$(22.5\pm4.5)\times10^{-1}$	$(46.8\pm9.4)\times10^{-1}$	$(29.6\pm5.9)\times10^{-1}$	$(18.2\pm3.6)\times10^{-1}$	$(6.6\pm6.6)\times10^{-1}$	$(4.9\pm2.5)\times10^{-2}$	–	–	$(7.5\pm2.3)\times10^{-1}$	$(9.3\pm2.8)\times10^{-5}$	$(29.6\pm8.9)\times10^{-3}$
G237.180–01.470	$(7.8\pm1.6)\times10^{-2}$	$(5.2\pm1.0)\times10^{-1}$	$(38.7\pm7.7)\times10^{-2}$	$(19.2\pm3.8)\times10^{-2}$	$(5.6\pm5.6)\times10^{-2}$	$(2.1\pm1.1)\times10^{-2}$	–	–	–	$(6.2\pm1.9)\times10^{-3}$	$(4.5\pm1.3)\times10^{-3}$
G237.210–01.440	$(31.9\pm6.4)\times10^{-2}$	$(8.1\pm1.6)\times10^{-1}$	$(6.3\pm1.3)\times10^{-1}$	$(31.2\pm6.3)\times10^{-2}$	$(9.3\pm9.3)\times10^{-2}$	$(4.3\pm2.2)\times10^{-2}$	$(4.9\pm1.5)\times10^{-1}$	–	–	$(25.3\pm7.6)\times10^{-3}$	$(22.8\pm6.8)\times10^{-3}$
G237.230–01.060	$(37.5\pm7.5)\times10^{+0}$	$(34.9\pm7.0)\times10^{+0}$	$(12.1\pm2.4)\times10^{+0}$	$(44.0\pm8.8)\times10^{-1}$	$(12.2\pm6.1)\times10^{-1}$	$(9.3\pm4.6)\times10^{-1}$	$(12.0\pm3.6)\times10^{-1}$	$(3.4\pm1.0)\times10^{-1}$	$(17.6\pm5.3)\times10^{-1}$	$(12.6\pm3.8)\times10^{-1}$	$(24.6\pm7.4)\times10^{-1}$
G237.240–01.080	$(28.0\pm5.6)\times10^{-1}$	$(7.2\pm1.4)\times10^{+0}$	$(36.3\pm7.3)\times10^{-1}$	$(14.6\pm2.9)\times10^{-1}$	$(4.9\pm4.9)\times10^{-1}$	$(11.4\pm5.7)\times10^{-2}$	–	–	–	$(18.9\pm5.7)\times10^{-2}$	$(15.9\pm4.8)\times10^{-2}$
G237.260–01.260	$(6.4\pm1.3)\times10^{+0}$	$(11.9\pm2.4)\times10^{+0}$	$(7.1\pm1.4)\times10^{+0}$	$(35.0\pm7.0)\times10^{-1}$	$(14.8\pm7.4)\times10^{-1}$	$(7.7\pm3.9)\times10^{-2}$	–	$(4.6\pm1.4)\times10^{-1}$	–	$(16.2\pm4.9)\times10^{-2}$	$(23.1\pm6.9)\times10^{-2}$
G237.260–01.280	$(8.3\pm1.7)\times10^{+1}$	$(9.5\pm1.9)\times10^{+1}$	$(36.2\pm7.2)\times10^{+0}$	$(13.9\pm2.8)\times10^{+0}$	$(3.8\pm1.9)\times10^{+0}$	$(2.0\pm1.0)\times10^{+0}$	$(30.6\pm9.2)\times10^{-1}$	$(15.7\pm4.7)\times10^{-1}$	$(20.8\pm6.3)\times10^{-1}$	$(24.4\pm7.3)\times10^{-1}$	$(28.9\pm8.7)\times10^{-1}$
G237.260–01.300	$(10.5\pm2.1)\times10^{+0}$	$(20.0\pm4.0)\times10^{+0}$	$(9.9\pm2.0)\times10^{+0}$	$(39.8\pm8.0)\times10^{-1}$	$(17.7\pm8.8)\times10^{-1}$	$(3.6\pm1.8)\times10^{-1}$	$(5.6\pm1.7)\times10^{-1}$	$(6.3\pm1.9)\times10^{-1}$	$(5.6\pm1.7)\times10^{-1}$	$(6.5\pm2.0)\times10^{-1}$	$(7.3\pm2.2)\times10^{-1}$
G237.320–01.280	$(23.0\pm4.6)\times10^{+1}$	$(10.0\pm2.0)\times10^{+1}$	$(27.2\pm5.4)\times10^{+0}$	$(8.6\pm1.7)\times10^{+0}$	$(2.6\pm2.6)\times10^{+0}$	$(2.2\pm1.1)\times10^{+0}$	$(3.6\pm1.1)\times10^{+0}$	$(3.6\pm1.1)\times10^{+0}$	$(26.4\pm7.9)\times10^{+0}$	$(4.0\pm1.2)\times10^{+0}$	$(17.4\pm5.2)\times10^{+0}$
G237.330–01.260	$(5.5\pm1.1)\times10^{-1}$	$(18.5\pm3.7)\times10^{-1}$	$(13.4\pm2.7)\times10^{-1}$	$(8.1\pm1.6)\times10^{-1}$	$(3.3\pm3.3)\times10^{-1}$	$(2.4\pm1.2)\times10^{-2}$	$(4.7\pm1.4)\times10^{-1}$	$(20.7\pm6.4)\times10^{-2}$	–	$(6.8\pm2.0)\times10^{-2}$	$(10.7\pm3.2)\times10^{-2}$
G237.460–01.790	–	$(6.0\pm1.2)\times10^{-1}$	$(9.5\pm1.9)\times10^{-1}$	$(5.9\pm1.2)\times10^{-1}$	$(3.3\pm1.7)\times10^{-1}$	–	–	–	–	$(30.8\pm9.3)\times10^{-5}$	$(9.9\pm3.0)\times10^{-3}$
G237.530–01.380	$(24.1\pm5.2)\times10^{-3}$	$(37.5\pm7.5)\times10^{-2}$	$(47.0\pm9.4)\times10^{-2}$	$(35.8\pm7.2)\times10^{-2}$	$(15.3\pm7.7)\times10^{-2}$	$(4.1\pm2.1)\times10^{-2}$	–	–	$(12.5\pm3.8)\times10^{-1}$	$(5.1\pm1.5)\times10^{-3}$	$(5.6\pm1.7)\times10^{-3}$
G237.540–00.660	$(6.1\pm1.2)\times10^{-2}$	$(27.9\pm5.6)\times10^{-2}$	$(18.6\pm3.7)\times10^{-2}$	$(13.9\pm2.8)\times10^{-2}$	$(3.0\pm1.5)\times10^{-2}$	$(2.1\pm1.0)\times10^{-2}$	$(4.9\pm1.5)\times10^{-1}$	$(25.2\pm7.7)\times10^{-2}$	–	$(12.5\pm3.7)\times10^{-3}$	$(11.5\pm3.4)\times10^{-3}$

Table A.3: continued

Name	F_{70} (Jy)	F_{160} (Jy)	F_{250} (Jy)	F_{350} (Jy)	F_{500} (Jy)	F_{8} (Jy)	$F_{12.1}$ (Jy)	$F_{14.7}$ (Jy)	F_{21} (Jy)	F_{14} (Jy)	F_{22} (Jy)
G237.550–00.640	$(11.4\pm2.3)\times10^{-2}$	$(5.5\pm1.1)\times10^{-1}$	$(30.1\pm6.0)\times10^{-2}$	$(21.7\pm4.4)\times10^{-2}$	$(8.9\pm4.5)\times10^{-2}$	–	–	–	$(12.8\pm3.9)\times10^{-1}$	$(8.3\pm2.5)\times10^{-3}$	$(7.4\pm2.2)\times10^{-3}$
G237.661–00.514	$(31.2\pm6.6)\times10^{-3}$	$(25.2\pm5.0)\times10^{-2}$	$(25.7\pm5.2)\times10^{-2}$	$(15.1\pm3.0)\times10^{-2}$	$(5.4\pm5.4)\times10^{-2}$	$(2.0\pm1.0)\times10^{-2}$	$(26.6\pm8.1)\times10^{-2}$	–	–	$(6.0\pm1.8)\times10^{-4}$	–
G237.660–01.790	–	$(36.0\pm7.2)\times10^{-2}$	$(35.8\pm7.2)\times10^{-2}$	$(19.8\pm4.0)\times10^{-2}$	$(7.6\pm3.8)\times10^{-2}$	–	$(9.7\pm2.9)\times10^{-1}$	–	–	$(26.6\pm8.0)\times10^{-4}$	$(15.0\pm4.5)\times10^{-4}$
G237.740–00.960	$(9.3\pm1.9)\times10^{+1}$	$(9.2\pm1.8)\times10^{+1}$	$(35.5\pm7.1)\times10^{+0}$	$(13.6\pm2.7)\times10^{+0}$	$(4.4\pm2.2)\times10^{+0}$	$(4.1\pm2.0)\times10^{+0}$	$(6.0\pm1.8)\times10^{+0}$	$(31.8\pm9.6)\times10^{-1}$	$(5.1\pm1.5)\times10^{+0}$	$(6.2\pm1.9)\times10^{+0}$	$(7.3\pm2.2)\times10^{+0}$
G237.740–00.970	$(7.3\pm1.5)\times10^{+0}$	$(9.4\pm1.9)\times10^{+0}$	$(31.3\pm6.3)\times10^{-1}$	$(10.2\pm2.1)\times10^{-1}$	$(4.7\pm4.7)\times10^{-1}$	$(5.3\pm2.7)\times10^{-1}$	$(6.6\pm2.0)\times10^{-1}$	$(6.0\pm1.8)\times10^{-1}$	–	$(6.5\pm2.0)\times10^{-1}$	$(5.6\pm1.7)\times10^{-1}$
G237.820–01.280	$(13.9\pm2.8)\times10^{-1}$	$(37.3\pm7.5)\times10^{-1}$	$(30.3\pm6.1)\times10^{-1}$	$(18.0\pm3.6)\times10^{-1}$	$(8.5\pm4.2)\times10^{-1}$	$(7.9\pm4.0)\times10^{-2}$	–	–	–	$(11.5\pm3.4)\times10^{-2}$	$(11.1\pm3.3)\times10^{-2}$
G238.260–01.720	$(5.9\pm1.2)\times10^{+0}$	$(12.3\pm2.5)\times10^{+0}$	$(5.9\pm1.2)\times10^{+0}$	$(24.7\pm4.9)\times10^{-1}$	$(10.3\pm5.2)\times10^{-1}$	$(3.9\pm1.9)\times10^{-1}$	$(5.0\pm1.5)\times10^{-1}$	–	$(13.9\pm4.2)\times10^{-1}$	$(5.4\pm1.6)\times10^{-1}$	$(4.0\pm1.2)\times10^{-1}$
G238.511–00.885	–	$(33.4\pm6.7)\times10^{-2}$	$(5.4\pm1.1)\times10^{-1}$	$(35.2\pm7.0)\times10^{-2}$	$(12.1\pm6.0)\times10^{-2}$	–	–	$(28.1\pm8.6)\times10^{-2}$	$(6.6\pm2.0)\times10^{-1}$	$(11.0\pm3.3)\times10^{-4}$	$(9.0\pm2.7)\times10^{-4}$
G238.540–00.920	$(13.6\pm2.7)\times10^{-2}$	$(42.1\pm8.4)\times10^{-2}$	$(44.1\pm8.8)\times10^{-2}$	$(26.7\pm5.3)\times10^{-2}$	$(10.0\pm5.0)\times10^{-2}$	$(6.0\pm3.0)\times10^{-2}$	–	$(3.5\pm1.0)\times10^{-1}$	$(5.1\pm1.6)\times10^{-1}$	$(5.1\pm1.5)\times10^{-4}$	$(26.4\pm7.9)\times10^{-4}$
G238.670–01.440	$(5.2\pm1.0)\times10^{+0}$	$(9.7\pm1.9)\times10^{+0}$	$(10.5\pm2.1)\times10^{+0}$	$(6.7\pm1.3)\times10^{+0}$	$(3.0\pm1.5)\times10^{+0}$	$(11.2\pm5.6)\times10^{-2}$	–	$(21.0\pm6.6)\times10^{-2}$	$(23.5\pm7.1)\times10^{-1}$	$(8.7\pm2.6)\times10^{-2}$	$(6.6\pm2.0)\times10^{-1}$
G238.690–01.860	$(33.6\pm6.7)\times10^{-2}$	$(7.0\pm1.4)\times10^{-1}$	$(7.1\pm1.4)\times10^{-1}$	$(43.7\pm8.8)\times10^{-2}$	$(1.6\pm1.6)\times10^{-1}$	$(5.0\pm2.5)\times10^{-2}$	–	–	–	$(24.1\pm7.2)\times10^{-3}$	$(3.6\pm1.1)\times10^{-2}$
G238.700–01.270	–	$(35.2\pm7.1)\times10^{-2}$	$(46.7\pm9.3)\times10^{-2}$	$(20.7\pm4.2)\times10^{-2}$	$(9.5\pm9.5)\times10^{-2}$	$(4.5\pm2.3)\times10^{-2}$	–	$(15.8\pm5.0)\times10^{-2}$	$(5.2\pm1.6)\times10^{-1}$	$(29.5\pm8.8)\times10^{-5}$	–
G238.770–01.810	$(6.7\pm1.3)\times10^{+0}$	$(8.3\pm1.7)\times10^{+0}$	$(34.3\pm6.9)\times10^{-1}$	$(15.7\pm3.1)\times10^{-1}$	$(4.5\pm4.5)\times10^{-1}$	$(18.1\pm9.1)\times10^{-2}$	$(4.7\pm1.4)\times10^{-1}$	$(29.6\pm9.0)\times10^{-2}$	$(7.8\pm2.4)\times10^{-1}$	$(27.4\pm8.2)\times10^{-2}$	$(3.8\pm1.1)\times10^{-1}$
G238.800–01.630	$(21.2\pm4.2)\times10^{-1}$	$(35.0\pm7.0)\times10^{-1}$	$(28.1\pm5.6)\times10^{-1}$	$(16.9\pm3.4)\times10^{-1}$	$(5.4\pm5.4)\times10^{-1}$	$(2.8\pm1.4)\times10^{-1}$	–	$(4.0\pm1.2)\times10^{-1}$	$(8.4\pm2.5)\times10^{-1}$	$(6.3\pm1.9)\times10^{-1}$	$(8.2\pm2.5)\times10^{-1}$
G238.960–01.680	$(21.1\pm4.2)\times10^{+0}$	$(17.9\pm3.6)\times10^{+0}$	$(6.8\pm1.4)\times10^{+0}$	$(24.7\pm4.9)\times10^{-1}$	$(7.0\pm7.0)\times10^{-1}$	$(3.2\pm1.6)\times10^{-1}$	–	$(8.8\pm2.6)\times10^{-1}$	$(27.0\pm8.1)\times10^{-1}$	$(7.3\pm2.2)\times10^{-1}$	$(3.8\pm1.1)\times10^{+0}$
G239.190–01.960	$(46.6\pm9.3)\times10^{-2}$	$(11.6\pm2.3)\times10^{-1}$	$(15.5\pm3.1)\times10^{-1}$	$(11.1\pm2.2)\times10^{-1}$	$(5.2\pm2.6)\times10^{-1}$	$(2.3\pm1.1)\times10^{-2}$	–	–	$(14.3\pm4.3)\times10^{-1}$	$(26.1\pm7.8)\times10^{-3}$	$(4.5\pm1.4)\times10^{-2}$
G239.300–00.630	$(7.5\pm1.5)\times10^{-2}$	$(15.7\pm3.1)\times10^{-2}$	$(48.6\pm9.7)\times10^{-2}$	$(36.2\pm7.2)\times10^{-2}$	$(1.4\pm1.4)\times10^{-1}$	–	–	–	$(8.6\pm2.6)\times10^{-1}$	$(3.5\pm1.1)\times10^{-3}$	$(10.4\pm3.1)\times10^{-3}$
G239.370–00.080	$(6.0\pm1.2)\times10^{-2}$	$(18.6\pm3.7)\times10^{-2}$	$(19.2\pm3.8)\times10^{-2}$	$(13.5\pm2.7)\times10^{-2}$	$(5.7\pm5.7)\times10^{-2}$	$(2.1\pm1.1)\times10^{-2}$	$(17.4\pm5.4)\times10^{-2}$	–	–	–	–
G239.370–01.690	$(47.9\pm9.6)\times10^{-1}$	$(5.5\pm1.1)\times10^{+0}$	$(34.7\pm6.9)\times10^{-1}$	$(23.6\pm4.7)\times10^{-1}$	$(7.2\pm7.2)\times10^{-1}$	$(4.6\pm2.3)\times10^{-2}$	$(27.5\pm8.5)\times10^{-2}$	–	–	$(5.6\pm1.7)\times10^{-2}$	$(3.5\pm1.0)\times10^{-1}$
G239.524–00.711	$(19.0\pm3.8)\times10^{-2}$	$(13.0\pm2.6)\times10^{-1}$	$(17.6\pm3.5)\times10^{-1}$	$(10.6\pm2.1)\times10^{-1}$	$(4.7\pm2.3)\times10^{-1}$	$(16.3\pm8.2)\times10^{-2}$	–	–	$(10.2\pm3.1)\times10^{-1}$	$(13.8\pm4.1)\times10^{-2}$	$(24.9\pm7.5)\times10^{-2}$
G239.630–02.090	$(41.2\pm8.2)\times10^{-2}$	$(43.4\pm8.7)\times10^{-1}$	$(5.1\pm1.0)\times10^{+0}$	$(33.6\pm6.7)\times10^{-1}$	$(16.4\pm8.2)\times10^{-1}$	$(5.0\pm2.5)\times10^{-2}$	–	–	$(5.6\pm1.8)\times10^{-1}$	$(7.7\pm2.3)\times10^{-2}$	$(10.6\pm3.2)\times10^{-2}$
G239.650–00.810	$(6.5\pm1.3)\times10^{-2}$	$(22.2\pm4.4)\times10^{-2}$	$(31.5\pm6.3)\times10^{-2}$	$(22.9\pm4.6)\times10^{-2}$	$(9.8\pm9.8)\times10^{-2}$	–	–	–	$(5.8\pm1.8)\times10^{-1}$	$(4.1\pm1.2)\times10^{-2}$	$(17.0\pm5.1)\times10^{-3}$
G239.660–02.040	$(18.9\pm3.8)\times10^{-2}$	$(8.4\pm1.7)\times10^{-1}$	$(11.2\pm2.2)\times10^{-1}$	$(8.4\pm1.7)\times10^{-1}$	$(3.6\pm1.8)\times10^{-1}$	$(4.1\pm2.1)\times10^{-2}$	–	–	$(4.5\pm1.4)\times10^{-1}$	$(6.6\pm2.0)\times10^{-3}$	$(8.0\pm2.4)\times10^{-3}$
G239.680–02.040	$(6.1\pm1.2)\times10^{-2}$	$(12.6\pm2.5)\times10^{-2}$	$(20.1\pm4.0)\times10^{-2}$	$(17.4\pm3.5)\times10^{-2}$	$(7.4\pm7.4)\times10^{-2}$	–	–	$(4.2\pm1.3)\times10^{-1}$	–	$(14.4\pm4.3)\times10^{-3}$	$(32.4\pm9.7)\times10^{-3}$
G239.950–01.810	–	$(45.8\pm9.2)\times10^{-2}$	$(8.4\pm1.7)\times10^{-1}$	$(5.4\pm1.1)\times10^{-1}$	$(2.1\pm2.1)\times10^{-1}$	–	–	–	$(4.2\pm1.3)\times10^{-1}$	–	–
G240.140–01.540	$(5.8\pm1.2)\times10^{-2}$	$(14.0\pm2.8)\times10^{-1}$	$(20.8\pm4.2)\times10^{-1}$	$(14.2\pm2.8)\times10^{-1}$	$(6.1\pm3.0)\times10^{-1}$	–	–	$(5.9\pm1.8)\times10^{-1}$	–	$(8.9\pm2.7)\times10^{-3}$	$(6.1\pm1.8)\times10^{-3}$
G240.170–01.590	–	$(41.0\pm8.4)\times10^{-3}$	$(18.9\pm3.8)\times10^{-2}$	$(13.7\pm2.8)\times10^{-2}$	$(6.2\pm3.1)\times10^{-2}$	–	$(5.8\pm1.8)\times10^{-1}$	–	–	$(28.1\pm8.4)\times10^{-4}$	$(6.1\pm1.8)\times10^{-3}$
G240.250–00.910	$(7.8\pm1.6)\times10^{-2}$	$(6.2\pm1.2)\times10^{-1}$	$(44.4\pm8.9)\times10^{-2}$	$(25.2\pm5.1)\times10^{-2}$	$(7.8\pm3.9)\times10^{-2}$	–	–	–	–	–	$(4.3\pm1.3)\times10^{-4}$
G240.490–00.070	–	$(6.9\pm1.4)\times10^{-1}$	$(5.0\pm1.0)\times10^{-1}$	$(29.5\pm5.9)\times10^{-2}$	$(11.9\pm5.9)\times10^{-2}$	–	$(21.1\pm6.5)\times10^{-2}$	–	$(10.1\pm3.1)\times10^{-1}$	$(27.7\pm8.3)\times10^{-3}$	$(21.2\pm6.4)\times10^{-3}$
G240.940–01.440	–	$(5.1\pm1.0)\times10^{-1}$	$(6.1\pm1.2)\times10^{-1}$	$(38.6\pm7.7)\times10^{-2}$	$(15.4\pm7.7)\times10^{-2}$	$(3.4\pm1.7)\times10^{-2}$	–	$(22.8\pm7.0)\times10^{-2}$	–	–	–
G240.990–01.470	$(19.1\pm3.8)\times10^{-2}$	$(9.5\pm1.9)\times10^{-1}$	$(12.2\pm2.4)\times10^{-1}$	$(7.1\pm1.4)\times10^{-1}$	$(2.8\pm1.4)\times10^{-1}$	$(2.7\pm1.3)\times10^{-2}$	$(30.0\pm9.2)\times10^{-2}$	–	–	$(9.6\pm2.9)\times10^{-3}$	$(20.1\pm6.0)\times10^{-3}$
G241.003–01.203	$(28.1\pm5.6)\times10^{-1}$	$(7.5\pm1.5)\times10^{+0}$	$(5.6\pm1.1)\times10^{+0}$	$(33.5\pm6.7)\times10^{-1}$	$(1.3\pm1.3)\times10^{+0}$	$(3.6\pm1.8)\times10^{-2}$	–	–	–	$(4.4\pm1.3)\times10^{-2}$	$(16.7\pm5.0)\times10^{-2}$
G241.010–01.200	$(28.1\pm5.6)\times10^{-1}$	$(7.5\pm1.5)\times10^{+0}$	$(5.6\pm1.1)\times10^{+0}$	$(33.5\pm6.7)\times10^{-1}$	$(1.3\pm1.3)\times10^{+0}$	$(3.4\pm1.7)\times10^{-2}$	–	–	–	$(4.4\pm1.3)\times10^{-2}$	$(16.7\pm5.0)\times10^{-2}$
G241.121–00.781	$(16.8\pm3.4)\times10^{-2}$	$(17.2\pm3.4)\times10^{-1}$	$(24.9\pm5.0)\times10^{-1}$	$(17.1\pm3.4)\times10^{-1}$	$(7.7\pm3.9)\times10^{-1}$	–	–	–	$(15.9\pm4.8)\times10^{-1}$	$(14.9\pm4.5)\times10^{-3}$	$(15.1\pm4.5)\times10^{-3}$
G241.140–01.170	–	$(5.4\pm1.1)\times10^{-1}$	$(13.8\pm2.8)\times10^{-1}$	$(11.7\pm2.3)\times10^{-1}$	$(5.7\pm2.9)\times10^{-1}$	$(4.0\pm2.0)\times10^{-2}$	–	–	$(11.0\pm3.3)\times10^{-1}$	–	–
G241.180–01.070	–	$(13.8\pm2.8)\times10^{-2}$	$(37.6\pm7.5)\times10^{-2}$	$(20.4\pm4.1)\times10^{-2}$	$(7.8\pm3.9)\times10^{-2}$	$(2.5\pm1.3)\times10^{-2}$	–	$(3.7\pm1.1)\times10^{-1}$	$(9.1\pm2.8)\times10^{-1}$	$(9.7\pm2.9)\times10^{-4}$	$(11.6\pm3.5)\times10^{-4}$
G241.190–00.780	$(14.3\pm2.9)\times10^{-2}$	$(46.7\pm9.4)\times10^{-2}$	$(9.3\pm1.9)\times10^{-1}$	$(7.9\pm1.6)\times10^{-1}$	$(3.5\pm1.8)\times10^{-1}$	–	–	–	$(7.6\pm2.3)\times10^{-1}$	–	–
G241.290–00.710	$(14.4\pm2.9)\times10^{-1}$	$(32.7\pm6.5)\times10^{-1}$	$(25.6\pm5.1)\times10^{-1}$	$(13.1\pm2.6)\times10^{-1}$	$(6.4\pm3.2)\times10^{-1}$	$(9.7\pm4.9)\times10^{-2}$	–	$(3.3\pm1.0)\times10^{-1}$	–	$(16.2\pm4.9)\times10^{-2}$	$(16.9\pm5.1)\times10^{-2}$
G241.390–02.030	–	$(6.8\pm1.4)\times10^{-1}$	$(8.1\pm1.6)\times10^{-1}$	$(5.2\pm1.0)\times10^{-1}$	$(2.0\pm1.0)\times10^{-1}$	–	–	–	–	–	–
G241.420–00.700	$(8.5\pm1.7)\times10^{-1}$	$(32.7\pm6.5)\times10^{-1}$	$(30.1\pm6.0)\times10^{-1}$	$(18.9\pm3.8)\times10^{-1}$	$(6.5\pm6.5)\times10^{-1}$	–	$(4.5\pm1.4)\times10^{-1}$	–	–	$(4.0\pm1.2)\times10^{-2}$	$(10.9\pm3.3)\times10^{-2}$
G241.530–00.600	$(5.2\pm1.0)\times10^{+1}$	$(42.9\pm8.6)\times10^{+0}$	$(15.1\pm3.0)\times10^{+0}$	$(5.7\pm1.1)\times10^{+0}$	$(17.5\pm8.7)\times10^{-1}$	$(15.2\pm7.6)\times10^{-1}$	$(16.1\pm4.8)\times10^{-1}$	$(7.2\pm2.2)\times10^{-1}$	$(21.2\pm6.4)\times10^{-1}$	$(19.3\pm5.8)\times10^{-1}$	$(23.2\pm7.0)\times10^{-1}$
G241.538–00.594	$(8.7\pm1.7)\times10^{+0}$	$(16.2\pm3.2)\times10^{+0}$	$(9.3\pm1.9)\times10^{+0}$	$(42.8\pm8.6)\times10^{-1}$	$(15.9\pm8.0)\times10^{-1}$	$(3.6\pm1.8)\times10^{-1}$	–	–	–	$(3.4\pm1.0)\times10^{-1}$	$(26.8\pm8.0)\times10^{-2}$
G241.560–00.590	$(8.4\pm1.7)\times10^{+1}$	$(8.3\pm1.7)\times10^{+1}$	$(29.5\pm5.9)\times10^{+0}$	$(11.9\pm2.4)\times10^{+0}$	$(3.7\pm1.8)\times10^{+0}$	$(2.1\pm1.0)\times10^{+0}$	$(29.0\pm8.7)\times10^{-1}$	$(14.9\pm4.5)\times10^{-1}$	$(24.7\pm7.4)\times10^{-1}$	$(23.5\pm7.0)\times10^{-1}$	$(25.7\pm7.7)\times10^{-1}$

Table A.3: continued

Name	F_{70} (Jy)	F_{160} (Jy)	F_{250} (Jy)	F_{350} (Jy)	F_{500} (Jy)	F_{8} (Jy)	$F_{12.1}$ (Jy)	$F_{14.7}$ (Jy)	F_{21} (Jy)	F_{14} (Jy)	F_{22} (Jy)
G241.570–00.640	$(31.3\pm6.3)\times10^{-1}$	$(23.8\pm4.8)\times10^{+0}$	$(24.4\pm4.9)\times10^{+0}$	$(16.0\pm3.2)\times10^{+0}$	$(7.6\pm3.8)\times10^{+0}$	$(2.1\pm1.1)\times10^{-1}$	$(4.2\pm1.3)\times10^{-1}$	–	$(10.8\pm3.2)\times10^{-1}$	$(31.6\pm9.5)\times10^{-2}$	$(3.5\pm1.1)\times10^{-1}$
G241.680–00.580	$(19.1\pm3.8)\times10^{+0}$	$(37.0\pm7.4)\times10^{+0}$	$(18.1\pm3.6)\times10^{+0}$	$(9.2\pm1.8)\times10^{+0}$	$(2.9\pm2.9)\times10^{+0}$	$(3.7\pm1.8)\times10^{-2}$	–	–	$(6.3\pm1.9)\times10^{-1}$	$(4.2\pm1.3)\times10^{-2}$	$(14.5\pm4.3)\times10^{-2}$
G242.190–00.780	–	$(18.3\pm3.7)\times10^{-2}$	$(19.2\pm3.8)\times10^{-2}$	$(11.0\pm2.2)\times10^{-2}$	$(3.1\pm3.1)\times10^{-2}$	–	–	–	–	$(3.6\pm1.1)\times10^{-3}$	$(5.0\pm1.5)\times10^{-3}$
G242.560–00.630	$(27.1\pm5.8)\times10^{-3}$	$(5.4\pm1.1)\times10^{-2}$	$(13.6\pm2.7)\times10^{-2}$	$(8.8\pm1.9)\times10^{-2}$	$(4.1\pm2.1)\times10^{-2}$	–	–	–	–	–	$(12.0\pm3.6)\times10^{-4}$
G242.590–00.240	$(15.1\pm3.0)\times10^{+0}$	$(19.8\pm4.0)\times10^{+0}$	$(6.7\pm1.3)\times10^{+0}$	$(20.8\pm4.2)\times10^{-1}$	$(5.0\pm5.0)\times10^{-1}$	$(4.2\pm2.1)\times10^{-1}$	$(8.8\pm2.6)\times10^{-1}$	$(4.0\pm1.2)\times10^{-1}$	$(12.4\pm3.7)\times10^{-1}$	$(6.8\pm2.0)\times10^{-1}$	$(7.4\pm2.2)\times10^{-1}$
G242.620–00.690	$(11.0\pm2.2)\times10^{-2}$	$(6.7\pm1.3)\times10^{-1}$	$(10.7\pm2.1)\times10^{-1}$	$(8.4\pm1.7)\times10^{-1}$	$(3.2\pm1.6)\times10^{-1}$	–	$(4.6\pm1.4)\times10^{-1}$	–	–	$(11.9\pm3.6)\times10^{-2}$	$(12.9\pm3.9)\times10^{-2}$
G242.640–00.700	$(32.8\pm6.9)\times10^{-3}$	$(5.3\pm1.1)\times10^{-1}$	$(9.9\pm2.0)\times10^{-1}$	$(7.9\pm1.6)\times10^{-1}$	$(2.9\pm2.9)\times10^{-1}$	–	$(28.7\pm8.8)\times10^{-2}$	$(25.2\pm7.7)\times10^{-2}$	–	$(5.9\pm1.8)\times10^{-3}$	$(9.9\pm3.0)\times10^{-3}$
G242.770–01.530	$(9.0\pm1.8)\times10^{-2}$	$(8.0\pm1.6)\times10^{-1}$	$(11.8\pm2.4)\times10^{-1}$	$(7.1\pm1.4)\times10^{-1}$	$(2.9\pm2.9)\times10^{-1}$	–	–	–	–	$(12.3\pm3.7)\times10^{-3}$	$(22.0\pm6.6)\times10^{-3}$
G242.880–02.250	$(5.4\pm1.1)\times10^{-2}$	$(7.1\pm1.4)\times10^{-1}$	$(7.0\pm1.4)\times10^{-1}$	$(41.9\pm8.4)\times10^{-2}$	$(17.1\pm8.5)\times10^{-2}$	–	–	$(4.2\pm1.3)\times10^{-1}$	–	$(5.4\pm1.6)\times10^{-3}$	$(4.6\pm1.4)\times10^{-3}$
G242.920–00.520	$(8.3\pm1.7)\times10^{-1}$	$(19.1\pm3.8)\times10^{-1}$	$(21.0\pm4.2)\times10^{-1}$	$(14.6\pm2.9)\times10^{-1}$	$(7.5\pm3.8)\times10^{-1}$	–	$(6.0\pm1.8)\times10^{-1}$	–	$(5.5\pm1.7)\times10^{-1}$	$(5.7\pm1.7)\times10^{-2}$	$(8.1\pm2.4)\times10^{-2}$
G242.940–00.450	$(22.8\pm4.6)\times10^{+0}$	$(34.6\pm6.9)\times10^{+0}$	$(16.6\pm3.3)\times10^{+0}$	$(7.4\pm1.5)\times10^{+0}$	$(1.8\pm1.8)\times10^{+0}$	$(13.2\pm6.6)\times10^{-1}$	$(20.9\pm6.3)\times10^{-1}$	$(20.0\pm6.0)\times10^{-1}$	$(4.4\pm1.3)\times10^{+0}$	$(21.5\pm6.4)\times10^{-1}$	$(4.6\pm1.4)\times10^{+0}$
G242.940–00.500	$(15.3\pm3.1)\times10^{-1}$	$(37.8\pm7.6)\times10^{-1}$	$(35.7\pm7.1)\times10^{-1}$	$(21.7\pm4.3)\times10^{-1}$	$(9.7\pm4.8)\times10^{-1}$	$(4.6\pm2.3)\times10^{-2}$	–	–	–	$(11.2\pm3.3)\times10^{-2}$	$(27.0\pm8.1)\times10^{-2}$
G243.150–00.170	$(6.3\pm1.3)\times10^{-1}$	$(6.8\pm1.4)\times10^{-1}$	$(10.3\pm2.1)\times10^{-1}$	$(7.6\pm1.5)\times10^{-1}$	$(3.5\pm1.8)\times10^{-1}$	$(5.0\pm2.5)\times10^{-2}$	$(17.3\pm5.4)\times10^{-2}$	–	–	$(21.0\pm6.3)\times10^{-3}$	$(5.1\pm1.5)\times10^{-3}$
G243.160–01.520	$(13.5\pm2.7)\times10^{-1}$	$(17.9\pm3.6)\times10^{-1}$	$(16.1\pm3.2)\times10^{-1}$	$(10.3\pm2.1)\times10^{-1}$	$(5.0\pm2.5)\times10^{-1}$	–	–	–	–	$(14.2\pm4.3)\times10^{-3}$	$(8.1\pm2.4)\times10^{-3}$
G243.190–00.160	$(21.2\pm4.3)\times10^{-2}$	$(5.8\pm1.2)\times10^{-1}$	$(5.6\pm1.1)\times10^{-1}$	$(36.9\pm7.4)\times10^{-2}$	$(16.8\pm8.4)\times10^{-2}$	–	$(25.1\pm7.7)\times10^{-2}$	$(6.3\pm1.9)\times10^{-1}$	$(5.0\pm1.5)\times10^{-1}$	$(8.4\pm2.5)\times10^{-3}$	$(18.5\pm5.5)\times10^{-3}$
G243.200–00.330	$(40.1\pm8.3)\times10^{-3}$	$(33.4\pm6.7)\times10^{-2}$	$(20.6\pm4.1)\times10^{-2}$	$(11.9\pm2.4)\times10^{-2}$	$(5.0\pm2.5)\times10^{-2}$	$(2.9\pm1.5)\times10^{-2}$	$(4.0\pm1.2)\times10^{-1}$	$(23.9\pm7.3)\times10^{-2}$	$(4.4\pm1.4)\times10^{-1}$	$(17.7\pm5.3)\times10^{-4}$	$(15.0\pm4.5)\times10^{-4}$
G243.450–01.620	$(27.2\pm5.4)\times10^{-2}$	$(6.4\pm1.3)\times10^{-1}$	$(5.1\pm1.0)\times10^{-1}$	$(33.1\pm6.6)\times10^{-2}$	$(12.6\pm6.3)\times10^{-2}$	$(9.0\pm4.5)\times10^{-2}$	–	–	–	$(8.4\pm2.5)\times10^{-4}$	$(10.7\pm3.2)\times10^{-4}$
G243.540–00.810	$(9.8\pm2.0)\times10^{-1}$	$(32.6\pm6.5)\times10^{-1}$	$(30.0\pm6.0)\times10^{-1}$	$(16.5\pm3.3)\times10^{-1}$	$(6.3\pm6.3)\times10^{-1}$	$(2.7\pm1.4)\times10^{-2}$	–	$(26.2\pm8.0)\times10^{-2}$	–	$(4.8\pm1.4)\times10^{-2}$	$(11.1\pm3.3)\times10^{-2}$
G243.770–01.420	$(19.3\pm4.4)\times10^{-3}$	$(23.0\pm4.6)\times10^{-2}$	$(39.9\pm8.0)\times10^{-2}$	$(24.4\pm4.9)\times10^{-2}$	$(9.1\pm9.1)\times10^{-2}$	–	–	–	–	–	–
G243.780–00.240	$(11.0\pm2.2)\times10^{-1}$	$(28.9\pm5.8)\times10^{-1}$	$(21.7\pm4.3)\times10^{-1}$	$(12.8\pm2.6)\times10^{-1}$	$(3.7\pm3.7)\times10^{-1}$	$(16.1\pm8.1)\times10^{-3}$	$(21.7\pm6.7)\times10^{-2}$	–	–	$(3.5\pm1.1)\times10^{-2}$	$(5.8\pm1.7)\times10^{-2}$
G243.860–00.870	–	$(6.3\pm1.3)\times10^{-1}$	$(11.4\pm2.3)\times10^{-1}$	$(8.2\pm1.6)\times10^{-1}$	$(3.5\pm1.7)\times10^{-1}$	$(5.4\pm2.7)\times10^{-2}$	$(28.6\pm8.7)\times10^{-2}$	–	$(3.3\pm1.0)\times10^{-1}$	–	–
G243.950–00.200	–	$(37.0\pm7.4)\times10^{-2}$	$(28.5\pm5.7)\times10^{-2}$	$(15.2\pm3.1)\times10^{-2}$	$(5.8\pm5.8)\times10^{-2}$	–	–	–	–	$(28.8\pm8.7)\times10^{-4}$	$(21.3\pm6.4)\times10^{-4}$
G244.410–01.970	$(12.8\pm2.6)\times10^{-2}$	$(41.3\pm8.3)\times10^{-2}$	$(11.5\pm2.3)\times10^{-1}$	$(10.3\pm2.1)\times10^{-1}$	$(5.9\pm3.0)\times10^{-1}$	–	–	–	$(9.3\pm2.8)\times10^{-1}$	$(30.3\pm9.1)\times10^{-3}$	$(5.5\pm1.6)\times10^{-2}$
G244.460–00.540	–	$(29.7\pm5.9)\times10^{-2}$	$(39.7\pm7.9)\times10^{-2}$	$(24.9\pm5.0)\times10^{-2}$	$(8.5\pm4.3)\times10^{-2}$	–	$(3.7\pm1.1)\times10^{-1}$	–	–	$(6.7\pm2.0)\times10^{-4}$	–
G244.760–00.320	$(5.9\pm1.2)\times10^{-1}$	$(6.1\pm1.2)\times10^{-1}$	$(8.5\pm1.7)\times10^{-1}$	$(6.8\pm1.4)\times10^{-1}$	$(3.1\pm1.5)\times10^{-1}$	–	$(6.5\pm2.0)\times10^{-1}$	–	–	$(3.6\pm1.1)\times10^{-3}$	$(7.0\pm2.1)\times10^{-3}$
G244.830–00.960	–	$(29.3\pm5.9)\times10^{-2}$	$(45.6\pm9.1)\times10^{-2}$	$(32.3\pm6.5)\times10^{-2}$	$(12.8\pm6.5)\times10^{-2}$	–	–	–	–	$(18.6\pm5.6)\times10^{-5}$	–
G245.070–00.210	–	$(17.8\pm3.6)\times10^{-2}$	$(44.0\pm8.8)\times10^{-2}$	$(24.4\pm4.9)\times10^{-2}$	$(10.5\pm5.2)\times10^{-2}$	–	$(26.4\pm8.0)\times10^{-2}$	–	–	$(5.2\pm1.6)\times10^{-3}$	$(32.4\pm9.7)\times10^{-4}$
G245.080–00.180	$(6.2\pm1.3)\times10^{-2}$	$(35.4\pm7.1)\times10^{-2}$	$(27.7\pm5.6)\times10^{-2}$	$(14.2\pm2.9)\times10^{-2}$	$(8.2\pm8.2)\times10^{-2}$	$(2.2\pm1.1)\times10^{-2}$	$(18.2\pm5.6)\times10^{-2}$	–	–	$(6.4\pm1.9)\times10^{-3}$	$(3.4\pm1.0)\times10^{-3}$
G245.100–00.990	$(17.1\pm3.4)\times10^{-1}$	$(5.0\pm1.0)\times10^{+0}$	$(34.8\pm7.0)\times10^{-1}$	$(18.4\pm3.7)\times10^{-1}$	$(5.8\pm5.8)\times10^{-1}$	$(5.4\pm2.7)\times10^{-2}$	–	–	–	$(11.1\pm3.3)\times10^{-2}$	$(14.3\pm4.3)\times10^{-2}$
G245.240–01.390	$(10.0\pm2.0)\times10^{-2}$	$(21.3\pm4.3)\times10^{-2}$	$(32.2\pm6.4)\times10^{-2}$	$(17.7\pm3.5)\times10^{-2}$	$(4.3\pm4.3)\times10^{-2}$	$(18.9\pm9.6)\times10^{-3}$	–	–	$(6.9\pm2.1)\times10^{-1}$	$(23.9\pm7.2)\times10^{-5}$	–
G245.300–00.300	$(18.8\pm3.8)\times10^{+0}$	$(28.8\pm5.8)\times10^{+0}$	$(11.3\pm2.3)\times10^{+0}$	$(46.3\pm9.3)\times10^{-1}$	$(15.2\pm7.6)\times10^{-1}$	$(7.7\pm3.8)\times10^{-1}$	$(6.1\pm1.8)\times10^{-1}$	$(17.4\pm5.4)\times10^{-2}$	–	$(9.8\pm2.9)\times10^{-1}$	$(6.4\pm1.9)\times10^{-1}$
G246.270–00.070	–	$(6.8\pm1.4)\times10^{-1}$	$(6.1\pm1.2)\times10^{-1}$	$(37.7\pm7.6)\times10^{-2}$	$(13.7\pm6.8)\times10^{-2}$	–	$(3.7\pm1.1)\times10^{-1}$	$(16.1\pm5.0)\times10^{-2}$	–	$(6.0\pm1.8)\times10^{-3}$	$(5.8\pm1.8)\times10^{-3}$
G246.970–01.720	–	$(21.5\pm4.3)\times10^{-2}$	$(41.4\pm8.3)\times10^{-2}$	$(30.0\pm6.0)\times10^{-2}$	$(11.9\pm6.0)\times10^{-2}$	–	$(24.3\pm7.5)\times10^{-2}$	–	–	–	–
G247.240–01.120	$(21.1\pm4.2)\times10^{-2}$	$(48.5\pm9.7)\times10^{-2}$	$(6.0\pm1.2)\times10^{-1}$	$(41.6\pm8.3)\times10^{-2}$	$(18.6\pm9.3)\times10^{-2}$	$(2.7\pm1.3)\times10^{-2}$	$(28.4\pm8.7)\times10^{-2}$	$(18.5\pm5.8)\times10^{-2}$	–	–	–
G247.280–00.560	–	$(39.7\pm7.9)\times10^{-2}$	$(18.5\pm3.7)\times10^{-2}$	$(13.0\pm2.7)\times10^{-2}$	$(5.1\pm2.6)\times10^{-2}$	–	–	–	–	$(31.0\pm9.3)\times10^{-4}$	$(17.7\pm5.3)\times10^{-4}$
G247.440–00.930	$(35.8\pm7.2)\times10^{-2}$	$(32.9\pm6.6)\times10^{-2}$	$(5.0\pm1.0)\times10^{-1}$	$(26.8\pm5.4)\times10^{-2}$	$(13.3\pm6.7)\times10^{-2}$	–	$(7.3\pm2.2)\times10^{-1}$	$(3.8\pm1.2)\times10^{-1}$	–	$(10.7\pm3.2)\times10^{-3}$	$(17.6\pm5.3)\times10^{-3}$
G247.460–00.820	–	$(39.3\pm7.9)\times10^{-2}$	$(48.4\pm9.7)\times10^{-2}$	$(29.8\pm6.0)\times10^{-2}$	$(10.3\pm5.2)\times10^{-2}$	$(18.6\pm9.4)\times10^{-3}$	–	$(21.1\pm6.4)\times10^{-2}$	–	–	$(4.6\pm1.4)\times10^{-4}$
G247.510+00.060	$(19.5\pm3.9)\times10^{-2}$	$(5.4\pm1.1)\times10^{-1}$	$(31.4\pm6.3)\times10^{-2}$	$(17.4\pm3.5)\times10^{-2}$	$(5.7\pm2.9)\times10^{-2}$	$(10.0\pm5.0)\times10^{-2}$	–	–	–	$(19.0\pm5.7)\times10^{-3}$	$(14.0\pm4.2)\times10^{-3}$
G247.510–00.570	–	$(47.9\pm9.6)\times10^{-2}$	$(29.9\pm6.0)\times10^{-2}$	$(26.6\pm5.4)\times10^{-2}$	$(15.0\pm7.5)\times10^{-2}$	$(2.8\pm1.4)\times10^{-2}$	–	–	–	$(16.3\pm4.9)\times10^{-4}$	–
G247.520+00.050	–	$(7.5\pm1.5)\times10^{-1}$	$(10.7\pm2.2)\times10^{-2}$	$(11.1\pm2.3)\times10^{-2}$	$(12.9\pm6.4)\times10^{-2}$	–	–	–	$(4.0\pm1.2)\times10^{-1}$	$(25.8\pm7.8)\times10^{-5}$	–
G247.520–00.240	$(15.2\pm3.0)\times10^{-2}$	$(33.1\pm6.6)\times10^{-2}$	$(21.2\pm4.2)\times10^{-2}$	$(10.7\pm2.2)\times10^{-2}$	$(4.1\pm4.1)\times10^{-2}$	–	–	–	–	$(8.0\pm2.4)\times10^{-3}$	$(7.1\pm2.1)\times10^{-3}$
G247.590–00.820	–	$(6.4\pm1.3)\times10^{-1}$	$(7.1\pm1.4)\times10^{-1}$	$(42.0\pm8.4)\times10^{-2}$	$(15.9\pm8.0)\times10^{-2}$	–	$(26.7\pm8.2)\times10^{-2}$	–	–	$(23.1\pm6.9)\times10^{-4}$	$(29.7\pm8.9)\times10^{-4}$
G247.610–00.830	$(29.0\pm6.2)\times10^{-3}$	$(46.1\pm9.2)\times10^{-2}$	$(6.5\pm1.3)\times10^{-1}$	$(43.9\pm8.8)\times10^{-2}$	$(1.7\pm1.7)\times10^{-1}$	–	–	–	$(3.7\pm1.1)\times10^{-1}$	–	$(11.3\pm3.4)\times10^{-4}$

Table A.3: continued

Name	F_{70} (Jy)	F_{160} (Jy)	F_{250} (Jy)	F_{350} (Jy)	F_{500} (Jy)	F_{8} (Jy)	$F_{12.1}$ (Jy)	$F_{14.7}$ (Jy)	F_{21} (Jy)	F_{14} (Jy)	F_{22} (Jy)
G247.630–00.550	$(5.4\pm1.1)\times10^{+1}$	$(8.0\pm1.6)\times10^{+1}$	$(34.3\pm6.9)\times10^{+0}$	$(14.9\pm3.0)\times10^{+0}$	$(5.2\pm2.6)\times10^{+0}$	$(16.3\pm8.2)\times10^{-1}$	–	$(10.4\pm3.1)\times10^{-1}$	$(30.2\pm9.1)\times10^{-1}$	$(22.1\pm6.6)\times10^{-1}$	$(21.4\pm6.4)\times10^{-1}$
G247.640–00.530	$(12.2\pm2.4)\times10^{+0}$	$(16.1\pm3.2)\times10^{+0}$	$(6.8\pm1.4)\times10^{+0}$	$(25.4\pm5.1)\times10^{-1}$	$(7.6\pm3.8)\times10^{-1}$	$(3.9\pm1.9)\times10^{-1}$	–	$(26.5\pm8.1)\times10^{-2}$	$(7.6\pm2.3)\times10^{-1}$	$(5.5\pm1.7)\times10^{-1}$	$(27.8\pm8.3)\times10^{-2}$
G247.890–00.990	$(7.4\pm1.5)\times10^{-2}$	$(13.0\pm2.6)\times10^{-2}$	$(22.8\pm4.6)\times10^{-2}$	$(11.8\pm2.4)\times10^{-2}$	$(4.4\pm4.4)\times10^{-2}$	–	–	–	–	$(9.2\pm2.8)\times10^{-4}$	–
G247.930–00.440	$(11.9\pm2.4)\times10^{-2}$	$(10.7\pm2.1)\times10^{-1}$	$(15.7\pm3.1)\times10^{-1}$	$(11.9\pm2.4)\times10^{-1}$	$(5.1\pm2.6)\times10^{-1}$	$(2.5\pm1.3)\times10^{-2}$	–	–	$(30.5\pm9.6)\times10^{-2}$	$(13.4\pm4.0)\times10^{-3}$	$(3.5\pm1.1)\times10^{-2}$
G248.000–00.430	$(20.7\pm4.1)\times10^{+0}$	$(5.7\pm1.1)\times10^{+1}$	$(28.1\pm5.6)\times10^{+0}$	$(11.9\pm2.4)\times10^{+0}$	$(4.3\pm2.2)\times10^{+0}$	$(12.8\pm6.4)\times10^{-1}$	$(10.8\pm3.2)\times10^{-1}$	$(3.7\pm1.1)\times10^{-1}$	–	$(19.7\pm5.9)\times10^{-1}$	$(15.7\pm4.7)\times10^{-1}$
G248.150–02.210	$(40.6\pm8.1)\times10^{-2}$	$(29.1\pm5.8)\times10^{-1}$	$(33.7\pm6.7)\times10^{-1}$	$(19.4\pm3.9)\times10^{-1}$	$(7.3\pm3.7)\times10^{-1}$	–	$(15.3\pm4.6)\times10^{-1}$	–	–	$(6.0\pm1.8)\times10^{-3}$	$(10.3\pm3.1)\times10^{-3}$
G248.440–00.910	–	$(16.1\pm3.2)\times10^{-2}$	$(28.8\pm5.8)\times10^{-2}$	$(15.8\pm3.2)\times10^{-2}$	$(6.6\pm3.3)\times10^{-2}$	–	$(24.8\pm7.6)\times10^{-2}$	–	–	$(9.6\pm2.9)\times10^{-4}$	$(3.7\pm1.1)\times10^{-4}$
G248.690–01.930	–	$(8.5\pm1.7)\times10^{-1}$	$(15.6\pm3.1)\times10^{-1}$	$(10.3\pm2.1)\times10^{-1}$	$(4.4\pm2.2)\times10^{-1}$	–	–	$(30.1\pm9.2)\times10^{-2}$	–	$(16.1\pm4.8)\times10^{-4}$	$(14.4\pm4.3)\times10^{-4}$
G248.700–01.010	–	$(47.2\pm9.4)\times10^{-2}$	$(31.3\pm6.3)\times10^{-2}$	$(17.9\pm3.6)\times10^{-2}$	$(7.6\pm3.8)\times10^{-2}$	–	–	–	$(7.1\pm2.2)\times10^{-1}$	$(12.1\pm3.6)\times10^{-4}$	$(13.8\pm4.1)\times10^{-4}$
G249.170–02.020	$(16.5\pm3.3)\times10^{-2}$	$(32.6\pm6.5)\times10^{-2}$	$(20.6\pm4.1)\times10^{-2}$	$(8.7\pm1.8)\times10^{-2}$	–	–	–	–	$(8.2\pm2.5)\times10^{-1}$	$(21.7\pm6.5)\times10^{-4}$	$(25.6\pm7.7)\times10^{-4}$
G249.390–01.410	$(7.0\pm1.4)\times10^{-2}$	$(25.7\pm5.1)\times10^{-2}$	$(28.8\pm5.8)\times10^{-2}$	$(15.7\pm3.3)\times10^{-2}$	$(5.9\pm5.9)\times10^{-2}$	$(2.9\pm1.5)\times10^{-2}$	–	–	–	$(9.1\pm2.7)\times10^{-3}$	$(32.9\pm9.9)\times10^{-4}$
G249.450–02.420	$(22.1\pm4.7)\times10^{-3}$	$(7.5\pm1.5)\times10^{-2}$	$(34.3\pm6.9)\times10^{-2}$	$(26.4\pm5.3)\times10^{-2}$	$(12.2\pm6.1)\times10^{-2}$	–	$(4.3\pm1.3)\times10^{-1}$	$(25.7\pm7.9)\times10^{-2}$	–	$(6.8\pm2.1)\times10^{-4}$	–
G249.530–02.500	$(27.0\pm5.4)\times10^{-2}$	–	$(26.5\pm5.3)\times10^{-2}$	$(17.8\pm3.6)\times10^{-2}$	$(5.8\pm2.9)\times10^{-2}$	–	$(28.5\pm8.9)\times10^{-2}$	–	–	–	$(11.1\pm3.3)\times10^{-4}$
G249.600–02.080	$(12.0\pm2.4)\times10^{+0}$	$(14.8\pm3.0)\times10^{+0}$	$(5.6\pm1.1)\times10^{+0}$	$(22.8\pm4.6)\times10^{-1}$	$(8.3\pm4.1)\times10^{-1}$	$(4.5\pm2.2)\times10^{-1}$	–	–	–	$(4.5\pm1.3)\times10^{-1}$	$(3.4\pm1.0)\times10^{-1}$
G249.680–02.100	$(22.9\pm4.6)\times10^{-2}$	$(18.7\pm3.7)\times10^{-1}$	$(39.5\pm7.9)\times10^{-1}$	$(28.1\pm5.6)\times10^{-1}$	$(12.9\pm6.4)\times10^{-1}$	$(9.1\pm4.6)\times10^{-2}$	–	$(12.1\pm3.6)\times10^{-1}$	–	$(8.7\pm2.6)\times10^{-2}$	$(4.5\pm1.4)\times10^{-2}$
G250.230–00.040	$(24.4\pm4.9)\times10^{-1}$	$(6.8\pm1.4)\times10^{+0}$	$(45.3\pm9.1)\times10^{-1}$	$(22.2\pm4.4)\times10^{-1}$	$(8.6\pm8.6)\times10^{-1}$	$(11.8\pm5.9)\times10^{-2}$	–	–	$(9.5\pm2.9)\times10^{-1}$	$(18.3\pm5.5)\times10^{-2}$	$(17.8\pm5.3)\times10^{-2}$
G250.270–00.980	$(27.2\pm5.8)\times10^{-3}$	$(27.1\pm5.4)\times10^{-2}$	$(5.1\pm1.0)\times10^{-1}$	$(32.9\pm6.6)\times10^{-2}$	$(14.7\pm7.4)\times10^{-2}$	$(2.8\pm1.4)\times10^{-2}$	–	–	–	$(4.3\pm1.3)\times10^{-3}$	$(3.7\pm1.1)\times10^{-3}$
G250.590–00.650	$(40.0\pm8.0)\times10^{+0}$	$(41.0\pm8.2)\times10^{+0}$	$(15.1\pm3.0)\times10^{+0}$	$(6.3\pm1.3)\times10^{+0}$	$(19.1\pm9.5)\times10^{-1}$	$(11.0\pm5.5)\times10^{-1}$	$(13.9\pm4.2)\times10^{-1}$	$(10.0\pm3.0)\times10^{-1}$	$(8.6\pm2.6)\times10^{-1}$	$(15.0\pm4.5)\times10^{-1}$	$(18.1\pm5.4)\times10^{-1}$
G250.900–01.530	$(18.2\pm3.6)\times10^{-2}$	$(6.9\pm1.4)\times10^{-1}$	$(7.7\pm1.5)\times10^{-1}$	$(5.6\pm1.1)\times10^{-1}$	$(2.7\pm1.3)\times10^{-1}$	–	$(20.0\pm6.3)\times10^{-2}$	–	–	$(12.0\pm3.6)\times10^{-4}$	$(6.8\pm2.1)\times10^{-4}$
G250.900–02.050	$(36.8\pm7.6)\times10^{-3}$	$(44.9\pm9.0)\times10^{-2}$	$(5.0\pm1.0)\times10^{-1}$	$(33.2\pm6.6)\times10^{-2}$	$(14.2\pm7.1)\times10^{-2}$	–	–	–	–	$(7.7\pm2.3)\times10^{-3}$	$(24.0\pm7.2)\times10^{-3}$
G250.910–01.280	$(9.8\pm2.0)\times10^{-2}$	$(5.2\pm1.0)\times10^{-1}$	$(49.3\pm9.9)\times10^{-2}$	$(25.3\pm5.1)\times10^{-2}$	$(10.8\pm5.4)\times10^{-2}$	–	–	$(32.5\pm9.8)\times10^{-2}$	–	$(4.1\pm1.2)\times10^{-3}$	$(31.0\pm9.3)\times10^{-4}$
G251.040–01.030	$(27.9\pm5.6)\times10^{-2}$	$(13.6\pm2.7)\times10^{+0}$	$(22.8\pm4.6)\times10^{+0}$	$(16.9\pm3.4)\times10^{+0}$	$(8.1\pm4.1)\times10^{+0}$	$(10.6\pm5.3)\times10^{-2}$	–	–	–	$(15.0\pm4.5)\times10^{-3}$	$(15.2\pm4.5)\times10^{-3}$
G251.070–00.980	$(32.3\pm6.5)\times10^{-1}$	$(38.7\pm7.7)\times10^{-1}$	$(36.3\pm7.3)\times10^{-1}$	$(22.0\pm4.4)\times10^{-1}$	$(9.4\pm9.4)\times10^{-1}$	$(2.2\pm1.1)\times10^{-2}$	–	$(32.5\pm9.8)\times10^{-2}$	$(7.4\pm2.2)\times10^{-1}$	$(18.0\pm5.4)\times10^{-2}$	$(7.2\pm2.1)\times10^{-1}$
G251.070–01.000	$(46.5\pm9.5)\times10^{-3}$	$(13.5\pm2.7)\times10^{-1}$	$(33.9\pm6.8)\times10^{-1}$	$(32.9\pm6.6)\times10^{-1}$	$(15.1\pm7.6)\times10^{-1}$	–	–	$(15.3\pm4.8)\times10^{-2}$	–	$(3.3\pm1.0)\times10^{-4}$	$(4.9\pm1.5)\times10^{-2}$
G251.080–00.990	$(5.4\pm1.1)\times10^{-1}$	$(19.0\pm3.8)\times10^{-1}$	$(42.6\pm8.5)\times10^{-1}$	$(31.9\pm6.4)\times10^{-1}$	$(14.1\pm7.0)\times10^{-1}$	–	–	–	–	$(5.9\pm1.8)\times10^{-3}$	$(11.5\pm3.5)\times10^{-2}$
G251.160–01.990	$(7.3\pm1.5)\times10^{-1}$	$(22.8\pm4.6)\times10^{-1}$	$(13.8\pm2.8)\times10^{-1}$	$(6.3\pm1.3)\times10^{-1}$	$(2.7\pm2.7)\times10^{-1}$	$(2.1\pm1.1)\times10^{-2}$	$(26.1\pm8.1)\times10^{-2}$	–	$(9.4\pm2.8)\times10^{-1}$	$(8.2\pm2.5)\times10^{-2}$	$(6.7\pm2.0)\times10^{-2}$
G251.190–01.970	$(5.8\pm1.2)\times10^{+1}$	$(6.4\pm1.3)\times10^{+1}$	$(24.9\pm5.0)\times10^{+0}$	$(10.3\pm2.1)\times10^{+0}$	$(3.0\pm1.5)\times10^{+0}$	$(2.5\pm1.2)\times10^{+0}$	$(3.6\pm1.1)\times10^{+0}$	$(9.6\pm2.9)\times10^{-1}$	$(17.7\pm5.3)\times10^{-1}$	$(28.6\pm8.6)\times10^{-1}$	$(23.0\pm6.9)\times10^{-1}$
G251.210–00.610	$(8.7\pm1.8)\times10^{-2}$	$(8.6\pm1.7)\times10^{-1}$	$(7.9\pm1.6)\times10^{-1}$	$(42.2\pm8.4)\times10^{-2}$	$(16.8\pm8.4)\times10^{-2}$	$(2.2\pm1.1)\times10^{-2}$	$(4.0\pm1.2)\times10^{-1}$	–	–	$(6.3\pm1.9)\times10^{-3}$	$(7.5\pm2.3)\times10^{-3}$
G251.230–01.950	$(8.8\pm1.8)\times10^{+1}$	$(8.3\pm1.7)\times10^{+1}$	$(38.8\pm7.8)\times10^{+0}$	$(16.8\pm3.4)\times10^{+0}$	$(5.0\pm5.0)\times10^{+0}$	$(18.4\pm9.2)\times10^{-1}$	$(22.0\pm6.6)\times10^{-1}$	$(3.6\pm1.1)\times10^{+0}$	$(13.6\pm4.1)\times10^{+0}$	$(27.0\pm8.1)\times10^{-1}$	$(10.7\pm3.2)\times10^{+0}$
G251.400–00.180	–	$(30.2\pm6.0)\times10^{-2}$	$(43.0\pm8.6)\times10^{-2}$	$(23.4\pm4.7)\times10^{-2}$	$(9.3\pm9.3)\times10^{-2}$	$(3.4\pm1.7)\times10^{-2}$	–	–	–	$(26.5\pm8.0)\times10^{-3}$	$(5.9\pm1.8)\times10^{-3}$
G251.410–00.980	–	$(5.1\pm1.0)\times10^{-1}$	$(49.2\pm9.9)\times10^{-2}$	$(26.2\pm5.2)\times10^{-2}$	$(5.9\pm3.0)\times10^{-2}$	–	–	–	–	$(18.9\pm5.7)\times10^{-5}$	$(8.7\pm2.6)\times10^{-4}$
G251.750–00.900	$(16.0\pm3.2)\times10^{-2}$	$(30.8\pm6.2)\times10^{-2}$	$(32.6\pm6.5)\times10^{-2}$	$(16.9\pm3.4)\times10^{-2}$	$(4.5\pm2.2)\times10^{-2}$	–	$(6.3\pm1.9)\times10^{-1}$	$(3.8\pm1.1)\times10^{-1}$	–	$(4.7\pm1.4)\times10^{-3}$	$(30.1\pm9.0)\times10^{-4}$
G251.750–01.010	–	$(22.5\pm4.5)\times10^{-2}$	$(26.9\pm5.4)\times10^{-2}$	$(14.3\pm2.9)\times10^{-2}$	$(5.8\pm2.9)\times10^{-2}$	–	–	–	–	$(27.3\pm8.2)\times10^{-4}$	$(3.5\pm1.1)\times10^{-3}$
G251.880–01.060	$(21.9\pm4.7)\times10^{-3}$	$(5.5\pm1.1)\times10^{-2}$	$(5.2\pm1.1)\times10^{-2}$	$(25.3\pm5.6)\times10^{-3}$	–	–	–	–	–	$(12.8\pm3.9)\times10^{-5}$	–
G251.900–01.060	$(9.7\pm1.9)\times10^{-2}$	$(32.3\pm6.5)\times10^{-2}$	$(40.2\pm8.0)\times10^{-2}$	$(24.8\pm5.0)\times10^{-2}$	$(12.9\pm6.5)\times10^{-2}$	–	$(20.8\pm6.5)\times10^{-2}$	–	–	$(7.4\pm2.2)\times10^{-4}$	$(11.3\pm3.4)\times10^{-4}$
G251.900–01.080	$(40.9\pm8.2)\times10^{-2}$	$(12.4\pm2.5)\times10^{-1}$	$(12.6\pm2.5)\times10^{-1}$	$(8.3\pm1.7)\times10^{-1}$	$(2.6\pm1.3)\times10^{-1}$	–	–	–	–	$(4.2\pm1.3)\times10^{-3}$	$(6.6\pm2.0)\times10^{-2}$
G251.920–01.090	$(5.4\pm1.1)\times10^{-1}$	$(18.3\pm3.7)\times10^{-1}$	$(20.7\pm4.1)\times10^{-1}$	$(13.5\pm2.7)\times10^{-1}$	$(6.4\pm3.2)\times10^{-1}$	$(7.7\pm3.8)\times10^{-2}$	$(25.6\pm7.9)\times10^{-2}$	$(3.6\pm1.1)\times10^{-1}$	$(13.1\pm3.9)\times10^{-1}$	–	–
G251.990–01.230	$(25.0\pm5.0)\times10^{-2}$	$(6.5\pm1.3)\times10^{-1}$	$(8.3\pm1.7)\times10^{-1}$	$(5.3\pm1.1)\times10^{-1}$	$(2.2\pm1.1)\times10^{-1}$	$(2.7\pm1.4)\times10^{-2}$	–	–	–	$(3.8\pm1.2)\times10^{-3}$	$(7.2\pm2.2)\times10^{-3}$
G252.080–01.290	$(35.7\pm7.1)\times10^{-2}$	$(16.3\pm3.3)\times10^{-1}$	$(23.8\pm4.8)\times10^{-1}$	$(16.2\pm3.3)\times10^{-1}$	$(8.0\pm4.0)\times10^{-1}$	$(4.6\pm2.3)\times10^{-2}$	–	–	–	$(5.0\pm1.5)\times10^{-2}$	$(14.4\pm4.3)\times10^{-2}$
G252.080–01.810	–	$(45.6\pm9.1)\times10^{-1}$	$(9.0\pm1.8)\times10^{+0}$	$(6.7\pm1.3)\times10^{+0}$	$(3.3\pm1.7)\times10^{+0}$	–	–	–	$(6.9\pm2.1)\times10^{-1}$	$(17.8\pm5.4)\times10^{-3}$	$(27.1\pm8.1)\times10^{-3}$
G252.090–01.270	–	$(14.4\pm2.9)\times10^{-1}$	$(28.3\pm5.7)\times10^{-1}$	$(26.7\pm5.3)\times10^{-1}$	$(14.4\pm7.2)\times10^{-1}$	–	$(20.6\pm6.4)\times10^{-2}$	–	–	$(15.1\pm4.5)\times10^{-4}$	$(13.2\pm3.9)\times10^{-3}$
G252.100–01.220	–	$(30.6\pm6.1)\times10^{-2}$	$(9.2\pm1.8)\times10^{-1}$	$(6.4\pm1.3)\times10^{-1}$	$(2.7\pm1.4)\times10^{-1}$	–	–	–	$(9.8\pm2.9)\times10^{-1}$	$(10.8\pm3.3)\times10^{-4}$	$(3.7\pm1.1)\times10^{-3}$
G252.110–01.270	$(7.9\pm1.6)\times10^{-1}$	$(43.4\pm8.7)\times10^{-2}$	$(33.3\pm6.7)\times10^{-2}$	$(25.3\pm5.4)\times10^{-2}$	$(10.5\pm5.4)\times10^{-2}$	–	–	$(30.3\pm9.2)\times10^{-2}$	–	$(7.3\pm2.2)\times10^{-2}$	$(18.4\pm5.5)\times10^{-2}$

Table A.3: continued

Name	F_{70} (Jy)	F_{160} (Jy)	F_{250} (Jy)	F_{350} (Jy)	F_{500} (Jy)	F_{8} (Jy)	$F_{12.1}$ (Jy)	$F_{14.7}$ (Jy)	F_{21} (Jy)	F_{14} (Jy)	F_{22} (Jy)
G252.120–01.170	$(6.0\pm1.2)\times10^{-1}$	$(20.3\pm4.1)\times10^{-1}$	$(28.7\pm5.7)\times10^{-1}$	$(21.5\pm4.3)\times10^{-1}$	$(8.7\pm4.4)\times10^{-1}$	–	–	$(29.9\pm9.1)\times10^{-2}$	–	$(19.1\pm5.7)\times10^{-4}$	$(32.2\pm9.7)\times10^{-3}$
G252.133–01.175	$(16.3\pm3.3)\times10^{-1}$	$(31.5\pm6.3)\times10^{-1}$	$(25.0\pm5.0)\times10^{-1}$	$(16.0\pm3.2)\times10^{-1}$	$(6.5\pm6.5)\times10^{-1}$	$(3.7\pm1.9)\times10^{-2}$	–	–	–	$(4.4\pm1.3)\times10^{-2}$	$(20.6\pm6.2)\times10^{-2}$
G252.140–01.180	$(16.9\pm3.4)\times10^{-1}$	$(32.1\pm6.4)\times10^{-1}$	$(25.3\pm5.1)\times10^{-1}$	$(15.1\pm3.0)\times10^{-1}$	$(6.5\pm6.5)\times10^{-1}$	$(3.2\pm1.6)\times10^{-2}$	–	–	–	$(4.4\pm1.3)\times10^{-2}$	$(20.6\pm6.2)\times10^{-2}$
G252.180–01.080	$(18.4\pm3.7)\times10^{-2}$	$(27.6\pm5.5)\times10^{-2}$	$(30.5\pm6.1)\times10^{-2}$	$(18.4\pm3.7)\times10^{-2}$	$(8.4\pm4.2)\times10^{-2}$	$(2.2\pm1.1)\times10^{-2}$	$(16.0\pm5.0)\times10^{-2}$	$(17.4\pm5.4)\times10^{-2}$	–	–	–
G252.480–01.570	$(7.5\pm1.5)\times10^{+0}$	$(34.8\pm7.0)\times10^{+0}$	$(31.1\pm6.2)\times10^{+0}$	$(19.8\pm4.0)\times10^{+0}$	$(7.4\pm3.7)\times10^{+0}$	$(2.1\pm1.1)\times10^{-1}$	–	$(4.3\pm1.3)\times10^{-1}$	$(17.2\pm5.2)\times10^{-1}$	$(4.3\pm1.3)\times10^{-1}$	$(13.1\pm3.9)\times10^{-1}$
G252.510–01.440	$(9.4\pm1.9)\times10^{-2}$	$(7.0\pm1.4)\times10^{-1}$	$(5.2\pm1.0)\times10^{-1}$	$(23.9\pm4.8)\times10^{-2}$	$(6.0\pm6.0)\times10^{-2}$	$(5.2\pm2.6)\times10^{-2}$	–	$(23.4\pm7.2)\times10^{-2}$	–	$(23.8\pm7.1)\times10^{-3}$	$(4.1\pm1.2)\times10^{-3}$
G252.680–01.530	$(14.6\pm2.9)\times10^{-2}$	$(8.9\pm1.8)\times10^{-1}$	$(5.3\pm1.1)\times10^{-1}$	$(25.0\pm5.0)\times10^{-2}$	$(7.2\pm7.2)\times10^{-2}$	–	–	–	–	$(4.6\pm1.4)\times10^{-3}$	$(3.6\pm1.1)\times10^{-3}$
G252.700–01.490	–	$(5.2\pm1.0)\times10^{-1}$	$(36.7\pm7.3)\times10^{-2}$	$(15.2\pm3.1)\times10^{-2}$	$(5.3\pm5.3)\times10^{-2}$	–	–	$(4.3\pm1.3)\times10^{-1}$	$(6.5\pm2.0)\times10^{-1}$	$(6.7\pm2.0)\times10^{-3}$	$(6.5\pm2.0)\times10^{-3}$
G252.840–00.470	–	$(24.1\pm4.8)\times10^{-2}$	$(26.7\pm5.4)\times10^{-2}$	$(14.4\pm2.9)\times10^{-2}$	$(8.2\pm4.1)\times10^{-2}$	–	$(5.7\pm1.7)\times10^{-1}$	$(15.3\pm4.8)\times10^{-2}$	–	–	$(24.3\pm7.3)\times10^{-4}$
G252.850–00.730	–	$(15.6\pm3.1)\times10^{-2}$	$(23.5\pm4.7)\times10^{-2}$	$(16.4\pm3.3)\times10^{-2}$	$(8.6\pm4.3)\times10^{-2}$	$(3.4\pm1.7)\times10^{-2}$	–	$(24.5\pm7.5)\times10^{-2}$	–	$(8.0\pm2.4)\times10^{-3}$	$(7.3\pm2.2)\times10^{-3}$
G253.030–01.990	–	$(8.1\pm1.6)\times10^{-1}$	$(5.5\pm1.1)\times10^{-1}$	$(30.2\pm6.2)\times10^{-2}$	$(5.9\pm3.0)\times10^{-2}$	–	–	$(4.3\pm1.3)\times10^{-1}$	–	–	$(24.5\pm7.4)\times10^{-4}$
G253.080–02.100	$(30.7\pm6.5)\times10^{-3}$	$(25.2\pm5.0)\times10^{-2}$	$(35.1\pm7.0)\times10^{-2}$	$(20.6\pm4.2)\times10^{-2}$	$(6.7\pm3.4)\times10^{-2}$	–	$(3.8\pm1.1)\times10^{-1}$	–	–	$(4.1\pm1.2)\times10^{-3}$	$(30.9\pm9.3)\times10^{-4}$
G253.100–01.350	–	$(26.0\pm5.2)\times10^{-1}$	$(38.6\pm7.7)\times10^{-1}$	$(26.4\pm5.3)\times10^{-1}$	$(11.0\pm5.5)\times10^{-1}$	–	–	–	–	$(5.6\pm1.7)\times10^{-3}$	$(5.5\pm1.6)\times10^{-3}$
G253.110–01.800	$(16.0\pm3.2)\times10^{-2}$	$(9.2\pm1.8)\times10^{-1}$	$(8.6\pm1.7)\times10^{-1}$	$(37.4\pm7.5)\times10^{-2}$	$(1.3\pm1.3)\times10^{-1}$	–	–	–	–	–	$(10.1\pm3.0)\times10^{-4}$
G253.110–02.120	$(23.9\pm4.8)\times10^{-2}$	$(21.5\pm4.3)\times10^{-1}$	$(26.0\pm5.2)\times10^{-1}$	$(16.3\pm3.3)\times10^{-1}$	$(6.2\pm3.1)\times10^{-1}$	–	–	–	–	$(18.2\pm5.5)\times10^{-4}$	$(7.4\pm2.2)\times10^{-3}$
G253.110–02.150	$(9.7\pm2.0)\times10^{-2}$	$(7.4\pm1.5)\times10^{-1}$	$(44.0\pm8.8)\times10^{-2}$	$(20.8\pm4.2)\times10^{-2}$	$(2.1\pm1.0)\times10^{-1}$	$(6.4\pm3.2)\times10^{-2}$	–	–	$(23.0\pm6.9)\times10^{-1}$	$(15.8\pm4.7)\times10^{-3}$	$(8.9\pm2.7)\times10^{-3}$
G253.120–02.060	–	$(13.7\pm2.8)\times10^{-2}$	$(23.6\pm4.7)\times10^{-2}$	$(13.7\pm2.9)\times10^{-2}$	$(4.6\pm4.6)\times10^{-2}$	$(3.3\pm1.7)\times10^{-2}$	–	$(5.3\pm1.6)\times10^{-1}$	$(5.2\pm1.6)\times10^{-1}$	$(32.7\pm9.8)\times10^{-4}$	$(11.8\pm3.5)\times10^{-4}$
G253.160–01.960	$(11.0\pm2.2)\times10^{-2}$	$(46.4\pm9.3)\times10^{-2}$	$(32.6\pm6.5)\times10^{-2}$	$(15.1\pm3.1)\times10^{-2}$	–	–	–	–	$(5.7\pm1.7)\times10^{-1}$	$(10.1\pm3.0)\times10^{-3}$	$(16.3\pm4.9)\times10^{-3}$
G253.230–01.350	$(20.6\pm4.6)\times10^{-3}$	$(23.5\pm4.7)\times10^{-2}$	$(19.0\pm3.8)\times10^{-2}$	$(12.4\pm2.5)\times10^{-2}$	$(3.4\pm1.7)\times10^{-2}$	–	–	–	$(5.9\pm1.8)\times10^{-1}$	$(12.9\pm3.9)\times10^{-3}$	$(18.9\pm5.7)\times10^{-3}$
G253.270–01.110	$(30.9\pm6.2)\times10^{-2}$	$(8.2\pm1.6)\times10^{-1}$	$(10.2\pm2.0)\times10^{-1}$	$(5.3\pm1.1)\times10^{-1}$	$(2.5\pm1.3)\times10^{-1}$	–	$(25.9\pm7.9)\times10^{-2}$	–	$(5.9\pm1.8)\times10^{-1}$	$(19.6\pm5.9)\times10^{-3}$	$(24.4\pm7.3)\times10^{-3}$
G253.290–01.010	$(6.2\pm1.3)\times10^{-2}$	$(22.8\pm4.6)\times10^{-2}$	$(19.8\pm4.0)\times10^{-2}$	$(10.7\pm2.3)\times10^{-2}$	–	$(18.2\pm9.2)\times10^{-3}$	–	–	$(4.1\pm1.3)\times10^{-1}$	$(3.3\pm1.0)\times10^{-2}$	$(8.5\pm2.5)\times10^{-3}$
G253.290–01.610	$(21.0\pm4.2)\times10^{+0}$	$(47.0\pm9.4)\times10^{+0}$	$(33.8\pm6.8)\times10^{+0}$	$(19.3\pm3.9)\times10^{+0}$	$(6.7\pm3.4)\times10^{+0}$	$(4.0\pm2.0)\times10^{-1}$	$(6.6\pm2.0)\times10^{-1}$	$(14.0\pm4.2)\times10^{-1}$	$(17.6\pm5.3)\times10^{-1}$	$(7.8\pm2.3)\times10^{-1}$	$(25.9\pm7.8)\times10^{-1}$
G253.300–01.080	$(22.1\pm4.4)\times10^{-2}$	$(14.7\pm2.9)\times10^{-1}$	$(19.7\pm3.9)\times10^{-1}$	$(11.9\pm2.4)\times10^{-1}$	$(4.6\pm2.3)\times10^{-1}$	–	–	–	–	$(14.5\pm4.4)\times10^{-2}$	$(6.9\pm2.1)\times10^{-2}$
G253.400–01.400	$(12.9\pm2.6)\times10^{+1}$	$(13.5\pm2.7)\times10^{+1}$	$(5.5\pm1.1)\times10^{+1}$	$(20.8\pm4.2)\times10^{+0}$	$(6.2\pm6.2)\times10^{+0}$	$(13.9\pm6.9)\times10^{-1}$	$(17.4\pm5.2)\times10^{-1}$	$(20.0\pm6.0)\times10^{-1}$	$(4.8\pm1.4)\times10^{+0}$	$(32.8\pm9.9)\times10^{-1}$	$(8.4\pm2.5)\times10^{+0}$
G253.400–01.420	$(17.2\pm3.4)\times10^{-1}$	$(39.7\pm7.9)\times10^{-1}$	$(33.6\pm6.7)\times10^{-1}$	$(21.5\pm4.3)\times10^{-1}$	$(9.0\pm9.0)\times10^{-1}$	$(5.6\pm2.8)\times10^{-2}$	–	–	–	$(17.9\pm5.4)\times10^{-2}$	$(3.8\pm1.1)\times10^{-1}$
G253.420–01.400	$(43.3\pm8.7)\times10^{-1}$	$(6.8\pm1.4)\times10^{+0}$	$(5.1\pm1.0)\times10^{+0}$	$(35.0\pm7.0)\times10^{-1}$	$(1.2\pm1.2)\times10^{+0}$	$(7.3\pm3.7)\times10^{-1}$	$(10.6\pm3.2)\times10^{-1}$	$(9.8\pm2.9)\times10^{-1}$	$(6.0\pm1.8)\times10^{-1}$	$(14.5\pm4.4)\times10^{-1}$	$(18.9\pm5.7)\times10^{-1}$
G253.430–01.370	$(8.7\pm1.7)\times10^{+0}$	$(9.2\pm1.8)\times10^{+0}$	$(5.3\pm1.1)\times10^{+0}$	$(29.5\pm5.9)\times10^{-1}$	$(1.1\pm1.1)\times10^{+0}$	$(3.5\pm1.8)\times10^{-1}$	$(3.4\pm1.0)\times10^{-1}$	$(9.1\pm2.7)\times10^{-1}$	$(16.7\pm5.0)\times10^{-1}$	$(7.3\pm2.2)\times10^{-1}$	$(17.4\pm5.2)\times10^{-1}$
G253.450–01.370	$(13.5\pm2.7)\times10^{+0}$	$(27.9\pm5.6)\times10^{+0}$	$(16.3\pm3.3)\times10^{+0}$	$(8.8\pm1.8)\times10^{+0}$	$(2.9\pm2.9)\times10^{+0}$	$(16.4\pm8.2)\times10^{-2}$	$(4.0\pm1.2)\times10^{-1}$	$(4.5\pm1.4)\times10^{-1}$	$(6.2\pm1.9)\times10^{-1}$	$(26.9\pm8.1)\times10^{-2}$	$(8.0\pm2.4)\times10^{-1}$
G253.460–01.410	$(23.2\pm4.6)\times10^{-2}$	$(5.1\pm1.0)\times10^{-1}$	$(42.9\pm8.6)\times10^{-2}$	$(47.7\pm9.6)\times10^{-2}$	$(2.5\pm1.3)\times10^{-1}$	–	–	$(14.6\pm4.4)\times10^{-1}$	$(6.7\pm2.0)\times10^{-1}$	$(4.5\pm1.4)\times10^{-4}$	$(13.4\pm4.0)\times10^{-3}$
G253.470–01.420	–	$(28.4\pm5.7)\times10^{-2}$	$(36.4\pm7.3)\times10^{-2}$	$(30.0\pm6.1)\times10^{-2}$	$(10.3\pm5.2)\times10^{-2}$	–	$(28.3\pm8.7)\times10^{-2}$	–	–	–	–
G253.480–01.290	$(44.9\pm9.2)\times10^{-3}$	$(20.8\pm4.2)\times10^{-2}$	$(40.0\pm8.0)\times10^{-2}$	$(22.9\pm4.8)\times10^{-2}$	$(9.9\pm5.1)\times10^{-2}$	$(4.8\pm2.4)\times10^{-2}$	$(19.2\pm6.0)\times10^{-2}$	–	–	$(5.5\pm1.6)\times10^{-4}$	–
G253.480–01.370	–	$(6.6\pm1.3)\times10^{-1}$	$(15.1\pm3.0)\times10^{-1}$	$(11.6\pm2.3)\times10^{-1}$	$(6.3\pm3.2)\times10^{-1}$	–	–	–	$(5.3\pm1.6)\times10^{-1}$	–	–
G253.503–01.237	$(12.1\pm2.4)\times10^{-1}$	$(9.2\pm1.8)\times10^{+0}$	$(10.9\pm2.2)\times10^{+0}$	$(6.8\pm1.4)\times10^{+0}$	$(3.2\pm1.6)\times10^{+0}$	–	–	$(22.1\pm6.8)\times10^{-2}$	–	–	$(9.0\pm2.7)\times10^{-2}$
G253.510–01.240	$(13.4\pm2.7)\times10^{-1}$	$(10.0\pm2.0)\times10^{+0}$	$(12.5\pm2.5)\times10^{+0}$	$(8.5\pm1.7)\times10^{+0}$	$(3.4\pm1.7)\times10^{+0}$	–	–	$(7.7\pm2.3)\times10^{-1}$	$(4.6\pm1.4)\times10^{-1}$	$(10.2\pm3.1)\times10^{-3}$	$(9.5\pm2.9)\times10^{-2}$
G253.510–01.260	$(5.7\pm1.1)\times10^{+0}$	$(10.9\pm2.2)\times10^{+0}$	$(7.8\pm1.6)\times10^{+0}$	$(42.4\pm8.5)\times10^{-1}$	$(16.1\pm8.1)\times10^{-1}$	$(10.9\pm5.5)\times10^{-2}$	–	–	–	$(22.4\pm6.7)\times10^{-2}$	$(6.8\pm2.0)\times10^{-1}$
G253.520–01.370	$(15.1\pm3.0)\times10^{-2}$	$(45.4\pm9.1)\times10^{-2}$	$(5.3\pm1.1)\times10^{-1}$	$(28.8\pm5.8)\times10^{-2}$	$(7.0\pm3.6)\times10^{-2}$	–	–	–	$(9.4\pm2.8)\times10^{-1}$	–	–
G253.530–00.420	$(37.1\pm7.4)\times10^{-1}$	$(11.4\pm2.3)\times10^{+0}$	$(9.0\pm1.8)\times10^{+0}$	$(46.6\pm9.3)\times10^{-1}$	$(16.4\pm8.2)\times10^{-1}$	$(14.0\pm7.0)\times10^{-2}$	$(4.6\pm1.4)\times10^{-1}$	$(4.8\pm1.4)\times10^{-1}$	$(11.3\pm3.4)\times10^{-1}$	$(19.9\pm6.0)\times10^{-2}$	$(5.8\pm1.7)\times10^{-1}$
G253.630–01.440	$(17.8\pm3.6)\times10^{-2}$	$(10.4\pm2.1)\times10^{-1}$	$(6.8\pm1.4)\times10^{-1}$	$(36.6\pm7.4)\times10^{-2}$	$(1.3\pm1.3)\times10^{-1}$	–	–	–	$(5.2\pm1.6)\times10^{-1}$	$(11.3\pm3.4)\times10^{-3}$	$(15.4\pm4.6)\times10^{-3}$
G253.770–01.300	$(39.4\pm7.9)\times10^{-2}$	$(5.5\pm1.1)\times10^{-1}$	$(40.7\pm8.2)\times10^{-2}$	$(20.6\pm4.3)\times10^{-2}$	$(7.1\pm7.1)\times10^{-2}$	–	$(26.2\pm8.0)\times10^{-2}$	–	$(6.9\pm2.1)\times10^{-1}$	$(12.1\pm3.6)\times10^{-3}$	$(13.0\pm3.9)\times10^{-3}$
G253.860–01.230	$(37.9\pm7.6)\times10^{-2}$	$(21.4\pm4.3)\times10^{-1}$	$(14.9\pm3.0)\times10^{-1}$	$(7.5\pm1.5)\times10^{-1}$	$(3.1\pm1.5)\times10^{-1}$	–	$(4.2\pm1.3)\times10^{-1}$	–	–	$(3.7\pm1.1)\times10^{-2}$	$(5.2\pm1.6)\times10^{-2}$
G253.870–01.200	$(15.2\pm3.0)\times10^{-2}$	$(14.5\pm2.9)\times10^{-1}$	$(19.2\pm3.8)\times10^{-1}$	$(12.8\pm2.6)\times10^{-1}$	$(5.6\pm2.8)\times10^{-1}$	–	–	–	$(4.0\pm1.2)\times10^{-1}$	–	$(14.6\pm4.4)\times10^{-3}$
G253.870–01.210	$(35.2\pm7.0)\times10^{-1}$	$(18.1\pm3.6)\times10^{+0}$	$(15.6\pm3.1)\times10^{+0}$	$(9.0\pm1.8)\times10^{+0}$	$(3.6\pm1.8)\times10^{+0}$	$(9.0\pm4.5)\times10^{-2}$	$(7.4\pm2.2)\times10^{-1}$	–	$(12.9\pm3.9)\times10^{-1}$	$(21.2\pm6.4)\times10^{-2}$	$(3.8\pm1.1)\times10^{-1}$
G253.880–01.540	–	$(11.5\pm2.3)\times10^{-1}$	$(10.2\pm2.0)\times10^{-1}$	$(48.1\pm9.7)\times10^{-2}$	$(2.2\pm1.1)\times10^{-1}$	$(3.3\pm1.7)\times10^{-2}$	$(10.9\pm3.3)\times10^{-1}$	–	–	$(14.9\pm4.5)\times10^{-3}$	$(10.8\pm3.2)\times10^{-3}$

Table A.3: continued

Name	F_{70} (Jy)	F_{160} (Jy)	F_{250} (Jy)	F_{350} (Jy)	F_{500} (Jy)	F_{8} (Jy)	$F_{12.1}$ (Jy)	$F_{14.7}$ (Jy)	F_{21} (Jy)	F_{14} (Jy)	F_{22} (Jy)
G253.890–00.470	$(12.7\pm2.5)\times10^{-1}$	$(5.1\pm1.0)\times10^{+0}$	$(44.1\pm8.8)\times10^{-1}$	$(29.6\pm5.9)\times10^{-1}$	$(1.2\pm1.2)\times10^{+0}$	–	$(21.9\pm6.8)\times10^{-2}$	$(30.0\pm9.1)\times10^{-2}$	$(4.2\pm1.3)\times10^{-1}$	$(6.0\pm1.8)\times10^{-4}$	$(9.2\pm2.8)\times10^{-3}$
G253.980–00.720	$(41.7\pm8.3)\times10^{-1}$	$(15.5\pm3.1)\times10^{+0}$	$(12.5\pm2.5)\times10^{+0}$	$(7.0\pm1.4)\times10^{+0}$	$(3.0\pm1.5)\times10^{+0}$	$(8.1\pm4.1)\times10^{-2}$	–	–	–	$(28.9\pm8.7)\times10^{-2}$	$(28.2\pm8.5)\times10^{-2}$
G254.052–00.566	$(9.0\pm1.8)\times10^{+1}$	$(10.8\pm2.2)\times10^{+1}$	$(5.0\pm1.0)\times10^{+1}$	$(19.9\pm4.0)\times10^{+0}$	$(6.9\pm3.4)\times10^{+0}$	$(13.6\pm6.8)\times10^{-1}$	$(24.0\pm7.2)\times10^{-1}$	$(3.4\pm1.0)\times10^{+0}$	$(14.5\pm4.4)\times10^{+0}$	$(28.7\pm8.6)\times10^{-1}$	$(13.6\pm4.1)\times10^{+0}$
G254.120–01.420	$(48.8\pm9.8)\times10^{-2}$	$(46.3\pm9.3)\times10^{-2}$	$(8.7\pm1.7)\times10^{-1}$	$(5.7\pm1.1)\times10^{-1}$	$(2.9\pm1.5)\times10^{-1}$	$(18.2\pm9.1)\times10^{-1}$	$(8.7\pm2.6)\times10^{-1}$	–	$(4.4\pm1.4)\times10^{-1}$	$(12.5\pm3.7)\times10^{-1}$	$(32.2\pm9.6)\times10^{-2}$
G254.232–00.136	$(19.5\pm3.9)\times10^{+0}$	$(30.8\pm6.2)\times10^{+0}$	$(15.6\pm3.1)\times10^{+0}$	$(6.4\pm1.3)\times10^{+0}$	$(2.0\pm1.0)\times10^{+0}$	$(6.1\pm3.0)\times10^{-1}$	$(11.8\pm3.5)\times10^{-1}$	–	$(8.4\pm2.5)\times10^{-1}$	$(8.7\pm2.6)\times10^{-1}$	$(9.7\pm2.9)\times10^{-1}$
G254.230–02.320	$(12.4\pm2.5)\times10^{-2}$	$(12.3\pm2.5)\times10^{-2}$	$(28.4\pm5.7)\times10^{-2}$	$(19.3\pm4.0)\times10^{-2}$	$(5.2\pm5.2)\times10^{-2}$	–	–	–	–	–	$(5.3\pm1.6)\times10^{-3}$
G254.390–01.010	–	$(13.8\pm2.8)\times10^{-2}$	$(18.8\pm3.8)\times10^{-2}$	$(16.7\pm3.4)\times10^{-2}$	$(4.1\pm4.1)\times10^{-2}$	–	–	–	–	$(4.6\pm1.4)\times10^{-3}$	$(24.8\pm7.4)\times10^{-4}$
G254.590–01.060	$(14.1\pm2.8)\times10^{-2}$	$(31.9\pm6.4)\times10^{-2}$	$(21.8\pm4.4)\times10^{-2}$	$(16.0\pm3.2)\times10^{-2}$	$(6.1\pm3.1)\times10^{-2}$	–	$(5.6\pm1.7)\times10^{-1}$	–	–	$(30.6\pm9.2)\times10^{-4}$	$(4.0\pm1.2)\times10^{-3}$
G254.660–01.250	$(8.5\pm1.7)\times10^{-2}$	$(12.4\pm2.5)\times10^{-1}$	$(13.4\pm2.7)\times10^{-1}$	$(8.4\pm1.7)\times10^{-1}$	$(3.1\pm1.5)\times10^{-1}$	$(8.7\pm4.3)\times10^{-2}$	–	$(22.2\pm6.8)\times10^{-2}$	–	$(3.5\pm1.1)\times10^{-3}$	–
G254.680–01.890	$(6.2\pm1.3)\times10^{-2}$	$(35.3\pm7.1)\times10^{-2}$	$(40.7\pm8.2)\times10^{-2}$	$(21.6\pm4.3)\times10^{-2}$	$(5.7\pm2.9)\times10^{-2}$	$(2.2\pm1.1)\times10^{-2}$	–	$(22.1\pm6.8)\times10^{-2}$	–	–	–
G254.760–01.240	$(6.5\pm1.3)\times10^{-2}$	$(12.1\pm2.4)\times10^{-1}$	$(18.3\pm3.7)\times10^{-1}$	$(11.7\pm2.3)\times10^{-1}$	$(4.5\pm2.2)\times10^{-1}$	–	–	$(5.4\pm1.6)\times10^{-1}$	$(7.1\pm2.2)\times10^{-1}$	$(29.5\pm8.9)\times10^{-4}$	–
G255.100–00.090	–	$(19.5\pm3.9)\times10^{-2}$	$(40.4\pm8.1)\times10^{-2}$	$(28.0\pm5.7)\times10^{-2}$	$(1.3\pm1.3)\times10^{-1}$	$(17.1\pm8.7)\times10^{-3}$	–	–	–	$(14.9\pm4.5)\times10^{-3}$	$(25.3\pm7.6)\times10^{-3}$
G255.170–00.570	$(5.4\pm1.1)\times10^{+0}$	$(8.5\pm1.7)\times10^{+0}$	$(35.9\pm7.2)\times10^{-1}$	$(14.3\pm2.9)\times10^{-1}$	$(4.1\pm4.1)\times10^{-1}$	$(2.5\pm1.2)\times10^{-1}$	$(4.6\pm1.4)\times10^{-1}$	$(28.4\pm8.6)\times10^{-2}$	$(7.6\pm2.3)\times10^{-1}$	$(4.5\pm1.3)\times10^{-1}$	$(31.5\pm9.4)\times10^{-2}$
G255.190–02.280	–	$(29.3\pm5.9)\times10^{-2}$	$(34.9\pm7.0)\times10^{-2}$	$(18.8\pm3.8)\times10^{-2}$	$(9.2\pm4.6)\times10^{-2}$	–	$(13.4\pm4.0)\times10^{-1}$	–	$(12.4\pm3.7)\times10^{-1}$	$(4.0\pm1.2)\times10^{-3}$	$(30.6\pm9.2)\times10^{-4}$
G255.200–02.290	–	$(17.9\pm3.6)\times10^{-2}$	$(23.0\pm4.6)\times10^{-2}$	$(9.8\pm2.0)\times10^{-2}$	$(4.9\pm2.5)\times10^{-2}$	–	$(6.9\pm2.1)\times10^{-1}$	$(5.5\pm1.7)\times10^{-1}$	$(15.7\pm4.7)\times10^{-1}$	$(9.0\pm2.7)\times10^{-3}$	$(4.4\pm1.3)\times10^{-3}$
G255.210–02.290	–	$(43.9\pm8.8)\times10^{-2}$	$(46.1\pm9.2)\times10^{-2}$	$(21.8\pm4.4)\times10^{-2}$	$(8.1\pm4.1)\times10^{-2}$	–	$(3.8\pm1.2)\times10^{-1}$	–	$(10.3\pm3.1)\times10^{-1}$	$(12.9\pm3.9)\times10^{-3}$	$(8.6\pm2.6)\times10^{-3}$
G255.401–00.918	$(16.9\pm3.4)\times10^{-2}$	$(12.6\pm2.5)\times10^{-1}$	$(18.1\pm3.6)\times10^{-1}$	$(15.9\pm3.2)\times10^{-1}$	$(9.1\pm4.6)\times10^{-1}$	–	–	$(3.3\pm1.0)\times10^{-1}$	–	$(15.0\pm4.5)\times10^{-3}$	$(24.1\pm7.2)\times10^{-3}$
G256.130–01.470	$(13.4\pm2.7)\times10^{+0}$	$(12.8\pm2.6)\times10^{+0}$	$(5.6\pm1.1)\times10^{+0}$	$(24.3\pm4.9)\times10^{-1}$	$(7.5\pm7.5)\times10^{-1}$	$(2.6\pm1.3)\times10^{-1}$	$(3.7\pm1.1)\times10^{-1}$	$(4.5\pm1.4)\times10^{-1}$	$(5.3\pm1.6)\times10^{-1}$	$(3.8\pm1.2)\times10^{-1}$	$(10.2\pm3.0)\times10^{-1}$
G256.150–01.370	$(33.5\pm6.7)\times10^{-1}$	$(7.2\pm1.4)\times10^{+0}$	$(38.6\pm7.7)\times10^{-1}$	$(18.6\pm3.7)\times10^{-1}$	$(4.9\pm4.9)\times10^{-1}$	$(2.5\pm1.3)\times10^{-2}$	–	–	–	$(15.5\pm4.7)\times10^{-2}$	$(26.8\pm8.0)\times10^{-2}$
G256.150–01.380	$(33.5\pm6.7)\times10^{-1}$	$(7.2\pm1.4)\times10^{+0}$	$(38.6\pm7.7)\times10^{-1}$	$(18.6\pm3.7)\times10^{-1}$	$(4.9\pm4.9)\times10^{-1}$	$(2.5\pm1.3)\times10^{-2}$	–	–	–	$(15.5\pm4.7)\times10^{-2}$	$(26.8\pm8.0)\times10^{-2}$
G256.190–01.540	$(31.4\pm6.3)\times10^{+0}$	$(28.2\pm5.6)\times10^{+0}$	$(8.8\pm1.8)\times10^{+0}$	$(29.0\pm5.8)\times10^{-1}$	$(6.2\pm6.2)\times10^{-1}$	$(5.4\pm2.7)\times10^{-1}$	$(7.1\pm2.1)\times10^{-1}$	$(27.5\pm8.4)\times10^{-2}$	–	$(9.2\pm2.8)\times10^{-1}$	$(7.3\pm2.2)\times10^{-1}$
G256.187–01.547	$(32.5\pm6.5)\times10^{+0}$	$(29.7\pm5.9)\times10^{+0}$	$(9.4\pm1.9)\times10^{+0}$	$(30.2\pm6.0)\times10^{-1}$	$(7.3\pm7.3)\times10^{-1}$	$(6.2\pm3.1)\times10^{-1}$	$(5.9\pm1.8)\times10^{-1}$	$(3.6\pm1.1)\times10^{-1}$	–	$(9.8\pm2.9)\times10^{-1}$	$(7.8\pm2.3)\times10^{-1}$
G256.430–01.630	–	$(10.4\pm2.1)\times10^{-2}$	$(13.3\pm2.7)\times10^{-2}$	$(4.9\pm1.0)\times10^{-2}$	–	$(8.9\pm4.5)\times10^{-2}$	$(5.7\pm1.7)\times10^{-1}$	$(3.6\pm1.1)\times10^{-1}$	–	$(21.5\pm6.5)\times10^{-4}$	$(15.7\pm4.7)\times10^{-4}$
G256.430–01.640	–	$(23.0\pm4.6)\times10^{-2}$	$(39.5\pm7.9)\times10^{-2}$	$(24.8\pm5.0)\times10^{-2}$	$(9.8\pm4.9)\times10^{-2}$	$(6.2\pm3.1)\times10^{-2}$	–	$(7.5\pm2.3)\times10^{-1}$	$(11.2\pm3.4)\times10^{-1}$	$(10.0\pm3.0)\times10^{-3}$	$(7.6\pm2.3)\times10^{-3}$
G256.440–01.610	$(15.6\pm3.1)\times10^{-2}$	$(7.1\pm1.4)\times10^{-1}$	$(5.9\pm1.2)\times10^{-1}$	$(39.4\pm7.9)\times10^{-2}$	$(15.6\pm7.8)\times10^{-2}$	–	–	–	$(8.7\pm2.6)\times10^{-1}$	$(22.5\pm6.8)\times10^{-3}$	$(20.8\pm6.2)\times10^{-3}$
G256.450–01.608	$(11.5\pm2.3)\times10^{-1}$	$(22.3\pm4.5)\times10^{-1}$	$(15.8\pm3.2)\times10^{-1}$	$(8.7\pm1.7)\times10^{-1}$	$(3.2\pm3.2)\times10^{-1}$	$(4.5\pm2.2)\times10^{-2}$	–	–	–	$(5.8\pm1.8)\times10^{-2}$	$(10.8\pm3.2)\times10^{-2}$
G256.620–00.050	–	$(20.9\pm4.2)\times10^{-2}$	$(39.4\pm7.9)\times10^{-2}$	$(28.8\pm5.8)\times10^{-2}$	$(1.4\pm1.4)\times10^{-1}$	–	$(4.5\pm1.4)\times10^{-1}$	$(14.9\pm4.7)\times10^{-2}$	–	$(23.0\pm6.9)\times10^{-4}$	–
G256.682–01.627	–	$(5.1\pm1.0)\times10^{-1}$	$(8.1\pm1.6)\times10^{-1}$	$(5.7\pm1.1)\times10^{-1}$	$(2.7\pm1.3)\times10^{-1}$	–	–	–	–	$(7.8\pm2.4)\times10^{-3}$	$(3.8\pm1.2)\times10^{-3}$
G256.690–00.040	–	$(8.4\pm1.7)\times10^{-1}$	$(7.5\pm1.5)\times10^{-1}$	$(6.8\pm1.4)\times10^{-1}$	$(2.4\pm1.2)\times10^{-1}$	–	–	–	–	–	$(5.7\pm1.7)\times10^{-3}$
G256.720–01.930	$(6.2\pm1.2)\times10^{+0}$	$(8.2\pm1.6)\times10^{+0}$	$(5.1\pm1.0)\times10^{+0}$	$(26.9\pm5.4)\times10^{-1}$	$(1.0\pm1.0)\times10^{+0}$	$(5.3\pm2.6)\times10^{-1}$	$(4.7\pm1.4)\times10^{-1}$	$(9.1\pm2.7)\times10^{-1}$	$(8.9\pm2.7)\times10^{-1}$	$(9.2\pm2.8)\times10^{-1}$	$(14.7\pm4.4)\times10^{-1}$
G256.730–01.670	$(9.6\pm1.9)\times10^{-2}$	$(5.7\pm1.1)\times10^{-1}$	$(6.4\pm1.3)\times10^{-1}$	$(40.8\pm8.2)\times10^{-2}$	$(15.2\pm7.6)\times10^{-2}$	–	–	–	$(10.9\pm3.3)\times10^{-1}$	–	–
G256.740–01.580	–	$(17.8\pm3.6)\times10^{-1}$	$(16.9\pm3.4)\times10^{-1}$	$(9.1\pm1.8)\times10^{-1}$	$(3.7\pm1.9)\times10^{-1}$	–	–	$(5.0\pm1.5)\times10^{-1}$	–	$(25.8\pm7.7)\times10^{-3}$	$(16.3\pm4.9)\times10^{-3}$
G256.750–00.060	–	$(24.0\pm4.8)\times10^{-2}$	$(33.0\pm6.6)\times10^{-2}$	$(30.7\pm6.2)\times10^{-2}$	$(15.4\pm7.8)\times10^{-2}$	–	–	$(22.6\pm6.9)\times10^{-2}$	$(3.6\pm1.1)\times10^{-1}$	$(9.0\pm2.7)\times10^{-3}$	$(19.0\pm5.7)\times10^{-3}$
G256.780–00.130	$(39.3\pm7.9)\times10^{-2}$	$(11.9\pm2.4)\times10^{-1}$	$(12.1\pm2.4)\times10^{-1}$	$(7.2\pm1.5)\times10^{-1}$	$(3.3\pm1.6)\times10^{-1}$	–	–	–	–	$(21.9\pm6.6)\times10^{-3}$	$(4.5\pm1.4)\times10^{-2}$
G256.780–02.070	$(5.0\pm1.0)\times10^{-2}$	$(39.0\pm7.8)\times10^{-2}$	$(31.3\pm6.3)\times10^{-2}$	$(18.7\pm3.8)\times10^{-2}$	$(8.6\pm4.3)\times10^{-2}$	$(6.2\pm3.1)\times10^{-2}$	–	–	–	$(11.3\pm3.4)\times10^{-4}$	–
G256.910–00.280	$(21.1\pm4.2)\times10^{-2}$	$(14.2\pm2.8)\times10^{-1}$	$(20.9\pm4.2)\times10^{-1}$	$(15.0\pm3.0)\times10^{-1}$	$(7.0\pm3.5)\times10^{-1}$	–	$(7.1\pm2.1)\times10^{-1}$	$(4.6\pm1.4)\times10^{-1}$	–	$(13.4\pm4.0)\times10^{-3}$	$(3.9\pm1.2)\times10^{-2}$
G256.920–01.830	$(6.7\pm1.4)\times10^{-2}$	$(5.8\pm1.2)\times10^{-1}$	$(26.7\pm5.4)\times10^{-2}$	$(11.5\pm2.4)\times10^{-2}$	–	–	–	$(25.8\pm7.9)\times10^{-2}$	$(14.1\pm4.2)\times10^{-1}$	$(6.2\pm1.9)\times10^{-3}$	$(21.0\pm6.3)\times10^{-4}$
G256.950–00.530	$(38.7\pm8.0)\times10^{-3}$	$(38.5\pm7.7)\times10^{-2}$	$(5.4\pm1.1)\times10^{-1}$	$(43.1\pm8.6)\times10^{-2}$	$(2.4\pm1.2)\times10^{-1}$	–	–	–	–	$(6.2\pm1.9)\times10^{-3}$	$(4.4\pm1.3)\times10^{-3}$
G256.990–00.570	$(28.0\pm5.9)\times10^{-3}$	$(33.7\pm6.8)\times10^{-2}$	$(33.9\pm6.8)\times10^{-2}$	$(22.1\pm4.4)\times10^{-2}$	$(8.0\pm4.0)\times10^{-2}$	–	–	–	$(6.8\pm2.1)\times10^{-1}$	$(6.4\pm1.9)\times10^{-4}$	$(30.7\pm9.2)\times10^{-4}$
G256.990–02.130	$(10.0\pm2.0)\times10^{-2}$	$(22.4\pm4.5)\times10^{-2}$	$(14.6\pm2.9)\times10^{-2}$	$(8.6\pm1.8)\times10^{-2}$	$(3.2\pm3.2)\times10^{-2}$	–	$(25.9\pm8.1)\times10^{-2}$	$(3.7\pm1.1)\times10^{-1}$	–	$(25.8\pm7.7)\times10^{-4}$	$(6.5\pm2.0)\times10^{-4}$
G257.010+00.000	$(8.8\pm1.8)\times10^{-2}$	$(25.2\pm5.0)\times10^{-2}$	$(27.3\pm5.5)\times10^{-2}$	$(16.5\pm3.3)\times10^{-2}$	$(6.9\pm6.9)\times10^{-2}$	$(19.5\pm9.9)\times10^{-3}$	–	–	$(5.6\pm1.7)\times10^{-1}$	$(7.7\pm2.3)\times10^{-3}$	$(15.2\pm4.6)\times10^{-3}$
G257.060–02.080	$(10.3\pm2.1)\times10^{-2}$	$(47.3\pm9.5)\times10^{-2}$	$(22.7\pm4.5)\times10^{-2}$	$(11.1\pm2.2)\times10^{-2}$	$(2.8\pm1.4)\times10^{-2}$	–	$(4.2\pm1.3)\times10^{-1}$	–	–	–	$(25.3\pm7.6)\times10^{-4}$
G257.227–00.902	$(19.6\pm4.4)\times10^{-3}$	$(28.4\pm5.7)\times10^{-1}$	$(28.2\pm5.6)\times10^{-1}$	$(16.4\pm3.3)\times10^{-1}$	$(7.1\pm3.6)\times10^{-1}$	$(2.4\pm1.2)\times10^{-1}$	–	$(11.5\pm3.4)\times10^{-1}$	–	$(22.4\pm6.7)\times10^{-2}$	$(6.3\pm1.9)\times10^{-2}$

Table A.3: continued

Name	F_{70} (Jy)	F_{160} (Jy)	F_{250} (Jy)	F_{350} (Jy)	F_{500} (Jy)	F_{8} (Jy)	$F_{12.1}$ (Jy)	$F_{14.7}$ (Jy)	F_{21} (Jy)	F_{14} (Jy)	F_{22} (Jy)
G257.240–00.700	–	$(17.5\pm3.5)\times10^{-2}$	$(30.6\pm6.1)\times10^{-2}$	$(16.2\pm3.3)\times10^{-2}$	$(4.7\pm2.3)\times10^{-2}$	$(5.0\pm2.5)\times10^{-2}$	–	–	$(4.6\pm1.4)\times10^{-1}$	$(30.2\pm9.0)\times10^{-4}$	–
G257.261–01.240	–	$(7.0\pm1.4)\times10^{-1}$	$(5.1\pm1.0)\times10^{-1}$	$(26.3\pm5.3)\times10^{-2}$	$(10.2\pm5.1)\times10^{-2}$	–	–	$(26.1\pm8.0)\times10^{-2}$	$(15.7\pm4.7)\times10^{-1}$	$(10.0\pm3.0)\times10^{-3}$	$(4.9\pm1.5)\times10^{-3}$
G257.282–00.336	$(22.2\pm4.4)\times10^{-2}$	$(41.2\pm8.2)\times10^{-1}$	$(5.1\pm1.0)\times10^{+0}$	$(33.7\pm6.7)\times10^{-1}$	$(15.1\pm7.6)\times10^{-1}$	$(3.0\pm1.5)\times10^{-1}$	–	–	–	$(3.8\pm1.1)\times10^{-1}$	$(5.7\pm1.7)\times10^{-1}$
G257.298–01.147	$(6.1\pm1.2)\times10^{-2}$	$(16.3\pm3.3)\times10^{-2}$	$(16.5\pm3.3)\times10^{-2}$	$(8.6\pm1.7)\times10^{-2}$	$(2.3\pm2.3)\times10^{-2}$	$(18.8\pm9.5)\times10^{-3}$	–	–	–	$(9.5\pm2.8)\times10^{-3}$	$(22.0\pm6.6)\times10^{-4}$
G257.320–01.063	$(29.1\pm5.8)\times10^{-1}$	$(16.1\pm3.2)\times10^{-1}$	$(7.1\pm1.4)\times10^{-1}$	$(34.6\pm6.9)\times10^{-2}$	$(1.2\pm1.2)\times10^{-1}$	$(3.6\pm1.8)\times10^{-1}$	$(9.9\pm3.0)\times10^{-1}$	$(7.4\pm2.2)\times10^{-1}$	$(18.1\pm5.4)\times10^{-1}$	$(9.7\pm2.9)\times10^{-1}$	$(25.8\pm7.7)\times10^{-1}$
G257.330–00.258	$(10.8\pm2.2)\times10^{-2}$	$(48.0\pm9.6)\times10^{-2}$	$(27.0\pm5.4)\times10^{-2}$	$(13.1\pm2.6)\times10^{-2}$	$(3.4\pm3.4)\times10^{-2}$	–	$(26.6\pm8.1)\times10^{-2}$	$(13.7\pm4.3)\times10^{-2}$	–	$(5.2\pm1.6)\times10^{-3}$	$(5.4\pm1.6)\times10^{-3}$
G257.340–00.360	$(11.7\pm2.3)\times10^{-2}$	$(10.9\pm2.2)\times10^{-1}$	$(7.2\pm1.4)\times10^{-1}$	$(43.4\pm8.7)\times10^{-2}$	$(16.6\pm8.3)\times10^{-2}$	–	$(19.8\pm6.1)\times10^{-2}$	$(3.6\pm1.1)\times10^{-1}$	$(11.7\pm3.5)\times10^{-1}$	$(18.1\pm5.4)\times10^{-3}$	$(26.6\pm8.0)\times10^{-3}$
G257.354–00.220	$(37.4\pm7.5)\times10^{-2}$	$(15.3\pm3.1)\times10^{-1}$	$(21.5\pm4.3)\times10^{-1}$	$(15.5\pm3.1)\times10^{-1}$	$(7.5\pm3.7)\times10^{-1}$	$(6.3\pm3.1)\times10^{-2}$	–	–	–	$(5.5\pm1.7)\times10^{-2}$	$(17.6\pm5.3)\times10^{-3}$
G257.374–00.276	$(22.2\pm4.9)\times10^{-3}$	$(6.7\pm1.3)\times10^{-1}$	$(9.4\pm1.9)\times10^{-1}$	$(6.3\pm1.3)\times10^{-1}$	$(2.6\pm1.3)\times10^{-1}$	–	$(6.8\pm2.1)\times10^{-1}$	$(23.2\pm7.1)\times10^{-2}$	–	–	–
G257.380–00.280	$(8.0\pm1.6)\times10^{-2}$	$(7.1\pm1.4)\times10^{-1}$	$(9.5\pm1.9)\times10^{-1}$	$(6.4\pm1.3)\times10^{-1}$	$(2.4\pm1.2)\times10^{-1}$	–	$(7.9\pm2.4)\times10^{-1}$	–	–	–	–
G257.460–00.610	$(16.9\pm3.4)\times10^{-2}$	$(36.4\pm7.3)\times10^{-2}$	$(38.3\pm7.7)\times10^{-2}$	$(20.4\pm4.1)\times10^{-2}$	$(8.4\pm8.4)\times10^{-2}$	–	$(16.0\pm5.0)\times10^{-2}$	$(19.8\pm6.1)\times10^{-2}$	–	$(5.2\pm1.6)\times10^{-3}$	$(5.7\pm1.7)\times10^{-3}$
G257.470–00.630	$(46.3\pm9.3)\times10^{-1}$	$(9.4\pm1.9)\times10^{+0}$	$(5.3\pm1.1)\times10^{+0}$	$(28.2\pm5.6)\times10^{-1}$	$(1.0\pm1.0)\times10^{+0}$	$(13.0\pm6.5)\times10^{-2}$	$(32.8\pm9.9)\times10^{-2}$	$(16.4\pm5.1)\times10^{-2}$	$(8.2\pm2.5)\times10^{-1}$	$(30.8\pm9.2)\times10^{-2}$	$(31.3\pm9.4)\times10^{-2}$
G257.510–02.250	$(13.0\pm2.6)\times10^{+0}$	$(11.2\pm2.2)\times10^{+0}$	$(5.2\pm1.0)\times10^{+0}$	$(22.3\pm4.5)\times10^{-1}$	$(7.9\pm7.9)\times10^{-1}$	$(12.5\pm6.2)\times10^{-2}$	–	–	$(3.6\pm1.1)\times10^{-1}$	$(18.5\pm5.5)\times10^{-2}$	$(12.4\pm3.7)\times10^{-1}$
G257.540–01.270	–	$(10.0\pm2.0)\times10^{-2}$	$(23.9\pm4.8)\times10^{-2}$	$(17.4\pm3.5)\times10^{-2}$	$(7.8\pm7.8)\times10^{-2}$	–	–	$(18.3\pm5.7)\times10^{-2}$	–	–	–
G257.540–01.630	$(34.4\pm6.9)\times10^{-2}$	$(33.5\pm6.7)\times10^{-2}$	$(19.6\pm3.9)\times10^{-2}$	$(14.3\pm2.9)\times10^{-2}$	$(3.2\pm3.2)\times10^{-2}$	–	–	–	–	$(4.6\pm1.4)\times10^{-2}$	$(12.8\pm3.8)\times10^{-2}$
G257.546–01.214	$(4.9\pm1.0)\times10^{-2}$	$(29.7\pm5.9)\times10^{-2}$	$(14.9\pm3.0)\times10^{-2}$	$(6.6\pm1.3)\times10^{-2}$	$(2.0\pm2.0)\times10^{-2}$	–	$(22.6\pm7.1)\times10^{-2}$	–	$(7.5\pm2.3)\times10^{-1}$	$(3.4\pm1.0)\times10^{-3}$	$(22.9\pm6.9)\times10^{-4}$
G257.560–00.480	$(21.8\pm4.4)\times10^{-2}$	$(35.1\pm7.0)\times10^{-2}$	$(27.5\pm5.5)\times10^{-2}$	$(15.3\pm3.1)\times10^{-2}$	$(6.1\pm6.1)\times10^{-2}$	–	$(19.3\pm6.0)\times10^{-2}$	–	–	$(8.5\pm2.5)\times10^{-3}$	$(32.8\pm9.9)\times10^{-4}$
G257.570–02.070	$(25.4\pm5.5)\times10^{-3}$	$(11.2\pm2.2)\times10^{-1}$	$(12.4\pm2.5)\times10^{-1}$	$(8.5\pm1.7)\times10^{-1}$	$(3.5\pm1.8)\times10^{-1}$	–	–	$(5.7\pm1.7)\times10^{-1}$	–	$(14.6\pm4.4)\times10^{-3}$	$(20.2\pm6.1)\times10^{-3}$
G257.610–00.660	$(15.2\pm3.1)\times10^{-2}$	$(19.4\pm3.9)\times10^{-2}$	$(30.2\pm6.1)\times10^{-2}$	$(16.7\pm3.4)\times10^{-2}$	$(8.0\pm8.0)\times10^{-2}$	–	–	–	–	$(10.2\pm3.1)\times10^{-3}$	$(5.7\pm1.7)\times10^{-3}$
G257.617–01.772	$(6.9\pm1.4)\times10^{-2}$	$(42.6\pm8.5)\times10^{-2}$	$(44.0\pm8.8)\times10^{-2}$	$(24.7\pm5.0)\times10^{-2}$	$(8.1\pm8.1)\times10^{-2}$	–	$(28.8\pm8.9)\times10^{-2}$	$(24.7\pm7.6)\times10^{-2}$	–	$(11.6\pm3.5)\times10^{-3}$	$(32.4\pm9.7)\times10^{-4}$
G257.630–00.590	–	$(21.9\pm4.4)\times10^{-2}$	$(24.8\pm5.0)\times10^{-2}$	$(16.3\pm3.3)\times10^{-2}$	$(6.0\pm3.0)\times10^{-2}$	$(3.5\pm1.8)\times10^{-2}$	–	–	–	$(16.6\pm5.0)\times10^{-3}$	$(8.9\pm2.7)\times10^{-3}$
G257.630–01.050	$(8.2\pm1.7)\times10^{-2}$	$(7.8\pm1.6)\times10^{-1}$	$(6.9\pm1.4)\times10^{-1}$	$(38.4\pm7.7)\times10^{-2}$	$(11.7\pm5.9)\times10^{-2}$	–	–	–	–	$(4.9\pm1.5)\times10^{-3}$	$(4.0\pm1.2)\times10^{-3}$
G257.640–00.959	–	$(49.5\pm9.9)\times10^{-2}$	$(6.0\pm1.2)\times10^{-1}$	$(32.8\pm6.6)\times10^{-2}$	$(10.0\pm5.0)\times10^{-2}$	$(7.4\pm3.7)\times10^{-2}$	$(7.0\pm2.1)\times10^{-1}$	–	–	–	$(19.2\pm5.8)\times10^{-4}$
G257.655–01.250	–	$(35.6\pm7.1)\times10^{-2}$	$(27.6\pm5.5)\times10^{-2}$	$(13.2\pm2.7)\times10^{-2}$	$(5.2\pm2.6)\times10^{-2}$	$(2.0\pm1.0)\times10^{-2}$	–	–	$(11.2\pm3.4)\times10^{-1}$	$(11.4\pm3.4)\times10^{-3}$	$(5.2\pm1.6)\times10^{-3}$
G257.808–01.277	$(22.2\pm4.4)\times10^{-2}$	$(43.8\pm8.8)\times10^{-2}$	$(37.7\pm7.5)\times10^{-2}$	$(20.6\pm4.1)\times10^{-2}$	$(8.6\pm8.6)\times10^{-2}$	$(3.2\pm1.6)\times10^{-2}$	$(18.2\pm5.7)\times10^{-2}$	–	–	$(9.0\pm2.7)\times10^{-3}$	$(18.7\pm5.6)\times10^{-3}$
G257.830–00.740	–	$(25.3\pm5.1)\times10^{-2}$	$(21.5\pm4.3)\times10^{-2}$	$(16.1\pm3.2)\times10^{-2}$	$(6.4\pm3.2)\times10^{-2}$	–	$(18.8\pm5.9)\times10^{-2}$	–	–	$(10.5\pm3.1)\times10^{-4}$	$(20.1\pm6.0)\times10^{-4}$
G257.842–01.085	$(11.0\pm2.2)\times10^{-1}$	$(34.4\pm6.9)\times10^{-1}$	$(22.6\pm4.5)\times10^{-1}$	$(12.7\pm2.5)\times10^{-1}$	$(3.8\pm3.8)\times10^{-1}$	$(2.5\pm1.2)\times10^{-2}$	–	–	–	$(3.6\pm1.1)\times10^{-2}$	$(6.5\pm2.0)\times10^{-2}$
G257.864–01.086	$(14.7\pm2.9)\times10^{-2}$	$(8.1\pm1.6)\times10^{-1}$	$(12.2\pm2.4)\times10^{-1}$	$(7.6\pm1.5)\times10^{-1}$	$(3.1\pm1.6)\times10^{-1}$	–	$(3.8\pm1.2)\times10^{-1}$	–	–	$(20.3\pm6.1)\times10^{-3}$	$(16.3\pm4.9)\times10^{-3}$
G257.865–01.495	$(11.3\pm2.3)\times10^{-2}$	$(6.3\pm1.3)\times10^{-1}$	$(42.0\pm8.4)\times10^{-2}$	$(21.4\pm4.3)\times10^{-2}$	$(7.1\pm3.6)\times10^{-2}$	–	–	–	–	$(17.5\pm5.3)\times10^{-4}$	$(17.4\pm5.2)\times10^{-4}$
G257.867–01.793	$(42.5\pm8.5)\times10^{-1}$	$(9.2\pm1.8)\times10^{+0}$	$(40.7\pm8.1)\times10^{-1}$	$(16.8\pm3.4)\times10^{-1}$	$(5.3\pm2.7)\times10^{-1}$	$(2.4\pm1.2)\times10^{-1}$	–	$(3.6\pm1.1)\times10^{-1}$	–	$(3.8\pm1.1)\times10^{-1}$	$(3.8\pm1.1)\times10^{-1}$
G257.879–01.729	$(11.0\pm2.2)\times10^{-2}$	$(17.6\pm3.5)\times10^{-1}$	$(15.3\pm3.1)\times10^{-1}$	$(7.9\pm1.6)\times10^{-1}$	$(2.9\pm1.5)\times10^{-1}$	–	–	–	–	$(31.3\pm9.4)\times10^{-3}$	$(5.5\pm1.7)\times10^{-2}$
G257.920–00.470	$(29.9\pm6.0)\times10^{-2}$	$(15.7\pm3.1)\times10^{-1}$	$(13.3\pm2.7)\times10^{-1}$	$(8.2\pm1.7)\times10^{-1}$	$(3.0\pm1.5)\times10^{-1}$	$(4.2\pm2.1)\times10^{-2}$	$(6.0\pm1.8)\times10^{-1}$	–	–	$(27.0\pm8.1)\times10^{-3}$	$(21.2\pm6.4)\times10^{-3}$
G257.932–01.387	$(17.7\pm3.5)\times10^{-1}$	$(11.4\pm2.3)\times10^{+0}$	$(9.0\pm1.8)\times10^{+0}$	$(45.1\pm9.0)\times10^{-1}$	$(11.9\pm5.9)\times10^{-1}$	$(2.2\pm1.1)\times10^{-1}$	–	$(11.3\pm3.4)\times10^{-1}$	–	$(5.6\pm1.7)\times10^{-1}$	$(4.3\pm1.3)\times10^{-1}$
G257.940–00.942	–	$(7.8\pm1.6)\times10^{-2}$	$(20.5\pm4.1)\times10^{-2}$	$(18.3\pm3.7)\times10^{-2}$	$(8.6\pm8.6)\times10^{-2}$	–	–	–	–	$(8.9\pm2.7)\times10^{-4}$	$(7.4\pm2.2)\times10^{-3}$
G257.950–00.170	$(29.5\pm5.9)\times10^{-2}$	$(8.0\pm1.6)\times10^{-1}$	$(5.4\pm1.1)\times10^{-1}$	$(29.4\pm5.9)\times10^{-2}$	$(8.2\pm4.1)\times10^{-2}$	–	–	$(17.8\pm5.5)\times10^{-2}$	$(5.2\pm1.6)\times10^{-1}$	$(8.0\pm2.4)\times10^{-3}$	$(5.2\pm1.6)\times10^{-3}$
G257.950–00.510	$(12.8\pm2.6)\times10^{-2}$	$(5.2\pm1.0)\times10^{-1}$	$(5.8\pm1.2)\times10^{-1}$	$(33.9\pm6.8)\times10^{-2}$	$(13.3\pm6.7)\times10^{-2}$	–	$(31.0\pm9.4)\times10^{-2}$	–	–	$(6.0\pm1.8)\times10^{-3}$	$(4.6\pm1.4)\times10^{-3}$
G257.960–00.940	$(8.5\pm1.7)\times10^{-2}$	$(32.1\pm6.4)\times10^{-2}$	$(5.3\pm1.1)\times10^{-1}$	$(44.3\pm8.9)\times10^{-2}$	$(2.3\pm1.1)\times10^{-1}$	$(2.4\pm1.2)\times10^{-2}$	–	$(27.4\pm8.3)\times10^{-2}$	–	$(21.8\pm6.5)\times10^{-4}$	$(13.3\pm4.0)\times10^{-3}$
G257.978–01.428	$(31.5\pm6.3)\times10^{-1}$	$(8.2\pm1.6)\times10^{+0}$	$(6.1\pm1.2)\times10^{+0}$	$(29.2\pm5.8)\times10^{-1}$	$(8.7\pm4.4)\times10^{-1}$	–	$(6.6\pm2.0)\times10^{-1}$	–	$(26.0\pm7.8)\times10^{-1}$	$(5.3\pm1.6)\times10^{-1}$	$(4.8\pm1.4)\times10^{-1}$
G258.000–00.300	$(17.4\pm3.5)\times10^{-2}$	$(14.9\pm3.0)\times10^{-1}$	$(12.4\pm2.5)\times10^{-1}$	$(5.9\pm1.2)\times10^{-1}$	$(2.5\pm1.2)\times10^{-1}$	–	$(4.3\pm1.3)\times10^{-1}$	$(4.3\pm1.3)\times10^{-1}$	$(7.3\pm2.2)\times10^{-1}$	$(18.4\pm5.5)\times10^{-3}$	$(20.2\pm6.1)\times10^{-3}$
G258.050–01.341	$(22.6\pm4.5)\times10^{-1}$	$(6.3\pm1.3)\times10^{+0}$	$(5.4\pm1.1)\times10^{+0}$	$(30.0\pm6.0)\times10^{-1}$	$(12.2\pm6.1)\times10^{-1}$	$(15.1\pm7.5)\times10^{-2}$	–	$(4.3\pm1.3)\times10^{-1}$	$(21.3\pm6.4)\times10^{-1}$	$(17.8\pm5.3)\times10^{-2}$	$(20.7\pm6.2)\times10^{-2}$
G258.047–01.604	$(18.4\pm3.7)\times10^{-2}$	$(7.3\pm1.5)\times10^{-1}$	$(6.4\pm1.3)\times10^{-1}$	$(34.6\pm7.1)\times10^{-2}$	$(1.0\pm1.0)\times10^{-1}$	–	–	–	–	$(22.4\pm6.7)\times10^{-3}$	$(20.9\pm6.3)\times10^{-3}$
G258.080–01.350	$(12.5\pm2.5)\times10^{-2}$	$(20.6\pm4.1)\times10^{-2}$	$(32.2\pm6.5)\times10^{-2}$	$(22.1\pm4.6)\times10^{-2}$	$(18.4\pm9.3)\times10^{-2}$	$(9.4\pm4.7)\times10^{-1}$	$(5.4\pm1.6)\times10^{-1}$	$(14.0\pm4.2)\times10^{-1}$	$(9.7\pm2.9)\times10^{-1}$	$(8.3\pm2.5)\times10^{-1}$	$(29.1\pm8.7)\times10^{-2}$
G258.080–01.563	–	$(27.6\pm5.5)\times10^{-2}$	$(43.4\pm8.7)\times10^{-2}$	$(28.1\pm5.6)\times10^{-2}$	$(9.9\pm9.9)\times10^{-2}$	–	–	–	–	–	–

Table A.3: continued

Name	F_{70} (Jy)	F_{160} (Jy)	F_{250} (Jy)	F_{350} (Jy)	F_{500} (Jy)	F_{8} (Jy)	$F_{12.1}$ (Jy)	$F_{14.7}$ (Jy)	F_{21} (Jy)	F_{14} (Jy)	F_{22} (Jy)
G258.081–01.561	–	$(27.6\pm5.5)\times10^{-2}$	$(43.4\pm8.7)\times10^{-2}$	$(28.1\pm5.6)\times10^{-2}$	$(9.9\pm9.9)\times10^{-2}$	–	–	–	–	–	–
G258.080–01.561	–	$(27.6\pm5.5)\times10^{-2}$	$(43.4\pm8.7)\times10^{-2}$	$(28.1\pm5.6)\times10^{-2}$	$(9.9\pm9.9)\times10^{-2}$	–	–	–	–	–	–
G258.081–01.558	–	$(27.6\pm5.5)\times10^{-2}$	$(43.4\pm8.7)\times10^{-2}$	$(28.1\pm5.6)\times10^{-2}$	$(9.9\pm9.9)\times10^{-2}$	–	–	–	–	–	–
G258.082–01.626	$(15.2\pm3.1)\times10^{-2}$	$(14.6\pm2.9)\times10^{-1}$	$(17.8\pm3.6)\times10^{-1}$	$(10.5\pm2.1)\times10^{-1}$	$(4.6\pm2.3)\times10^{-1}$	$(12.0\pm6.0)\times10^{-2}$	–	$(7.5\pm2.3)\times10^{-1}$	–	–	–
G258.140–00.350	$(5.9\pm1.2)\times10^{-2}$	$(16.2\pm3.2)\times10^{-2}$	$(13.0\pm2.6)\times10^{-2}$	$(8.8\pm1.8)\times10^{-2}$	$(3.6\pm1.8)\times10^{-2}$	–	–	$(25.6\pm7.8)\times10^{-2}$	–	$(10.2\pm3.0)\times10^{-3}$	$(19.7\pm5.9)\times10^{-3}$
G258.182–01.512	$(13.2\pm2.6)\times10^{-2}$	$(8.6\pm1.7)\times10^{-1}$	$(6.2\pm1.2)\times10^{-1}$	$(34.2\pm6.9)\times10^{-2}$	$(16.2\pm8.1)\times10^{-2}$	–	$(6.0\pm1.8)\times10^{-1}$	–	–	$(13.5\pm4.1)\times10^{-3}$	$(6.9\pm2.1)\times10^{-3}$
G258.194–02.221	$(27.7\pm5.6)\times10^{-2}$	$(18.8\pm3.8)\times10^{-1}$	$(17.1\pm3.4)\times10^{-1}$	$(10.7\pm2.1)\times10^{-1}$	$(4.8\pm2.4)\times10^{-1}$	–	$(3.8\pm1.2)\times10^{-1}$	–	$(20.6\pm6.2)\times10^{-1}$	$(8.0\pm2.4)\times10^{-3}$	–
G258.190–02.277	–	$(16.5\pm3.3)\times10^{-1}$	$(13.7\pm2.7)\times10^{-1}$	$(8.2\pm1.6)\times10^{-1}$	$(3.1\pm1.6)\times10^{-1}$	$(4.5\pm2.3)\times10^{-2}$	$(9.3\pm2.8)\times10^{-1}$	–	–	$(15.3\pm4.6)\times10^{-3}$	$(6.4\pm1.9)\times10^{-3}$
G258.255–01.233	$(40.9\pm8.2)\times10^{-2}$	$(7.6\pm1.5)\times10^{-1}$	$(5.1\pm1.0)\times10^{-1}$	$(30.6\pm6.1)\times10^{-2}$	$(13.6\pm6.8)\times10^{-2}$	–	–	–	–	$(27.4\pm8.2)\times10^{-3}$	$(18.1\pm5.4)\times10^{-3}$
G258.260–00.870	–	$(24.4\pm4.9)\times10^{-2}$	$(27.3\pm5.5)\times10^{-2}$	$(15.1\pm3.0)\times10^{-2}$	$(6.0\pm3.0)\times10^{-2}$	–	$(23.9\pm7.3)\times10^{-2}$	$(13.6\pm4.3)\times10^{-2}$	$(3.2\pm1.0)\times10^{-1}$	$(9.5\pm2.9)\times10^{-3}$	$(30.1\pm9.0)\times10^{-4}$
G258.300–00.520	$(34.0\pm6.8)\times10^{-2}$	$(5.5\pm1.1)\times10^{-1}$	$(6.9\pm1.4)\times10^{-1}$	$(34.3\pm6.9)\times10^{-2}$	$(12.7\pm6.4)\times10^{-2}$	$(4.7\pm2.4)\times10^{-2}$	–	–	$(8.5\pm2.6)\times10^{-1}$	$(19.7\pm5.9)\times10^{-3}$	$(12.3\pm3.7)\times10^{-3}$
G258.300–02.163	$(9.7\pm1.9)\times10^{-1}$	$(39.7\pm7.9)\times10^{-1}$	$(41.7\pm8.3)\times10^{-1}$	$(25.0\pm5.0)\times10^{-1}$	$(12.0\pm6.0)\times10^{-1}$	$(2.3\pm1.2)\times10^{-1}$	$(5.6\pm1.7)\times10^{-1}$	–	$(5.6\pm1.7)\times10^{-1}$	$(4.6\pm1.4)\times10^{-2}$	$(5.0\pm1.5)\times10^{-2}$
G258.319–00.920	–	$(18.5\pm3.7)\times10^{-1}$	$(18.6\pm3.7)\times10^{-1}$	$(10.0\pm2.0)\times10^{-1}$	$(3.4\pm1.7)\times10^{-1}$	–	–	–	–	–	–
G258.340–02.190	$(22.2\pm4.8)\times10^{-3}$	$(41.4\pm8.3)\times10^{-2}$	$(7.9\pm1.6)\times10^{-1}$	$(48.7\pm9.8)\times10^{-2}$	$(2.2\pm1.1)\times10^{-1}$	–	–	–	–	$(32.2\pm9.7)\times10^{-3}$	$(19.7\pm5.9)\times10^{-3}$
G258.384–01.113	–	$(15.7\pm3.1)\times10^{-1}$	$(11.0\pm2.2)\times10^{-1}$	$(6.5\pm1.3)\times10^{-1}$	$(2.7\pm1.4)\times10^{-1}$	$(2.9\pm1.4)\times10^{-2}$	$(7.7\pm2.3)\times10^{-1}$	–	–	$(32.2\pm9.7)\times10^{-3}$	$(12.9\pm3.9)\times10^{-3}$
G258.420–00.940	$(23.4\pm4.7)\times10^{-2}$	$(6.3\pm1.3)\times10^{-1}$	$(6.0\pm1.2)\times10^{-1}$	$(29.5\pm5.9)\times10^{-2}$	$(13.8\pm6.9)\times10^{-2}$	$(2.5\pm1.3)\times10^{-2}$	–	–	–	$(19.7\pm5.9)\times10^{-3}$	$(16.5\pm5.0)\times10^{-3}$
G258.430–00.940	–	$(19.1\pm3.8)\times10^{-2}$	$(38.7\pm7.7)\times10^{-2}$	$(26.9\pm5.4)\times10^{-2}$	$(10.2\pm5.1)\times10^{-2}$	–	–	–	$(7.3\pm2.2)\times10^{-1}$	$(6.5\pm2.0)\times10^{-3}$	$(5.7\pm1.7)\times10^{-3}$
G258.427–01.444	$(32.7\pm6.5)\times10^{-2}$	$(5.8\pm1.2)\times10^{-1}$	$(26.3\pm5.3)\times10^{-2}$	$(10.5\pm2.1)\times10^{-2}$	$(2.1\pm2.1)\times10^{-2}$	$(4.6\pm2.3)\times10^{-2}$	$(16.8\pm5.3)\times10^{-2}$	$(3.4\pm1.0)\times10^{-1}$	–	$(29.1\pm8.7)\times10^{-3}$	$(22.8\pm6.9)\times10^{-3}$
G258.532–01.188	$(16.3\pm3.3)\times10^{-1}$	$(8.4\pm1.7)\times10^{+0}$	$(5.9\pm1.2)\times10^{+0}$	$(30.8\pm6.2)\times10^{-1}$	$(11.9\pm5.9)\times10^{-1}$	$(3.8\pm1.9)\times10^{-1}$	–	–	–	$(14.3\pm4.3)\times10^{-2}$	$(8.4\pm2.5)\times10^{-2}$
G258.610–01.920	$(6.3\pm1.3)\times10^{+1}$	$(12.3\pm2.5)\times10^{+1}$	$(5.5\pm1.1)\times10^{+1}$	$(21.6\pm4.3)\times10^{+0}$	$(7.5\pm3.7)\times10^{+0}$	$(2.7\pm1.3)\times10^{+0}$	$(30.2\pm9.1)\times10^{-1}$	$(27.7\pm8.3)\times10^{-1}$	$(4.3\pm1.3)\times10^{+0}$	$(3.8\pm1.1)\times10^{+0}$	$(27.0\pm8.1)\times10^{-1}$
G258.660–00.390	$(16.3\pm3.3)\times10^{-2}$	$(47.3\pm9.5)\times10^{-2}$	$(7.0\pm1.4)\times10^{-1}$	$(40.5\pm8.1)\times10^{-2}$	$(18.3\pm9.2)\times10^{-2}$	–	–	$(6.3\pm1.9)\times10^{-1}$	–	$(3.6\pm1.1)\times10^{-3}$	$(4.1\pm1.2)\times10^{-3}$
G258.667–01.050	–	$(8.2\pm1.6)\times10^{-1}$	$(12.3\pm2.5)\times10^{-1}$	$(7.2\pm1.4)\times10^{-1}$	$(2.7\pm1.3)\times10^{-1}$	–	–	$(6.3\pm1.9)\times10^{-1}$	–	$(5.9\pm1.8)\times10^{-3}$	$(10.4\pm3.1)\times10^{-3}$
G258.718–01.168	$(8.8\pm1.8)\times10^{-1}$	$(24.8\pm5.0)\times10^{-1}$	$(12.7\pm2.5)\times10^{-1}$	$(5.2\pm1.0)\times10^{-1}$	$(2.0\pm2.0)\times10^{-1}$	$(6.2\pm3.1)\times10^{-2}$	–	–	–	$(9.1\pm2.7)\times10^{-2}$	$(5.5\pm1.7)\times10^{-2}$
G258.733–01.335	$(12.4\pm2.5)\times10^{-1}$	$(48.5\pm9.7)\times10^{-1}$	$(26.2\pm5.2)\times10^{-1}$	$(12.0\pm2.4)\times10^{-1}$	$(3.9\pm1.9)\times10^{-1}$	$(10.2\pm5.1)\times10^{-2}$	$(4.6\pm1.4)\times10^{-1}$	–	$(10.8\pm3.3)\times10^{-1}$	$(15.8\pm4.7)\times10^{-2}$	$(8.4\pm2.5)\times10^{-2}$
G258.743–01.291	$(28.4\pm5.7)\times10^{-1}$	$(14.7\pm2.9)\times10^{+0}$	$(7.8\pm1.6)\times10^{+0}$	$(38.3\pm7.7)\times10^{-1}$	$(14.5\pm7.3)\times10^{-1}$	$(4.5\pm2.3)\times10^{-1}$	$(3.3\pm1.0)\times10^{-1}$	–	$(3.9\pm1.2)\times10^{+0}$	$(4.0\pm1.2)\times10^{-1}$	$(25.5\pm7.7)\times10^{-2}$
G258.790–00.970	$(22.2\pm4.4)\times10^{-2}$	$(6.5\pm1.3)\times10^{-1}$	$(44.4\pm8.9)\times10^{-2}$	$(19.7\pm4.0)\times10^{-2}$	$(8.2\pm4.1)\times10^{-2}$	–	$(24.2\pm7.5)\times10^{-2}$	–	$(15.5\pm4.7)\times10^{-1}$	$(4.7\pm1.4)\times10^{-3}$	$(3.6\pm1.1)\times10^{-3}$
G258.792–01.422	$(42.4\pm8.5)\times10^{-2}$	$(13.7\pm2.7)\times10^{-1}$	$(26.5\pm5.3)\times10^{-1}$	$(15.5\pm3.1)\times10^{-1}$	$(6.8\pm3.4)\times10^{-1}$	$(12.9\pm6.5)\times10^{-2}$	–	–	$(20.3\pm6.1)\times10^{-1}$	$(9.0\pm2.7)\times10^{-3}$	–
G258.822–01.402	$(10.5\pm2.1)\times10^{-2}$	$(21.9\pm4.4)\times10^{-1}$	$(24.2\pm4.8)\times10^{-1}$	$(14.5\pm2.9)\times10^{-1}$	$(5.9\pm2.9)\times10^{-1}$	–	–	$(12.8\pm3.8)\times10^{-1}$	$(5.4\pm1.6)\times10^{-1}$	$(31.0\pm9.3)\times10^{-4}$	–
G258.842–01.446	$(42.4\pm8.5)\times10^{-2}$	$(35.4\pm7.1)\times10^{-1}$	$(38.5\pm7.7)\times10^{-1}$	$(25.5\pm5.1)\times10^{-1}$	$(11.4\pm5.7)\times10^{-1}$	–	–	–	–	$(3.4\pm1.0)\times10^{-2}$	$(17.9\pm5.4)\times10^{-3}$
G258.860–01.397	–	$(16.8\pm3.4)\times10^{-2}$	$(7.8\pm1.6)\times10^{-1}$	$(6.3\pm1.3)\times10^{-1}$	$(2.4\pm1.2)\times10^{-1}$	–	$(24.0\pm7.4)\times10^{-2}$	–	–	–	–
G258.870–01.475	$(33.1\pm6.9)\times10^{-3}$	$(8.0\pm1.6)\times10^{-1}$	$(13.5\pm2.7)\times10^{-1}$	$(8.6\pm1.7)\times10^{-1}$	$(3.4\pm1.7)\times10^{-1}$	–	$(24.0\pm7.5)\times10^{-2}$	$(24.7\pm7.6)\times10^{-2}$	$(4.1\pm1.3)\times10^{-1}$	–	$(12.5\pm3.7)\times10^{-4}$
G258.880–00.720	$(42.3\pm8.5)\times10^{-2}$	$(14.6\pm2.9)\times10^{-1}$	$(18.8\pm3.8)\times10^{-1}$	$(11.4\pm2.3)\times10^{-1}$	$(4.5\pm2.3)\times10^{-1}$	–	–	–	–	–	–
G258.878–01.440	–	$(38.7\pm7.7)\times10^{-2}$	$(6.1\pm1.2)\times10^{-1}$	$(36.3\pm7.3)\times10^{-2}$	$(1.1\pm1.1)\times10^{-1}$	–	–	–	$(5.5\pm1.7)\times10^{-1}$	–	–
G258.885–01.498	$(11.6\pm2.3)\times10^{-2}$	$(7.5\pm1.5)\times10^{-1}$	$(16.0\pm3.2)\times10^{-1}$	$(12.1\pm2.4)\times10^{-1}$	$(5.0\pm2.5)\times10^{-1}$	$(4.3\pm2.2)\times10^{-2}$	$(3.3\pm1.0)\times10^{-1}$	–	$(8.2\pm2.5)\times10^{-1}$	–	–
G258.910–01.450	–	$(49.7\pm9.9)\times10^{-2}$	$(9.8\pm2.0)\times10^{-1}$	$(7.9\pm1.6)\times10^{-1}$	$(3.5\pm1.8)\times10^{-1}$	$(4.7\pm2.4)\times10^{-2}$	–	–	–	$(6.5\pm2.0)\times10^{-3}$	–
G258.930–00.730	$(43.8\pm8.8)\times10^{-2}$	$(8.3\pm1.7)\times10^{-1}$	$(22.0\pm4.4)\times10^{-1}$	$(12.9\pm2.6)\times10^{-1}$	$(6.2\pm3.1)\times10^{-1}$	–	–	–	–	–	–
G258.960–00.720	–	$(5.3\pm1.1)\times10^{-1}$	$(40.2\pm8.1)\times10^{-2}$	$(26.5\pm5.5)\times10^{-2}$	$(17.9\pm9.0)\times10^{-2}$	$(5.1\pm2.6)\times10^{-2}$	–	$(20.0\pm6.1)\times10^{-2}$	–	$(12.1\pm3.6)\times10^{-4}$	$(25.0\pm7.5)\times10^{-4}$
G258.965–01.475	$(28.7\pm5.7)\times10^{-2}$	$(26.4\pm5.3)\times10^{-1}$	$(28.2\pm5.6)\times10^{-1}$	$(18.2\pm3.6)\times10^{-1}$	$(7.1\pm3.5)\times10^{-1}$	$(7.1\pm3.6)\times10^{-2}$	$(6.3\pm1.9)\times10^{-1}$	–	–	$(4.7\pm1.4)\times10^{-2}$	$(7.2\pm2.2)\times10^{-2}$
G259.002–01.498	$(25.1\pm5.0)\times10^{-2}$	$(38.0\pm7.6)\times10^{-1}$	$(23.4\pm4.7)\times10^{-1}$	$(11.2\pm2.2)\times10^{-1}$	$(6.3\pm3.1)\times10^{-1}$	–	$(4.5\pm1.4)\times10^{-1}$	–	–	$(15.8\pm4.7)\times10^{-2}$	$(15.0\pm4.5)\times10^{-2}$
G259.018–01.550	$(9.9\pm2.0)\times10^{+1}$	$(13.4\pm2.7)\times10^{+1}$	$(5.6\pm1.1)\times10^{+1}$	$(23.9\pm4.8)\times10^{+0}$	$(8.4\pm4.2)\times10^{+0}$	$(3.6\pm1.8)\times10^{+0}$	$(3.6\pm1.1)\times10^{+0}$	$(19.6\pm5.9)\times10^{-1}$	–	$(4.5\pm1.4)\times10^{+0}$	$(3.7\pm1.1)\times10^{+0}$
G259.031–00.496	–	$(5.2\pm1.0)\times10^{-1}$	$(6.9\pm1.4)\times10^{-1}$	$(36.5\pm7.4)\times10^{-2}$	$(11.9\pm6.0)\times10^{-2}$	–	$(25.8\pm7.9)\times10^{-2}$	–	–	$(4.2\pm1.3)\times10^{-3}$	$(33.1\pm9.9)\times10^{-4}$
G259.052–01.140	$(34.1\pm6.8)\times10^{-2}$	$(13.7\pm2.7)\times10^{-1}$	$(12.4\pm2.5)\times10^{-1}$	$(8.0\pm1.6)\times10^{-1}$	$(3.1\pm1.5)\times10^{-1}$	–	$(11.0\pm3.3)\times10^{-1}$	–	$(5.8\pm1.8)\times10^{-1}$	$(12.9\pm3.9)\times10^{-3}$	$(15.6\pm4.7)\times10^{-3}$
G259.050–01.538	$(12.6\pm2.5)\times10^{+1}$	$(11.6\pm2.3)\times10^{+1}$	$(39.6\pm7.9)\times10^{+0}$	$(14.2\pm2.8)\times10^{+0}$	$(5.3\pm2.6)\times10^{+0}$	$(2.3\pm1.1)\times10^{+0}$	$(16.2\pm4.9)\times10^{-1}$	$(16.1\pm4.8)\times10^{-1}$	$(31.1\pm9.3)\times10^{-1}$	$(3.5\pm1.0)\times10^{+0}$	$(6.9\pm2.1)\times10^{+0}$

Table A.3: continued

Name	F_{70} (Jy)	F_{160} (Jy)	F_{250} (Jy)	F_{350} (Jy)	F_{500} (Jy)	F_{8} (Jy)	$F_{12.1}$ (Jy)	$F_{14.7}$ (Jy)	F_{21} (Jy)	F_{14} (Jy)	F_{22} (Jy)
G259.045–01.557	$(20.6\pm4.1)\times10^{+1}$	$(15.5\pm3.1)\times10^{+1}$	$(49.7\pm9.9)\times10^{+0}$	$(18.8\pm3.8)\times10^{+0}$	$(5.2\pm2.6)\times10^{+0}$	$(3.8\pm1.9)\times10^{+0}$	$(5.5\pm1.7)\times10^{+0}$	$(4.0\pm1.2)\times10^{+0}$	$(14.3\pm4.3)\times10^{+0}$	$(6.1\pm1.8)\times10^{+0}$	$(15.6\pm4.7)\times10^{+0}$
G259.080–00.050	–	$(43.6\pm8.7)\times10^{-2}$	$(34.1\pm6.9)\times10^{-2}$	$(15.4\pm3.2)\times10^{-2}$	$(6.8\pm6.8)\times10^{-2}$	–	$(17.9\pm5.6)\times10^{-2}$	–	–	$(12.9\pm3.9)\times10^{-3}$	$(12.9\pm3.9)\times10^{-3}$
G259.078–01.620	$(26.7\pm5.3)\times10^{+0}$	$(33.7\pm6.7)\times10^{+0}$	$(13.3\pm2.7)\times10^{+0}$	$(46.7\pm9.4)\times10^{-1}$	$(12.8\pm6.4)\times10^{-1}$	$(6.5\pm3.3)\times10^{-1}$	$(13.5\pm4.1)\times10^{-1}$	$(5.1\pm1.5)\times10^{-1}$	–	$(8.4\pm2.5)\times10^{-1}$	$(8.4\pm2.5)\times10^{-1}$
G259.112–01.437	$(36.1\pm7.2)\times10^{-2}$	$(39.9\pm8.0)\times10^{-1}$	$(5.3\pm1.1)\times10^{+0}$	$(34.0\pm6.8)\times10^{-1}$	$(15.4\pm7.7)\times10^{-1}$	–	–	–	–	–	–
G259.133–01.426	–	$(41.5\pm8.3)\times10^{-1}$	$(5.8\pm1.2)\times10^{+0}$	$(40.4\pm8.1)\times10^{-1}$	$(19.5\pm9.8)\times10^{-1}$	–	–	–	$(5.7\pm1.8)\times10^{-1}$	–	–
G259.153–01.337	–	$(34.2\pm6.8)\times10^{-1}$	$(39.1\pm7.8)\times10^{-1}$	$(26.9\pm5.4)\times10^{-1}$	$(13.4\pm6.7)\times10^{-1}$	$(12.4\pm6.2)\times10^{-2}$	–	$(5.7\pm1.7)\times10^{-1}$	–	–	–
G259.165–01.217	–	$(10.8\pm2.2)\times10^{-1}$	$(16.6\pm3.3)\times10^{-1}$	$(11.4\pm2.3)\times10^{-1}$	$(5.5\pm2.7)\times10^{-1}$	–	$(20.1\pm6.3)\times10^{-2}$	–	$(4.0\pm1.3)\times10^{-1}$	$(6.0\pm1.8)\times10^{-2}$	$(5.3\pm1.6)\times10^{-2}$
G259.172–01.253	$(41.5\pm8.5)\times10^{-3}$	$(11.8\pm2.4)\times10^{-1}$	$(10.5\pm2.1)\times10^{-1}$	$(6.1\pm1.2)\times10^{-1}$	$(2.2\pm1.1)\times10^{-1}$	$(8.6\pm4.3)\times10^{-2}$	$(18.0\pm5.7)\times10^{-2}$	–	–	$(13.1\pm3.9)\times10^{-4}$	$(5.1\pm1.5)\times10^{-3}$
G259.167–01.313	$(6.5\pm1.3)\times10^{-2}$	$(14.9\pm3.0)\times10^{-1}$	$(17.4\pm3.5)\times10^{-1}$	$(9.3\pm1.9)\times10^{-1}$	$(4.5\pm2.3)\times10^{-1}$	–	–	–	–	$(11.2\pm3.4)\times10^{-3}$	$(7.4\pm2.2)\times10^{-3}$
G259.190–00.030	$(33.6\pm7.6)\times10^{-3}$	$(5.6\pm1.1)\times10^{-1}$	$(5.4\pm1.1)\times10^{-1}$	$(25.8\pm5.2)\times10^{-2}$	$(9.0\pm9.0)\times10^{-2}$	–	–	–	–	$(29.8\pm8.9)\times10^{-4}$	$(6.1\pm1.8)\times10^{-3}$
G259.200+00.000	$(27.1\pm5.4)\times10^{-2}$	$(5.4\pm1.1)\times10^{-1}$	$(7.2\pm1.4)\times10^{-1}$	$(37.5\pm7.6)\times10^{-2}$	$(1.0\pm1.0)\times10^{-1}$	–	–	–	–	–	$(26.0\pm7.8)\times10^{-4}$
G259.200–00.010	$(13.3\pm2.7)\times10^{-2}$	$(19.3\pm3.9)\times10^{-1}$	$(13.5\pm2.7)\times10^{-1}$	$(7.0\pm1.4)\times10^{-1}$	$(2.3\pm1.1)\times10^{-1}$	$(9.1\pm4.5)\times10^{-2}$	$(31.9\pm9.7)\times10^{-2}$	$(5.6\pm1.7)\times10^{-1}$	–	$(5.4\pm1.6)\times10^{-2}$	$(4.3\pm1.3)\times10^{-2}$
G259.198–01.272	–	$(45.5\pm9.1)\times10^{-1}$	$(43.7\pm8.7)\times10^{-1}$	$(29.5\pm5.9)\times10^{-1}$	$(14.0\pm7.0)\times10^{-1}$	$(13.2\pm6.6)\times10^{-2}$	–	$(11.0\pm3.3)\times10^{-1}$	–	$(23.4\pm7.0)\times10^{-3}$	$(16.5\pm5.0)\times10^{-3}$
G259.215–01.389	–	$(5.1\pm1.0)\times10^{+0}$	$(7.3\pm1.5)\times10^{+0}$	$(46.5\pm9.3)\times10^{-1}$	$(2.2\pm1.1)\times10^{+0}$	$(4.9\pm2.5)\times10^{-2}$	–	–	–	$(3.7\pm1.1)\times10^{-2}$	$(4.0\pm1.2)\times10^{-2}$
G259.217–01.390	–	$(5.4\pm1.1)\times10^{+0}$	$(7.5\pm1.5)\times10^{+0}$	$(48.5\pm9.7)\times10^{-1}$	$(2.4\pm1.2)\times10^{+0}$	$(9.9\pm4.9)\times10^{-2}$	–	–	–	$(4.3\pm1.3)\times10^{-2}$	$(4.5\pm1.4)\times10^{-2}$
G259.230–00.030	$(6.2\pm1.3)\times10^{-2}$	$(28.8\pm5.8)\times10^{-2}$	$(29.0\pm5.8)\times10^{-2}$	$(23.6\pm4.8)\times10^{-2}$	$(11.5\pm5.7)\times10^{-2}$	$(3.1\pm1.6)\times10^{-2}$	–	–	–	$(8.0\pm2.4)\times10^{-3}$	$(15.6\pm4.7)\times10^{-3}$
G259.230–00.300	$(13.7\pm2.7)\times10^{-2}$	$(42.6\pm8.5)\times10^{-2}$	$(22.6\pm4.5)\times10^{-2}$	$(12.1\pm2.4)\times10^{-2}$	$(4.1\pm2.0)\times10^{-2}$	–	–	–	–	$(9.6\pm2.9)\times10^{-3}$	$(11.1\pm3.3)\times10^{-3}$
G259.240–00.320	–	$(7.2\pm1.4)\times10^{-1}$	$(7.1\pm1.4)\times10^{-1}$	$(44.6\pm8.9)\times10^{-2}$	$(17.7\pm8.9)\times10^{-2}$	–	–	–	$(11.2\pm3.4)\times10^{-1}$	$(17.0\pm5.1)\times10^{-3}$	$(31.7\pm9.5)\times10^{-3}$
G259.237–01.627	$(44.3\pm8.9)\times10^{+0}$	$(44.6\pm8.9)\times10^{+0}$	$(17.5\pm3.5)\times10^{+0}$	$(6.8\pm1.4)\times10^{+0}$	$(2.2\pm1.1)\times10^{+0}$	$(9.9\pm4.9)\times10^{-1}$	$(14.3\pm4.3)\times10^{-1}$	$(9.9\pm3.0)\times10^{-1}$	$(8.0\pm2.4)\times10^{-1}$	$(14.1\pm4.2)\times10^{-1}$	$(25.7\pm7.7)\times10^{-1}$
G259.250–00.050	$(6.0\pm1.2)\times10^{-1}$	$(8.7\pm1.7)\times10^{-1}$	$(17.7\pm3.5)\times10^{-1}$	$(13.2\pm2.7)\times10^{-1}$	$(4.6\pm2.3)\times10^{-1}$	$(2.2\pm1.1)\times10^{-2}$	$(6.8\pm2.0)\times10^{-1}$	$(19.5\pm6.0)\times10^{-2}$	–	–	$(20.8\pm6.2)\times10^{-3}$
G259.245–01.227	$(10.6\pm2.1)\times10^{-1}$	$(41.7\pm8.3)\times10^{-1}$	$(5.3\pm1.1)\times10^{+0}$	$(35.0\pm7.0)\times10^{-1}$	$(13.9\pm7.0)\times10^{-1}$	$(9.1\pm4.6)\times10^{-2}$	$(3.4\pm1.0)\times10^{-1}$	–	–	–	–
G259.250–02.020	–	$(34.3\pm6.9)\times10^{-1}$	$(36.1\pm7.2)\times10^{-1}$	$(22.4\pm4.5)\times10^{-1}$	$(9.6\pm4.8)\times10^{-1}$	$(2.4\pm1.2)\times10^{-2}$	$(3.4\pm1.0)\times10^{-1}$	–	$(24.4\pm7.3)\times10^{-1}$	$(4.6\pm1.4)\times10^{-2}$	$(4.7\pm1.4)\times10^{-2}$
G259.270–00.330	–	$(8.0\pm1.6)\times10^{-2}$	$(20.4\pm4.1)\times10^{-2}$	$(11.0\pm2.2)\times10^{-2}$	$(4.1\pm4.1)\times10^{-2}$	–	–	–	–	$(5.7\pm1.7)\times10^{-3}$	–
G259.272–01.238	$(8.4\pm1.7)\times10^{-1}$	$(9.2\pm1.8)\times10^{+0}$	$(10.8\pm2.2)\times10^{+0}$	$(6.5\pm1.3)\times10^{+0}$	$(2.7\pm1.4)\times10^{+0}$	$(12.5\pm6.2)\times10^{-2}$	–	–	$(12.0\pm3.6)\times10^{-1}$	$(4.2\pm1.3)\times10^{-2}$	$(29.0\pm8.7)\times10^{-3}$
G259.292–01.955	$(12.3\pm2.5)\times10^{+0}$	$(17.8\pm3.6)\times10^{+0}$	$(8.7\pm1.7)\times10^{+0}$	$(40.0\pm8.0)\times10^{-1}$	$(1.1\pm1.1)\times10^{+0}$	$(14.9\pm7.5)\times10^{-2}$	$(6.4\pm1.9)\times10^{-1}$	$(3.8\pm1.2)\times10^{-1}$	$(19.8\pm5.9)\times10^{-1}$	$(4.0\pm1.2)\times10^{-1}$	$(13.2\pm4.0)\times10^{-1}$
G259.302–01.220	–	$(25.6\pm5.1)\times10^{-1}$	$(33.8\pm6.8)\times10^{-1}$	$(23.3\pm4.7)\times10^{-1}$	$(10.1\pm5.0)\times10^{-1}$	$(4.2\pm2.1)\times10^{-2}$	–	–	$(6.9\pm2.1)\times10^{-1}$	–	–
G259.320–01.740	$(17.8\pm3.6)\times10^{-2}$	$(9.7\pm1.9)\times10^{-1}$	$(11.7\pm2.3)\times10^{-1}$	$(7.7\pm1.5)\times10^{-1}$	$(3.6\pm1.8)\times10^{-1}$	–	$(5.1\pm1.5)\times10^{-1}$	–	–	$(12.2\pm3.7)\times10^{-3}$	$(9.8\pm2.9)\times10^{-3}$
G259.320–01.780	–	$(13.5\pm2.7)\times10^{-2}$	$(31.0\pm6.2)\times10^{-2}$	$(26.4\pm5.5)\times10^{-2}$	$(17.5\pm8.8)\times10^{-2}$	–	$(3.5\pm1.1)\times10^{-1}$	–	–	–	$(12.5\pm3.7)\times10^{-3}$
G259.340–01.444	$(30.6\pm6.1)\times10^{-1}$	$(8.1\pm1.6)\times10^{+0}$	$(5.1\pm1.0)\times10^{+0}$	$(27.9\pm5.6)\times10^{-1}$	$(1.0\pm1.0)\times10^{+0}$	–	–	–	–	$(6.2\pm1.9)\times10^{-3}$	$(12.7\pm3.8)\times10^{-2}$
G259.330–01.780	$(36.2\pm7.2)\times10^{-1}$	$(5.6\pm1.1)\times10^{+0}$	$(35.1\pm7.0)\times10^{-1}$	$(16.4\pm3.3)\times10^{-1}$	$(6.3\pm6.3)\times10^{-1}$	–	–	–	–	$(10.5\pm3.1)\times10^{-3}$	$(19.5\pm5.9)\times10^{-2}$
G259.340–00.450	$(42.9\pm8.6)\times10^{-2}$	$(19.2\pm3.8)\times10^{-1}$	$(16.8\pm3.4)\times10^{-1}$	$(9.2\pm1.8)\times10^{-1}$	$(3.2\pm1.6)\times10^{-1}$	–	–	$(6.9\pm2.1)\times10^{-1}$	$(9.2\pm2.8)\times10^{-1}$	$(30.4\pm9.1)\times10^{-3}$	$(23.8\pm7.2)\times10^{-3}$
G259.338–01.445	$(30.6\pm6.1)\times10^{-1}$	$(8.1\pm1.6)\times10^{+0}$	$(5.1\pm1.0)\times10^{+0}$	$(27.9\pm5.6)\times10^{-1}$	$(1.0\pm1.0)\times10^{+0}$	–	–	–	–	$(6.2\pm1.9)\times10^{-3}$	$(12.7\pm3.8)\times10^{-2}$
G259.360–01.740	$(16.4\pm3.3)\times10^{-2}$	$(37.4\pm7.5)\times10^{-2}$	$(25.3\pm5.1)\times10^{-2}$	$(12.6\pm2.6)\times10^{-2}$	$(3.8\pm1.9)\times10^{-2}$	–	–	–	$(5.2\pm1.6)\times10^{-1}$	$(11.0\pm3.3)\times10^{-3}$	$(6.4\pm1.9)\times10^{-3}$
G259.368–01.192	$(14.6\pm2.9)\times10^{-2}$	$(23.9\pm4.8)\times10^{-1}$	$(30.7\pm6.1)\times10^{-1}$	$(18.1\pm3.6)\times10^{-1}$	$(7.3\pm3.6)\times10^{-1}$	$(6.7\pm3.3)\times10^{-2}$	–	$(9.9\pm3.0)\times10^{-1}$	$(13.3\pm4.0)\times10^{-1}$	$(14.0\pm4.2)\times10^{-3}$	$(6.6\pm2.0)\times10^{-3}$
G259.383–01.083	$(5.0\pm1.0)\times10^{-1}$	$(34.7\pm6.9)\times10^{-1}$	$(27.2\pm5.4)\times10^{-1}$	$(16.3\pm3.3)\times10^{-1}$	$(7.1\pm3.6)\times10^{-1}$	$(2.5\pm1.2)\times10^{-2}$	–	$(18.8\pm5.8)\times10^{-2}$	–	$(8.4\pm2.5)\times10^{-2}$	$(9.0\pm2.7)\times10^{-2}$
G259.390–00.180	$(10.1\pm2.0)\times10^{-2}$	$(9.5\pm1.9)\times10^{-1}$	$(10.5\pm2.1)\times10^{-1}$	$(5.6\pm1.1)\times10^{-1}$	$(18.4\pm9.2)\times10^{-2}$	–	$(5.8\pm1.7)\times10^{-1}$	$(17.5\pm5.4)\times10^{-2}$	–	$(5.2\pm1.6)\times10^{-4}$	$(29.4\pm8.8)\times10^{-4}$
G259.390–01.710	$(28.9\pm5.8)\times10^{-2}$	–	$(47.0\pm9.4)\times10^{-2}$	$(33.8\pm6.9)\times10^{-2}$	$(16.7\pm8.4)\times10^{-2}$	–	–	$(6.6\pm2.0)\times10^{-1}$	$(8.5\pm2.6)\times10^{-1}$	$(4.5\pm1.3)\times10^{-4}$	–
G259.400–01.075	$(46.8\pm9.4)\times10^{-1}$	$(27.6\pm5.5)\times10^{+0}$	$(23.2\pm4.6)\times10^{+0}$	$(12.7\pm2.5)\times10^{+0}$	$(5.4\pm2.7)\times10^{+0}$	$(2.4\pm1.2)\times10^{-1}$	$(16.4\pm4.9)\times10^{-1}$	–	–	$(6.3\pm1.9)\times10^{-1}$	$(6.0\pm1.8)\times10^{-1}$
G259.405–01.162	$(30.4\pm6.1)\times10^{-2}$	$(22.0\pm4.4)\times10^{-1}$	$(20.1\pm4.0)\times10^{-1}$	$(12.0\pm2.4)\times10^{-1}$	$(4.5\pm2.3)\times10^{-1}$	–	–	$(13.8\pm4.3)\times10^{-2}$	$(7.8\pm2.4)\times10^{-1}$	$(3.9\pm1.2)\times10^{-2}$	$(3.4\pm1.0)\times10^{-2}$
G259.410–01.488	–	$(6.3\pm1.3)\times10^{+0}$	$(11.0\pm2.2)\times10^{+0}$	$(6.7\pm1.3)\times10^{+0}$	$(3.6\pm1.8)\times10^{+0}$	$(2.4\pm1.2)\times10^{-1}$	–	$(15.9\pm5.0)\times10^{-2}$	$(22.6\pm6.8)\times10^{-1}$	$(22.1\pm6.6)\times10^{-3}$	–
G259.409–01.302	$(9.7\pm2.0)\times10^{-2}$	$(9.4\pm1.9)\times10^{-1}$	$(12.8\pm2.6)\times10^{-1}$	$(7.0\pm1.4)\times10^{-1}$	$(2.5\pm1.3)\times10^{-1}$	–	–	$(23.0\pm7.0)\times10^{-2}$	$(13.0\pm3.9)\times10^{-1}$	–	$(33.1\pm9.9)\times10^{-4}$
G259.410–01.710	–	$(8.2\pm1.6)\times10^{-1}$	$(10.2\pm2.0)\times10^{-1}$	$(8.5\pm1.7)\times10^{-1}$	$(5.2\pm2.6)\times10^{-1}$	–	–	–	–	–	–
G259.417–01.065	$(8.2\pm1.6)\times10^{-1}$	$(33.7\pm6.7)\times10^{-1}$	$(25.6\pm5.1)\times10^{-1}$	$(13.6\pm2.7)\times10^{-1}$	$(5.6\pm2.8)\times10^{-1}$	–	$(5.0\pm1.5)\times10^{-1}$	–	–	$(7.4\pm2.2)\times10^{-2}$	$(10.2\pm3.1)\times10^{-2}$

Table A.3: continued

Name	F_{70} (Jy)	F_{160} (Jy)	F_{250} (Jy)	F_{350} (Jy)	F_{500} (Jy)	F_{8} (Jy)	$F_{12.1}$ (Jy)	$F_{14.7}$ (Jy)	F_{21} (Jy)	F_{14} (Jy)	F_{22} (Jy)
G259.440–01.080	$(5.4\pm1.1)\times10^{+0}$	$(29.3\pm5.9)\times10^{+0}$	$(23.7\pm4.7)\times10^{+0}$	$(13.7\pm2.7)\times10^{+0}$	$(6.1\pm3.0)\times10^{+0}$	$(3.2\pm1.6)\times10^{-1}$	$(10.4\pm3.1)\times10^{-1}$	$(22.7\pm6.8)\times10^{-1}$	$(27.4\pm8.2)\times10^{-1}$	$(6.8\pm2.0)\times10^{-1}$	$(6.2\pm1.9)\times10^{-1}$
G259.450–00.330	$(38.3\pm7.7)\times10^{-2}$	$(8.8\pm1.8)\times10^{-1}$	$(43.9\pm8.8)\times10^{-2}$	$(18.4\pm3.7)\times10^{-2}$	$(5.3\pm2.6)\times10^{-2}$	–	$(16.3\pm5.1)\times10^{-2}$	–	$(6.7\pm2.0)\times10^{-1}$	$(33.1\pm9.9)\times10^{-3}$	$(4.2\pm1.3)\times10^{-2}$
G259.463–01.065	$(19.8\pm4.0)\times10^{-1}$	$(10.6\pm2.1)\times10^{+0}$	$(10.4\pm2.1)\times10^{+0}$	$(6.5\pm1.3)\times10^{+0}$	$(2.6\pm1.3)\times10^{+0}$	$(18.1\pm9.1)\times10^{-2}$	$(6.4\pm1.9)\times10^{-1}$	$(4.2\pm1.3)\times10^{-1}$	$(8.8\pm2.7)\times10^{-1}$	$(3.4\pm1.0)\times10^{-1}$	$(28.1\pm8.4)\times10^{-2}$
G259.457–01.110	$(5.9\pm1.2)\times10^{-1}$	$(6.2\pm1.2)\times10^{+0}$	$(6.6\pm1.3)\times10^{+0}$	$(42.5\pm8.5)\times10^{-1}$	$(18.5\pm9.3)\times10^{-1}$	$(9.6\pm4.8)\times10^{-2}$	–	$(16.2\pm5.1)\times10^{-2}$	$(4.5\pm1.4)\times10^{-1}$	$(15.9\pm4.8)\times10^{-2}$	$(15.9\pm4.8)\times10^{-2}$
G259.560–00.930	$(10.3\pm2.1)\times10^{+1}$	$(7.8\pm1.6)\times10^{+1}$	$(27.5\pm5.5)\times10^{+0}$	$(10.8\pm2.2)\times10^{+0}$	$(3.6\pm1.8)\times10^{+0}$	$(14.5\pm7.2)\times10^{-1}$	$(17.3\pm5.2)\times10^{-1}$	$(12.7\pm3.8)\times10^{-1}$	$(32.5\pm9.7)\times10^{-1}$	$(18.2\pm5.5)\times10^{-1}$	$(4.4\pm1.3)\times10^{+0}$
G259.570–01.020	$(24.5\pm4.9)\times10^{-1}$	$(7.2\pm1.4)\times10^{+0}$	$(5.6\pm1.1)\times10^{+0}$	$(36.7\pm7.3)\times10^{-1}$	$(13.6\pm6.8)\times10^{-1}$	$(13.4\pm6.7)\times10^{-2}$	$(6.2\pm1.9)\times10^{-1}$	–	–	$(9.8\pm2.9)\times10^{-2}$	$(20.6\pm6.2)\times10^{-2}$
G259.570–01.430	$(5.4\pm1.1)\times10^{+0}$	$(5.7\pm1.1)\times10^{+0}$	$(36.8\pm7.4)\times10^{-1}$	$(21.9\pm4.4)\times10^{-1}$	$(9.0\pm9.0)\times10^{-1}$	$(5.7\pm2.9)\times10^{-2}$	$(27.9\pm8.6)\times10^{-2}$	–	–	$(14.7\pm4.4)\times10^{-2}$	$(7.6\pm2.3)\times10^{-1}$
G259.610–01.300	$(48.4\pm9.7)\times10^{-1}$	$(10.4\pm2.1)\times10^{+0}$	$(6.3\pm1.3)\times10^{+0}$	$(37.1\pm7.4)\times10^{-1}$	$(1.2\pm1.2)\times10^{+0}$	$(10.9\pm5.5)\times10^{-2}$	$(26.8\pm8.2)\times10^{-2}$	–	$(4.6\pm1.4)\times10^{-1}$	$(3.7\pm1.1)\times10^{-1}$	$(9.2\pm2.8)\times10^{-1}$
G259.640–01.320	$(17.4\pm3.5)\times10^{+0}$	$(27.2\pm5.4)\times10^{+0}$	$(12.5\pm2.5)\times10^{+0}$	$(43.8\pm8.8)\times10^{-1}$	$(18.3\pm9.1)\times10^{-1}$	$(9.5\pm4.7)\times10^{-1}$	$(8.8\pm2.7)\times10^{-1}$	$(27.5\pm8.4)\times10^{-2}$	$(16.1\pm4.8)\times10^{-1}$	$(13.2\pm4.0)\times10^{-1}$	$(14.6\pm4.4)\times10^{-1}$
G259.652–01.313	$(10.6\pm2.1)\times10^{+0}$	$(12.9\pm2.6)\times10^{+0}$	$(5.8\pm1.2)\times10^{+0}$	$(24.6\pm4.9)\times10^{-1}$	$(1.0\pm1.0)\times10^{+0}$	$(6.1\pm3.1)\times10^{-1}$	$(10.8\pm3.3)\times10^{-1}$	$(5.4\pm1.6)\times10^{-1}$	$(10.5\pm3.2)\times10^{-1}$	$(9.5\pm2.8)\times10^{-1}$	$(14.2\pm4.3)\times10^{-1}$
G259.668–01.318	$(42.6\pm8.5)\times10^{+0}$	$(5.3\pm1.1)\times10^{+1}$	$(24.0\pm4.8)\times10^{+0}$	$(9.8\pm2.0)\times10^{+0}$	$(3.3\pm3.3)\times10^{+0}$	$(6.1\pm3.1)\times10^{-1}$	$(13.6\pm4.1)\times10^{-1}$	$(10.5\pm3.2)\times10^{-1}$	$(4.6\pm1.4)\times10^{+0}$	$(12.9\pm3.9)\times10^{-1}$	$(4.9\pm1.5)\times10^{+0}$
G259.700–01.280	$(28.8\pm5.8)\times10^{+0}$	$(5.2\pm1.0)\times10^{+1}$	$(29.6\pm5.9)\times10^{+0}$	$(15.2\pm3.0)\times10^{+0}$	$(6.9\pm3.5)\times10^{+0}$	$(10.8\pm5.4)\times10^{-1}$	–	$(12.8\pm3.9)\times10^{-1}$	–	$(9.0\pm2.7)\times10^{-1}$	$(21.2\pm6.4)\times10^{-1}$
G259.711–01.934	$(23.8\pm4.8)\times10^{-2}$	$(8.7\pm1.7)\times10^{-1}$	$(12.9\pm2.6)\times10^{-1}$	$(8.6\pm1.7)\times10^{-1}$	$(3.8\pm1.9)\times10^{-1}$	–	–	$(5.7\pm1.7)\times10^{-1}$	$(13.9\pm4.2)\times10^{-1}$	–	–
G259.750–01.340	$(5.5\pm1.1)\times10^{+0}$	$(11.7\pm2.3)\times10^{+0}$	$(5.1\pm1.0)\times10^{+0}$	$(22.1\pm4.4)\times10^{-1}$	$(6.9\pm3.4)\times10^{-1}$	$(2.5\pm1.3)\times10^{-1}$	$(10.3\pm3.1)\times10^{-1}$	–	–	$(4.2\pm1.3)\times10^{-1}$	$(4.0\pm1.2)\times10^{-1}$
G259.860–02.030	$(5.1\pm1.0)\times10^{-2}$	$(7.6\pm1.5)\times10^{-2}$	$(10.4\pm2.1)\times10^{-2}$	$(47.3\pm9.9)\times10^{-3}$	$(2.0\pm2.0)\times10^{-2}$	–	$(27.3\pm8.5)\times10^{-2}$	$(24.8\pm7.7)\times10^{-2}$	–	$(31.0\pm9.3)\times10^{-4}$	–
G259.870–02.400	$(20.6\pm4.1)\times10^{-2}$	$(10.6\pm2.1)\times10^{+0}$	$(15.9\pm3.2)\times10^{+0}$	$(11.8\pm2.4)\times10^{+0}$	$(5.1\pm2.6)\times10^{+0}$	$(12.2\pm6.1)\times10^{-2}$	–	$(7.7\pm2.3)\times10^{-1}$	–	–	–
G259.880–02.020	$(24.1\pm4.8)\times10^{-2}$	$(25.7\pm5.1)\times10^{-2}$	$(17.1\pm3.4)\times10^{-2}$	$(10.6\pm2.2)\times10^{-2}$	$(2.1\pm2.1)\times10^{-2}$	–	–	–	–	$(6.0\pm1.8)\times10^{-3}$	$(6.1\pm1.8)\times10^{-3}$
G259.880–02.410	$(20.7\pm4.1)\times10^{-2}$	$(23.3\pm4.7)\times10^{-1}$	$(38.1\pm7.6)\times10^{-1}$	$(26.8\pm5.4)\times10^{-1}$	$(11.7\pm5.9)\times10^{-1}$	–	$(4.6\pm1.4)\times10^{-1}$	–	–	$(14.8\pm4.5)\times10^{-3}$	$(4.8\pm1.4)\times10^{-2}$
G259.890–02.420	$(34.2\pm6.9)\times10^{-2}$	$(47.0\pm9.4)\times10^{-1}$	$(5.4\pm1.1)\times10^{+0}$	$(38.9\pm7.8)\times10^{-1}$	$(16.2\pm8.1)\times10^{-1}$	–	–	–	–	$(5.7\pm1.7)\times10^{-3}$	$(18.1\pm5.4)\times10^{-3}$
G259.900–01.970	–	$(15.6\pm3.1)\times10^{-2}$	$(12.1\pm2.5)\times10^{-2}$	$(5.6\pm1.3)\times10^{-2}$	–	–	$(31.8\pm9.8)\times10^{-2}$	–	–	$(3.4\pm1.0)\times10^{-3}$	$(19.9\pm6.0)\times10^{-4}$
G259.900–02.430	$(44.3\pm8.9)\times10^{-2}$	$(23.3\pm4.7)\times10^{-1}$	$(28.3\pm5.7)\times10^{-1}$	$(20.0\pm4.0)\times10^{-1}$	$(7.9\pm7.9)\times10^{-1}$	–	–	–	–	$(8.0\pm2.4)\times10^{-3}$	$(5.9\pm1.8)\times10^{-2}$
G259.950–01.330	$(8.3\pm1.7)\times10^{-2}$	$(40.0\pm8.0)\times10^{-2}$	$(22.6\pm4.5)\times10^{-2}$	$(11.3\pm2.4)\times10^{-2}$	$(6.2\pm6.2)\times10^{-2}$	$(17.0\pm8.6)\times10^{-3}$	$(3.7\pm1.1)\times10^{-1}$	$(22.9\pm7.0)\times10^{-2}$	$(6.8\pm2.1)\times10^{-1}$	$(8.6\pm2.6)\times10^{-3}$	$(27.8\pm8.3)\times10^{-4}$
G260.000–00.160	$(6.4\pm1.3)\times10^{+0}$	$(5.1\pm1.0)\times10^{+1}$	$(40.1\pm8.0)\times10^{+0}$	$(21.2\pm4.2)\times10^{+0}$	$(8.8\pm4.4)\times10^{+0}$	$(3.0\pm1.5)\times10^{-1}$	–	$(9.7\pm2.9)\times10^{-1}$	–	$(13.9\pm4.2)\times10^{-1}$	$(14.8\pm4.4)\times10^{-1}$
G225.472–01.674	$(9.0\pm1.8)\times10^{-2}$	$(36.9\pm7.4)\times10^{-2}$	$(24.1\pm4.8)\times10^{-2}$	$(15.2\pm3.1)\times10^{-2}$	$(3.7\pm3.7)\times10^{-2}$	–	–	–	–	–	$(5.0\pm1.5)\times10^{-3}$
G226.125–00.316	$(21.5\pm4.3)\times10^{-2}$	$(8.4\pm1.7)\times10^{-2}$	$(20.7\pm4.3)\times10^{-2}$	$(15.2\pm3.5)\times10^{-2}$	–	$(4.4\pm2.2)\times10^{-2}$	$(20.9\pm6.5)\times10^{-2}$	$(4.1\pm1.2)\times10^{-1}$	–	$(5.8\pm1.7)\times10^{-4}$	–
G232.062–00.126	$(15.3\pm3.1)\times10^{-2}$	$(10.3\pm2.1)\times10^{-1}$	$(14.0\pm2.8)\times10^{-1}$	$(8.2\pm1.6)\times10^{-1}$	$(3.4\pm1.7)\times10^{-1}$	$(9.1\pm4.6)\times10^{-2}$	$(25.8\pm7.9)\times10^{-2}$	$(7.6\pm2.3)\times10^{-1}$	–	$(3.6\pm1.1)\times10^{-2}$	$(3.6\pm1.1)\times10^{-2}$
G231.841–01.752	$(23.8\pm4.8)\times10^{-2}$	$(5.7\pm1.1)\times10^{-1}$	$(5.9\pm1.2)\times10^{-1}$	$(31.3\pm6.3)\times10^{-2}$	$(13.4\pm6.7)\times10^{-2}$	–	$(27.7\pm8.6)\times10^{-2}$	–	$(7.1\pm2.2)\times10^{-1}$	$(21.8\pm6.5)\times10^{-3}$	$(8.1\pm2.4)\times10^{-3}$
G232.894–00.613	$(49.0\pm9.8)\times10^{-2}$	$(7.8\pm1.6)\times10^{-1}$	$(17.2\pm3.4)\times10^{-1}$	$(10.7\pm2.1)\times10^{-1}$	$(5.4\pm2.7)\times10^{-1}$	–	–	–	$(15.2\pm4.6)\times10^{-1}$	$(4.4\pm1.3)\times10^{-3}$	$(9.1\pm2.7)\times10^{-3}$
G233.067–01.271	$(32.8\pm6.6)\times10^{-2}$	$(12.7\pm2.5)\times10^{-1}$	$(12.8\pm2.6)\times10^{-1}$	$(7.5\pm1.5)\times10^{-1}$	$(3.8\pm1.9)\times10^{-1}$	–	–	$(14.5\pm4.4)\times10^{-1}$	$(7.7\pm2.3)\times10^{-1}$	$(8.9\pm2.7)\times10^{-2}$	$(5.9\pm1.8)\times10^{-2}$
G233.840–00.183	$(38.5\pm7.7)\times10^{+1}$	$(20.6\pm4.1)\times10^{+1}$	$(6.2\pm1.2)\times10^{+1}$	$(23.6\pm4.7)\times10^{+0}$	$(6.3\pm6.3)\times10^{+0}$	$(15.2\pm7.6)\times10^{+0}$	$(21.1\pm6.3)\times10^{+0}$	$(28.3\pm8.5)\times10^{+0}$	$(10.4\pm3.1)\times10^{+1}$	$(31.7\pm9.5)\times10^{-1}$	$(10.1\pm3.0)\times10^{+0}$
G233.757–01.269	$(14.8\pm3.0)\times10^{-2}$	$(29.1\pm5.8)\times10^{-2}$	$(49.5\pm9.9)\times10^{-2}$	$(40.7\pm8.2)\times10^{-2}$	$(19.2\pm9.6)\times10^{-2}$	$(7.3\pm3.7)\times10^{-2}$	–	$(24.6\pm7.5)\times10^{-2}$	–	$(11.1\pm3.3)\times10^{-3}$	$(8.1\pm2.4)\times10^{-3}$
G234.476–00.003	$(6.0\pm1.2)\times10^{+0}$	$(18.3\pm3.7)\times10^{+0}$	$(12.8\pm2.6)\times10^{+0}$	$(7.0\pm1.4)\times10^{+0}$	$(2.8\pm1.4)\times10^{+0}$	$(3.8\pm1.9)\times10^{-1}$	–	$(11.5\pm3.5)\times10^{-1}$	–	$(5.6\pm1.7)\times10^{-1}$	$(3.9\pm1.2)\times10^{-1}$
G242.625–00.878	$(6.1\pm1.2)\times10^{-1}$	$(10.0\pm2.0)\times10^{-1}$	$(13.8\pm2.8)\times10^{-1}$	$(9.2\pm1.8)\times10^{-1}$	$(3.0\pm1.5)\times10^{-1}$	–	–	$(4.4\pm1.3)\times10^{-1}$	$(7.8\pm2.4)\times10^{-1}$	$(26.0\pm7.8)\times10^{-4}$	$(25.1\pm7.5)\times10^{-4}$
G247.796–00.823	$(16.5\pm3.3)\times10^{-2}$	$(21.1\pm4.2)\times10^{-2}$	$(20.4\pm4.1)\times10^{-2}$	$(22.0\pm4.4)\times10^{-2}$	$(2.4\pm1.2)\times10^{-1}$	$(12.2\pm6.1)\times10^{-2}$	–	$(26.1\pm7.9)\times10^{-2}$	$(7.1\pm2.2)\times10^{-1}$	$(13.7\pm4.1)\times10^{-3}$	$(16.0\pm4.8)\times10^{-3}$
G252.029–01.864	–	–	$(18.1\pm3.6)\times10^{-2}$	$(8.5\pm1.7)\times10^{-2}$	$(4.0\pm2.0)\times10^{-2}$	–	–	–	–	$(16.6\pm5.0)\times10^{-4}$	$(16.5\pm4.9)\times10^{-4}$
G252.173–01.872	$(9.6\pm1.9)\times10^{-2}$	$(26.7\pm5.3)\times10^{-2}$	$(38.8\pm7.8)\times10^{-2}$	$(23.2\pm4.7)\times10^{-2}$	$(8.1\pm4.1)\times10^{-2}$	–	–	–	–	$(25.1\pm7.5)\times10^{-4}$	$(31.5\pm9.5)\times10^{-4}$
G253.950–00.563	$(40.0\pm8.0)\times10^{-1}$	$(20.7\pm4.1)\times10^{+0}$	$(15.8\pm3.2)\times10^{+0}$	$(8.8\pm1.8)\times10^{+0}$	$(3.9\pm2.0)\times10^{+0}$	$(2.3\pm1.2)\times10^{-1}$	–	–	–	$(5.0\pm1.5)\times10^{-1}$	$(5.6\pm1.7)\times10^{-1}$
G256.422–02.208	–	$(10.3\pm2.1)\times10^{-1}$	$(16.2\pm3.2)\times10^{-1}$	$(10.1\pm2.0)\times10^{-1}$	$(3.7\pm1.9)\times10^{-1}$	$(7.5\pm3.7)\times10^{-2}$	$(10.0\pm3.0)\times10^{-1}$	–	–	$(18.3\pm5.5)\times10^{-3}$	$(22.5\pm6.7)\times10^{-3}$
G257.870–01.498	$(14.0\pm2.8)\times10^{-2}$	$(5.9\pm1.2)\times10^{-1}$	$(41.2\pm8.2)\times10^{-2}$	$(24.1\pm4.8)\times10^{-2}$	$(7.5\pm3.8)\times10^{-2}$	–	–	–	–	$(18.4\pm5.5)\times10^{-4}$	$(21.1\pm6.3)\times10^{-4}$
G257.894–01.885	$(11.5\pm2.3)\times10^{-2}$	$(5.9\pm1.2)\times10^{-1}$	$(5.5\pm1.1)\times10^{-1}$	$(27.7\pm5.6)\times10^{-2}$	$(10.1\pm5.1)\times10^{-2}$	–	–	–	$(6.7\pm2.1)\times10^{-1}$	$(12.2\pm3.6)\times10^{-3}$	$(4.8\pm1.4)\times10^{-3}$
G258.090–01.577	$(33.1\pm6.6)\times10^{-2}$	$(5.9\pm1.2)\times10^{-2}$	$(20.8\pm4.2)\times10^{-2}$	$(17.8\pm3.6)\times10^{-2}$	$(9.2\pm4.6)\times10^{-2}$	–	–	$(4.3\pm1.3)\times10^{-1}$	–	$(20.2\pm6.1)\times10^{-4}$	$(18.6\pm5.6)\times10^{-4}$
G258.114–01.904	$(35.3\pm7.1)\times10^{-2}$	$(23.8\pm4.8)\times10^{-2}$	$(25.7\pm5.2)\times10^{-2}$	$(16.2\pm3.4)\times10^{-2}$	$(7.1\pm7.1)\times10^{-2}$	–	–	–	–	–	–
G258.347–02.182	$(21.3\pm4.7)\times10^{-3}$	$(17.2\pm3.4)\times10^{-2}$	$(47.3\pm9.5)\times10^{-2}$	$(26.7\pm5.4)\times10^{-2}$	$(16.4\pm8.2)\times10^{-2}$	–	–	–	–	$(27.6\pm8.3)\times10^{-3}$	$(19.0\pm5.7)\times10^{-3}$

Table A.3: continued

Name	F_{70} (Jy)	F_{160} (Jy)	F_{250} (Jy)	F_{350} (Jy)	F_{500} (Jy)	F_{8} (Jy)	$F_{12.1}$ (Jy)	$F_{14.7}$ (Jy)	F_{21} (Jy)	F_{14} (Jy)	F_{22} (Jy)
G258.681–01.774	–	$(27.1\pm5.4)\times10^{-2}$	$(28.6\pm5.7)\times10^{-2}$	$(16.5\pm3.4)\times10^{-2}$	$(7.0\pm7.0)\times10^{-2}$	–	–	–	–	–	–
G258.691–01.773	–	$(28.5\pm5.7)\times10^{-2}$	$(19.2\pm3.9)\times10^{-2}$	$(10.9\pm2.4)\times10^{-2}$	–	–	$(3.4\pm1.0)\times10^{-1}$	–	–	$(7.8\pm2.3)\times10^{-3}$	$(5.3\pm1.6)\times10^{-3}$
G259.408–00.860	$(27.3\pm5.5)\times10^{-2}$	$(6.1\pm1.2)\times10^{-1}$	$(35.2\pm7.0)\times10^{-2}$	$(19.3\pm3.9)\times10^{-2}$	$(6.0\pm3.1)\times10^{-2}$	$(16.7\pm8.5)\times10^{-3}$	$(3.5\pm1.1)\times10^{-1}$	$(3.8\pm1.2)\times10^{-1}$	–	$(16.5\pm4.9)\times10^{-3}$	$(15.7\pm4.7)\times10^{-3}$
G259.446–00.838	–	$(30.0\pm6.0)\times10^{-2}$	$(30.8\pm6.2)\times10^{-2}$	$(17.9\pm3.7)\times10^{-2}$	$(6.2\pm3.1)\times10^{-2}$	–	–	$(23.0\pm7.0)\times10^{-2}$	$(4.1\pm1.3)\times10^{-1}$	$(10.8\pm3.2)\times10^{-3}$	$(6.7\pm2.0)\times10^{-3}$
G259.643–00.659	$(6.7\pm1.4)\times10^{-2}$	$(48.8\pm9.8)\times10^{-2}$	$(48.7\pm9.8)\times10^{-2}$	$(24.0\pm4.8)\times10^{-2}$	$(9.6\pm4.8)\times10^{-2}$	–	–	–	$(4.0\pm1.2)\times10^{-1}$	$(9.8\pm2.9)\times10^{-3}$	$(5.8\pm1.8)\times10^{-3}$
G259.480–01.135	$(20.0\pm4.5)\times10^{-3}$	$(8.3\pm1.7)\times10^{-1}$	$(10.8\pm2.2)\times10^{-1}$	$(5.1\pm1.0)\times10^{-1}$	$(2.2\pm1.1)\times10^{-1}$	–	$(23.0\pm7.1)\times10^{-2}$	–	$(9.0\pm2.7)\times10^{-1}$	$(20.8\pm6.2)\times10^{-3}$	$(20.8\pm6.2)\times10^{-3}$
G259.691–00.614	$(15.3\pm3.1)\times10^{-2}$	$(7.6\pm1.5)\times10^{-1}$	$(36.4\pm7.3)\times10^{-2}$	$(22.1\pm4.4)\times10^{-2}$	–	$(3.2\pm1.6)\times10^{-2}$	–	–	$(4.6\pm1.4)\times10^{-1}$	$(4.5\pm1.3)\times10^{-2}$	$(24.4\pm7.3)\times10^{-3}$
G259.545–00.807	–	$(9.8\pm2.0)\times10^{-1}$	$(11.1\pm2.2)\times10^{-1}$	$(7.9\pm1.6)\times10^{-1}$	$(3.3\pm1.7)\times10^{-1}$	–	$(20.4\pm6.3)\times10^{-2}$	$(6.5\pm2.0)\times10^{-1}$	$(6.2\pm1.9)\times10^{-1}$	$(31.9\pm9.6)\times10^{-3}$	$(25.8\pm7.7)\times10^{-3}$
G259.847–00.465	$(10.3\pm2.1)\times10^{-2}$	$(5.6\pm1.1)\times10^{-1}$	$(6.1\pm1.2)\times10^{-1}$	$(30.1\pm6.0)\times10^{-2}$	$(15.9\pm8.0)\times10^{-2}$	$(7.3\pm3.7)\times10^{-2}$	$(21.5\pm6.7)\times10^{-2}$	–	$(7.7\pm2.3)\times10^{-1}$	$(32.0\pm9.6)\times10^{-3}$	$(22.0\pm6.6)\times10^{-3}$
G259.908–01.942	$(13.0\pm2.6)\times10^{-2}$	$(6.8\pm1.4)\times10^{-1}$	$(6.9\pm1.4)\times10^{-1}$	$(18.2\pm3.7)\times10^{-2}$	$(7.1\pm3.6)\times10^{-2}$	–	–	$(5.8\pm1.7)\times10^{-1}$	$(15.1\pm4.5)\times10^{-1}$	$(22.7\pm6.8)\times10^{-3}$	$(26.4\pm7.9)\times10^{-3}$

Table A.4: Source parameters obtained from the SEDs for all sources: Galactic longitude ℓ and latitude b, heliocentric distance $R_{\rm hel}$, aperture diameter $D_{\rm app}$, linear size $D_{\rm lin}$, evolutionary class, dust temperature $T_{\rm dust}$, and optical depth τ_{350}.

Name	$\ell_{\rm app}$ (deg)	$b_{\rm app}$ (deg)	$R_{\rm hel}$ (kpc)	$D_{\rm app}$ ($''$)	$D_{\rm lin}$ (pc)	Class	$T_{\rm dust}$ (K)	τ_{350}
G225.020–00.590	225.017	−0.588	1.3	88.9	0.13	Quiescent	10.3 ± 0.7	$(20.6 \pm 8.4) \times 10^{-5}$
G225.030+00.060	225.029	0.058	1.6	68.3	0.11	Protostellar	15.8 ± 0.2	$(126.6 \pm 6.4) \times 10^{-7}$
G225.080+00.060	225.082	0.060	1.6	63.3	0.10	YSO	14.6 ± 0.6	$(41.1 \pm 7.8) \times 10^{-6}$
G225.160–00.830	225.160	−0.835	1.7	69.6	0.12	YSO	19.9 ± 1.4	$(19.7 \pm 4.9) \times 10^{-6}$
G225.160–00.840	225.163	−0.841	1.7	65.9	0.11	Protostellar	16.5 ± 2.0	$(16.0 \pm 7.9) \times 10^{-6}$
G225.170–00.750	225.167	−0.746	1.3	53.1	0.06	YSO	16.5 ± 1.9	$(2.5 \pm 1.2) \times 10^{-5}$
G225.210–01.110	225.215	−1.110	1.3	200.0	0.31	Quiescent	12.0 ± 0.1	$(32.1 \pm 1.9) \times 10^{-5}$
G225.220–01.200	225.220	−1.195	1.2	59.3	0.07	Quiescent	17.7 ± 0.6	$(26.9 \pm 3.6) \times 10^{-6}$
G225.230–00.960	225.228	−0.961	1.3	89.5	0.13	Quiescent	16.1 ± 0.5	$(51.4 \pm 7.0) \times 10^{-6}$
G225.240–01.110	225.243	−1.106	1.2	42.5	0.03	Quiescent	15.3 ± 0.2	$(48.7 \pm 2.4) \times 10^{-6}$
G225.300–01.090	225.300	−1.093	1.3	55.3	0.07	YSO	12.7 ± 1.8	$(10.7 \pm 7.7) \times 10^{-5}$
G225.320–00.280	225.319	−0.277	1.3	90.5	0.13	Quiescent	13.1 ± 0.6	$(25.6 \pm 5.3) \times 10^{-5}$
G225.320–01.100	225.323	−1.103	1.3	85.7	0.12	Quiescent	9.7 ± 0.9	$(4.8 \pm 3.0) \times 10^{-4}$
G225.320–01.170	225.315	−1.170	1.2	51.8	0.05	Protostellar	14.8 ± 2.0	$(11.9 \pm 7.0) \times 10^{-5}$
G225.330–00.540	225.330	−0.535	1.6	42.5	0.04	YSO	21.0 ± 3.4	$(4.9 \pm 2.6) \times 10^{-4}$
G225.330–01.120	225.333	−1.120	1.3	47.5	0.05	Protostellar	14.5 ± 0.3	$(101.3 \pm 8.6) \times 10^{-6}$
G225.370–01.380	225.373	−1.376	1.2	51.8	0.05	YSO	17.2 ± 0.6	$(27.1 \pm 3.4) \times 10^{-6}$
G225.380–00.540	225.378	−0.543	1.4	77.6	0.12	Quiescent	12.8 ± 0.2	$(32.1 \pm 2.8) \times 10^{-5}$
G225.390–00.990	225.390	−0.985	1.3	48.6	0.05	Protostellar	14.9 ± 0.6	$(9.8 \pm 1.6) \times 10^{-5}$
G225.390–01.370	225.387	−1.371	1.2	74.5	0.09	Protostellar	14.1 ± 2.1	$(5.3 \pm 3.6) \times 10^{-5}$
G225.400–00.560	225.400	−0.562	1.4	42.7	0.04	YSO	19.9 ± 2.1	$(19.5 \pm 7.3) \times 10^{-5}$
G225.440–00.390	225.437	−0.388	1.6	132.3	0.25	YSO	14.8 ± 0.6	$(17.2 \pm 2.9) \times 10^{-5}$
G225.460–01.680	225.461	−1.678	1.4	44.8	0.04	Protostellar	18.6 ± 0.1	$(36.4 \pm 1.1) \times 10^{-6}$
G225.470–01.680	225.466	−1.676	1.4	42.5	0.04	Protostellar	20.3 ± 0.4	$(24.6 \pm 1.6) \times 10^{-6}$
G225.480–00.230	225.479	−0.233	1.4	157.5	0.26	Quiescent	11.5 ± 0.1	$(50.0 \pm 2.6) \times 10^{-5}$
G225.480–01.790	225.480	−1.795	1.4	46.1	0.05	YSO	21.0 ± 1.2	$(6.8 \pm 1.3) \times 10^{-5}$
G225.480–01.800	225.480	−1.795	1.4	42.5	0.04	YSO	22.4 ± 1.5	$(5.1 \pm 2.7) \times 10^{-5}$
G225.490–00.400	225.487	−0.402	1.6	157.5	0.30	YSO	15.0 ± 0.1	$(156.1 \pm 5.6) \times 10^{-6}$
G225.490–01.780	225.493	−1.781	1.4	64.9	0.09	Protostellar	21.3 ± 1.3	$(5.5 \pm 1.1) \times 10^{-5}$
G225.490–01.810	225.486	−1.808	1.4	101.7	0.16	YSO	21.1 ± 3.8	$(5.9 \pm 3.5) \times 10^{-5}$
G225.500–01.230	225.497	−1.226	1.0	45.1	0.03	Quiescent	19.5 ± 0.9	$(54.8 \pm 8.6) \times 10^{-7}$
G225.500–01.770	225.498	−1.773	1.4	42.5	0.04	Protostellar	20.1 ± 0.4	$(66.9 \pm 4.4) \times 10^{-6}$
G225.510–01.230	225.515	−1.230	1.0	47.0	0.04	Protostellar	16.3 ± 0.8	$(16.4 \pm 3.1) \times 10^{-6}$
G225.510–01.740	225.506	−1.738	1.3	200.0	0.31	YSO	25.7 ± 2.5	$(1.9 \pm 1.4) \times 10^{-6}$
G225.510–01.780	225.510	−1.778	1.4	131.2	0.21	YSO	18.1 ± 0.2	$(86.0 \pm 2.7) \times 10^{-6}$
G225.660–00.220	225.655	−0.220	1.6	111.6	0.20	Protostellar	16.2 ± 0.3	$(83.4 \pm 6.4) \times 10^{-6}$
G225.780–00.940	225.780	−0.943	1.3	75.1	0.10	Quiescent	12.3 ± 0.2	$(10.1 \pm 1.0) \times 10^{-4}$
G225.980+00.080	225.982	0.078	1.6	66.1	0.11	Protostellar	20.2 ± 1.6	$(18.7 \pm 5.0) \times 10^{-6}$
G226.117–00.349	226.117	−0.352	1.3	42.5	0.03	YSO	25.8 ± 2.0	$(16.6 \pm 3.5) \times 10^{-5}$
G226.280–02.070	226.280	−2.068	1.1	55.9	0.06	Protostellar	18.0 ± 0.3	$(24.9 \pm 1.5) \times 10^{-6}$
G226.330–02.030	226.333	−2.033	1.1	72.8	0.08	Quiescent	16.2 ± 0.5	$(36.5 \pm 4.5) \times 10^{-6}$
G226.353–00.766	226.353	−0.768	1.3	42.5	0.03	YSO	24.9 ± 6.9	$(10.6 \pm 8.3) \times 10^{-4}$
G226.670–02.060	226.668	−2.058	1.3	73.2	0.10	Quiescent	16.2 ± 0.8	$(26.3 \pm 5.2) \times 10^{-6}$
G227.040–00.900	227.042	−0.898	6.0	51.8	0.27	YSO	13.0 ± 0.3	$(19.2 \pm 2.2) \times 10^{-5}$
G227.180–00.460	227.177	−0.463	1.7	42.5	0.05	Quiescent	19.1 ± 0.6	$(44.1 \pm 4.8) \times 10^{-7}$
G227.230–00.830	227.230	−0.832	1.7	78.5	0.14	Quiescent	15.2 ± 0.7	$(39.0 \pm 8.2) \times 10^{-6}$

Table A.4: continued

Name	$\ell_{\rm app}$ (deg)	$b_{\rm app}$ (deg)	$R_{\rm hel}$ (kpc)	$D_{\rm app}$ ($''$)	$D_{\rm lin}$ (pc)	Class	$T_{\rm dust}$ (K)	τ_{350}
G227.570–01.140	227.567	−1.143	8.9	42.5	0.24	YSO	20.6 ± 2.1	$(11.4 \pm 3.9) \times 10^{-5}$
G227.650–01.286	227.652	−1.285	8.7	42.5	0.23	Quiescent	14.6 ± 0.2	$(77.0 \pm 4.0) \times 10^{-6}$
G227.689–00.121	227.691	−0.122	5.0	125.4	0.73	YSO	26.1 ± 6.6	$(6.0 \pm 4.2) \times 10^{-6}$
G227.792–00.104	227.793	−0.105	4.7	129.9	0.71	YSO	24.5 ± 2.5	$(26.8 \pm 7.7) \times 10^{-6}$
G227.800–00.080	227.798	−0.077	4.9	68.4	0.34	YSO	20.2 ± 4.7	$(2.7 \pm 2.2) \times 10^{-5}$
G227.800–00.140	227.801	−0.137	5.0	80.2	0.43	Protostellar	24.3 ± 6.2	$(3.6 \pm 2.6) \times 10^{-5}$
G227.810–00.120	227.813	−0.123	5.0	42.5	0.13	YSO	21.9 ± 0.9	$(9.8 \pm 1.3) \times 10^{-5}$
G227.815–00.129	227.815	−0.123	5.0	42.5	0.13	YSO	22.2 ± 2.1	$(11.0 \pm 3.2) \times 10^{-5}$
G227.820–00.140	227.821	−0.137	4.9	109.1	0.61	YSO	23.9 ± 0.8	$(97.0 \pm 9.4) \times 10^{-6}$
G227.820–00.160	227.815	−0.160	4.9	90.1	0.49	YSO	23.9 ± 0.6	$(5.5 \pm 1.2) \times 10^{-5}$
G227.862–00.243	227.861	−0.242	5.0	63.5	0.32	YSO	19.1 ± 1.7	$(5.0 \pm 1.6) \times 10^{-5}$
G227.880–01.780	227.879	−1.779	1.6	74.0	0.13	Quiescent	9.9 ± 0.9	$(1.9 \pm 1.2) \times 10^{-4}$
G227.910–01.880	227.910	−1.879	1.6	99.6	0.18	Quiescent	14.7 ± 0.3	$(85.4 \pm 8.6) \times 10^{-6}$
G227.940–00.139	227.941	−0.138	6.6	42.5	0.17	Protostellar	13.7 ± 0.2	$(14.7 \pm 1.0) \times 10^{-5}$
G228.030+00.010	228.032	0.012	4.9	50.1	0.20	Quiescent	13.9 ± 0.6	$(8.9 \pm 1.9) \times 10^{-5}$
G228.030+00.020	228.031	0.015	4.9	48.6	0.19	Quiescent	13.3 ± 0.4	$(11.0 \pm 1.5) \times 10^{-5}$
G228.027–00.924	228.027	−0.923	3.3	60.4	0.19	Quiescent	12.5 ± 0.5	$(13.1 \pm 3.0) \times 10^{-5}$
G228.026–00.946	228.027	−0.945	3.3	88.0	0.32	Quiescent	13.1 ± 0.2	$(95.1 \pm 7.1) \times 10^{-6}$
G228.300–00.970	228.300	−0.975	3.2	53.9	0.15	Protostellar	16.6 ± 0.1	$(29.5 \pm 3.0) \times 10^{-6}$
G228.710–00.910	228.713	−0.908	4.3	66.4	0.29	YSO	12.4 ± 0.8	$(12.5 \pm 4.2) \times 10^{-5}$
G229.750+00.030	229.748	0.027	7.2	83.6	0.66	Quiescent	16.4 ± 1.1	$(4.7 \pm 1.3) \times 10^{-5}$
G229.770+00.040	229.767	0.042	7.0	63.8	0.44	Protostellar	20.3 ± 4.0	$(6.2 \pm 4.1) \times 10^{-5}$
G229.770+00.060	229.772	0.060	7.1	55.5	0.36	YSO	23.4 ± 1.1	$(22.7 \pm 3.2) \times 10^{-5}$
G229.780+00.050	229.777	0.053	7.4	42.5	0.20	YSO	24.9 ± 0.2	$(66.3 \pm 4.5) \times 10^{-6}$
G229.790–00.680	229.787	−0.682	3.6	42.5	0.10	Quiescent	11.8 ± 0.2	$(26.0 \pm 2.8) \times 10^{-5}$
G229.800–00.360	229.805	−0.360	7.4	55.6	0.38	Protostellar	13.9 ± 2.0	$(2.4 \pm 1.6) \times 10^{-4}$
G229.900–00.650	229.903	−0.653	3.6	59.2	0.20	Protostellar	12.3 ± 0.3	$(16.3 \pm 2.1) \times 10^{-5}$
G230.340–00.610	230.340	−0.608	3.4	69.2	0.24	YSO	26.5 ± 0.4	$(60.5 \pm 6.9) \times 10^{-6}$
G230.350–00.600	230.353	−0.598	3.4	59.9	0.20	YSO	29.9 ± 1.0	$(7.5 \pm 1.6) \times 10^{-5}$
G230.390–00.780	230.390	−0.785	3.5	55.9	0.18	Quiescent	18.9 ± 0.6	$(17.6 \pm 2.0) \times 10^{-6}$
G230.940–00.400	230.938	−0.403	3.6	60.5	0.21	Protostellar	13.6 ± 0.4	$(9.3 \pm 1.2) \times 10^{-5}$
G231.010–00.180	231.010	−0.175	2.9	88.5	0.28	YSO	19.4 ± 0.1	$(37.5 \pm 2.6) \times 10^{-6}$
G231.070–00.130	231.065	−0.130	2.9	100.2	0.33	YSO	21.0 ± 5.0	$(12.1 \pm 9.2) \times 10^{-5}$
G231.130–00.320	231.127	−0.317	2.8	70.7	0.21	YSO	20.7 ± 1.0	$(13.1 \pm 2.1) \times 10^{-5}$
G231.140–00.330	231.140	−0.335	2.8	157.5	0.52	YSO	20.4 ± 0.7	$(14.2 \pm 1.6) \times 10^{-5}$
G231.240–00.390	231.239	−0.392	2.5	200.0	0.60	YSO	20.7 ± 0.6	$(5.0 \pm 1.3) \times 10^{-5}$
G231.250–00.330	231.250	−0.327	2.8	69.9	0.20	YSO	22.0 ± 0.5	$(40.3 \pm 3.1) \times 10^{-6}$
G231.260–00.290	231.257	−0.287	2.9	78.0	0.24	YSO	20.2 ± 1.3	$(7.9 \pm 1.7) \times 10^{-5}$
G231.280–00.260	231.282	−0.260	2.6	61.0	0.15	Protostellar	18.8 ± 3.4	$(5.8 \pm 3.7) \times 10^{-5}$
G231.280–00.280	231.280	−0.282	2.6	158.9	0.49	YSO	20.6 ± 4.1	$(5.8 \pm 3.8) \times 10^{-5}$
G231.290–00.360	231.294	−0.357	4.1	61.0	0.24	Protostellar	22.9 ± 2.0	$(1.7 \pm 1.1) \times 10^{-5}$
G231.300–00.310	231.299	−0.310	1.7	74.3	0.13	Protostellar	14.0 ± 0.9	$(13.7 \pm 4.1) \times 10^{-5}$
G231.310–00.290	231.314	−0.287	1.7	42.5	0.05	YSO	23.6 ± 0.6	$(21.9 \pm 4.6) \times 10^{-6}$
G231.320–00.280	231.320	−0.280	2.6	50.7	0.11	Protostellar	22.1 ± 0.3	$(51.0 \pm 6.4) \times 10^{-6}$
G231.330–00.380	231.329	−0.378	2.5	200.0	0.60	YSO	18.9 ± 1.0	$(11.2 \pm 2.0) \times 10^{-5}$
G231.330–00.690	231.328	−0.688	3.5	62.8	0.22	YSO	14.8 ± 1.7	$(5.5 \pm 2.8) \times 10^{-5}$
G231.470–01.860	231.466	−1.863	3.7	144.6	0.63	Protostellar	13.9 ± 0.1	$(164.8 \pm 8.3) \times 10^{-6}$
G231.540–00.880	231.543	−0.883	3.7	49.8	0.15	Protostellar	16.5 ± 0.9	$(12.2 \pm 2.6) \times 10^{-6}$
G231.590–00.840	231.588	−0.840	3.7	42.5	0.10	Quiescent	15.2 ± 0.7	$(34.7 \pm 6.6) \times 10^{-6}$

Table A.4: continued

Name	$\ell_{\rm app}$ (deg)	$b_{\rm app}$ (deg)	$R_{\rm hel}$ (kpc)	$D_{\rm app}$ ($''$)	$D_{\rm lin}$ (pc)	Class	$T_{\rm dust}$ (K)	τ_{350}
G231.610–01.260	231.613	−1.258	3.3	70.2	0.24	Quiescent	15.2 ± 0.5	$(57.2 \pm 8.5) \times 10^{-6}$
G231.740–01.760	231.736	−1.761	3.9	200.0	0.93	Protostellar	12.7 ± 0.6	$(4.4 \pm 1.0) \times 10^{-5}$
G231.760–00.250	231.760	−0.252	2.4	83.9	0.22	Quiescent	10.9 ± 0.3	$(9.8 \pm 1.7) \times 10^{-5}$
G231.770–00.350	231.765	−0.350	2.3	67.0	0.16	Protostellar	17.2 ± 3.2	$(2.5 \pm 1.8) \times 10^{-5}$
G231.793–01.970	231.798	−1.970	4.0	42.5	0.11	YSO	30.1 ± 1.6	$(32.6 \pm 4.1) \times 10^{-5}$
G231.930–01.500	231.930	−1.497	7.4	60.6	0.43	YSO	18.6 ± 0.5	$(23.9 \pm 2.4) \times 10^{-5}$
G231.940–01.510	231.937	−1.513	7.3	42.5	0.19	Protostellar	24.2 ± 0.3	$(82.4 \pm 7.4) \times 10^{-6}$
G232.075–02.276	232.076	−2.276	3.7	42.5	0.10	YSO	28.2 ± 1.1	$(9.9 \pm 2.4) \times 10^{-4}$
G232.220+00.190	232.220	0.185	1.3	59.9	0.07	Protostellar	14.4 ± 1.0	$(9.0 \pm 2.7) \times 10^{-5}$
G232.220–01.070	232.222	−1.068	3.8	56.4	0.20	Quiescent	14.0 ± 0.5	$(33.5 \pm 5.3) \times 10^{-6}$
G232.230+00.180	232.230	0.176	1.6	42.5	0.04	Quiescent	10.9 ± 0.5	$(30.4 \pm 8.0) \times 10^{-5}$
G232.240+00.130	232.242	0.127	1.5	67.4	0.10	Protostellar	13.8 ± 0.4	$(55.8 \pm 7.0) \times 10^{-6}$
G232.250+00.060	232.252	0.057	1.5	45.8	0.05	Quiescent	15.6 ± 0.5	$(49.5 \pm 6.3) \times 10^{-6}$
G232.250+00.070	232.248	0.070	1.5	42.5	0.04	Quiescent	14.1 ± 0.4	$(81.7 \pm 9.8) \times 10^{-6}$
G232.490–00.300	232.487	−0.297	1.5	70.8	0.11	Protostellar	12.8 ± 0.1	$(55.6 \pm 1.8) \times 10^{-5}$
G232.500–00.040	232.498	−0.038	1.5	42.5	0.04	Quiescent	13.0 ± 0.6	$(14.0 \pm 3.4) \times 10^{-5}$
G232.504–01.223	232.503	−1.223	2.2	42.5	0.06	YSO	15.8 ± 2.0	$(6.7 \pm 3.7) \times 10^{-5}$
G232.590–01.190	232.592	−1.188	1.9	70.0	0.14	Protostellar	19.7 ± 2.2	$(6.5 \pm 2.4) \times 10^{-6}$
G232.600+00.100	232.600	0.103	1.5	51.0	0.06	Quiescent	11.8 ± 0.6	$(26.4 \pm 7.3) \times 10^{-5}$
G232.600–01.320	232.603	−1.317	4.2	47.6	0.16	Quiescent	14.5 ± 0.4	$(25.2 \pm 3.2) \times 10^{-6}$
G232.640–00.420	232.640	−0.423	2.0	65.4	0.13	Quiescent	17.9 ± 0.4	$(14.2 \pm 1.2) \times 10^{-6}$
G232.680+00.160	232.680	0.155	1.3	42.5	0.03	Protostellar	18.5 ± 1.9	$(2.7 \pm 1.0) \times 10^{-5}$
G232.710–00.240	232.713	−0.243	1.6	42.5	0.04	Quiescent	12.0 ± 0.5	$(11.7 \pm 2.5) \times 10^{-5}$
G232.760+00.050	232.763	0.048	1.6	42.5	0.04	Protostellar	14.1 ± 0.6	$(27.3 \pm 5.2) \times 10^{-5}$
G232.760–00.240	232.758	−0.237	1.6	63.6	0.10	Protostellar	15.9 ± 0.7	$(6.5 \pm 1.1) \times 10^{-5}$
G232.770–00.340	232.765	−0.340	2.0	42.5	0.05	Protostellar	12.7 ± 0.3	$(21.3 \pm 2.8) \times 10^{-5}$
G232.770–00.350	232.773	−0.347	2.0	42.5	0.05	Quiescent	12.5 ± 0.2	$(22.8 \pm 1.9) \times 10^{-5}$
G232.770–00.360	232.770	−0.357	2.0	65.1	0.13	Quiescent	10.9 ± 0.8	$(20.6 \pm 8.1) \times 10^{-5}$
G232.790+00.150	232.785	0.150	2.0	53.9	0.10	YSO	19.0 ± 0.1	$(66.9 \pm 1.7) \times 10^{-5}$
G232.790–01.400	232.793	−1.402	4.8	63.5	0.30	Protostellar	16.6 ± 0.4	$(4.3 \pm 1.1) \times 10^{-5}$
G232.810+00.180	232.808	0.183	1.9	95.7	0.20	YSO	21.9 ± 1.3	$(15.5 \pm 3.8) \times 10^{-5}$
G232.820–00.840	232.822	−0.843	4.2	70.4	0.31	Protostellar	10.5 ± 0.7	$(12.8 \pm 5.3) \times 10^{-5}$
G232.894–01.389	232.897	−1.392	4.1	45.0	0.13	Protostellar	14.7 ± 0.6	$(7.5 \pm 1.5) \times 10^{-5}$
G232.930+00.040	232.932	0.042	1.6	65.9	0.11	Quiescent	12.4 ± 0.5	$(18.0 \pm 3.9) \times 10^{-5}$
G232.940–01.000	232.940	−1.000	3.9	57.4	0.21	Protostellar	15.4 ± 0.6	$(40.9 \pm 6.9) \times 10^{-6}$
G232.950–00.790	232.947	−0.793	4.1	95.6	0.44	YSO	15.2 ± 1.1	$(4.7 \pm 1.4) \times 10^{-5}$
G232.970–00.780	232.970	−0.777	4.1	47.9	0.15	Quiescent	15.8 ± 1.0	$(30.9 \pm 8.4) \times 10^{-6}$
G233.030+00.140	233.028	0.137	1.6	42.5	0.04	Quiescent	10.0 ± 0.8	$(5.6 \pm 3.0) \times 10^{-4}$
G233.100–00.380	233.098	−0.377	1.6	42.5	0.04	Protostellar	17.0 ± 0.3	$(109.3 \pm 6.6) \times 10^{-6}$
G233.140–01.220	233.137	−1.223	4.4	50.3	0.19	Quiescent	15.4 ± 0.9	$(4.4 \pm 1.2) \times 10^{-5}$
G233.140–01.540	233.144	−1.537	4.5	75.2	0.36	YSO	18.2 ± 0.4	$(32.1 \pm 2.4) \times 10^{-6}$
G233.180–01.710	233.177	−1.708	4.6	95.3	0.49	Quiescent	13.8 ± 0.2	$(19.2 \pm 1.4) \times 10^{-5}$
G233.250+00.100	233.246	0.097	3.5	42.5	0.09	Protostellar	16.1 ± 0.4	$(12.5 \pm 1.3) \times 10^{-5}$
G233.250–00.360	233.250	−0.365	4.1	58.6	0.23	Quiescent	15.4 ± 2.7	$(1.5 \pm 1.2) \times 10^{-5}$
G233.290–00.310	233.293	−0.312	4.0	65.3	0.26	Quiescent	12.3 ± 0.6	$(12.1 \pm 3.3) \times 10^{-5}$
G233.320–00.320	233.320	−0.318	4.0	42.5	0.11	Protostellar	15.9 ± 0.2	$(53.0 \pm 3.1) \times 10^{-6}$
G233.380–01.600	233.382	−1.596	7.8	46.7	0.28	Protostellar	14.6 ± 0.1	$(50.8 \pm 1.3) \times 10^{-6}$
G233.730–01.330	233.730	−1.333	7.6	42.5	0.20	Protostellar	23.4 ± 0.2	$(78.6 \pm 5.0) \times 10^{-6}$
G233.736–00.197	233.733	−0.198	3.9	44.0	0.12	YSO	31.1 ± 1.4	$(33.0 \pm 9.2) \times 10^{-5}$

Table A.4: continued

Name	$\ell_{\rm app}$ (deg)	$b_{\rm app}$ (deg)	$R_{\rm hel}$ (kpc)	$D_{\rm app}$ ($''$)	$D_{\rm lin}$ (pc)	Class	$T_{\rm dust}$ (K)	τ_{350}
G233.750–01.270	233.753	−1.270	7.6	71.8	0.57	Protostellar	12.2 ± 0.1	$(86.9 \pm 5.5) \times 10^{-6}$
G233.760–01.250	233.758	−1.251	7.7	53.2	0.36	Protostellar	13.0 ± 0.4	$(9.7 \pm 1.5) \times 10^{-5}$
G233.810–00.110	233.806	−0.107	3.9	200.0	0.93	Quiescent	20.6 ± 1.1	$(5.6 \pm 1.3) \times 10^{-6}$
G233.980–01.860	233.979	−1.858	4.3	64.0	0.27	Quiescent	12.2 ± 1.2	$(7.8 \pm 4.0) \times 10^{-5}$
G234.033–00.537	234.032	−0.538	3.8	144.2	0.64	YSO	19.1 ± 0.6	$(66.4 \pm 7.9) \times 10^{-6}$
G234.050–00.130	234.049	−0.132	3.7	56.3	0.19	YSO	17.7 ± 0.5	$(18.5 \pm 2.1) \times 10^{-5}$
G234.050–01.910	234.053	−1.906	4.4	42.5	0.12	Quiescent	17.4 ± 2.7	$(17.2 \pm 9.9) \times 10^{-6}$
G234.234–00.717	234.232	−0.718	3.7	58.5	0.21	Protostellar	17.8 ± 0.4	$(72.1 \pm 6.3) \times 10^{-6}$
G234.260–01.490	234.258	−1.493	6.7	50.3	0.28	YSO	27.4 ± 0.4	$(73.5 \pm 8.6) \times 10^{-6}$
G234.270–01.500	234.271	−1.496	6.6	42.5	0.17	YSO	25.9 ± 0.5	$(63.2 \pm 8.7) \times 10^{-6}$
G234.333–00.651	234.333	−0.647	3.4	126.7	0.50	YSO	19.6 ± 1.6	$(6.8 \pm 1.9) \times 10^{-5}$
G234.450–01.070	234.453	−1.071	7.7	42.5	0.20	Protostellar	17.1 ± 1.9	$(22.7 \pm 9.9) \times 10^{-5}$
G234.468–00.393	234.472	−0.392	3.7	42.9	0.10	YSO	16.1 ± 1.4	$(10.5 \pm 3.8) \times 10^{-4}$
G234.493–00.829	234.495	−0.825	7.7	42.5	0.20	Protostellar	15.7 ± 0.5	$(11.9 \pm 1.6) \times 10^{-5}$
G234.501–00.863	234.498	−0.867	7.7	194.3	1.78	Quiescent	13.7 ± 1.0	$(13.2 \pm 5.4) \times 10^{-5}$
G234.570–01.003	234.572	−1.003	3.9	110.2	0.49	Protostellar	14.6 ± 0.8	$(4.3 \pm 1.1) \times 10^{-5}$
G234.580–01.030	234.578	−1.033	3.9	42.7	0.11	Protostellar	13.9 ± 0.1	$(65.5 \pm 2.2) \times 10^{-6}$
G234.590–01.080	234.587	−1.080	1.9	63.6	0.12	YSO	22.5 ± 0.8	$(5.1 \pm 1.6) \times 10^{-6}$
G234.620–00.197	234.623	−0.200	3.7	200.0	0.88	YSO	18.4 ± 0.7	$(48.5 \pm 7.0) \times 10^{-5}$
G234.650–01.580	234.653	−1.578	6.6	54.0	0.32	YSO	14.6 ± 0.1	$(29.4 \pm 1.2) \times 10^{-5}$
G234.660+00.070	234.655	0.070	2.4	200.0	0.57	YSO	16.9 ± 0.5	$(16.7 \pm 2.0) \times 10^{-5}$
G234.710–00.910	234.713	−0.913	7.6	42.5	0.20	YSO	30.9 ± 0.8	$(11.6 \pm 1.8) \times 10^{-5}$
G234.720–00.820	234.720	−0.823	7.9	42.5	0.21	Protostellar	21.7 ± 1.8	$(21.6 \pm 5.8) \times 10^{-6}$
G234.715–00.911	234.717	−0.913	7.6	42.5	0.20	YSO	31.3 ± 0.8	$(12.4 \pm 1.9) \times 10^{-5}$
G234.730–00.750	234.725	−0.750	7.8	44.0	0.23	YSO	28.9 ± 0.4	$(9.9 \pm 1.0) \times 10^{-5}$
G234.730–00.810	234.732	−0.813	7.9	42.5	0.21	Protostellar	19.7 ± 0.8	$(13.0 \pm 1.8) \times 10^{-5}$
G234.764–00.282	234.760	−0.278	3.8	200.0	0.91	YSO	27.7 ± 8.0	$(4.6 \pm 3.5) \times 10^{-5}$
G234.860–00.090	234.862	−0.090	3.8	42.5	0.10	YSO	24.7 ± 4.1	$(18.7 \pm 9.0) \times 10^{-5}$
G234.880–00.130	234.882	−0.127	3.7	64.9	0.24	YSO	20.6 ± 1.5	$(8.0 \pm 1.9) \times 10^{-5}$
G234.890–00.180	234.893	−0.178	3.8	135.8	0.60	YSO	21.8 ± 0.6	$(54.3 \pm 4.4) \times 10^{-6}$
G235.050–01.530	235.052	−1.533	8.3	47.0	0.30	YSO	21.8 ± 1.5	$(5.3 \pm 1.2) \times 10^{-4}$
G235.220–01.670	235.217	−1.668	8.4	59.0	0.47	Protostellar	11.9 ± 0.1	$(18.3 \pm 1.1) \times 10^{-5}$
G235.348–01.687	235.350	−1.687	8.4	42.5	0.22	Protostellar	20.2 ± 0.8	$(65.6 \pm 9.2) \times 10^{-6}$
G235.347–01.740	235.348	−1.737	8.3	51.4	0.37	Protostellar	14.0 ± 0.1	$(157.1 \pm 4.9) \times 10^{-6}$
G235.389–01.655	235.387	−1.655	8.4	42.5	0.22	YSO	31.5 ± 1.3	$(20.7 \pm 5.5) \times 10^{-5}$
G235.532–01.675	235.533	−1.675	8.5	105.3	1.02	YSO	13.2 ± 1.7	$(2.2 \pm 1.4) \times 10^{-4}$
G235.590–01.520	235.593	−1.517	7.2	42.5	0.19	Protostellar	25.8 ± 0.9	$(11.6 \pm 3.0) \times 10^{-6}$
G235.680–00.030	235.683	−0.027	4.3	42.5	0.11	Quiescent	12.7 ± 1.1	$(12.6 \pm 5.8) \times 10^{-5}$
G235.690–01.240	235.687	−1.243	7.4	42.5	0.20	YSO	30.7 ± 1.2	$(28.9 \pm 7.3) \times 10^{-5}$
G235.780+00.010	235.783	0.013	4.6	93.2	0.48	YSO	14.6 ± 0.4	$(10.0 \pm 1.2) \times 10^{-5}$
G236.180–01.830	236.179	−1.828	2.6	42.5	0.07	YSO	17.9 ± 1.0	$(9.1 \pm 1.9) \times 10^{-4}$
G236.420–00.710	236.418	−0.708	2.2	42.5	0.06	Quiescent	14.5 ± 0.4	$(12.4 \pm 1.6) \times 10^{-5}$
G236.490–00.590	236.490	−0.588	2.2	66.5	0.15	Quiescent	12.1 ± 0.5	$(18.2 \pm 3.8) \times 10^{-5}$
G236.570–00.460	236.570	−0.458	4.4	59.0	0.25	YSO	23.1 ± 5.1	$(5.6 \pm 3.7) \times 10^{-6}$
G236.600–02.130	236.595	−2.129	2.3	48.8	0.09	YSO	20.7 ± 4.7	$(10.0 \pm 7.5) \times 10^{-4}$
G236.600–02.290	236.597	−2.293	2.3	72.8	0.18	Protostellar	12.7 ± 1.5	$(8.6 \pm 5.4) \times 10^{-4}$
G236.600–02.310	236.597	−2.306	2.3	42.5	0.06	YSO	15.9 ± 0.7	$(38.4 \pm 7.5) \times 10^{-5}$
G236.610–02.110	236.607	−2.106	2.2	42.7	0.06	YSO	14.9 ± 0.9	$(6.1 \pm 1.7) \times 10^{-4}$
G236.620+00.000	236.616	−0.002	4.2	42.5	0.11	Quiescent	13.0 ± 0.6	$(6.9 \pm 1.7) \times 10^{-5}$

Table A.4: continued

Name	$\ell_{\rm app}$ (deg)	$b_{\rm app}$ (deg)	$R_{\rm hel}$ (kpc)	$D_{\rm app}$ ($''$)	$D_{\rm lin}$ (pc)	Class	$T_{\rm dust}$ (K)	τ_{350}
G236.630–01.150	236.632	−1.153	2.4	72.7	0.18	Protostellar	13.4 ± 0.2	$(75.8 \pm 5.9) \times 10^{-6}$
G236.880–01.010	236.878	−1.011	7.9	61.9	0.48	Protostellar	14.5 ± 0.1	$(81.3 \pm 2.2) \times 10^{-6}$
G237.000–01.840	236.999	−1.839	8.0	42.5	0.21	YSO	26.9 ± 1.2	$(13.9 \pm 1.7) \times 10^{-5}$
G237.050–00.770	237.047	−0.773	2.0	77.6	0.17	Quiescent	15.5 ± 1.8	$(3.5 \pm 1.7) \times 10^{-5}$
G237.100–00.820	237.097	−0.823	1.9	65.5	0.13	Quiescent	14.2 ± 0.4	$(84.3 \pm 9.9) \times 10^{-6}$
G237.110–00.300	237.107	−0.297	5.1	42.5	0.14	Quiescent	15.1 ± 0.2	$(57.8 \pm 3.6) \times 10^{-6}$
G237.110–00.790	237.108	−0.786	2.0	85.9	0.19	YSO	15.3 ± 0.3	$(25.4 \pm 2.3) \times 10^{-5}$
G237.110–00.990	237.112	−0.991	1.9	55.7	0.10	YSO	15.7 ± 0.3	$(72.2 \pm 5.3) \times 10^{-6}$
G237.170–00.960	237.175	−0.960	1.9	42.5	0.05	YSO	18.6 ± 0.9	$(31.3 \pm 5.4) \times 10^{-5}$
G237.180–01.470	237.180	−1.468	6.8	43.8	0.20	Protostellar	18.7 ± 2.7	$(3.3 \pm 1.7) \times 10^{-5}$
G237.210–01.440	237.213	−1.441	7.1	44.1	0.21	Protostellar	18.4 ± 1.5	$(5.5 \pm 1.6) \times 10^{-5}$
G237.230–01.060	237.228	−1.061	7.6	61.3	0.45	YSO	31.3 ± 2.2	$(13.6 \pm 6.0) \times 10^{-5}$
G237.240–01.080	237.243	−1.076	7.6	42.5	0.20	YSO	24.0 ± 0.1	$(158.3 \pm 6.7) \times 10^{-6}$
G237.260–01.260	237.257	−1.256	7.1	47.7	0.26	YSO	20.5 ± 2.7	$(4.0 \pm 1.8) \times 10^{-4}$
G237.260–01.280	237.260	−1.278	6.8	64.6	0.44	YSO	29.3 ± 0.8	$(42.4 \pm 7.5) \times 10^{-5}$
G237.260–01.300	237.262	−1.303	6.7	42.5	0.18	YSO	24.8 ± 1.4	$(39.8 \pm 6.4) \times 10^{-5}$
G237.320–01.280	237.318	−1.281	7.7	42.5	0.20	YSO	41.3 ± 2.5	$(3.5 \pm 1.1) \times 10^{-4}$
G237.330–01.260	237.327	−1.256	7.6	42.5	0.20	YSO	17.5 ± 2.1	$(16.5 \pm 7.7) \times 10^{-5}$
G237.460–01.790	237.463	−1.793	2.1	42.6	0.06	Quiescent	13.2 ± 0.4	$(30.5 \pm 4.4) \times 10^{-5}$
G237.530–01.380	237.531	−1.383	7.4	53.7	0.35	YSO	13.6 ± 2.1	$(9.4 \pm 7.1) \times 10^{-5}$
G237.540–00.660	237.538	−0.657	5.5	73.4	0.42	Protostellar	17.6 ± 1.9	$(8.1 \pm 3.3) \times 10^{-6}$
G237.550–00.640	237.547	−0.637	5.1	70.0	0.37	YSO	18.5 ± 1.8	$(13.2 \pm 4.6) \times 10^{-6}$
G237.661–00.514	237.662	−0.515	5.1	42.5	0.14	Protostellar	15.6 ± 0.3	$(44.2 \pm 3.6) \times 10^{-6}$
G237.660–01.790	237.661	−1.788	2.1	68.9	0.15	Quiescent	16.1 ± 1.5	$(20.2 \pm 7.7) \times 10^{-6}$
G237.740–00.960	237.742	−0.957	1.9	77.7	0.16	YSO	30.1 ± 1.0	$(27.2 \pm 5.8) \times 10^{-5}$
G237.740–00.970	237.743	−0.973	1.9	42.5	0.05	YSO	29.4 ± 0.6	$(8.4 \pm 1.1) \times 10^{-5}$
G237.820–01.280	237.822	−1.277	7.4	68.7	0.52	YSO	16.7 ± 0.3	$(16.3 \pm 1.2) \times 10^{-5}$
G238.260–01.720	238.257	−1.723	2.1	42.5	0.06	YSO	24.9 ± 0.3	$(24.0 \pm 1.0) \times 10^{-5}$
G238.511–00.885	238.512	−0.888	2.1	58.6	0.12	Quiescent	13.3 ± 0.6	$(8.7 \pm 2.1) \times 10^{-5}$
G238.540–00.920	238.537	−0.917	2.1	60.8	0.12	YSO	15.4 ± 0.4	$(38.7 \pm 3.9) \times 10^{-6}$
G238.670–01.440	238.673	−1.442	1.8	97.7	0.20	YSO	14.9 ± 2.2	$(4.2 \pm 2.8) \times 10^{-4}$
G238.690–01.860	238.692	−1.863	9.1	42.5	0.24	Protostellar	15.4 ± 1.7	$(13.3 \pm 6.2) \times 10^{-5}$
G238.700–01.270	238.697	−1.272	1.8	42.5	0.05	Quiescent	15.3 ± 1.2	$(7.2 \pm 2.6) \times 10^{-5}$
G238.770–01.810	238.772	−1.810	9.1	42.5	0.24	YSO	26.8 ± 2.2	$(12.4 \pm 2.7) \times 10^{-5}$
G238.800–01.630	238.800	−1.632	1.6	42.5	0.04	YSO	16.9 ± 1.6	$(3.8 \pm 1.4) \times 10^{-4}$
G238.960–01.680	238.958	−1.683	1.7	42.5	0.05	YSO	31.2 ± 1.3	$(15.5 \pm 3.8) \times 10^{-5}$
G239.190–01.960	239.189	−1.956	8.3	77.1	0.68	YSO	13.5 ± 0.7	$(15.0 \pm 3.8) \times 10^{-5}$
G239.300–00.630	239.302	−0.627	6.0	42.5	0.16	YSO	10.7 ± 0.5	$(4.0 \pm 1.2) \times 10^{-4}$
G239.370–00.080	239.371	−0.080	6.2	42.5	0.16	Protostellar	14.7 ± 0.3	$(44.6 \pm 4.1) \times 10^{-6}$
G239.370–01.690	239.367	−1.693	1.8	42.5	0.05	YSO	18.1 ± 3.3	$(4.2 \pm 2.8) \times 10^{-4}$
G239.524–00.711	239.525	−0.712	6.1	73.6	0.47	YSO	14.1 ± 1.1	$(14.4 \pm 5.2) \times 10^{-5}$
G239.630–02.090	239.627	−2.086	7.7	91.7	0.79	YSO	14.3 ± 0.4	$(27.1 \pm 3.3) \times 10^{-5}$
G239.650–00.810	239.647	−0.807	6.0	44.7	0.19	YSO	13.2 ± 1.5	$(10.0 \pm 5.6) \times 10^{-5}$
G239.660–02.040	239.657	−2.043	7.7	74.1	0.60	YSO	13.4 ± 1.9	$(12.3 \pm 8.3) \times 10^{-5}$
G239.680–02.040	239.684	−2.039	7.6	42.5	0.20	Protostellar	12.3 ± 0.2	$(10.4 \pm 1.1) \times 10^{-5}$
G239.950–01.810	239.947	−1.806	1.7	42.5	0.05	Quiescent	12.6 ± 0.5	$(32.0 \pm 6.3) \times 10^{-5}$
G240.140–01.540	240.138	−1.541	2.9	96.8	0.32	Protostellar	13.3 ± 0.3	$(12.8 \pm 1.4) \times 10^{-5}$
G240.170–01.590	240.166	−1.593	6.8	57.4	0.37	Quiescent	10.0 ± 0.7	$(11.3 \pm 5.4) \times 10^{-5}$
G240.250–00.910	240.247	−0.908	1.7	69.9	0.12	Protostellar	18.3 ± 0.7	$(16.7 \pm 2.4) \times 10^{-6}$

Table A.4: continued

Name	$\ell_{\rm app}$ (deg)	$b_{\rm app}$ (deg)	$R_{\rm hel}$ (kpc)	$D_{\rm app}$ ($''$)	$D_{\rm lin}$ (pc)	Class	$T_{\rm dust}$ (K)	τ_{350}
G240.490–00.070	240.492	−0.068	6.4	58.0	0.35	Quiescent	17.7 ± 0.9	$(31.5 \pm 6.0) \times 10^{-6}$
G240.940–01.440	240.943	−1.440	6.1	68.9	0.43	Quiescent	14.5 ± 0.3	$(52.2 \pm 5.3) \times 10^{-6}$
G240.990–01.470	240.990	−1.468	1.7	46.0	0.06	Protostellar	14.6 ± 2.0	$(2.2 \pm 1.3) \times 10^{-4}$
G241.003–01.203	241.007	−1.202	5.9	42.5	0.16	YSO	17.5 ± 2.2	$(6.9 \pm 3.4) \times 10^{-4}$
G241.010–01.200	241.007	−1.202	6.2	42.5	0.16	YSO	17.5 ± 2.2	$(6.9 \pm 3.3) \times 10^{-4}$
G241.121–00.781	241.120	−0.783	6.6	68.2	0.46	YSO	13.4 ± 0.2	$(30.9 \pm 2.3) \times 10^{-5}$
G241.140–01.170	241.138	−1.170	6.0	91.7	0.61	Quiescent	10.8 ± 1.2	$(2.5 \pm 1.7) \times 10^{-4}$
G241.180–01.070	241.180	−1.070	6.1	49.9	0.25	Quiescent	12.0 ± 1.1	$(11.1 \pm 5.4) \times 10^{-5}$
G241.190–00.780	241.192	−0.777	6.4	67.4	0.44	Protostellar	11.7 ± 0.2	$(22.4 \pm 2.5) \times 10^{-5}$
G241.290–00.710	241.292	−0.708	6.5	42.5	0.17	YSO	17.8 ± 1.5	$(27.7 \pm 9.0) \times 10^{-5}$
G241.390–02.030	241.390	−2.027	1.7	79.8	0.15	Quiescent	14.5 ± 0.3	$(52.0 \pm 5.5) \times 10^{-6}$
G241.420–00.700	241.418	−0.703	6.8	42.5	0.18	YSO	15.9 ± 0.3	$(51.0 \pm 4.1) \times 10^{-5}$
G241.530–00.600	241.527	−0.603	6.8	54.5	0.33	YSO	31.9 ± 1.6	$(20.9 \pm 6.3) \times 10^{-5}$
G241.538–00.594	241.535	−0.597	6.6	54.5	0.32	YSO	21.8 ± 0.8	$(32.8 \pm 3.7) \times 10^{-5}$
G241.560–00.590	241.563	−0.587	6.6	79.8	0.57	YSO	30.5 ± 0.8	$(21.8 \pm 3.7) \times 10^{-5}$
G241.570–00.640	241.568	−0.642	6.6	162.4	1.27	YSO	15.0 ± 0.3	$(35.6 \pm 3.1) \times 10^{-5}$
G241.680–00.580	241.680	−0.575	6.5	42.5	0.17	YSO	22.9 ± 4.1	$(9.9 \pm 5.4) \times 10^{-4}$
G242.190–00.780	242.192	−0.780	6.3	45.0	0.20	Quiescent	15.6 ± 0.6	$(28.7 \pm 4.4) \times 10^{-6}$
G242.560–00.630	242.563	−0.627	6.1	42.5	0.16	Protostellar	11.7 ± 0.6	$(7.1 \pm 2.2) \times 10^{-5}$
G242.590–00.240	242.586	−0.240	2.0	42.5	0.05	YSO	29.5 ± 1.0	$(17.3 \pm 3.8) \times 10^{-5}$
G242.620–00.690	242.623	−0.687	6.1	54.6	0.30	YSO	12.7 ± 0.4	$(26.8 \pm 4.1) \times 10^{-5}$
G242.640–00.700	242.640	−0.698	6.1	42.5	0.16	Protostellar	12.0 ± 0.3	$(52.7 \pm 6.1) \times 10^{-5}$
G242.770–01.530	242.770	−1.535	1.8	43.7	0.05	Protostellar	13.6 ± 0.5	$(30.9 \pm 5.1) \times 10^{-5}$
G242.880–02.250	242.879	−2.251	2.0	66.8	0.14	Protostellar	15.7 ± 0.2	$(47.8 \pm 2.5) \times 10^{-6}$
G242.920–00.520	242.923	−0.520	5.9	56.1	0.31	YSO	14.3 ± 0.2	$(30.8 \pm 2.3) \times 10^{-5}$
G242.940–00.450	242.940	−0.450	5.9	42.5	0.16	YSO	24.9 ± 4.0	$(6.8 \pm 3.1) \times 10^{-4}$
G242.940–00.500	242.936	−0.503	5.8	55.2	0.29	YSO	15.8 ± 0.6	$(35.9 \pm 5.9) \times 10^{-5}$
G243.150–00.170	243.150	−0.173	4.9	88.8	0.48	Protostellar	13.0 ± 1.7	$(8.8 \pm 5.8) \times 10^{-5}$
G243.160–01.520	243.156	−1.523	1.6	98.4	0.18	Protostellar	15.8 ± 1.4	$(5.3 \pm 1.9) \times 10^{-5}$
G243.190–00.160	243.189	−0.163	4.9	70.6	0.36	YSO	15.3 ± 0.2	$(40.5 \pm 2.1) \times 10^{-6}$
G243.200–00.330	243.200	−0.327	5.4	58.7	0.30	YSO	19.0 ± 0.7	$(10.4 \pm 1.4) \times 10^{-6}$
G243.450–01.620	243.450	−1.615	1.8	68.5	0.13	Protostellar	16.7 ± 0.5	$(29.0 \pm 3.7) \times 10^{-6}$
G243.540–00.810	243.538	−0.812	2.2	42.5	0.06	YSO	16.5 ± 2.7	$(4.2 \pm 2.8) \times 10^{-4}$
G243.770–01.420	243.773	−1.420	1.7	42.5	0.05	Protostellar	13.0 ± 0.6	$(13.3 \pm 3.0) \times 10^{-5}$
G243.780–00.240	243.783	−0.243	6.2	42.5	0.16	Protostellar	17.6 ± 0.6	$(26.0 \pm 3.5) \times 10^{-5}$
G243.860–00.870	243.863	−0.873	2.2	62.4	0.14	Quiescent	12.3 ± 0.6	$(23.2 \pm 5.9) \times 10^{-5}$
G243.950–00.200	243.947	−0.202	6.1	42.5	0.16	Quiescent	17.9 ± 1.0	$(30.7 \pm 6.4) \times 10^{-6}$
G244.410–01.970	244.413	−1.968	9.5	72.5	0.72	YSO	10.6 ± 0.2	$(38.8 \pm 3.8) \times 10^{-5}$
G244.460–00.540	244.462	−0.543	2.0	60.4	0.12	Quiescent	14.2 ± 0.6	$(46.9 \pm 9.5) \times 10^{-6}$
G244.760–00.320	244.763	−0.323	5.8	92.9	0.60	Protostellar	13.0 ± 0.2	$(69.0 \pm 5.5) \times 10^{-6}$
G244.830–00.960	244.828	−0.958	1.9	55.0	0.10	Quiescent	13.1 ± 0.4	$(9.5 \pm 1.3) \times 10^{-5}$
G245.070–00.210	245.067	−0.208	5.3	51.5	0.23	Quiescent	12.2 ± 1.1	$(11.8 \pm 5.9) \times 10^{-5}$
G245.080–00.180	245.078	−0.178	2.1	42.5	0.06	Protostellar	17.8 ± 2.7	$(3.0 \pm 1.7) \times 10^{-5}$
G245.100–00.990	245.103	−0.993	8.7	42.5	0.23	YSO	18.8 ± 0.4	$(32.1 \pm 2.3) \times 10^{-5}$
G245.240–01.390	245.235	−1.390	1.4	42.5	0.04	YSO	14.0 ± 0.9	$(7.6 \pm 2.4) \times 10^{-5}$
G245.300–00.300	245.302	−0.298	5.6	58.6	0.31	YSO	27.3 ± 1.5	$(19.7 \pm 7.5) \times 10^{-5}$
G246.270–00.070	246.272	−0.068	5.2	71.7	0.39	Quiescent	16.2 ± 0.4	$(33.4 \pm 3.2) \times 10^{-6}$
G246.970–01.720	246.966	−1.718	5.4	49.4	0.22	Quiescent	12.3 ± 0.5	$(13.7 \pm 2.7) \times 10^{-5}$
G247.240–01.120	247.240	−1.117	2.0	50.7	0.09	Protostellar	13.7 ± 1.4	$(12.1 \pm 5.7) \times 10^{-5}$

Table A.4: continued

Name	$\ell_{\rm app}$ (deg)	$b_{\rm app}$ (deg)	$R_{\rm hel}$ (kpc)	$D_{\rm app}$ ($''$)	$D_{\rm lin}$ (pc)	Class	$T_{\rm dust}$ (K)	τ_{350}
G247.280–00.560	247.280	−0.555	2.4	54.8	0.12	Quiescent	20.2 ± 3.3	$(10.3 \pm 5.6) \times 10^{-6}$
G247.440–00.930	247.440	−0.925	2.0	73.8	0.16	Protostellar	13.9 ± 0.7	$(39.5 \pm 9.7) \times 10^{-6}$
G247.460–00.820	247.457	−0.817	2.2	49.3	0.09	Quiescent	14.6 ± 0.6	$(7.7 \pm 1.4) \times 10^{-5}$
G247.510+00.060	247.505	0.060	5.3	70.3	0.39	Protostellar	20.2 ± 4.1	$(8.9 \pm 6.1) \times 10^{-6}$
G247.510–00.570	247.508	−0.573	5.3	66.7	0.36	Quiescent	16.1 ± 1.9	$(2.6 \pm 1.2) \times 10^{-5}$
G247.520+00.050	247.518	0.047	5.3	72.4	0.40	Quiescent	24.6 ± 1.9	$(3.3 \pm 2.0) \times 10^{-6}$
G247.520–00.240	247.517	−0.238	1.8	42.5	0.05	Protostellar	19.8 ± 0.5	$(16.7 \pm 1.4) \times 10^{-6}$
G247.590–00.820	247.593	−0.823	5.5	54.3	0.27	Quiescent	15.3 ± 0.4	$(79.5 \pm 9.5) \times 10^{-6}$
G247.610–00.830	247.610	−0.828	2.0	42.5	0.05	Protostellar	13.5 ± 0.3	$(20.1 \pm 1.9) \times 10^{-5}$
G247.630–00.550	247.630	−0.552	5.4	119.0	0.74	YSO	26.8 ± 5.5	$(15.3 \pm 8.4) \times 10^{-5}$
G247.640–00.530	247.643	−0.533	5.5	62.0	0.33	YSO	28.0 ± 0.6	$(9.4 \pm 1.3) \times 10^{-5}$
G247.890–00.990	247.887	−0.993	2.2	42.5	0.06	Protostellar	13.5 ± 1.0	$(6.0 \pm 2.1) \times 10^{-5}$
G247.930–00.440	247.932	−0.440	5.1	64.6	0.33	YSO	13.0 ± 1.4	$(2.5 \pm 1.4) \times 10^{-4}$
G248.000–00.430	248.005	−0.430	5.0	137.6	0.80	YSO	23.7 ± 1.2	$(12.4 \pm 4.8) \times 10^{-5}$
G248.150–02.210	248.155	−2.210	2.1	93.9	0.22	Protostellar	15.1 ± 0.5	$(12.7 \pm 1.9) \times 10^{-5}$
G248.440–00.910	248.440	−0.912	1.9	51.8	0.08	Quiescent	13.3 ± 1.8	$(5.4 \pm 3.5) \times 10^{-5}$
G248.690–01.930	248.687	−1.933	2.1	94.4	0.22	Quiescent	12.6 ± 0.5	$(12.0 \pm 2.3) \times 10^{-5}$
G248.700–01.010	248.698	−1.011	1.9	71.5	0.14	Quiescent	18.5 ± 0.5	$(11.3 \pm 1.1) \times 10^{-6}$
G249.170–02.020	249.175	−2.019	2.1	52.0	0.09	YSO	21.4 ± 1.3	$(8.0 \pm 1.6) \times 10^{-6}$
G249.390–01.410	249.386	−1.411	1.7	46.1	0.06	Protostellar	15.4 ± 2.3	$(4.2 \pm 2.8) \times 10^{-5}$
G249.450–02.420	249.451	−2.418	2.8	50.0	0.12	Protostellar	9.9 ± 0.6	$(2.9 \pm 1.2) \times 10^{-4}$
G249.530–02.500	249.533	−2.496	2.7	53.6	0.13	Protostellar	15.6 ± 2.4	$(3.0 \pm 1.5) \times 10^{-5}$
G249.600–02.080	249.600	−2.075	11.6	59.7	0.66	YSO	28.6 ± 0.2	$(85.5 \pm 4.1) \times 10^{-6}$
G249.680–02.100	249.683	−2.101	1.8	89.7	0.18	Protostellar	12.0 ± 0.4	$(44.0 \pm 8.3) \times 10^{-5}$
G250.230–00.040	250.228	−0.038	5.0	42.5	0.13	YSO	19.6 ± 0.3	$(35.9 \pm 1.6) \times 10^{-5}$
G250.270–00.980	250.273	−0.980	6.5	65.5	0.43	Protostellar	12.6 ± 1.7	$(8.2 \pm 5.6) \times 10^{-5}$
G250.590–00.650	250.592	−0.650	7.8	64.2	0.50	YSO	29.9 ± 0.8	$(18.1 \pm 2.9) \times 10^{-5}$
G250.900–01.530	250.900	−1.535	5.1	73.1	0.39	Protostellar	14.2 ± 1.1	$(7.1 \pm 2.5) \times 10^{-5}$
G250.900–02.050	250.899	−2.048	4.7	63.5	0.30	Protostellar	14.6 ± 0.1	$(51.2 \pm 2.3) \times 10^{-6}$
G250.910–01.280	250.905	−1.280	1.4	65.7	0.09	Protostellar	16.7 ± 0.5	$(26.3 \pm 3.1) \times 10^{-6}$
G251.040–01.030	251.040	−1.035	1.2	200.0	0.29	Protostellar	12.5 ± 1.7	$(4.4 \pm 3.1) \times 10^{-4}$
G251.070–00.980	251.068	−0.982	1.4	42.5	0.04	YSO	15.8 ± 0.2	$(61.0 \pm 2.7) \times 10^{-5}$
G251.070–01.000	251.073	−0.997	1.4	65.0	0.09	Protostellar	10.8 ± 0.2	$(13.5 \pm 1.8) \times 10^{-4}$
G251.080–00.990	251.083	−0.990	1.4	65.4	0.09	YSO	11.6 ± 0.4	$(10.4 \pm 2.1) \times 10^{-4}$
G251.160–01.990	251.159	−1.991	5.5	42.5	0.15	YSO	21.2 ± 1.8	$(8.6 \pm 2.5) \times 10^{-5}$
G251.190–01.970	251.192	−1.973	5.4	66.3	0.36	YSO	29.2 ± 1.2	$(28.9 \pm 7.8) \times 10^{-5}$
G251.210–00.610	251.215	−0.610	4.5	68.3	0.32	Protostellar	16.8 ± 2.2	$(4.0 \pm 2.1) \times 10^{-5}$
G251.230–01.950	251.232	−1.953	5.3	42.5	0.14	YSO	25.6 ± 5.4	$(14.9 \pm 8.7) \times 10^{-4}$
G251.400–00.180	251.405	−0.180	4.6	42.5	0.12	Quiescent	14.2 ± 1.9	$(9.7 \pm 6.1) \times 10^{-5}$
G251.410–00.980	251.412	−0.982	1.8	61.8	0.11	Quiescent	17.0 ± 1.6	$(27.2 \pm 9.8) \times 10^{-6}$
G251.750–00.900	251.753	−0.896	1.9	71.4	0.14	Protostellar	16.4 ± 1.3	$(15.0 \pm 4.7) \times 10^{-6}$
G251.750–01.010	251.747	−1.013	1.7	54.8	0.08	Quiescent	15.2 ± 0.7	$(28.1 \pm 5.3) \times 10^{-6}$
G251.880–01.060	251.877	−1.060	1.7	42.5	0.05	Protostellar	16.8 ± 1.0	$(6.4 \pm 1.6) \times 10^{-6}$
G251.900–01.060	251.900	−1.065	1.7	60.5	0.10	Protostellar	14.2 ± 0.2	$(48.3 \pm 3.8) \times 10^{-6}$
G251.900–01.080	251.902	−1.081	4.4	53.0	0.21	Protostellar	15.3 ± 0.7	$(15.4 \pm 2.9) \times 10^{-5}$
G251.920–01.090	251.925	−1.090	1.7	95.4	0.18	YSO	14.3 ± 1.2	$(9.9 \pm 3.9) \times 10^{-5}$
G251.990–01.230	251.992	−1.233	1.7	66.5	0.11	Protostellar	14.2 ± 2.4	$(8.3 \pm 6.6) \times 10^{-5}$
G252.080–01.290	252.082	−1.290	1.7	67.8	0.12	YSO	13.3 ± 1.1	$(3.1 \pm 1.2) \times 10^{-4}$
G252.080–01.810	252.083	−1.813	1.7	99.0	0.19	Quiescent	12.0 ± 0.2	$(83.4 \pm 9.1) \times 10^{-5}$

Table A.4: continued

Name	$\ell_{\rm app}$ (deg)	$b_{\rm app}$ (deg)	$R_{\rm hel}$ (kpc)	$D_{\rm app}$ ($''$)	$D_{\rm lin}$ (pc)	Class	$T_{\rm dust}$ (K)	τ_{350}
G252.090–01.270	252.087	−1.271	1.7	106.8	0.21	Quiescent	11.4 ± 0.1	$(33.0 \pm 2.3) \times 10^{-5}$
G252.100–01.220	252.097	−1.223	1.7	63.0	0.11	Quiescent	11.1 ± 0.7	$(27.6 \pm 9.6) \times 10^{-5}$
G252.110–01.270	252.108	−1.266	1.7	58.3	0.09	YSO	15.8 ± 2.3	$(3.3 \pm 2.1) \times 10^{-5}$
G252.120–01.170	252.123	−1.171	1.7	56.0	0.09	Protostellar	13.2 ± 0.3	$(57.1 \pm 5.8) \times 10^{-5}$
G252.133–01.175	252.135	−1.178	1.7	42.5	0.05	YSO	16.6 ± 2.3	$(3.7 \pm 2.1) \times 10^{-4}$
G252.140–01.180	252.137	−1.178	1.7	42.5	0.05	YSO	17.0 ± 2.3	$(3.4 \pm 1.8) \times 10^{-4}$
G252.180–01.080	252.182	−1.083	4.5	46.8	0.16	Protostellar	14.6 ± 0.8	$(5.3 \pm 1.2) \times 10^{-5}$
G252.480–01.570	252.481	−1.573	1.5	55.9	0.08	YSO	16.1 ± 1.6	$(2.9 \pm 1.2) \times 10^{-3}$
G252.510–01.440	252.508	−1.441	1.3	42.5	0.03	Protostellar	19.2 ± 1.1	$(41.5 \pm 8.4) \times 10^{-6}$
G252.680–01.530	252.680	−1.526	1.0	42.5	0.03	Protostellar	20.4 ± 0.2	$(37.8 \pm 3.3) \times 10^{-6}$
G252.700–01.490	252.703	−1.490	1.5	42.5	0.04	Quiescent	20.4 ± 1.2	$(23.7 \pm 4.8) \times 10^{-6}$
G252.840–00.470	252.837	−0.473	1.7	56.0	0.09	Quiescent	15.3 ± 0.6	$(27.6 \pm 4.4) \times 10^{-6}$
G252.850–00.730	252.855	−0.730	5.0	64.9	0.33	Quiescent	13.1 ± 0.1	$(35.9 \pm 1.6) \times 10^{-6}$
G253.030–01.990	253.028	−1.992	1.5	85.5	0.14	Quiescent	19.7 ± 2.1	$(10.7 \pm 3.9) \times 10^{-6}$
G253.080–02.100	253.080	−2.101	1.5	46.8	0.05	Protostellar	14.3 ± 1.0	$(6.4 \pm 2.0) \times 10^{-5}$
G253.100–01.350	253.100	−1.355	1.5	90.7	0.15	Quiescent	13.3 ± 0.3	$(27.0 \pm 3.2) \times 10^{-5}$
G253.110–01.800	253.108	−1.800	1.0	44.6	0.03	Protostellar	17.7 ± 1.2	$(7.6 \pm 2.0) \times 10^{-5}$
G253.110–02.120	253.113	−2.121	1.5	65.1	0.10	Protostellar	14.6 ± 0.4	$(24.5 \pm 3.0) \times 10^{-5}$
G253.110–02.150	253.111	−2.153	1.7	72.7	0.13	YSO	19.5 ± 1.0	$(13.0 \pm 4.2) \times 10^{-6}$
G253.120–02.060	253.123	−2.063	1.5	42.5	0.04	Quiescent	13.2 ± 0.7	$(7.2 \pm 2.0) \times 10^{-5}$
G253.160–01.960	253.163	−1.963	1.7	49.7	0.07	YSO	19.5 ± 0.8	$(18.4 \pm 2.6) \times 10^{-6}$
G253.230–01.350	253.233	−1.347	1.5	47.2	0.05	YSO	16.8 ± 1.0	$(21.5 \pm 5.1) \times 10^{-6}$
G253.270–01.110	253.273	−1.107	1.5	81.5	0.13	YSO	15.0 ± 0.7	$(5.1 \pm 1.0) \times 10^{-5}$
G253.290–01.010	253.290	−1.015	1.5	57.7	0.08	YSO	16.9 ± 2.5	$(13.8 \pm 8.4) \times 10^{-6}$
G253.290–01.610	253.293	−1.612	1.0	50.0	0.04	YSO	18.2 ± 1.4	$(25.9 \pm 7.5) \times 10^{-4}$
G253.300–01.080	253.298	−1.078	1.5	84.9	0.14	Protostellar	14.2 ± 1.5	$(11.5 \pm 5.7) \times 10^{-5}$
G253.400–01.400	253.397	−1.400	1.5	42.5	0.04	YSO	29.5 ± 1.3	$(14.5 \pm 4.0) \times 10^{-4}$
G253.400–01.420	253.402	−1.422	1.8	42.5	0.05	YSO	16.2 ± 0.4	$(54.0 \pm 5.3) \times 10^{-5}$
G253.420–01.400	253.420	−1.402	1.5	46.2	0.05	YSO	16.7 ± 1.6	$(6.6 \pm 2.5) \times 10^{-4}$
G253.430–01.370	253.432	−1.367	1.8	42.5	0.05	YSO	20.1 ± 1.7	$(4.2 \pm 1.2) \times 10^{-4}$
G253.450–01.370	253.450	−1.367	1.5	42.5	0.04	YSO	20.3 ± 2.0	$(12.5 \pm 4.2) \times 10^{-4}$
G253.460–01.410	253.460	−1.407	1.5	77.8	0.13	YSO	13.8 ± 1.4	$(5.1 \pm 2.5) \times 10^{-5}$
G253.470–01.420	253.468	−1.417	1.5	65.8	0.10	Quiescent	13.4 ± 0.5	$(5.3 \pm 1.0) \times 10^{-5}$
G253.480–01.290	253.485	−1.290	1.5	55.3	0.08	Protostellar	12.9 ± 0.8	$(7.7 \pm 2.3) \times 10^{-5}$
G253.480–01.370	253.477	−1.373	1.5	50.6	0.06	Quiescent	11.5 ± 0.3	$(66.8 \pm 8.5) \times 10^{-5}$
G253.503–01.237	253.505	−1.238	1.5	61.8	0.09	Protostellar	14.5 ± 1.8	$(11.7 \pm 6.4) \times 10^{-4}$
G253.510–01.240	253.507	−1.243	1.5	61.8	0.09	YSO	14.1 ± 0.3	$(15.4 \pm 1.5) \times 10^{-4}$
G253.510–01.260	253.513	−1.260	1.5	56.9	0.08	YSO	18.4 ± 1.4	$(4.3 \pm 1.2) \times 10^{-4}$
G253.520–01.370	253.517	−1.368	1.5	58.8	0.08	Protostellar	15.7 ± 1.4	$(4.2 \pm 1.5) \times 10^{-5}$
G253.530–00.420	253.530	−0.415	3.5	70.2	0.25	YSO	18.1 ± 1.7	$(3.3 \pm 1.1) \times 10^{-4}$
G253.630–01.440	253.633	−1.437	1.8	45.3	0.06	YSO	19.2 ± 0.3	$(53.3 \pm 3.3) \times 10^{-6}$
G253.770–01.300	253.772	−1.303	1.8	42.9	0.05	YSO	18.6 ± 0.3	$(36.9 \pm 2.4) \times 10^{-6}$
G253.860–01.230	253.858	−1.227	1.6	57.1	0.09	Protostellar	19.1 ± 0.2	$(72.0 \pm 2.1) \times 10^{-6}$
G253.870–01.200	253.872	−1.202	1.6	50.1	0.07	Protostellar	13.8 ± 0.2	$(38.2 \pm 2.7) \times 10^{-5}$
G253.870–01.210	253.865	−1.210	1.6	106.9	0.19	YSO	16.7 ± 0.4	$(34.0 \pm 3.3) \times 10^{-5}$
G253.880–01.540	253.877	−1.537	4.0	77.3	0.33	Quiescent	17.5 ± 1.5	$(3.3 \pm 1.1) \times 10^{-5}$
G253.890–00.470	253.893	−0.467	1.6	42.5	0.04	YSO	15.9 ± 0.5	$(77.9 \pm 9.4) \times 10^{-5}$
G253.980–00.720	253.975	−0.720	4.0	134.9	0.63	YSO	17.2 ± 0.8	$(15.4 \pm 2.8) \times 10^{-5}$
G254.052–00.566	254.048	−0.562	3.7	53.0	0.17	YSO	26.7 ± 6.0	$(10.6 \pm 6.4) \times 10^{-4}$

Table A.4: continued

Name	$\ell_{\rm app}$ (deg)	$b_{\rm app}$ (deg)	$R_{\rm hel}$ (kpc)	$D_{\rm app}$ ($''$)	$D_{\rm lin}$ (pc)	Class	$T_{\rm dust}$ (K)	τ_{350}
G254.120–01.420	254.117	−1.423	4.6	80.4	0.40	YSO	12.4 ± 1.3	$(10.1 \pm 5.4) \times 10^{-5}$
G254.232–00.136	254.235	−0.132	3.5	75.3	0.28	YSO	25.1 ± 1.2	$(19.1 \pm 2.6) \times 10^{-5}$
G254.230–02.320	254.234	−2.316	3.7	42.5	0.10	Protostellar	11.8 ± 0.6	$(14.6 \pm 4.5) \times 10^{-5}$
G254.390–01.010	254.387	−1.007	7.8	42.5	0.21	Quiescent	12.9 ± 1.2	$(8.1 \pm 3.8) \times 10^{-5}$
G254.590–01.060	254.592	−1.058	3.9	48.8	0.15	Protostellar	16.9 ± 1.1	$(25.3 \pm 6.5) \times 10^{-6}$
G254.660–01.250	254.657	−1.246	1.4	83.0	0.13	Protostellar	15.1 ± 0.4	$(68.5 \pm 8.0) \times 10^{-6}$
G254.680–01.890	254.684	−1.891	1.6	51.2	0.07	Protostellar	15.8 ± 1.3	$(4.1 \pm 1.4) \times 10^{-5}$
G254.760–01.240	254.757	−1.241	1.6	92.1	0.16	YSO	13.5 ± 0.5	$(11.2 \pm 2.1) \times 10^{-5}$
G255.100–00.090	255.102	−0.093	7.3	42.5	0.19	Quiescent	12.0 ± 0.8	$(20.0 \pm 7.3) \times 10^{-5}$
G255.170–00.570	255.169	−0.567	8.6	42.5	0.23	YSO	26.9 ± 0.4	$(12.0 \pm 1.3) \times 10^{-5}$
G255.190–02.280	255.195	−2.279	1.4	81.1	0.12	Quiescent	15.1 ± 0.8	$(17.7 \pm 4.1) \times 10^{-6}$
G255.200–02.290	255.201	−2.286	1.4	63.8	0.09	Quiescent	15.7 ± 1.3	$(14.4 \pm 5.1) \times 10^{-6}$
G255.210–02.290	255.211	−2.289	1.4	78.6	0.12	Quiescent	16.6 ± 1.5	$(16.5 \pm 5.8) \times 10^{-6}$
G255.401–00.918	255.402	−0.920	8.3	79.1	0.71	Protostellar	12.5 ± 0.3	$(25.9 \pm 3.6) \times 10^{-5}$
G256.130–01.470	256.130	−1.465	8.9	42.5	0.24	YSO	26.4 ± 4.5	$(20.1 \pm 9.3) \times 10^{-5}$
G256.150–01.370	256.150	−1.375	8.9	42.5	0.24	YSO	22.3 ± 1.5	$(21.6 \pm 4.6) \times 10^{-5}$
G256.150–01.380	256.150	−1.375	8.9	42.5	0.24	YSO	22.3 ± 1.5	$(21.6 \pm 4.6) \times 10^{-5}$
G256.190–01.540	256.187	−1.543	9.3	42.5	0.25	YSO	32.5 ± 1.7	$(19.0 \pm 5.9) \times 10^{-5}$
G256.187–01.547	256.187	−1.545	9.4	42.5	0.25	YSO	32.3 ± 1.4	$(20.3 \pm 5.5) \times 10^{-5}$
G256.430–01.630	256.430	−1.630	1.5	55.3	0.08	Quiescent	16.3 ± 2.8	$(9.1 \pm 6.5) \times 10^{-6}$
G256.430–01.640	256.432	−1.642	1.5	70.9	0.11	Quiescent	13.1 ± 0.6	$(4.6 \pm 1.0) \times 10^{-5}$
G256.440–01.610	256.440	−1.605	1.5	56.0	0.08	YSO	16.2 ± 0.5	$(56.0 \pm 7.4) \times 10^{-6}$
G256.450–01.608	256.453	−1.607	9.1	42.5	0.24	YSO	18.3 ± 1.4	$(16.1 \pm 4.4) \times 10^{-5}$
G256.620–00.050	256.622	−0.048	7.7	42.5	0.20	Quiescent	12.2 ± 0.2	$(19.0 \pm 2.0) \times 10^{-5}$
G256.682–01.627	256.683	−1.628	4.7	82.3	0.42	Quiescent	12.9 ± 1.1	$(8.0 \pm 3.5) \times 10^{-5}$
G256.690–00.040	256.692	−0.043	7.7	71.2	0.57	Quiescent	14.6 ± 1.1	$(7.4 \pm 2.4) \times 10^{-5}$
G256.720–01.930	256.723	−1.930	4.7	42.5	0.12	YSO	19.7 ± 1.4	$(4.1 \pm 1.0) \times 10^{-4}$
G256.730–01.670	256.727	−1.667	4.7	51.9	0.21	Protostellar	14.9 ± 0.4	$(89.2 \pm 9.8) \times 10^{-6}$
G256.740–01.580	256.740	−1.577	1.2	87.6	0.12	Quiescent	16.5 ± 0.4	$(54.5 \pm 5.0) \times 10^{-6}$
G256.750–00.060	256.748	−0.063	7.9	60.4	0.46	Quiescent	12.5 ± 0.4	$(8.1 \pm 1.4) \times 10^{-5}$
G256.780–00.130	256.783	−0.127	7.9	56.6	0.41	Protostellar	15.5 ± 0.1	$(122.1 \pm 4.0) \times 10^{-6}$
G256.780–02.070	256.780	−2.068	1.5	59.3	0.09	Protostellar	16.8 ± 0.3	$(22.4 \pm 1.7) \times 10^{-6}$
G256.910–00.280	256.907	−0.277	7.6	72.3	0.58	Protostellar	13.1 ± 0.1	$(25.3 \pm 1.2) \times 10^{-5}$
G256.920–01.830	256.920	−1.828	4.8	63.1	0.30	YSO	20.0 ± 0.6	$(9.6 \pm 2.8) \times 10^{-6}$
G256.950–00.530	256.952	−0.528	5.5	75.9	0.44	Protostellar	12.8 ± 0.6	$(7.1 \pm 1.6) \times 10^{-5}$
G256.990–00.570	256.992	−0.572	5.5	48.1	0.21	YSO	15.3 ± 0.4	$(50.2 \pm 5.6) \times 10^{-6}$
G256.990–02.130	256.995	−2.130	4.9	42.5	0.13	Protostellar	18.7 ± 0.6	$(14.7 \pm 1.8) \times 10^{-6}$
G257.010+00.000	257.013	0.003	5.8	42.5	0.15	YSO	15.1 ± 2.0	$(5.3 \pm 3.2) \times 10^{-5}$
G257.060–02.080	257.060	−2.085	4.8	58.3	0.27	Protostellar	21.8 ± 0.3	$(73.7 \pm 8.5) \times 10^{-7}$
G257.227–00.902	257.228	−0.900	6.0	117.0	0.81	Protostellar	13.5 ± 0.2	$(11.7 \pm 2.6) \times 10^{-5}$
G257.240–00.700	257.243	−0.697	2.2	52.1	0.10	Quiescent	13.8 ± 1.3	$(4.7 \pm 2.1) \times 10^{-5}$
G257.261–01.240	257.260	−1.245	1.2	64.4	0.08	Quiescent	18.5 ± 0.2	$(211.2 \pm 8.8) \times 10^{-7}$
G257.282–00.336	257.278	−0.333	5.9	103.7	0.69	YSO	14.1 ± 0.6	$(22.2 \pm 4.4) \times 10^{-5}$
G257.298–01.147	257.298	−1.147	2.9	42.5	0.08	Protostellar	16.3 ± 2.9	$(2.3 \pm 1.6) \times 10^{-5}$
G257.320–01.063	257.320	−1.063	2.7	42.5	0.07	YSO	25.0 ± 5.7	$(2.8 \pm 1.8) \times 10^{-5}$
G257.330–00.258	257.328	−0.257	5.6	42.5	0.15	Protostellar	21.5 ± 0.1	$(167.8 \pm 7.4) \times 10^{-7}$
G257.340–00.360	257.340	−0.355	5.9	74.1	0.46	YSO	18.3 ± 0.7	$(25.7 \pm 3.5) \times 10^{-6}$
G257.354–00.220	257.353	−0.220	5.6	126.2	0.82	Protostellar	13.3 ± 0.9	$(8.3 \pm 2.8) \times 10^{-5}$
G257.374–00.276	257.373	−0.277	1.3	57.6	0.07	Protostellar	13.6 ± 0.3	$(14.9 \pm 1.8) \times 10^{-5}$

Table A.4: continued

Name	ℓ_{app} (deg)	b_{app} (deg)	R_{hel} (kpc)	D_{app} ($''$)	D_{lin} (pc)	Class	T_{dust} (K)	τ_{350}
G257.380–00.280	257.377	−0.277	1.3	57.6	0.07	Protostellar	13.9 ± 0.4	$(13.9 \pm 1.9) \times 10^{-5}$
G257.460–00.610	257.458	−0.608	5.6	42.5	0.15	Protostellar	15.8 ± 0.5	$(59.9 \pm 8.0) \times 10^{-6}$
G257.470–00.630	257.473	−0.633	5.6	46.3	0.19	YSO	20.7 ± 2.7	$(3.2 \pm 1.4) \times 10^{-4}$
G257.510–02.250	257.509	−2.253	9.7	42.5	0.26	YSO	25.5 ± 6.5	$(2.0 \pm 1.4) \times 10^{-4}$
G257.540–01.270	257.538	−1.271	7.7	42.5	0.20	Quiescent	11.4 ± 0.4	$(14.8 \pm 3.0) \times 10^{-5}$
G257.540–01.630	257.540	−1.625	1.3	42.5	0.03	YSO	18.1 ± 1.8	$(23.5 \pm 8.6) \times 10^{-6}$
G257.546–01.214	257.545	−1.211	2.3	42.5	0.06	YSO	20.8 ± 0.4	$(10.2 \pm 1.7) \times 10^{-6}$
G257.560–00.480	257.557	−0.482	5.9	42.5	0.16	Protostellar	17.5 ± 3.0	$(3.2 \pm 2.1) \times 10^{-5}$
G257.570–02.070	257.574	−2.066	10.0	64.4	0.64	Protostellar	14.5 ± 0.2	$(128.1 \pm 8.5) \times 10^{-6}$
G257.610–00.660	257.608	−0.658	5.8	42.5	0.15	Protostellar	13.7 ± 1.3	$(7.8 \pm 3.5) \times 10^{-5}$
G257.617–01.772	257.617	−1.771	2.5	42.5	0.07	Protostellar	15.7 ± 0.5	$(71.6 \pm 8.9) \times 10^{-6}$
G257.630–00.590	257.633	−0.590	5.6	62.5	0.35	Quiescent	14.7 ± 1.1	$(25.3 \pm 8.4) \times 10^{-6}$
G257.630–01.050	257.628	−1.053	2.0	63.0	0.12	Protostellar	17.0 ± 1.0	$(39.1 \pm 8.8) \times 10^{-6}$
G257.640–00.959	257.638	−0.958	2.3	70.2	0.17	Quiescent	15.3 ± 1.0	$(3.7 \pm 1.0) \times 10^{-5}$
G257.655–01.250	257.655	−1.251	6.0	64.4	0.39	Quiescent	18.6 ± 1.7	$(10.8 \pm 3.6) \times 10^{-6}$
G257.808–01.277	257.807	−1.276	8.0	42.5	0.21	Protostellar	16.9 ± 3.1	$(4.8 \pm 3.5) \times 10^{-5}$
G257.830–00.740	257.830	−0.735	2.3	54.7	0.11	Quiescent	15.5 ± 0.7	$(26.3 \pm 5.2) \times 10^{-6}$
G257.842–01.085	257.842	−1.085	8.5	42.5	0.23	Protostellar	19.0 ± 1.3	$(21.1 \pm 5.4) \times 10^{-5}$
G257.864–01.086	257.863	−1.086	8.1	66.8	0.55	Protostellar	13.6 ± 0.6	$(13.9 \pm 3.1) \times 10^{-5}$
G257.865–01.495	257.867	−1.493	2.3	48.5	0.09	Protostellar	19.6 ± 0.5	$(25.9 \pm 2.4) \times 10^{-6}$
G257.867–01.793	257.869	−1.793	4.9	74.2	0.38	YSO	25.1 ± 0.2	$(53.2 \pm 3.2) \times 10^{-6}$
G257.879–01.729	257.879	−1.724	1.3	96.8	0.14	Protostellar	16.9 ± 0.1	$(37.0 \pm 2.2) \times 10^{-6}$
G257.920–00.470	257.920	−0.467	5.6	88.3	0.55	Protostellar	16.5 ± 0.9	$(45.2 \pm 9.5) \times 10^{-6}$
G257.932–01.387	257.932	−1.386	4.7	170.6	0.95	YSO	18.6 ± 2.5	$(4.9 \pm 2.3) \times 10^{-5}$
G257.940–00.942	257.938	−0.941	8.6	42.5	0.23	Quiescent	10.7 ± 0.2	$(19.4 \pm 2.1) \times 10^{-5}$
G257.950–00.170	257.948	−0.167	5.5	58.4	0.30	YSO	19.3 ± 1.0	$(24.5 \pm 4.5) \times 10^{-6}$
G257.950–00.510	257.946	−0.513	5.6	50.5	0.24	Protostellar	15.2 ± 0.7	$(7.6 \pm 1.6) \times 10^{-5}$
G257.960–00.940	257.962	−0.940	8.6	48.4	0.33	Protostellar	12.2 ± 0.1	$(20.8 \pm 1.0) \times 10^{-5}$
G257.978–01.428	257.978	−1.428	4.7	194.9	1.09	YSO	19.3 ± 1.1	$(23.0 \pm 4.8) \times 10^{-6}$
G258.000–00.300	258.000	−0.302	4.7	78.6	0.40	YSO	18.0 ± 0.6	$(35.8 \pm 4.7) \times 10^{-6}$
G258.050–01.341	258.050	−1.341	5.2	110.3	0.66	YSO	16.9 ± 1.6	$(10.3 \pm 3.8) \times 10^{-5}$
G258.047–01.604	258.048	−1.604	4.7	42.5	0.12	Protostellar	17.0 ± 0.6	$(7.9 \pm 1.0) \times 10^{-5}$
G258.080–01.350	258.078	−1.348	5.2	92.6	0.54	YSO	12.4 ± 1.3	$(3.0 \pm 1.6) \times 10^{-5}$
G258.080–01.563	258.080	−1.561	4.7	42.5	0.12	Quiescent	13.2 ± 0.4	$(14.0 \pm 2.3) \times 10^{-5}$
G258.081–01.561	258.080	−1.561	4.7	42.5	0.12	Quiescent	13.2 ± 0.4	$(14.0 \pm 2.3) \times 10^{-5}$
G258.080–01.561	258.080	−1.561	4.7	42.5	0.12	Quiescent	13.2 ± 0.4	$(14.0 \pm 2.3) \times 10^{-5}$
G258.081–01.558	258.080	−1.561	4.7	42.5	0.12	Quiescent	13.2 ± 0.4	$(14.0 \pm 2.3) \times 10^{-5}$
G258.082–01.626	258.081	−1.624	4.7	79.9	0.41	Protostellar	14.6 ± 0.4	$(10.7 \pm 1.2) \times 10^{-5}$
G258.140–00.350	258.139	−0.353	2.7	64.0	0.17	Protostellar	16.3 ± 0.6	$(9.4 \pm 1.4) \times 10^{-6}$
G258.182–01.512	258.181	−1.513	4.7	72.3	0.36	Protostellar	18.0 ± 2.2	$(2.3 \pm 1.0) \times 10^{-5}$
G258.194–02.221	258.193	−2.221	2.3	98.8	0.26	YSO	15.9 ± 0.2	$(53.7 \pm 2.4) \times 10^{-6}$
G258.190–02.277	258.190	−2.276	2.1	76.4	0.17	Quiescent	16.8 ± 2.3	$(5.9 \pm 3.2) \times 10^{-5}$
G258.255–01.233	258.253	−1.231	8.7	79.0	0.74	Protostellar	18.1 ± 1.5	$(16.7 \pm 5.1) \times 10^{-6}$
G258.260–00.870	258.263	−0.873	8.3	67.6	0.57	Quiescent	15.4 ± 0.5	$(18.3 \pm 2.7) \times 10^{-6}$
G258.300–00.520	258.300	−0.525	6.1	75.9	0.49	YSO	15.4 ± 1.4	$(3.4 \pm 1.4) \times 10^{-5}$
G258.300–02.163	258.301	−2.163	6.1	130.4	0.93	YSO	15.2 ± 2.1	$(8.4 \pm 5.1) \times 10^{-5}$
G258.319–00.920	258.320	−0.920	1.3	104.1	0.15	Quiescent	16.3 ± 0.7	$(42.7 \pm 7.8) \times 10^{-6}$
G258.340–02.190	258.343	−2.189	4.8	62.8	0.30	Protostellar	12.7 ± 0.9	$(13.0 \pm 4.9) \times 10^{-5}$
G258.384–01.113	258.382	−1.110	8.4	99.8	0.95	Quiescent	17.9 ± 1.1	$(23.0 \pm 5.1) \times 10^{-6}$

Table A.4: continued

Name	$\ell_{\rm app}$ (deg)	$b_{\rm app}$ (deg)	$R_{\rm hel}$ (kpc)	$D_{\rm app}$ ($''$)	$D_{\rm lin}$ (pc)	Class	$T_{\rm dust}$ (K)	τ_{350}
G258.420–00.940	258.417	−0.940	8.7	79.0	0.74	Protostellar	16.8 ± 0.8	$(21.6 \pm 4.2) \times 10^{-6}$
G258.430–00.940	258.433	−0.942	8.7	51.0	0.38	Quiescent	12.2 ± 0.6	$(11.8 \pm 3.1) \times 10^{-5}$
G258.427–01.444	258.426	−1.443	1.9	42.5	0.05	Protostellar	26.0 ± 2.1	$(9.4 \pm 5.5) \times 10^{-6}$
G258.532–01.188	258.532	−1.186	2.3	200.0	0.55	Protostellar	18.8 ± 2.2	$(2.5 \pm 1.0) \times 10^{-5}$
G258.610–01.920	258.608	−1.916	2.1	200.0	0.50	YSO	25.6 ± 0.3	$(92.4 \pm 6.8) \times 10^{-6}$
G258.660–00.390	258.663	−0.393	2.8	71.1	0.21	Protostellar	13.8 ± 0.6	$(6.3 \pm 1.2) \times 10^{-5}$
G258.667–01.050	258.667	−1.048	2.1	94.1	0.22	Quiescent	13.9 ± 0.7	$(6.2 \pm 1.5) \times 10^{-5}$
G258.718–01.168	258.720	−1.168	6.9	42.5	0.18	Protostellar	23.5 ± 0.2	$(58.7 \pm 3.3) \times 10^{-6}$
G258.733–01.335	258.733	−1.335	2.4	67.7	0.17	YSO	22.0 ± 0.2	$(58.3 \pm 4.1) \times 10^{-6}$
G258.743–01.291	258.743	−1.290	7.0	200.0	1.67	YSO	21.0 ± 0.1	$(23.9 \pm 1.1) \times 10^{-6}$
G258.790–00.970	258.788	−0.973	2.4	52.8	0.11	YSO	20.1 ± 1.3	$(20.2 \pm 4.3) \times 10^{-6}$
G258.792–01.422	258.793	−1.420	2.1	120.2	0.29	YSO	12.8 ± 0.7	$(11.1 \pm 3.1) \times 10^{-5}$
G258.822–01.402	258.823	−1.402	2.1	90.9	0.21	YSO	15.1 ± 0.3	$(100.6 \pm 8.8) \times 10^{-6}$
G258.842–01.446	258.843	−1.445	1.9	108.5	0.24	Protostellar	14.7 ± 1.3	$(13.3 \pm 5.3) \times 10^{-5}$
G258.860–01.397	258.860	−1.395	1.9	65.6	0.13	Quiescent	9.8 ± 0.7	$(4.1 \pm 1.9) \times 10^{-4}$
G258.870–01.475	258.872	−1.477	2.1	68.0	0.15	YSO	13.1 ± 0.6	$(17.0 \pm 3.6) \times 10^{-5}$
G258.880–00.720	258.883	−0.723	1.9	98.6	0.21	Protostellar	14.4 ± 0.4	$(7.9 \pm 1.1) \times 10^{-5}$
G258.878–01.440	258.878	−1.440	1.9	43.0	0.05	Quiescent	13.5 ± 0.6	$(16.8 \pm 3.9) \times 10^{-5}$
G258.885–01.498	258.885	−1.498	1.9	65.8	0.13	YSO	11.7 ± 1.4	$(3.7 \pm 2.5) \times 10^{-4}$
G258.910–01.450	258.910	−1.448	1.9	85.6	0.18	Quiescent	11.9 ± 0.2	$(13.3 \pm 1.5) \times 10^{-5}$
G258.930–00.730	258.927	−0.727	1.9	82.8	0.17	Protostellar	11.8 ± 0.8	$(2.7 \pm 1.0) \times 10^{-4}$
G258.960–00.720	258.962	−0.723	1.9	64.4	0.12	Quiescent	16.2 ± 1.2	$(30.0 \pm 8.9) \times 10^{-6}$
G258.965–01.475	258.967	−1.473	6.5	113.3	0.84	Protostellar	15.0 ± 1.3	$(8.1 \pm 3.0) \times 10^{-5}$
G259.002–01.498	259.005	−1.502	6.5	85.0	0.60	YSO	17.6 ± 0.3	$(6.9 \pm 1.1) \times 10^{-5}$
G259.018–01.550	259.018	−1.550	6.3	112.9	0.82	YSO	27.5 ± 5.9	$(2.6 \pm 1.5) \times 10^{-4}$
G259.031–00.496	259.030	−0.497	2.6	60.0	0.15	Quiescent	15.0 ± 1.1	$(6.2 \pm 2.0) \times 10^{-5}$
G259.052–01.140	259.055	−1.142	6.5	86.5	0.62	YSO	15.9 ± 0.3	$(51.3 \pm 4.6) \times 10^{-6}$
G259.050–01.538	259.050	−1.537	6.5	91.1	0.66	YSO	31.4 ± 1.6	$(20.4 \pm 6.5) \times 10^{-5}$
G259.045–01.557	259.045	−1.557	6.5	82.8	0.59	YSO	33.3 ± 1.6	$(27.7 \pm 7.7) \times 10^{-5}$
G259.080–00.050	259.082	−0.048	1.4	42.5	0.04	Quiescent	18.8 ± 0.8	$(29.2 \pm 4.6) \times 10^{-6}$
G259.078–01.620	259.078	−1.620	6.5	49.9	0.27	YSO	28.8 ± 0.7	$(26.1 \pm 4.5) \times 10^{-5}$
G259.112–01.437	259.112	−1.437	2.4	121.5	0.34	Protostellar	13.9 ± 0.3	$(17.2 \pm 1.5) \times 10^{-5}$
G259.133–01.426	259.133	−1.427	2.4	168.1	0.48	Quiescent	13.4 ± 0.1	$(119.5 \pm 4.1) \times 10^{-6}$
G259.153–01.337	259.153	−1.337	2.2	134.3	0.34	Quiescent	14.3 ± 0.1	$(101.2 \pm 4.5) \times 10^{-6}$
G259.165–01.217	259.165	−1.217	2.2	141.5	0.36	Quiescent	13.1 ± 0.3	$(51.8 \pm 5.7) \times 10^{-6}$
G259.172–01.253	259.170	−1.252	2.2	71.9	0.17	Protostellar	16.0 ± 0.1	$(58.1 \pm 3.1) \times 10^{-6}$
G259.167–01.313	259.167	−1.312	2.2	97.4	0.24	Protostellar	15.2 ± 1.1	$(5.9 \pm 1.8) \times 10^{-5}$
G259.190–00.030	259.187	−0.027	1.1	42.5	0.03	Protostellar	16.9 ± 0.2	$(64.4 \pm 5.5) \times 10^{-6}$
G259.200+00.000	259.197	−0.002	1.4	42.5	0.04	Protostellar	14.7 ± 0.9	$(13.7 \pm 3.9) \times 10^{-5}$
G259.200–00.010	259.203	−0.012	1.4	69.1	0.10	Protostellar	17.6 ± 0.9	$(5.8 \pm 3.1) \times 10^{-5}$
G259.198–01.272	259.197	−1.270	2.2	171.7	0.45	Quiescent	15.2 ± 0.3	$(55.6 \pm 4.9) \times 10^{-6}$
G259.215–01.389	259.217	−1.390	6.4	162.2	1.23	Quiescent	13.6 ± 0.7	$(14.3 \pm 3.6) \times 10^{-5}$
G259.217–01.390	259.217	−1.390	6.4	162.2	1.23	Quiescent	13.7 ± 1.0	$(14.8 \pm 5.3) \times 10^{-5}$
G259.230–00.030	259.232	−0.033	2.2	60.7	0.13	Protostellar	14.2 ± 2.1	$(4.1 \pm 2.8) \times 10^{-5}$
G259.230–00.300	259.233	−0.298	1.9	48.0	0.07	Protostellar	21.4 ± 0.9	$(11.7 \pm 1.5) \times 10^{-6}$
G259.240–00.320	259.243	−0.317	5.6	73.5	0.43	Quiescent	15.5 ± 0.2	$(42.9 \pm 2.6) \times 10^{-6}$
G259.237–01.627	259.237	−1.627	6.8	64.7	0.44	YSO	29.9 ± 1.0	$(19.7 \pm 4.1) \times 10^{-5}$
G259.250–00.050	259.248	−0.052	2.2	59.9	0.13	Protostellar	12.1 ± 0.6	$(4.3 \pm 1.1) \times 10^{-4}$
G259.245–01.227	259.245	−1.227	5.0	130.8	0.76	Protostellar	14.1 ± 0.3	$(14.3 \pm 1.5) \times 10^{-5}$

Table A.4: continued

Name	ℓ_{app} (deg)	b_{app} (deg)	R_{hel} (kpc)	D_{app} ($''$)	D_{lin} (pc)	Class	T_{dust} (K)	τ_{350}
G259.250–02.020	259.252	−2.022	6.1	99.9	0.69	Quiescent	15.2 ± 0.1	$(127.2 \pm 3.7) \times 10^{-6}$
G259.270–00.330	259.265	−0.330	1.9	45.7	0.06	Quiescent	12.0 ± 1.0	$(7.3 \pm 3.3) \times 10^{-5}$
G259.272–01.238	259.272	−1.238	2.2	127.0	0.32	YSO	14.8 ± 1.4	$(2.5 \pm 1.0) \times 10^{-4}$
G259.292–01.955	259.292	−1.955	6.1	45.4	0.20	YSO	24.0 ± 4.2	$(3.5 \pm 1.8) \times 10^{-4}$
G259.302–01.220	259.300	−1.218	2.2	88.4	0.21	Quiescent	13.4 ± 1.0	$(24.9 \pm 8.7) \times 10^{-5}$
G259.320–01.740	259.320	−1.735	1.9	83.5	0.17	Protostellar	14.2 ± 0.4	$(7.6 \pm 1.1) \times 10^{-5}$
G259.320–01.780	259.323	−1.782	1.9	42.5	0.05	Quiescent	11.1 ± 0.1	$(24.3 \pm 1.7) \times 10^{-5}$
G259.340–01.444	259.338	−1.445	1.9	42.5	0.05	YSO	19.3 ± 0.4	$(44.5 \pm 3.7) \times 10^{-5}$
G259.330–01.780	259.333	−1.778	1.9	42.5	0.05	YSO	20.6 ± 0.3	$(23.3 \pm 1.2) \times 10^{-5}$
G259.340–00.450	259.342	−0.448	2.4	89.1	0.24	YSO	17.0 ± 0.5	$(47.4 \pm 5.7) \times 10^{-6}$
G259.338–01.445	259.338	−1.445	1.9	42.5	0.05	YSO	19.3 ± 0.4	$(44.5 \pm 3.7) \times 10^{-5}$
G259.360–01.740	259.357	−1.737	1.9	54.0	0.09	YSO	19.8 ± 2.3	$(11.8 \pm 4.7) \times 10^{-6}$
G259.368–01.192	259.368	−1.190	6.5	88.3	0.63	YSO	14.5 ± 0.5	$(15.5 \pm 2.4) \times 10^{-5}$
G259.383–01.083	259.388	−1.083	6.2	64.4	0.40	Protostellar	17.0 ± 1.7	$(16.0 \pm 6.4) \times 10^{-5}$
G259.390–00.180	259.393	−0.177	2.2	60.5	0.13	Protostellar	15.8 ± 0.9	$(7.8 \pm 1.8) \times 10^{-5}$
G259.390–01.710	259.387	−1.707	1.9	75.3	0.15	YSO	13.3 ± 0.1	$(500.1 \pm 8.5) \times 10^{-7}$
G259.400–01.075	259.400	−1.072	6.4	135.9	1.02	YSO	17.1 ± 0.5	$(28.4 \pm 3.3) \times 10^{-5}$
G259.405–01.162	259.403	−1.162	6.0	75.2	0.48	YSO	16.2 ± 2.8	$(9.7 \pm 6.9) \times 10^{-5}$
G259.410–01.488	259.408	−1.488	2.2	187.7	0.49	Quiescent	13.0 ± 0.5	$(18.9 \pm 3.6) \times 10^{-5}$
G259.409–01.302	259.408	−1.303	2.2	73.4	0.17	YSO	14.6 ± 0.8	$(8.5 \pm 2.2) \times 10^{-5}$
G259.410–01.710	259.413	−1.708	1.9	73.0	0.15	Quiescent	13.1 ± 0.5	$(13.8 \pm 2.5) \times 10^{-5}$
G259.417–01.065	259.417	−1.065	6.5	57.2	0.35	YSO	18.0 ± 0.1	$(148.4 \pm 2.1) \times 10^{-6}$
G259.440–01.080	259.438	−1.078	6.2	200.0	1.48	YSO	17.0 ± 2.7	$(14.1 \pm 8.8) \times 10^{-5}$
G259.450–00.330	259.452	−0.328	1.7	62.4	0.10	YSO	24.4 ± 0.2	$(84.7 \pm 5.4) \times 10^{-7}$
G259.463–01.065	259.462	−1.067	6.4	177.3	1.35	YSO	15.5 ± 0.5	$(10.8 \pm 1.4) \times 10^{-5}$
G259.457–01.110	259.457	−1.110	6.2	153.0	1.12	YSO	15.0 ± 0.2	$(106.2 \pm 5.6) \times 10^{-6}$
G259.560–00.930	259.563	−0.927	6.0	49.1	0.24	YSO	32.5 ± 1.5	$(4.6 \pm 1.2) \times 10^{-4}$
G259.570–01.020	259.568	−1.022	6.0	57.4	0.32	YSO	16.7 ± 1.9	$(4.5 \pm 2.0) \times 10^{-4}$
G259.570–01.430	259.570	−1.435	2.2	42.5	0.06	YSO	18.6 ± 2.1	$(3.8 \pm 1.5) \times 10^{-4}$
G259.610–01.300	259.608	−1.302	6.3	42.5	0.17	YSO	19.3 ± 0.9	$(57.8 \pm 9.5) \times 10^{-5}$
G259.640–01.320	259.643	−1.317	6.3	66.7	0.43	YSO	26.8 ± 1.6	$(16.1 \pm 6.6) \times 10^{-5}$
G259.652–01.313	259.652	−1.315	6.3	42.5	0.17	YSO	26.1 ± 5.9	$(2.1 \pm 1.3) \times 10^{-4}$
G259.668–01.318	259.668	−1.318	6.4	42.5	0.17	YSO	26.7 ± 7.3	$(8.1 \pm 6.0) \times 10^{-4}$
G259.700–01.280	259.703	−1.277	6.3	200.0	1.50	YSO	20.6 ± 2.7	$(9.8 \pm 4.3) \times 10^{-5}$
G259.711–01.934	259.715	−1.933	2.0	106.1	0.24	YSO	13.1 ± 1.4	$(6.8 \pm 3.6) \times 10^{-5}$
G259.750–01.340	259.748	−1.343	6.3	56.3	0.33	YSO	25.1 ± 0.1	$(118.4 \pm 5.1) \times 10^{-6}$
G259.860–02.030	259.860	−2.035	2.5	42.5	0.07	Protostellar	15.0 ± 1.2	$(17.4 \pm 6.1) \times 10^{-6}$
G259.870–02.400	259.870	−2.403	2.0	110.1	0.25	Protostellar	13.0 ± 0.2	$(86.8 \pm 6.9) \times 10^{-5}$
G259.880–02.020	259.884	−2.018	2.0	42.5	0.05	Protostellar	18.3 ± 1.2	$(18.4 \pm 4.6) \times 10^{-6}$
G259.880–02.410	259.882	−2.413	2.0	55.8	0.10	Protostellar	12.9 ± 0.3	$(82.4 \pm 9.7) \times 10^{-5}$
G259.890–02.420	259.894	−2.421	2.0	62.1	0.12	Protostellar	14.2 ± 0.2	$(67.4 \pm 5.3) \times 10^{-5}$
G259.900–01.970	259.904	−1.970	2.0	42.5	0.05	Quiescent	18.6 ± 3.1	$(10.8 \pm 6.7) \times 10^{-6}$
G259.900–02.430	259.900	−2.425	2.0	42.5	0.05	Protostellar	13.9 ± 0.2	$(79.6 \pm 4.9) \times 10^{-5}$
G259.950–01.330	259.952	−1.327	6.9	42.5	0.18	YSO	21.0 ± 0.8	$(15.4 \pm 2.0) \times 10^{-6}$
G260.000–00.160	260.000	−0.157	1.7	200.0	0.41	YSO	17.7 ± 1.4	$(19.9 \pm 6.0) \times 10^{-5}$
G225.472–01.674	225.468	−1.675	1.4	42.5	0.04	Protostellar	18.3 ± 1.1	$(26.8 \pm 5.9) \times 10^{-6}$
G226.125–00.316	226.120	−0.315	1.2	42.5	0.03	Protostellar	11.2 ± 0.5	$(14.1 \pm 3.9) \times 10^{-5}$
G232.062–00.126	232.067	−0.125	1.7	121.4	0.24	Protostellar	14.2 ± 0.5	$(39.6 \pm 6.7) \times 10^{-6}$
G231.841–01.752	231.846	−1.752	4.3	66.6	0.29	YSO	16.0 ± 2.5	$(3.6 \pm 2.3) \times 10^{-5}$

Table A.4: continued

Name	ℓ_{app} (deg)	b_{app} (deg)	R_{hel} (kpc)	D_{app} ($''$)	D_{lin} (pc)	Class	T_{dust} (K)	τ_{350}
G232.894–00.613	232.892	−0.612	3.9	97.7	0.43	YSO	12.1 ± 0.6	$(14.2 \pm 3.7) \times 10^{-5}$
G233.067–01.271	233.068	−1.273	4.0	133.9	0.62	YSO	15.6 ± 0.2	$(22.6 \pm 1.5) \times 10^{-6}$
G233.840–00.183	233.835	−0.183	3.8	42.5	0.10	YSO	36.5 ± 8.3	$(11.2 \pm 5.5) \times 10^{-4}$
G233.757–01.269	233.753	−1.270	2.6	71.8	0.19	Protostellar	12.2 ± 0.1	$(86.9 \pm 5.5) \times 10^{-6}$
G234.476–00.003	234.474	−0.007	2.5	158.5	0.47	YSO	18.5 ± 2.2	$(9.1 \pm 3.9) \times 10^{-5}$
G242.625–00.878	242.620	−0.878	6.1	140.7	1.01	YSO	13.9 ± 0.6	$(33.3 \pm 7.0) \times 10^{-6}$
G247.796–00.823	247.800	−0.827	2.0	112.2	0.26	YSO	12.9 ± 1.5	$(15.7 \pm 9.4) \times 10^{-6}$
G252.029–01.864	252.028	−1.869	5.0	49.5	0.20	Quiescent	20.1 ± 2.6	$(9.9 \pm 3.4) \times 10^{-6}$
G252.173–01.872	252.168	−1.873	7.1	49.7	0.29	Protostellar	14.0 ± 0.7	$(6.9 \pm 1.7) \times 10^{-5}$
G253.950–00.563	253.953	−0.567	4.2	200.0	1.00	YSO	17.6 ± 0.2	$(83.7 \pm 3.1) \times 10^{-6}$
G256.422–02.208	256.418	−2.208	1.5	124.8	0.22	Quiescent	13.5 ± 1.6	$(5.3 \pm 3.1) \times 10^{-5}$
G257.870–01.498	257.867	−1.495	1.3	48.5	0.05	Protostellar	18.3 ± 0.7	$(32.9 \pm 4.9) \times 10^{-6}$
G257.894–01.885	257.890	−1.883	1.3	59.0	0.07	YSO	17.0 ± 2.7	$(3.4 \pm 2.1) \times 10^{-5}$
G258.090–01.577	258.095	−1.576	1.6	64.4	0.10	Protostellar	10.2 ± 0.4	$(10.2 \pm 2.5) \times 10^{-5}$
G258.114–01.904	258.110	−1.904	1.8	46.8	0.06	Protostellar	14.9 ± 0.1	$(438.4 \pm 7.6) \times 10^{-7}$
G258.347–02.182	258.346	−2.186	1.3	62.8	0.08	Protostellar	11.6 ± 0.9	$(10.7 \pm 4.9) \times 10^{-5}$
G258.681–01.774	258.681	−1.778	6.6	42.5	0.17	Quiescent	15.4 ± 0.3	$(50.9 \pm 3.7) \times 10^{-6}$
G258.691–01.773	258.688	−1.776	6.4	42.5	0.17	Quiescent	18.6 ± 2.1	$(19.2 \pm 8.2) \times 10^{-6}$
G259.408–00.860	259.408	−0.865	4.0	52.7	0.18	Protostellar	20.5 ± 0.9	$(17.1 \pm 2.4) \times 10^{-6}$
G259.446–00.838	259.443	−0.837	6.4	51.9	0.29	Quiescent	15.8 ± 0.6	$(33.2 \pm 4.9) \times 10^{-6}$
G259.643–00.659	259.638	−0.658	1.7	68.8	0.12	YSO	16.6 ± 1.6	$(23.4 \pm 8.7) \times 10^{-6}$
G259.480–01.135	259.480	−1.130	6.7	75.3	0.54	YSO	14.7 ± 0.2	$(64.9 \pm 9.4) \times 10^{-6}$
G259.691–00.614	259.693	−0.618	1.7	89.8	0.17	YSO	21.1 ± 0.3	$(61.0 \pm 7.5) \times 10^{-7}$
G259.545–00.807	259.540	−0.807	1.9	88.5	0.19	Quiescent	14.3 ± 0.2	$(65.9 \pm 4.7) \times 10^{-6}$
G259.847–00.465	259.850	−0.468	1.7	87.4	0.16	YSO	15.9 ± 1.3	$(21.5 \pm 7.5) \times 10^{-6}$
G259.908–01.942	259.905	−1.945	2.5	90.1	0.25	YSO	20.4 ± 0.7	$(7.5 \pm 2.1) \times 10^{-6}$

Table A.5: Physical parameters derived from the dust SEDs for all sources: bolometric luminosity L, clump mass M, column density N_{H_2}, and luminosity-to-mass ratio L/M.

Name	L ($L_\odot$)	M ($M_\odot$)	N_{H_2} (cm^{-2})	L/M ($L_\odot/M_\odot$)
G225.020–00.590	$(49.5\pm3.2)\times10^{-2}$	$(5.3\pm1.7)\times10^{+0}$	$(31.8\pm1.6)\times10^{20}$	$(9.3\pm3.0)\times10^{-2}$
G225.030+00.060	$(383.5\pm4.7)\times10^{-3}$	$(31.6\pm8.7)\times10^{-2}$	$(22.1\pm1.8)\times10^{19}$	$(12.1\pm3.3)\times10^{-1}$
G225.080+00.060	$(58.0\pm2.5)\times10^{-2}$	$(9.0\pm2.5)\times10^{-1}$	$(54.8\pm5.3)\times10^{19}$	$(6.4\pm1.8)\times10^{-1}$
G225.160–00.830	$(29.1\pm2.1)\times10^{-1}$	$(6.2\pm1.7)\times10^{-1}$	$(27.6\pm2.4)\times10^{19}$	$(4.7\pm1.3)\times10^{+0}$
G225.160–00.840	$(56.5\pm6.9)\times10^{-2}$	$(3.6\pm1.1)\times10^{-1}$	$(28.0\pm2.9)\times10^{19}$	$(15.8\pm5.1)\times10^{-1}$
G225.170–00.750	$(64.5\pm7.6)\times10^{-2}$	$(24.4\pm8.0)\times10^{-2}$	$(33.8\pm5.7)\times10^{19}$	$(26.4\pm9.2)\times10^{-1}$
G225.210–01.110	$(97.8\pm1.1)\times10^{-1}$	$(4.4\pm1.3)\times10^{+1}$	$(146.0\pm1.4)\times10^{20}$	$(22.4\pm6.8)\times10^{-2}$
G225.220–01.200	$(56.7\pm2.0)\times10^{-2}$	$(28.7\pm9.2)\times10^{-2}$	$(34.6\pm3.8)\times10^{19}$	$(19.8\pm6.4)\times10^{-1}$
G225.230–00.960	$(166.7\pm5.5)\times10^{-2}$	$(14.9\pm4.6)\times10^{-1}$	$(79.0\pm3.8)\times10^{19}$	$(11.2\pm3.5)\times10^{-1}$
G225.240–01.110	$(223.8\pm2.6)\times10^{-3}$	$(26.0\pm8.4)\times10^{-2}$	$(6.1\pm1.5)\times10^{20}$	$(8.6\pm2.8)\times10^{-1}$
G225.300–01.090	$(37.7\pm5.3)\times10^{-2}$	$(11.9\pm4.0)\times10^{-1}$	$(15.0\pm2.3)\times10^{20}$	$(3.2\pm1.2)\times10^{-1}$
G225.320–00.280	$(75.1\pm3.2)\times10^{-1}$	$(7.3\pm2.3)\times10^{+0}$	$(40.6\pm2.0)\times10^{20}$	$(10.2\pm3.2)\times10^{-1}$
G225.320–01.100	$(17.3\pm1.6)\times10^{+0}$	$(11.4\pm3.6)\times10^{+0}$	$(71.9\pm4.2)\times10^{20}$	$(15.1\pm5.0)\times10^{-1}$
G225.320–01.170	$(7.9\pm1.1)\times10^{-1}$	$(8.4\pm2.9)\times10^{-1}$	$(15.1\pm2.7)\times10^{20}$	$(9.4\pm3.5)\times10^{-1}$
G225.330–00.540	$(55.4\pm9.0)\times10^{+0}$	$(5.0\pm1.6)\times10^{+0}$	$(8.0\pm2.2)\times10^{21}$	$(11.0\pm3.9)\times10^{+0}$
G225.330–01.120	$(511.7\pm9.5)\times10^{-3}$	$(8.2\pm2.5)\times10^{-1}$	$(12.6\pm2.0)\times10^{20}$	$(6.2\pm1.9)\times10^{-1}$
G225.370–01.380	$(40.0\pm1.3)\times10^{-2}$	$(22.4\pm7.2)\times10^{-2}$	$(32.4\pm5.0)\times10^{19}$	$(17.9\pm5.8)\times10^{-1}$
G225.380–00.540	$(242.4\pm4.1)\times10^{-2}$	$(7.8\pm2.3)\times10^{+0}$	$(48.9\pm3.0)\times10^{20}$	$(30.9\pm9.1)\times10^{-2}$
G225.390–00.990	$(59.6\pm2.2)\times10^{-2}$	$(7.8\pm2.4)\times10^{-1}$	$(13.9\pm2.7)\times10^{20}$	$(7.6\pm2.4)\times10^{-1}$
G225.390–01.370	$(22.6\pm3.3)\times10^{-1}$	$(7.7\pm2.7)\times10^{-1}$	$(64.6\pm5.7)\times10^{19}$	$(2.9\pm1.1)\times10^{+0}$
G225.400–00.560	$(85.1\pm9.2)\times10^{-1}$	$(15.1\pm4.7)\times10^{-1}$	$(37.5\pm9.2)\times10^{20}$	$(5.6\pm1.9)\times10^{+0}$
G225.440–00.390	$(146.4\pm5.5)\times10^{-1}$	$(17.0\pm4.7)\times10^{+0}$	$(366.3\pm8.3)\times10^{19}$	$(8.6\pm2.4)\times10^{-1}$
G225.460–01.680	$(797.4\pm6.3)\times10^{-3}$	$(30.4\pm8.9)\times10^{-2}$	$(37.2\pm6.7)\times10^{19}$	$(26.3\pm7.7)\times10^{-1}$
G225.470–01.680	$(77.9\pm1.5)\times10^{-2}$	$(18.7\pm5.5)\times10^{-2}$	$(29.9\pm5.7)\times10^{19}$	$(4.2\pm1.2)\times10^{+0}$
G225.480–00.230	$(842.6\pm7.8)\times10^{-2}$	$(5.1\pm1.5)\times10^{+1}$	$(139.9\pm2.2)\times10^{20}$	$(16.7\pm4.9)\times10^{-2}$
G225.480–01.790	$(39.9\pm2.3)\times10^{-1}$	$(6.3\pm1.9)\times10^{-1}$	$(7.8\pm1.5)\times10^{20}$	$(6.4\pm1.9)\times10^{+0}$
G225.480–01.800	$(43.0\pm2.8)\times10^{-1}$	$(3.5\pm1.1)\times10^{-1}$	$(5.6\pm1.4)\times10^{20}$	$(12.3\pm3.8)\times10^{+0}$
G225.490–00.400	$(135.6\pm1.1)\times10^{-1}$	$(16.2\pm4.8)\times10^{+0}$	$(355.4\pm5.5)\times10^{19}$	$(8.4\pm2.5)\times10^{-1}$
G225.490–01.780	$(69.9\pm4.2)\times10^{-1}$	$(9.0\pm2.7)\times10^{-1}$	$(78.6\pm7.8)\times10^{19}$	$(7.8\pm2.4)\times10^{+0}$
G225.490–01.810	$(22.3\pm4.1)\times10^{+0}$	$(25.0\pm8.6)\times10^{-1}$	$(121.1\pm6.2)\times10^{19}$	$(8.9\pm3.5)\times10^{+0}$
G225.500–01.230	$(79.6\pm3.5)\times10^{-3}$	$(23.1\pm8.6)\times10^{-3}$	$(8.4\pm1.9)\times10^{19}$	$(3.5\pm1.3)\times10^{+0}$
G225.500–01.770	$(259.6\pm5.0)\times10^{-2}$	$(4.9\pm1.5)\times10^{-1}$	$(7.2\pm1.7)\times10^{20}$	$(5.3\pm1.6)\times10^{+0}$
G225.510–01.230	$(92.5\pm4.3)\times10^{-3}$	$(7.6\pm2.8)\times10^{-2}$	$(19.8\pm3.7)\times10^{19}$	$(12.2\pm4.5)\times10^{-1}$
G225.510–01.740	$(81.0\pm7.8)\times10^{-1}$	$(8.9\pm3.0)\times10^{-2}$	$(529.6\pm6.3)\times10^{18}$	$(9.1\pm3.2)\times10^{+1}$
G225.510–01.780	$(169.7\pm1.5)\times10^{-1}$	$(6.1\pm1.8)\times10^{+0}$	$(159.6\pm3.6)\times10^{19}$	$(27.8\pm8.2)\times10^{-1}$
G225.660–00.220	$(82.9\pm1.6)\times10^{-1}$	$(5.9\pm1.6)\times10^{+0}$	$(241.3\pm7.5)\times10^{19}$	$(14.0\pm3.9)\times10^{-1}$
G225.780–00.940	$(497.8\pm9.5)\times10^{-2}$	$(19.6\pm6.0)\times10^{+0}$	$(14.5\pm1.0)\times10^{21}$	$(25.3\pm7.8)\times10^{-2}$
G225.980+00.080	$(27.3\pm2.2)\times10^{-1}$	$(4.5\pm1.3)\times10^{-1}$	$(23.2\pm2.2)\times10^{19}$	$(6.1\pm1.8)\times10^{+0}$
G226.117–00.349	$(30.1\pm2.3)\times10^{+0}$	$(10.8\pm3.4)\times10^{-1}$	$(24.8\pm5.0)\times10^{20}$	$(27.9\pm9.0)\times10^{+0}$
G226.280–02.070	$(429.3\pm6.8)\times10^{-3}$	$(18.8\pm6.4)\times10^{-2}$	$(27.0\pm3.3)\times10^{19}$	$(22.8\pm7.7)\times10^{-1}$
G226.330–02.030	$(59.3\pm1.8)\times10^{-2}$	$(4.8\pm1.6)\times10^{-1}$	$(40.2\pm2.7)\times10^{19}$	$(12.3\pm4.2)\times10^{-1}$
G226.353–00.766	$(10.6\pm2.9)\times10^{+1}$	$(6.7\pm2.8)\times10^{+0}$	$(17.6\pm6.5)\times10^{21}$	$(15.7\pm7.8)\times10^{+0}$
G226.670–02.060	$(67.4\pm3.3)\times10^{-2}$	$(4.7\pm1.5)\times10^{-1}$	$(31.4\pm2.3)\times10^{19}$	$(14.4\pm4.5)\times10^{-1}$
G227.040–00.900	$(208.0\pm4.7)\times10^{-1}$	$(8.7\pm1.8)\times10^{+1}$	$(56.7\pm8.3)\times10^{20}$	$(23.8\pm5.0)\times10^{-2}$
G227.180–00.460	$(146.1\pm4.4)\times10^{-3}$	$(5.1\pm1.4)\times10^{-2}$	$(6.3\pm1.4)\times10^{19}$	$(28.5\pm7.9)\times10^{-1}$
G227.230–00.830	$(141.6\pm6.9)\times10^{-2}$	$(15.7\pm4.3)\times10^{-1}$	$(78.4\pm5.0)\times10^{19}$	$(9.0\pm2.5)\times10^{-1}$
G227.570–01.140	$(36.2\pm3.7)\times10^{+1}$	$(12.7\pm2.9)\times10^{+1}$	$(5.2\pm1.1)\times10^{21}$	$(28.6\pm7.1)\times10^{-1}$

Table A.5: continued

Name	L ($L_\odot$)	M ($M_\odot$)	N_{H_2} (cm^{-2})	L/M ($L_\odot/M_\odot$)
G227.650–01.286	$(144.8 \pm 1.7) \times 10^{-1}$	$(7.8 \pm 1.6) \times 10^{+1}$	$(35.0 \pm 8.2) \times 10^{20}$	$(18.6 \pm 3.8) \times 10^{-2}$
G227.689–00.121	$(14.4 \pm 3.7) \times 10^{+1}$	$(8.7 \pm 2.9) \times 10^{+0}$	$(26.4 \pm 1.0) \times 10^{19}$	$(16.5 \pm 6.9) \times 10^{+0}$
G227.792–00.104	$(39.4 \pm 4.0) \times 10^{+1}$	$(35.8 \pm 8.3) \times 10^{+0}$	$(72.9 \pm 1.9) \times 10^{19}$	$(11.0 \pm 2.8) \times 10^{+0}$
G227.800–00.080	$(5.1 \pm 1.2) \times 10^{+1}$	$(11.3 \pm 3.5) \times 10^{+0}$	$(8.3 \pm 1.2) \times 10^{20}$	$(4.5 \pm 1.8) \times 10^{+0}$
G227.800–00.140	$(20.4 \pm 5.2) \times 10^{+1}$	$(22.0 \pm 7.2) \times 10^{+0}$	$(88.6 \pm 8.7) \times 10^{19}$	$(9.3 \pm 3.8) \times 10^{+0}$
G227.810–00.120	$(76.6 \pm 3.2) \times 10^{+0}$	$(16.3 \pm 3.5) \times 10^{+0}$	$(23.0 \pm 5.1) \times 10^{20}$	$(4.7 \pm 1.0) \times 10^{+0}$
G227.815–00.129	$(87.5 \pm 8.2) \times 10^{+0}$	$(18.3 \pm 4.2) \times 10^{+0}$	$(23.9 \pm 6.2) \times 10^{20}$	$(4.8 \pm 1.2) \times 10^{+0}$
G227.820–00.140	$(84.0 \pm 2.8) \times 10^{+1}$	$(10.3 \pm 2.2) \times 10^{+1}$	$(41.8 \pm 1.4) \times 10^{20}$	$(8.2 \pm 1.8) \times 10^{+0}$
G227.820–00.160	$(361.1 \pm 9.3) \times 10^{+0}$	$(36.8 \pm 7.8) \times 10^{+0}$	$(154.1 \pm 7.4) \times 10^{19}$	$(9.8 \pm 2.1) \times 10^{+0}$
G227.862–00.243	$(39.4 \pm 3.5) \times 10^{+0}$	$(18.5 \pm 4.2) \times 10^{+0}$	$(12.4 \pm 1.3) \times 10^{20}$	$(21.2 \pm 5.2) \times 10^{-1}$
G227.880–01.780	$(38.7 \pm 3.6) \times 10^{-2}$	$(5.0 \pm 1.5) \times 10^{+0}$	$(22.0 \pm 1.7) \times 10^{20}$	$(7.7 \pm 2.3) \times 10^{-2}$
G227.910–01.880	$(313.1 \pm 7.1) \times 10^{-2}$	$(4.5 \pm 1.3) \times 10^{+0}$	$(149.5 \pm 5.8) \times 10^{19}$	$(6.9 \pm 1.9) \times 10^{-1}$
G227.940–00.139	$(163.5 \pm 2.3) \times 10^{-1}$	$(5.9 \pm 1.2) \times 10^{+1}$	$(4.8 \pm 1.0) \times 10^{21}$	$(27.9 \pm 5.8) \times 10^{-2}$
G228.030+00.010	$(54.5 \pm 2.5) \times 10^{-1}$	$(19.6 \pm 4.2) \times 10^{+0}$	$(19.8 \pm 3.2) \times 10^{20}$	$(27.9 \pm 6.1) \times 10^{-2}$
G228.030+00.020	$(49.4 \pm 1.3) \times 10^{-1}$	$(22.9 \pm 4.8) \times 10^{+0}$	$(22.3 \pm 3.6) \times 10^{20}$	$(21.6 \pm 4.6) \times 10^{-2}$
G228.027–00.924	$(28.8 \pm 1.2) \times 10^{-1}$	$(14.1 \pm 3.2) \times 10^{+0}$	$(22.4 \pm 2.3) \times 10^{20}$	$(20.4 \pm 4.7) \times 10^{-2}$
G228.026–00.946	$(622.3 \pm 9.5) \times 10^{-1}$	$(23.0 \pm 5.1) \times 10^{+0}$	$(27.5 \pm 1.4) \times 10^{20}$	$(27.1 \pm 6.0) \times 10^{-1}$
G228.300–00.970	$(268.9 \pm 2.4) \times 10^{-2}$	$(22.6 \pm 5.0) \times 10^{-1}$	$(49.5 \pm 7.2) \times 10^{19}$	$(11.9 \pm 2.6) \times 10^{-1}$
G228.710–00.910	$(54.8 \pm 3.5) \times 10^{-1}$	$(31.0 \pm 6.9) \times 10^{+0}$	$(29.8 \pm 2.7) \times 10^{20}$	$(17.6 \pm 4.1) \times 10^{-2}$
G229.750+00.030	$(63.7 \pm 4.4) \times 10^{+0}$	$(8.6 \pm 1.9) \times 10^{+1}$	$(152.7 \pm 9.1) \times 10^{19}$	$(7.4 \pm 1.7) \times 10^{-1}$
G229.770+00.040	$(19.5 \pm 3.9) \times 10^{+1}$	$(6.5 \pm 1.9) \times 10^{+1}$	$(20.2 \pm 2.3) \times 10^{20}$	$(3.0 \pm 1.0) \times 10^{+0}$
G229.770+00.060	$(101.8 \pm 4.9) \times 10^{+1}$	$(18.4 \pm 3.9) \times 10^{+1}$	$(8.7 \pm 1.1) \times 10^{21}$	$(5.5 \pm 1.2) \times 10^{+0}$
G229.780+00.050	$(300.1 \pm 2.6) \times 10^{+0}$	$(34.7 \pm 7.1) \times 10^{+0}$	$(44.1 \pm 9.6) \times 10^{20}$	$(8.6 \pm 1.8) \times 10^{+0}$
G229.790–00.680	$(243.3 \pm 4.7) \times 10^{-2}$	$(17.1 \pm 3.7) \times 10^{+0}$	$(41.7 \pm 9.1) \times 10^{20}$	$(14.2 \pm 3.1) \times 10^{-2}$
G229.800–00.360	$(52.0 \pm 7.3) \times 10^{+0}$	$(23.3 \pm 5.8) \times 10^{+1}$	$(10.3 \pm 1.5) \times 10^{21}$	$(22.3 \pm 6.4) \times 10^{-2}$
G229.900–00.650	$(379.4 \pm 9.3) \times 10^{-2}$	$(22.7 \pm 5.0) \times 10^{+0}$	$(36.0 \pm 3.9) \times 10^{20}$	$(16.7 \pm 3.7) \times 10^{-2}$
G230.340–00.610	$(173.8 \pm 2.7) \times 10^{+0}$	$(8.5 \pm 1.9) \times 10^{+0}$	$(100.0 \pm 7.8) \times 10^{19}$	$(20.4 \pm 4.5) \times 10^{+0}$
G230.350–00.600	$(33.4 \pm 1.1) \times 10^{+1}$	$(8.1 \pm 1.8) \times 10^{+0}$	$(12.0 \pm 1.3) \times 10^{20}$	$(41.4 \pm 9.2) \times 10^{+0}$
G230.390–00.780	$(41.3 \pm 1.3) \times 10^{-1}$	$(20.1 \pm 4.4) \times 10^{-1}$	$(27.5 \pm 3.3) \times 10^{19}$	$(20.5 \pm 4.6) \times 10^{-1}$
G230.940–00.400	$(47.6 \pm 1.3) \times 10^{-1}$	$(12.6 \pm 2.8) \times 10^{+0}$	$(15.3 \pm 1.7) \times 10^{20}$	$(37.8 \pm 8.3) \times 10^{-2}$
G231.010–00.180	$(357.9 \pm 2.6) \times 10^{-1}$	$(5.9 \pm 1.3) \times 10^{+0}$	$(59.4 \pm 3.0) \times 10^{19}$	$(6.1 \pm 1.4) \times 10^{+0}$
G231.070–00.130	$(17.3 \pm 4.1) \times 10^{+1}$	$(26.2 \pm 8.5) \times 10^{+0}$	$(21.5 \pm 1.3) \times 10^{20}$	$(6.6 \pm 2.7) \times 10^{+0}$
G231.130–00.320	$(75.2 \pm 3.7) \times 10^{+0}$	$(13.0 \pm 3.0) \times 10^{+0}$	$(21.4 \pm 1.7) \times 10^{20}$	$(5.8 \pm 1.4) \times 10^{+0}$
G231.140–00.330	$(39.7 \pm 1.4) \times 10^{+1}$	$(6.9 \pm 1.6) \times 10^{+1}$	$(346.1 \pm 5.4) \times 10^{19}$	$(5.8 \pm 1.3) \times 10^{+0}$
G231.240–00.390	$(83.3 \pm 2.3) \times 10^{+0}$	$(11.5 \pm 3.2) \times 10^{+0}$	$(109.4 \pm 1.1) \times 10^{19}$	$(7.2 \pm 2.0) \times 10^{+0}$
G231.250–00.330	$(390.8 \pm 9.6) \times 10^{-1}$	$(39.1 \pm 8.9) \times 10^{-1}$	$(74.4 \pm 5.8) \times 10^{19}$	$(10.0 \pm 2.3) \times 10^{+0}$
G231.260–00.290	$(48.7 \pm 3.1) \times 10^{+0}$	$(10.2 \pm 2.4) \times 10^{+0}$	$(118.4 \pm 7.7) \times 10^{19}$	$(4.8 \pm 1.2) \times 10^{+0}$
G231.280–00.260	$(16.1 \pm 2.9) \times 10^{+0}$	$(3.7 \pm 1.1) \times 10^{+0}$	$(8.4 \pm 1.1) \times 10^{20}$	$(4.3 \pm 1.5) \times 10^{+0}$
G231.280–00.280	$(15.2 \pm 3.0) \times 10^{+1}$	$(24.3 \pm 7.4) \times 10^{+0}$	$(99.3 \pm 2.1) \times 10^{19}$	$(6.3 \pm 2.3) \times 10^{+0}$
G231.290–00.360	$(30.1 \pm 2.6) \times 10^{+0}$	$(29.9 \pm 7.0) \times 10^{-1}$	$(43.2 \pm 4.8) \times 10^{19}$	$(10.1 \pm 2.5) \times 10^{+0}$
G231.300–00.310	$(35.7 \pm 2.3) \times 10^{-1}$	$(4.4 \pm 1.2) \times 10^{+0}$	$(15.5 \pm 1.1) \times 10^{20}$	$(8.2 \pm 2.3) \times 10^{-1}$
G231.310–00.290	$(365.4 \pm 9.1) \times 10^{-2}$	$(22.2 \pm 6.0) \times 10^{-2}$	$(23.6 \pm 5.7) \times 10^{19}$	$(16.5 \pm 4.5) \times 10^{+0}$
G231.320–00.280	$(196.0 \pm 2.8) \times 10^{-1}$	$(19.7 \pm 4.6) \times 10^{-1}$	$(58.2 \pm 8.4) \times 10^{19}$	$(9.9 \pm 2.3) \times 10^{+0}$
G231.330–00.380	$(26.1 \pm 1.3) \times 10^{+1}$	$(7.0 \pm 1.7) \times 10^{+1}$	$(192.2 \pm 1.9) \times 10^{19}$	$(37.5 \pm 9.2) \times 10^{-1}$
G231.330–00.690	$(49.4 \pm 5.6) \times 10^{-1}$	$(7.2 \pm 1.8) \times 10^{+0}$	$(80.0 \pm 9.0) \times 10^{19}$	$(6.8 \pm 1.8) \times 10^{-1}$
G231.470–01.860	$(486.2 \pm 5.2) \times 10^{-1}$	$(13.7 \pm 3.0) \times 10^{+1}$	$(386.2 \pm 7.1) \times 10^{19}$	$(35.5 \pm 7.7) \times 10^{-2}$
G231.540–00.880	$(133.2 \pm 7.0) \times 10^{-2}$	$(11.7 \pm 2.7) \times 10^{-1}$	$(28.0 \pm 4.7) \times 10^{19}$	$(11.4 \pm 2.6) \times 10^{-1}$
G231.590–00.840	$(149.5 \pm 6.4) \times 10^{-2}$	$(25.7 \pm 5.8) \times 10^{-1}$	$(5.8 \pm 1.3) \times 10^{20}$	$(5.8 \pm 1.3) \times 10^{-1}$
G231.610–01.260	$(53.5 \pm 1.8) \times 10^{-1}$	$(9.0 \pm 2.0) \times 10^{+0}$	$(13.3 \pm 1.0) \times 10^{20}$	$(6.0 \pm 1.3) \times 10^{-1}$

Table A.5: continued

Name	L ($L_\odot$)	M ($M_\odot$)	N_{H_2} (cm^{-2})	L/M ($L_\odot/M_\odot$)
G231.740–01.760	$(47.1\pm2.1)\times10^{+0}$	$(9.5\pm2.1)\times10^{+1}$	$(460.5\pm4.6)\times10^{19}$	$(4.9\pm1.1)\times10^{-1}$
G231.760–00.250	$(104.3\pm2.9)\times10^{-2}$	$(9.0\pm2.1)\times10^{+0}$	$(167.4\pm9.5)\times10^{19}$	$(11.6\pm2.8)\times10^{-2}$
G231.770–00.350	$(22.2\pm4.1)\times10^{-1}$	$(14.0\pm4.2)\times10^{-1}$	$(39.3\pm4.5)\times10^{19}$	$(15.9\pm5.7)\times10^{-1}$
G231.793–01.970	$(27.2\pm1.4)\times10^{+2}$	$(30.4\pm6.7)\times10^{+0}$	$(8.3\pm1.9)\times10^{21}$	$(8.9\pm2.0)\times10^{+1}$
G231.930–01.500	$(40.8\pm1.1)\times10^{+1}$	$(26.9\pm5.5)\times10^{+1}$	$(10.4\pm1.1)\times10^{21}$	$(15.2\pm3.2)\times10^{-1}$
G231.940–01.510	$(247.5\pm2.9)\times10^{+0}$	$(40.5\pm8.3)\times10^{+0}$	$(25.6\pm6.0)\times10^{20}$	$(6.1\pm1.3)\times10^{+0}$
G232.075–02.276	$(196.2\pm8.0)\times10^{+1}$	$(7.0\pm1.5)\times10^{+1}$	$(22.5\pm5.4)\times10^{21}$	$(28.2\pm6.3)\times10^{+0}$
G232.220+00.190	$(68.7\pm4.6)\times10^{-2}$	$(12.3\pm3.8)\times10^{-1}$	$(16.6\pm1.9)\times10^{20}$	$(5.6\pm1.8)\times10^{-1}$
G232.220–01.070	$(165.5\pm5.5)\times10^{-2}$	$(4.6\pm1.0)\times10^{+0}$	$(72.5\pm9.1)\times10^{19}$	$(36.3\pm8.2)\times10^{-2}$
G232.230+00.180	$(35.8\pm1.6)\times10^{-2}$	$(27.7\pm7.7)\times10^{-1}$	$(38.6\pm8.7)\times10^{20}$	$(13.0\pm3.7)\times10^{-2}$
G232.240+00.130	$(55.5\pm1.5)\times10^{-2}$	$(12.1\pm3.5)\times10^{-1}$	$(77.1\pm6.6)\times10^{19}$	$(4.6\pm1.3)\times10^{-1}$
G232.250+00.060	$(46.6\pm1.4)\times10^{-2}$	$(4.8\pm1.4)\times10^{-1}$	$(6.2\pm1.2)\times10^{20}$	$(9.8\pm2.8)\times10^{-1}$
G232.250+00.070	$(39.6\pm1.0)\times10^{-2}$	$(6.6\pm1.9)\times10^{-1}$	$(8.7\pm2.0)\times10^{20}$	$(6.0\pm1.8)\times10^{-1}$
G232.490–00.300	$(407.0\pm2.6)\times10^{-2}$	$(12.7\pm3.6)\times10^{+0}$	$(12.8\pm1.0)\times10^{21}$	$(32.0\pm9.1)\times10^{-2}$
G232.500–00.040	$(39.6\pm1.9)\times10^{-2}$	$(11.1\pm3.2)\times10^{-1}$	$(15.2\pm3.4)\times10^{20}$	$(3.6\pm1.0)\times10^{-1}$
G232.504–01.223	$(49.8\pm6.4)\times10^{-1}$	$(13.1\pm3.6)\times10^{-1}$	$(8.7\pm2.3)\times10^{20}$	$(3.8\pm1.2)\times10^{+0}$
G232.590–01.190	$(17.0\pm1.9)\times10^{-1}$	$(21.7\pm6.0)\times10^{-2}$	$(20.9\pm1.8)\times10^{19}$	$(7.8\pm2.3)\times10^{+0}$
G232.600+00.100	$(63.0\pm3.2)\times10^{-2}$	$(31.3\pm9.0)\times10^{-1}$	$(29.0\pm4.3)\times10^{20}$	$(20.1\pm5.9)\times10^{-2}$
G232.600–01.320	$(134.3\pm3.7)\times10^{-2}$	$(30.5\pm6.6)\times10^{-1}$	$(54.1\pm8.9)\times10^{19}$	$(44.0\pm9.6)\times10^{-2}$
G232.640–00.420	$(107.9\pm2.5)\times10^{-2}$	$(5.6\pm1.4)\times10^{-1}$	$(24.5\pm2.3)\times10^{19}$	$(19.3\pm4.9)\times10^{-1}$
G232.680+00.160	$(58.5\pm5.9)\times10^{-2}$	$(25.4\pm7.7)\times10^{-2}$	$(4.7\pm1.3)\times10^{20}$	$(23.1\pm7.4)\times10^{-1}$
G232.710–00.240	$(241.0\pm9.2)\times10^{-3}$	$(10.6\pm3.0)\times10^{-1}$	$(18.3\pm4.1)\times10^{20}$	$(22.8\pm6.5)\times10^{-2}$
G232.760+00.050	$(30.9\pm1.2)\times10^{-1}$	$(28.1\pm7.8)\times10^{-1}$	$(38.1\pm8.4)\times10^{20}$	$(11.0\pm3.1)\times10^{-1}$
G232.760–00.240	$(152.2\pm6.4)\times10^{-2}$	$(14.0\pm3.9)\times10^{-1}$	$(84.2\pm8.2)\times10^{19}$	$(10.9\pm3.1)\times10^{-1}$
G232.770–00.340	$(93.3\pm2.3)\times10^{-2}$	$(34.0\pm8.6)\times10^{-1}$	$(26.0\pm6.1)\times10^{20}$	$(27.4\pm6.9)\times10^{-2}$
G232.770–00.350	$(90.6\pm1.4)\times10^{-2}$	$(36.2\pm9.1)\times10^{-1}$	$(28.5\pm6.2)\times10^{20}$	$(25.0\pm6.3)\times10^{-2}$
G232.770–00.360	$(133.0\pm9.4)\times10^{-1}$	$(7.2\pm1.9)\times10^{+0}$	$(37.7\pm3.7)\times10^{20}$	$(18.5\pm5.0)\times10^{-1}$
G232.790+00.150	$(603.2\pm4.4)\times10^{-1}$	$(17.5\pm4.4)\times10^{+0}$	$(11.8\pm1.5)\times10^{21}$	$(34.5\pm8.6)\times10^{-1}$
G232.790–01.400	$(140.0\pm3.1)\times10^{-1}$	$(9.8\pm2.1)\times10^{+0}$	$(86.3\pm8.3)\times10^{19}$	$(14.3\pm3.1)\times10^{-1}$
G232.810+00.180	$(76.2\pm4.6)\times10^{+0}$	$(8.2\pm2.3)\times10^{+0}$	$(31.3\pm1.4)\times10^{20}$	$(9.3\pm2.7)\times10^{+0}$
G232.820–00.840	$(119.7\pm8.1)\times10^{-1}$	$(33.8\pm7.6)\times10^{+0}$	$(31.5\pm2.6)\times10^{20}$	$(35.4\pm8.3)\times10^{-2}$
G232.894–01.389	$(36.5\pm1.6)\times10^{-1}$	$(7.5\pm1.6)\times10^{+0}$	$(13.2\pm2.4)\times10^{20}$	$(4.9\pm1.1)\times10^{-1}$
G232.930+00.040	$(107.9\pm4.5)\times10^{-2}$	$(4.1\pm1.1)\times10^{+0}$	$(25.6\pm2.3)\times10^{20}$	$(26.4\pm7.4)\times10^{-2}$
G232.940–01.000	$(42.4\pm1.7)\times10^{-1}$	$(6.4\pm1.4)\times10^{+0}$	$(65.9\pm7.9)\times10^{19}$	$(6.7\pm1.5)\times10^{-1}$
G232.950–00.790	$(73.0\pm5.1)\times10^{+0}$	$(22.7\pm5.1)\times10^{+0}$	$(40.5\pm1.8)\times10^{20}$	$(32.2\pm7.6)\times10^{-1}$
G232.970–00.780	$(32.3\pm2.1)\times10^{-1}$	$(37.5\pm8.5)\times10^{-1}$	$(7.9\pm1.5)\times10^{20}$	$(8.6\pm2.0)\times10^{-1}$
G233.030+00.140	$(43.8\pm3.7)\times10^{-2}$	$(4.8\pm1.4)\times10^{+0}$	$(6.3\pm1.6)\times10^{21}$	$(9.1\pm2.7)\times10^{-2}$
G233.100–00.380	$(163.7\pm2.5)\times10^{-2}$	$(10.8\pm3.0)\times10^{-1}$	$(17.1\pm4.0)\times10^{20}$	$(15.1\pm4.2)\times10^{-1}$
G233.140–01.220	$(42.6\pm2.6)\times10^{-1}$	$(6.7\pm1.5)\times10^{+0}$	$(8.3\pm1.4)\times10^{20}$	$(6.4\pm1.5)\times10^{-1}$
G233.140–01.540	$(177.5\pm3.7)\times10^{-1}$	$(12.4\pm2.6)\times10^{+0}$	$(76.8\pm5.3)\times10^{19}$	$(14.3\pm3.1)\times10^{-1}$
G233.180–01.710	$(359.5\pm5.3)\times10^{-1}$	$(12.2\pm2.6)\times10^{+1}$	$(44.1\pm1.9)\times10^{20}$	$(29.4\pm6.2)\times10^{-2}$
G233.250+00.100	$(110.8\pm2.8)\times10^{-1}$	$(8.0\pm1.8)\times10^{+0}$	$(28.0\pm6.6)\times10^{20}$	$(13.8\pm3.0)\times10^{-1}$
G233.250–00.360	$(36.4\pm6.4)\times10^{-1}$	$(26.7\pm7.4)\times10^{-1}$	$(35.4\pm5.6)\times10^{19}$	$(13.6\pm4.5)\times10^{-1}$
G233.290–00.310	$(54.7\pm2.8)\times10^{-1}$	$(24.0\pm5.3)\times10^{+0}$	$(22.9\pm2.1)\times10^{20}$	$(22.8\pm5.2)\times10^{-2}$
G233.320–00.320	$(382.5\pm5.2)\times10^{-2}$	$(4.5\pm1.0)\times10^{+0}$	$(10.6\pm2.4)\times10^{20}$	$(8.4\pm1.9)\times10^{-1}$
G233.380–01.600	$(908.5\pm5.0)\times10^{-2}$	$(39.0\pm8.0)\times10^{+0}$	$(17.6\pm3.2)\times10^{20}$	$(23.3\pm4.8)\times10^{-2}$
G233.730–01.330	$(243.6\pm2.0)\times10^{+0}$	$(43.0\pm8.8)\times10^{+0}$	$(27.7\pm6.0)\times10^{20}$	$(5.7\pm1.2)\times10^{+0}$
G233.736–00.197	$(118.6\pm5.4)\times10^{+1}$	$(27.9\pm6.1)\times10^{+0}$	$(47.6\pm9.3)\times10^{20}$	$(42.5\pm9.5)\times10^{+0}$
G233.750–01.270	$(127.6\pm1.5)\times10^{-1}$	$(14.6\pm3.0)\times10^{+1}$	$(40.4\pm3.0)\times10^{20}$	$(8.8\pm1.8)\times10^{-2}$

Table A.5: continued

Name	L ($L_\odot$)	M ($M_\odot$)	N_{H_2} (cm^{-2})	L/M ($L_\odot/M_\odot$)
G233.760–01.250	$(207.7 \pm 6.3) \times 10^{-1}$	$(9.8 \pm 2.0) \times 10^{+1}$	$(43.8 \pm 5.6) \times 10^{20}$	$(21.2 \pm 4.4) \times 10^{-2}$
G233.810–00.110	$(175.6 \pm 9.1) \times 10^{+0}$	$(8.0 \pm 1.8) \times 10^{+0}$	$(170.7 \pm 1.7) \times 10^{19}$	$(22.0 \pm 5.0) \times 10^{+0}$
G233.980–01.860	$(32.5 \pm 3.1) \times 10^{-1}$	$(16.5 \pm 3.8) \times 10^{+0}$	$(21.5 \pm 2.3) \times 10^{20}$	$(19.7 \pm 5.0) \times 10^{-2}$
G234.033–00.537	$(180.5 \pm 6.1) \times 10^{+0}$	$(5.9 \pm 1.3) \times 10^{+1}$	$(153.1 \pm 2.9) \times 10^{19}$	$(30.7 \pm 6.8) \times 10^{-1}$
G234.050–00.130	$(61.4 \pm 1.9) \times 10^{+0}$	$(23.0 \pm 5.0) \times 10^{+0}$	$(43.4 \pm 5.1) \times 10^{20}$	$(26.7 \pm 5.9) \times 10^{-1}$
G234.050–01.910	$(7.0 \pm 1.1) \times 10^{+1}$	$(25.1 \pm 6.7) \times 10^{-1}$	$(5.1 \pm 1.4) \times 10^{20}$	$(27.7 \pm 8.6) \times 10^{+0}$
G234.234–00.717	$(197.2 \pm 4.6) \times 10^{-1}$	$(9.8 \pm 2.1) \times 10^{+0}$	$(14.1 \pm 1.5) \times 10^{20}$	$(20.2 \pm 4.4) \times 10^{-1}$
G234.260–01.490	$(526.1 \pm 8.6) \times 10^{+0}$	$(35.0 \pm 7.2) \times 10^{+0}$	$(20.8 \pm 3.3) \times 10^{20}$	$(15.0 \pm 3.1) \times 10^{+0}$
G234.270–01.500	$(73.9 \pm 1.3) \times 10^{+1}$	$(6.9 \pm 1.4) \times 10^{+1}$	$(16.5 \pm 3.9) \times 10^{20}$	$(10.7 \pm 2.2) \times 10^{+0}$
G234.333–00.651	$(12.8 \pm 1.0) \times 10^{+1}$	$(34.5 \pm 8.1) \times 10^{+0}$	$(151.9 \pm 3.9) \times 10^{19}$	$(37.1 \pm 9.2) \times 10^{-1}$
G234.450–01.070	$(15.7 \pm 1.7) \times 10^{+1}$	$(13.6 \pm 3.2) \times 10^{+1}$	$(8.1 \pm 2.2) \times 10^{21}$	$(11.5 \pm 3.0) \times 10^{-1}$
G234.468–00.393	$(91.0 \pm 7.9) \times 10^{+0}$	$(7.7 \pm 1.8) \times 10^{+1}$	$(17.7 \pm 4.2) \times 10^{21}$	$(11.8 \pm 2.9) \times 10^{-1}$
G234.493–00.829	$(83.5 \pm 2.7) \times 10^{+0}$	$(7.1 \pm 1.5) \times 10^{+1}$	$(42.3 \pm 9.3) \times 10^{20}$	$(11.7 \pm 2.5) \times 10^{-1}$
G234.501–00.863	$(63.7 \pm 4.6) \times 10^{+1}$	$(16.4 \pm 3.5) \times 10^{+2}$	$(856.8 \pm 9.2) \times 10^{19}$	$(38.9 \pm 8.9) \times 10^{-2}$
G234.570–01.003	$(109.5 \pm 6.3) \times 10^{-1}$	$(25.3 \pm 5.6) \times 10^{+0}$	$(227.8 \pm 7.5) \times 10^{19}$	$(43.3 \pm 9.9) \times 10^{-2}$
G234.580–01.030	$(190.9 \pm 1.3) \times 10^{-2}$	$(5.4 \pm 1.2) \times 10^{+0}$	$(15.0 \pm 3.3) \times 10^{20}$	$(35.3 \pm 7.6) \times 10^{-2}$
G234.590–01.080	$(124.2 \pm 4.3) \times 10^{-2}$	$(12.8 \pm 3.4) \times 10^{-2}$	$(80.1 \pm 8.6) \times 10^{18}$	$(9.7 \pm 2.6) \times 10^{+0}$
G234.620–00.197	$(189.3 \pm 7.5) \times 10^{+1}$	$(7.5 \pm 1.6) \times 10^{+2}$	$(167.2 \pm 1.7) \times 10^{20}$	$(25.2 \pm 5.6) \times 10^{-1}$
G234.650–01.580	$(650.5 \pm 6.1) \times 10^{-1}$	$(16.9 \pm 3.5) \times 10^{+1}$	$(9.5 \pm 1.3) \times 10^{21}$	$(38.4 \pm 7.9) \times 10^{-2}$
G234.660+00.070	$(169.9 \pm 5.1) \times 10^{+0}$	$(8.7 \pm 2.1) \times 10^{+1}$	$(502.0 \pm 4.9) \times 10^{19}$	$(19.5 \pm 4.7) \times 10^{-1}$
G234.710–00.910	$(154.1 \pm 3.8) \times 10^{+1}$	$(6.0 \pm 1.2) \times 10^{+1}$	$(41.3 \pm 9.7) \times 10^{20}$	$(25.7 \pm 5.3) \times 10^{+0}$
G234.720–00.820	$(45.2 \pm 3.8) \times 10^{+0}$	$(13.8 \pm 3.1) \times 10^{+0}$	$(8.0 \pm 1.9) \times 10^{20}$	$(32.8 \pm 7.9) \times 10^{-1}$
G234.715–00.911	$(181.5 \pm 4.4) \times 10^{+1}$	$(6.6 \pm 1.3) \times 10^{+1}$	$(41.5 \pm 9.1) \times 10^{20}$	$(27.7 \pm 5.7) \times 10^{+0}$
G234.730–00.750	$(99.5 \pm 1.5) \times 10^{+1}$	$(5.8 \pm 1.2) \times 10^{+1}$	$(35.8 \pm 8.4) \times 10^{20}$	$(17.2 \pm 3.5) \times 10^{+0}$
G234.730–00.810	$(142.4 \pm 5.7) \times 10^{+0}$	$(7.9 \pm 1.6) \times 10^{+1}$	$(5.7 \pm 1.3) \times 10^{21}$	$(17.9 \pm 3.8) \times 10^{-1}$
G234.764–00.282	$(24.8 \pm 7.1) \times 10^{+2}$	$(7.9 \pm 2.8) \times 10^{+1}$	$(60.5 \pm 1.0) \times 10^{20}$	$(3.1 \pm 1.5) \times 10^{+1}$
G234.860–00.090	$(17.1 \pm 2.9) \times 10^{+1}$	$(13.7 \pm 3.7) \times 10^{+0}$	$(3.7 \pm 1.0) \times 10^{21}$	$(12.4 \pm 4.0) \times 10^{+0}$
G234.880–00.130	$(74.9 \pm 5.3) \times 10^{+0}$	$(13.0 \pm 2.9) \times 10^{+0}$	$(18.3 \pm 1.8) \times 10^{20}$	$(5.8 \pm 1.4) \times 10^{+0}$
G234.890–00.180	$(290.2 \pm 7.5) \times 10^{+0}$	$(41.7 \pm 9.0) \times 10^{+0}$	$(143.6 \pm 3.0) \times 10^{19}$	$(7.0 \pm 1.5) \times 10^{+0}$
G235.050–01.530	$(15.6 \pm 1.1) \times 10^{+2}$	$(4.9 \pm 1.1) \times 10^{+2}$	$(20.4 \pm 4.1) \times 10^{21}$	$(31.9 \pm 7.2) \times 10^{-1}$
G235.220–01.670	$(190.3 \pm 2.0) \times 10^{-1}$	$(28.6 \pm 5.8) \times 10^{+1}$	$(8.7 \pm 1.0) \times 10^{21}$	$(6.7 \pm 1.4) \times 10^{-2}$
G235.348–01.687	$(74.3 \pm 3.1) \times 10^{+0}$	$(5.5 \pm 1.1) \times 10^{+1}$	$(27.7 \pm 6.2) \times 10^{20}$	$(13.6 \pm 2.9) \times 10^{-1}$
G235.347–01.740	$(407.0 \pm 2.7) \times 10^{-1}$	$(17.6 \pm 3.6) \times 10^{+1}$	$(6.8 \pm 1.0) \times 10^{21}$	$(23.1 \pm 4.7) \times 10^{-2}$
G235.389–01.655	$(36.9 \pm 1.6) \times 10^{+2}$	$(15.4 \pm 3.2) \times 10^{+1}$	$(8.6 \pm 2.1) \times 10^{21}$	$(23.9 \pm 5.1) \times 10^{+0}$
G235.532–01.675	$(15.7 \pm 2.0) \times 10^{+1}$	$(11.7 \pm 2.8) \times 10^{+2}$	$(182.0 \pm 7.3) \times 10^{20}$	$(13.4 \pm 3.6) \times 10^{-2}$
G235.590–01.520	$(64.4 \pm 2.2) \times 10^{+0}$	$(5.5 \pm 1.2) \times 10^{+0}$	$(39.0 \pm 7.6) \times 10^{19}$	$(11.7 \pm 2.5) \times 10^{+0}$
G235.680–00.030	$(25.8 \pm 2.3) \times 10^{-1}$	$(11.1 \pm 2.6) \times 10^{+0}$	$(18.6 \pm 3.9) \times 10^{20}$	$(23.2 \pm 5.7) \times 10^{-2}$
G235.690–01.240	$(32.4 \pm 1.3) \times 10^{+2}$	$(14.4 \pm 3.0) \times 10^{+1}$	$(10.8 \pm 2.4) \times 10^{21}$	$(22.6 \pm 4.8) \times 10^{+0}$
G235.780+00.010	$(256.5 \pm 6.9) \times 10^{-1}$	$(5.8 \pm 1.2) \times 10^{+1}$	$(26.8 \pm 1.2) \times 10^{20}$	$(43.9 \pm 9.4) \times 10^{-2}$
G236.180–01.830	$(67.8 \pm 3.8) \times 10^{+0}$	$(27.0 \pm 6.4) \times 10^{+0}$	$(13.1 \pm 3.2) \times 10^{21}$	$(25.1 \pm 6.1) \times 10^{-1}$
G236.420–00.710	$(141.9 \pm 3.9) \times 10^{-2}$	$(23.9 \pm 5.8) \times 10^{-1}$	$(14.2 \pm 2.7) \times 10^{20}$	$(5.9 \pm 1.5) \times 10^{-1}$
G236.490–00.590	$(182.2 \pm 7.1) \times 10^{-2}$	$(8.3 \pm 2.0) \times 10^{+0}$	$(31.7 \pm 2.8) \times 10^{20}$	$(21.9 \pm 5.4) \times 10^{-2}$
G236.570–00.460	$(7.6 \pm 1.7) \times 10^{+0}$	$(13.9 \pm 4.2) \times 10^{-1}$	$(14.8 \pm 2.8) \times 10^{19}$	$(5.5 \pm 2.1) \times 10^{+0}$
G236.600–02.130	$(18.3 \pm 4.2) \times 10^{+1}$	$(3.1 \pm 1.0) \times 10^{+1}$	$(17.3 \pm 4.2) \times 10^{21}$	$(5.9 \pm 2.4) \times 10^{+0}$
G236.600–02.290	$(16.9 \pm 2.1) \times 10^{+0}$	$(5.6 \pm 1.5) \times 10^{+1}$	$(18.2 \pm 1.5) \times 10^{21}$	$(30.4 \pm 9.0) \times 10^{-2}$
G236.600–02.310	$(82.0 \pm 3.8) \times 10^{-1}$	$(9.0 \pm 2.2) \times 10^{+0}$	$(5.8 \pm 1.3) \times 10^{21}$	$(9.1 \pm 2.3) \times 10^{-1}$
G236.610–02.110	$(130.4 \pm 8.0) \times 10^{-1}$	$(12.5 \pm 3.1) \times 10^{+0}$	$(8.2 \pm 1.7) \times 10^{21}$	$(10.4 \pm 2.7) \times 10^{-1}$
G236.620+00.000	$(150.8 \pm 7.1) \times 10^{-2}$	$(6.0 \pm 1.3) \times 10^{+0}$	$(14.4 \pm 2.8) \times 10^{20}$	$(25.1 \pm 5.6) \times 10^{-2}$
G236.630–01.150	$(195.4 \pm 3.1) \times 10^{-2}$	$(5.5 \pm 1.3) \times 10^{+0}$	$(129.2 \pm 9.4) \times 10^{19}$	$(35.8 \pm 8.5) \times 10^{-2}$

Table A.5: continued

Name	L ($L_\odot$)	M ($M_\odot$)	N_{H_2} (cm^{-2})	L/M ($L_\odot/M_\odot$)
G236.880–01.010	$(255.3\pm1.5)\times10^{-1}$	$(10.8\pm2.2)\times10^{+1}$	$(35.6\pm3.6)\times10^{20}$	$(23.6\pm4.8)\times10^{-2}$
G237.000–01.840	$(98.9\pm4.5)\times10^{+1}$	$(9.2\pm1.9)\times10^{+1}$	$(5.5\pm1.3)\times10^{21}$	$(10.7\pm2.3)\times10^{+0}$
G237.050–00.770	$(23.9\pm2.8)\times10^{-1}$	$(19.0\pm5.3)\times10^{-1}$	$(53.4\pm3.9)\times10^{19}$	$(12.6\pm3.8)\times10^{-1}$
G237.100–00.820	$(153.1\pm3.9)\times10^{-2}$	$(27.8\pm7.2)\times10^{-1}$	$(17.0\pm1.5)\times10^{20}$	$(5.5\pm1.4)\times10^{-1}$
G237.110–00.300	$(453.3\pm6.4)\times10^{-2}$	$(9.2\pm1.9)\times10^{+0}$	$(12.2\pm2.7)\times10^{20}$	$(4.9\pm1.0)\times10^{-1}$
G237.110–00.790	$(161.4\pm3.5)\times10^{-1}$	$(16.8\pm4.2)\times10^{+0}$	$(71.6\pm3.7)\times10^{20}$	$(9.6\pm2.4)\times10^{-1}$
G237.110–00.990	$(166.4\pm2.9)\times10^{-2}$	$(17.7\pm4.5)\times10^{-1}$	$(10.3\pm1.4)\times10^{20}$	$(9.4\pm2.4)\times10^{-1}$
G237.170–00.960	$(110.5\pm5.2)\times10^{-1}$	$(4.7\pm1.2)\times10^{+0}$	$(43.3\pm8.4)\times10^{20}$	$(23.7\pm6.3)\times10^{-1}$
G237.180–01.470	$(22.4\pm3.2)\times10^{+0}$	$(13.2\pm3.3)\times10^{+0}$	$(8.3\pm2.2)\times10^{20}$	$(17.0\pm4.9)\times10^{-1}$
G237.210–01.440	$(51.9\pm4.1)\times10^{+0}$	$(26.0\pm5.7)\times10^{+0}$	$(15.4\pm3.0)\times10^{20}$	$(20.0\pm4.7)\times10^{-1}$
G237.230–01.060	$(38.7\pm2.7)\times10^{+2}$	$(14.7\pm3.2)\times10^{+1}$	$(46.3\pm5.0)\times10^{20}$	$(26.3\pm5.9)\times10^{+0}$
G237.240–01.080	$(504.4\pm2.7)\times10^{+0}$	$(8.2\pm1.7)\times10^{+1}$	$(4.5\pm1.1)\times10^{21}$	$(6.1\pm1.3)\times10^{+0}$
G237.260–01.260	$(56.3\pm7.4)\times10^{+1}$	$(22.3\pm5.4)\times10^{+1}$	$(16.4\pm3.7)\times10^{21}$	$(25.2\pm7.0)\times10^{-1}$
G237.260–01.280	$(73.5\pm2.0)\times10^{+2}$	$(36.4\pm7.5)\times10^{+1}$	$(11.5\pm1.1)\times10^{21}$	$(20.2\pm4.2)\times10^{+0}$
G237.260–01.300	$(123.1\pm7.0)\times10^{+1}$	$(13.8\pm2.9)\times10^{+1}$	$(9.9\pm2.4)\times10^{21}$	$(8.9\pm2.0)\times10^{+0}$
G237.320–01.280	$(23.8\pm1.5)\times10^{+3}$	$(19.0\pm4.0)\times10^{+1}$	$(11.3\pm2.8)\times10^{21}$	$(12.5\pm2.8)\times10^{+1}$
G237.330–01.260	$(12.5\pm1.5)\times10^{+1}$	$(9.5\pm2.2)\times10^{+1}$	$(4.6\pm1.3)\times10^{21}$	$(13.2\pm3.5)\times10^{-1}$
G237.460–01.790	$(225.4\pm6.6)\times10^{-2}$	$(5.0\pm1.3)\times10^{+0}$	$(38.7\pm8.6)\times10^{20}$	$(4.5\pm1.1)\times10^{-1}$
G237.530–01.380	$(21.4\pm3.4)\times10^{+0}$	$(7.9\pm2.0)\times10^{+1}$	$(29.9\pm4.8)\times10^{20}$	$(27.3\pm8.2)\times10^{-2}$
G237.540–00.660	$(53.3\pm5.7)\times10^{-1}$	$(5.9\pm1.4)\times10^{+0}$	$(33.6\pm2.8)\times10^{19}$	$(9.1\pm2.3)\times10^{-1}$
G237.550–00.640	$(11.1\pm1.1)\times10^{+0}$	$(6.5\pm1.5)\times10^{+0}$	$(34.3\pm3.0)\times10^{19}$	$(17.1\pm4.3)\times10^{-1}$
G237.661–00.514	$(414.9\pm7.9)\times10^{-2}$	$(7.1\pm1.5)\times10^{+0}$	$(8.7\pm1.9)\times10^{20}$	$(5.8\pm1.2)\times10^{-1}$
G237.660–01.790	$(11.1\pm1.0)\times10^{-1}$	$(9.2\pm2.4)\times10^{-1}$	$(31.5\pm2.7)\times10^{19}$	$(12.1\pm3.4)\times10^{-1}$
G237.740–00.960	$(72.6\pm2.5)\times10^{+1}$	$(12.4\pm3.2)\times10^{+0}$	$(54.6\pm3.7)\times10^{20}$	$(5.9\pm1.5)\times10^{+1}$
G237.740–00.970	$(69.6\pm1.4)\times10^{+0}$	$(9.7\pm2.5)\times10^{-1}$	$(9.1\pm2.1)\times10^{20}$	$(7.1\pm1.8)\times10^{+1}$
G237.820–01.280	$(198.0\pm3.8)\times10^{+0}$	$(21.5\pm4.4)\times10^{+1}$	$(77.0\pm6.3)\times10^{20}$	$(9.2\pm1.9)\times10^{-1}$
G238.260–01.720	$(841.5\pm9.5)\times10^{-1}$	$(4.1\pm1.0)\times10^{+0}$	$(35.2\pm8.2)\times10^{20}$	$(20.8\pm5.1)\times10^{+0}$
G238.511–00.885	$(104.8\pm5.1)\times10^{-2}$	$(28.8\pm7.2)\times10^{-1}$	$(10.5\pm1.2)\times10^{20}$	$(36.4\pm9.3)\times10^{-2}$
G238.540–00.920	$(118.1\pm2.8)\times10^{-2}$	$(13.9\pm3.4)\times10^{-1}$	$(49.9\pm5.1)\times10^{19}$	$(8.5\pm2.1)\times10^{-1}$
G238.670–01.440	$(27.8\pm4.2)\times10^{+0}$	$(27.4\pm8.2)\times10^{+0}$	$(100.1\pm5.0)\times10^{20}$	$(10.2\pm3.4)\times10^{-1}$
G238.690–01.860	$(72.5\pm7.8)\times10^{+0}$	$(13.3\pm3.1)\times10^{+1}$	$(5.9\pm1.5)\times10^{21}$	$(5.4\pm1.4)\times10^{-1}$
G238.700–01.270	$(76.4\pm6.2)\times10^{-2}$	$(7.8\pm2.1)\times10^{-1}$	$(8.3\pm2.1)\times10^{20}$	$(9.8\pm2.8)\times10^{-1}$
G238.770–01.810	$(107.9\pm8.7)\times10^{+1}$	$(12.9\pm2.8)\times10^{+1}$	$(6.8\pm1.6)\times10^{21}$	$(8.4\pm1.9)\times10^{+0}$
G238.800–01.630	$(25.4\pm2.4)\times10^{+0}$	$(4.7\pm1.3)\times10^{+0}$	$(4.9\pm1.0)\times10^{21}$	$(5.4\pm1.6)\times10^{+0}$
G238.960–01.680	$(30.7\pm1.2)\times10^{+2}$	$(38.6\pm8.0)\times10^{+0}$	$(26.0\pm6.2)\times10^{20}$	$(7.9\pm1.7)\times10^{+1}$
G239.190–01.960	$(78.1\pm4.1)\times10^{+0}$	$(36.1\pm7.6)\times10^{+1}$	$(69.6\pm4.5)\times10^{20}$	$(21.6\pm4.7)\times10^{-2}$
G239.300–00.630	$(82.0\pm3.9)\times10^{-1}$	$(9.4\pm2.0)\times10^{+1}$	$(8.7\pm2.1)\times10^{21}$	$(8.7\pm1.9)\times10^{-2}$
G239.370–00.080	$(445.3\pm9.0)\times10^{-2}$	$(13.1\pm2.7)\times10^{+0}$	$(10.3\pm2.4)\times10^{20}$	$(34.1\pm7.1)\times10^{-2}$
G239.370–01.690	$(16.4\pm3.0)\times10^{+0}$	$(5.7\pm1.8)\times10^{+0}$	$(6.1\pm1.6)\times10^{21}$	$(2.9\pm1.1)\times10^{+0}$
G239.524–00.711	$(108.4\pm8.5)\times10^{+0}$	$(11.2\pm2.5)\times10^{+1}$	$(44.6\pm3.5)\times10^{20}$	$(9.7\pm2.3)\times10^{-1}$
G239.630–02.090	$(219.0\pm5.8)\times10^{+0}$	$(7.0\pm1.4)\times10^{+2}$	$(140.5\pm6.5)\times10^{20}$	$(31.5\pm6.5)\times10^{-2}$
G239.650–00.810	$(15.4\pm1.7)\times10^{+0}$	$(28.3\pm6.6)\times10^{+0}$	$(23.9\pm6.0)\times10^{20}$	$(5.5\pm1.4)\times10^{-1}$
G239.660–02.040	$(44.6\pm6.2)\times10^{+0}$	$(21.4\pm5.3)\times10^{+1}$	$(36.6\pm2.9)\times10^{20}$	$(20.9\pm5.9)\times10^{-2}$
G239.680–02.040	$(54.1\pm1.0)\times10^{-1}$	$(5.7\pm1.2)\times10^{+1}$	$(25.8\pm5.0)\times10^{20}$	$(9.5\pm2.0)\times10^{-2}$
G239.950–01.810	$(99.3\pm3.8)\times10^{-2}$	$(32.4\pm8.8)\times10^{-1}$	$(38.3\pm8.5)\times10^{20}$	$(30.7\pm8.4)\times10^{-2}$
G240.140–01.540	$(81.7\pm1.8)\times10^{-1}$	$(24.3\pm5.5)\times10^{+0}$	$(37.1\pm1.6)\times10^{20}$	$(33.6\pm7.6)\times10^{-2}$
G240.170–01.590	$(44.1\pm3.2)\times10^{-1}$	$(6.9\pm1.5)\times10^{+1}$	$(31.7\pm4.0)\times10^{20}$	$(6.4\pm1.5)\times10^{-2}$
G240.250–00.910	$(119.0\pm4.7)\times10^{-2}$	$(5.1\pm1.4)\times10^{-1}$	$(24.7\pm2.0)\times10^{19}$	$(23.3\pm6.4)\times10^{-1}$
G240.490–00.070	$(28.6\pm1.5)\times10^{+0}$	$(18.6\pm3.9)\times10^{+0}$	$(9.4\pm1.1)\times10^{20}$	$(15.4\pm3.4)\times10^{-1}$

Table A.5: continued

Name	L ($L_\odot$)	M ($M_\odot$)	N_{H_2} (cm^{-2})	L/M ($L_\odot/M_\odot$)
G240.940–01.440	$(123.3\pm2.8)\times10^{-1}$	$(36.1\pm7.5)\times10^{+0}$	$(15.9\pm1.4)\times10^{20}$	$(34.1\pm7.1)\times10^{-2}$
G240.990–01.470	$(23.8\pm3.2)\times10^{-1}$	$(26.8\pm8.0)\times10^{-1}$	$(28.3\pm6.5)\times10^{20}$	$(8.9\pm2.9)\times10^{-1}$
G241.003–01.203	$(19.7\pm2.5)\times10^{+1}$	$(16.8\pm4.1)\times10^{+1}$	$(21.4\pm5.9)\times10^{21}$	$(11.7\pm3.2)\times10^{-1}$
G241.010–01.200	$(21.7\pm2.7)\times10^{+1}$	$(19.7\pm4.7)\times10^{+1}$	$(22.7\pm6.2)\times10^{21}$	$(11.0\pm3.0)\times10^{-1}$
G241.121–00.781	$(582.3\pm9.0)\times10^{-1}$	$(26.4\pm5.4)\times10^{+1}$	$(116.0\pm9.5)\times10^{20}$	$(22.1\pm4.6)\times10^{-2}$
G241.140–01.170	$(14.5\pm1.7)\times10^{+1}$	$(29.0\pm6.9)\times10^{+1}$	$(71.0\pm3.7)\times10^{20}$	$(5.0\pm1.3)\times10^{-1}$
G241.180–01.070	$(45.2\pm4.1)\times10^{-1}$	$(35.7\pm8.1)\times10^{+0}$	$(24.9\pm4.4)\times10^{20}$	$(12.6\pm3.1)\times10^{-2}$
G241.190–00.780	$(159.2\pm3.2)\times10^{-1}$	$(17.3\pm3.6)\times10^{+1}$	$(74.2\pm6.3)\times10^{20}$	$(9.2\pm1.9)\times10^{-2}$
G241.290–00.710	$(17.7\pm1.5)\times10^{+1}$	$(8.4\pm1.9)\times10^{+1}$	$(6.9\pm1.8)\times10^{21}$	$(21.0\pm5.0)\times10^{-1}$
G241.390–02.030	$(127.1\pm2.9)\times10^{-2}$	$(19.9\pm5.3)\times10^{-1}$	$(79.4\pm4.7)\times10^{19}$	$(6.4\pm1.7)\times10^{-1}$
G241.420–00.700	$(123.9\pm2.4)\times10^{+0}$	$(18.9\pm3.9)\times10^{+1}$	$(15.5\pm3.4)\times10^{21}$	$(6.6\pm1.4)\times10^{-1}$
G241.530–00.600	$(43.3\pm2.1)\times10^{+2}$	$(12.0\pm2.5)\times10^{+1}$	$(46.9\pm5.9)\times10^{20}$	$(36.0\pm7.8)\times10^{+0}$
G241.538–00.594	$(79.1\pm2.8)\times10^{+1}$	$(17.9\pm3.7)\times10^{+1}$	$(9.1\pm1.1)\times10^{21}$	$(44.2\pm9.4)\times10^{-1}$
G241.560–00.590	$(67.7\pm1.8)\times10^{+2}$	$(25.4\pm5.3)\times10^{+1}$	$(52.5\pm3.1)\times10^{20}$	$(26.6\pm5.6)\times10^{+0}$
G241.570–00.640	$(80.2\pm1.6)\times10^{+1}$	$(17.5\pm3.6)\times10^{+2}$	$(259.7\pm3.8)\times10^{20}$	$(45.9\pm9.5)\times10^{-2}$
G241.680–00.580	$(14.0\pm2.5)\times10^{+2}$	$(32.8\pm8.9)\times10^{+1}$	$(3.5\pm1.0)\times10^{22}$	$(4.3\pm1.4)\times10^{+0}$
G242.190–00.780	$(62.1\pm2.2)\times10^{-1}$	$(9.1\pm1.9)\times10^{+0}$	$(5.6\pm1.0)\times10^{20}$	$(6.8\pm1.5)\times10^{-1}$
G242.560–00.630	$(178.5\pm9.8)\times10^{-2}$	$(16.7\pm3.7)\times10^{+0}$	$(17.0\pm4.0)\times10^{20}$	$(10.7\pm2.4)\times10^{-2}$
G242.590–00.240	$(121.9\pm4.0)\times10^{+0}$	$(21.4\pm5.4)\times10^{-1}$	$(21.9\pm4.8)\times10^{20}$	$(5.7\pm1.4)\times10^{+1}$
G242.620–00.690	$(64.5\pm1.9)\times10^{+0}$	$(11.9\pm2.5)\times10^{+1}$	$(58.8\pm7.2)\times10^{20}$	$(5.4\pm1.1)\times10^{-1}$
G242.640–00.700	$(157.0\pm3.3)\times10^{-1}$	$(13.6\pm2.8)\times10^{+1}$	$(10.8\pm2.5)\times10^{21}$	$(11.6\pm2.4)\times10^{-2}$
G242.770–01.530	$(225.0\pm7.6)\times10^{-2}$	$(37.3\pm9.8)\times10^{-1}$	$(37.4\pm8.2)\times10^{20}$	$(6.0\pm1.6)\times10^{-1}$
G242.880–02.250	$(180.2\pm2.3)\times10^{-2}$	$(18.0\pm4.5)\times10^{-1}$	$(57.8\pm5.0)\times10^{19}$	$(10.0\pm2.5)\times10^{-1}$
G242.920–00.520	$(63.6\pm1.1)\times10^{+0}$	$(12.5\pm2.6)\times10^{+1}$	$(9.0\pm1.1)\times10^{21}$	$(5.1\pm1.1)\times10^{-1}$
G242.940–00.450	$(21.4\pm3.4)\times10^{+2}$	$(16.1\pm4.2)\times10^{+1}$	$(15.5\pm3.8)\times10^{21}$	$(13.3\pm4.1)\times10^{+0}$
G242.940–00.500	$(134.7\pm5.3)\times10^{+0}$	$(13.3\pm2.8)\times10^{+1}$	$(10.7\pm1.5)\times10^{21}$	$(10.1\pm2.2)\times10^{-1}$
G243.150–00.170	$(17.8\pm2.3)\times10^{+0}$	$(5.3\pm1.3)\times10^{+1}$	$(24.5\pm1.5)\times10^{20}$	$(33.9\pm9.5)\times10^{-2}$
G243.160–01.520	$(31.1\pm2.7)\times10^{-1}$	$(26.9\pm7.7)\times10^{-1}$	$(73.3\pm3.1)\times10^{19}$	$(11.5\pm3.5)\times10^{-1}$
G243.190–00.160	$(86.0\pm1.0)\times10^{-1}$	$(15.5\pm3.3)\times10^{+0}$	$(120.6\pm9.4)\times10^{19}$	$(5.6\pm1.2)\times10^{-1}$
G243.200–00.330	$(78.1\pm3.0)\times10^{-1}$	$(43.7\pm9.3)\times10^{-1}$	$(32.9\pm4.0)\times10^{19}$	$(17.9\pm3.8)\times10^{-1}$
G243.450–01.620	$(129.3\pm4.2)\times10^{-2}$	$(9.6\pm2.5)\times10^{-1}$	$(33.6\pm2.7)\times10^{19}$	$(13.4\pm3.6)\times10^{-1}$
G243.540–00.810	$(14.9\pm2.5)\times10^{+0}$	$(7.7\pm2.3)\times10^{+0}$	$(6.9\pm2.1)\times10^{21}$	$(19.4\pm6.5)\times10^{-1}$
G243.770–01.420	$(48.4\pm2.1)\times10^{-2}$	$(13.1\pm3.5)\times10^{-1}$	$(16.6\pm3.7)\times10^{20}$	$(3.7\pm1.0)\times10^{-1}$
G243.780–00.240	$(87.6\pm3.0)\times10^{+0}$	$(7.2\pm1.5)\times10^{+1}$	$(6.7\pm1.3)\times10^{21}$	$(12.2\pm2.6)\times10^{-1}$
G243.860–00.870	$(151.0\pm7.4)\times10^{-1}$	$(9.4\pm2.3)\times10^{+0}$	$(32.1\pm3.5)\times10^{20}$	$(16.1\pm4.1)\times10^{-1}$
G243.950–00.200	$(100.3\pm5.5)\times10^{-1}$	$(7.7\pm1.7)\times10^{+0}$	$(7.1\pm1.6)\times10^{20}$	$(13.0\pm2.9)\times10^{-1}$
G244.410–01.970	$(72.9\pm1.2)\times10^{+0}$	$(11.9\pm2.4)\times10^{+2}$	$(18.6\pm1.3)\times10^{21}$	$(6.1\pm1.3)\times10^{-2}$
G244.460–00.540	$(79.3\pm3.5)\times10^{-2}$	$(14.5\pm3.7)\times10^{-1}$	$(59.9\pm6.4)\times10^{19}$	$(5.5\pm1.4)\times10^{-1}$
G244.760–00.320	$(156.3\pm2.5)\times10^{-1}$	$(7.4\pm1.5)\times10^{+1}$	$(37.1\pm1.7)\times10^{20}$	$(21.2\pm4.4)\times10^{-2}$
G244.830–00.960	$(74.9\pm2.1)\times10^{-2}$	$(21.6\pm5.5)\times10^{-1}$	$(14.5\pm1.9)\times10^{20}$	$(34.7\pm9.0)\times10^{-2}$
G245.070–00.210	$(54.2\pm5.1)\times10^{-1}$	$(25.6\pm5.9)\times10^{+0}$	$(19.6\pm3.1)\times10^{20}$	$(21.1\pm5.2)\times10^{-2}$
G245.080–00.180	$(15.4\pm2.3)\times10^{-1}$	$(4.8\pm1.4)\times10^{-1}$	$(31.0\pm9.2)\times10^{19}$	$(3.2\pm1.1)\times10^{+0}$
G245.100–00.990	$(351.0\pm6.9)\times10^{+0}$	$(25.4\pm5.2)\times10^{+1}$	$(11.6\pm2.5)\times10^{21}$	$(13.8\pm2.8)\times10^{-1}$
G245.240–01.390	$(28.7\pm1.9)\times10^{-2}$	$(4.9\pm1.5)\times10^{-1}$	$(7.6\pm1.9)\times10^{20}$	$(5.9\pm1.8)\times10^{-1}$
G245.300–00.300	$(136.2\pm7.3)\times10^{+1}$	$(7.0\pm1.5)\times10^{+1}$	$(37.6\pm4.2)\times10^{20}$	$(19.5\pm4.3)\times10^{+0}$
G246.270–00.070	$(115.2\pm2.7)\times10^{-1}$	$(15.4\pm3.2)\times10^{+0}$	$(76.1\pm5.8)\times10^{19}$	$(7.5\pm1.6)\times10^{-1}$
G246.970–01.720	$(49.1\pm1.8)\times10^{-1}$	$(31.8\pm6.7)\times10^{+0}$	$(26.3\pm4.3)\times10^{20}$	$(15.4\pm3.3)\times10^{-2}$
G247.240–01.120	$(11.1\pm1.1)\times10^{+0}$	$(26.5\pm7.1)\times10^{-1}$	$(21.3\pm3.8)\times10^{20}$	$(4.2\pm1.2)\times10^{+0}$
G247.280–00.560	$(17.0\pm2.8)\times10^{-1}$	$(4.3\pm1.3)\times10^{-1}$	$(15.2\pm2.7)\times10^{19}$	$(3.9\pm1.3)\times10^{+0}$

Table A.5: continued

Name	L ($L_\odot$)	M ($M_\odot$)	N_{H_2} (cm^{-2})	L/M ($L_\odot/M_\odot$)
G247.440–00.930	$(90.4 \pm 4.7) \times 10^{-2}$	$(16.1 \pm 4.1) \times 10^{-1}$	$(63.4 \pm 4.7) \times 10^{19}$	$(5.6 \pm 1.5) \times 10^{-1}$
G247.460–00.820	$(124.6 \pm 4.9) \times 10^{-2}$	$(19.1 \pm 4.7) \times 10^{-1}$	$(10.0 \pm 1.6) \times 10^{20}$	$(6.5 \pm 1.6) \times 10^{-1}$
G247.510+00.060	$(23.0 \pm 4.7) \times 10^{+0}$	$(4.2 \pm 1.2) \times 10^{+0}$	$(33.2 \pm 3.7) \times 10^{19}$	$(5.5 \pm 2.0) \times 10^{+0}$
G247.510–00.570	$(16.9 \pm 2.0) \times 10^{-1}$	$(25.6 \pm 6.7) \times 10^{-1}$	$(49.0 \pm 4.8) \times 10^{19}$	$(6.6 \pm 1.9) \times 10^{-1}$
G247.520+00.050	$(13.4 \pm 1.0) \times 10^{+0}$	$(17.4 \pm 4.0) \times 10^{-1}$	$(14.9 \pm 1.2) \times 10^{19}$	$(7.7 \pm 1.9) \times 10^{+0}$
G247.520–00.240	$(102.8 \pm 2.5) \times 10^{-2}$	$(19.8 \pm 5.2) \times 10^{-2}$	$(22.2 \pm 4.9) \times 10^{19}$	$(5.2 \pm 1.4) \times 10^{+0}$
G247.590–00.820	$(175.2 \pm 4.8) \times 10^{-2}$	$(30.6 \pm 7.7) \times 10^{-1}$	$(17.4 \pm 2.2) \times 10^{20}$	$(5.7 \pm 1.5) \times 10^{-1}$
G247.610–00.830	$(125.4 \pm 2.4) \times 10^{-2}$	$(29.4 \pm 7.4) \times 10^{-1}$	$(23.9 \pm 5.2) \times 10^{20}$	$(4.3 \pm 1.1) \times 10^{-1}$
G247.630–00.550	$(34.3 \pm 7.1) \times 10^{+2}$	$(20.5 \pm 6.0) \times 10^{+1}$	$(38.9 \pm 1.5) \times 10^{20}$	$(16.7 \pm 6.0) \times 10^{+0}$
G247.640–00.530	$(83.6 \pm 1.7) \times 10^{+1}$	$(33.9 \pm 7.1) \times 10^{+0}$	$(16.3 \pm 1.7) \times 10^{20}$	$(24.7 \pm 5.2) \times 10^{+0}$
G247.890–00.990	$(45.0 \pm 3.2) \times 10^{-2}$	$(9.8 \pm 2.5) \times 10^{-1}$	$(6.8 \pm 1.6) \times 10^{20}$	$(4.6 \pm 1.2) \times 10^{-1}$
G247.930–00.440	$(25.8 \pm 2.8) \times 10^{+0}$	$(8.7 \pm 2.0) \times 10^{+1}$	$(58.9 \pm 6.4) \times 10^{20}$	$(29.8 \pm 7.7) \times 10^{-2}$
G248.000–00.430	$(167.3 \pm 8.2) \times 10^{+1}$	$(17.0 \pm 3.6) \times 10^{+1}$	$(47.8 \pm 1.0) \times 10^{20}$	$(9.9 \pm 2.2) \times 10^{+0}$
G248.150–02.210	$(86.2 \pm 3.0) \times 10^{-1}$	$(10.1 \pm 2.5) \times 10^{+0}$	$(157.8 \pm 6.9) \times 10^{19}$	$(8.6 \pm 2.1) \times 10^{-1}$
G248.440–00.910	$(44.6 \pm 5.9) \times 10^{-2}$	$(9.7 \pm 2.8) \times 10^{-1}$	$(5.8 \pm 1.1) \times 10^{20}$	$(4.6 \pm 1.5) \times 10^{-1}$
G248.690–01.930	$(28.2 \pm 1.1) \times 10^{-1}$	$(9.4 \pm 2.3) \times 10^{+0}$	$(190.2 \pm 8.5) \times 10^{19}$	$(30.0 \pm 7.5) \times 10^{-2}$
G248.700–01.010	$(116.7 \pm 3.2) \times 10^{-2}$	$(4.3 \pm 1.1) \times 10^{-1}$	$(20.5 \pm 1.6) \times 10^{19}$	$(27.0 \pm 7.0) \times 10^{-1}$
G249.170–02.020	$(127.1 \pm 7.9) \times 10^{-2}$	$(18.6 \pm 4.9) \times 10^{-2}$	$(9.9 \pm 1.6) \times 10^{19}$	$(6.8 \pm 1.9) \times 10^{+0}$
G249.390–01.410	$(8.8 \pm 1.3) \times 10^{-1}$	$(4.9 \pm 1.5) \times 10^{-1}$	$(5.7 \pm 1.3) \times 10^{20}$	$(18.0 \pm 6.2) \times 10^{-1}$
G249.450–02.420	$(83.2 \pm 5.4) \times 10^{-2}$	$(11.8 \pm 2.8) \times 10^{+0}$	$(33.0 \pm 5.3) \times 10^{20}$	$(7.0 \pm 1.7) \times 10^{-2}$
G249.530–02.500	$(12.7 \pm 2.0) \times 10^{-1}$	$(14.9 \pm 4.1) \times 10^{-1}$	$(5.7 \pm 1.0) \times 10^{20}$	$(8.5 \pm 2.7) \times 10^{-1}$
G249.600–02.080	$(350.8 \pm 2.5) \times 10^{+1}$	$(34.8 \pm 7.0) \times 10^{+1}$	$(53.0 \pm 6.4) \times 10^{20}$	$(10.1 \pm 2.0) \times 10^{+0}$
G249.680–02.100	$(49.7 \pm 1.7) \times 10^{-1}$	$(22.0 \pm 5.8) \times 10^{+0}$	$(78.6 \pm 4.0) \times 10^{20}$	$(22.6 \pm 6.0) \times 10^{-2}$
G250.230–00.040	$(171.4 \pm 2.2) \times 10^{+0}$	$(47.3 \pm 9.9) \times 10^{+0}$	$(7.8 \pm 1.8) \times 10^{21}$	$(36.3 \pm 7.6) \times 10^{-1}$
G250.270–00.980	$(13.2 \pm 1.8) \times 10^{+0}$	$(5.2 \pm 1.3) \times 10^{+1}$	$(19.6 \pm 2.0) \times 10^{20}$	$(25.5 \pm 7.1) \times 10^{-2}$
G250.590–00.650	$(47.4 \pm 1.2) \times 10^{+2}$	$(20.8 \pm 4.3) \times 10^{+1}$	$(57.1 \pm 4.7) \times 10^{20}$	$(22.9 \pm 4.7) \times 10^{+0}$
G250.900–01.530	$(116.0 \pm 8.8) \times 10^{-1}$	$(30.1 \pm 6.7) \times 10^{+0}$	$(17.0 \pm 1.3) \times 10^{20}$	$(38.6 \pm 9.1) \times 10^{-2}$
G250.900–02.050	$(936.1 \pm 9.4) \times 10^{-2}$	$(12.9 \pm 2.7) \times 10^{+0}$	$(103.8 \pm 9.9) \times 10^{19}$	$(7.2 \pm 1.5) \times 10^{-1}$
G250.910–01.280	$(66.6 \pm 2.0) \times 10^{-2}$	$(4.1 \pm 1.2) \times 10^{-1}$	$(34.0 \pm 3.2) \times 10^{19}$	$(16.4 \pm 4.9) \times 10^{-1}$
G251.040–01.030	$(15.0 \pm 2.0) \times 10^{+0}$	$(4.7 \pm 1.6) \times 10^{+1}$	$(120.8 \pm 1.4) \times 10^{20}$	$(3.2 \pm 1.2) \times 10^{-1}$
G251.070–00.980	$(125.3 \pm 1.3) \times 10^{-1}$	$(4.2 \pm 1.2) \times 10^{+0}$	$(8.2 \pm 1.9) \times 10^{21}$	$(30.1 \pm 8.8) \times 10^{-1}$
G251.070–01.000	$(265.8 \pm 5.8) \times 10^{-2}$	$(22.1 \pm 6.5) \times 10^{+0}$	$(15.8 \pm 1.5) \times 10^{21}$	$(12.0 \pm 3.6) \times 10^{-2}$
G251.080–00.990	$(48.9 \pm 1.8) \times 10^{-1}$	$(16.3 \pm 4.8) \times 10^{+0}$	$(11.8 \pm 1.1) \times 10^{21}$	$(30.1 \pm 9.0) \times 10^{-2}$
G251.160–01.990	$(75.0 \pm 6.5) \times 10^{+0}$	$(14.4 \pm 3.3) \times 10^{+0}$	$(16.1 \pm 4.1) \times 10^{20}$	$(5.2 \pm 1.3) \times 10^{+0}$
G251.190–01.970	$(35.8 \pm 1.5) \times 10^{+2}$	$(11.5 \pm 2.4) \times 10^{+1}$	$(55.7 \pm 4.8) \times 10^{20}$	$(31.3 \pm 6.8) \times 10^{+0}$
G251.210–00.610	$(14.6 \pm 1.9) \times 10^{+0}$	$(10.0 \pm 2.5) \times 10^{+0}$	$(71.9 \pm 7.9) \times 10^{19}$	$(14.5 \pm 4.1) \times 10^{-1}$
G251.230–01.950	$(38.6 \pm 8.1) \times 10^{+2}$	$(23.0 \pm 6.8) \times 10^{+1}$	$(28.9 \pm 9.1) \times 10^{21}$	$(16.8 \pm 6.1) \times 10^{+0}$
G251.400–00.180	$(10.4 \pm 1.4) \times 10^{+0}$	$(9.3 \pm 2.3) \times 10^{+0}$	$(15.4 \pm 4.3) \times 10^{20}$	$(11.1 \pm 3.1) \times 10^{-1}$
G251.410–00.980	$(11.2 \pm 1.0) \times 10^{-1}$	$(6.9 \pm 1.9) \times 10^{-1}$	$(39.4 \pm 4.6) \times 10^{19}$	$(16.1 \pm 4.7) \times 10^{-1}$
G251.750–00.900	$(73.9 \pm 5.8) \times 10^{-2}$	$(5.5 \pm 1.5) \times 10^{-1}$	$(22.8 \pm 1.8) \times 10^{19}$	$(13.4 \pm 3.7) \times 10^{-1}$
G251.750–01.010	$(50.9 \pm 2.2) \times 10^{-2}$	$(4.5 \pm 1.2) \times 10^{-1}$	$(30.6 \pm 4.4) \times 10^{19}$	$(11.3 \pm 3.1) \times 10^{-1}$
G251.880–01.060	$(102.5 \pm 6.1) \times 10^{-3}$	$(6.1 \pm 1.8) \times 10^{-2}$	$(8.3 \pm 2.2) \times 10^{19}$	$(16.9 \pm 5.0) \times 10^{-1}$
G251.900–01.060	$(461.3 \pm 7.8) \times 10^{-2}$	$(7.0 \pm 1.5) \times 10^{+0}$	$(77.3 \pm 9.2) \times 10^{19}$	$(6.6 \pm 1.4) \times 10^{-1}$
G251.900–01.080	$(24.0 \pm 1.0) \times 10^{+0}$	$(24.0 \pm 5.2) \times 10^{+0}$	$(35.8 \pm 5.1) \times 10^{20}$	$(10.0 \pm 2.2) \times 10^{-1}$
G251.920–01.090	$(19.0 \pm 1.7) \times 10^{+0}$	$(5.1 \pm 1.4) \times 10^{+0}$	$(22.7 \pm 1.0) \times 10^{20}$	$(3.7 \pm 1.1) \times 10^{+0}$
G251.990–01.230	$(12.6 \pm 2.2) \times 10^{-1}$	$(16.0 \pm 5.3) \times 10^{-1}$	$(12.5 \pm 1.4) \times 10^{20}$	$(7.9 \pm 3.0) \times 10^{-1}$
G252.080–01.290	$(57.2 \pm 4.6) \times 10^{-1}$	$(7.8 \pm 2.2) \times 10^{+0}$	$(52.9 \pm 5.4) \times 10^{20}$	$(7.4 \pm 2.1) \times 10^{-1}$
G252.080–01.810	$(111.3 \pm 2.2) \times 10^{-1}$	$(4.5 \pm 1.2) \times 10^{+1}$	$(135.5 \pm 5.4) \times 10^{20}$	$(24.9 \pm 6.7) \times 10^{-2}$
G252.090–01.270	$(379.0 \pm 4.7) \times 10^{-2}$	$(21.8 \pm 5.8) \times 10^{+0}$	$(95.2 \pm 3.1) \times 10^{20}$	$(17.4 \pm 4.6) \times 10^{-2}$

Table A.5: continued

Name	L ($L_\odot$)	M ($M_\odot$)	N_{H_2} (cm^{-2})	L/M ($L_\odot/M_\odot$)
G252.100–01.220	$(94.5 \pm 5.6) \times 10^{-2}$	$(5.7 \pm 1.6) \times 10^{+0}$	$(40.4 \pm 4.3) \times 10^{20}$	$(16.5 \pm 4.6) \times 10^{-2}$
G252.110–01.270	$(49.9 \pm 7.4) \times 10^{-1}$	$(7.2 \pm 2.3) \times 10^{-1}$	$(11.6 \pm 1.8) \times 10^{20}$	$(7.0 \pm 2.4) \times 10^{+0}$
G252.120–01.170	$(402.4 \pm 8.2) \times 10^{-2}$	$(10.4 \pm 2.8) \times 10^{+0}$	$(66.2 \pm 8.1) \times 10^{20}$	$(3.9 \pm 1.0) \times 10^{-1}$
G252.133–01.175	$(8.5 \pm 1.2) \times 10^{+0}$	$(4.0 \pm 1.2) \times 10^{+0}$	$(5.4 \pm 1.4) \times 10^{21}$	$(21.5 \pm 7.2) \times 10^{-1}$
G252.140–01.180	$(8.7 \pm 1.2) \times 10^{+0}$	$(3.5 \pm 1.0) \times 10^{+0}$	$(5.3 \pm 1.5) \times 10^{21}$	$(25.0 \pm 8.1) \times 10^{-1}$
G252.180–01.080	$(42.3 \pm 2.2) \times 10^{+0}$	$(6.4 \pm 1.4) \times 10^{+0}$	$(8.6 \pm 1.7) \times 10^{20}$	$(6.6 \pm 1.5) \times 10^{+0}$
G252.480–01.570	$(62.1 \pm 6.4) \times 10^{+0}$	$(4.1 \pm 1.2) \times 10^{+1}$	$(40.7 \pm 5.3) \times 10^{21}$	$(15.3 \pm 4.8) \times 10^{-1}$
G252.510–01.440	$(112.6 \pm 6.4) \times 10^{-2}$	$(30.3 \pm 8.7) \times 10^{-2}$	$(4.6 \pm 1.1) \times 10^{20}$	$(3.7 \pm 1.1) \times 10^{+0}$
G252.680–01.530	$(674.4 \pm 6.2) \times 10^{-3}$	$(12.0 \pm 4.3) \times 10^{-2}$	$(34.2 \pm 7.4) \times 10^{19}$	$(5.6 \pm 2.0) \times 10^{+0}$
G252.700–01.490	$(90.0 \pm 5.4) \times 10^{-2}$	$(17.1 \pm 5.0) \times 10^{-2}$	$(23.0 \pm 5.3) \times 10^{19}$	$(5.3 \pm 1.6) \times 10^{+0}$
G252.840–00.470	$(44.3 \pm 1.6) \times 10^{-2}$	$(4.5 \pm 1.2) \times 10^{-1}$	$(34.8 \pm 4.3) \times 10^{19}$	$(9.9 \pm 2.7) \times 10^{-1}$
G252.850–00.730	$(272.7 \pm 2.5) \times 10^{-2}$	$(10.5 \pm 2.2) \times 10^{+0}$	$(91.1 \pm 8.4) \times 10^{19}$	$(25.9 \pm 5.4) \times 10^{-2}$
G253.030–01.990	$(13.3 \pm 1.4) \times 10^{-1}$	$(3.7 \pm 1.1) \times 10^{-1}$	$(27.7 \pm 1.7) \times 10^{19}$	$(3.6 \pm 1.2) \times 10^{+0}$
G253.080–02.100	$(46.7 \pm 3.2) \times 10^{-2}$	$(6.0 \pm 1.8) \times 10^{-1}$	$(6.2 \pm 1.2) \times 10^{20}$	$(7.8 \pm 2.3) \times 10^{-1}$
G253.100–01.350	$(41.9 \pm 1.0) \times 10^{-1}$	$(9.5 \pm 2.7) \times 10^{+0}$	$(33.6 \pm 1.6) \times 10^{20}$	$(4.4 \pm 1.3) \times 10^{-1}$
G253.110–01.800	$(63.0 \pm 4.3) \times 10^{-2}$	$(25.3 \pm 9.3) \times 10^{-2}$	$(9.8 \pm 2.4) \times 10^{20}$	$(24.9 \pm 9.3) \times 10^{-1}$
G253.110–02.120	$(323.5 \pm 8.7) \times 10^{-2}$	$(4.5 \pm 1.3) \times 10^{+0}$	$(31.0 \pm 2.9) \times 10^{20}$	$(7.3 \pm 2.1) \times 10^{-1}$
G253.110–02.150	$(23.2 \pm 1.1) \times 10^{-1}$	$(34.0 \pm 9.3) \times 10^{-2}$	$(55.8 \pm 4.3) \times 10^{19}$	$(6.8 \pm 1.9) \times 10^{+0}$
G253.120–02.060	$(22.2 \pm 1.2) \times 10^{-2}$	$(5.1 \pm 1.5) \times 10^{-1}$	$(7.8 \pm 1.8) \times 10^{20}$	$(4.3 \pm 1.3) \times 10^{-1}$
G253.160–01.960	$(130.4 \pm 5.3) \times 10^{-2}$	$(24.6 \pm 6.7) \times 10^{-2}$	$(17.4 \pm 2.9) \times 10^{19}$	$(5.3 \pm 1.5) \times 10^{+0}$
G253.230–01.350	$(65.6 \pm 3.9) \times 10^{-2}$	$(22.6 \pm 6.6) \times 10^{-2}$	$(26.1 \pm 4.4) \times 10^{19}$	$(28.9 \pm 8.6) \times 10^{-1}$
G253.270–01.110	$(167.2 \pm 7.6) \times 10^{-2}$	$(13.3 \pm 3.8) \times 10^{-1}$	$(73.9 \pm 4.4) \times 10^{19}$	$(12.6 \pm 3.6) \times 10^{-1}$
G253.290–01.010	$(10.9 \pm 1.6) \times 10^{-1}$	$(19.3 \pm 6.3) \times 10^{-2}$	$(38.3 \pm 5.4) \times 10^{19}$	$(5.6 \pm 2.0) \times 10^{+0}$
G253.290–01.610	$(44.4 \pm 3.5) \times 10^{+0}$	$(12.3 \pm 4.5) \times 10^{+0}$	$(40.3 \pm 6.9) \times 10^{21}$	$(3.6 \pm 1.4) \times 10^{+0}$
G253.300–01.080	$(45.6 \pm 4.9) \times 10^{-1}$	$(3.5 \pm 1.1) \times 10^{+0}$	$(164.7 \pm 9.8) \times 10^{19}$	$(13.0 \pm 4.2) \times 10^{-1}$
G253.400–01.400	$(54.2 \pm 2.3) \times 10^{+1}$	$(10.9 \pm 3.1) \times 10^{+0}$	$(17.8 \pm 4.0) \times 10^{21}$	$(5.0 \pm 1.4) \times 10^{+1}$
G253.400–01.420	$(157.8 \pm 3.7) \times 10^{-1}$	$(6.4 \pm 1.7) \times 10^{+0}$	$(5.7 \pm 1.3) \times 10^{21}$	$(24.8 \pm 6.5) \times 10^{-1}$
G253.420–01.400	$(39.7 \pm 3.8) \times 10^{+0}$	$(6.5 \pm 1.9) \times 10^{+0}$	$(9.7 \pm 1.9) \times 10^{21}$	$(6.1 \pm 1.9) \times 10^{+0}$
G253.430–01.370	$(53.0 \pm 4.5) \times 10^{+0}$	$(5.0 \pm 1.4) \times 10^{+0}$	$(6.4 \pm 1.3) \times 10^{21}$	$(10.5 \pm 3.0) \times 10^{+0}$
G253.450–01.370	$(55.4 \pm 5.4) \times 10^{+0}$	$(10.0 \pm 3.0) \times 10^{+0}$	$(18.7 \pm 4.9) \times 10^{21}$	$(5.5 \pm 1.7) \times 10^{+0}$
G253.460–01.410	$(67.7 \pm 7.0) \times 10^{-2}$	$(15.5 \pm 4.7) \times 10^{-1}$	$(120.8 \pm 8.3) \times 10^{19}$	$(4.4 \pm 1.4) \times 10^{-1}$
G253.470–01.420	$(42.7 \pm 1.7) \times 10^{-2}$	$(10.7 \pm 3.1) \times 10^{-1}$	$(73.6 \pm 6.8) \times 10^{19}$	$(4.0 \pm 1.2) \times 10^{-1}$
G253.480–01.290	$(35.3 \pm 2.1) \times 10^{-2}$	$(9.2 \pm 2.7) \times 10^{-1}$	$(15.3 \pm 2.1) \times 10^{20}$	$(3.8 \pm 1.1) \times 10^{-1}$
G253.480–01.370	$(131.1 \pm 2.9) \times 10^{-2}$	$(7.0 \pm 2.0) \times 10^{+0}$	$(6.6 \pm 1.0) \times 10^{21}$	$(18.7 \pm 5.3) \times 10^{-2}$
G253.503–01.237	$(16.1 \pm 1.9) \times 10^{+0}$	$(18.8 \pm 5.8) \times 10^{+0}$	$(17.2 \pm 2.0) \times 10^{21}$	$(8.5 \pm 2.8) \times 10^{-1}$
G253.510–01.240	$(147.4 \pm 3.0) \times 10^{-1}$	$(25.7 \pm 7.3) \times 10^{+0}$	$(17.7 \pm 1.7) \times 10^{21}$	$(5.7 \pm 1.6) \times 10^{-1}$
G253.510–01.260	$(35.9 \pm 2.8) \times 10^{+0}$	$(8.8 \pm 2.4) \times 10^{+0}$	$(73.3 \pm 9.2) \times 10^{20}$	$(4.1 \pm 1.2) \times 10^{+0}$
G253.520–01.370	$(68.0 \pm 5.9) \times 10^{-2}$	$(6.3 \pm 1.9) \times 10^{-1}$	$(56.1 \pm 7.2) \times 10^{19}$	$(10.7 \pm 3.3) \times 10^{-1}$
G253.530–00.420	$(13.8 \pm 1.3) \times 10^{+1}$	$(4.7 \pm 1.1) \times 10^{+1}$	$(72.8 \pm 6.2) \times 10^{20}$	$(29.5 \pm 7.5) \times 10^{-1}$
G253.630–01.440	$(271.1 \pm 4.7) \times 10^{-2}$	$(7.0 \pm 1.8) \times 10^{-1}$	$(52.0 \pm 9.4) \times 10^{19}$	$(3.9 \pm 1.0) \times 10^{+0}$
G253.770–01.300	$(163.3 \pm 2.9) \times 10^{-2}$	$(4.2 \pm 1.1) \times 10^{-1}$	$(37.3 \pm 9.1) \times 10^{19}$	$(3.9 \pm 1.0) \times 10^{+0}$
G253.860–01.230	$(484.9 \pm 4.1) \times 10^{-2}$	$(11.3 \pm 3.1) \times 10^{-1}$	$(8.7 \pm 1.0) \times 10^{20}$	$(4.3 \pm 1.2) \times 10^{+0}$
G253.870–01.200	$(246.2 \pm 3.7) \times 10^{-2}$	$(4.7 \pm 1.3) \times 10^{+0}$	$(42.6 \pm 6.8) \times 10^{20}$	$(5.3 \pm 1.5) \times 10^{-1}$
G253.870–01.210	$(361.3 \pm 8.7) \times 10^{-1}$	$(19.1 \pm 5.3) \times 10^{+0}$	$(55.0 \pm 1.9) \times 10^{20}$	$(18.9 \pm 5.2) \times 10^{-1}$
G253.880–01.540	$(16.9 \pm 1.5) \times 10^{+0}$	$(7.3 \pm 1.7) \times 10^{+0}$	$(42.1 \pm 2.8) \times 10^{19}$	$(23.3 \pm 5.7) \times 10^{-1}$
G253.890–00.470	$(80.2 \pm 2.3) \times 10^{-1}$	$(7.2 \pm 2.0) \times 10^{+0}$	$(12.8 \pm 2.4) \times 10^{21}$	$(11.2 \pm 3.1) \times 10^{-1}$
G253.980–00.720	$(200.1 \pm 9.5) \times 10^{+0}$	$(11.0 \pm 2.4) \times 10^{+1}$	$(56.7 \pm 1.3) \times 10^{20}$	$(18.2 \pm 4.1) \times 10^{-1}$
G254.052–00.566	$(25.2 \pm 5.7) \times 10^{+2}$	$(9.6 \pm 3.0) \times 10^{+1}$	$(18.4 \pm 3.8) \times 10^{21}$	$(2.6 \pm 1.0) \times 10^{+1}$
G254.120–01.420	$(31.9 \pm 3.3) \times 10^{+1}$	$(34.8 \pm 8.2) \times 10^{+0}$	$(28.6 \pm 1.9) \times 10^{20}$	$(9.2 \pm 2.3) \times 10^{+0}$

Table A.5: continued

Name	L ($L_\odot$)	M ($M_\odot$)	N_{H_2} (cm^{-2})	L/M ($L_\odot/M_\odot$)
G254.232–00.136	$(53.0\pm2.6)\times10^{+1}$	$(30.5\pm6.8)\times10^{+0}$	$(38.0\pm2.5)\times10^{20}$	$(17.4\pm4.0)\times10^{+0}$
G254.230–02.320	$(144.0\pm7.9)\times10^{-2}$	$(8.0\pm1.8)\times10^{+0}$	$(21.6\pm5.3)\times10^{20}$	$(17.9\pm4.2)\times10^{-2}$
G254.390–01.010	$(79.7\pm7.2)\times10^{-1}$	$(40.9\pm9.2)\times10^{+0}$	$(23.1\pm5.5)\times10^{20}$	$(19.5\pm4.7)\times10^{-2}$
G254.590–01.060	$(130.5\pm8.6)\times10^{-1}$	$(9.3\pm2.0)\times10^{+0}$	$(34.9\pm5.3)\times10^{19}$	$(14.0\pm3.1)\times10^{-1}$
G254.660–01.250	$(154.4\pm4.2)\times10^{-2}$	$(17.6\pm5.2)\times10^{-1}$	$(96.3\pm5.4)\times10^{19}$	$(8.8\pm2.6)\times10^{-1}$
G254.680–01.890	$(60.0\pm4.8)\times10^{-2}$	$(5.3\pm1.5)\times10^{-1}$	$(48.6\pm7.6)\times10^{19}$	$(11.3\pm3.4)\times10^{-1}$
G254.760–01.240	$(214.7\pm8.2)\times10^{-2}$	$(4.6\pm1.3)\times10^{+0}$	$(150.2\pm7.0)\times10^{19}$	$(4.7\pm1.3)\times10^{-1}$
G255.100–00.090	$(19.9\pm1.3)\times10^{+0}$	$(6.9\pm1.5)\times10^{+1}$	$(4.2\pm1.0)\times10^{21}$	$(28.7\pm6.5)\times10^{-2}$
G255.170–00.570	$(104.8\pm1.5)\times10^{+1}$	$(7.2\pm1.5)\times10^{+1}$	$(30.9\pm5.9)\times10^{20}$	$(14.5\pm3.0)\times10^{+0}$
G255.190–02.280	$(44.4\pm2.3)\times10^{-2}$	$(4.0\pm1.2)\times10^{-1}$	$(22.8\pm1.4)\times10^{19}$	$(11.1\pm3.4)\times10^{-1}$
G255.200–02.290	$(23.5\pm2.0)\times10^{-2}$	$(18.6\pm5.7)\times10^{-2}$	$(20.1\pm2.2)\times10^{19}$	$(12.6\pm4.0)\times10^{-1}$
G255.210–02.290	$(78.8\pm7.0)\times10^{-2}$	$(3.5\pm1.1)\times10^{-1}$	$(16.7\pm1.1)\times10^{19}$	$(22.4\pm7.2)\times10^{-1}$
G255.401–00.918	$(61.5\pm1.6)\times10^{+0}$	$(5.2\pm1.1)\times10^{+2}$	$(92.8\pm5.8)\times10^{20}$	$(11.9\pm2.5)\times10^{-2}$
G256.130–01.470	$(16.1\pm2.7)\times10^{+2}$	$(14.2\pm3.8)\times10^{+1}$	$(7.7\pm2.2)\times10^{21}$	$(11.4\pm3.6)\times10^{+0}$
G256.150–01.370	$(62.4\pm4.2)\times10^{+1}$	$(15.5\pm3.3)\times10^{+1}$	$(7.6\pm1.9)\times10^{21}$	$(40.3\pm9.1)\times10^{-1}$
G256.150–01.380	$(62.4\pm4.2)\times10^{+1}$	$(15.5\pm3.3)\times10^{+1}$	$(7.6\pm1.9)\times10^{21}$	$(40.3\pm9.1)\times10^{-1}$
G256.190–01.540	$(46.4\pm2.4)\times10^{+2}$	$(13.4\pm2.8)\times10^{+1}$	$(5.4\pm1.2)\times10^{21}$	$(34.6\pm7.4)\times10^{+0}$
G256.187–01.547	$(49.9\pm2.2)\times10^{+2}$	$(14.6\pm3.0)\times10^{+1}$	$(5.5\pm1.3)\times10^{21}$	$(34.1\pm7.2)\times10^{+0}$
G256.430–01.630	$(15.9\pm2.7)\times10^{-2}$	$(9.6\pm3.2)\times10^{-2}$	$(16.5\pm3.1)\times10^{19}$	$(16.6\pm6.3)\times10^{-1}$
G256.430–01.640	$(37.5\pm1.7)\times10^{-2}$	$(9.3\pm2.7)\times10^{-1}$	$(76.2\pm6.1)\times10^{19}$	$(4.0\pm1.2)\times10^{-1}$
G256.440–01.610	$(149.8\pm4.8)\times10^{-2}$	$(7.8\pm2.2)\times10^{-1}$	$(10.9\pm1.4)\times10^{20}$	$(19.3\pm5.5)\times10^{-1}$
G256.450–01.608	$(18.8\pm1.4)\times10^{+1}$	$(12.2\pm2.6)\times10^{+1}$	$(6.3\pm1.4)\times10^{21}$	$(15.5\pm3.5)\times10^{-1}$
G256.620–00.050	$(96.9\pm1.9)\times10^{-1}$	$(7.8\pm1.6)\times10^{+1}$	$(39.9\pm8.8)\times10^{20}$	$(12.4\pm2.6)\times10^{-2}$
G256.682–01.627	$(93.5\pm8.1)\times10^{-1}$	$(31.1\pm7.1)\times10^{+0}$	$(21.4\pm1.3)\times10^{20}$	$(30.1\pm7.3)\times10^{-2}$
G256.690–00.040	$(30.0\pm2.2)\times10^{+0}$	$(10.3\pm2.2)\times10^{+1}$	$(24.3\pm1.9)\times10^{20}$	$(29.0\pm6.6)\times10^{-2}$
G256.720–01.930	$(35.3\pm2.6)\times10^{+1}$	$(44.3\pm9.8)\times10^{+0}$	$(8.2\pm1.9)\times10^{21}$	$(8.0\pm1.9)\times10^{+0}$
G256.730–01.670	$(80.8\pm2.0)\times10^{-1}$	$(14.2\pm3.0)\times10^{+0}$	$(16.1\pm2.4)\times10^{20}$	$(5.7\pm1.2)\times10^{-1}$
G256.740–01.580	$(164.6\pm3.8)\times10^{-2}$	$(10.8\pm3.5)\times10^{-1}$	$(62.3\pm3.3)\times10^{19}$	$(15.3\pm4.9)\times10^{-1}$
G256.750–00.060	$(105.1\pm3.6)\times10^{-1}$	$(8.0\pm1.7)\times10^{+1}$	$(35.4\pm3.8)\times10^{20}$	$(13.1\pm2.8)\times10^{-2}$
G256.780–00.130	$(647.6\pm5.0)\times10^{-1}$	$(9.8\pm2.0)\times10^{+1}$	$(34.0\pm4.0)\times10^{20}$	$(6.6\pm1.4)\times10^{-1}$
G256.780–02.070	$(58.4\pm1.1)\times10^{-1}$	$(35.6\pm7.5)\times10^{-1}$	$(31.7\pm3.5)\times10^{19}$	$(16.4\pm3.5)\times10^{-1}$
G256.910–00.280	$(569.2\pm5.6)\times10^{-1}$	$(29.9\pm6.1)\times10^{+1}$	$(80.5\pm6.3)\times10^{20}$	$(19.0\pm3.9)\times10^{-2}$
G256.920–01.830	$(73.0\pm2.1)\times10^{-1}$	$(19.2\pm4.1)\times10^{-1}$	$(15.7\pm1.6)\times10^{19}$	$(38.1\pm8.3)\times10^{-1}$
G256.950–00.530	$(97.3\pm4.2)\times10^{-1}$	$(35.9\pm7.6)\times10^{+0}$	$(20.7\pm1.5)\times10^{20}$	$(27.1\pm5.9)\times10^{-2}$
G256.990–00.570	$(69.4\pm1.8)\times10^{-1}$	$(10.6\pm2.2)\times10^{+0}$	$(8.5\pm1.4)\times10^{20}$	$(6.5\pm1.4)\times10^{-1}$
G256.990–02.130	$(35.7\pm1.2)\times10^{-1}$	$(17.9\pm4.0)\times10^{-1}$	$(26.2\pm6.5)\times10^{19}$	$(20.0\pm4.5)\times10^{-1}$
G257.010+00.000	$(10.4\pm1.4)\times10^{+0}$	$(9.6\pm2.4)\times10^{+0}$	$(10.1\pm2.9)\times10^{20}$	$(10.8\pm3.1)\times10^{-1}$
G257.060–02.080	$(78.8\pm1.0)\times10^{-1}$	$(15.1\pm3.2)\times10^{-1}$	$(11.7\pm1.3)\times10^{19}$	$(5.2\pm1.1)\times10^{+0}$
G257.227–00.902	$(499.1\pm7.4)\times10^{-1}$	$(14.8\pm3.1)\times10^{+1}$	$(298.7\pm8.6)\times10^{19}$	$(33.7\pm7.0)\times10^{-2}$
G257.240–00.700	$(61.0\pm5.6)\times10^{-2}$	$(11.7\pm3.1)\times10^{-1}$	$(6.3\pm1.1)\times10^{20}$	$(5.2\pm1.4)\times10^{-1}$
G257.261–01.240	$(681.8\pm7.8)\times10^{-3}$	$(22.9\pm7.3)\times10^{-2}$	$(24.5\pm2.4)\times10^{19}$	$(29.8\pm9.5)\times10^{-1}$
G257.282–00.336	$(26.2\pm1.1)\times10^{+1}$	$(25.0\pm5.3)\times10^{+1}$	$(54.2\pm2.0)\times10^{20}$	$(10.5\pm2.3)\times10^{-1}$
G257.298–01.147	$(18.3\pm3.2)\times10^{-1}$	$(7.0\pm2.0)\times10^{-1}$	$(29.6\pm8.6)\times10^{19}$	$(26.2\pm8.8)\times10^{-1}$
G257.320–01.063	$(9.6\pm2.2)\times10^{+1}$	$(8.8\pm2.8)\times10^{-1}$	$(6.4\pm2.3)\times10^{20}$	$(10.9\pm4.3)\times10^{+1}$
G257.330–00.258	$(1191.5\pm6.5)\times10^{-2}$	$(27.8\pm5.8)\times10^{-1}$	$(27.8\pm6.1)\times10^{19}$	$(42.9\pm9.0)\times10^{-1}$
G257.340–00.360	$(245.5\pm9.2)\times10^{-1}$	$(15.6\pm3.3)\times10^{+0}$	$(48.9\pm3.4)\times10^{19}$	$(15.8\pm3.4)\times10^{-1}$
G257.354–00.220	$(54.3\pm3.8)\times10^{+0}$	$(12.0\pm2.6)\times10^{+1}$	$(282.2\pm7.3)\times10^{19}$	$(4.5\pm1.0)\times10^{-1}$
G257.374–00.276	$(158.3\pm3.9)\times10^{-1}$	$(31.6\pm6.6)\times10^{+0}$	$(19.5\pm2.3)\times10^{20}$	$(5.0\pm1.0)\times10^{-1}$
G257.380–00.280	$(165.4\pm4.8)\times10^{-1}$	$(30.0\pm6.2)\times10^{+0}$	$(17.8\pm2.1)\times10^{20}$	$(5.5\pm1.2)\times10^{-1}$

Table A.5: continued

Name	L ($L_\odot$)	M ($M_\odot$)	N_{H_2} (cm^{-2})	L/M ($L_\odot/M_\odot$)
G257.460–00.610	$(73.3\pm2.3)\times10^{-1}$	$(9.3\pm2.0)\times10^{+0}$	$(9.7\pm2.3)\times10^{20}$	$(7.8\pm1.7)\times10^{-1}$
G257.470–00.630	$(30.0\pm3.9)\times10^{+1}$	$(6.5\pm1.6)\times10^{+1}$	$(6.2\pm1.4)\times10^{21}$	$(4.6\pm1.3)\times10^{+0}$
G257.510–02.250	$(16.6\pm4.2)\times10^{+2}$	$(18.3\pm5.9)\times10^{+1}$	$(9.0\pm3.2)\times10^{21}$	$(9.1\pm3.7)\times10^{+0}$
G257.540–01.270	$(53.0\pm1.8)\times10^{-1}$	$(5.8\pm1.2)\times10^{+1}$	$(33.7\pm8.1)\times10^{20}$	$(9.2\pm1.9)\times10^{-2}$
G257.540–01.630	$(16.3\pm1.6)\times10^{-1}$	$(15.5\pm5.0)\times10^{-2}$	$(25.8\pm5.5)\times10^{19}$	$(10.5\pm3.5)\times10^{+0}$
G257.546–01.214	$(117.5\pm2.0)\times10^{-2}$	$(17.5\pm4.2)\times10^{-2}$	$(11.4\pm2.7)\times10^{19}$	$(6.7\pm1.6)\times10^{+0}$
G257.560–00.480	$(9.8\pm1.7)\times10^{+0}$	$(6.2\pm1.7)\times10^{+0}$	$(5.8\pm1.8)\times10^{20}$	$(15.9\pm5.0)\times10^{-1}$
G257.570–02.070	$(71.0\pm1.0)\times10^{+0}$	$(30.7\pm6.2)\times10^{+1}$	$(98.1\pm9.3)\times10^{20}$	$(23.2\pm4.7)\times10^{-2}$
G257.610–00.660	$(72.1\pm6.6)\times10^{-1}$	$(12.8\pm2.9)\times10^{+0}$	$(15.0\pm3.9)\times10^{20}$	$(5.6\pm1.4)\times10^{-1}$
G257.617–01.772	$(169.8\pm5.0)\times10^{-2}$	$(16.0\pm3.8)\times10^{-1}$	$(9.5\pm2.1)\times10^{20}$	$(10.6\pm2.5)\times10^{-1}$
G257.630–00.590	$(132.6\pm9.8)\times10^{-1}$	$(9.3\pm2.1)\times10^{+0}$	$(65.4\pm6.7)\times10^{19}$	$(14.3\pm3.3)\times10^{-1}$
G257.630–01.050	$(22.1\pm1.3)\times10^{-1}$	$(12.4\pm3.2)\times10^{-1}$	$(46.8\pm4.8)\times10^{19}$	$(17.9\pm4.7)\times10^{-1}$
G257.640–00.959	$(17.3\pm1.1)\times10^{-1}$	$(19.0\pm4.7)\times10^{-1}$	$(48.8\pm3.8)\times10^{19}$	$(9.1\pm2.3)\times10^{-1}$
G257.655–01.250	$(15.2\pm1.4)\times10^{+0}$	$(4.8\pm1.1)\times10^{+0}$	$(21.6\pm2.3)\times10^{19}$	$(31.5\pm7.7)\times10^{-1}$
G257.808–01.277	$(31.0\pm5.6)\times10^{+0}$	$(22.3\pm6.1)\times10^{+0}$	$(13.3\pm4.2)\times10^{20}$	$(13.9\pm4.5)\times10^{-1}$
G257.830–00.740	$(87.6\pm4.0)\times10^{-2}$	$(9.0\pm2.2)\times10^{-1}$	$(36.4\pm4.6)\times10^{19}$	$(9.8\pm2.4)\times10^{-1}$
G257.842–01.085	$(18.5\pm1.3)\times10^{+1}$	$(11.5\pm2.5)\times10^{+1}$	$(6.6\pm1.3)\times10^{21}$	$(16.1\pm3.6)\times10^{-1}$
G257.864–01.086	$(49.1\pm2.2)\times10^{+0}$	$(16.5\pm3.4)\times10^{+1}$	$(28.0\pm2.4)\times10^{20}$	$(29.8\pm6.4)\times10^{-2}$
G257.865–01.495	$(247.9\pm6.5)\times10^{-2}$	$(6.5\pm1.6)\times10^{-1}$	$(34.2\pm6.2)\times10^{19}$	$(38.2\pm9.2)\times10^{-1}$
G257.867–01.793	$(312.9\pm2.4)\times10^{+0}$	$(17.7\pm3.7)\times10^{+0}$	$(92.6\pm6.1)\times10^{19}$	$(17.7\pm3.7)\times10^{+0}$
G257.879–01.729	$(248.2\pm1.7)\times10^{-2}$	$(10.3\pm3.2)\times10^{-1}$	$(52.3\pm2.3)\times10^{19}$	$(24.0\pm7.3)\times10^{-1}$
G257.920–00.470	$(47.2\pm2.5)\times10^{+0}$	$(33.4\pm7.1)\times10^{+0}$	$(121.5\pm5.9)\times10^{19}$	$(14.1\pm3.1)\times10^{-1}$
G257.932–01.387	$(31.3\pm4.1)\times10^{+1}$	$(8.4\pm2.1)\times10^{+1}$	$(183.7\pm2.9)\times10^{19}$	$(3.7\pm1.1)\times10^{+0}$
G257.940–00.942	$(91.7\pm1.6)\times10^{-1}$	$(11.4\pm2.3)\times10^{+1}$	$(5.7\pm1.2)\times10^{21}$	$(8.0\pm1.6)\times10^{-2}$
G257.950–00.170	$(170.9\pm9.1)\times10^{-1}$	$(7.6\pm1.6)\times10^{+0}$	$(46.0\pm5.6)\times10^{19}$	$(22.5\pm5.0)\times10^{-1}$
G257.950–00.510	$(121.1\pm5.9)\times10^{-1}$	$(17.4\pm3.7)\times10^{+0}$	$(14.7\pm2.2)\times10^{20}$	$(7.0\pm1.5)\times10^{-1}$
G257.960–00.940	$(178.2\pm1.6)\times10^{-1}$	$(16.6\pm3.4)\times10^{+1}$	$(53.0\pm8.5)\times10^{20}$	$(10.7\pm2.2)\times10^{-2}$
G257.978–01.428	$(24.8\pm1.5)\times10^{+1}$	$(5.0\pm1.1)\times10^{+1}$	$(174.4\pm1.9)\times10^{19}$	$(5.0\pm1.1)\times10^{+0}$
G258.000–00.300	$(31.5\pm1.1)\times10^{+0}$	$(17.0\pm3.6)\times10^{+0}$	$(75.5\pm5.1)\times10^{19}$	$(18.6\pm4.0)\times10^{-1}$
G258.050–01.341	$(17.9\pm1.7)\times10^{+1}$	$(9.2\pm2.1)\times10^{+1}$	$(39.7\pm1.4)\times10^{20}$	$(19.3\pm4.8)\times10^{-1}$
G258.047–01.604	$(154.9\pm5.2)\times10^{-1}$	$(8.1\pm1.7)\times10^{+0}$	$(12.3\pm2.8)\times10^{20}$	$(19.2\pm4.2)\times10^{-1}$
G258.080–01.350	$(37.7\pm4.0)\times10^{+1}$	$(17.3\pm4.1)\times10^{+0}$	$(30.7\pm1.6)\times10^{20}$	$(21.8\pm5.7)\times10^{+0}$
G258.080–01.563	$(43.0\pm1.4)\times10^{-1}$	$(13.9\pm2.9)\times10^{+0}$	$(22.9\pm5.4)\times10^{20}$	$(31.0\pm6.7)\times10^{-2}$
G258.081–01.561	$(43.0\pm1.4)\times10^{-1}$	$(13.9\pm2.9)\times10^{+0}$	$(22.9\pm5.4)\times10^{20}$	$(31.0\pm6.7)\times10^{-2}$
G258.080–01.561	$(43.0\pm1.4)\times10^{-1}$	$(13.9\pm2.9)\times10^{+0}$	$(22.9\pm5.4)\times10^{20}$	$(31.0\pm6.7)\times10^{-2}$
G258.081–01.558	$(43.0\pm1.4)\times10^{-1}$	$(13.9\pm2.9)\times10^{+0}$	$(22.9\pm5.4)\times10^{20}$	$(31.0\pm6.7)\times10^{-2}$
G258.082–01.626	$(209.3\pm5.3)\times10^{-1}$	$(37.7\pm8.0)\times10^{+0}$	$(24.2\pm1.5)\times10^{20}$	$(5.5\pm1.2)\times10^{-1}$
G258.140–00.350	$(72.0\pm2.6)\times10^{-2}$	$(6.2\pm1.5)\times10^{-1}$	$(19.4\pm2.0)\times10^{19}$	$(11.7\pm2.8)\times10^{-1}$
G258.182–01.512	$(14.6\pm1.7)\times10^{+0}$	$(6.9\pm1.7)\times10^{+0}$	$(52.5\pm4.4)\times10^{19}$	$(21.1\pm5.7)\times10^{-1}$
G258.194–02.221	$(617.3\pm6.6)\times10^{-2}$	$(5.6\pm1.3)\times10^{+0}$	$(69.2\pm2.7)\times10^{19}$	$(11.1\pm2.7)\times10^{-1}$
G258.190–02.277	$(56.8\pm7.8)\times10^{-1}$	$(30.1\pm8.5)\times10^{-1}$	$(71.4\pm5.5)\times10^{19}$	$(18.9\pm5.9)\times10^{-1}$
G258.255–01.233	$(54.7\pm4.6)\times10^{+0}$	$(36.7\pm8.1)\times10^{+0}$	$(65.8\pm4.4)\times10^{19}$	$(14.9\pm3.5)\times10^{-1}$
G258.260–00.870	$(108.6\pm3.8)\times10^{-1}$	$(23.8\pm4.9)\times10^{+0}$	$(47.3\pm4.2)\times10^{19}$	$(45.7\pm9.6)\times10^{-2}$
G258.300–00.520	$(27.3\pm2.6)\times10^{+0}$	$(21.2\pm4.8)\times10^{+0}$	$(63.8\pm4.8)\times10^{19}$	$(12.9\pm3.2)\times10^{-1}$
G258.300–02.163	$(13.8\pm1.9)\times10^{+1}$	$(16.0\pm4.0)\times10^{+1}$	$(185.7\pm5.1)\times10^{19}$	$(8.6\pm2.5)\times10^{-1}$
G258.319–00.920	$(203.7\pm9.2)\times10^{-2}$	$(14.2\pm4.4)\times10^{-1}$	$(58.6\pm2.1)\times10^{19}$	$(14.3\pm4.5)\times10^{-1}$
G258.340–02.190	$(133.1\pm9.9)\times10^{-1}$	$(28.5\pm6.4)\times10^{+0}$	$(23.8\pm2.4)\times10^{20}$	$(4.7\pm1.1)\times10^{-1}$
G258.384–01.113	$(101.0\pm6.0)\times10^{+0}$	$(7.2\pm1.5)\times10^{+1}$	$(70.1\pm2.8)\times10^{19}$	$(14.1\pm3.1)\times10^{-1}$
G258.420–00.940	$(54.1\pm2.7)\times10^{+0}$	$(43.1\pm9.0)\times10^{+0}$	$(78.9\pm5.2)\times10^{19}$	$(12.5\pm2.7)\times10^{-1}$

Table A.5: continued

Name	L ($L_\odot$)	M ($M_\odot$)	N_{H_2} (cm^{-2})	L/M ($L_\odot/M_\odot$)
G258.430–00.940	$(163.8\pm8.0)\times10^{-1}$	$(10.3\pm2.2)\times10^{+1}$	$(26.5\pm4.0)\times10^{20}$	$(15.9\pm3.4)\times10^{-2}$
G258.427–01.444	$(52.6\pm4.2)\times10^{-1}$	$(11.3\pm3.0)\times10^{-2}$	$(14.1\pm3.6)\times10^{19}$	$(4.6\pm1.3)\times10^{+1}$
G258.532–01.188	$(44.0\pm5.1)\times10^{+0}$	$(10.3\pm2.7)\times10^{+0}$	$(411.3\pm4.6)\times10^{18}$	$(4.3\pm1.2)\times10^{+0}$
G258.610–01.920	$(745.7\pm7.3)\times10^{+0}$	$(29.8\pm7.3)\times10^{+0}$	$(219.4\pm2.1)\times10^{19}$	$(25.1\pm6.2)\times10^{+0}$
G258.660–00.390	$(25.4\pm1.1)\times10^{-1}$	$(4.9\pm1.1)\times10^{+0}$	$(92.5\pm7.4)\times10^{19}$	$(5.2\pm1.2)\times10^{-1}$
G258.667–01.050	$(25.0\pm1.3)\times10^{-1}$	$(4.6\pm1.1)\times10^{+0}$	$(111.2\pm5.0)\times10^{19}$	$(5.5\pm1.4)\times10^{-1}$
G258.718–01.168	$(156.4\pm1.1)\times10^{+0}$	$(16.1\pm3.3)\times10^{+0}$	$(11.1\pm2.4)\times10^{20}$	$(9.7\pm2.0)\times10^{+0}$
G258.733–01.335	$(331.7\pm2.8)\times10^{-1}$	$(30.1\pm7.1)\times10^{-1}$	$(64.7\pm5.5)\times10^{19}$	$(11.0\pm2.6)\times10^{+0}$
G258.743–01.291	$(848.2\pm4.2)\times10^{+0}$	$(16.0\pm3.3)\times10^{+1}$	$(133.1\pm1.3)\times10^{19}$	$(5.3\pm1.1)\times10^{+0}$
G258.790–00.970	$(30.3\pm1.9)\times10^{-1}$	$(6.1\pm1.5)\times10^{-1}$	$(21.8\pm3.2)\times10^{19}$	$(4.9\pm1.2)\times10^{+0}$
G258.792–01.422	$(45.8\pm2.5)\times10^{-1}$	$(12.7\pm3.2)\times10^{+0}$	$(191.9\pm5.3)\times10^{19}$	$(36.0\pm9.3)\times10^{-2}$
G258.822–01.402	$(61.8\pm1.2)\times10^{-1}$	$(7.1\pm1.7)\times10^{+0}$	$(169.8\pm8.1)\times10^{19}$	$(8.8\pm2.2)\times10^{-1}$
G258.842–01.446	$(90.1\pm8.1)\times10^{-1}$	$(10.8\pm2.9)\times10^{+0}$	$(203.3\pm7.4)\times10^{19}$	$(8.3\pm2.4)\times10^{-1}$
G258.860–01.397	$(88.0\pm6.2)\times10^{-2}$	$(11.4\pm3.0)\times10^{+0}$	$(62.9\pm5.8)\times10^{20}$	$(7.7\pm2.1)\times10^{-2}$
G258.870–01.475	$(208.9\pm8.8)\times10^{-2}$	$(5.4\pm1.4)\times10^{+0}$	$(21.1\pm1.9)\times10^{20}$	$(3.9\pm1.0)\times10^{-1}$
G258.880–00.720	$(34.7\pm1.1)\times10^{-1}$	$(5.2\pm1.3)\times10^{+0}$	$(104.8\pm4.2)\times10^{19}$	$(6.6\pm1.7)\times10^{-1}$
G258.878–01.440	$(97.4\pm4.6)\times10^{-2}$	$(20.2\pm5.3)\times10^{-1}$	$(17.7\pm4.0)\times10^{20}$	$(4.8\pm1.3)\times10^{-1}$
G258.885–01.498	$(12.9\pm1.5)\times10^{+0}$	$(11.0\pm3.1)\times10^{+0}$	$(56.8\pm6.3)\times10^{20}$	$(11.8\pm3.6)\times10^{-1}$
G258.910–01.450	$(146.0\pm3.0)\times10^{-2}$	$(6.8\pm1.7)\times10^{+0}$	$(25.4\pm1.4)\times10^{20}$	$(21.5\pm5.5)\times10^{-2}$
G258.930–00.730	$(26.6\pm1.8)\times10^{-1}$	$(11.5\pm3.0)\times10^{+0}$	$(45.8\pm2.8)\times10^{20}$	$(23.2\pm6.3)\times10^{-2}$
G258.960–00.720	$(113.5\pm8.2)\times10^{-2}$	$(8.5\pm2.3)\times10^{-1}$	$(63.2\pm6.8)\times10^{19}$	$(13.3\pm3.7)\times10^{-1}$
G258.965–01.475	$(101.6\pm8.6)\times10^{+0}$	$(14.4\pm3.2)\times10^{+1}$	$(244.1\pm7.9)\times10^{19}$	$(7.0\pm1.7)\times10^{-1}$
G259.002–01.498	$(151.8\pm2.3)\times10^{+0}$	$(5.7\pm1.2)\times10^{+1}$	$(19.5\pm1.0)\times10^{20}$	$(26.5\pm5.5)\times10^{-1}$
G259.018–01.550	$(8.7\pm1.9)\times10^{+3}$	$(4.2\pm1.2)\times10^{+2}$	$(68.2\pm3.0)\times10^{20}$	$(20.9\pm7.7)\times10^{+0}$
G259.031–00.496	$(26.3\pm2.0)\times10^{-1}$	$(29.5\pm7.2)\times10^{-1}$	$(10.1\pm1.2)\times10^{20}$	$(8.9\pm2.3)\times10^{-1}$
G259.052–01.140	$(416.9\pm8.9)\times10^{-1}$	$(5.4\pm1.1)\times10^{+1}$	$(150.2\pm7.5)\times10^{19}$	$(7.7\pm1.6)\times10^{-1}$
G259.050–01.538	$(88.1\pm4.5)\times10^{+2}$	$(19.8\pm4.2)\times10^{+1}$	$(48.2\pm2.3)\times10^{20}$	$(44.6\pm9.7)\times10^{+0}$
G259.045–01.557	$(154.0\pm7.3)\times10^{+2}$	$(25.1\pm5.3)\times10^{+1}$	$(97.4\pm5.5)\times10^{20}$	$(6.1\pm1.3)\times10^{+1}$
G259.080–00.050	$(86.2\pm3.7)\times10^{-2}$	$(17.7\pm5.3)\times10^{-2}$	$(34.1\pm8.3)\times10^{19}$	$(4.9\pm1.5)\times10^{+0}$
G259.078–01.620	$(222.7\pm5.6)\times10^{+1}$	$(8.1\pm1.7)\times10^{+1}$	$(58.6\pm9.5)\times10^{20}$	$(27.5\pm5.7)\times10^{+0}$
G259.112–01.437	$(152.8\pm2.8)\times10^{-1}$	$(28.3\pm6.7)\times10^{+0}$	$(246.3\pm6.5)\times10^{19}$	$(5.4\pm1.3)\times10^{-1}$
G259.133–01.426	$(162.2\pm1.1)\times10^{-1}$	$(38.2\pm9.0)\times10^{+0}$	$(543.1\pm7.4)\times10^{19}$	$(4.2\pm1.0)\times10^{-1}$
G259.153–01.337	$(105.4\pm1.0)\times10^{-1}$	$(17.2\pm4.2)\times10^{+0}$	$(286.2\pm6.2)\times10^{19}$	$(6.1\pm1.5)\times10^{-1}$
G259.165–01.217	$(65.2\pm1.4)\times10^{-1}$	$(9.6\pm2.3)\times10^{+0}$	$(158.9\pm3.0)\times10^{19}$	$(6.8\pm1.7)\times10^{-1}$
G259.172–01.253	$(339.2\pm1.5)\times10^{-2}$	$(27.9\pm6.8)\times10^{-1}$	$(68.9\pm5.2)\times10^{19}$	$(12.2\pm2.9)\times10^{-1}$
G259.167–01.313	$(51.1\pm3.6)\times10^{-1}$	$(4.9\pm1.2)\times10^{+0}$	$(87.6\pm3.9)\times10^{19}$	$(10.4\pm2.7)\times10^{-1}$
G259.190–00.030	$(493.8\pm4.6)\times10^{-3}$	$(23.5\pm8.0)\times10^{-2}$	$(6.8\pm1.5)\times10^{20}$	$(21.0\pm7.1)\times10^{-1}$
G259.200+00.000	$(70.2\pm4.4)\times10^{-2}$	$(8.3\pm2.5)\times10^{-1}$	$(11.5\pm2.6)\times10^{20}$	$(8.5\pm2.6)\times10^{-1}$
G259.200–00.010	$(52.3\pm2.7)\times10^{-1}$	$(9.5\pm2.8)\times10^{-1}$	$(79.6\pm6.4)\times10^{19}$	$(5.5\pm1.7)\times10^{+0}$
G259.198–01.272	$(135.3\pm2.8)\times10^{-1}$	$(15.7\pm3.8)\times10^{+0}$	$(184.5\pm2.4)\times10^{19}$	$(8.6\pm2.1)\times10^{-1}$
G259.215–01.389	$(164.9\pm8.5)\times10^{+0}$	$(46.8\pm9.9)\times10^{+1}$	$(574.7\pm8.8)\times10^{19}$	$(35.3\pm7.7)\times10^{-2}$
G259.217–01.390	$(18.8\pm1.4)\times10^{+1}$	$(4.9\pm1.1)\times10^{+2}$	$(580.0\pm9.2)\times10^{19}$	$(38.6\pm8.9)\times10^{-2}$
G259.230–00.030	$(18.0\pm2.6)\times10^{-1}$	$(15.3\pm4.4)\times10^{-1}$	$(9.4\pm1.3)\times10^{20}$	$(11.8\pm3.8)\times10^{-1}$
G259.230–00.300	$(157.3\pm6.3)\times10^{-2}$	$(19.5\pm5.1)\times10^{-2}$	$(21.2\pm3.9)\times10^{19}$	$(8.1\pm2.1)\times10^{+0}$
G259.240–00.320	$(208.4\pm3.0)\times10^{-1}$	$(21.0\pm4.4)\times10^{+0}$	$(82.4\pm6.0)\times10^{19}$	$(9.9\pm2.1)\times10^{-1}$
G259.237–01.627	$(39.0\pm1.3)\times10^{+2}$	$(12.5\pm2.6)\times10^{+1}$	$(60.8\pm5.7)\times10^{20}$	$(31.3\pm6.6)\times10^{+0}$
G259.250–00.050	$(34.1\pm1.6)\times10^{-1}$	$(14.6\pm3.6)\times10^{+0}$	$(87.2\pm9.1)\times10^{20}$	$(23.4\pm5.9)\times10^{-2}$
G259.245–01.227	$(77.1\pm1.8)\times10^{+0}$	$(18.2\pm3.8)\times10^{+1}$	$(322.9\pm7.4)\times10^{19}$	$(42.4\pm8.9)\times10^{-2}$
G259.250–02.020	$(983.1\pm6.7)\times10^{-1}$	$(14.3\pm2.9)\times10^{+1}$	$(31.7\pm1.2)\times10^{20}$	$(6.9\pm1.4)\times10^{-1}$

Table A.5: continued

Name	L ($L_\odot$)	M ($M_\odot$)	N_{H_2} (cm^{-2})	L/M ($L_\odot/M_\odot$)
G259.270–00.330	$(24.7\pm2.0)\times10^{-2}$	$(9.0\pm2.4)\times10^{-1}$	$(6.5\pm1.3)\times10^{20}$	$(27.4\pm7.7)\times10^{-2}$
G259.272–01.238	$(32.7\pm3.0)\times10^{+0}$	$(37.4\pm9.7)\times10^{+0}$	$(356.9\pm9.4)\times10^{19}$	$(8.7\pm2.4)\times10^{-1}$
G259.292–01.955	$(8.5\pm1.5)\times10^{+2}$	$(8.3\pm2.2)\times10^{+1}$	$(8.1\pm1.9)\times10^{21}$	$(10.3\pm3.3)\times10^{+0}$
G259.302–01.220	$(22.7\pm1.6)\times10^{+0}$	$(18.1\pm4.6)\times10^{+0}$	$(51.1\pm2.7)\times10^{20}$	$(12.6\pm3.3)\times10^{-1}$
G259.320–01.740	$(267.2\pm8.0)\times10^{-2}$	$(36.1\pm9.3)\times10^{-1}$	$(21.3\pm1.2)\times10^{20}$	$(7.4\pm1.9)\times10^{-1}$
G259.320–01.780	$(448.6\pm5.3)\times10^{-3}$	$(28.9\pm7.6)\times10^{-1}$	$(29.5\pm7.2)\times10^{20}$	$(15.5\pm4.1)\times10^{-2}$
G259.340–01.444	$(235.3\pm5.5)\times10^{-1}$	$(5.7\pm1.5)\times10^{+0}$	$(7.7\pm1.8)\times10^{21}$	$(4.1\pm1.1)\times10^{+0}$
G259.330–01.780	$(205.7\pm3.1)\times10^{-1}$	$(28.9\pm7.4)\times10^{-1}$	$(35.2\pm7.7)\times10^{20}$	$(7.1\pm1.8)\times10^{+0}$
G259.340–00.450	$(71.8\pm2.2)\times10^{-1}$	$(4.3\pm1.0)\times10^{+0}$	$(68.8\pm3.5)\times10^{19}$	$(16.6\pm4.0)\times10^{-1}$
G259.338–01.445	$(235.3\pm5.5)\times10^{-1}$	$(5.7\pm1.5)\times10^{+0}$	$(7.7\pm1.8)\times10^{21}$	$(4.1\pm1.1)\times10^{+0}$
G259.360–01.740	$(13.1\pm1.5)\times10^{-1}$	$(24.2\pm6.9)\times10^{-2}$	$(15.8\pm2.5)\times10^{19}$	$(5.4\pm1.7)\times10^{+0}$
G259.368–01.192	$(66.4\pm2.2)\times10^{+0}$	$(16.0\pm3.3)\times10^{+1}$	$(32.8\pm1.7)\times10^{20}$	$(41.5\pm8.7)\times10^{-2}$
G259.383–01.083	$(12.1\pm1.2)\times10^{+1}$	$(8.0\pm1.8)\times10^{+1}$	$(38.0\pm3.9)\times10^{20}$	$(15.2\pm3.8)\times10^{-1}$
G259.390–00.180	$(30.0\pm1.7)\times10^{-1}$	$(26.5\pm6.6)\times10^{-1}$	$(88.6\pm9.3)\times10^{19}$	$(11.3\pm2.9)\times10^{-1}$
G259.390–01.710	$(836.1\pm3.8)\times10^{-3}$	$(19.5\pm5.0)\times10^{-1}$	$(87.4\pm6.1)\times10^{19}$	$(4.3\pm1.1)\times10^{-1}$
G259.400–01.075	$(96.8\pm2.9)\times10^{+1}$	$(6.7\pm1.4)\times10^{+2}$	$(59.2\pm1.3)\times10^{20}$	$(14.5\pm3.0)\times10^{-1}$
G259.405–01.162	$(8.0\pm1.4)\times10^{+1}$	$(6.4\pm1.7)\times10^{+1}$	$(20.3\pm1.9)\times10^{20}$	$(12.5\pm4.0)\times10^{-1}$
G259.410–01.488	$(223.0\pm8.4)\times10^{-1}$	$(5.8\pm1.4)\times10^{+1}$	$(509.7\pm5.6)\times10^{19}$	$(38.5\pm9.5)\times10^{-2}$
G259.409–01.302	$(30.4\pm1.7)\times10^{-1}$	$(4.1\pm1.0)\times10^{+0}$	$(128.7\pm9.9)\times10^{19}$	$(7.3\pm1.9)\times10^{-1}$
G259.410–01.710	$(196.2\pm7.1)\times10^{-2}$	$(5.2\pm1.3)\times10^{+0}$	$(21.0\pm1.6)\times10^{20}$	$(38.0\pm9.9)\times10^{-2}$
G259.417–01.065	$(1281.4\pm5.0)\times10^{-1}$	$(6.5\pm1.3)\times10^{+1}$	$(37.2\pm4.4)\times10^{20}$	$(19.6\pm4.0)\times10^{-1}$
G259.440–01.080	$(10.6\pm1.7)\times10^{+2}$	$(6.7\pm1.7)\times10^{+2}$	$(650.0\pm8.0)\times10^{19}$	$(15.8\pm4.8)\times10^{-1}$
G259.450–00.330	$(351.8\pm2.9)\times10^{-2}$	$(17.6\pm4.7)\times10^{-2}$	$(10.8\pm1.1)\times10^{19}$	$(20.0\pm5.4)\times10^{+0}$
G259.463–01.065	$(42.0\pm1.3)\times10^{+1}$	$(44.5\pm9.2)\times10^{+1}$	$(350.4\pm4.3)\times10^{19}$	$(9.4\pm2.0)\times10^{-1}$
G259.457–01.110	$(214.5\pm2.6)\times10^{+0}$	$(29.7\pm6.1)\times10^{+1}$	$(319.9\pm5.3)\times10^{19}$	$(7.2\pm1.5)\times10^{-1}$
G259.560–00.930	$(61.7\pm2.8)\times10^{+2}$	$(11.9\pm2.5)\times10^{+1}$	$(10.2\pm1.7)\times10^{21}$	$(5.2\pm1.1)\times10^{+1}$
G259.570–01.020	$(21.7\pm2.5)\times10^{+1}$	$(16.8\pm4.0)\times10^{+1}$	$(10.6\pm1.3)\times10^{21}$	$(12.9\pm3.4)\times10^{-1}$
G259.570–01.430	$(36.1\pm4.0)\times10^{+0}$	$(6.8\pm1.8)\times10^{+0}$	$(5.3\pm1.3)\times10^{21}$	$(5.3\pm1.5)\times10^{+0}$
G259.610–01.300	$(50.1\pm2.3)\times10^{+1}$	$(13.6\pm2.9)\times10^{+1}$	$(9.7\pm1.9)\times10^{21}$	$(36.8\pm7.9)\times10^{-1}$
G259.640–01.320	$(168.0\pm9.8)\times10^{+1}$	$(7.9\pm1.7)\times10^{+1}$	$(46.9\pm4.1)\times10^{20}$	$(21.4\pm4.7)\times10^{+0}$
G259.652–01.313	$(9.4\pm2.1)\times10^{+2}$	$(4.7\pm1.4)\times10^{+1}$	$(3.9\pm1.4)\times10^{21}$	$(20.2\pm7.7)\times10^{+0}$
G259.668–01.318	$(33.8\pm9.3)\times10^{+2}$	$(18.8\pm6.4)\times10^{+1}$	$(19.1\pm7.6)\times10^{21}$	$(18.0\pm7.9)\times10^{+0}$
G259.700–01.280	$(20.6\pm2.7)\times10^{+2}$	$(4.8\pm1.2)\times10^{+2}$	$(103.4\pm1.2)\times10^{20}$	$(4.3\pm1.2)\times10^{+0}$
G259.711–01.934	$(28.5\pm3.1)\times10^{+0}$	$(5.7\pm1.6)\times10^{+0}$	$(109.9\pm4.3)\times10^{19}$	$(5.0\pm1.5)\times10^{+0}$
G259.750–01.340	$(640.4\pm3.6)\times10^{+0}$	$(45.0\pm9.3)\times10^{+0}$	$(24.3\pm2.8)\times10^{20}$	$(14.2\pm2.9)\times10^{+0}$
G259.860–02.030	$(31.9\pm2.5)\times10^{-2}$	$(34.0\pm8.6)\times10^{-2}$	$(19.6\pm5.1)\times10^{19}$	$(9.4\pm2.5)\times10^{-1}$
G259.870–02.400	$(298.5\pm4.7)\times10^{-1}$	$(8.1\pm2.0)\times10^{+1}$	$(247.4\pm7.8)\times10^{20}$	$(36.8\pm9.2)\times10^{-2}$
G259.880–02.020	$(92.8\pm6.3)\times10^{-2}$	$(27.4\pm7.2)\times10^{-2}$	$(17.0\pm3.5)\times10^{19}$	$(33.9\pm9.2)\times10^{-1}$
G259.880–02.410	$(78.4\pm1.8)\times10^{-1}$	$(19.4\pm4.9)\times10^{+0}$	$(9.3\pm1.1)\times10^{21}$	$(4.0\pm1.0)\times10^{-1}$
G259.890–02.420	$(124.6\pm2.1)\times10^{-1}$	$(20.5\pm5.1)\times10^{+0}$	$(10.4\pm1.1)\times10^{21}$	$(6.1\pm1.5)\times10^{-1}$
G259.900–01.970	$(53.9\pm8.9)\times10^{-2}$	$(13.9\pm4.5)\times10^{-2}$	$(13.6\pm4.5)\times10^{19}$	$(3.9\pm1.4)\times10^{+0}$
G259.900–02.430	$(742.7\pm9.5)\times10^{-2}$	$(11.1\pm2.8)\times10^{+0}$	$(9.7\pm2.3)\times10^{21}$	$(6.7\pm1.7)\times10^{-1}$
G259.950–01.330	$(145.9\pm5.7)\times10^{-1}$	$(44.3\pm9.7)\times10^{-1}$	$(35.3\pm8.9)\times10^{19}$	$(32.9\pm7.4)\times10^{-1}$
G260.000–00.160	$(12.8\pm1.0)\times10^{+1}$	$(4.2\pm1.2)\times10^{+1}$	$(596.0\pm6.3)\times10^{19}$	$(30.1\pm8.7)\times10^{-1}$
G225.472–01.674	$(46.9\pm2.8)\times10^{-2}$	$(21.6\pm6.5)\times10^{-2}$	$(45.5\pm9.0)\times10^{19}$	$(21.8\pm6.6)\times10^{-1}$
G226.125–00.316	$(111.2\pm5.1)\times10^{-3}$	$(6.8\pm2.3)\times10^{-1}$	$(28.9\pm7.3)\times10^{20}$	$(16.4\pm5.7)\times10^{-2}$
G232.062–00.126	$(199.0\pm7.2)\times10^{-2}$	$(34.9\pm9.4)\times10^{-1}$	$(68.7\pm1.9)\times10^{19}$	$(5.7\pm1.6)\times10^{-1}$
G231.841–01.752	$(9.4\pm1.4)\times10^{+0}$	$(9.0\pm2.4)\times10^{+0}$	$(88.4\pm9.7)\times10^{19}$	$(10.4\pm3.2)\times10^{-1}$
G232.894–00.613	$(105.9\pm5.2)\times10^{-1}$	$(5.6\pm1.2)\times10^{+1}$	$(208.9\pm8.8)\times10^{19}$	$(19.0\pm4.3)\times10^{-2}$

Table A.5: continued

Name	L ($L_\odot$)	M ($M_\odot$)	N_{H_2} (cm^{-2})	L/M ($L_\odot/M_\odot$)
G233.067–01.271	$(127.8 \pm 2.0) \times 10^{-1}$	$(19.0 \pm 4.1) \times 10^{+0}$	$(48.9 \pm 1.0) \times 10^{19}$	$(6.7 \pm 1.4) \times 10^{-1}$
G233.840–00.183	$(12.3 \pm 2.8) \times 10^{+3}$	$(8.3 \pm 2.6) \times 10^{+1}$	$(22.0 \pm 6.3) \times 10^{21}$	$(14.8 \pm 5.7) \times 10^{+1}$
G233.757–01.269	$(130.9 \pm 1.6) \times 10^{-1}$	$(6.6 \pm 1.3) \times 10^{+1}$	$(17.8 \pm 1.3) \times 10^{20}$	$(19.9 \pm 4.1) \times 10^{-2}$
G234.476–00.003	$(12.3 \pm 1.5) \times 10^{+1}$	$(34.4 \pm 9.0) \times 10^{+0}$	$(241.3 \pm 4.3) \times 10^{19}$	$(3.6 \pm 1.0) \times 10^{+0}$
G242.625–00.878	$(25.2 \pm 1.1) \times 10^{+0}$	$(9.7 \pm 2.0) \times 10^{+1}$	$(205.4 \pm 4.1) \times 10^{19}$	$(26.0 \pm 5.6) \times 10^{-2}$
G247.796–00.823	$(52.3 \pm 6.2) \times 10^{-2}$	$(17.2 \pm 4.8) \times 10^{-1}$	$(131.9 \pm 4.7) \times 10^{19}$	$(30.4 \pm 9.2) \times 10^{-2}$
G252.029–01.864	$(56.2 \pm 7.3) \times 10^{-1}$	$(16.7 \pm 4.2) \times 10^{-1}$	$(25.7 \pm 5.0) \times 10^{19}$	$(33.6 \pm 9.4) \times 10^{-1}$
G252.173–01.872	$(105.4 \pm 5.4) \times 10^{-1}$	$(33.1 \pm 7.1) \times 10^{+0}$	$(13.9 \pm 2.2) \times 10^{20}$	$(31.9 \pm 7.0) \times 10^{-2}$
G253.950–00.563	$(326.4 \pm 3.2) \times 10^{+0}$	$(14.8 \pm 3.2) \times 10^{+1}$	$(245.8 \pm 2.4) \times 10^{19}$	$(22.0 \pm 4.7) \times 10^{-1}$
G256.422–02.208	$(27.3 \pm 3.2) \times 10^{-1}$	$(3.4 \pm 1.0) \times 10^{+0}$	$(76.3 \pm 2.1) \times 10^{19}$	$(8.0 \pm 2.6) \times 10^{-1}$
G257.870–01.498	$(69.2 \pm 2.8) \times 10^{-2}$	$(25.4 \pm 7.8) \times 10^{-2}$	$(36.9 \pm 5.5) \times 10^{19}$	$(27.3 \pm 8.5) \times 10^{-1}$
G257.894–01.885	$(7.9 \pm 1.3) \times 10^{-1}$	$(3.5 \pm 1.2) \times 10^{-1}$	$(54.3 \pm 8.2) \times 10^{19}$	$(22.4 \pm 8.5) \times 10^{-1}$
G258.090–01.577	$(185.0 \pm 7.0) \times 10^{-3}$	$(19.2 \pm 5.4) \times 10^{-1}$	$(14.3 \pm 1.5) \times 10^{20}$	$(9.6 \pm 2.7) \times 10^{-2}$
G258.114–01.904	$(487.3 \pm 1.9) \times 10^{-3}$	$(5.9 \pm 1.6) \times 10^{-1}$	$(7.3 \pm 1.4) \times 10^{20}$	$(8.3 \pm 2.2) \times 10^{-1}$
G258.347–02.182	$(66.9 \pm 5.5) \times 10^{-2}$	$(11.2 \pm 3.5) \times 10^{-1}$	$(20.9 \pm 2.2) \times 10^{20}$	$(6.0 \pm 2.0) \times 10^{-1}$
G258.681–01.774	$(75.9 \pm 1.3) \times 10^{-2}$	$(12.9 \pm 3.2) \times 10^{-1}$	$(10.0 \pm 2.2) \times 10^{20}$	$(5.9 \pm 1.5) \times 10^{-1}$
G258.691–01.773	$(10.5 \pm 1.2) \times 10^{+0}$	$(4.7 \pm 1.2) \times 10^{+0}$	$(7.2 \pm 2.0) \times 10^{20}$	$(22.3 \pm 6.2) \times 10^{-1}$
G259.408–00.860	$(72.1 \pm 3.0) \times 10^{-1}$	$(18.7 \pm 4.1) \times 10^{-1}$	$(20.7 \pm 2.7) \times 10^{19}$	$(38.5 \pm 8.7) \times 10^{-1}$
G259.446–00.838	$(78.8 \pm 2.8) \times 10^{-1}$	$(11.6 \pm 2.5) \times 10^{+0}$	$(8.7 \pm 1.4) \times 10^{20}$	$(6.8 \pm 1.5) \times 10^{-1}$
G259.643–00.659	$(11.5 \pm 1.1) \times 10^{-1}$	$(5.7 \pm 1.6) \times 10^{-1}$	$(35.8 \pm 3.3) \times 10^{19}$	$(20.4 \pm 6.1) \times 10^{-1}$
G259.480–01.135	$(327.7 \pm 4.5) \times 10^{-1}$	$(46.6 \pm 9.6) \times 10^{+0}$	$(18.5 \pm 1.3) \times 10^{20}$	$(7.0 \pm 1.4) \times 10^{-1}$
G259.691–00.614	$(324.1 \pm 5.0) \times 10^{-2}$	$(29.0 \pm 7.8) \times 10^{-2}$	$(24.8 \pm 1.2) \times 10^{19}$	$(11.2 \pm 3.0) \times 10^{+0}$
G259.545–00.807	$(225.2 \pm 3.5) \times 10^{-2}$	$(36.7 \pm 9.4) \times 10^{-1}$	$(94.4 \pm 4.8) \times 10^{19}$	$(6.1 \pm 1.6) \times 10^{-1}$
G259.847–00.465	$(28.2 \pm 2.4) \times 10^{-1}$	$(8.1 \pm 2.3) \times 10^{-1}$	$(46.6 \pm 2.6) \times 10^{19}$	$(3.5 \pm 1.0) \times 10^{+0}$
G259.908–01.942	$(35.4 \pm 1.2) \times 10^{-1}$	$(5.9 \pm 1.4) \times 10^{-1}$	$(31.4 \pm 1.5) \times 10^{19}$	$(6.0 \pm 1.4) \times 10^{+0}$

Bibliography

Aguirre, J. E., Ginsburg, A. G., Dunham, M. K., et al. 2011, ApJS, 192, 4 (Cited on page 30.)

Anderson, L. D., Bania, T. M., Balser, D. S., et al. 2014, ApJS, 212, 1 (Cited on pages 116 and 131.)

Bacmann, A., Lefloch, B., Ceccarelli, C., et al. 2002, A&A, 389, L6 (Cited on page 54.)

Bartschi, B. Y., Morse, D. E., & Woolston, T. L. 1996, Johns Hopkins APL Technical Digest, 17, 215 (Cited on page 12.)

Benjamin et al., R. A. & et al. 2003, PASP, 115, 953 (Cited on page 30.)

Bernard, J.-P., Paradis, D., Marshall, D. J., et al. 2010, A&A, 518, L88 (Cited on page 42.)

Bertin, E. & Arnouts, S. 1996, A&AS, 117, 393 (Cited on pages 76 and 96.)

Bertoldi, F. & McKee, C. F. 1992, ApJ, 395, 140 (Cited on pages 48 and 49.)

Beuther, H., Henning, T., Linz, H., et al. 2010, A&A, 518, L78 (Cited on pages 20 and 40.)

Bloemen, J. B. G. M., Bennett, K., Bignami, G. F., et al. 1984, A&A, 135, 12 (Cited on page 73.)

Bolatto, A. D., Wolfire, M., & Leroy, A. K. 2013, ARA&A, 51, 207 (Cited on pages 9 and 10.)

Bonnell, I. A., Clarke, C. J., Bate, M. R., & Pringle, J. E. 2001, MNRAS, 324, 573 (Cited on page 7.)

Bonnor, W. B. 1955, MNRAS, 115, 310 (Cited on page 49.)

Boomsma, R., Oosterloo, T. A., Fraternali, F., van der Hulst, J. M., & Sancisi, R. 2008, A&A, 490, 555 (Cited on page 93.)

Brand, J. & Blitz, L. 1993, A&A, 275, 67 (Cited on pages 23, 83, 86 and 96.)

Brand, J. & Wouterloot, J. G. A. 1995, A&A, 303, 851 (Cited on page 101.)

Breen, S. L., Fuller, G. A., Caswell, J. L., et al. 2015, MNRAS, 450, 4109 (Cited on page 55.)

Brunthaler, A., Reid, M. J., Menten, K. M., et al. 2009, ApJ, 693, 424 (Cited on page 43.)

Busfield, A. L., Purcell, C. R., Hoare, M. G., et al. 2006, MNRAS, 366, 1096 (Cited on page 43.)

Carey, S. J., Noriega-Crespo, A., Mizuno, D. R., et al. 2009, PASP, 121, 76 (Cited on pages 30 and 32.)

Caselli, P., Walmsley, C. M., Terzieva, R., & Herbst, E. 1998, ApJ, 499, 234 (Cited on page 54.)

Caswell, J. L., Murray, J. D., Roger, R. S., Cole, D. J., & Cooke, D. J. 1975, A&A, 45, 239 (Cited on page 43.)

Churchwell, E., Babler, B. L., Meade, M. R., et al. 2009, PASP, 121, 213 (Cited on page 35.)

Colombo, D., Hughes, A., Schinnerer, E., et al. 2014, ApJ, 784, 3 (Cited on page 95.)

Colombo, D., Rosolowsky, E., Ginsburg, A., Duarte-Cabral, A., & Hughes, A. 2015, MNRAS, 454, 2067 (Cited on page 132.)

Compiégne, M. 2010, in Astronomical Society of the Pacific Conference Series, Vol. 438, The Dynamic Interstellar Medium: A Celebration of the Canadian Galactic Plane Survey, ed. R. Kothes, T. L. Landecker, & A. G. Willis, 55 (Cited on page 21.)

Compiègne, M., Flagey, N., Noriega-Crespo, A., et al. 2010, ApJ, 724, L44 (Cited on page 21.)

Contreras, Y., Schuller, F., Urquhart, J. S., et al. 2013, A&A, 549, A45 (Cited on pages 11, 30, 35, 59, 64 and 76.)

Crutcher, R. M. 2012, ARA&A, 50, 29 (Cited on pages 50 and 51.)

Csengeri, T., Leurini, S., Wyrowski, F., et al. 2016, A&A, 586, A149 (Cited on pages 31, 32 and 56.)

Csengeri, T., Urquhart, J. S., Schuller, F., et al. 2014, A&A, 565, A75 (Cited on pages 11, 30, 38, 49, 52, 53, 114, 124 and 131.)

Dame, T. M., Hartmann, D., & Thaddeus, P. 2001, ApJ, 547, 792 (Cited on pages 13, 82, 83, 84, 88, 90, 91, 92, 96 and 134.)

Davies, B., Clark, J. S., Trombley, C., et al. 2012, MNRAS, 419, 1871 (Cited on page 43.)

de Villiers, H. M., Chrysostomou, A., Thompson, M. A., et al. 2014, MNRAS, 444, 566 (Cited on page 56.)

de Villiers, H. M., Chrysostomou, A., Thompson, M. A., et al. 2015, MNRAS, 449, 119 (Cited on page 56.)

de Wit, W. J., Testi, L., Palla, F., Vanzi, L., & Zinnecker, H. 2004, A&A, 425, 937 (Cited on page 29.)

Dent, W. R. F., Matthews, H. E., & Ward-Thompson, D. 1998, MNRAS, 301, 1049 (Cited on page 9.)

Diplas, A. & Savage, B. D. 1991, ApJ, 377, 126 (Cited on page 4.)

Dobbs, C. & Baba, J. 2014, PASA, 31, e035 (Cited on pages 5 and 88.)

Draine, B. T. 2003, ARA&A, 41, 241 (Cited on page 9.)

Eden, D. J., Moore, T. J. T., Morgan, L. K., Thompson, M. A., & Urquhart, J. S. 2013, MNRAS, 431, 1587 (Cited on page 123.)

Eden, D. J., Moore, T. J. T., Urquhart, J. S., et al. 2015, MNRAS, 452, 289 (Cited on pages 113 and 123.)

Egan, M. P., Price, S. D., Kraemer, K. E., et al. 2003, VizieR Online Data Catalog, 5114, 0 (Cited on pages 31, 32 and 37.)

Elia, D., Molinari, S., Fukui, Y., et al. 2013, ApJ, 772, 45 (Cited on pages 34, 102 and 123.)

Elia, D. & Pezzuto, S. 2016, MNRAS, 461, 1328 (Cited on pages 42 and 54.)

Elia, D., Schisano, E., Molinari, S., et al. 2010, A&A, 518, L97 (Cited on page 40.)

Ester, M., Kriegel, H.-P., Sander, J., & Xu, X. 1996 (AAAI Press), 226–231 (Cited on page 95.)

Feng, S., Beuther, H., Zhang, Q., et al. 2016, ApJ, 828, 100 (Cited on page 54.)

Ferrière, K. M. 2001, Reviews of Modern Physics, 73, 1031 (Cited on page 10.)

Gallaway, M., Thompson, M. A., Lucas, P. W., et al. 2013, MNRAS, 430, 808 (Cited on page 56.)

Galyardt, J. & Shelton, R. L. 2016, ApJ, 816, L18 (Cited on page 93.)

Gerhard, O. 2011, Memorie della Societa Astronomica Italiana Supplementi, 18, 185 (Cited on page 5.)

Giannetti, A., Leurini, S., König, C., et al. 2017a, A&A, 606, L12 (Cited on pages 9, 10, 73, 100 and 102.)

Giannetti, A., Leurini, S., Wyrowski, F., et al. 2017b, A&A, 603, A33 (Cited on pages 31, 55, 57, 107 and 132.)

Giannetti, A., Wyrowski, F., Brand, J., et al. 2014, A&A, 570, A65 (Cited on pages 30, 31, 32, 34, 35, 43, 48, 49, 54 and 132.)

Giannetti, A., Wyrowski, F., Leurini, S., et al. 2015, A&A, 580, L7 (Cited on pages 35 and 43.)

Green, J. A., Caswell, J. L., Fuller, G. A., et al. 2012, MNRAS, 420, 3108 (Cited on pages 84 and 116.)

Green, J. A. & McClure-Griffiths, N. M. 2011, MNRAS, 417, 2500 (Cited on page 43.)

Griffin, M. J., Abergel, A., Abreu, A., et al. 2010, A&A, 518, L3 (Cited on pages 12, 37 and 99.)

Güsten, R., Nyman, L. Å., Schilke, P., et al. 2006, A&A, 454, L13 (Cited on pages 11, 23, 30 and 133.)

Gutermuth, R. A. & Heyer, M. 2015, AJ, 149, 64 (Cited on page 32.)

Guzmán, A. E., Sanhueza, P., Contreras, Y., et al. 2015, ApJ, 815, 130 (Cited on pages 21, 66 and 67.)

Heiles, C. 1979, ApJ, 229, 533 (Cited on pages 93 and 97.)

Herbst, E. & van Dishoeck, E. F. 2009, ARA&A, 47, 427 (Cited on page 11.)

Heyer, M. & Dame, T. M. 2015, ARA&A, 53, 583 (Cited on pages 5, 73, 111, 112, 113, 115, 116, 117, 131 and 246.)

Heyer, M., Gutermuth, R., Urquhart, J. S., et al. 2016, A&A, 588, A29 (Cited on page 32.)

Hildebrand, R. H. 1983, QJRAS, 24, 267 (Cited on page 47.)

Hoare, M. G., Purcell, C. R., Churchwell, E. B., et al. 2012, PASP, 124, 939 (Cited on pages 30 and 32.)

Immer, K., Reid, M. J., Menten, K. M., Brunthaler, A., & Dame, T. M. 2013, A&A, 553, A117 (Cited on page 43.)

Immer, K., Schuller, F., Omont, A., & Menten, K. M. 2012, A&A, 537, A121 (Cited on page 43.)

Izumi, N., Kobayashi, N., Yasui, C., et al. 2014, ApJ, 795, 66 (Cited on page 121.)

Jackson, J. M., Rathborne, J. M., Foster, J. B., et al. 2013, PASA, 30, 57 (Cited on page 66.)

Jackson, J. M., Rathborne, J. M., Shah, R. Y., et al. 2006, ApJS, 163, 145 (Cited on page 134.)

Kauffmann, J., Bertoldi, F., Bourke, T. L., Evans, II, N. J., & Lee, C. W. 2008, A&A, 487, 993 (Cited on page 48.)

Kauffmann, J., Pillai, T., & Goldsmith, P. F. 2013, ApJ, 779, 185 (Cited on pages 49, 50 and 51.)

Kauffmann, J., Pillai, T., Shetty, R., Myers, P. C., & Goodman, A. A. 2010a, ApJ, 712, 1137 (Cited on pages 48 and 49.)

Kauffmann, J., Pillai, T., Shetty, R., Myers, P. C., & Goodman, A. A. 2010b, ApJ, 716, 433 (Cited on pages 115, 124 and 131.)

Kennicutt, R. C. 2005, in IAU Symposium, Vol. 227, Massive Star Birth: A Crossroads of Astrophysics, ed. R. Cesaroni, M. Felli, E. Churchwell, & M. Walmsley, 3–11 (Cited on pages 5, 7 and 29.)

Kim, B. G., Kawamura, A., Yonekura, Y., & Fukui, Y. 2004, PASJ, 56, 313 (Cited on page 102.)

Klein, B., Hochgürtel, S., Krämer, I., et al. 2012, A&A, 542, L3 (Cited on page 24.)

Kobayashi, N., Yasui, C., Tokunaga, A. T., & Saito, M. 2008, ApJ, 683, 178 (Cited on page 4.)

König, C., Urquhart, J. S., Csengeri, T., et al. 2017, A&A, 599, A139 (Cited on pages 3, 20, 29, 64, 68, 99, 100, 106, 107, 124, 129, 130 and 132.)

Koo, J.-R., Lee, J. W., & Hong, K. 2017, AJ, 154, 235 (Cited on page 88.)

Kroupa, P. 2001, MNRAS, 322, 231 (Cited on page 6.)

Kurayama, T., Nakagawa, A., Sawada-Satoh, S., et al. 2011, PASJ, 63, 513 (Cited on page 43.)

Larson, R. B. 1981, MNRAS, 194, 809 (Cited on page 103.)

Lucas, P. W., Hoare, M. G., Longmore, A., et al. 2008, MNRAS, 391, 136 (Cited on page 30.)

Lumsden, S. L., Hoare, M. G., Urquhart, J. S., et al. 2013, ApJS, 208, 11 (Cited on page 116.)

Mainzer, A., Bauer, J., Grav, T., et al. 2011, ApJ, 731, 53 (Cited on page 13.)

McClure-Griffiths, N. M., Dickey, J. M., Gaensler, B. M., & Green, A. J. 2004, ApJ, 607, L127 (Cited on pages 90, 91, 92 and 96.)

McClure-Griffiths, N. M., Dickey, J. M., Gaensler, B. M., Green, A. J., & Haverkorn, M. 2006, ApJ, 652, 1339 (Cited on pages 85, 93, 94, 97 and 121.)

McClure-Griffiths, N. M., Pisano, D. J., Calabretta, M. R., et al. 2009, ApJS, 181, 398 (Cited on pages 13, 87 and 88.)

McKee, C. F. & Tan, J. C. 2003, ApJ, 585, 850 (Cited on page 7.)

Melia, F. & Falcke, H. 2001, ARA&A, 39, 309 (Cited on page 4.)

Mills, E. A. C. 2017, ArXiv e-prints [arXiv:1705.05332] (Cited on page 5.)

Miville-Deschênes, M.-A., Murray, N., & Lee, E. J. 2017, ApJ, 834, 57 (Cited on page 95.)

Moisés, A. P., Damineli, A., Figuerêdo, E., et al. 2011, MNRAS, 411, 705 (Cited on page 43.)

Molinari, S., Pezzuto, S., Cesaroni, R., et al. 2008, A&A, 481, 345 (Cited on pages 3, 52, 113, 114 and 118.)

Molinari, S., Schisano, E., Elia, D., et al. 2016, A&A, 591, A149 (Cited on pages 46, 64 and 76.)

Molinari, S., Schisano, E., Faustini, F., et al. 2017, CUTEX: CUrvature Thresholding EXtractor, Astrophysics Source Code Library (Cited on page 64.)

Molinari, S., Swinyard, B., Bally, J., et al. 2010, PASP, 122, 314 (Cited on pages 12, 30, 31, 37, 76 and 99.)

Moore, T. J. T., Urquhart, J. S., Morgan, L. K., & Thompson, M. A. 2012, MNRAS, 426, 701 (Cited on page 123.)

Motte, F., Bontemps, S., & Louvet, F. 2017, ArXiv e-prints [arXiv:1706.00118] (Cited on page 7.)

Motte, F., Zavagno, A., Bontemps, S., et al. 2010, A&A, 518, L77 (Cited on pages 34 and 40.)

Mottram, J. C., Hoare, M. G., Davies, B., et al. 2011a, ApJ, 730, L33 (Cited on pages 52, 53, 114 and 124.)

Mottram, J. C., Hoare, M. G., Urquhart, J. S., et al. 2011b, A&A, 525, A149 (Cited on pages 40 and 130.)

Nguyen Luong, Q., Motte, F., Hennemann, M., et al. 2011, A&A, 535, A76 (Cited on page 40.)

Ossenkopf, V. & Henning, T. 1994, A&A, 291, 943 (Cited on pages 9, 20, 40 and 47.)

Park, G., Koo, B.-C., Kang, J.-h., et al. 2016, ApJ, 827, L27 (Cited on page 93.)

Pilbratt, G. L., Riedinger, J. R., Passvogel, T., et al. 2010, A&A, 518, L1 (Cited on page 37.)

Pillai, T. 2016, in EAS Publications Series, Vol. 75, EAS Publications Series, 245–250 (Cited on page 54.)

Pineda, J. L., Langer, W. D., Velusamy, T., & Goldsmith, P. F. 2013, A&A, 554, A103 (Cited on pages 132 and 133.)

Planck Collaboration, Ade, P. A. R., Aghanim, N., et al. 2015, A&A, 576, A104 (Cited on page 93.)

Poglitsch, A., Waelkens, C., Geis, N., et al. 2010, A&A, 518, L2 (Cited on pages 12, 37 and 99.)

Price, S. D., Egan, M. P., Carey, S. J., Mizuno, D. R., & Kuchar, T. A. 2001, AJ, 121, 2819 (Cited on pages 12, 30, 32 and 99.)

Price, S. D., Egan, M. P., & Shipman, R. F. 1999, in Astronomical Society of the Pacific Conference Series, Vol. 177, Astrophysics with Infrared Surveys: A Prelude to SIRTF, ed. M. D. Bicay, R. M. Cutri, & B. F. Madore, 394 (Cited on page 12.)

Purcell, C. R., Hoare, M. G., Cotton, W. D., et al. 2013, ApJS, 205, 1 (Cited on pages 30 and 32.)

Ragan, S. E., Moore, T. J. T., Eden, D. J., et al. 2018, MNRAS, 479, 2361 (Cited on page 123.)

Razali, Nornadiah; Wah, Y. B. 2011, Journal of Statistical Modeling and Analytics, 2, 21 (Cited on page 35.)

Reid, M. J., Dame, T. M., Menten, K. M., & Brunthaler, A. 2016, ApJ, 823, 77 (Cited on page 88.)

Reid, M. J. & Honma, M. 2014, ARA&A, 52, 339 (Cited on page 21.)

Reid, M. J., Menten, K. M., Brunthaler, A., et al. 2014, ApJ, 783, 130 (Cited on pages 5, 23, 34, 60, 83, 85, 87, 88, 89, 121 and 122.)

Risacher, C., Güsten, R., Stutzki, J., et al. 2016, A&A, 595, A34 (Cited on page 133.)

Robitaille, T. P., Whitney, B. A., Indebetouw, R., & Wood, K. 2007, ApJS, 169, 328 (Cited on pages 42 and 46.)

Roman-Duval, J., Jackson, J. M., Heyer, M., et al. 2009, ApJ, 699, 1153 (Cited on page 43.)

Roman-Duval, J., Jackson, J. M., Heyer, M., Rathborne, J., & Simon, R. 2010, ApJ, 723, 492 (Cited on page 123.)

Rudolph, A. L., Simpson, J. P., Haas, M. R., Erickson, E. F., & Fich, M. 1997, ApJ, 489, 94 (Cited on page 73.)

Salpeter, E. E. 1955, ApJ, 121, 161 (Cited on page 6.)

Sandstrom, K. M., Leroy, A. K., Walter, F., et al. 2013, ApJ, 777, 5 (Cited on page 101.)

Sanna, A., Reid, M. J., Menten, K. M., et al. 2014, ApJ, 781, 108 (Cited on page 43.)

Sato, M., Reid, M. J., Brunthaler, A., & Menten, K. M. 2010, ApJ, 720, 1055 (Cited on page 43.)

Sato, M., Wu, Y. W., Immer, K., et al. 2014, ApJ, 793, 72 (Cited on page 43.)

Schuller, F., Beuther, H., Bontemps, S., et al. 2010, The Messenger, 141, 20 (Cited on page 11.)

Schuller, F., Csengeri, T., Urquhart, J. S., et al. 2017, A&A, 601, A124 (Cited on pages 22 and 134.)

Schuller, F., Menten, K. M., Contreras, Y., et al. 2009, A&A, 504, 415 (Cited on pages 3, 11, 30, 47 and 59.)

Schulman, E. 1996, PASP, 108, 460 (Cited on page 93.)

Shetty, R., Kauffmann, J., Schnee, S., & Goodman, A. A. 2009a, ApJ, 696, 676 (Cited on page 20.)

Shetty, R., Kauffmann, J., Schnee, S., Goodman, A. A., & Ercolano, B. 2009b, ApJ, 696, 2234 (Cited on page 20.)

Siringo, G., Kreysa, E., Kovács, A., et al. 2009, A&A, 497, 945 (Cited on pages 11 and 30.)

Snell, R. L., Dickman, R. L., & Huang, Y.-L. 1990, ApJ, 352, 139 (Cited on page 43.)

Sridharan, T. K., Beuther, H., Schilke, P., Menten, K. M., & Wyrowski, F. 2002, ApJ, 566, 931 (Cited on page 30.)

Stephens, M. A. 1974, Journal of the American Statistical Association, 69, 730 (Cited on page 35.)

Stutzki, J. & Guesten, R. 1990, ApJ, 356, 513 (Cited on page 11.)

Tan, J. C. 2016, in IAU Symposium, Vol. 315, From Interstellar Clouds to Star-Forming Galaxies: Universal Processes?, ed. P. Jablonka, P. André, & F. van der Tak, 154–162 (Cited on page 54.)

Tan, J. C., Beltran, M. T., Caselli, P., et al. 2014, ArXiv e-prints [arXiv:1402.0919] (Cited on page 7.)

Thompson, M. A., White, G. J., Morgan, L. K., et al. 2004, A&A, 414, 1017 (Cited on page 40.)

Traficante, A., Fuller, G. A., Peretto, N., Pineda, J. E., & Molinari, S. 2015, MNRAS, 451, 3089 (Cited on page 34.)

Urban, A., Evans, II, N. J., & Doty, S. D. 2009, ApJ, 698, 1341 (Cited on page 42.)

Urquhart, J. S., Busfield, A. L., Hoare, M. G., et al. 2007, A&A, 461, 11 (Cited on page 32.)

Urquhart, J. S., Csengeri, T., Wyrowski, F., et al. 2014a, A&A, 568, A41 (Cited on pages 11, 30, 43, 59 and 64.)

Urquhart, J. S., Figura, C. C., Moore, T. J. T., et al. 2014b, MNRAS, 437, 1791 (Cited on pages 30, 46 and 245.)

Urquhart, J. S., Hoare, M. G., Lumsden, S. L., et al. 2012, MNRAS, 420, 1656 (Cited on pages 35 and 43.)

Urquhart, J. S., König, C., Giannetti, A., et al. 2018, MNRAS, 473, 1059 (Cited on pages 3, 20, 21, 23, 59, 60, 61, 62, 63, 64, 66, 67, 68, 69, 75, 83, 99, 104, 106, 107, 110, 111, 113, 114, 115, 118, 123, 124, 125, 129 and 130.)

Urquhart, J. S., Moore, T. J. T., Csengeri, T., et al. 2014c, MNRAS, 443, 1555 (Cited on pages 30, 32, 34, 48, 49, 52, 67, 68, 76 and 115.)

Urquhart, J. S., Moore, T. J. T., Menten, K. M., et al. 2015, MNRAS, 446, 3461 (Cited on pages 34 and 116.)

Urquhart, J. S., Moore, T. J. T., Schuller, F., et al. 2013a, MNRAS, 431, 1752 (Cited on pages 30 and 55.)

Urquhart, J. S., Morgan, L. K., Figura, C. C., et al. 2011, MNRAS, 418, 1689 (Cited on page 66.)

Urquhart, J. S., Morgan, L. K., & Thompson, M. A. 2009, A&A, 497, 789 (Cited on page 32.)

Urquhart, J. S., Thompson, M. A., Moore, T. J. T., et al. 2013b, MNRAS, 435, 400 (Cited on page 30.)

Vallée, J. P. 2015, MNRAS, 450, 4277 (Cited on pages 87, 88 and 89.)

van Dishoeck, E. F. 2014, Faraday Discussions, 168, 9 (Cited on page 10.)

Vassilev, V., Meledin, D., Lapkin, I., et al. 2008, A&A, 490, 1157 (Cited on page 23.)

Walsh, A. J., Breen, S. L., Britton, T., et al. 2011, in EAS Publications Series, Vol. 52, EAS Publications Series, ed. M. Röllig, R. Simon, V. Ossenkopf, & J. Stutzki, 135–138 (Cited on page 57.)

Walsh, A. J., Burton, M. G., Hyland, A. R., & Robinson, G. 1998, MNRAS, 301, 640 (Cited on page 32.)

Walsh, A. J., Hyland, A. R., Robinson, G., & Burton, M. G. 1997, MNRAS, 291, 261 (Cited on page 30.)

Walsh, A. J., Macdonald, G. H., Alvey, N. D. S., Burton, M. G., & Lee, J.-K. 2003, A&A, 410, 597 (Cited on page 30.)

Walsh, A. J., Purcell, C. R., Longmore, S. N., et al. 2014, MNRAS, 442, 2240 (Cited on page 57.)

Whitney, B. A., Robitaille, T. P., Wood, K., Denzmore, P., & Bjorkman, J. E. 2005, in Protostars and Planets V Posters, Vol. 1286, 8460 (Cited on page 46.)

Wienen, M., Wyrowski, F., Menten, K. M., et al. 2015, A&A, 579, A91 (Cited on pages 34 and 43.)

Wienen, M., Wyrowski, F., Schuller, F., et al. 2012, A&A, 544, A146 (Cited on page 66.)

Woltjer, L. 1974, in Astrophysics and Space Science Library, Vol. 45, Supernovae and Supernova Remnants, ed. C. B. Cosmovici, 323 (Cited on page 93.)

Wood, D. O. S. & Churchwell, E. 1989, ApJS, 69, 831 (Cited on page 30.)

Wright, E. L., Eisenhardt, P. R. M., Mainzer, A. K., et al. 2010, AJ, 140, 1868 (Cited on pages 13, 30, 31, 37 and 99.)

Wu, Y. W., Sato, M., Reid, M. J., et al. 2014, A&A, 566, A17 (Cited on page 43.)

Wyrowski, F., Güsten, R., Menten, K. M., et al. 2016, A&A, 585, A149 (Cited on pages 31 and 34.)

Xu, Y., Moscadelli, L., Reid, M. J., et al. 2011, ApJ, 733, 25 (Cited on page 43.)

Xu, Y., Reid, M. J., Menten, K. M., et al. 2009, ApJ, 693, 413 (Cited on page 43.)

Young, E. T., Becklin, E. E., Marcum, P. M., et al. 2012, ApJ, 749, L17 (Cited on page 133.)

Zhang, B., Moscadelli, L., Sato, M., et al. 2014, ApJ, 781, 89 (Cited on page 43.)

Zhang, B., Reid, M. J., Menten, K. M., et al. 2013, ApJ, 775, 79 (Cited on page 43.)

Zhang, B., Zheng, X. W., Reid, M. J., et al. 2009, ApJ, 693, 419 (Cited on page 43.)

Zinnecker, H. & Yorke, H. W. 2007, ARA&A, 45, 481 (Cited on page 29.)

List of Figures

List of Tables

Publications

Refereed

König, C.; Urquhart, J. S.; Csengeri, T.; Leurini, S.; Wyrowski, F.; Giannetti, A.; Wienen, M.; Pillai, T.; Kauffmann, J.; Menten, K. M.; Schuller, F.: "*ATLASGAL-selected massive clumps in the inner Galaxy. III. Dust continuum characterization of an evolutionary sample*", 2017, A&A, 599A, 139K (DOI: 10.1051/0004-6361/201526841

Refereed (co-authored)

Eden, D. J., Moore, T. J. T., Urquhart, J. S., Elia, D., Plume, R., **König, C.**, Baldeschi, A., Schisano, E., Rigby, A. J., Morgan, L. K., Thompson, M. A.: "*Extreme star formation in the Milky Way: luminosity distributions of young stellar objects in W49A and W51*", 2018, MNRAS, 477, 3369 (DOI: 10.1093/mnras/sty606)

Tang, X. D., Henkel, C., Wyrowski, F., Giannetti, A., Menten, K. M., Csengeri, T., Leurini, S., Urquhart, J. S., **König, C.**, Güsten, R., Lin, Y. X., Zheng, X. W., Esimbek, J., Zhou, J. J.: "*ATLASGAL-selected massive clumps in the inner Galaxy. VI. Kinetic temperature and spatial density measured with formaldehyde*", 2018, A&A, 611, A6 (DOI: 10.1051/0004-6361/201732168)

Urquhart, J. S., **König, C.**, Giannetti, A., Leurini, S., Moore, T. J. T., Eden, D. J., Pillai, T., Thompson, M. A., Braiding, C., Burton, M. G., Csengeri, T., Dempsey, J. T., Figura, C., Froebrich, D., Menten, K. M., Schuller, F., Smith, M. D., Wyrowski, F.: "*ATLASGAL - properties of a complete sample of Galactic clumps*", 2018, MNRAS, 473, 1059 (DOI: 10.1093/mnras/stx2258)

Giannetti, A., Leurini, S., **König, C.**, Urquhart, J. S., Pillai, T., Brand, J., Kauffmann, J., Wyrowski, F., Menten, K. M.: "*Galactocentric variation of the gas-to-dust ratio and its relation with metallicity*", 2017, A&A, 606, L12 (DOI: 10.1051/0004-6361/201731728)

Giannetti, A., Leurini, S., Wyrowski, F., Urquhart, J., Csengeri, T., Menten, K. M., **König, C.**, Güsten, R.: "*ATLASGAL-selected massive clumps in the inner Galaxy. V. Temperature structure and evolution*", 2017, A&A, 603, A33 (DOI: 10.1051/0004-6361/201630048)

Tang, X. D., Henkel, C., Menten, K. M., Zheng, X. W., Esimbek, J., Zhou, J. J., Yeh, C. C., **König, C.**, Yuan, Y., He, Y. X., Li, D. L.: "*Kinetic temperature of massive star forming molecular clumps measured with formaldehyde*", 2017, A&A, 598, A30 (DOI: 10.1051/0004-6361/201629694)

Wyrowski, F., Güsten, R., Menten, K. M., Wiesemeyer, H., Csengeri, T., Heyminck, S., Klein, B., **König, C.**, Urquhart, J. S.: "*Infall through the evolution of high-mass star-forming clumps*", 2016, A&A, 585, A149 (DOI: 10.1051/0004-6361/201526361)

Tremblay, C. D., Walsh, A. J., Longmore, S. N., Urquhart, J. S., **König, C.**: "*A Search for High-Mass Stars Forming in Isolation using CORNISH and ATLASGAL*", 2015, PASA, 32, e047 (DOI: 10.1017/pasa.2015.48)

Urquhart, J. S., Moore, T. J. T., Menten, K. M., **König, C.**, Wyrowski, F., Thompson, M. A., Csengeri, T., Leurini, S., Eden, D. J.: "*The almost ubiquitous association of 6.7-GHz methanol masers with dust*", 2015, MNRAS, 446, 3461 (DOI: 10.1093/mnras/stu2300)

Immer, K., Galván-Madrid, R., **König, C.**, Liu, H. B., Menten, K. M.: "*Diversity of chemistry and excitation conditions in the high-mass star forming complex W33*", 2014, A&A, 572, A63 (DOI: 10.1051/0004-6361/201423780)

Urquhart, J. S., Moore, T. J. T., Csengeri, T., Wyrowski, F., Schuller, F., Hoare, M. G., Lumsden, S. L., Mottram, J. C., Thompson, M. A., Menten, K. M., Walmsley, C. M., Bronfman, L., Pfalzner, S., **König, C.**, Wienen, M.: "*ATLASGAL - towards a complete sample of massive star forming clumps*", 2014, MNRAS, 443, 1555 (DOI: 10.1093/mnras/stu1207)

Urquhart, J. S., Moore, T. J. T., Schuller, F., Wyrowski, F., Menten, K. M., Thompson, M. A., Csengeri, T., Walmsley, C. M., Bronfman, L., **König, C.**: "*ATLASGAL - environments of 6.7 GHz methanol masers*", 2013, MNRAS, 431, 1752 (DOI: 10.1093/mnras/stt287)

Muders, D., Hafok, H., Wyrowski, F., Polehampton, E., Belloche, A., **König, C.**, Schaaf, R., Schuller, F., Hatchell, J., van der Tak, F.: "*APECS - the Atacama pathfinder experiment control system*", 2006, A&A, 454, L25 (DOI: 10.1051/0004-6361:20065359)

Proceedings

Wyrowski, F., Güsten, R., Menten, K. M., Wiesemeyer, H., Csengeri, T., **König, C.**, Urquhart, J. S.: "*SOFIA follow-ups of massive clumps from the ATLASGAL galactic plane survey*", 2015, EAS, 75, 281 (DOI: 10.1051/eas/1575056)

Leurini, S., Pillai, T., Jones, P., Csengeri, T., **König, C.**, Stanke, T., Wyrowski, F., Menten, K. M., Caselli, P., Cunningham, M., Testi, L.: "*G351.77-0.51: ridge formation caught in the act*", 2015, EAS, 75, 265 (DOI: 10.1051/eas/1575052)

Muders, D., Hafok, H., Wyrowski, F., Polehampton, E., Belloche, A., **König, C.**, Schaaf, R.: "*APECS - The Atacama Pathfinder Experiment Control System*", 2006, ASPC, 351, 200

Submitted / In Preparation

Leurini, S.; Schisano, E.; Pillai, T.; Giannetti, A.; Urquhart, J. S.; Csengeri, T., Casu, S.; Cunningham, M.; Elia, D., Jones; P. A., **König, C.**; Molinari, S.; Testi, L.; Stanke, T.; Wyrowski, F.; Menten, K. M.: "*Characterizing the high-mass star forming filament G351.776−0.527 with Herschel and APEX dust continuum and gas observations*", 2018, A&A, submitted

König, C.; Urquhart, J.S.; Wyrowski, F.; Giannetti, A.; Colombo, D.; et al.: "*A New Search for Star Forming Regions in the Outer Galaxy*", in prep.